A COMPLEMENTARY STUDY OF PEROVSKITES : COMBINING DIFFRACTION, SOLID-STATE NMR AND FIRST-PRINCIPLES DFT CALCULATIONS

Karen Elizabeth Johnston

A Thesis Submitted for the Degree of PhD
at the
University of St Andrews

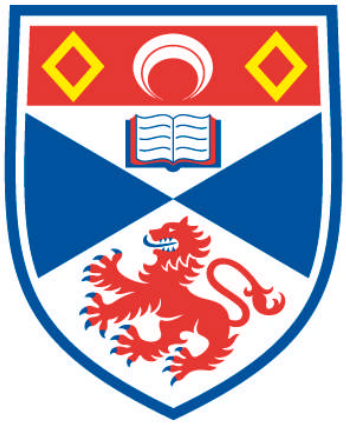

2010

A Complementary Study of Perovskites: Combining Diffraction, Solid-State NMR and First-Principles DFT Calculations

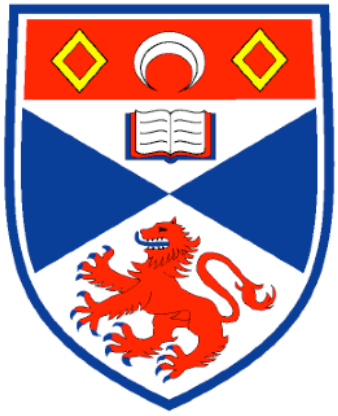

University
of
St Andrews

A thesis presented for the degree of

Doctor of Philosophy

in the Faculty of Science of the University of St Andrews

by Karen Elizabeth Johnston, BSc (Hons), AMRSC

July 2010

Declaration

I, Karen Elizabeth Johnston, herby certify that this thesis, which is approximately 63,000 words in length, has been written by me, that it is the record of work carried out by me and that it has not been submitted in any previous application for a higher degree.

I was submitted as a research student in September, 2006 and as a candidate for the degree of PhD in September, 2007; the higher study for which this is a record was carried out in the University of St Andrews between 2006 and 2010.

Date …… Signature of Candidate ……

I hereby certify that the candidate has fulfilled the conditions of the Resolution and Regulations appropriate for the degree of PhD in the University of St Andrews and that the candidate is qualified to submit this thesis in application for that degree.

Date …… Signature of Supervisor ……

Signature of Supervisor ……

In submitting this thesis to the University of St Andrews I understand that I am giving permission for it to be made available for use in accordance with the regulations of the University Library for the time being in force, subject to any copyright vested in the work not being affected thereby. I also understand that the title and the abstract will be published, and that a copy of the work may be made and supplied to any bona fide library or research worker, that my thesis will be electronically accessible for personal or research use unless exempt by award of an embargo as requested below, and that the library has the right to migrate my thesis into new electronic forms as required to ensure continued access to the thesis. I have obtained any third-party copyright permissions that may be

required in order to allow such access and migration, or have requested the appropriate embargo below.

The following is an agreed request by candidate and supervisor regarding the electronic publication of this thesis:

Embargo on both printed copy and electronic copy for the same fixed period of two years on the following ground: publication would preclude future publication.

Date …… Signature of Candidate ……

Signature of Supervisor …….

Signature of Supervisor …….

Abstract

Perovskites, ABX_3, and their associated solid-solutions are a particularly important and attractive area of research within materials chemistry. Owing to their structural and compositional flexibility and potential physical properties they are one of the largest classes of materials currently under investigation. This thesis is concerned with the synthesis and structural characterisation of several perovskite-based materials using a combined approach of high-resolution synchrotron X-ray and neutron powder diffraction (NPD), solid-state Nuclear Magnetic Resonance (NMR) and first-principles Density Functional Theory (DFT) calculations.

Initial investigations concentrated on room temperature $NaNbO_3$, a perovskite widely debated in the literatue. Published crystallographic data indicate $NaNbO_3$ possesses two crystallographically distinct Na sites in space group Pbcm. Whilst some of our materials appear in agreement with this (notably a commercially purchased sample) many of our laboratory-synthesised samples of $NaNbO_3$ routinely comprise of two phases, which we show to be the antiferroelectric Pbcm and polar $P2_1ma$ polymorphs. Several different synthetic methods were utilised during this investigation and the quantity of each phase present was found to vary as a function of preparative method. ^{23}Na, ^{93}Nb and ^{17}O DFT calculations were used in conjunction with experiment to aid in spectral analysis, assignment and interpretation. In addition, *ab initio* random structure searching (AIRSS) was utilised in an attempt to predict the most stable phases of $NaNbO_3$. This proved to be both successful and highly informative.

A series of $NaNbO_3$-related solid-solutions, namely $K_xNa_{1-x}NbO_3$ (KNN), $Li_xNa_{1-x}NbO_3$ (LNN) and $Na_{1-x}Sr_{x/2}\square_{x/2}NbO_3$ (SNN) have also been synthesised and characterised. The substitution of K^+, Li^+ and Sr^{2+} cations onto the A site appears to produce the same polar $P2_1ma$ phase initially identified in the room temperature $NaNbO_3$ investigation. The abrupt change in cation size in the KNN and LNN series, and the introduction of vacancies in the SNN series, is thought to result in a structural distortion which, in turn, causes the formation of the $P2_1ma$ phase.

A low temperature synchrotron X-ray powder diffraction study (12 < T < 295 K) was completed for a sample of $NaNbO_3$ composed of the $P2_1ma$ polymorph (~90%) and a small quantity of the Pbcm phase (~10%). A region of phase coexistence was identified between the $P2_1ma$, R3c and Pbcm phases over a relatively large temperature range. Full conversion of the $P2_1ma$ phase to the low temperature R3c phase was not possible and, consistently, the $P2_1ma$ phase was the most abundant phase present. Factors such as structural, strain, crystallite size and morphology are thought to be crucial in determining the exact phases of $NaNbO_3$ produced, both at low and room temperature.

The solid-solution $La_{1-x}Y_xScO_3$ was also investigated. Compositions x = 0, 0.2, 0.4, 0.6, 0.8 and 1 were successfully synthesised and characterised. Refined high-resolution NPD data indicates that an orthorhombic structure, in space group Pbnm, was retained throughout the solid-solution. Using ^{45}Sc and ^{89}Y MAS NMR each sample was found to exhibit disorder, believed to result from both a distribution of quadrupole and chemical shifts. NMR parameters were calculated for several model Sc and Y compounds using DFT methods to determine the feasibility and accuracy of ^{45}Sc and ^{89}Y DFT calculations. These proved successful and subsequent calculations were completed for the end members $LaScO_3$ and $YScO_3$. DFT calculations were also utilised to gain insight into the disorder exhibited in the $La_{1-x}Y_xScO_3$ solid-solution.

Acknowledgements

Firstly, and most importantly, I would like to thank my supervisors, Professor Philip Lightfoot and Dr Sharon Ashbrook, for giving me the opportunity to complete this research. To Phil, thank you for the many interesting and thought-provoking discussions over the last few years! To Sharon, thank you for being not only an excellent supervisor but also a friend and mentor. Your constant support, guidance and enthusiasm towards this research has been a significant factor towards the overall success of this project.

Much of the work completed within this thesis would not have been possible without the excellent assistance and guidance of various beamline scientists and facility managers. Special thanks to Professor Kevin Knight at HRPD for experimental assistance and useful discussion regarding the work completed on $NaNbO_3$. Many thanks also to Dr Ron Smith at POLARIS, Dr Chiu Tang, Dr Julia Parker and Dr Alistair Lennie at beamline I11, Diamond and Dr Dinu Igua at the 850 MHz Solid-State NMR Facility, Warwick. A special thank you to Professor Stephen Wimperis at the University of Glasgow for use of his spectrometer. Thank you to Dr Herbert Fruchtl, Dr Manfred Buck and Mr Ross Blackley for computational and experimental assistance at the University of St Andrews.

Several areas of this research were completed in collaboration with external researchers. Therefore, I would like to thank Professor Chris Pickard and Dr Maria Baias for their structure searching work using AIRSS. I would also like to thank Professor Clare Grey and Dr Frédéric Blanc for their experimental assistance with isotopic enrichment of several of our samples. Each of their contributions to this project are greatly appreciated. I would also like to thank Pierre-Yves Calvez and Charlotte Cree for their contributions to this work.

Many thanks go to both the past and present Lightfoot and Ashbrook group members for making each day in the lab more enjoyable; in particular to Dr John Griffin for his excellent experimental advice and constant supply of funny moments, to Dr Thushitha Mahenthirarajah, Alexandra Gibbs and Sandra Reisinger thank you for experimental

assistance during data collection and, most importantly, the supply of gingerbread men during the writing of this thesis, to Martin Mitchell and Stephanie Moore thank you for the many entertaining moments that have kept me going over the last few months! Very special thanks to Dr Dave Aldous for his invaluable help and advice in all things solid-state over the last five years. I would also like to thank my friends both in and out of the chemistry department, in particular Emma Whitelaw, Jason Gillespie and Andy Young for their support.

An unreserved thank you goes to my parents, Robert and Hilda. You have supported me through the many high and low points over the last few years and for that I am indebted to you both. Thank you for your constant belief and encouragement. To my sister Pamela, thank you for keeping 'morale' high and bringing a smile to my face even through the toughest of times. Finally, to Charlie, your constant encouragement has helped to keep me going during the most difficult stages of this work. Thank you for the many happy and funny moments we have shared over the last few years!

Contents

Abstract i
Acknowledgements iii
Contents v
List of Symbols and Abbreviations xi
Publications xvi

1 Background and Introduction 1

1.1 Perovskites 1
1.2 Perovskite Distortions 1
1.3 Glazer Notation 4
1.4 Cation Substitutions 8
1.5 Cation Ordering 10
1.5.1 A Site Ordering 10
1.5.2 B Site Ordering 13
1.5.3 Simultaneous A and B Site Ordering 16
1.6 Layered Perovskites 17
1.6.1 Aurivillius Phases 18
1.6.2 Ruddlesden-Popper Phases 18
1.6.3 Dion-Jacobson Phases 20
1.6.4 Brownmillerites 21
1.7 Physical Properties 22
1.7.1 Piezoelectricity 22
1.7.2 Pyroelectricity 22
1.7.3 Ferroelectricity 23
1.7.4 Applications of Perovskites 25
1.8 A Multidisciplinary Approach 25
1.9 Thesis Overview 27

2 Experimental Techniques

2.1 Crystal Symmetry 29

2.1.1 Crystal Systems and Lattices 29
2.1.2 Point Groups and Space Groups 29
2.1.3 Miller Planes 32
2.1.4 The Reciprocal Lattice 33
2.2 Diffraction Techniques 34
2.2.1 X-rays 34
2.2.2 Generation of X-rays 34
2.2.3 X-ray Scattering and Powder Diffraction 36
2.2.4 Conventional X-ray Diffraction 38
2.2.5 Generation of Synchrotron X-rays 38
2.2.6 Synchrotron X-ray Diffraction 41
2.2.7 Neutron Diffraction 41
2.2.8 Generation of Neutrons 42
2.2.9 POLARIS 44
2.2.10 High Resolution Powder Diffractometer (HRPD) 44
2.2.11 Comparison of Diffraction Techniques 45
2.3 Rietveld Analysis 46
2.4 Basic Principles of NMR 49
2.4.1 Nuclear Magnetism 49
2.4.2 The Vector Model 50
2.4.3 Relaxation 52
2.4.4 Fourier Transformation 53
2.4.5 Density Operator Formalism 54
2.4.6 Coherence 55
2.5 NMR Interactions 56
2.5.1 Chemical Shift Anisotropy (CSA) 58
2.5.2 Dipolar Coupling 61
2.5.3 Scalar Couplings 64
2.6 Magic-Angle Spinning 65
2.7 Dipoar Decoupling 67
2.8 Quadrupolar Interactions 69
2.8.1 Introduction 69
2.8.2 First-Order Quadrupolar Interactions 70
2.8.3 Removal of First-Order Effects 72

2.8.4 Second-Order Quadrupolar Interactions 73
2.8.5 Removal of Second-Order Quadrupolar Broadening 76
2.8.6 Double Rotation (DOR) 77
2.9 Multiple-Quantum Magic-Angle Spinning (MQMAS) 78
2.9.1 Introduction 78
2.9.2 The MQMAS Experiment 79
2.9.3 Higher-Order MQMAS 87
2.9.4 Extraction of NMR Parameters 88
2.9.5 MQMAS and Disorder 92
2.10 Density Functional Theory (DFT) Calculations 98
2.10.1 Introduction 98
2.10.2 First-Principles Calculations 99
2.10.3 Solving the Schrödinger Equation 101
2.10.4 The Born-Oppenheimer Approximation 101
2.10.5 Density Functional Theory (DFT) 102
2.10.6 Planewaves and Pseudopotentials 103
2.11 CASTEP 107
2.11.1 Convergence Studies 107
2.11.2 Structural Optimisation 108
2.11.3 Computational Methods 118

3 The Polar Phase of $NaNbO_3$: A Combined Study 121

3.1 Introduction 121
3.2 Experimental 124
3.2.1 Synthesis 124
3.2.2 X-ray and Neutron Powder Diffraction 125
3.2.3 NMR Spectroscopy 126
3.2.4 Calculations 127
3.2.5 Second Harmonic Generation (SHG) 128
3.2.6 Scanning Electron Microscopy (SEM) 128
3.3 Experimental Results 128
3.3.1 Commercial Sample 128

3.3.2 Solid-State Preparation 131
3.3.3 Molten Salt Preparation 152
3.3.4 Sol-Gel Preparation 161
3.3.5 ^{93}Nb MAS NMR 173
3.3.6 Static ^{93}Nb NMR Spectra 178
3.3.7 ^{17}O Enrichment of $NaNbO_3$ 184
3.4 DFT Calculations 189
3.5 Discussion 197
3.6 Prediction of Perovskites using *Ab Initio* Random Structure Searching (AIRSS) 207
3.6.1 Introduction to AIRSS 207
3.6.2 AIRSS Computational Details 208
3.6.3 Structure Searching $NaNbO_3$ 208
3.7 A Third Polymorph? 213
3.8 Conclusions 216

4 Synthesis and Characterisation of $NaNbO_3$-based Solid-Solutions 219

4.1 Introduction 219
4.2 Experimental 223
4.2.1 Synthesis 223
4.2.2 X-ray and Neutron Powder Diffraction 223
4.2.3 NMR Spectroscopy 223
4.3 Results and Discussion 224
4.3.1 Low Percentage K Doping 224
4.3.1.1 $K_{0.01}Na_{0.99}NbO_3$ 224
4.3.1.2 Higher Percentage Doping ($0.02 \leq x \leq 0.05$) 236
4.3.2 Low Percentage Li Doping ($Li_xNa_{1-x}NbO_3$) 253
4.3.3 The $Na_{1-x}Sr_{x/2}\square_{x/2}NbO_3$ Solid-Solution 280
4.4 Discussion 292
4.5 Conclusions 293

5 A Low Temperature s-PXRD Study of $NaNbO_3$ 295

5.1 Introduction 295
5.2 Experimental 297
5.2.1 Synthesis 297
5.2.2 High-Resolution X-ray Diffraction 298
5.3 Results and Discussion 298
5.4 Conclusions 320

6 The Synthesis and Characterisation of $La_{1-x}Y_xScO_3$ 325

6.1 Introduction 325
6.2 Experimental 328
6.2.1 Synthesis 328
6.2.2 X-ray and Neutron Powder Diffraction 329
6.2.3 NMR Spectroscopy 329
6.2.4 Scandium Referencing 330
6.2.5 Calculations 332
6.3 Results and Discussion 333
6.3.1 $LaScO_3$ 333
6.3.2 $YScO_3$ 341
6.3.3 $La_{1-x}Y_xScO_3$ 347
6.3.3.1 Neutron Diffraction Analysis 347
6.3.3.2 ^{45}Sc MAS NMR Analysis 358
6.3.3.3 ^{89}Y NMR Analysis 365
6.3.4 ^{17}O Enrichment of $LaScO_3$ 370
6.3.5 Density Functional Theory (DFT) Calculations 374
6.3.5.1 $LaScO_3$ and $YScO_3$ 374
6.3.5.2 Gaining Insight into Disorder using DFT 380
6.4 Conclusions 389

7 Conclusions and Future Work 391

7.1 Conclusions 391
7.2 Future Work 394

References 397

Appendices (see attached CD)

I
II
III
IV
V

List of Symbols and Abbreviations

□	Vacancy
2θ	Angle between X-ray source and detector
Å	Angstrom, 1×10^{-10} m
B_0	Magnetic field strength
B_1	Strength of applied pulse
B_0^{eff}	Effective static magnetic field
C_Q	Quadrupolar coupling constant
d	Parameter describing the distortion of the octahedra in a rhombohedral perovskite
d_{hkl}	Interplanar d-spacing
eV	Electron volts
E_C	Coercive field
E_{cut}	Cut-off energy
f	Scattering factor or form factor of an atom
f.u.	Formula units
$\hat{H}$	Hamiltonian
I	Intrinsic spin angular momentum
I	Spin quantum number
J	Isotropic J-coupling or scalar coupling
m_I	Magnetic spin quantum number
$\mathbf{M_0}$	Bulk magnetization vector
M	Metal cation
n_A	Number of electrons in the outer electron shells of the A atom
N_A	Principal quantum number of the A atom
ppm	Parts per million
P	Polarisation
P_R	Remnant polarisation
P_S	Saturation polarisation
P_Q	Quadrupolar product
r	Ionic radius
r_C	Core radius

R_p	R-profile
Ry	Rygbergs
s	Orthorhombic strain
sc	Parameter describing the displacement of the A-site cation from its ideal position
S_y	Structural refinement residual
t	Goldschmidt tolerance factor
tc	Parameter describing the displacement of the B-site cation from its ideal position
T_1	Longitudinal or spin-lattice relaxation
T_2	Transverse of spin-spin relaxation
T_C	Curie temperature
$\mathbf{V}$	EFG tensor
wR_p	R-weighted profile
y_{oi}	Observed intensity
y_{ci}	Calculated intensity
γ	Gyromagnetic ratio
δ	Deshielding parameter
δ_{iso}	Isotropic chemical shift
δ_Q	Isotropic quadrupolar shift
$\Delta\alpha$	Difference in polarisabilities of the B and B′ cations
$\Delta\sigma_{cs}$	Shielding anisotropy
$\Delta\nu_{1/2}$	Difference in linewidth
$d^1_{mm'}(\alpha)$	Wigner induced rotation matrix element
η_{CS}	Asymmetry parameter of the shielding interaction
η_Q	Asymmetry parameter of the quadrupolar interaction
λ	Wavelength
$\boldsymbol{\sigma}$	Shielding second-rank tensor
σ	Stress
σ_{iso}	Isotropic shielding
$\sigma(t)$	Density operator
$\sigma_{i,j}(t)$	Elements of the density matrix
χ^2	Parameter measuring the goodness of fit

$\Psi(t)$	Wavefunction
ω	Oxygen octahedral rotation angle
ω_0	Larmor frequency (in rad s^{-1})
ω_D^{PAS}	Dipolar splitting parameter in the PAS
ω_Q^{PAS}	Quadrupolar splitting parameter in the PAS
Ω	Offset frequency
ABX_3	General formula for a ternary perovskite where A is the larger cation occupying the 12-coordinate site, B is the smaller cation occupying the 6-fold coordinate site and X is the anion, commonly oxygen
$A_2BB'X_6$	General formula for a double perovskite where B and B′ are the 6-fold coordinate site
$A_3B_2B'X_{12}$	General formula for a 2:1 ordered perovskite
$A_4B_3B'X_{12}$	General formula for 3:1 ordered perovskite
AIRSS	*Ab Initio* Random Structure Searching
$[A_{n-1}BnO_{3n+1}]^{2-}$	General formula for Aurivillius phases
$A'[A_{n-1}B_nO_{3n+1}]$	General formula for Dion-Jacobson phases
APS	Argonne Advanced Photon Source
CMR	Colossal magnetoresistance
CSA	Chemical Shift Anisotropy
CW	Continous wave
$dist_{CS}$	Distribution of chemical shift environments
$dist_Q$	Distribution of quadrupolar contributions
DAS	Dynamic-Angle Spinning
DFT	Density Functionl Theory
DOR	Double rotation
EDX	Energy Dispersive X-ray Spectroscopy
EFG	Electric Field Gradient
ESRF	European Synchrotron Radiation Faciltity
FAM	Fast Amplitude Modulation
FID	Free Induction Decay
FT	Fourier transform
GIPAW	Gauge-Including Projector Augmented Wave

GGA	General Gradient Approximation
GSAS	General Structure Analysis System
hkl	Miller indices
HRPD	High Resolution Powder Diffractometer
ICSD	Inorganic Crystal Structure Database
ILL	Institute Laue-Langevin
KNN	Potassium sodium niobate ($K_xNa_{1-x}NbO_3$)
l-PXRD	Laboratory Powder X-ray Diffraction
LDA	Local Density Approximation
LNN	Lithium sodium niobate ($Li_xNa_{1-x}NbO_3$)
$M_2[A_{n-1}B_nO_{3n+1}]$	General formual for Ruddlesden-Popper phases
MACs	Multi-analysing crystal detectors
MAS	Magic-Angle Spinning
MPB	Morphotropic Phase Boundary
MQMAS	Multiple-Quantum Magic-Angle Spinning
NLO	Nonlinear optic
NMR	Nuclear Magnetic Resonance
NPD	Neutron Powder Diffraction
PAS	Principle Axis System
PAW	Projector Augmented Wave
PBE	Perdew-Burke-Ernzerhof
PFM	Piezoelectric Force Microscopy
POTATO	Program Originated To Analyse Tilted Octahedra
PZT	Lead zirconium titanate
rf	Radiofrequency radiation
s-PXRD	Synchrotron Powder X-ray Diffraction
SEM	Scanning Electron Microscopy
SHG	Second Harmonic Generation
SNN	Strontium sodium niobate ($Na_{1-x}Sr_{x/2}\square_{x/2}NbO_3$)
SOLA	Solids Line Shapes Analysis program
SPAM	Soft Pulse Added Mixing
SSZ	Scandia-stabilised zirconia
TEM	Transmission Electron Microscopy
TOF	Time-of-Flight

TPPM	Two Pulse Phase Modulation decoupling
TTB	Tetragonal Tungsten Bronze
XRD	X-ray diffraction

Publications

K. E. Johnston, C. C. Tang, J. E. Parker, K. S. Knight, P. Lightfoot and S. E. Ashbrook, *J. Am. Chem. Soc.*, 2010, **132**, 8732.

S. W. Reader, M. R. Mitchell, K. E. Johnston, C. J. Pickard, K. R. Whittle and S. E. Ashbrook, *J. Phys. Chem. C*, 2009, **113**, 18874.

P. S. Berdonosov, D. O. Charkin, K. S. Knight, K. E. Johnston, R. J. Goff, V. A. Dolgikh and P. Lightfoot, *J. Solid State Chem.*, 2006, **179**, 3437.

Chapter 1
Background and Introduction

1.1 Perovskites

Perovskite, $CaTiO_3$, was initially discovered in the Ural Mountains of Russia by Gustav Rose in 1839 and named after the Russian mineralogist L. A. Perovski (1792 – 1865).[1] Since its discovery the name perovskite has been utilised to describe hundreds of materials with stoichiometry ABX_3. Perovskites are three-dimensional framework structures, constructed of corner-sharing BX_6 octahedra. The A-site cation, conventionally the larger of the two metal ions, is commonly either a rare earth or alkali earth metal. The smaller B-site cation, typically a transition metal, is surrounded by the anions X, usually O^{2-}, forming BO_6 octahedra. 'Ideal' perovskite is cubic, as shown in Figure 1.1. The A-site cations (green) are located on each corner of the cube, whilst the B-site cations (blue) are placed in the centre of the cube with the anions (red) positioned at the centre of each of the cube faces. Ideal coordination geometries for the A- and B-site cations are 12 and 6 fold respectively. A cubic close packed array is conventionally formed between the A-site cations and anions, whilst the B-site cation is positioned in 1/4 of the octahedral holes formed between the two. The size of A is vital in enabling such a close packed arrangement to occur.

1.2 Perovskite Distortions

In reality, compounds adopting the perovskite structure are often of lower symmetry owing to distortion or, more commonly, tilting of the octahedra. As a direct consequence there are considerably more distorted perovskites known than there are cubic.[2] Octahedral tilting is considered an intrinsic property of perovkites and is a direct consequence of the relative sizes and charge of both the A- and B-site cations situated within the structure. The mechanism and degree of such tilting plays a

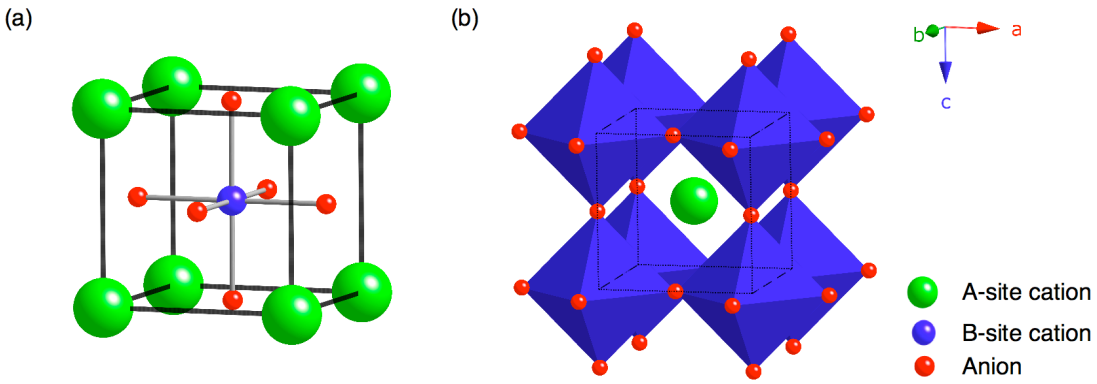

Figure 1.1: Cubic perovskite, $CaTiO_3$, with the origin centred on (a) the B-site cation and (b) the A-site cation.

significant role in the symmetry adopted by a structure. The level of distortion or strain imposed upon a structure is commonly measured using a parameter known as the tolerance factor, t, first introduced by Goldschmidt,[3]

$$t = \frac{r_A + r_X}{\sqrt{2}(r_B + r_X)}, \qquad (1.1)$$

where r_A, r_B and r_X are the ionic radii of A, B and X respectively.[4,5] When t is close to unity the degree of distortion observed is low. Large deviations from unity however result in increasing levels of strain upon the perovskite structure, commonly imposed by inappropriately sized ions for their allocated site, i.e., either too large or too small. In order to relieve such strain from the structure the BX_6 octahedra undergo some degree of rotation, accompanied by a corresponding shift of the A-site cation. When $0.85 < t < 1.06$ a perovskite structure, or suitably distorted version, will be adopted. In addition, when using the Shannon and Prewitt radii[K5] for $0.9 < t < 1.0$ the structure is often cubic and therefore more like an ideal structure. Values outside this range indicate the perovskite structure cannot meet the coordination requirements of the two chosen cations, hence a different structural arrangement is required. This is often the case when A and B cations of similar size are used.

The perovskite structure is routinely modified, either by cation displacements, tilting or distortion of the octahedra or, more commonly, a

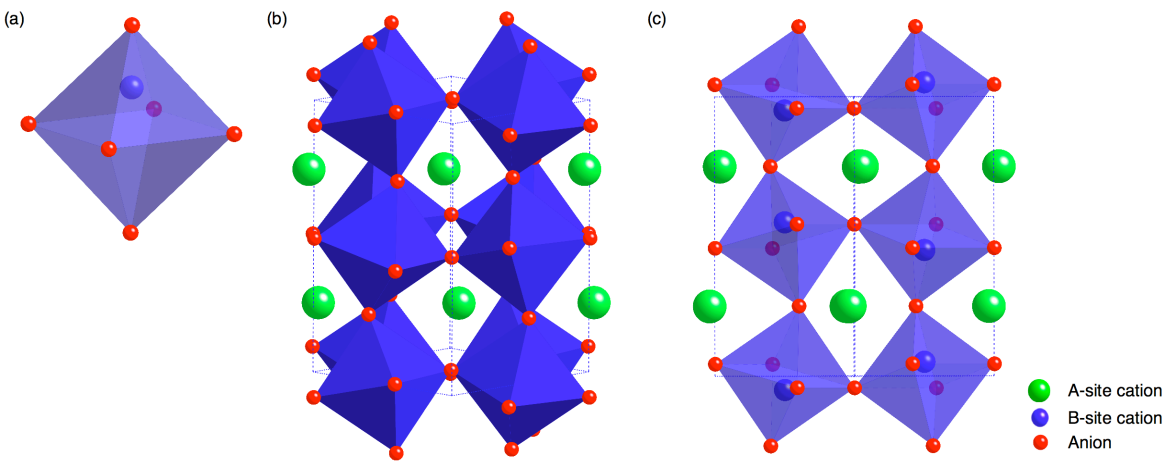

Figure 1.2: (a) A schematic representation of an exaggerated B-site cation displacement, (b) an example of octahderal tilting in perovskites and (c) a perovskite exhibiting both a B-site cation displacement and octahedral tilting.

combination of the two, as illustrated in Figure 1.2. Cation displacements are small shifts of the A- and/or B-site cations from their ideal positions. B site displacements are more common and are often directly related to the physical properties exhibited by a material, for example the ferroelectric displacement of the Ti^{4+} cation in $BaTiO_3$.[6,7] A schematic representation of an exaggerated B-site cation displacement is shown in Figure 1.2(a). Such displacements commonly give rise only to very slight distortions of the octahedra, hence they are relatively simple to deal with and have very little effect on the lattice parameters of a structure. Tilting of the octahedra (Figure 1.2(b)) have a considerably greater effect on the lattice parameters and are, in effect, more difficult to accurately describe. Numerous papers within the literature have attempted to depict methods for describing and illustrating how the various tilting mechanisms operate and, in turn, how they may be classified. Extensive work has been completed in this area by Megaw,[8] Darlington,[8] O'Keeffe and Hyde,[9] Thomas,[10-12] Zhou and Goodenough,[13] Howard and Stokes.[14,15] To date, however, Glazer[16] has provided the most exhaustive and comprehensive study of octahedral tilting mechanisms and, in turn, developed an accurate and detailed notation for describing the most commonly encountered tilts. The notation established by Glazer is by far the most influential and has, in turn, become the standard notation adopted within

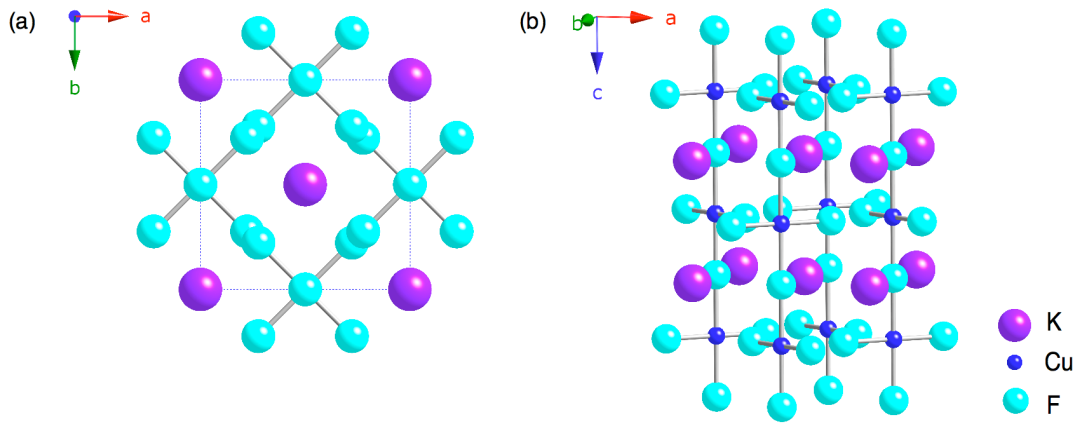

Figure 1.3: The crystal structure of $KCuF_3$ viewed (a) along c and (b) across the ab plane.

the perovskite literature. Octahedral distortions are commonly caused by electronic instabilities of the enclosed metal ion.[17] In particular, perovskites containing Jahn-Teller ions such as Cu^{2+} and Mn^{3+} routinely exhibit cooperative Jahn-Teller distortions, for example $KCuF_3$[17] shown in Figure 1.3. As a result they also commonly display many interesting physical properties such as charge and spin ordering.[18]

1.3 Glazer Notation

Octahedral tilting is commonly observed when the A-site cation is too small to fully occupy the 12 coordinate site. Under such circumstances the BO_6 octahedra are forced to tilt or rotate in order to accommodate its size. An associated effect of such tilting is greater flexibility in the coordination of the A-site cation (8 – 12) whilst leaving the B site environment essentially unchanged. Glazer[16] recognised that cooperative rotations give rise to as many as 23 different tilting mechanisms. The work presented within his original paper concentrated solely on the tilting systems adopted, with no discussion regarding cation displacements and/or octahedral distortions. The tilting mechanism adopted within a structure is extremely important as the overall symmetry follows that of the tilts.

Table 1.1: Glazer notation and initial space group allocation by Glazer. The two possible space group ambiguities, for tilts $a^+a^+c^-$ and $a^+a^+a^-$, are denoted by *.

	Tilt System Number	Tilt System Symbol	Space Group
Three-tilt systems	1	$a^+b^+c^+$	Immm
	2	$a^+b^+b^+$	Immm
	3	$a^+a^+a^+$	$Im\bar{3}$
	4	$a^+b^+c^-$	Pmmn*
	5	$a^+a^+c^-$	Pmmn
	6	$a^+b^+b^-$	Pmmn
	7	$a^+a^+a^-$	Pmmn*
	8	$a^+b^-c^-$	$A2_1/m11$
	9	$a^+a^-c^-$	$A2_1/m11$
	10	$a^+b^-b^-$	Pnma
	11	$a^+a^-a^-$	Pnma
	12	$a^-b^-c^-$	$F\bar{1}$
	13	$a^-b^-b^-$	I2/a
	14	$a^-a^-a^-$	$R\bar{3}c$
Two-tilt systems	15	$a^0b^+c^+$	Immm
	16	$a^0b^+b^+$	I4/m
	17	$a^0b^+c^-$	Bmmb
	18	$a^0b^+b^-$	Bmmb
	19	$a^0b^-c^-$	F2/m11
	20	$a^0b^-b^-$	Imcm
One-tilt systems	21	$a^0a^0c^+$	C4/mmb
	22	$a^0a^0c^-$	F4/mmc
Zero-tilt systems	23	$a^0a^0a^0$	$Pm\bar{3}m$

Fundamentally Glazer's work was based on the sole assumption that octahedra are rigid and regular and, when tilted, they produce a considerable effect on neighbouring octahedra. Glazer realised the complexity in trying to visualise and describe the effects on successive octahedra and therefore his initial work concentrated on understanding feasible tilting modes for individual octahedra. Glazer's notation provides

an accurate and effective method for comparing the various tilts exhibited by different structures. The notation, $a^{\pm}b^{\pm}c^{\pm}$, describes a tilting mechanism by specifying rotations of the octahedra about the three Cartesian axes. Each rotation is described by two parameters, a letter and a superscript. The letter indicates the magnitude of the rotation about that axis relative to the magnitude of all other rotations about the other Cartesian axes whilst the superscript denotes whether rotations in adjacent layers are in or out-of-phase. A positive superscript indicates adjacent octahedra tilt in the same direction, negative values indicate they rotate in opposite directions. Repetition of a letter represents equal tilts along different rotation axes. A simple example is 'ideal' perovskite (cubic) in which no tilts are observed, resulting in the notation $a^0a^0a^0$. The tilt $a^+b^-b^-$ indicates the rotation about the x axis to be different to that about the y and z axes. Similarly, the superscript indicates that rotations of two neighbouring octahedra along the x axis are in the same direction, whilst neighbouring octahedra along the y and z axes rotate in opposite directions. All 23 Glazer systems are listed in Table 1.1 and classified according to the number of tilts exhibited.

In addition to the notation Glazer also assigned space groups (see Chapter 2, section 2.1.2) to each tilt system identified. All space group allocations can also be found in Table 1.1. Interestingly, however, in recent years it has been suggested that Glazer was incorrect in his initial space group assignment for certain tilt systems, in particular $a^+a^+c^-$ and $a^+a^+a^-$.[19] Leinenweber and Parise completed an extensive structural investigation for the perovskite $CaFeTi_2O_6$ and within this study they concluded that the tilt exhibited, $a^+a^+c^-$, was incorrectly assigned by Glazer to space group Pmmn. Their findings suggested space group $P4_2/nmc$ to be a more accurate description of the observed tilt.

The two one-tilt systems $a^0a^0c^+$ and $a^0a^0c^-$ are shown in Figures 1.4(a) and (b) respectively. When two neighbouring octahedra rotate in the same direction they are in-phase with one another resulting in the tilt $a^0a^0c^+$ (Figure 1.4(a)). If, however, the two rotate in opposite directions they become out-of-phase, resulting in the tilt illustrated in Figure 1.4(b). When viewed along the c-axis these simple one-tilt systems provide a

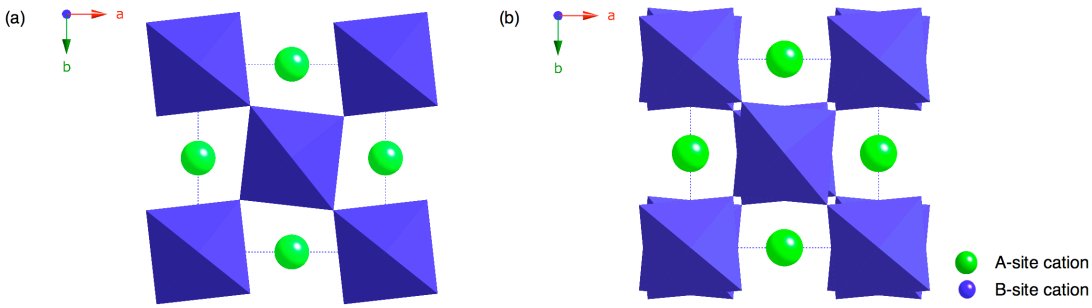

Figure 1.4: Examples of the one-tilt Glazer systems (a) $a^0a^0a^+$ and (b) $a^0a^0c^-$.

convenient way of visualising Glazer notation. In reality, however, systems routinely adopt more than one tilt hence visualisation becomes increasingly difficult. The most commonly encountered tilt system is $a^-a^-b^+$, displaying three different tilts resulting in an orthorhombic distortion, commonly associated with $GdFeO_3$ (Figure 1.5). Interestingly, this mechanism is also adopted by naturally occurring perovskite, $CaTiO_3$, thereby making it orthorhombic as opposed to the ideal 'cubic' structure.

By careful consideration of the interatomic distances between the octahedra centres Glazer's work extended to include a relation between the tilting mechanism observed and the symmetry adopted within a particular system, details of which can be found in his original publication.[16] Unfortunately, Glazer did not expand this information into detailed structural models complete with atomic coordinates for each of the systems described. In 1997 Woodward[20,21] completed an extensive review of Glazer's work and attempted to translate his original classifications into complete structural models by developing a FORTRAN program known as POTATO (Program Originated To Analyse Tilted Octahedra). Using the Glazer symbol, rotation angle about each of the Cartesian axes and the metal to oxygen bond lengths as input POTATO was capable of outputting a unit cell description of the compound, complete with atomic coordinates. This was successfully undertaken for many of the tilt systems originally proposed by Glazer.

Woodward's investigation did, however, highlight several areas of discrepancy. Using POTATO, six tilt systems posed considerable problems when calculating appropriate space groups and structural

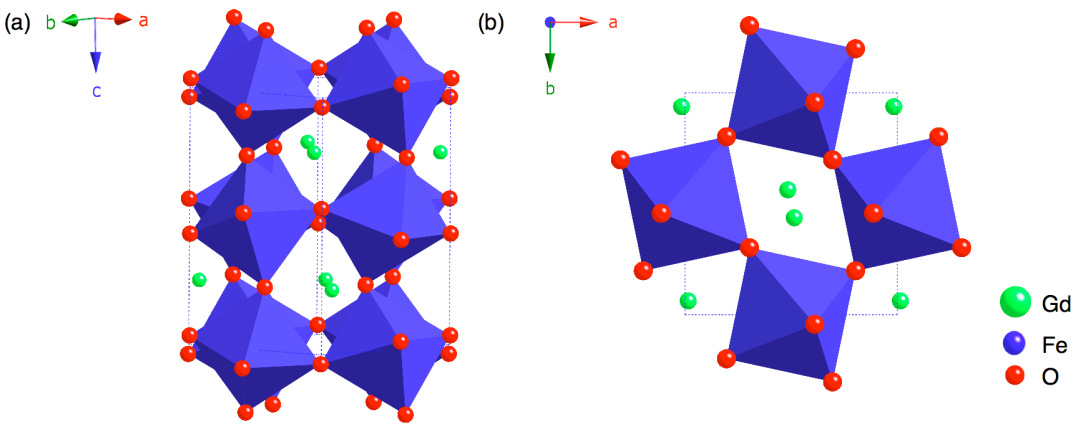

Figure 1.5: The crystal structure of $GdFeO_3$ displaying the most commonly encountered Glazer tilt, $a^-a^-b^+$, as viewed (a) across the ab plane and (b) down the c axis.

models, namely $a^+b^+c^-$, $a^+a^+c^-$, $a^+b^+b^-$, $a^+a^+a^-$, $a^0b^+c^-$ and $a^0b^+b^-$. Interestingly, the two tilts reported in the literature as being wrongly assigned by Glazer were amongst these six. Woodward suggested such discrepancies existed owing to octahedral distortions being an inherent geometric property of tilt systems and that slight distortions of the octahedra were always necessary to retain the overall connectivity of the octahedra. In turn for such structures it is extremely challenging to uniquely define a space group as the symmetry adopted by the unit cell depends upon the initial distortion of the octahedra. Woodward therefore concluded that it was not possible to rigorously assign space groups for the six problematic crystal systems and, in reality, compounds adopting such tilting mechanisms would favour the most symmetric configuration and space group. Therefore, the original space group assignment by Glazer for the tilts $a^+a^+c^-$ and $a^+a^+a^-$ was not necessarily incorrect, but rather extremely difficult to accurately and precisely assign.

1.4 Cation Substitutions

Since the discovery of $BaTiO_3$, perovskites have been a subject of significant interest and are studied extensively for their interesting and useful physical properties. They are currently one of the most heavily researched fields within solid-state chemistry.

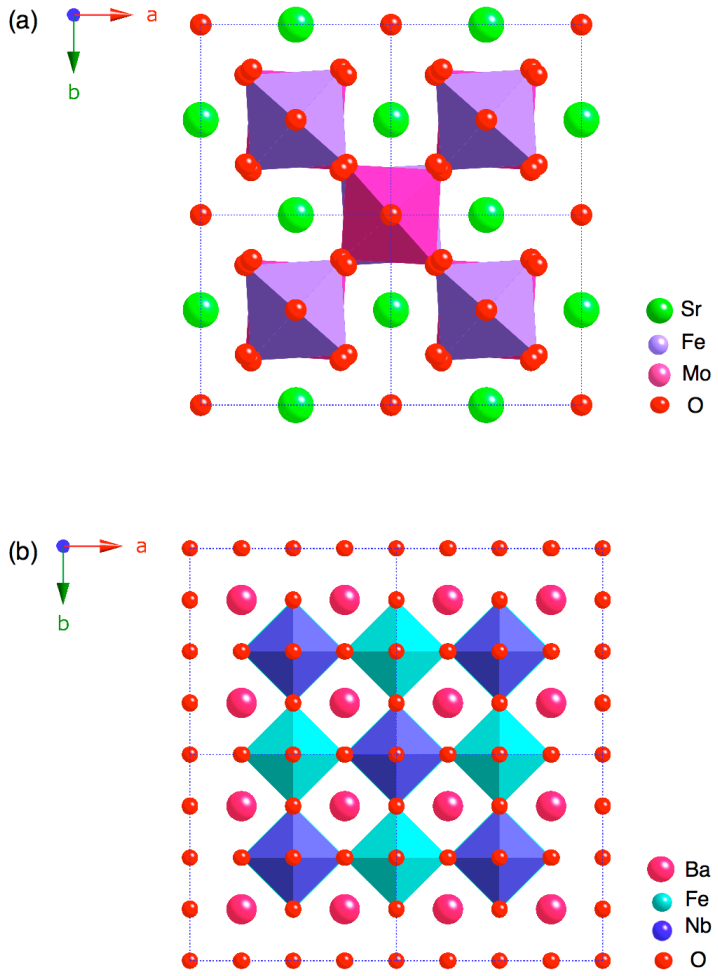

Figure 1.6: Two examples of double perovskites, $A_2BB'X_6$. In (a) Sr_2FeMoO_6 and (b) Ba_2FeNbO_6.

Perovskites are renowned for their compositional flexibility and ease of distortion, and hence the perovskite family is routinely extended by cation substitutions at either the A or B sites, leading to the formation of many useful solid-solutions; $A_{1-x}A'_xBX_3$ and $AB_{1-x}B'_xX_3$. When x = 0.5 perovskites of this nature are generally written as $AA'B_2X_6$ and $A_2BB'X_6$, commonly known as double or double-edge perovskites, two examples of which, namely Sr_2FeMoO_6 and Ba_2FeNbO_6, are shown in Figures 1.6(a) and (b) respectively.[22,23] By careful consideration of parameters such as the tolerance factor it is often possible to 'tune' solid-solutions to exhibit very specific physical properties such as ferroelectricity, piezoelectricity, superconductivity and ionic conductivity. Solid-solutions routinely

undergo interesting first- or second-order phase transitions with corresponding shifts in lattice parameters and cation displacements. In some cases dramatic structural changes may occur resulting in a Morphotropic Phase Boundary (MPB). The term MPB, initially used by Jaffe *et al.*,[24] to described a phase boundary in lead zirconium titanate (PZT) (x = 0.48) where an abrupt change from rhombohedral to tetragonal symmetry was observed over an extremely small compositional range. This term is now routinely utilised to describe systems exhibiting similar behaviour. For example, exceptional piezoelectric responses, believed to be comparable to those exhibited by PZT, were recently identified in the 50:50 region, i.e., x = 0.5 of the $Na_{1-x}K_xNbO_3$ (KNN) phase diagram.[25,26] Such perovskites are, therefore, both a crucial and hugely attractive area of research within solid-state chemistry, with many potential applications to a variety of materials and devices.

Double perovskites are currently under extensive investigation owing, principally, to their magnetic and magnetoresistive properties.[27] B site substitutions in such perovskites are investigated more frequently as changes to the octahedral environment commonly contribute to the generation of useful properties. Many A site substitutions are also widely known and within this particular investigation work has been completed on a variety of A site substituted systems, namely $Na_{1-x}K_xNbO_3$ and $La_{1-x}Y_xScO_3$. A specific discussion of each can be found in Chapters 4 and 6 respectively. Ultimately, cation substitutions are driven by either specifically desired physical properties or potential applications of a particular material to certain devices. In many cases it is extremely challenging to accurately predict what effects will occur within a specific system, therefore simple trial and error methods are often necessary.

1.5 Cation Ordering

1.5.1 A site Ordering

Cation ordering across the A site occurs less often[28] and is typically only observed in anion deficient, double or triple-perovskites, for example $YBa_2Cu_3O_{7-x}$,[29,30] $LnBaFe_2O_{5+x}$[31-33] and $YBa_2Fe_3O_{8+x}$,[34] respectively. More

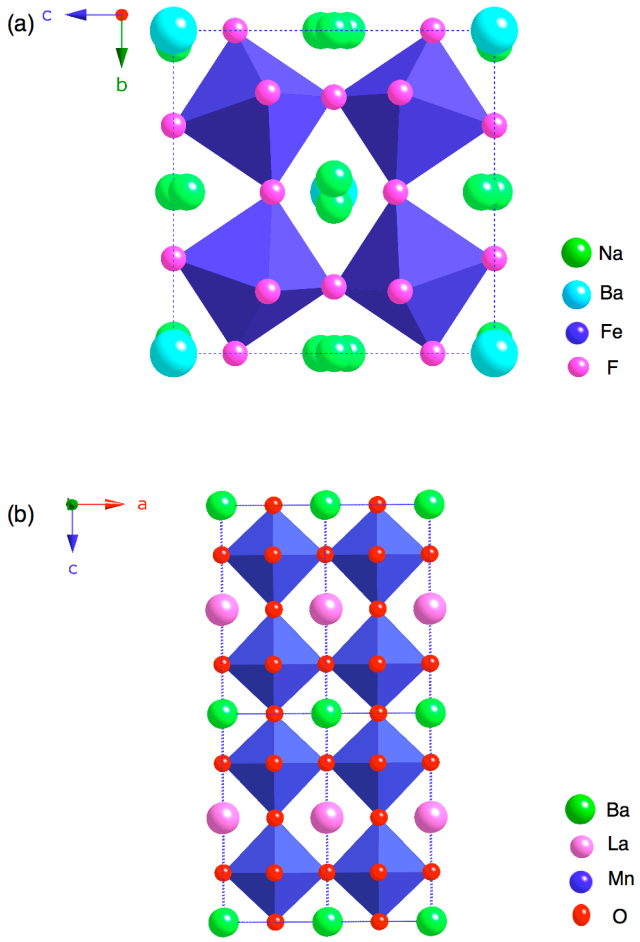

Figure 1.7: (a) An example of rock-salt ordering of the A-site cations in $Na_2BaFe_4F_{12}$,[38] and (b) an example of layered ordering of the A-site cations in $BaLaMn_2O_6$.[39,40]

recently, nonstoichiometric perovskites, $A_{1-x}BO_3$, have been shown to display layered cation ordering over the A site.[35-37] In many cases, to achieve ordering on the A site specific and often extreme experimental conditions such as high-pressure synthesis using diamond anvil cells are required to try and force the cations to order. Rock-salt ordering across the A site is exceptionally rare with only a single report of such behaviour in the literature, the A-site deficient $Na_2BaFe_4F_{12}$ shown in Figure 1.7(a).[38] Layered ordering, in contrast, occurs more readily on the A site, an example of which is $BaLaMn_2O_6$, illustrated in Figure 1.7(b).[39,40]

The anion environment plays a crucial role in the understanding of why rock-salt ordering is not favourable or often feasible across the A site.[41] When rock-salt ordering is exhibited across the B site in a system $A_2BB'X_6$ a mechanism is required to relieve stress and strain from the

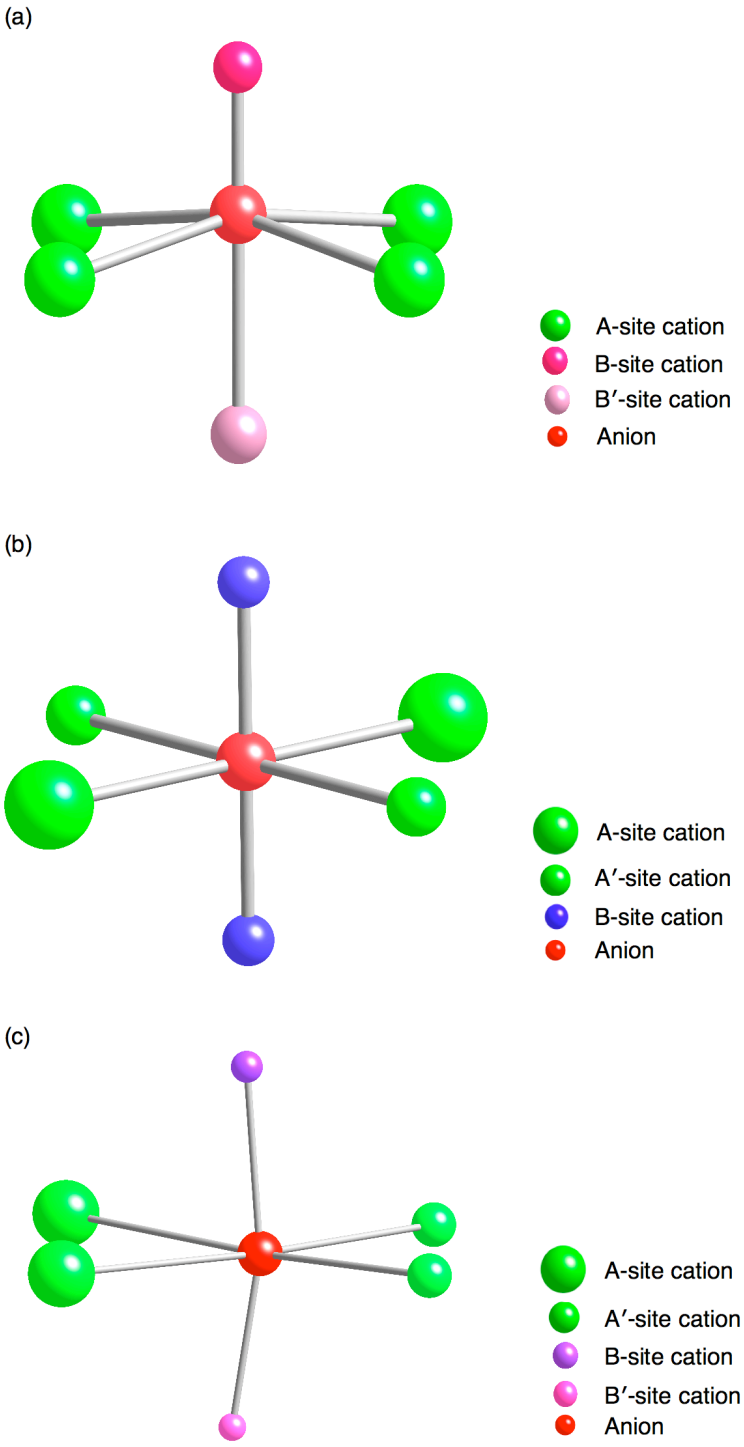

Figure 1.8: The anion environment for perovskites exhibiting: (a) rock salt ordering of the B-site cations, (b) rock salt ordering of the A-site cations and (c) layered ordering of the A-site cations.

structure, and therefore the anion moves towards the smaller of the two B-site cations, as shown in Figure 1.8(a). In a similar manner, if the position of the anion is considered in the system $AA'B_2X_6$ the anion is 'locked' in a plane coordinated to four A-site cations and two B-site cations (Figure 1.8(b)). As previously stated for cation ordering to occur there must be a significant mismatch in ionic radii and when a structure is as illustrated in Figure 1.8(b) there is no available space for movement or displacement of the anion to deal with such a mismatch. The anion is therefore held rigidly in a highly unstable formation. Rock-salt ordering across the A site is therefore not energetically feasible or favourable when there is a significant mismatch in ionic radii. Layered ordering is therefore highly favourable in such circumstances and is often adopted by many structures, as shown in Figure 1.8(c). In this case there is sufficient space for the anion to move when a significant difference in ionic radii is observed. Interestingly, layered ordering on the A site is not generally observed in stoichiometric perovskites in the absence of rock-salt ordering of B-site cations, as seen for example in $NaLaTi_2O_6$.[42] This does not exhibit long-range ordering of the Na^+ and La^{3+} cations as there is no octahedral site ordering.

1.5.2 B Site Ordering

In $A_2BB'X_6$-type perovskites the distribution of the B and B′ cations across the B site can be either random or regular. B-site cation ordering is highly desirable and, as a direct result, has been studied extensively within the perovskite literature.[43-47] It is well reported that octahedral-site cation ordering is particularly favourable when the stoichiometry is $A_2BB'X_6$ and there is a large difference in oxidation state and/or ionic radii of the B and B′ cations. If B is replaced by a cation of similar size there will be very little change to the size and shape of the already distorted octahedron. Such a small change produces no real effect on the stability of the structure, resulting in the B and B′ cations being randomly distributed over the B site. If, however, the deformation of the octahedron is very large after substitution the B-site cations will prefer to be in a certain

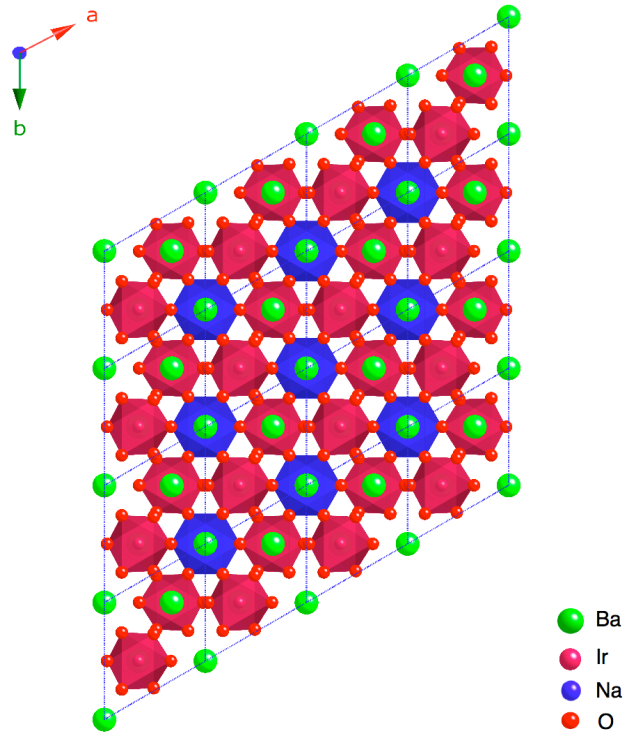

Figure 1.9: Example of a 2:1 ordered perovskite, Ba_3IrNaO_6.[49]

conformation so their arrangement can stabilise the perovskite structure, resulting in ordering of the cations. The extent of deformation exhibited by an octahedron depends upon both the difference in the ionic radii and the charges of the B and B′ cations. The polarisabilities of both B and B′ also play an integral role, as one may be more susceptible to deformation when under the action of the neighbouring ion. Therefore, all such factors must be taken into account when considering the potential for cation ordering across the B site. There are two major classifications for octahedral-site ordering; rock-salt and layered. The most commonly adopted within perovskite structures is rock-salt,[48] in which the cations B and B′ order into alternate octahedra. Octahedral-site ordering may occur for many different compositions, for example 2:1 ordered, $A_3B_2B'X_{12}$, and 3:1 ordered perovskites, $A_4B_3B'X_{12}$. Figure 1.9 illustrates Ba_3IrNaO_6, an example of a 2:1 ordered perovskite.[49]

Over many years there have been several attempts to devise a simple method for predicting whether perovskite-based systems will be ordered or disordered.[50-53] Liu *et al.*,[46] proposed an elementary set of

equations to predict order or disorder within $A_2BB'X_6$ compounds. Their work began by defining two variables, X and Y, as shown in Equations 1.2 and 1.3 respectively,

$$X = \left(\left| \frac{Z_B}{r_B} - \frac{Z_{B'}}{r_{B'}} \right| \right) \tag{1.2}$$

$$Y = \left(\frac{100 \times |\Delta\alpha|}{N_A \times n_A} \right) , \tag{1.3}$$

where $\Delta\alpha$ is the difference in polarisabilities of the B and B′ cations; N_A and n_A are the principal quantum number and the number of electrons in the outer electron shells of the A atom respectively; Z_B / r_B and $Z_{B'} / r_{B'}$ are the ratios of the charges to the ionic radii of the B and B′ cations, respectively. When X > 1.8 the compound will be ordered, irrespective of the value of Y. However, if X < 1.8 the compound resides in a region between order and disorder and an additional parameter, Y_0 (Equation 1.4), is required to determine precisely where in the order-disorder phase diagram the compound lies.

$$Y_0 = -1.9X + 2.3 \tag{1.4}$$

Liu determined that an order-disorder transition region exists when $Y_0 = \pm$ 0.3. Hence, if $Y > Y_0 + 0.3$ the compound will be ordered and if $Y < Y_0 -$ 0.3 it will be disordered. In cases where $Y_0 - 0.3 < Y < Y_0 + 0.3$ the compound resides in the order-disorder transition region or is partially ordered. All methods of this type can be extremely useful as an aid to predicting whether ordering will occur however, in reality, factors such as temperature, cooling rate and particle size often affect whether a compound is ordered or disordered. It is virtually impossible to model such factors using simple equations; hence it is often extremely difficult for simple prediction systems to accurately match experimental results.

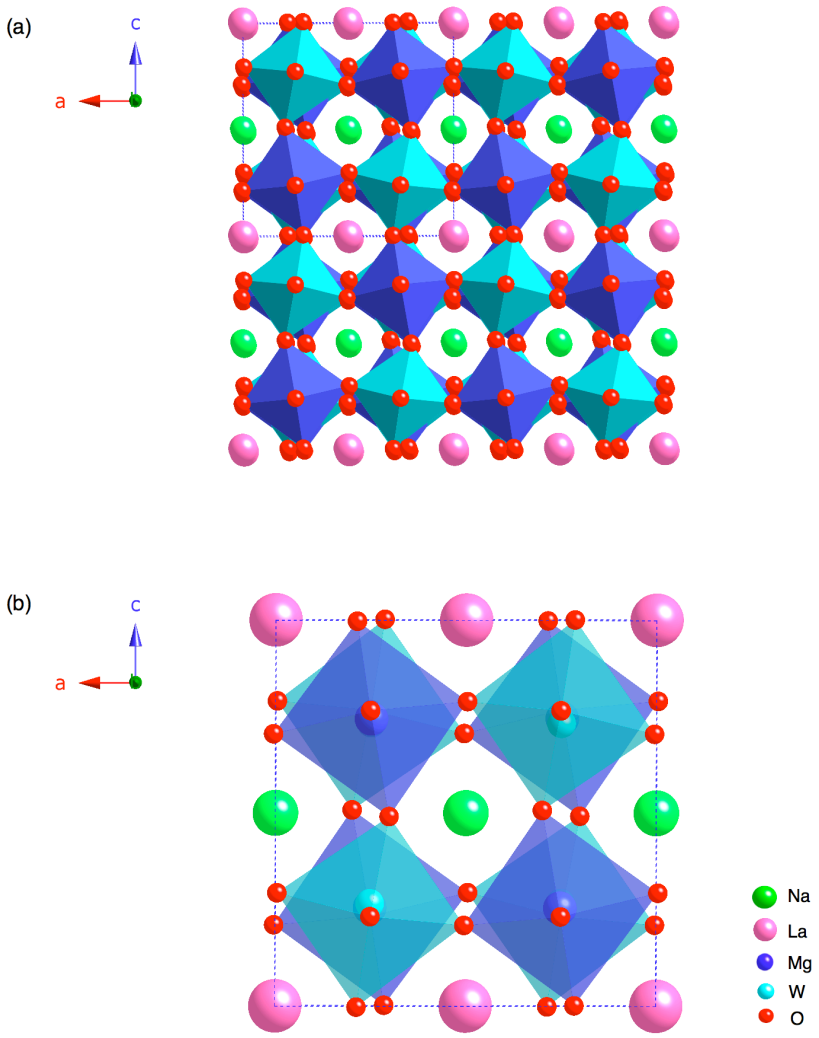

Figure 1.10: (a) The crystal structure of $NaLaMgWO_6$, a perovskite exhibiting simultaneous ordering of the A- and B-site cations. (b) An expansion of the unit cell in the $NaLaMgWO_6$ structure highlighting the simultaneous ordering observed.[54-56]

1.5.3 Simultaneous A and B Site Ordering

According to the literature only rarely can ordering be exhibited simultaneously across both the A and B sites. The first reported example of such behaviour was $NaLaMgWO_6$,[54-56] exhibiting rock-salt ordering of the Mg^{2+}/W^{6+} and layered ordering of the Na^{+}/La^{3+} ions, as illustrated in Figure 1.10. This compound is highly informative as it provides a valuable connection between B-site cation displacements and layered ordering, an area previously ignored within the perovskite literature.

Within the structure a Jahn-Teller distortion forces a displacement of the B′ cation which, in turn, stabilises layered ordering of the Na^+ and La^{3+} cations.[54] More recently such behaviour has also been reported for $NaLaScNbO_6$[41] and is believed to occur when the B′ cation is a d^0 transition metal in a high oxidation state. Subsequently, the following compounds have also been discovered to exhibit simultaneous ordering of the A- and B-site cations $KLaMgTeO_6$,[57] $NaLaMgTeO_6$,[57] $KLaMgWO_6$,[58] $NaLaCoWO_6$[59] and $NaLaNiWO_6$.[59] Now there is a better understanding of simultaneous ordering of the A- and B-site cations it is highly probable research will continue in this field. This will, presumably, lead to the development of methods for accurately predicting when simultaneous cation ordering will occur in such systems.

1.6 Layered Perovskites

Perovskites are currently one of the most heavily researched areas of solid-state chemistry owing to their extensive structural and compositional versatility. The basic perovskite unit, ABX_3, is routinely utilised as a structural 'building block' for a variety of diverse and interesting materials. In addition to the many solid-solutions and double perovskites previously discussed a variety of layered perovskite structures exist including Aurivillius, Ruddlesden-Popper and Dion-Jacobson phases, and Brownmillerites.

Perovskites possess both the ability and flexibility to exhibit various stacking mechanisms, producing a variety of layered perovskites. In recent years A_2BO_4-type oxides have received significant interest owing to the discovery of superconductivity within their structures.[60-62] Based upon the K_2NiF_4-type structure,[63,64] A_2BO_4 oxides form corner-sharing BO_6 sheets with rocksalt layers containing A-site cations lying between. An effective stacking system again requires the A- and B-site cations to be accurately matched to reduce the degree of tilting and rotation observed by the BO_6 octahedra. There are numerous stacking systems available with single, double or even triple perovskite layers separated by rock-salt or fluorite-type layers.

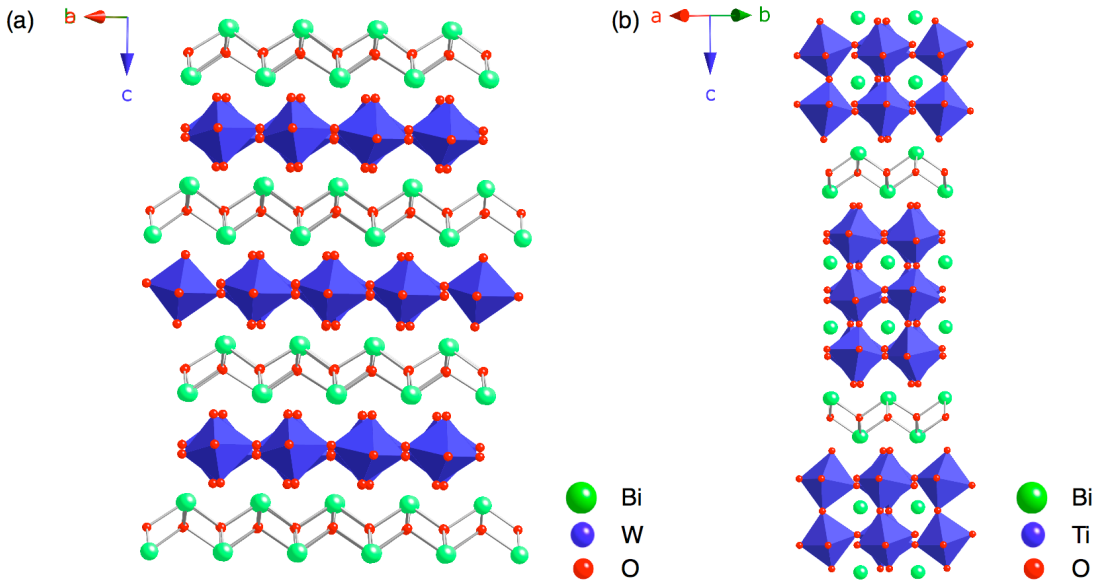

Figure 1.11: (a) Single-layer Aurivillius phase, Bi_2WO_6[67] and (b) 3-layer Aurivillius phase, $Bi_4Ti_3O_{12}$.[69]

1.6.1 Aurivillius Phases

Aurivillius phases are just one of many families of layered perovskites. First discovered over 50 years ago by B. Aurivillius[65,66] they exhibit a characteristic structure composed of $[A_{n-1}B_nO_{3n+1}]^{2-}$ perovskite-type blocks separated by $[Bi_2O_2]^{2+}$ fluorite-type layers, where A is a large 12-coordinate cation and B is a smaller 6-coordinate cation. An extensive family of Aurivillius phases exist and are classified according to the number of repeat perovskite layers, denoted by the integer *n*. Single-layer (Bi_2WO_6[67]), 2-layer ($SrBi_2Ta_2O_9$[68]), 3-layer ($Bi_4Ti_3O_{12}$[69]) 4-layer ($Bi_5Ti_3FeO_{15}$[70]) and mixed layer ($Bi_4Ti_3O_{12}$[71] mixed with $BaBi_2Nb_2O_9$[65]) Aurivillius phases are all widely known, two examples of which are shown in Figure 1.11.

1.6.2 Ruddlesden-Popper Phases

Work by Ruddlesden and Popper in 1957 led to the successful preparation of compositions such as Sr_2TiO_4, Ca_2MnO_4 and $SrLaAlO_4$,[72] regarded as the oxide derivatives of the well-known K_2NiF_4 structure. Successful determination of the structure $Sr_3Ti_2O_7$[73] a year later gave rise

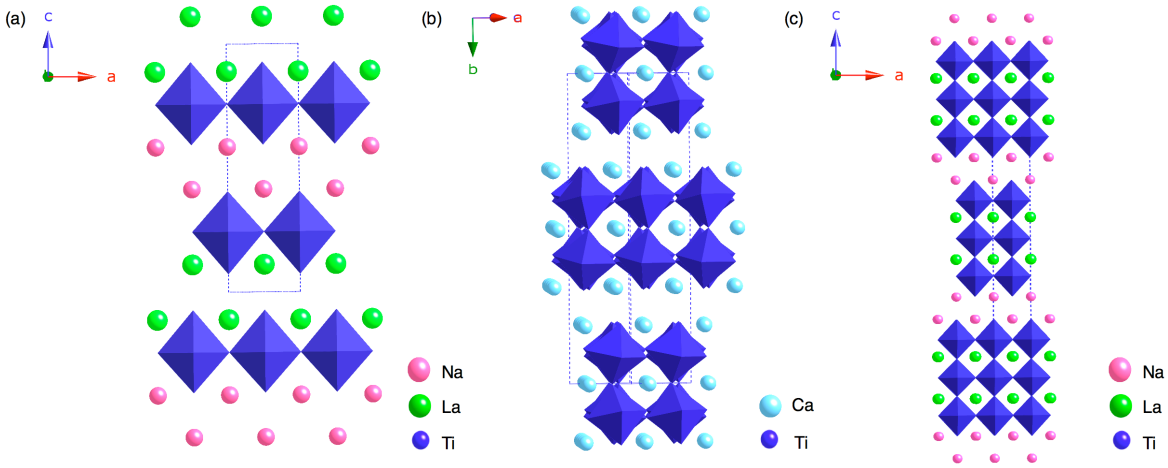

Figure 1.12: (a) 1-layer, $NaLaTiO_4$,[74] (b) 2-layer, $Ca_3Ti_2O_7$,[75] and (c) 3-layer, $Na_2La_2Ti_3O_{10}$,[76] Ruddlesden-Popper phases.

to a new family of layered perovskites now widely known as Ruddlesden-Popper phases, with general formula $M_2[A_{n-1}B_nO_{3n+1}]$. As expected with layered perovskites there are many 1-, 2- and 3-layer phases known, including $NaLaTiO_4$,[74] $Ca_3Ti_2O_7$[75] and $Na_2La_2Ti_3O_{10}$,[76] as shown in Figures 1.12(a), (b) and (c) respectively. Several Ruddlesden-Popper phases are known to possess ionic conduction capabilities, believed to occur through the interlayer region. A number have also been discovered to possess Colossal Magnetoresistance (CMR), thereby making such materials more desirable for use in devices. In recent years, several investigations have concentrated solely on 3-layer Ruddlesden-Popper phases with alkali metals in the interlayer and various lanthanides (Ln = La, Nd, Sm and Gd) on the A site within the perovskite blocks.[77] Such studies concluded that the lanthanide radius played a vital role in the ionic conductivity of a particular phase; a decrease in ionic size was accompanied by an increase in ionic conductivity. Trends in cation size are extremely important as they can often influence the physical properties exhibited by a particular perovskite or perovskite-based system.

The scope of interest for Ruddlesden-Popper phases has been extended by the possibility of proton conduction and many such studies are currently being undertaken.[78] Several Ruddlesden-Popper phases are well-known superconductors, for example the 1987 Nobel Prize in Physics

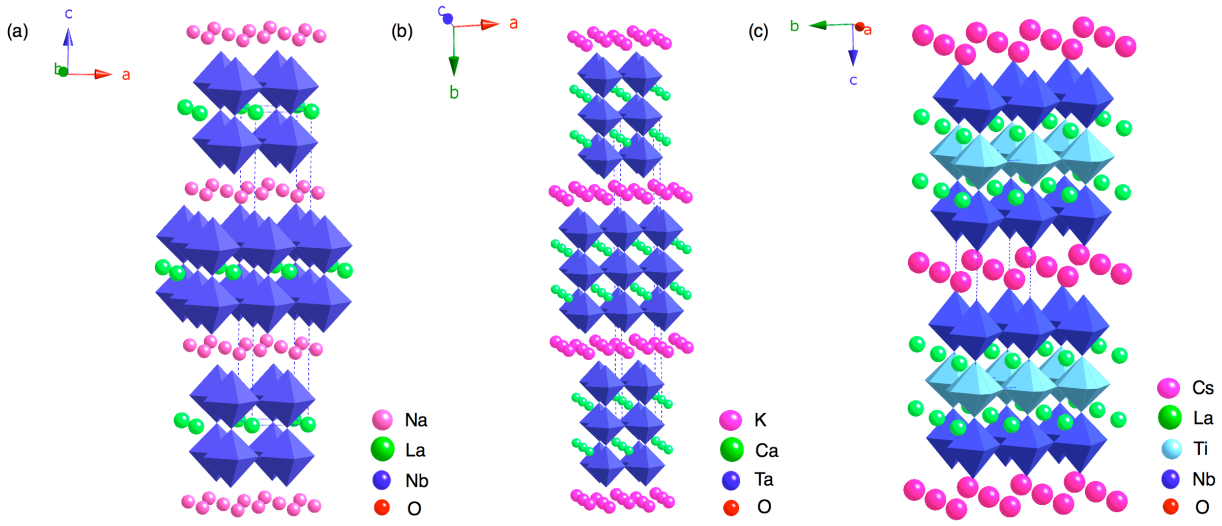

Figure 1.13: (a) 2-layer, $NaLaNb_2O_7$,[82] (b) 3-layer, $KCa_2Ta_3O_{10}$[83] and (c) $CsLa_2Ti_2NbO_{10}$ Dion-Jacobson phases.

was awarded to Bednorz and Müller for their discovery of superconductivity in ceramics materials, namely $(La,Ba)_2CuO_4$.[79] Many other additional phases have also been found to exhibit superconducting behaviour, including Sr_2RuO_4. Their practical application is, however, limited owing to the exceptionally low temperatures required to achieve such properties.

1.6.3 Dion-Jacobson Phases

One class of layered perovskites very closely related to Ruddlesden-Popper phases is the Dion-Jacobson family, general formula $A'[A_{n-1}B_nO_{3n+1}]$.[80,81] Structurally the two phases are extremely similar, with the only differences occurring in the composition of the interlayer. Ruddlesden-Popper phases have a double interlayer of cations whereas Dion-Jacobson phases possess only a single layer. Conventionally small alkali metals such as Li^+, Na^+ and K^+ are utilised in the interlayers of Ruddlesden-Popper phases. However, Dion-Jacobson phases are capable of accommodating larger cations such as Rb^+ and Cs^+, owing, predominantly, to the presence of a single interlayer. Commonly 3-layer Dion-Jacobson phases have compositions with divalent or trivalent cations on the A site of the perovskite block which, in turn, affects the valence of

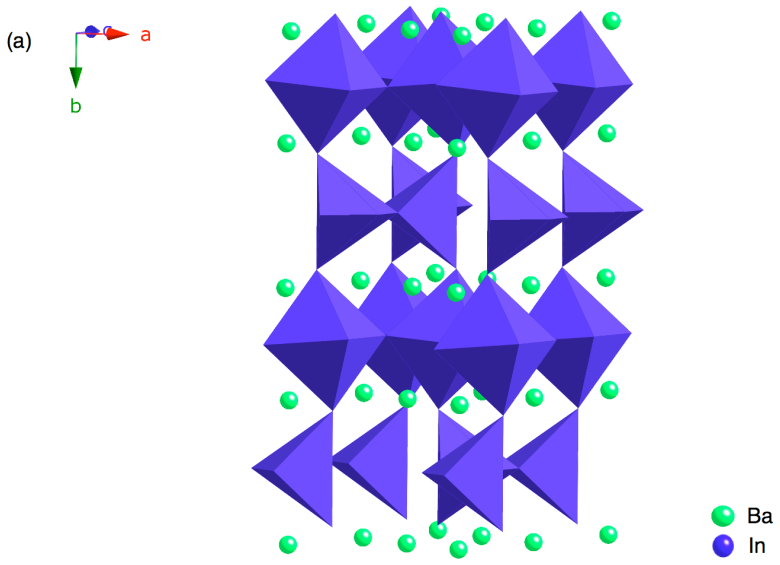

Figure 1.14: Example of the brownmillerite structure, $Ba_2In_2O_5$.[91]

the cation on the B site. For divalent cations the B site is usually fully occupied either by Nb^{5+} or Ta^{5+}. Trivalent cations however produce mixed valence on the B site. To date, there are no documented reports of single layer oxide Dion-Jacobson phases. Solely 2-layer ($NaLaNb_2O_7$[82]) and 3-layer ($KCa_2Ta_3O_{10}$[83]) oxide phases have been reported. Three examples of Dion-Jacobson phases are shown in Figures 1.13(a), (b) and (c) respectively. There are only very few known cases of Dion-Jacobson phases with greater than 3 layers.[84-87]

1.6.4 Brownmillerites

Brownmillerites are anion deficient derivatives of the perovskite structure, named after L. T. Brownmiller who first discovered the mineral $Ca_2[Fe,Al]_2O_5$.[88] The brownmillerite structure, shown in Figure 1.14, is composed of alternating layers of corner-sharing octahedra and distorted tetrahedra with oxygen vacancies in the ab plane.[89] Brownmillerites are studied extensively owing to their conduction capabilities.[90]

1.7 Physical Properties

Perovskites, or their derivatives, routinely possess enhanced physical properties such as ferro-, piezo- or pyroelectric behaviour, all of which are desired in a variety of materials and devices throughout solid-state chemistry. This is the principal reason perovskite-based materials are of such importance and significance.

1.7.1 Piezoelectricity

Piezoelectric ceramics respond to mechanical stress, becoming polarised and developing electrical charges on opposite crystal faces. The magnitude of the piezoelectric response observed depends upon both the crystal structure of the material and direction of the applied stress. Polarisation will, therefore, only occur when mechanical stress is applied in specific directions. The polarisation, P, and stress, σ, observed are related to the piezoelectric coefficient, d, by Equation 1.5. Conversely, the opposite is true, piezoelectrics can also develop a mechanical stress due to the application of an electric field.[91]

$$P = d\sigma \tag{1.5}$$

Potentially the most influential piezoelectric ceramic in materials science is $Pb[Zr_xTi_{1-x}]O_3$ (PZT).[24] Since its discovery in 1952 it has received considerable attention and is still heavily investigated. At varying compositions within the solid-solution different physical properties are exhibited. For example, it is known to be both ferroelectric ($x \geq 0.1$) and antiferroelectric ($x < 0.1$). To date, the largest dielectric responses were recorded when $x = 0.52$ at the MPB.[92-95]

1.7.2 Pyroelectricity[96]

Pyroelectric materials are closely related to ferroelectrics; however, the fundamental difference between the two is that the direction of the

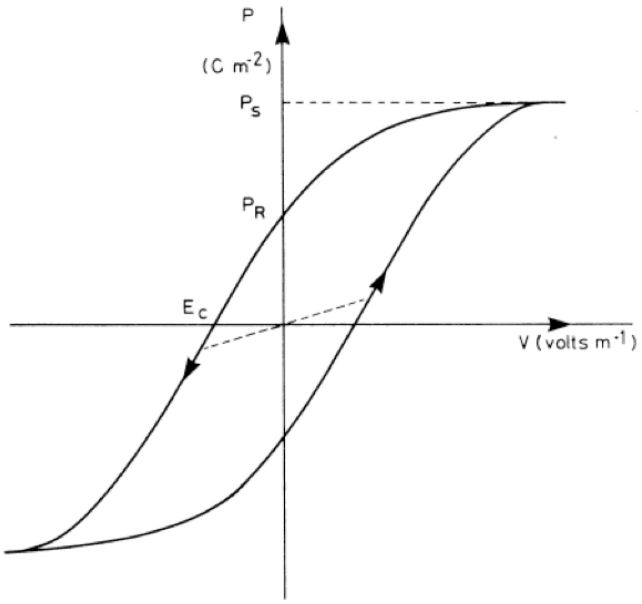

Figure 1.15: An example of a hysteresis loop of a ferroelectric material.[99]

saturation polarisation, P_S, cannot be reversed by application of an electric field. Temperature plays an integral role within pyroelectric materials, and only when the sample is heated will a change in P_S (Equation 1.6) be observed, as there will then be a change in the magnitude of the dipoles. The temperature dependence of P_S is given by

$$\Delta P_S = \pi \Delta T \tag{1.6}$$

where π is the pyroelectric coefficient.

Ferroelectric, piezoelectric and pyroelectric behaviour are closely related. By definition, ferroelectric materials are also pyroelectric and piezoelectric. In addition, pyroelectric materials are also piezoelectric. However, it must be noted that the reverse does not always hold, i.e., not all piezoelectric materials are pyroelectric.

1.7.3 Ferroelectricity

Ferroelectric behaviour was initially discovered in 1920 with the first ferroelectrically active material reported; Rochelle salt (potassium sodium tartrate), now known to rapidly lose all ferroelectric ability when

its composition is slightly changed, thereby preventing any potential industrial application.[97] At that time ferroelectricity was considered a scientific curiosity and believed to be an order/disorder phenomenon associated with hydrogen bonding, and its true scientific importance had, at that stage, not been established. In 1945, $BaTiO_3$ was found to possess similar behaviour and, as a direct result, is now one of the most widely known and utilised ferroelectric materials. $BaTiO_3$ exhibits a significant displacement of the Ti^{4+} cation within the octahedron, resulting in long-range ordering of the dipoles. This type of displacement is routinely adopted by many perovskites. Of the several hundred ferroelectrics now known a large percentage are disordered perovskite structures displaying significant octahedral cation displacements.

To be ferroelectrically active a material must be non-centrosymmetric and exhibit spontaneous polarisation which may be reversed upon the application of an electric field. Polarisation is achieved by the presence of a net dipole moment, commonly the result of cation displacements. The temperature above which polarisation is lost is defined as the Curie temperature, T_C. When a potential difference is applied across a ferroelectric material the polarisation is increased until a saturation polarisation, P_S, is reached. Once the voltage has been removed a remnant polarisation, P_R, remains. To reduce the polarisation to zero a reverse field is required, known as a coercive field, E_C. The behaviour of a ferroelectric material under the application of a potential difference can be described by a hysteresis loop, as shown in Figure 1.15.[98] Ferroelectric materials are distinguished from ordinary dielectrics due to this behaviour, as common dielectrics do not possess the ability to retain large residual polarisations once the applied voltage has been removed. To be successfully utilised in commercial and industrial applications relatively high values of T_C are desired, i.e., close to room temperature. However, it is often extremely challenging to produce materials with adequate values, as many materials exhibit interesting ferroelectric properties at extremely low temperatures.

1.7.4 Applications of Perovskites

Currently, the largest commercial application of ferroelectrics is in capacitors using materials such as $BaTiO_3$ and PZT. In recent years there has been significant interest and research into finding potential 'green' replacements for PZT owing to toxicity issues regarding the presence and continued use of heavy metals such as lead. Therefore, a compound exhibiting piezoelectric responses equal to or superior to PZT needs to be discovered. Compounds containing heavy metal ions are renowned for producing exceptional piezoelectric and ferroelectric responses, but their use is limited owing to their toxic nature. Piezoelectrics have been routinely utilised as transducers to convert mechanical to electrical energy in a variety of diverse materials, for example they are applied as bimorphs in microphones, earphones and loudspeakers.[99] Pyroelectric materials are routinely used in infrared radiation detectors.[99] By far, materials exhibiting ferroelectric behaviour provide the greatest number of potential applications.

1.8 A Multidisciplinary Approach

The work presented within this thesis is the result of a multidisciplinary investigation combining two principal characterisation techniques within solid-state chemistry, namely powder diffraction and solid-state Nuclear Magnetic Resonance (NMR). When compared with X-ray and neutron powder diffraction, solid-state NMR is a relatively new technique with the first application of NMR to solids occurring in 1945 by Felix Bloch and Edward Mills Purcell.[100,101] This revolutionised chemistry. Bloch and Purcell later collected a Nobel Prize in physics (1952) for their contributions.

Powder diffraction and solid-state NMR are now recognised as being highly complementary to one another. Powder diffraction examines the long-range order of a material whereas solid-state NMR investigates and determines more local, short-range structural effects. Therefore, when used in combination they aid considerably in obtaining a better structural

understanding and characterisation of a solid. Powder diffraction is principally used to identify the symmetry adopted within a structure. However, in some cases, this can be difficult to accurately determine using laboratory diffractometers owing to poor resolution. Hence, high-resolution data is often required, commonly synchrotron X-ray or neutron powder diffraction. The source utilised is often related to the material under investigation; for example, in some cases the sample may be too sensitive to be bombarded with neutrons and therefore high energy X-rays would be more favourable. Within this particular investigation a variety of dense ternary oxides have been investigated and for such materials neutron diffraction is often the only plausible option to successfully determine subtle structural effects such as phase transitions.

High-resolution solid-state NMR data has also been essential throughout this investigation. Lineshapes acquired in solution-state spectra are inherently narrower than those observed in the solid state owing principally to the presence of molecular motion when in solution. This motion averages any potential sources of broadening such as chemical shift anisotropies (CSA) or dipolar couplings.[102] In solids, however, there is usually no such averaging and therefore lines are often broadened. To obtain high-resolution spectra various experiments can be utilised to average the interactions that cause such broadenings and produce well resolved lineshapes. Specific details of these experiments can be found in Chapter 2. In many cases, solid-state NMR can provide additional information regarding the dynamics of a particular system and, in turn, provide essential structural information for often highly complex systems. Dynamics cannot be investigated easily using diffraction techniques and therefore solid-state NMR enables hugely important and significant additional information to be obtained for any system.

In addition, Density Functional Theory (DFT) calculations have been utilised routinely throughout this investigation. These calculations provide a direct link not only between experiment and theory but also between diffraction and NMR. Using DFT it is possible to calculate the NMR parameters for a particular structure and to do this an initial structural model is required, often provided by diffraction studies. DFT

calculations are therefore a direct and convenient way of bridging the two techniques whilst also providing additional information often lost by experiment.

1.9 Thesis Overview

This thesis is concerned with the synthesis and structural characterisation of several perovskite systems using high-resolution powder diffraction, solid-state NMR and first-principles DFT calculations. Chapter 2 begins by introducing many of the basic principles of crystal symmetry and powder diffraction. The generation and practical implementation of both X-rays and neutrons to high-resolution powder diffraction experiments is also discussed. A basic description of the theory used in structural refinement is presented and the Rietveld method is introduced. The NMR phenomenon is also introduced within Chapter 2 and includes detailed considerations of the many interactions present during the course of an NMR experiment. In particular, a detailed description of the quadrupolar interaction and its effect upon NMR spectra is given. In addition, a detailed discussion regarding the practical implementation of first-principles calculations to periodic systems using DFT methods for the calculation of NMR parameters is given, and many of the basic methodologies relevant to the calculation of NMR parameters using first-principles DFT calculations are introduced.

Chapter 3 presents a detailed structural study of room temperature $NaNbO_3$. Particular focus is placed on the effect of different synthetic methods on the different phases of $NaNbO_3$ formed and their respective quantities. Conventional solid-state, molten salt and sol-gel techniques have been investigated and compared. A detailed discussion regarding the structural subtleties of the $NaNbO_3$ system is given and considerable emphasis is placed on the need for a multidisciplinary approach to achieve an accurate and complete structural conclusion. Both high-resolution X-ray and neutron powder diffraction data will be presented. In addition, ^{23}Na, ^{93}Nb and ^{17}O MAS NMR data and DFT calculations are presented, each of which highlights the importance of using a combined

approach to characterise structurally complex compounds such as $NaNbO_3$.

Chapter 4 concentrates on the structural characterisation of several analogous $NaNbO_3$-based solid-solutions, namely $K_xNa_{1-x}NbO_3$, $Li_xNa_{1-x}NbO_3$ and $Na_{1-x}Sr_{x/2}\square_{x/2}NbO_3$. An understanding of the structure adopted after doping with the cations Na^+, Li^+ and Sr^{2+} is developed. The structural trends exhibited by each series are compared and the origin of the structural changes are discussed. Again, high-resolution X-ray and neutron powder diffraction techniques have been utilised to establish the structural subtleties exhibited by each system. The results obtained from each dataset will be presented in conjunction with the ^{23}Na MAS NMR data.

In Chapter 5 a low temperature structural study is presented using a sample of $NaNbO_3$ synthesised using a sol-gel approach. The same sample was initially characterised at room temperature in Chapter 3. Using high-resolution X-ray diffraction the structural changes observed as a function of temperature are discussed.

Chapter 6 presents a detailed structural study of $LaScO_3$, $YScO_3$ and the related solid-solution $La_{1-x}Y_xScO_3$ for compositions x = 0.2, 0.4, 0.6 and 0.8. High-resolution neutron diffraction data will be presented in conjunction with conventional and two-dimensional ^{45}Sc and ^{89}Y MAS NMR data and DFT calculations. The structural trends exhibited are presented and discussed, with possible reasoning as to why the observed changes occur.

Chapter 7 summarises the findings presented and suggests possible directions for future work.

Chapter 2

Experimental Techniques

2.1 Crystal Symmetry

2.1.1 Crystal Systems and Lattices[104,105]

Crystalline solids can be described by a periodic arrangement of atoms or ions in space. The simplest repeating portion of the structure, known as the asymmetric unit, yields the unit cell when translated, rotated or reflected. The unit cell can then be translated along all three dimensions to produce an infinite lattice, defined as an array of equivalent points in three dimensions. The lattice provides no information regarding the positional coordinates of any atoms; it simply displays the translational symmetry within a structure by locating equivalent positions. Increasing symmetry produces relationships between the various cell parameters that, in turn, leads to the definition of crystal classes. In total there are seven possible crystal systems (Figure 2.1) used to describe crystal structures, each governed by a minimum number of symmetry operations, as summarised in Table 2.1. As a direct consequence, a unit cell in each crystal system can be described using axes a, b and c, and angles α, β, and γ. Three-dimensional structures can also be described according to their lattice type, of which there are four possibilities; primitive (P), body centred (I), face centred (F) and side centred (C), illustrated in Figure 2.2. When combined with the seven crystal systems they give rise to the Bravais lattices, of which there are fourteen unique combinations.

2.1.2 Point Groups and Space Groups[104,105,106]

To fully describe a crystal structure more than simply the crystal system and lattice type are required. Crystals, owing to their infinite repeating structures, also possess some degree of space symmetry as opposed to solely point symmetry. There are 32 different point groups,

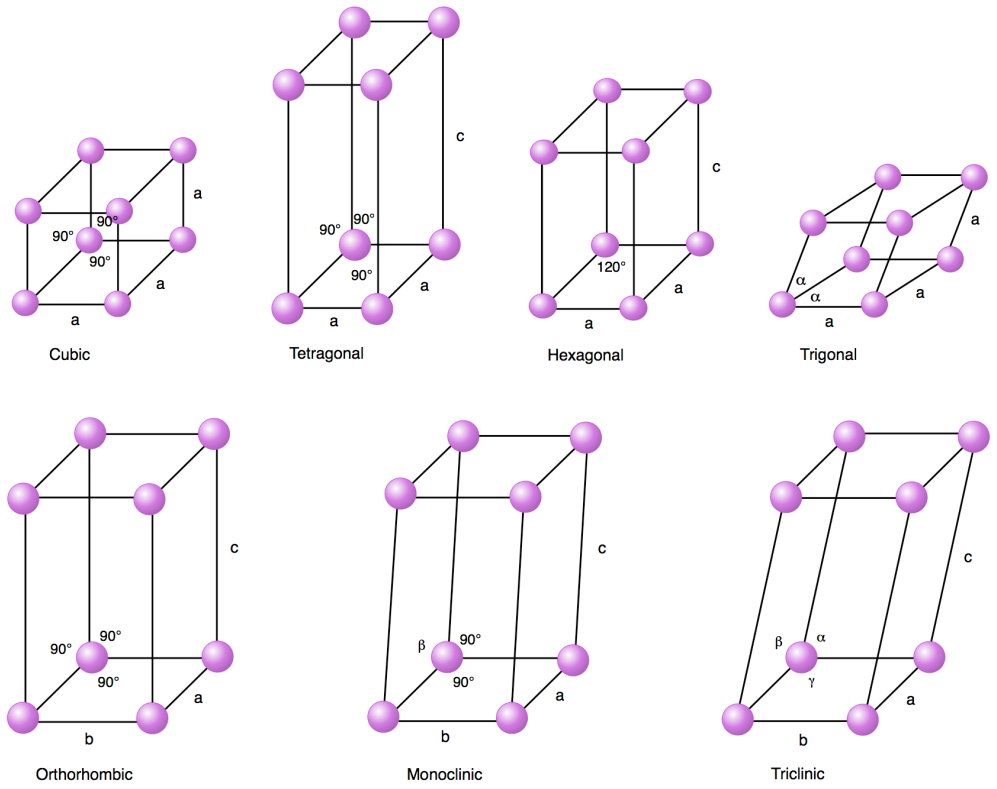

Figure 2.1: The seven crystal systems.

each of which provides information regarding the symmetry around a single point (rotations or mirror plane reflections). Point groups are therefore ideal for studying finite-sized molecules. In contrast, symmetry elements in the solid-state do not pass through a single point, instead they are regularly arranged as periodic solids. Space symmetry combines point symmetry elements with incremental translational steps giving rise to screw axes and glide planes. The symmetry of any system can then be characterised using a space group, a convenient and concise notation which utilises a set of pre-determined symbols to accurately summarise the symmetry elements exhibited. Space groups are extremely important as they provide key information regarding the crystal system, lattice type and elements of both the point and space symmetry exhibited by any one structure. In turn, they are routinely utilised throughout solid-state chemistry to describe all crystal structures. There are 230 space groups in total and the symmetry properties for each are well characterised. Details for each can be found in the International Tables for Crystallography, Volume A.[107]

Table 2.1: The seven crystal systems.[105]

Crystal Class	Symmetry Operation	Imposed Unit Cell Dimensions
Cubic	Four three-fold axes at 109.28° to each other	$a = b = c$ $\alpha = \beta = \gamma = 90°$
Tetragonal	One four-fold acis or one four-fold improper axis	$a = b \neq c$ $\alpha = \beta = \gamma = 90$
Hexagonal	One six-fold axis or one six-fold improper axis	$a = b = c$ $\alpha = \beta = 90°, \gamma = 120°$
Trigonal	One three-fold axis	$a = b = c$ $\alpha = \beta = \gamma \neq 90°$
Orthorhombic	Any combination of three mutually perpendicular two-fold axes or symmetry planes	$a \neq b \neq c$ $\alpha = \beta = \gamma = 90°$
Monoclinic	One two-fold axis or one symmetry plane	$a \neq b \neq c$ $\alpha = \gamma = 90°, \beta \neq 90°$
Triclinic	None	None

Space groups can be further classified into one of two categories; centrosymmetric or non-centrosymmetric. Structures that are non-centrosymmetric do not possess an inversion centre which often leads to many interesting physical properties, such as ferroelectricity. Solid-solutions are commonly synthesised, in which carefully selected cations are doped into the perovskite structure to try and force a structural transition to a non-centrosymmetric space group. In many cases, this is highly successful, enabling the physical properties exhibited by a particular perovskite to be 'tuned'. Perovskites in polar (non-centrosymmetric) space groups are therefore highly desirable as they commonly exhibit interesting physical properties that ultimately lead to many potential applications.

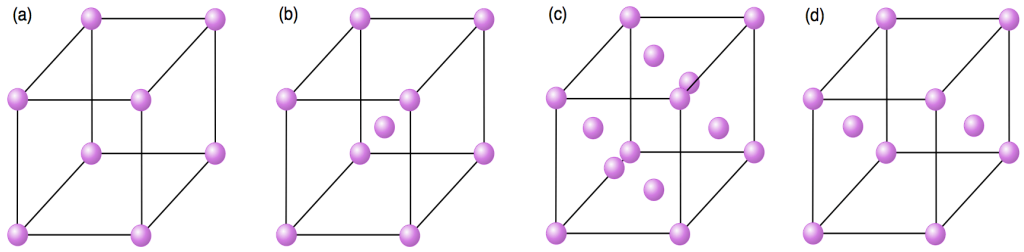

Figure 2.2: The four lattice types (a) primative, (b) body centred, (c) face centred and (d) side centred.

2.1.3 Miller Planes[108,109]

Bragg's Law, Equation 2.1, considers crystals as being composed of layers or planes of atoms, known as Miller planes, where adjacent planes are separated by an interplanar d-spacing, d_{hkl}. These planes are described by a set of integers known as Miller indices, commonly denoted as (*hkl*). Bragg's Law[110] governs diffraction, the physical process by which a beam of particles is refracted by a crystal and is given by

$$n\lambda = 2d_{hkl}\sin\theta \qquad (2.1)$$

where n is an integer value, λ is the wavelength of the radiation used, d is the spacing between the lattice planes within a crystal and θ is the angle between the incident beam and the sample. Consider the path of two X-ray beams reflected from two adjacent planes within a crystal, as illustrated in Figure 2.3. The beam reflected from the lowest of the three planes travels an extra distance, XY + YZ. When this path length difference is an integer number of wavelengths constructive interference results and Bragg's Law is satisfied. Bragg's Law imposes extremely stringent conditions on the angles at which reflections may occur and if the angle of incidence is incorrect by even a few tenths of a degree cancellation of the reflected beams will occur. In reality diffraction patterns are plotted as a function of 2θ rather than θ as 2θ corresponds to the angle between the X-ray source and the detector, i.e., the path of incident and reflected X-rays. Bragg's Law is considered a highly simplistic model to describe how X-rays are reflected in reality. The

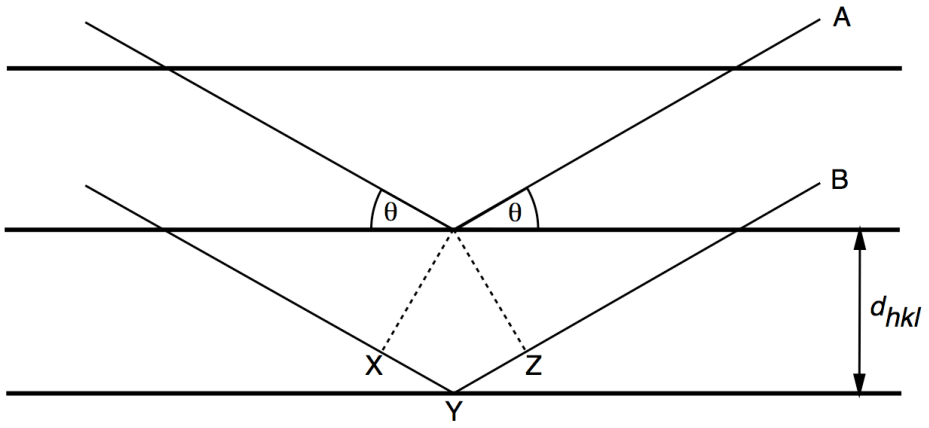

Figure 2.3: X-rays reflecting off adjacent planes.

'planes' described by Bragg are merely a concept rather than a physical reality. Crystal structures are large three-dimensional networks resulting from a regularly repeating unit cell, as previously discussed. Planes can be used to divide up the unit cell into various different orientations and it is this concept of planes that is utilised in the derivation of Bragg's Law. For extremely simple crystal structures the planes can correspond to layers of atoms however, in reality, this is generally not the case as atoms are commonly located on sites that do not correspond to such 'layers'.

2.1.4 The Reciprocal Lattice[111-114]

The reciprocal lattice is essential in the understanding of diffraction. To fully comprehend the concept of reciprocal space it first must be understood that diffraction patterns do not display the real-space reflections of a crystal. Instead, all diffraction patterns are functions that exist as a regular three-dimensional lattice known as the reciprocal lattice, defined with reference to a particular Bravais lattice. The reciprocal lattice is a vector perpendicular to the Miller planes and can be regarded as the Fourier transform of the real space or direct lattice of a crystal. The magnitude of this vector is the reciprocal of the interplanar distance and the reciprocal lattice parameters can be calculated from those of the crystal lattice in real space by $1/d_{hkl}$, where d_{hkl} is the spacing between the Miller planes.

2.2 Diffraction Techniques

The powder diffraction techniques utilised within this particular study can be separated into three main categories conventional (laboratory) X-ray diffraction, high-resolution synchrotron X-ray diffraction and high-resolution neutron diffraction.

2.2.1 X-rays

X-rays, electromagnetic radiation of wavelength ~1 Å, were initially discovered by Wilhelm C. Röntgen in 1895. The first description of X-ray diffraction (XRD) and subsequent diffraction pattern of a crystal followed seventeen years later by Max von Laue and Paul Knipping.[115] X-rays possess a wavelength comparable to interatomic distances making them suitable for the structural characterisation of many complex solids. In 1913 William H. Bragg and his son, William L. Bragg, devised a method and equation (Bragg's Law) to describe diffraction that revolutionised the technique and is now universally used as the basis for X-ray diffraction geometry, as previously discussed in section 2.1.3.

2.2.2 Generation of X-rays[108,116,117]

Laboratory X-rays are conventionally generated using an X-ray tube, where a beam of electrons (produced from a tungsten filament) is accelerated towards a metal target, commonly copper. As electrons penetrate the metal target they decelerate and generate radiation with a continuous range of wavelengths, known as Bremsstrahlung or 'white radiation'. The X-ray tube used to produce monochromatic radiation is evacuated and held under vacuum to avoid collision of the incident electrons and/or X-rays with air particles.

The accelerated incident electrons possess sufficient energy to ionize some of the 1s electrons in the copper and upon impact an electron is expelled from the inner shell and an electron of higher energy from an outer orbital, typically a 2p or 3p electron, drops down to occupy the

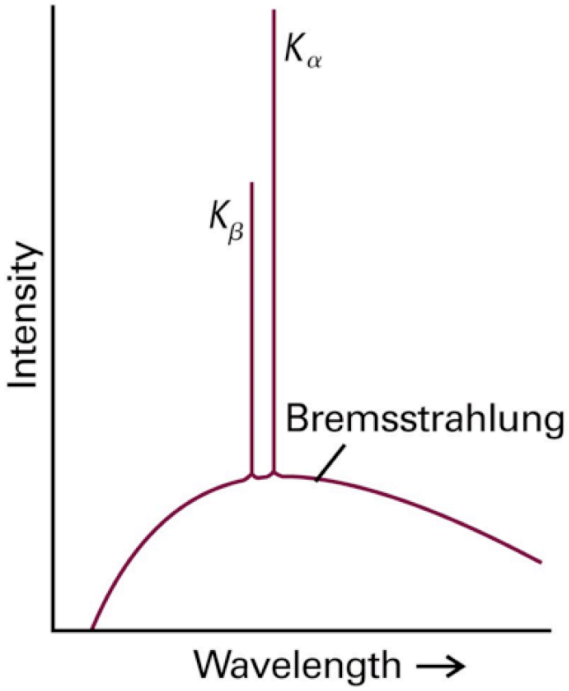

Figure 2.4: Bremsstrahlung radiation.[118]

vacant shell. Such electronic transitions result in the release of monochromatic X-rays and peaks corresponding to this radiation are superimposed onto the broad featureless Bremsstrahlung background, as shown in Figure 2.4. For copper the $2p \rightarrow 1s$ transition, K_α, has a wavelength λ = 1.5418 Å whilst the $3p \rightarrow 1s$ transition, K_β, has a wavelength λ = 1.3922 Å. The K_α transition occurs more frequently and is, in turn, more intense when compared with K_β transitions. As K_α radiation is more desirable for use in X-ray diffraction experiments, a method is required to accurately separate out the K_α and K_β radiation. Various metals filters, known as monochromators, can be utilised to successfully split the two; however their effectiveness is dependent upon the metal target initially used. For copper, Ni foil is extremely effective as a monochromator as it successfully absorbs the K_β radiation leaving a monochromatic beam of Cu K_α radiation.

The desirable K_α radiation is, in reality, a doublet composed of $K_{\alpha1}$ = 1.54051 Å and $K_{\alpha2}$ = 1.54433 Å. This is a consequence of spin multiplicity in the p shells , and therefore the 'K_α line' in the copper spectrum has two

lines instead of one. Patterns obtained by X-ray diffraction using both $K_{\alpha1}$ and $K_{\alpha2}$ often appear broadened and poorly resolved. Therefore, to overcome this problem and improve resolution the weaker $K_{\alpha2}$ beam can be removed from the incident radiation using an appropriate monochromator. Most modern diffractometers currently operate using monochromatic X-rays composed of solely Cu $K_{\alpha1}$ radiation.

2.2.3 X-ray Scattering and Powder Diffraction

X-rays interact with electrons present in matter and, upon contact with an inorganic compound or crystal a beam of X-rays, will be scattered in various directions by the electron density. The scattering factor or form factor, f, of an atom is directly proportional to the atomic number, Z, or, more accurately, the number of electrons possessed by a particular atom. There is a fall off in scattering power for X-rays owing to the finite size of the electron cloud, highlighted in Figure 2.5 for Ca^{2+} and F^{-}. The scattering factor is also dependent on the scattering angle, $\sin\theta/\lambda$, also illustrated in Figure 2.5. Atoms such as oxygen and hydrogen scatter X-rays weakly therefore it is often extremely challenging to locate their position when much heavier elements are present. The more electrons an atom possesses the more intense the scattered X-rays will be. Compounds containing several elements of similar atomic number can be exceptionally difficult to characterise as each element will scatter the X-rays in essentially the same manner. The structure factor, F_{hkl}, is related to the scattered intensity in any diffraction pattern and the structure factor for a particular reflection can be defined as

$$F_{hkl} = \sum_{i=1}^{N} f_i \exp(2\pi i(hx_i + ky_i + lz_i)) \qquad (2.2)$$

where f_i is the scattering factor, hkl are the Miller indices of a particular plane and (x_i, y_i, z_i) are the fractional coordinates of each of the atoms within the unit cell. The intensity of this reflection is given by

$$I_{hkl} = F_{hkl}^2 \quad . \qquad (2.3)$$

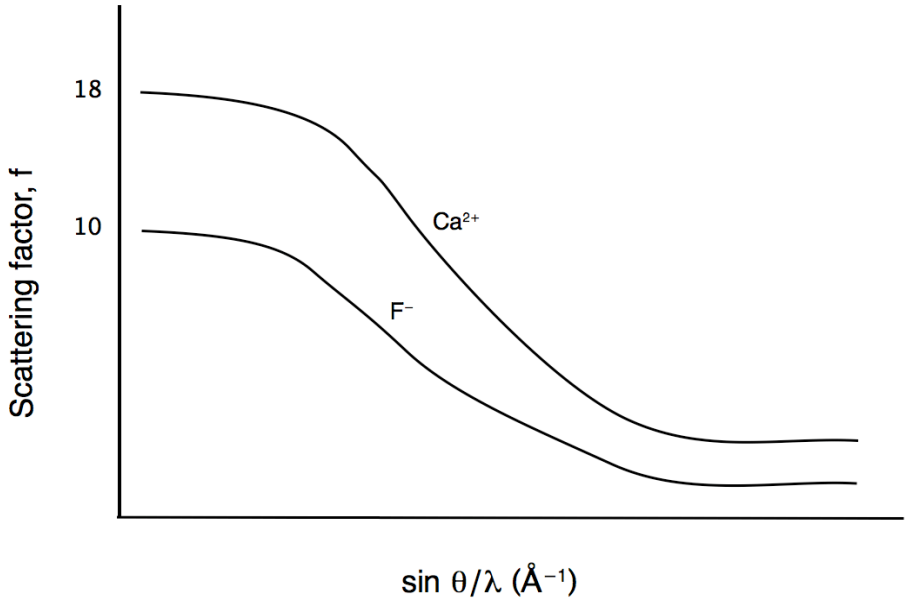

Figure 2.5: Fall off in scattering power for X-rays.

Polycrystalline samples are composed of millions of tiny crystallites, each with a different orientation. As a result, when an X-ray beam strikes a powdered sample it is diffracted as cones of radiation in all possible directions, as illustrated in Figure 2.6. Each cone is composed of a set of closely spaced dots, each of which represents diffraction from a single crystallite within the sample. When large numbers of crystallites are present the dots join together resulting in one continuous cone. To convert these 'cones' of radiation to a real space diffraction pattern a transformation from three to two-dimensional space is required, i.e., envisage taking a 'slice' through one particular cone from its point to its base, this is then represented in the diffraction pattern obtained. A highly diffracting (electron rich) atom with a very distinct location will produce an intense, narrow peak in the powder pattern. The converse is also true with broad peaks indicating weakly diffracting atoms. The powder pattern obtained is characteristic of the sample under analysis.

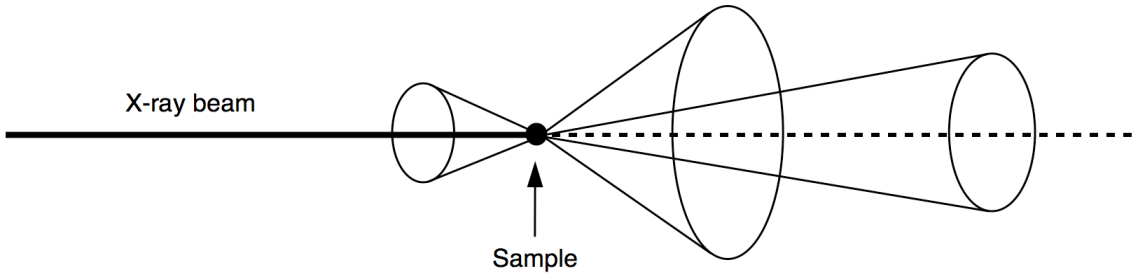

Figure 2.6: Cones of radiation produced in diffraction.

2.2.4 Conventional X-ray Diffraction

All "laboratory" powder diffraction (l-PXRD) experiments were completed on a Stoe STADI-P X-ray diffractometer equipped with a position-sensitive detector (PSD) and using Cu anodes with primary beam (Ge Crystal) monochromation, producing Cu $K_{\alpha 1}$ radiation (λ = 1.54056 Å). Samples were ground to a fine powder and mounted between two lightly greased Mylar film disks. Once prepared the film was mounted onto a sample disk. Diffraction patterns were initially collected from 5° to 70° (2θ angles) in steps of 0.02° using a continuous scan time of 12 s. Where necessary, higher quality patterns were obtained by increasing the scanning rate.

2.2.5 Generation of Synchrotron X-rays[115,116,119]

Synchrotron light is emitted when a beam of electrons travelling close to the speed of light is bent by a powerful magnetic field and the light produced spans the entire electromagnetic spectrum, producing X-rays, infrared and ultraviolet light. To date, there are approximately 50 operating synchrotrons in the world, the three biggest being the APS (USA), ESRF (France) and Spring-8 (Japan). Synchrotron radiation is currently of considerable use in the structural characterisation of many

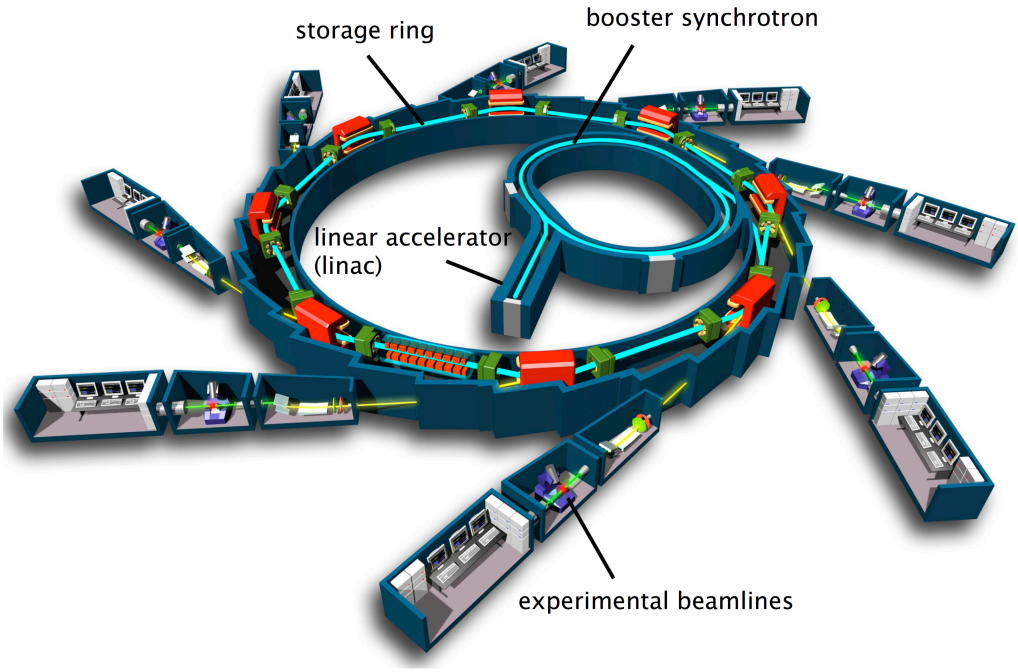

Figure 2.7: A schematic representation of a synchrotron facility.[120]

complex solids and is utilised across many disciplines, principally chemistry, physics and biology.

For example, at Diamond Synchrotron Light Source[121] electrons are produced in an electron gun and accelerated through a series of three particle accelerators namely the linear accelerator (linac), booster synchrotron and large storage ring, as shown in Figure 2.7. The electrons are initially accelerated to 100 MeV using the linear accelerator, after which they enter into the booster synchrotron where they follow a specially designed trajectory composed of both straight and semicircular curved sections. To drive the electrons round the bends within the booster synchrotron dipole bending magnets are utilised. When in the straight sections a radiofrequency (rf) voltage source is used to further accelerate the electrons until they reach an energy of 3 GeV. Once the correct energy is reached electrons are transferred into the third and final particle accelerator, the storage ring. In a similar manner to conventional X-ray sources the storage ring is held under vacuum to prevent interaction or collision of the electrons with air particles.

Electrons emit very intense beams of X-rays, infrared and ultraviolet light called synchrotron light as they travel round the storage ring. As this occurs the electrons become lighter and their path through the ring begins to change until they eventually hit a wall and are lost. To compensate for this loss the RF system in the booster ring provides each electron with a 'kick' each time they complete one cycle of the ring. This 'kick' replaces the energy lost in the previous cycle enabling them to then follow the correct path. The length of time the electrons remain in the storage ring is defined as the lifetime of the beam. When circulating in the ring the electrons collide with the few particles that remain in the vacuum and are then lost, thereby requiring new electrons to be added. Modern third generation synchrotron sources, such as Diamond Light Source Synchrotron,[121] function using a 'top-up' mode where the electron beam is topped up at regular intervals. This is a highly advantageous system as the beam is highly stable and the quality of beam produced remains high for longer periods of time.

The dimensions of the storage ring are dependent solely upon the research facility utilised. The work presented within this particular investigation used Diamond Light Source Synchrotron, Didcot, United Kingdom.[121] Diamond's storage ring has a circumference of 562 m and is composed of 24 straight sections that are angled together to form a closed loop. Inside the storage ring 48 large electromagnets or dipole magnets are utilised to curve the electron beam between adjacent straight sections. Beamlines are strategically placed at tangents to the ring to guide narrow beams of synchrotron light into the various experimental hutches. Each beamline is specifically designed for a particular type of experiment, for example high-resolution powder diffraction, small molecule diffraction and diffraction using extreme conditions (such as diamond anvil high pressure cells). Synchrotron X-rays are more intense than laboratory sources and offer a wide range of tunable wavelengths. Synchrotron sources are a highly desirable facility and, as a result, user time available is becoming increasingly limited.

2.2.6 Synchrotron X-ray Diffraction

All high-resolution X-ray diffraction data was collected using beamline I11 (high-resolution powder diffractometer) at Diamond Light Source Synchrotron ($\lambda = 0.827267$ Å), shown in Figure 2.8.[122-124] Within this particular study both room and low temperature diffraction experiments were completed using this facility. Room temperature samples were loaded into 0.5 mm or 0.7 mm glass capillaries and mounted on brass capillary spinners. The low temperature investigation was conducted using a PheniX cryostat (11 – 295 K) in which the sample was loaded into an aluminium capillary and mounted onto a flat brass plate that employed a continuous 'rocking' motion throughout data collection. Peaks resulting from the aluminium capillary were present in all low temperature diffraction patterns obtained and for ease of analysis these peaks were excluded from the data during Rietveld refinement. All data was automatically collected from 5° to 145° using the five multi-analysing crystal detectors (MACs), each composed of 9 Si (111) analysing crystals and 9 detectors. Typical collection times were between thirty minutes and one hour. Only data up to and including 70° was utilised and analysed using the General Structure Analysis System (GSAS) software package.[125]

2.2.7 Neutron Diffraction[126]

The neutron is an uncharged particle with spin 1/2 and mass 1.675×10^{-27} kg. Neutrons, unlike X-rays, are scattered by atomic nuclei, thereby making neutron diffraction isotope specific. This can be of considerable use when trying to distinguish between different isotopes of the same element, as each will scatter neutrons in a different manner. The scattering factor for neutrons is therefore not proportional to the number of electrons and, in turn, does not diminish with scattering angle, as shown in Figure 2.9. Neutrons are exceptionally effective in locating lighter elements, such as oxygen and hydrogen, when in the presence of much heavier elements such as bismuth and lead. Unlike X-rays neutrons possess spin, I = 1/2, therefore they have the ability to interact with any

(a)

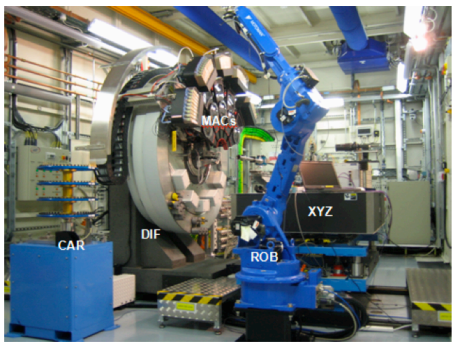

(b)

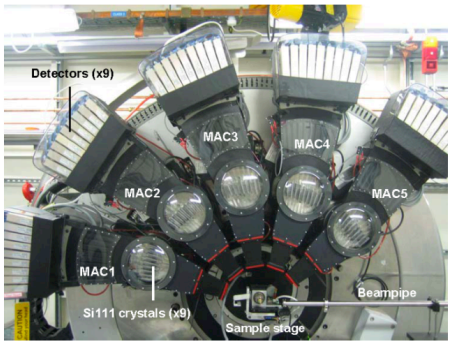

Figure 2.8: Beamline I11 at Diamond Light Source Synchrotron.[124]

magnetic species in a sample, making them an invaluable tool for solving complex magnetic structures. If magnetic centres of interest are present there will be additional interactions with the neutrons bombarding the sample, resulting in the appearance of extra peaks in the diffraction pattern obtained. However, there are many associated disadvantages of the technique, principally the high running and maintenance costs, the complexity of generating neutrons and the large sample quantities required (typically 5 g for powder diffraction). Furthermore, user time allocated at neutron sources is becoming increasingly limited and, in turn, highly competitive.

2.2.8 Generation of Neutrons[127,128]

Neutrons are generated from one of two sources, either a nuclear reactor or a spallation source. The first of these relies upon a series of controlled chain reactions of neutron-induced fission of a heavy nucleus, most commonly ^{235}U. In a spallation source a heavy metal target is bombarded by high energy protons (~50 MeV), generated using a linear particle accelerator. Modern spallation sources utilise a synchrotron in conjunction with the linear accelerator to produce higher energy protons (~800 MeV). During collision of the protons with the metal target enough energy is imparted to the target to produce spallation neutrons. However, the neutrons produced in each case are too high in energy and possess too short a wavelength to be utilised in diffraction experiments. Therefore, to

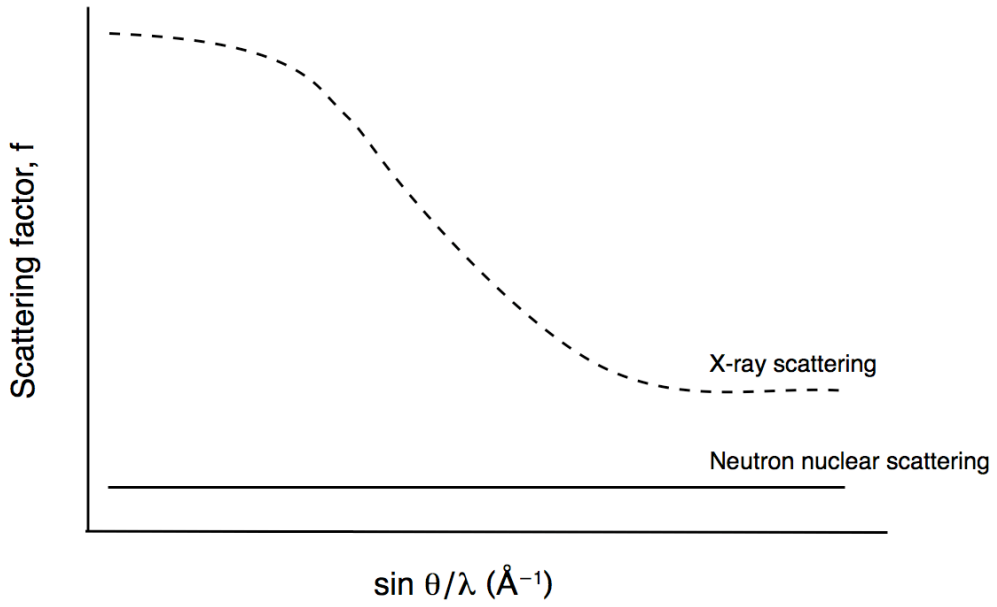

Figure 2.9: Schematic representation of the neutron scattering factor.

be used effectively the neutrons need to be slowed, i.e., reduce their frequency, using a moderator, the type of which varies depending upon the facility used. Once the neutrons have been slowed sufficiently to reduce their frequency the corresponding wavelength will be increased. There are, however, fundamental differences between the neutrons produced by a nuclear reactor and those from a spallation source. Neutrons from nuclear reactors need to be passed through a monochromator to reduce the neutrons incident on a sample to a single or 'fixed' wavelength. In this type of experiment the detector is then moved during data collection. An example of a fixed wavelength facility is the high-resolution D2B diffractometer (λ = 1.594 Å) at the Institut Laue-Langevin (ILL), Grenoble.[128] In contrast, neutrons from spallation sources arrive at an instrument in 'bunches'; hence neutrons possessing a variety of wavelengths are utilised and separated according to their different velocities. In such cases, fixed detector banks are used because each of the wavelengths will diffract off the *hkl* planes in the structure with different d-spacings. This technique is known as time-of-flight (TOF) neutron diffraction and one example of such a diffractometer is POLARIS at the ISIS neutron spallation source, United Kingdom.[129] Within this particular

structural investigation solely TOF neutron diffraction experiments have been completed, specific details of which can be found in the following sections.

2.2.9 POLARIS[130-133]

POLARIS is a medium resolution TOF neutron powder diffractometer located at the ISIS neutron spallation source, Rutherford Appleton Laboratories, Didcot, United Kingdom. POLARIS consists of three fixed detector banks, backscattering (130-160°), 90 degrees (85-95°) and low angle (28-42°) composed of ^{3}He tube, ZnS scintillator and ^{3}He tube detectors respectively. The sample is conventionally held in a cylindrical vanadium can in a tank evacuated to pressures of ~0.1 mbar. Samples are held under vacuum principally to avoid collision of the incident and scattered neutrons with air. All experiments completed using POLARIS were under ambient reaction conditions with use of the sample changer. Once collected, all datasets were normalised using the GENIE program and converted into GSAS format for compatibility with the GSAS software.

2.2.10 High Resolution Powder Diffractometer (HRPD)[134,135]

HRPD is the high-resolution TOF neutron powder diffractometer situated at the ISIS neutron spallation source, Rutherford Appleton Laboratories, Didcot, United Kingdom.[129] To gain the required high-resolution HRPD possesses an extended flight path and is therefore located ~100 m from the ISIS target at the end of the neutron guide. HRPD is utilised principally in the study of complex materials exhibiting subtle structural variations such as phase transitions, hence extremely accurate and precise crystallographic data is required to characterise such changes. HRPD is currently the highest resolution neutron powder diffractometer of its type in the world and consists of three fixed detector banks, the backscattering (160-176°), 90 degree (87-93°) and low angle (28-32°) banks. Both the backscattering and 90 degree banks are composed of

ZnS scintillator detectors whilst the low angle bank uses ^{3}He tube detectors. The highest resolution data is acquired using the backscattering bank with a $\delta d/d$ resolution of ~4 x 10^{-4} and can record out to d-spacings of up to 6 Å. The measurable d-spacing range can be extended to over 20 Å using the complementary detectors at 90 degrees and low angle; however, the resolution is considerably reduced. Samples are conventionally held in vanadium cans, the size of which varies depending upon sample quantity. All experiments were completed under ambient reaction conditions. Once collected, all datasets were normalised using the GENIE program and converted to the relevant GSAS format for compatibility with the GSAS software.

2.2.11 Comparison of Diffraction Techniques

Laboratory X-ray diffraction is typically only sufficient to determine phase purity owing to relatively low resolution and poor data quality. Synchrotron X-ray and neutron diffraction are superior techniques owing, fundamentally, to higher resolution. A comparison of data obtained from each of the three sources is shown in Figure 2.10 and highlights the considerable differences in peak definition and overall resolution. In particular, the signal-to-noise ratio is greatly improved in both the synchrotron XRD and neutron data when compared with the laboratory XRD data. Neutron diffraction is often essential in the structural characterisation of dense ternary oxides as location of the oxygen atoms within such structures is extremely challenging and requires well-resolved, precise crystallographic data. Neutron diffraction is also known to enhance superstructure peaks within such solids; hence it is possible to identify any superstructure characteristics exhibited. Within this particular investigation neutron diffraction was of considerable use as it enabled the key identification of subtle structural discrepancies otherwise unseen using high-resolution X-ray methods.

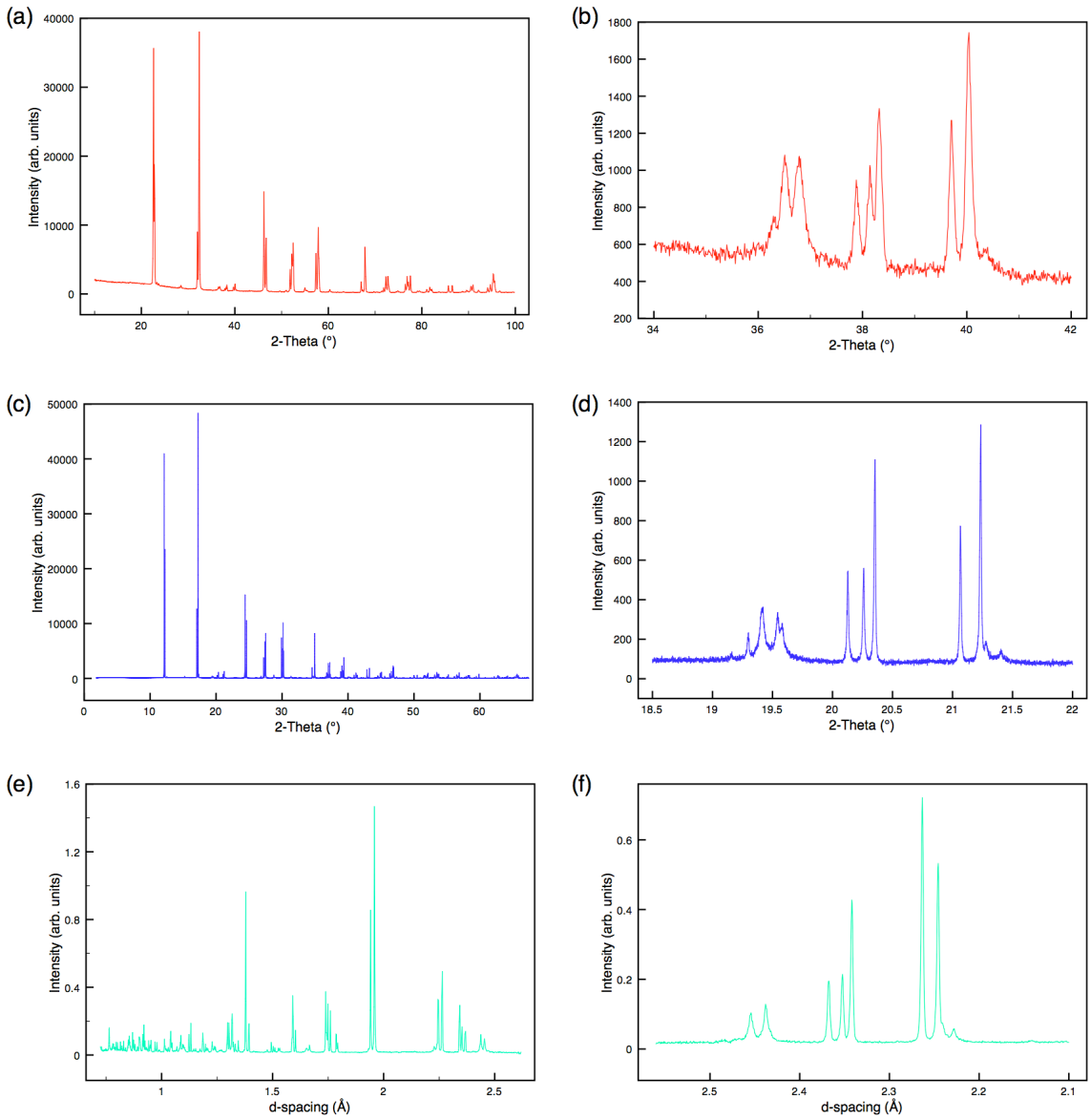

Figure 2.10: Comparison of Rietveld profiles for commercial $NaNbO_3$ (Aldrich) obtained from (a) conventional "laboratory" XRD, (c) synchrotron XRD and (e) neutron powder diffraction. (b, d, f) show corresponding expansions of the 'superstructure' peaks, highlighting the differences observed in resolution between the three techniques.

2.3 Rietveld Analysis[136]

The use of powder diffraction techniques in the determination of crystal structures is extremely challenging. However, it is one of the most common uses of powder data and the procedure adopted to complete

such structural investigations is that of the Rietveld method, originally proposed by Hugo Rietveld.[137-139] To use this particular technique some prior knowledge of the structural model is required, enabling the refinement process to be simplified considerably.

Polycrystalline samples routinely generate a considerable number of peaks within any powder diffraction pattern, the majority of which occur at low d-spacings. Owing to the quantity of peaks generated they often overlap with one another making it virtually impossible to accurately identify and fit each individual peak. The Rietveld method provides an accurate solution to such a problem by attempting to fit a structural model to the pattern as a whole, thereby avoiding the problem of indexing and fitting each peak separately. The method adopted within this particular type of refinement is a least squares minimisation, in which model parameters for a theoretical structure are refined until a reasonable degree of fit is achieved with the experimental powder pattern. The theoretical model utilised is commonly obtained from the Inorganic Crystal Structure Database.[140] Structural refinement involves the adjustment of factors such as the background coefficients, detector zero point, instrumental parameters, lattice parameters, profile coefficients, isotropic and anisotropic thermal factors and atomic positional coordinates. During any structural refinement the residual, S_y, (as detailed by Equation 2.4, where the parameter y_{oi} corresponds to the observed intensity and y_{ci} is the calculated intensity) is minimised using a least squares method.

$$S_y = \sum_i \frac{1}{y_i}(y_{oi} - y_{ci})^2 \qquad (2.4)$$

When S_y is a minimum the 'best' possible fit between the calculated and experimental patterns is achieved. However, this does not take into consideration the chemical accuracy of the model. To determine the quality of fit obtained R-factors such as the R-profile, R_p, and R-weighted profile, R_{wp}, are utilised, given by Equations 2.5 and 2.6 respectively. Profile weighting is hugely important within the Rietveld method as it attempts to fit all peaks in the pattern equally, with no preference given to

peaks of higher intensity. Therefore, to prevent peaks of greater intensity dominating any refinement the parameter $1/y_i$ is used. This enables peaks of weaker intensity to be fitted with the same preference as peaks exhibiting the greatest intensity in any diffraction pattern.

$$R_p = \frac{\sum_i |y_{oi} - y_{ci}|}{\sum_i y_{oi}} \tag{2.5}$$

$$R_{wp} = \left[\frac{\sum_i \frac{1}{y_i}(y_{oi} - y_{ci})}{\sum_i \frac{1}{y_i}(y_{oi})^2} \right]^{\frac{1}{2}} \tag{2.6}$$

$$\chi^2 = \frac{\sum_i \frac{1}{y_i}(y_{oi} - y_{ci})^2}{N - P + C} \tag{2.7}$$

An additional parameter used to establish the quality of a fit is given by χ^2, Equation 2.7, where N is the number of observations, P is the number of refined parameters and C is the number of constraints. This parameter is particularly useful as it indicates the 'goodness' of fit. When χ^2 is equal to one this is indicative of a perfect fit. Therefore, to determine the quality of Rietveld fit the closeness of χ^2 to one is measured. All structural refinements were completed using GSAS.

2.4 Basic Principles of NMR

Nuclear Magnetic Resonance (NMR) is a hugely powerful technique and is widely used in the study and characterisation of complex structures. Almost all stable elements in the periodic table possess active nuclei and therefore NMR is routinely utilised, both in solution and in the solid state.

2.4.1 Nuclear Magnetism

Nuclei possess an intrinsic spin angular momentum, **I**, with a corresponding spin quantum number, I, related to the composition of the nucleus. I may be zero or any positive integer or half-integer value. The magnitude of the spin angular momentum is given by

$$|\mathbf{I}| = \hbar\left[I(I+1)\right]^{1/2} \quad . \tag{2.8}$$

The projection of this angular momentum vector onto the z-axis is given by $I_z = m_I\hbar$, where m_I is the magnetic quantum number with values ranging from −I to +I, resulting in 2I + 1 states degenerate in energy. The circulating charge creates a magnetic dipole moment, $\boldsymbol{\mu}$, given by

$$\boldsymbol{\mu} = \gamma\mathbf{I} \quad , \tag{2.9}$$

where γ is the gyromagnetic ratio of the nucleus. The orientation of $\boldsymbol{\mu}$ is either parallel (if γ is positive) or anti-parallel (if γ is negative) to **I**. In the absence of an external magnetic field all 2I + 1 orientations of I are degenerate in energy and orientated at random. Upon application of a strong magnetic field, B_0, the axis of quantization is defined and the nuclear spins align themselves relative to B_0. Upon doing so the degeneracy of the 2I + 1 is lifted, as shown in Figure 2.11 for spin I = 1/2, 1 and 3/2 nuclei. When the field is applied along the z-axis the energy is given by

$$E = -\mu_Z B_0 \quad , \tag{2.10}$$

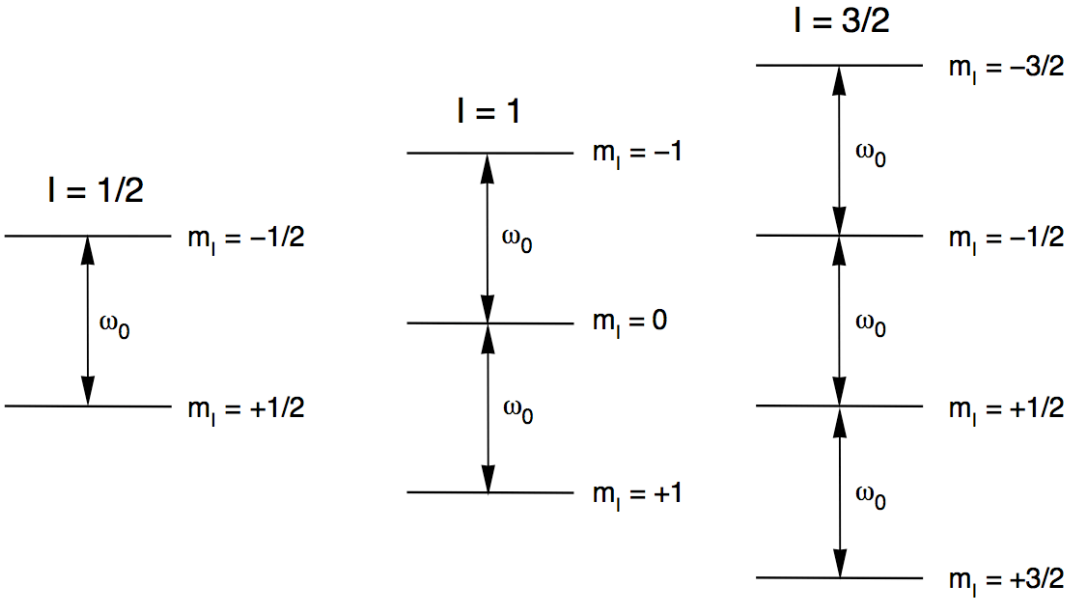

Figure 2.11: The effect of the Zeeman interaction upon the nuclear energy levels for spin (a) I = 1/2, (b) I = 1 and (c) I = 3/2 nuclei.

where μ_Z is the projection of the magnetic dipole moment onto the z-axis and B_0 is the applied magnetic field in this direction. This is known as the Zeeman interaction. In a macroscopic sample at thermal equilibrium there will be a very slight excess of spins in the lower energy level which gives rise to a net or bulk magnetization vector, $\mathbf{M_0}$. In NMR the spectroscopic selection rule for an observable transition is $\Delta m_I = \pm 1$ and the frequency of any such transition is therefore given by

$$\omega_0 = \frac{\Delta E}{\hbar} = -\gamma B_0 \quad , \tag{2.11}$$

where ω_0 is the Larmor frequency with units of rad s^{-1}.

2.4.2 The Vector Model

Although spin must be treated quantum mechanically, it is possible to treat the ensemble of spins in a macroscopic sample in a classical way. The 'vector model' was first proposed by Bloch and is now routinely utilised as a geometrical interpretation of the basic principles involved in NMR.[141] Modern spectrometers commonly employ pulsed NMR methods

in which short pulses of intense linearly oscillating radiofrequency (rf) radiation is applied to a sample. The frequency of this radiation, ω_{rf}, is close to the resonance frequency, ω_0. The applied pulse, with strength B_1 and duration τ_p, interacts with the nuclear spins in a sample, exciting all resonances simultaneously, thereby affecting the orientation of the bulk magnetization vector, $\mathbf{M_0}$, as shown in Figure 2.12. Pulsed NMR methods are highly advantageous over previous continuous wave (CW) methods as the experiment can be repeated more rapidly which, in turn, improves signal-to-noise which can be limiting in NMR spectroscopy owing to the low Boltzmann population differences. The interaction of a pulse with a sample is extremely difficult to visualise in the laboratory frame and so a 'rotating frame' is utilised. This is a frame of reference which itself is rotating about the z-axis at a frequency ω_{rf}. In this frame, the bulk magnetization vector precesses around the magnetic field at a frequency Ω, with an effective magnetic field, B_0^{eff}, along the z-axis.

$$\Omega = \omega_0 - \omega_{rf} \tag{2.12}$$

$$B_0^{eff} = \frac{\Omega}{\gamma} = -B_0 - \frac{\omega_{rf}}{\gamma} \quad . \tag{2.13}$$

In the rotating frame a pulse can be described as a static field, B_1, applied perpendicular to B_0. If applied along x the bulk magnetization vector, $\mathbf{M_0}$, nutates into the xy plane. Once the pulse is removed $\mathbf{M_0}$ undergoes free precession at a frequency $\Omega = \omega_0 - \omega_{rf}$, as shown in Figure 2.12. The angle through which the magnetization nutates during the pulse is defined as the 'flip angle', β,

$$\beta = \omega_1 \tau_p \quad , \tag{2.14}$$

where $\omega_1 = -\gamma B_1$ and τ_p is the duration of the pulse. Flip angles commonly utilised in NMR experiments are $\beta = 90°$, where the magnetization is placed in the xy plane, and $\beta = 180°$, where the magnetization is inverted to lie along the −z-axis.

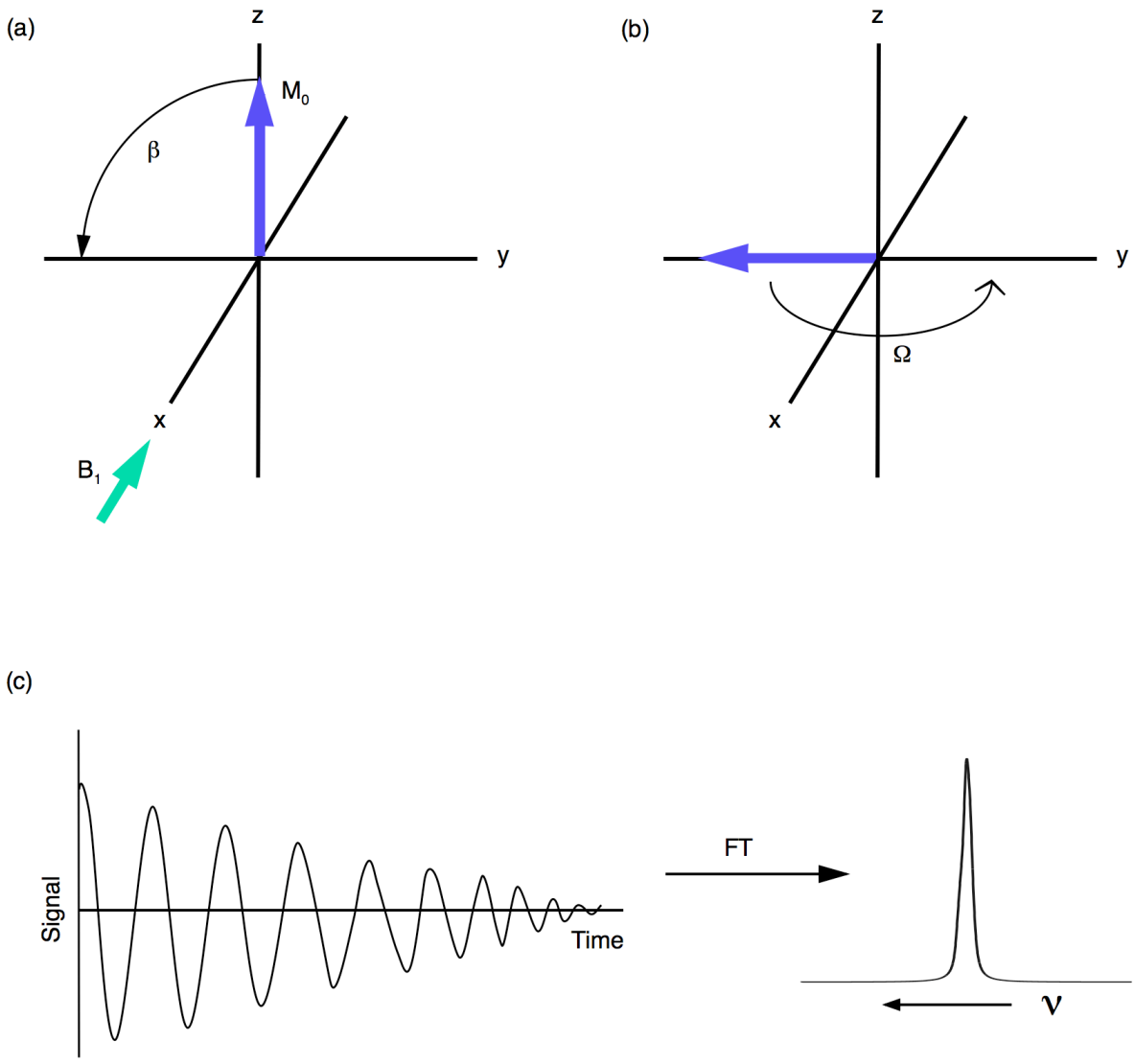

Figure 2.12: (a) Vector model representation of the effect of a pulse applied along the x axis of the rotating frame on the bulk magnetization vector M_0. (b) After nutation into the yx plane the vector undergoes free precession at frequency Ω. (c) A schematic representation of an FID and corresponding spectrum post Fourier transformation and phasing.

2.4.3 Relaxation

Various relaxation effects, returning the system to equilibrium, dampen the precession of the magnetization around the z-axis. Transverse or spin-spin relaxation, characterised by a time constant T_2, is defined as the loss of magnetization from the xy plane and occurs through

interaction between the spins. Longitudinal or spin-lattice relaxation, with time constant T_1, describes the return of the z component of the magnetization to equilibrium. Values of T_1 are sample dependent and, in some cases, are extremely long. For example, in solids ^{89}Y (I = 1/2) has typical T_1 values on the order of hundreds to thousands of seconds. As a result, this determines the rate at which experiments can be repeated. The damped precession of $\mathbf{M_0}$ is known as the free induction decay (FID) and is the signal detected when an induced voltage is detected in the receiver coil. The FID is a time-domain signal and to convert to a frequency-based spectrum Fourier Transformation (FT) is required.[142,143]

2.4.4 Fourier Transformation

The FID obtained is the sum of many different oscillating waves, each with a different frequency, amplitude and phase. This signal is commonly detected using a technique known as quadrature detection[144] which enables simultaneous measurement of both the x and y components of the FID. For each resonance observed in the spectrum two signals are acquired, one a cosine and the other a sine function of the offset frequency Ω, decaying at a rate of $1/T_2$ (owing to transverse relaxation effects). These signals are the real and imaginary parts of a complex time-domain signal, s(t), given by[145,146]

$$s(t) = \left[\cos\Omega t + i\sin\Omega t\right]\exp(-t/T_2) \tag{2.15}$$

$$s(t) = \exp(i\Omega t)\exp(-t/T_2) \quad t \geq 0 \tag{2.16}$$

$$s(t) = 0 \quad t < 0 \ . \tag{2.17}$$

The signal is then converted to a frequency-domain spectrum S(ω) by Fourier transformation

$$S(\omega) = \int_0^\infty s(t)e^{-i\omega t}dt \ . \tag{2.18}$$

The frequency-domain function, S(ω), is composed of both real and imaginary parts, given by Equations 2.20 and 2.21, respectively. The real part corresponds to an absorptive Lorentzian lineshape and the imaginary part the corresponding dispersive Lorentzian.

$$S(\omega) = A(\Delta\omega) - iD(\Delta\omega) \tag{2.19}$$

$$A(\Delta\omega) = \frac{1/T_2}{(1/T_2)^2 + (\Delta\omega)^2} \tag{2.20}$$

$$D(\Delta\omega) = \frac{\Delta\omega}{(1/T_2)^2 + (\Delta\omega)^2} \quad . \tag{2.21}$$

Spectral lineshapes, in reality, are neither purely real or imaginary. They instead possess an arbitrary phase composed of both the real and imaginary parts and to obtain absorption-phase lineshapes a process known as 'phasing' is required post Fourier transformation. This is achieved by taking linear combinations of the real and imaginary parts of the spectrum until the desired lineshape is achieved. A schematic representation of an FID and corresponding spectrum, post Fourier transformation and phasing, are shown in Figure 2.12(c).

2.4.5 Density Operator Formalism

Macroscopic samples are known to contain large numbers of nuclear spin systems, each of which may be described quantum mechanically by a wavefunction, Ψ(t). Each wavefunction may be expanded as a linear combination of the elements of an orthogonal basis set $|i\rangle$:

$$\Psi(t) = \sum_i c_i(t)|i\rangle \quad , \tag{2.22}$$

where $c_i(t)$ are time-dependent coefficients. A more compact approach involves using a density operator, σ(t), whose matrix representation is termed the density matrix.[147] The elements of this matrix, $\sigma_{i,j}(t)$, are the products of the expansion coefficients of the wavefunction Ψ(t), i.e.,

$$\sigma_{i,j}(t) = \langle i|\sigma(t)|j\rangle$$

$$= \overline{c_i(t)c_j(t)^*} \quad , \tag{2.23}$$

where the overbar and * denote an ensemble average and complex conjugate, respectively. The density operator formalism,[147] when compared with the classical vector model description, is a more rigorous and compact quantum mechanical approach to describe the ensemble of spins during the course of an NMR experiment. For a spin $I > 1/2$ nucleus quantum mechanical behaviour is a more convenient description.

2.4.6 Coherence

Consider an ensemble of non-interacting spins. Each spin, with wavefunction $\Psi(t)$, can be described as a superposition of the states $|\alpha\rangle$ and $|\beta\rangle$. The contributions to these states, described by coefficients $c_\alpha(t)$ and $c_\beta(t)$, possess both a time and phase dependence. At $t = 0$, the complex superposition coefficients $c_\alpha(t)$ and $c_\beta(t)$ have phases ϕ_α and ϕ_β, respectively and $\Psi(t)$ is given by,

$$\Psi(t) = c_\alpha(t)e^{i\phi_\alpha}|\alpha\rangle + c_\beta(t)e^{i\phi_\beta}|\beta\rangle \quad . \tag{2.24}$$

The matrix representation of the density operator, $\sigma(t)$, for the system therefore takes the following form

$$\sigma(t) = \begin{pmatrix} c_\alpha c_\alpha^* & c_\alpha c_\beta^* e^{i(\phi_\alpha - \phi_\beta)} \\ c_\beta c_\alpha^* e^{i(\phi_\beta - \phi_\alpha)} & c_\beta c_\beta^* \end{pmatrix} \quad . \tag{2.25}$$

The diagonal elements $c_\alpha c_\alpha^*$ and $c_\beta c_\beta^*$ are equal to $|c_\alpha^2|$ and $|c_\beta^2|$ respectively, thus, they refer to the populations of the $|\alpha\rangle$ and $|\beta\rangle$ spin states. If the relative phases of each of the spins are the same then the off-diagonal elements $c_\alpha c_\beta^* e^{i(\phi_\alpha - \phi_\beta)}$ and $c_\beta c_\alpha^* e^{i(\phi_\beta - \phi_\alpha)}$ will have non-zero magnitude. In

such cases there is said to be phase coherence between the spins. The converse is also true, if each spin exhibits a random phase difference, then the off-diagonal elements in the density matrix will, on average, sum to zero and in such cases no coherence exists in the ensemble. Consider the density matrix for a single spin I = 3/2 nucleus where the chosen basis set is the set of eigenstates of the Zeeman Hamiltonian, i.e., m_I = 3/2, 1/2, −1/2, −3/2. The density matrix is of the form

$$\sigma(t) = \begin{pmatrix} \sigma_{1,1}(t) & \sigma_{1,2}(t) & \sigma_{1,3}(t) & \sigma_{1,4}(t) \\ \sigma_{2,1}(t) & \sigma_{2,2}(t) & \sigma_{2,3}(t) & \sigma_{2,4}(t) \\ \sigma_{3,1}(t) & \sigma_{3,2}(t) & \sigma_{3,3}(t) & \sigma_{3,4}(t) \\ \sigma_{4,1}(t) & \sigma_{4,2}(t) & \sigma_{4,3}(t) & \sigma_{4,4}(t) \end{pmatrix}, \tag{2.26}$$

where the elements $\sigma_{i,i\pm1}(t)$ represent coherences with $\Delta m_I = \pm1$, commonly denoted as coherence order p = ±1. It is these coherences which are directly observable in an NMR experiment. However, by convention only p = −1 coherences are detected when quadrature detection[144] is utilised. The elements $\sigma_{i,i\pm2}(t)$ and $\sigma_{i,i\pm3}(t)$ represent multiple-quantum coherences, i.e., those with coherence orders of p = ±2 and ±3 respectively. Although these are not directly observable they are utilised in many important NMR experiments.

2.5 NMR Interactions

There are many important interactions in NMR, the most dominant of which is usually the Zeeman interaction. These interactions, including the Zeeman interaction, can be described by a Hamiltonian, H, given in general form by,

$$H = I \cdot R \cdot X \tag{2.27}$$

$$H = (I_x\, I_y\, I_z) \begin{pmatrix} R_{xx} & R_{xy} & R_{xz} \\ R_{yx} & R_{yy} & R_{yz} \\ R_{zx} & R_{zy} & R_{zz} \end{pmatrix} \begin{pmatrix} X_x \\ X_y \\ X_z \end{pmatrix}, \tag{2.28}$$

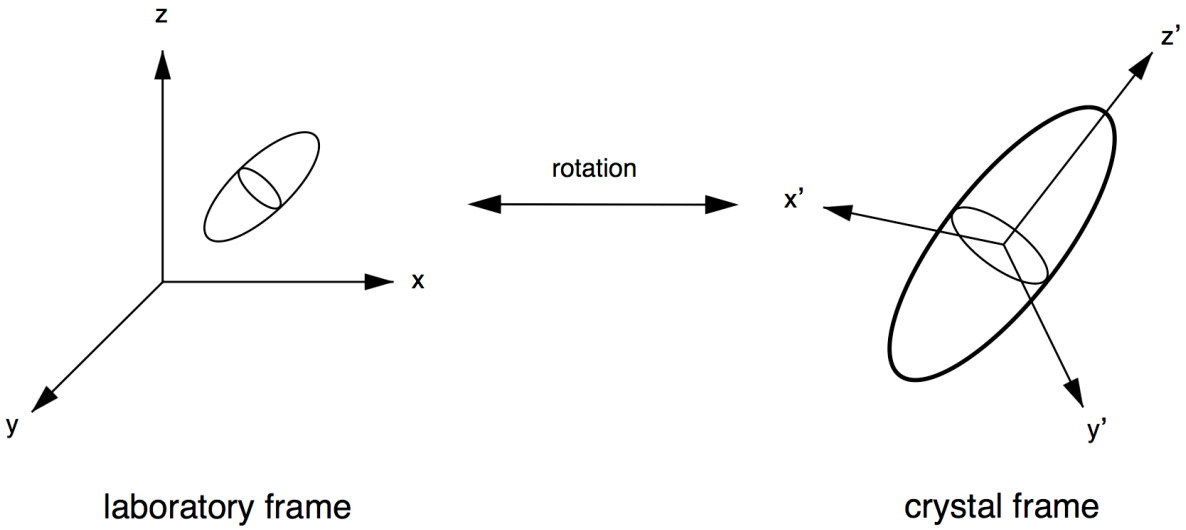

Figure 2.13: Schematic representation of the transformation of a tensor between the laboratory frame and the PAS.

where I is the spin angular momentum operator, R is a second-rank Cartesian tensor defining the interaction and X represents either a second spin operator or a magnetic field. Hence the total Hamiltonian, H, for any nucleus may be expressed as the sum of the individual Hamiltonian contributions for the Zeeman interaction, H_Z, the applied radiofrequency pulse, H_{rf}, dipolar, H_D, chemical shielding, H_{CS}, scalar, H_J, and quadrupolar, H_Q, interactions given by,

$$H = H_Z + H_{rf} + H_D + H_{CS} + H_J + H_Q \quad . \tag{2.29}$$

It is convenient to describe an interaction within a frame, defined by the magnitude and shape of the interaction itself. This is known as the Principal Axis System, or PAS, a frame where the second-rank tensor defining the interaction is defined such that all off-diagonal elements are zero. A schematic representation of the PAS is shown in Figure 2.13. To convert between the laboratory frame and the PAS a rotation is required, thereby highlighting the angular dependence of many of the interactions.

2.5.1 Chemical Shift Anisotropy (CSA)

The field experienced by a nuclear spin, in reality, is not the applied magnetic field, B_0. In a magnetic field, the electrons around a nucleus circulate and, in turn, generate a small magnetic field, B′, which either opposes or augments the applied field. Consequently, this changes the field experienced by the nucleus and perturbs the Larmor frequency

$$\omega' = -\gamma B_0(1-\sigma) \quad , \tag{2.30}$$

where σ is a shielding parameter. In reality, the shielding is orientation dependent and is described by a second-rank tensor, $\boldsymbol{\sigma}$. The Hamiltonian describing the chemical shielding, H_{CS}, is given by

$$H_{CS} = \mathbf{I}\cdot\boldsymbol{\sigma}\cdot\gamma\mathbf{B_0} \quad . \tag{2.31}$$

When B_0 is defined to be along the z-axis the secular approximation may be applied and the Hamiltonian becomes

$$H_{CS} = \gamma B_0 \sigma_{zz} I_z \quad . \tag{2.32}$$

More usually the shielding tensor is expressed in the PAS. In this frame the tensor can be represented by an ellipsoid, as illustrated in Figure 2.14, and is defined by three parameters, the isotropic shielding, σ_{iso}, the shielding anisotropy, $\Delta\sigma_{CS}$, and the asymmetry, η_{CS}, given by

$$\sigma_{iso} = \frac{1}{3}(\sigma_{11} + \sigma_{22} + \sigma_{33}) \tag{2.33}$$

$$\Delta\sigma_{CS} = (\sigma_{33} - \sigma_{iso}) \tag{2.34}$$

$$\eta_{CS} = \frac{(\sigma_{11} - \sigma_{22})}{(\sigma_{33} - \sigma_{iso})} \quad , \quad 0 < \eta_{CS} < 1 \tag{2.35}$$

where σ_{11}, σ_{22} and σ_{33} are the three principal components of the tensor. To convert from the PAS to the laboratory frame a rotation is necessary,

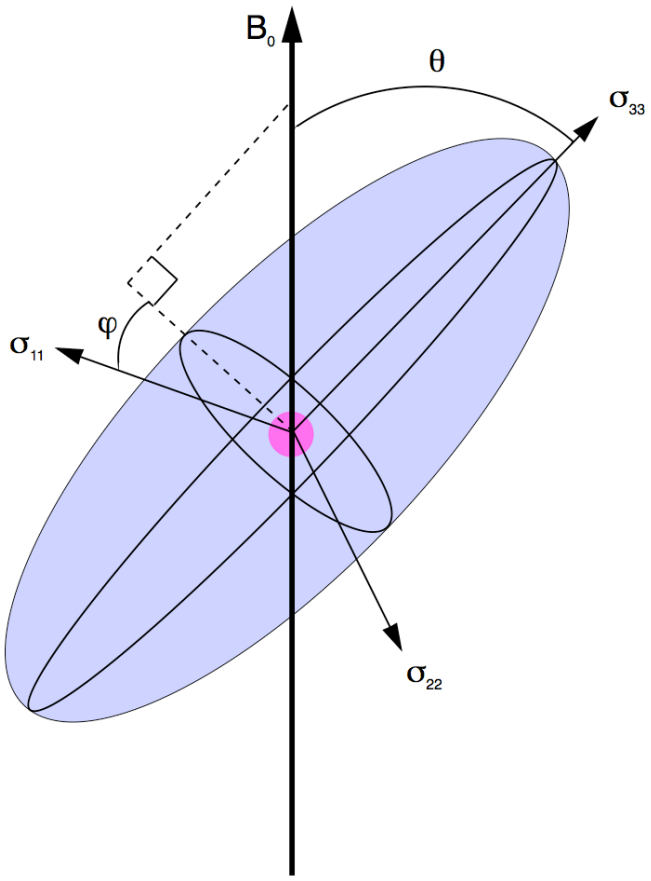

Figure 2.14: A schematic representation of the shielding tensor in the PAS, where σ_{11}, σ_{22} and σ_{33} are the three principal components of the tensor. The angles θ and ϕ are the angles defining the orientation of the tensor relative to the magnetic field B_0.

revealing the angular dependence of the chemical shielding. This is highlighted in the σ_{zz} component[148] of the shielding tensor, given by

$$\sigma_{zz} = \sigma_{iso} + \frac{\Delta\sigma_{CS}}{2}\left[(3\cos^2\theta - 1) + \eta_{CS}(\sin^2\theta\cos 2\varphi)\right] . \qquad (2.36)$$

For different orientations of the shielding tensor PAS, a different chemical shift is observed. In solution the chemical shielding is averaged solely to its isotropic value, shown in Equation 2.33, by rapid molecular tumbling and, as a result, lineshapes are inherently sharp and narrow. Solids, however, are often densely packed and therefore do not usually exhibit such molecular motion, hence they display the full extent of the CSA, producing extremely broad spectra. Powders are composed of millions of tiny crystallites, each with a different orientation with respect to B_0, hence

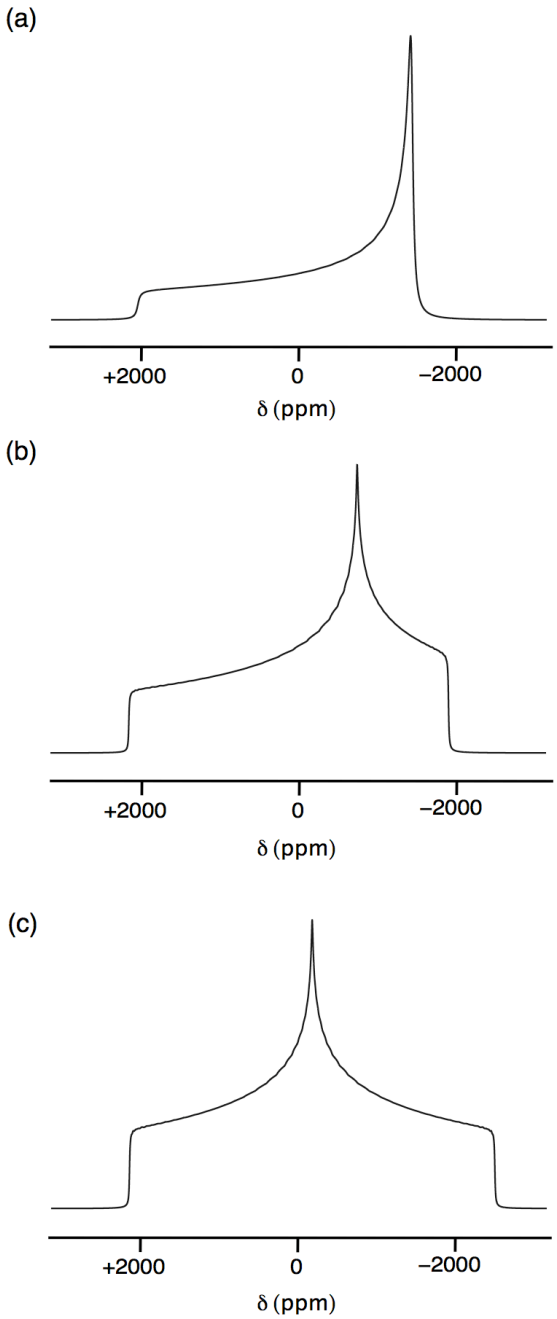

Figure 2.15: Simulated CSA lineshapes for a spin I = 1/2 nucleus with $\Delta\sigma_{CS}$ = 2000 ppm and asymmetry, η_{CS}, (a) 0, (b) 0.5 and (c) 1.

shifts from all possible orientations will be observed resulting in broad 'powder-pattern' lineshapes. Powdered CSA lineshapes simulated with η_{CS} = 0, 0.5 and 1 are shown in Figures 2.15(a), (b) and (c), respectively. The lineshapes simulated highlight how the shape of the powder-pattern line observed varies depending upon η_{CS}. Specific details are given in the figure caption.

The shielding is an inconvenient measure of the chemical shift and therefore a deshielding parameter, δ, is used, defined by

$$\delta = 10^6 \left(\frac{\omega - \omega_{ref}}{\omega_{ref}}\right) \tag{2.37}$$

where ω and ω_{ref} are the resonance frequencies of the nucleus of interest and a standard or reference.[149] The chemical shift of a nucleus is a property that reflects the environment the nucleus experiences. It therefore provides valuable information regarding the electron distribution around the nucleus. The chemical shift is dimensionless and quoted in parts per million (ppm).

2.5.2 Dipolar Coupling

The nuclear magnetic dipole moments of nuclei produce small localised magnetic fields that, in turn, interact with dipole moments of nearby nuclei. This through space interaction, referred to as dipolar coupling, is orientationally dependent, as the effect of the localised field from one spin to another depends upon the relative position of the two spins. This interaction is averaged to zero in solution by rapid molecular tumbling. In solids, however, the dipolar interaction produces an associated broadening of the observed spectrum. In the laboratory frame the dipolar Hamiltonian, H_D, between two spins I and S contains many orientationally dependent terms, and therefore a truncated form is usually used. Hence, for two homonuclear spins (I = S), separated by an internuclear distance r_{IS}, a truncated version of the dipolar Hamiltonian after the secular approximation is given by[150]

$$H_D^{IS} = \omega_D \left[3I_z S_z - \mathbf{I} \cdot \mathbf{S}\right] , \tag{2.38}$$

where ω_D is the dipolar splitting parameter, given by

$$\omega_D = \omega_D^{PAS} \left(\frac{3\cos^2\theta - 1}{2}\right) \tag{2.39}$$

with[151,152]

$$\omega_D^{PAS} = \frac{-\mu_0}{4\pi}\frac{\gamma_I\gamma_S\hbar}{r_{IS}^3} \tag{2.40}$$

where r_{IS} is the internuclear distance between two spins I and S. It must be noted that the dipolar tensor is always axially symmetric, with $\eta_D = 0$. For two heteronuclear spins ($I \neq S$) further truncation of the Hamiltonian is required, reducing it to[153]

$$H_D = \omega_D\left[2I_zS_z\right] \ . \tag{2.41}$$

Consider two isolated heteronuclear spin 1/2 nuclei I and S. A schematic representation of the energy levels for such a system is given in Figure 2.16(a). The effect of the heteronuclear dipolar coupling on the spectrum is to split each single transition into a doublet separated by $2\omega_D$, also shown in Figure 2.16(a). The dipolar interaction, in a similar manner to the CSA, is orientationally dependent, therefore the dipolar splitting observed depends upon the angle between the internuclear vector and the magnetic field. The variation of this angle produces an associated effect on the dipolar splitting also observed. In powdered or polycrystalline samples an average over all possible orientations is observed, resulting in a 'Pake doublet' lineshape, an example of which is shown in Figure 2.16(a). For two homonuclear spins I = S only two possible transitions are allowed, these are shown in Figure 2.16(b). The effect of homonuclear dipolar coupling on a spectrum is to split the single transition into a doublet, separated by $3\omega_D$, as shown in Figure 2.16(b). Powdered samples therefore result in a Pake doublet lineshape with a maximum splitting of $3\omega_D$, also shown in Figure 2.16(b).

In reality it is extremely rare to find two isolated spins, and hence there are many dipolar couplings involved between numerous spins. As a direct consequence of these interactions lineshapes typically exhibit an associated Gaussian broadening. Spectral lineshapes displaying different degrees of Gaussian broadening simulated to highlight the effect of such broadening on the observed lineshapes are shown in Figure 2.17. The

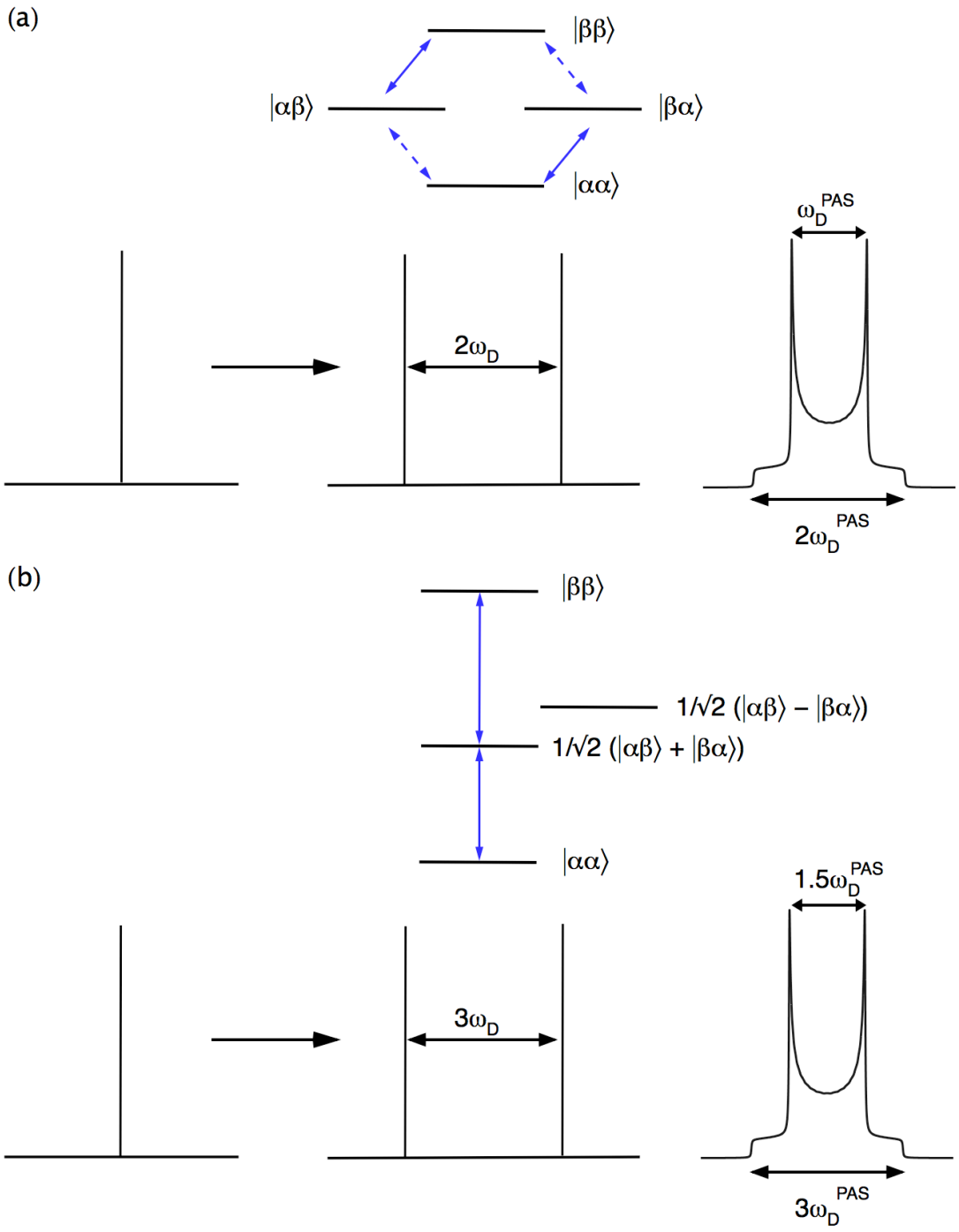

Figure 2.16: Schematic energy level diagrams for (a) two heteronuclear dipolar coupled I ≠ S = 1/2 nuclei and (b) two homonuclear dipolar coupled I = 1/2 nuclei. In each case, the single transition is split into a doublet by $2\omega_D$ and $3\omega_D$ in (a) and (b), respectively for a single orientation. For a powdered sample an average over all possible orientations is observed, resulting in a Pake doublet powder pattern lineshape.

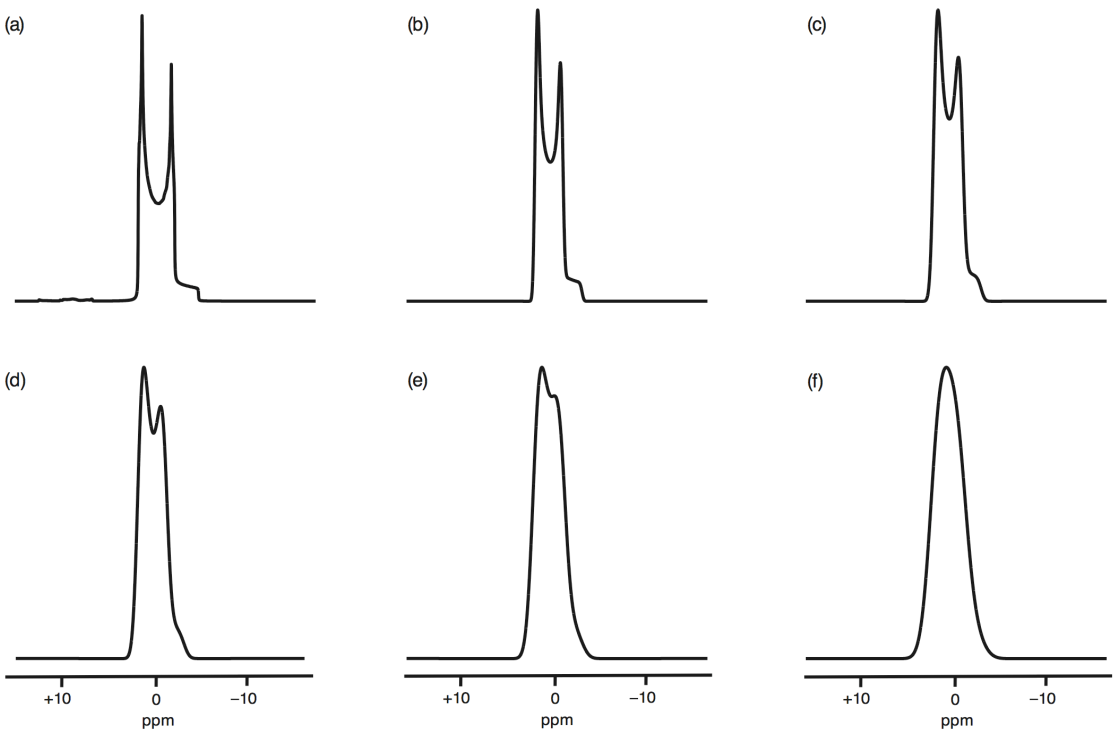

Figure 2.17: Second-order broadened quadrupolar (I = 3/2) lineshapes (see section 2.8 regarding quadrupolar interactions) simulated with C_Q = 2 MHz, η_Q = 0, $\omega_0/2\pi$ = 158.75 MHz and linebroadening of (a) 100, (b) 200, (c) 300, (d) 400, (e) 500 and (f) 600 Hz.

broadening exhibited can often lead to the loss of distinct features in the lineshape. For example in Figure 2.17(a) a distinct set of 'horns' are displayed which begin to diminish (Figures (b-e)) as the extent of Gaussian broadening is increased. The distinct features are then fully removed when the broadening is dominant, as illustrated in Figure 2.17(f). This type of broadening often hinders the extraction of any structurally relevant information. Hence, a method for removing such sources of broadening is highly desirable.

2.5.3 Scalar Couplings

In solids the scalar or J-coupling is usually the smallest of the contributions to the total Hamiltonian. In solution, high-resolution spectra commonly exhibit complex splitting patterns as a direct result of scalar couplings. For two J-coupled spins I and S the Hamiltonian[154] is given by

$$H_J = 2\pi \mathbf{J} \,.\, \mathbf{I} \,.\, \mathbf{S} \quad , \tag{2.42}$$

where **J** is a second-rank tensor defining the interaction. When B_0 is defined to be along the z-axis the secular approximation may be applied and the Hamiltonian becomes

$$H_J = 2\pi J I_z S_z \quad . \tag{2.43}$$

where J is the isotropic J-coupling or scalar coupling and is equal to the average of the diagonal elements of the J-coupling tensor. Scalar couplings are a through-bond interaction mediated by the electrons within the chemical bond. J-couplings are often present in solid-state NMR spectra; however, they are commonly only on the order of a few tens of hertz, and are therefore usually dominated by larger anisotropic interactions such as CSA and dipolar couplings. Despite this, the coupling is often utilised for the successful transfer of magnetization from one spin to another.

2.6 Magic-Angle Spinning

Magic-angle spinning (MAS) is a method for suppressing anisotropic interactions such as CSA and dipolar couplings by the introduction of artificial motion upon a solid.[155-157] The technique involves rapid rotation of the sample about an axis orientated at an angle of 54.736° relative to the external magnetic field, B_0, as illustrated in Figure 2.18(a).

Both CSA and dipolar interactions possess an orientation dependence proportional to $3\cos^2\theta - 1$, as shown in Equations 2.36 and 2.39 respectively. When $\theta = 54.736°$ the interaction is removed. However, for a powdered solid all crystallites must be orientated at θ simultaneously to remove the interaction. This is, in reality, not feasible and a method capable of imposing an average orientation on the whole sample is required. Magic-angle spinning achieves this by fast rotation of the sample around an angle where $3\cos^2\theta - 1$ is reduced to zero. MAS is

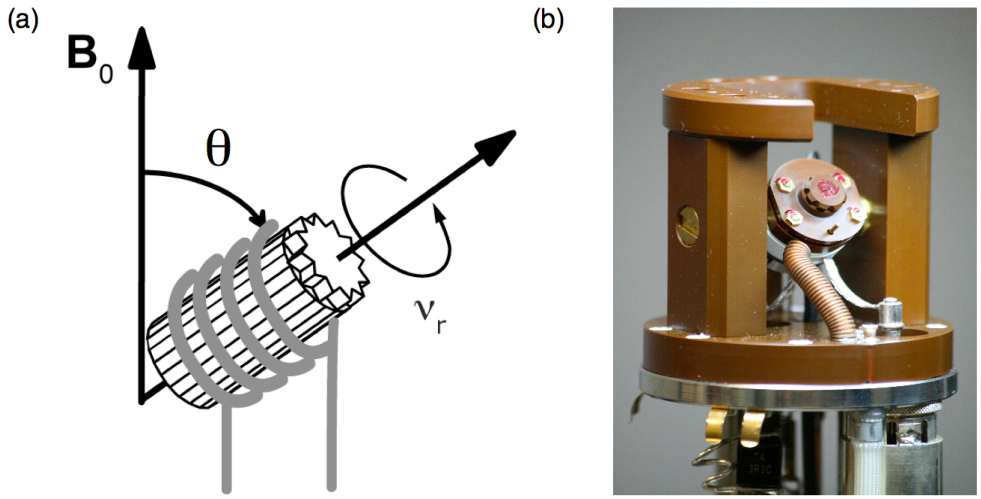

Figure 2.18: (a) Schematic representation of a rotor at the magic angle of θ = 54.736° and (b) picture of an MAS probe showing the stator block containing the coil inclined at the magic angle.

therefore a successful method for averaging many of the anisotropic interactions within solid-state NMR to their isotropic value. To successfully suppress the interactions the spinning rate must usually be equal to or greater than the anisotropy of the interaction being removed. MAS rates of up to 30 kHz are routinely possible, and with considerable advances in probe design, faster MAS rates of up to 65 kHz are now feasible commercially. If the spinning rate is insufficient to suppress the interaction the lineshape breaks up into an envelope of spinning sidebands separated from the centreband by the spinning speed, as shown in Figure 2.19. As the rate of spinning changes the centreband position remains unchanged. Broad sideband patterns severely hinder the extraction of important structural data, and hence fast spinning rates are desirable. Both CSA and several heteronuclear dipolar couplings are typically of the order of a few kilohertz, and hence they can be averaged relatively easily by MAS.[158] In contrast, homonuclear dipolar couplings can only be removed when very fast MAS rates are utilised as the spinning rate needs to be greater than the homonuclear dipolar coupling linewidth, e.g., $^{1}H - {}^{1}H$ dipolar couplings can often be 80 - 100 kHz. It is challenging to routinely use such speeds and therefore alternative methods capable of removing homonuclear dipolar couplings are more

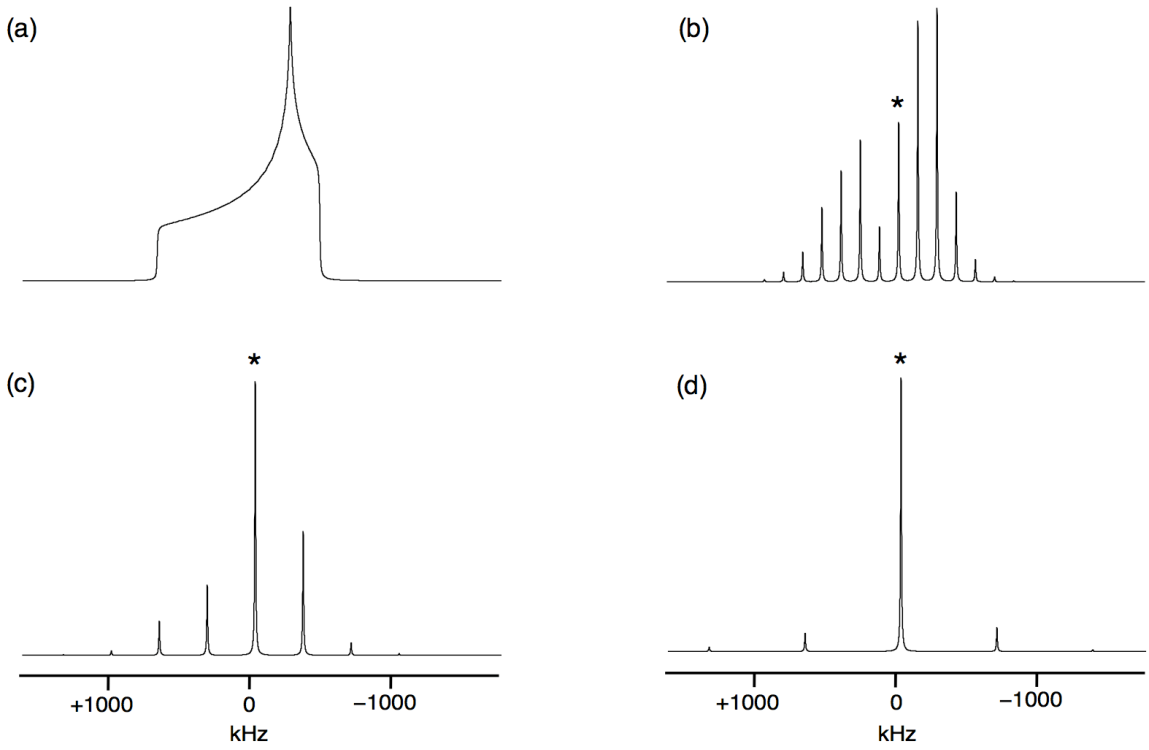

Figure 2.19: Simulated I = 1/2 lineshapes with $\Delta\sigma_{CS}$ = 300 ppm, η_{CS} = 0.3 at MAS rates of (a) 0 kHz, (b) 2 kHz, (c) 5 kHz and (d) 10 kHz. The isotopic centreband is marked with *.

commonly used, such as decoupling (see later section). Magic-angle spinning significantly improves the resolution of a spectrum, thereby making it feasible to accurately determine the number of distinct sites in addition to their respective chemical shifts and relative populations.

2.7 Dipolar Decoupling

At moderate MAS frequencies the heteronuclear dipolar coupling interaction is not fully removed, resulting in large homogeneous broadenings. Hence, very fast MAS rates are required to successfully remove the effects of such couplings. An alternative method for removing the dipolar couplings is a technique known as heteronuclear dipolar decoupling.[159,160] This is a hugely powerful method involving continuous irradiation of the spin not under observation during acquisition of the FID. Decoupling can be applied either static or under MAS, and when utilised under MAS further narrowing of the lineshape is commonly

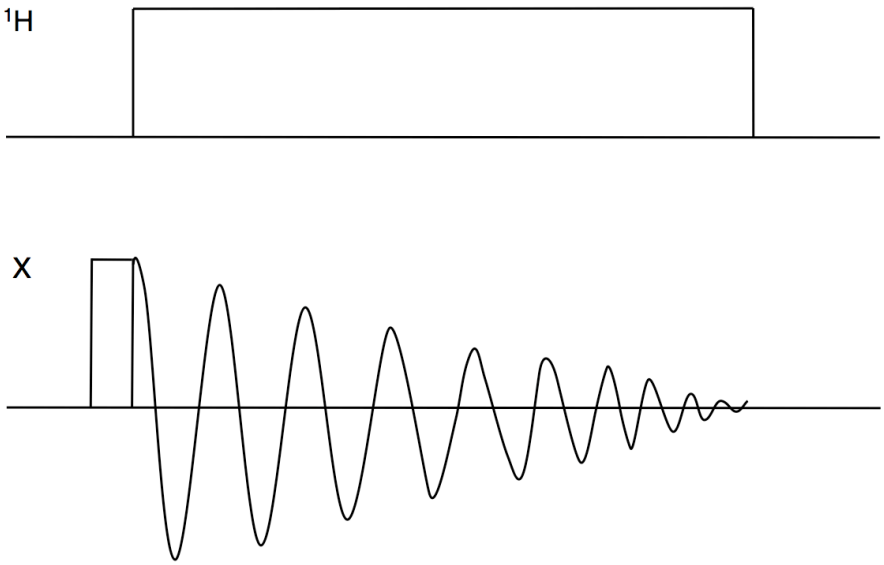

Figure 2.20: A schematic representation of a continuous wave (CW) pulse sequence used for ^{1}H decoupling of an X nucleus FID.

observed. Different schemes for decoupling exist, the simplest of which is continuous wave (CW) decoupling.[161] Consider two dipolar-coupled ^{1}H and ^{13}C spins where the ^{13}C spins are to be observed. The method consists of applying continuous irradiation of very high power, commonly 100-1000 watts, at the frequency of the proton resonance. The required pulse sequence for the ^{13}C nuclei is then applied and the ^{13}C FID is acquired whilst the ^{1}H is irradiated with high power rf pulses. This method of decoupling is relatively easy to implement and an example of the sequence used for CW decoupling is shown in Figure 2.20. It must be noted that this type of decoupling requires very high rf powers for effective decoupling. Alternatively, other decoupling pulse sequences may be used such as Two Pulse Phase Modulated (TPPM) which, in contrast to CW methods, incorporates phase modulation of the rf to achieve more efficient decoupling.[162]

As described previously, homonuclear dipolar couplings can only be removed when the MAS rate is greater than the homonuclear dipolar linewidth. Where this is not possible the effects of homonuclear dipolar couplings may be removed by homonuclear decoupling. Unlike

heteronuclear decoupling, it is not possible to pulse and acquire simultaneously on two identical spins. Therefore, a 'windowed' approach is required in which pulses are applied to remove the dipolar interaction and points of the FID are collected in small windows between each of the pulses applied. This type of sequence is technically challenging to implement.

2.8 Quadrupolar Interactions

2.8.1 Introduction

The periodic table is dominated by quadrupolar nuclei, with approximately 75% of the NMR-active species possessing a spin quantum number greater than 1/2. Quadrupolar interactions are therefore a relatively common occurrence in NMR.

Quadrupolar nuclei possess a nuclear electric quadrupole moment, eQ, that interacts with the electric field gradient (EFG), generated at the nucleus by other atoms present in the sample.[163] This interaction, known as the quadrupolar interaction, is extremely strong and, in turn, produces an inhomogeneous broadening, commonly of the order of megahertz, in the solid-state NMR spectra of quadrupolar nuclei. The quadrupolar interaction is orientationally dependent and in its PAS it may be described by three principal components; V_{xx}, V_{yy} and V_{zz}. The magnitude of the EFG is given by $eQ = V_{zz}$ and the shape of its cross-section can be represented by an asymmetry parameter, η_Q (Equation 2.45). The magnitude of the quadrupolar interaction is given, in Hz, by the quadrupolar coupling constant, C_Q,[163]

$$C_Q = \frac{eQV_{zz}}{h} = \frac{e^2qQ}{h} \tag{2.44}$$

$$\eta_Q = \frac{V_{xx} - V_{yy}}{V_{zz}} \quad 0 < \eta_Q < 1 \ . \tag{2.45}$$

As stated previously, the total Hamiltonian, H, for a particular nucleus depends upon many contributions. The quadrupolar interaction is often

very large but, in many cases, remains smaller than the more dominant Zeeman interaction. The Hamiltonian describing the quadrupolar interaction is given by[164]

$$H_Q = \frac{eQ}{2I(2I-1)\hbar}\mathbf{I}\cdot\mathbf{V}\cdot\mathbf{I} \tag{2.46}$$

$$H_Q = \frac{eQ}{2I(2I-1)\hbar}(I_x\, I_y\, I_z)\begin{pmatrix} V_{xx} & V_{xy} & V_{xz} \\ V_{yx} & V_{yy} & V_{yz} \\ V_{zx} & V_{zy} & V_{zz} \end{pmatrix}\begin{pmatrix} I_x \\ I_y \\ I_z \end{pmatrix} . \tag{2.47}$$

Hence, the total Hamiltonian for a quadrupolar nucleus, neglecting for the moment contributions from smaller interactions such as chemical shift anisotropy, dipolar and scalar couplings, may be expressed as the sum of the individual Hamiltonians for the Zeeman and quadrupolar interactions, given by

$$H = H_Z + H_Q \ . \tag{2.48}$$

In the PAS the quadrupolar tensor, **V**, is diagonal and the Hamiltonian is given by[164]

$$H_Q = \frac{3e^2qQ}{4I(2I-1)\hbar}\left[I_z^2 - \frac{1}{3}I(I+1) + \frac{\eta_Q}{3}(I_x^2 - I_y^2)\right] . \tag{2.49}$$

2.8.2 First-Order Quadrupolar Interactions

The effect of the quadrupolar interaction may be described as a perturbation of the Zeeman energy levels and can therefore be described using perturbation theory.[165] The quadrupolar interaction perturbs all energy levels and, to a first-order approximation, splits the original degenerate transitions at ω_0 into 2I transitions, equally spaced by $2\omega_Q$. In Figure 2.21 the Zeeman energy levels for spin I = 1 and I = 3/2 nuclei are shown, displaying two and three degenerate transitions at ω_0, respectively.

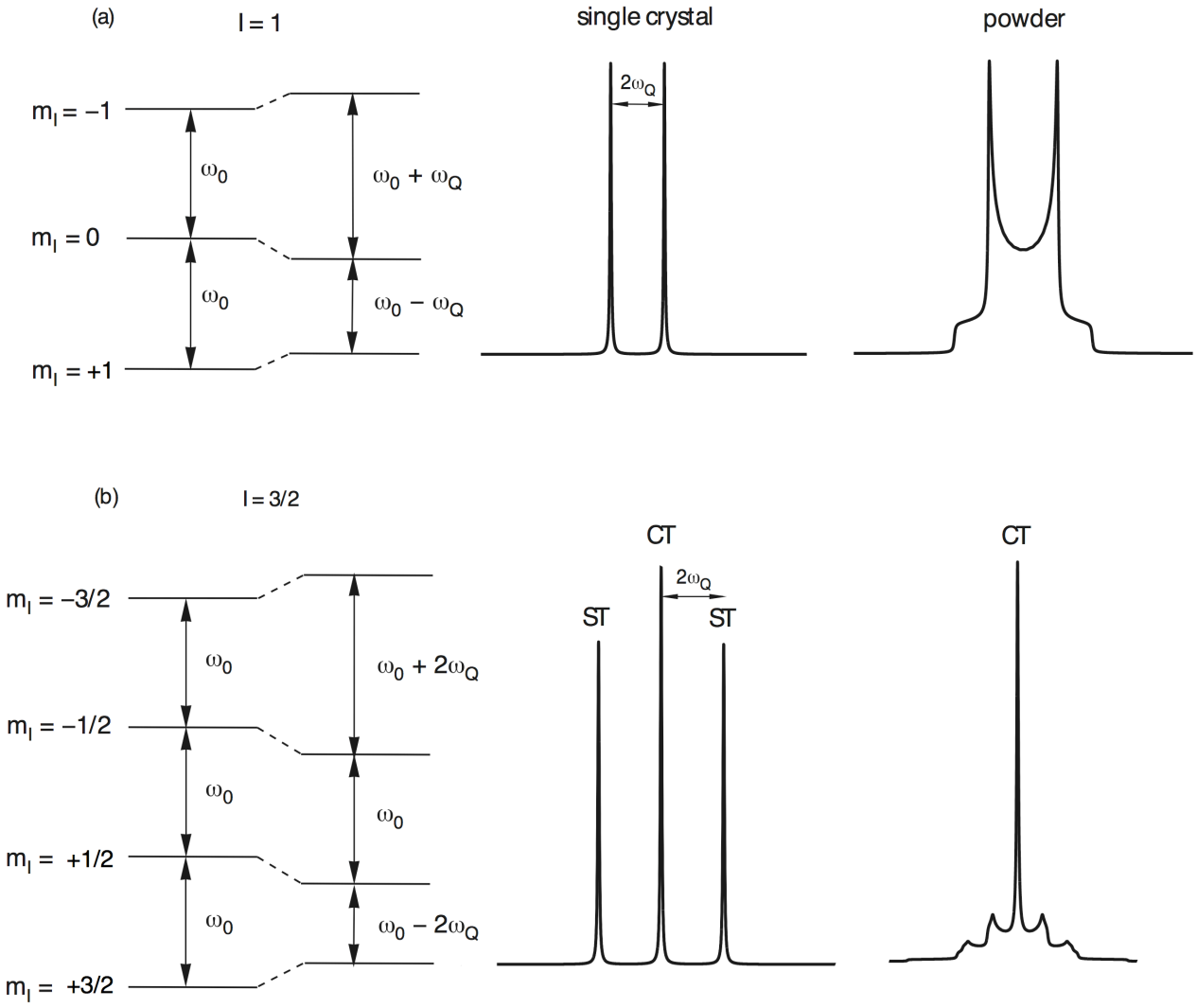

Figure 2.21: First-order perturbation of the Zeeman energy levels by the quadrupolar interaction for systems with (a) I = 1 and (b) I = 3/2. Also shown are resulting spectra for each spin system with 2I non-degenerate transitions separated by $2\omega_Q$, and corresponding spectra for a powder distribution of crystallites. In each case the central transition and satellite transitions are marked by CT and ST, respectively.

Also shown is the effect of the quadrupolar interaction, to a first-order approximation, on the energy levels. The quadrupolar splitting parameter, ω_Q, is given by

$$\omega_Q = \frac{(\omega_Q^{PAS})}{2}(3\cos^2\theta - 1 + \eta_Q(\sin^2\theta\cos\phi)) \qquad (2.50)$$

with

$$\omega_Q^{PAS} = \frac{3\pi C_Q}{2I(2I-1)} \quad , \tag{2.51}$$

given in rad s^{-1}, where the angles θ and ϕ define the orientation of the PAS of the EFG with respect to the external magnetic field.

For I = 3/2 nuclei, all energy levels are perturbed by the first-order quadrupolar interaction. However, for single-quantum transitions only the frequency of the central transition ($m_I = +1/2 \leftrightarrow -1/2$) remains unchanged at ω_0. The frequency of the outer transitions, termed satellite transitions with $m_I = \pm 1/2 \leftrightarrow \pm 3/2$, is now dependent upon the quadrupolar splitting parameter, ω_Q. This highlights a vital distinction between quadrupolar nuclei with integer and half-integer spins. For nuclei with half-integer spin quantum numbers the central transition is not affected to first-order by the quadrupolar interaction, producing a sharp peak in the centre of the spectrum. No such transition exists in the case of integer spins, and hence all transitions exhibit a perturbation by the quadrupolar interaction. These differences are highlighted in Figure 2.21.

Polycrystalline samples are composed of millions of tiny crystallites, each with a different orientation with respect to B_0, and hence in a similar manner to the CSA they commonly exhibit broad 'powder pattern' lineshapes, as a direct result of the orientational dependence of ω_Q. The width of each lineshape is directly proportional to C_Q therefore a measure of the linewidth can give a good indication as to the magnitude of the quadrupolar interaction. Examples of powdered lineshapes for spin I = 1 nuclei have been simulated with varying η_Q values and are shown in Figure 2.22.

2.8.3 Removal of First-Order Effects

For static samples substantial inhomogeneous broadening is exhibited for quadrupolar nuclei owing to the quadrupolar interaction. Therefore, a method for removing this interaction and obtaining high-resolution spectra is highly desirable. Examination of the first-order

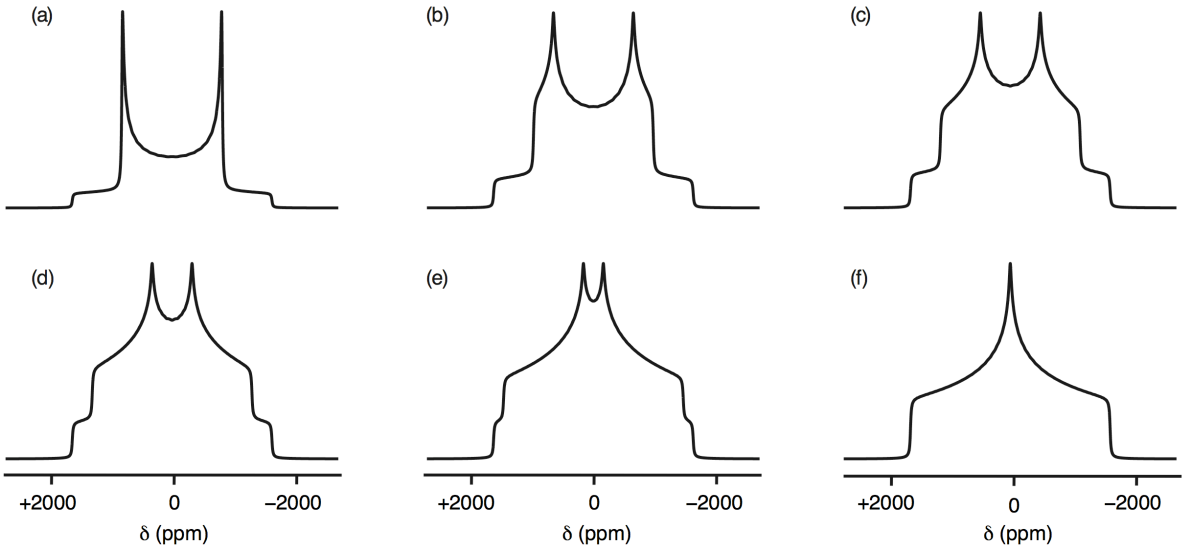

Figure 2.22: Powdered spin I = 1 lineshapes simulated under static conditions with C_Q = 2 MHz and η_Q = 0, 0.2, 0.4, 0.6, 0.8 and 1 in (a-f) respectively.

quadrupolar interaction (Equation 2.50) reveals an angular dependence similar to that previously identified for the chemical shift anisotropy and dipolar couplings, $3\cos^2\theta - 1$. Therefore, under MAS the quadrupolar interaction should be removed to first order. As previously described in section 2.6 MAS is only effective when the MAS rate is similar or greater than the anisotropy of the interaction attempting to be removed. Quadrupolar interactions are commonly many megahertz in magnitude and therefore fast MAS rates would be required to fully remove the interaction. For integer spins, if the MAS rate is too slow the spectrum will be broken up into a series of spinning sidebands. For half-integer spins under MAS only the satellite transitions are affected, the central transition is not broadened to first-order.

2.8.4 Second-Order Quadrupolar Interactions

When the quadrupolar interaction is relatively small a first-order approximation is sufficient to describe the effect upon the spectrum. However, in reality, for many solids this interaction is very large and a first-order perturbation approximation is no longer sufficient. When this

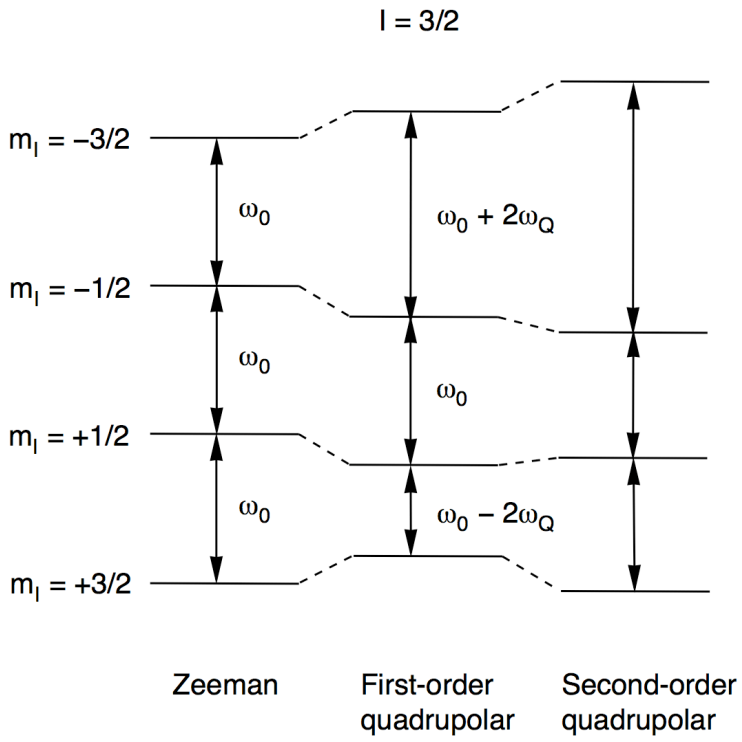

Figure 2.23: Perturbation of the Zeeman energy levels arising from the quadrupolar interaction to a first- and second-order approximation for a I = 3/2 system. Although not broadened by the first-order quaderupolar interaction, the central-transition is broadened by the second-order quadrupolar interaction.

is the case second-order terms are required to describe the perturbation of the Zeeman energy levels by the quadrupolar interaction. The four energy levels for a spin I = 3/2 nucleus are shown in Figure 2.23 under the effect of the Zeeman interaction, the first-order quadrupolar interaction and the second-order quadrupolar interaction. Both the central (CT) and satellite transitions (ST) are affected by the second-order quadrupolar interaction. The second-order perturbation to a transition frequency $m_I \leftrightarrow -m_I$ as defined, under MAS with $\eta_Q = 0$, is given by

$$E^2_{|m_I\rangle} - E^2_{|-m_I\rangle} = \frac{(\omega_Q^{PAS})^2}{\omega_0}[A^0(I,m_I) + A^2(I,m_I)d^2_{00}(\theta)d^2_{00}(\chi) + A^4(I,m_I)d^4_{00}(\theta)d^4_{00}(\chi)] \quad (2.52)$$

where $A^n(I,m_I)$ are spin and energy level dependent coefficients, θ is the angle between the rotor axis and the applied field (i.e., 54.736°) and

$d^1_{mm}(\alpha)$ are Wigner reduced rotation matrix elements.[166] It can be seen that the second-order interaction is composed of three distinct terms: an isotropic shift (proportional to $A^0(I, m_I)$), a second-rank anisotropic term (proportional to $A^2(I, m_I)d^2_{00}(\theta)d^2_{00}(\chi)$) and a fourth-rank anisotropic term (proportional to $A^4(I, m_I)d^4_{00}(\theta)d^4_{00}(\chi)$). The spin-dependent coefficients $A^n(I, m_I)$ are listed in Table 2.2 for half-integer spins.

For a spin I = 3/2 nucleus (again with $\eta_Q = 0$) Equation 2.52 may be expressed more simply as

$$E^2_{|1/2\rangle} - E^2_{|-1/2\rangle} = \frac{(\omega_Q^{PAS})^2}{\omega_0}\left[-\frac{2}{5} - \frac{8}{7}d^2_{00}(\theta)d^2_{00}(\chi) + \frac{54}{35}d^4_{00}(\theta)d^4_{00}(\chi)\right] \quad (2.53)$$

where

$$d^2_{00}(\theta) = \frac{1}{2}(3\cos^2\theta - 1) \quad (2.54)$$

$$d^4_{00}(\theta) = \frac{1}{8}(35\cos^4\theta - 30\cos^2\theta + 3) \quad . \quad (2.55)$$

The second-rank element, $d^2_{00}(\theta)$, has the same orientational dependence as the chemical shift anisotropy, dipolar and scalar couplings, and hence this broadening may be removed under MAS. The fourth-rank element, however, possesses a much more complex orientational dependence. This term is averaged to zero only when $\theta = 30.56°$ or $70.12°$. Hence, it is not feasible for conventional MAS to remove completely the anisotropic second-order quadrupolar broadening.

As shown previously, the central transition of a half-integer quadrupolar nucleus was not broadened, to a first-order approximation, by the quadrupolar interaction. This transition does, however, experience a second-order broadening. To illustrate the effect of this broadening on NMR spectra of half-integer nuclei, second-order broadened central transition powder pattern lineshapes have been simulated under MAS for a spin I = 3/2 nucleus with varying η_Q values, as shown in Figure 2.24. The central transition, previously unaffected to first order, now exhibits a complex 'powder pattern' lineshape that is shifted from the centre of the spectrum. The magnitude of the second-order quadrupolar interaction is

Table 2.2: Coefficients for zero-, second- and fourth-rank terms in Equation 2.50 for half-integer spin nuclei.

I	m_I	$A^0(I,m_I)$	$A^2(I,m_I)$	$A^4(I,m_I)$
I = 3/2	1/2	−2/5	−8/7	54/35
	3/2	6/5	0	−6/5
I = 5/2	1/2	−16/15	−64/21	144/35
	3/2	−4/5	−40/7	228/35
	5/2	20/3	40/21	−60/7
I = 7/2	1/2	−30/15	−120/21	270/35
	3/2	−54/15	−96/7	606/35
	5/2	30/15	−240/21	330/35
	7/2	294/15	168/21	−966/35
I = 9/2	1/2	−48/15	−192/21	432/35
	3/2	−108/15	−168/7	1092/35
	5/2	−60/15	−600/21	1140/35
	7/2	168/15	−336/21	168/35
	9/2	648/15	432/21	−2332/35

proportional to $(\omega_Q^{PAS})^2/\omega_0$, and so it is considerably smaller than the first-order quadrupolar interaction, proportional to ω_Q^{PAS}. The position of the NMR resonance for a quadrupolar nucleus is the sum of the isotropic chemical shift, δ_{iso}, and the isotropic quadrupolar shift, δ_Q.

2.8.5 Removal of Second-Order Quadrupolar Broadening

Second-order quadrupolar broadening of NMR spectra often hinders the extraction of important information regarding the number of crystallographically distinct sites or the relative populations of different sites within a sample as it cannot be removed by MAS. Hence, a technique capable of removing such broadenings and achieving high-resolution spectra for quadrupolar nuclei exhibiting such effects is required. For example, two-dimensional techniques such as double

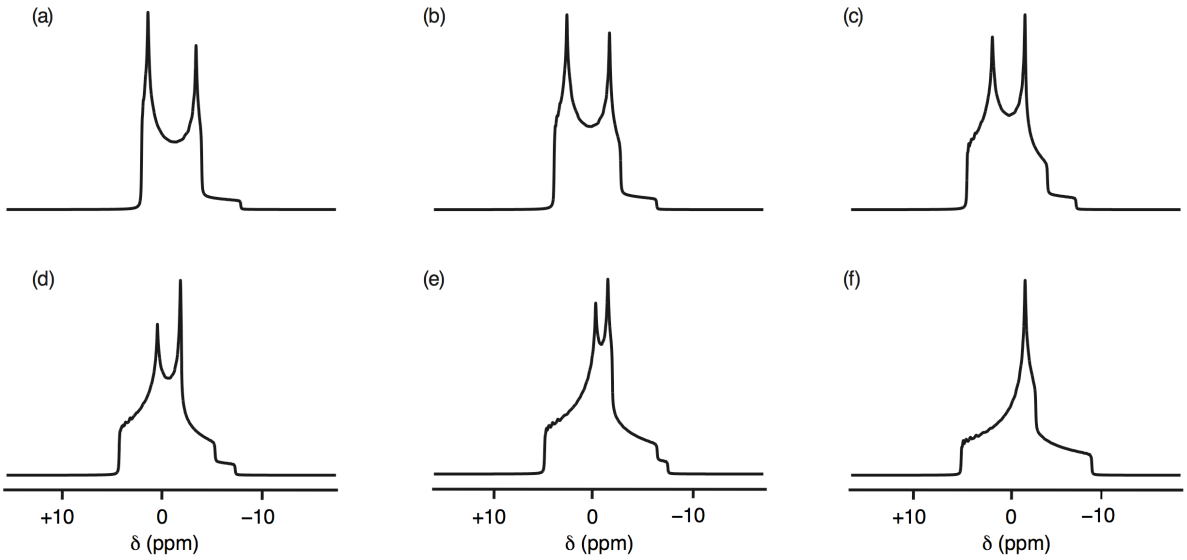

Figure 2.24: Second-order broadened central-transition MAS powder lineshapes for a I = 3/2 system simulated with C_Q = 2 MHz, $\omega_0/2\pi$ = 158.75 MHz and asymmetry, η_Q, of (a) 0, (b) 0.2, (c) 0.4, (d) 0.6, (e) 0.8 and (f) 1.

rotation[167,168] (DOR), dynamic-angle spinning[169,170] (DAS) or multiple-quantum (MQ) MAS may be utilised.[171]

2.8.6 Double Rotation (DOR)

One possible method for obtaining high-resolution NMR spectra for quadrupolar nuclei is the double rotation (DOR) technique.[167,168] In Equation 2.53 it was shown that the second- and fourth-rank anisotropic quadrupolar broadenings possessed different angular dependencies; hence, to remove both interactions simultaneously, rotation of the sample would need to occur around two different angles. DOR achieves high-resolution spectra by spinning the sample, by means of a double rotor, simultaneously at two different angles, one being the magic angle, θ, which averages the second-rank anisotropic broadening contribution, whilst the other angle (θ_R = 30.56° or 70.12°) averages the fourth-rank terms to zero. A schematic representation of the apparatus used in DOR is shown in Figure 2.25. Furthermore, the use of the magic angle removes any additional CSA or dipolar interactions from the spectrum. However, it must be noted that DOR, despite producing high-resolution spectra, is

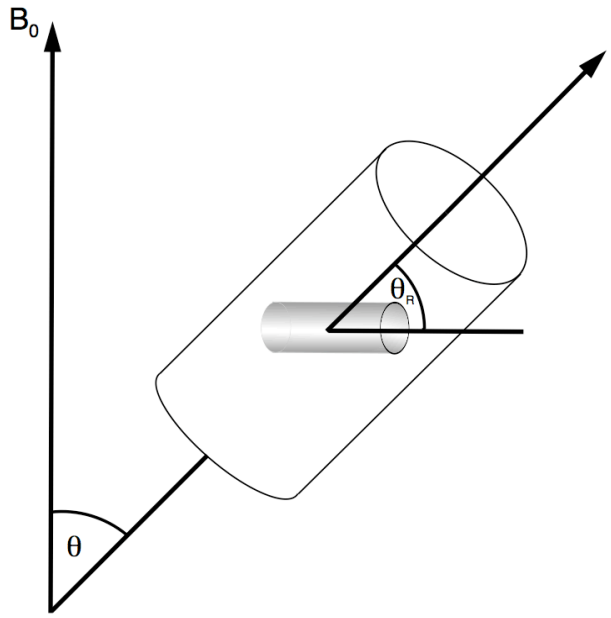

Figure 2.25: Schematic representation of the DOR experiment. Shown are two rotors, one spinning inside the other. The outer rotor spins about an axis inclined at 54.736° to the applied magnetic field, B_0, whilst the inner rotor spins about an axis inclined at 30.65° (or 70.12°) relative to the outer rotor.

an extremely specialist technique and its practical application is limited owing to technical restrictions on the spinning speed of the outer rotor. The mechanical complexity of the technique leads to the requirement of expensive hardware different to that utilised for conventional MAS.

2.9 Multiple-Quantum Magic-Angle Spinning (MQMAS)

2.9.1 Introduction

Owing to the technical demands and complex practical implementation of methods such as DOR, alternative methods for the acquisition of high-resolution spectra have been developed in recent years. In 1995, Frydman and Harwood[171] suggested a method for removing second-order quadrupolar broadening which utilises the hardware conventionally used for MAS. The experiment, now termed multiple-quantum magic-angle spinning (MQMAS), is a two-dimensional technique which correlates multiple- and single-quantum coherences under MAS. The coherences exploited in MQMAS are the symmetric m_I

$\leftrightarrow -m_I$ coherences, i.e., triple-quantum ($+3/2 \leftrightarrow -3/2$), five-quantum ($+5/2 \leftrightarrow -5/2$) etc. Note that these coherences cannot be directly observed. Owing to the ease of its implementation the development of MQMAS has resulted in renewed interest in high-resolution NMR in a wide range of quadrupolar nuclei.

2.9.2 The MQMAS Experiment

The original MQMAS experiment used two pulses to excite multiple-quantum coherences.[171] However, it has subsequently been shown that single-pulse excitation[172,173] is a more efficient method to excite such coherences for nuclei with half-integer spin, as shown in Figure 2.26.[174-176] In MQMAS experiments multiple-quantum coherences are first excited using a high power rf pulse, and these then evolve during a time period t_1. The pulse utilised needs to be sufficiently high in power to efficiently excite multiple-quantum coherences. To select the desired coherence changes and ensure that no unwanted coherences are carried forward for the remainder of the pulse sequence a process known as phase cycling is required. Additional details regarding phase cycling can be found in Appendix I. The experiment is conducted under MAS and therefore it may be assumed that the second-rank second-order anisotropic broadening is averaged to zero throughout the experiment. Hence, the only anisotropy that arises during t_1 is due to the fourth-rank term. At the end of t_1 a second rf pulse is applied which converts the remaining multiple-quantum coherence to observable single-quantum coherences. A two-dimensional time domain dataset is obtained, displaying the evolution of single- and multiple-quantum coherences in the t_2 and t_1 dimensions respectively.

The key feature of the MQMAS technique is its ability to refocus fourth-rank anisotropic broadenings whilst retaining isotropic shifts. The second-order perturbation to the frequency of the central transition of a spin $I = 3/2$ nucleus under MAS conditions was shown earlier in Equation

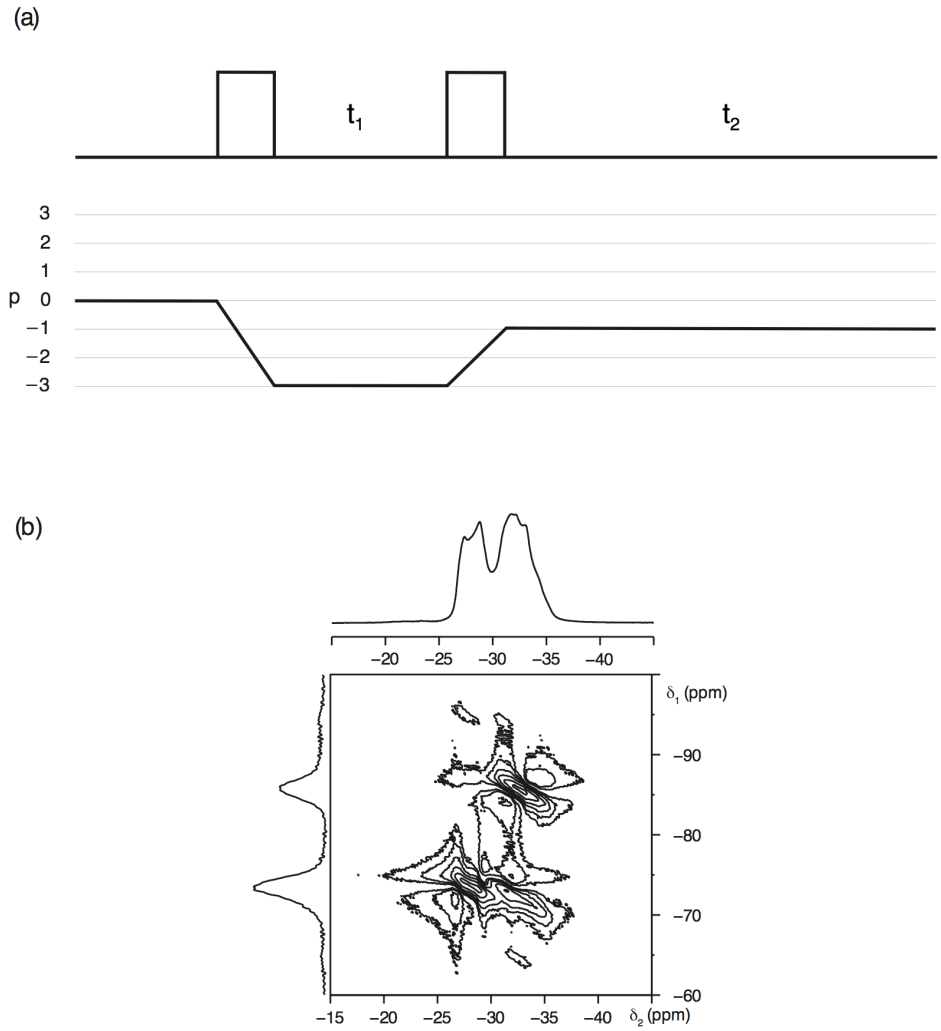

Figure 2.26: (a) Pulse sequence and coherence transfer pathway diagram for the two-pulse MQMAS NMR experiment adapted from that of Frydman and Harwood.[171] (b) Conventional ^{97}Rb MAS (14.1 T) NMR spectrum and triple-quantum MAS NMR spectrum of $RbNO_3$, recorded using the pulse sequence shown in (a). The spectrum is the result of averaging 96 transients with a recycle interval of 0.25 s for each of the 512 increments of 60.0 μs. The MAS rate was 12.5 kHz.

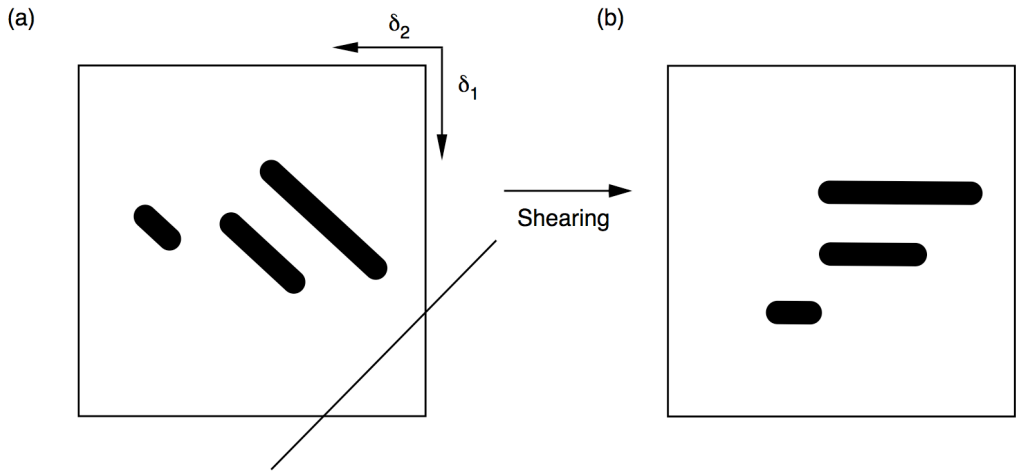

Figure 2.27: Schematic representation of a spectrum resulting from an MQMAS experiment. Shown in (a) are a series of ridges aligned along a gradient equal to the MQMAS ratio, R. To obtain an isotropic projection a projection orthogonal to the ridges is obtained, as shown in (a). This isotropic projection is free from quadrupolar broadening but retains the isotropic shifts. Shown in (b) is the spectrum post shearing, exhibiting a series of ridges parallel to δ_2. An isotropic spectrum is then obtained from a projection onto δ_1.

2.53. A similar expression may be obtained for the frequency of the triple-quantum transition for a I = 3/2 nucleus under MAS, given for $\eta_Q = 0$ by

$$E^2_{|3/2\rangle} - E^2_{|-3/2\rangle} = \frac{6}{5} - \frac{6}{5} d^4_{00}(\theta) d^4_{00}(\chi) \quad . \tag{2.56}$$

It can be seen from equations 2.53 and 2.56 that the ratio of the coefficients in the single- and triple-quantum expressions is different for the isotropic and anisotropic fourth-rank terms, i.e., $A^0(I,3/2)/A^0(I,1/2)$ and $A^4(I,3/2)/A^4(I,1/2)$. Using this property it is possible to refocus the anisotropic terms and retain solely the isotropic shifts to produce a high-resolution spectrum. It must be noted that the ratio of the coefficients of the anisotropic fourth-rank terms under single- and multiple-quantum coherences, $A^4(I,m_I)/A^4(I,1/2)$, is different for each spin system and coherence order. It is this value, termed the MQMAS ratio, R, that determines the point during t_2 at which the anisotropic broadening will be refocused. In addition, this value also determines the gradient along

which each ridge lineshape will be aligned in the two-dimensional spectrum obtained. For example, for a spin $I = 3/2$ nucleus $A^4(I,3/2)/A^4(I,1/2) = (-6/5)/(54/35) = -7/9$. All coefficients $A^n(I,m_I)$ are given in Table 2.2.

The two-dimensional time-domain dataset obtained during any MQMAS experiment is then Fourier transformed to produce a spectrum displaying signal corresponding to the multiple-quantum spectrum in the δ_1 dimension and the anisotropic powder pattern associated with the central transition in the δ_2 dimension. A schematic representation of an MQMAS spectrum obtained post Fourier transformation is shown in Figure 2.27(a). To achieve an isotropic spectrum a projection orthogonal to the ridge lineshape is required, as shown in Figure 2.27(a). This projection is free from all quadrupolar broadening but retains the isotropic shifts. In practice it is easier to use mathematical transformation known as shearing to obtain an isotropic projection in the δ_1 dimension. This transforms the spectrum so that the ridges appear parallel to δ_2. An example of a sheared spectrum is also shown in Figure 2.27(b). The isotropic spectrum is then more easily extracted.

Spectra recorded using the original MQMAS experiment give rise to undesirable 'phase-twist' lineshapes. A two-dimensional ^{87}Rb ($I = 3/2$) spectrum of $RbNO_3$ recorded using the original MQMAS pulse sequence is shown in Figure 2.26(b). The spectrum displays distorted lineshapes, each of which is aligned along R $(-7/9)$. There are three crystallographically distinct resonances in the ^{87}Rb MQMAS NMR spectrum of $RbNO_3$. However, owing to considerable distortion of the lineshape, caused by 'phase-twists', it is difficult to accurately observe the third site. Phase-twist lineshapes result from the real part of the two-dimensional Lorentzian containing both absorption and dispersion mode lineshapes. These are entangled in a complex manner and the lineshapes cannot be phased correctly. This is a major drawback of the original MQMAS sequence and, as a result, adjustments to the original experiment have been made to ensure pure-phase lineshapes are obtained. These 'modified' experiments are of two distinct types; amplitude- and phase-modulated with respect to t_1. The first of these, amplitude-modulated

experiments, produce pure-phase spectra if there is simultaneous selection of two symmetrical coherence pathways (e.g., p = ± 3) and if their transfer to the observable signal has the same efficiency. This sequence was first proposed by Amoureux[177] in 1996 for I = 3/2 nuclei. A modified version of this sequence was later proposed, again by Amoureux, which contained a filter through a population state, as shown in Figure 2.28.[178] This amplitude-modulated pulse sequence, known as a z-filter experiment, consists of the conventional triple-quantum excitation and conversion pulses in addition to a selective 90° pulse, used to convert the populations temporarily stored along the z-axis to observable signal. This sequence ensures equal combination of p = ±3 and can be implemented for all spins, and therefore it is a highly robust technique. Once obtained, the dataset is Fourier transformed to reveal a series of ridge lineshapes, each of which is aligned along an axis with a gradient equal to the MQMAS ratio, R, for that particular nucleus. For example, the spectrum obtained for a spin I = 3/2 nucleus will contain a series of ridges, each with a slope of −7/9. For convenience, spectra recorded using a z-filter pulse sequence are commonly shown post shearing.[179] Two-dimensional ^{87}Rb (I = 3/2) spectra recorded for $RbNO_3$ using a z-filtered pulse sequence are shown in Figures 2.28(a) and (b). The spectra shown are both prior to and post shearing.

Alternatively, a second type of experiment may be used in which a single coherence pathway is selected and the signal is phase-modulated in t_1. Initially proposed by Massiot *et al.*,[180] this is commonly achieved using a shifted-echo pulse sequence, shown in Figure 2.29. Unlike the original MQMAS experiment shifted-echo pulse sequences always result in the acquisition of pure-phase lineshapes owing to the acquisition of a whole echo. To successfully acquire a whole echo using a shifted-echo pulse sequence the correct coherence pathway must first be selected. This depends upon both the spin under investigation and the sign of the MQMAS ratio. For example, for a spin I = 3/2 nucleus R is negative and to successfully acquire a whole echo the pathway through negative multiple-quantum coherence, p = −3, (marked by the solid line in Figure 2.29) must be followed. The converse is true for I = 5/2, 7/2 and 9/2

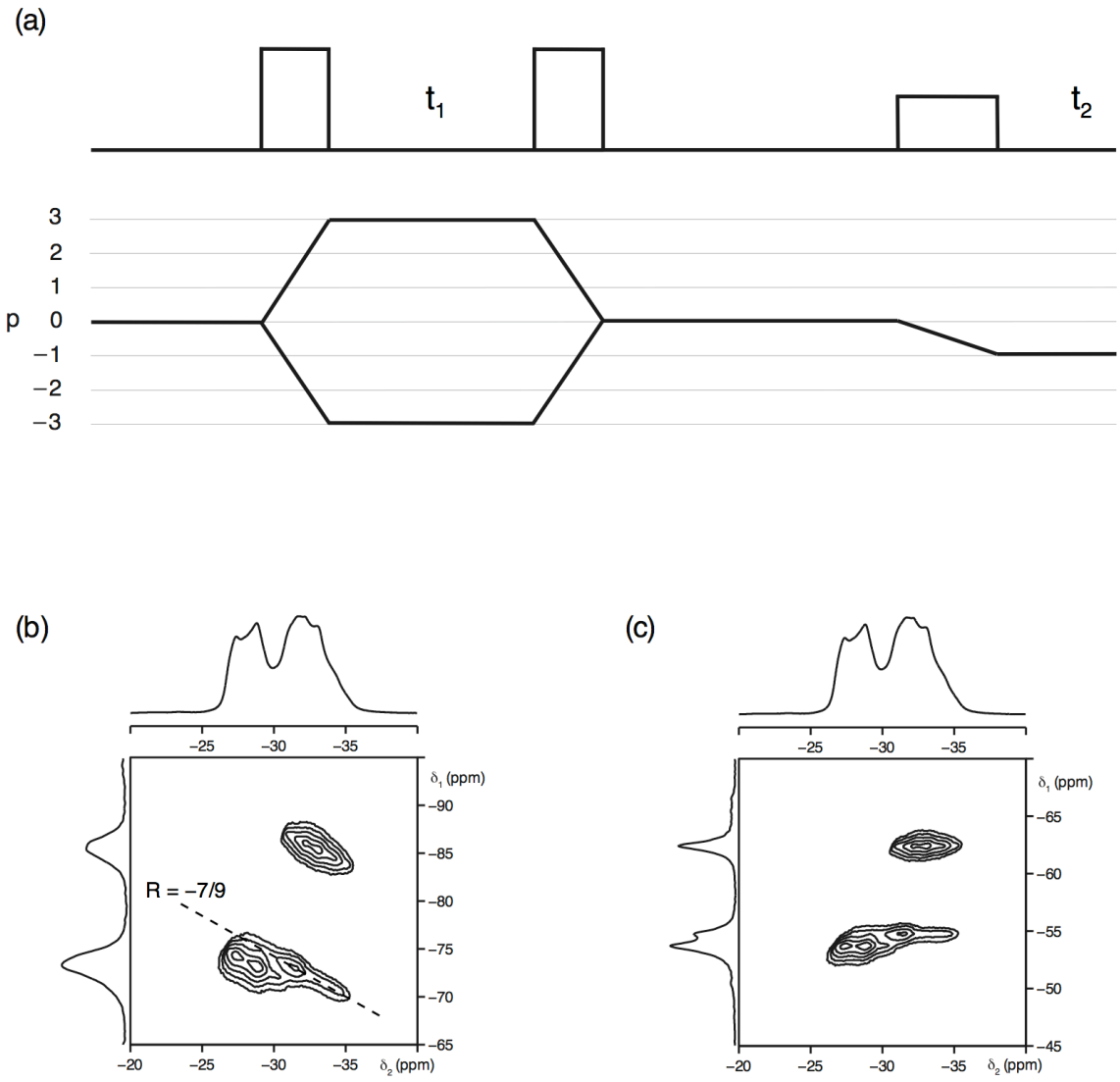

Figure 2.28: (a) Pulse sequence and coherence transfer pathway diagram for the z-filtered MQMAS NMR experiment of Amoureux.[178] (b, c) Conventional ^{97}Rb MAS (14.1 T) NMR spectra, triple-quantum MAS NMR spectra and corresponding projections for $Rb(NO)_3$, recorded using the pulse sequence shown in (a). Each spectrum is the result of averaging averaging 72 transients with a recycle interval of 0.25 s for each of the 512 increments of 60.0 μs. The two-dimensional spectrum shown in (b) exhibits a series of ridges aligned along a gradient of −7/9 (the MQMAS ratio for I = 3/2). The ^{97}Rb MAS NMR spectrum shown in (c) is post shearing, displaying a series of ridge lineshapes parallel to δ_2 and corresponding isotropic projection in the δ_1 dimension. The MAS rate was 12.5 kHz.

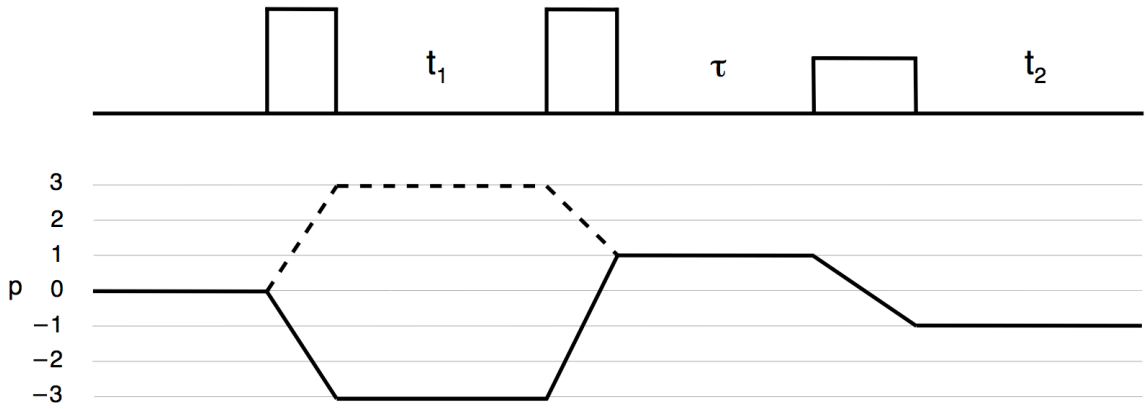

Figure 2.29: Pulse sequence and coherence transfer pathway diagram for the shifted-echo MQMAS experiment of Massiot *et al.*[180] The solid line denotes the correct coherence pathway for spin I = 3/2 nuclei and the dashed line denotes the correct coherence pathway for spin I = 5/2, 7/2 and 9/2 nuclei.

nuclei, i.e., the pathway though positive multiple-quantum coherence, p = +3, must be followed, denoted by the dashed line in Figure 2.29. For shifted-echo experiments it is important to determine the echo interval, τ, as it needs to be sufficiently long enough to acquire a whole echo. Transverse relaxation is, however, a limiting factor in precisely how far the echo can be shifted into the acquisition period, t_2. If τ is too long relaxation may begin to effect data acquisition. Hence, when relaxation causes a detrimental effect it is better to use a z-filtered experiment. Similar to the z-filtered experiment, the spectrum acquired using a shifted-echo contains a series of ridges aligned along an axis with a gradient equal to the MQMAS ratio. Hence, they too require post acquisition processing (shearing) in order to obtain ridges which appear parallel to δ_2.

Brown and Wimperis later proposed a split-t_1 approach, which may be applied to both phase- and amplitude-modulated experiments.[181] The phase-modulated split-t_1 pulse sequence, shown in Figure 2.30(a), divides the t_1 time period into two fractional contributions, kt_1 and $k't_1$, which are related to the MQMAS ratio. The key feature of each of the MQMAS experiments discussed thus far is the refocusing of the fourth-rank anisotropic broadening which occurs at some point in the t_2 period. However, if the t_1 period is split into single- and triple-quantum evolution

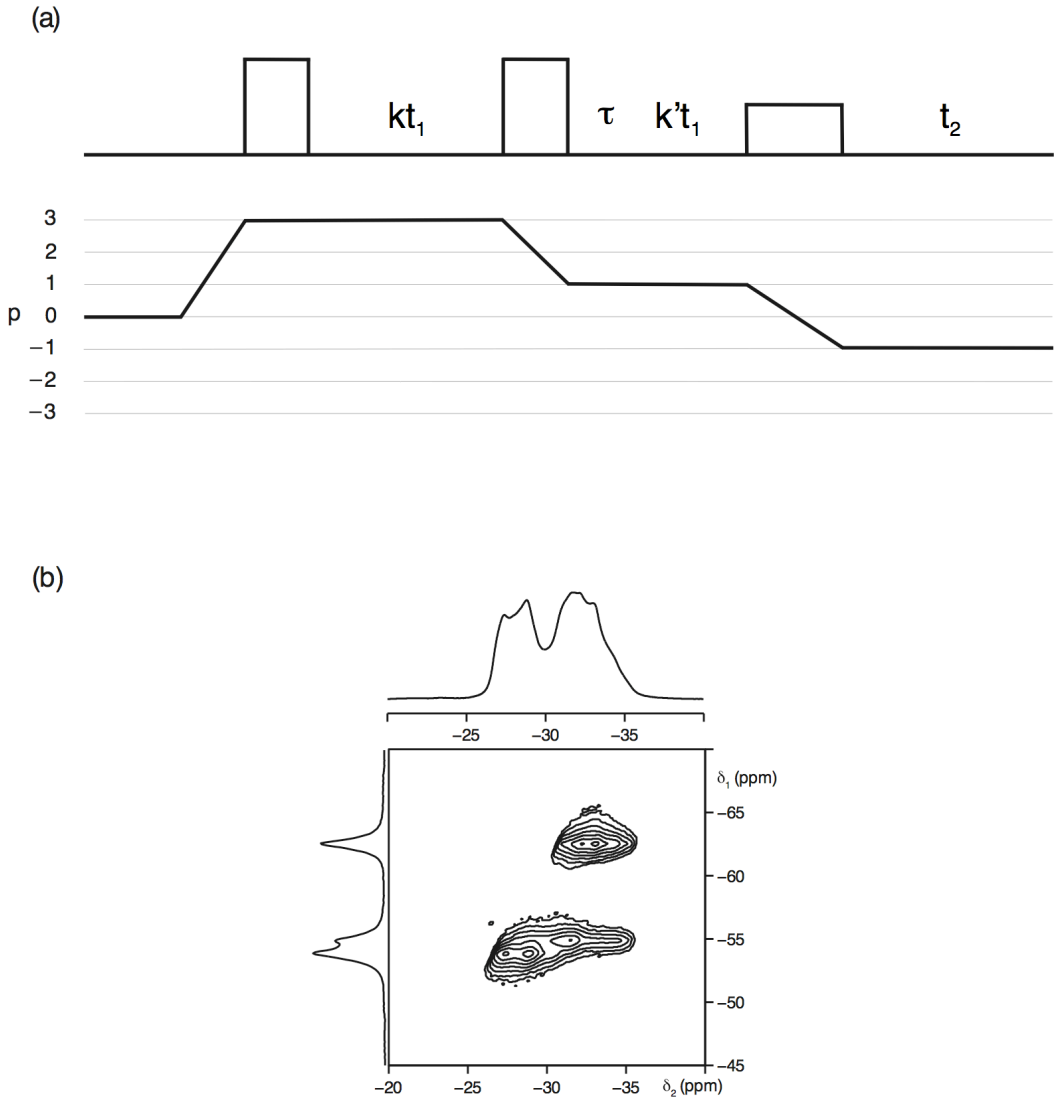

Figure 2.30: (a) Pulse sequence and coherence transfer pathway diagram for the I = 3/2 phase-modulated split-t_1 pulse sequence of Brown and Wimperis,[181] for spins I > 3/2 the $k't_1$ evolution period is placed after the 180° pulse. The t_1 time period is split into two fractional contributions, kt_1 and $k't_1$, which are related to the MQMAS ratio. (b) Conventional ^{97}Rb MAS (14.1 T) NMR spectrum, triple-quantum MAS NMR spectrum and corresponding isotropic projections for $RbNO_3$ recorded using the pulse sequence shown in (a). The triple-quantum MAS NMR spectrum is the result of averaging 96 transients with a recycle interval of 0.25 s for each of the 512 increments of 60.0 μs. The MAS rate was 12.5 kHz.

periods in a ratio determined by the relevant MQMAS ratio then the fourth-rank anisotropic broadening can be refocused at the end of the t_1 period, resulting in ridges which appear parallel to the δ_2 axis. Hence, no additional shearing transformation is required. For example, using this pulse sequence for a spin I = 3/2 nucleus a whole echo is generated utilising a coherence pathway through p = +3, with k = 9/16 t_1 and k' = 7/16 t_1. As a direct result of the splitting of the t_1 period, the spectrum produced contains ridges parallel to δ_2 without the need for shearing. The split-t_1 approach is commonly added to phase-modulated experiments with relative ease. However, it is more challenging to add to amplitude-modulated experiments as complex phase cycling is required to ensure the correct coherence transfer pathways are correlated. A two-dimensional ^{87}Rb (I = 3/2) spectrum of $RbNO_3$, recorded using a phase-modulated split-t_1 pulse sequence is shown in Figure 2.30(b), displaying three distinct resonances, in good agreement with the literature. This spectrum is also in good agreement with the sheared $RbNO_3$ spectrum shown in Figure 2.28(c) obtained using a z-filtered experiment. In each spectrum the isotropic projection onto the δ_1 axis clearly indicate the three sites.

2.9.3 Higher-Order MQMAS

There are various versions of the MQMAS technique including three-, five-, seven- and nine-quantum experiments. There is, however, considerable debate within the literature regarding the associated advantages and disadvantages of using experiments with greater changes in coherence order. Higher-order, principally five- (quintuple-) quantum MAS experiments, were initially introduced by Fernandez and Amoureux in 1995.[182,183] Their early work reported 'extraordinarily high' resolution for spectra recorded using the five-quantum MAS experiment. Work by Wang *et al.*,[184] also suggested similar findings by successfully resolving two aluminum sites which could not be resolved using conventional triple-quantum methods. However, in later years the initial excitement surrounding higher-order MQMAS experiments began to diminish as more experiments were completed.

Numerous investigations have since been completed to compare the associated advantages and disadvantages of higher-order MQMAS experiments and, as a result, there is now a better understanding that many factors need to be considered when deciding which order of multiple-quantum MAS NMR experiment to utilise. Pike[185] and co-workers concluded that multiple-quantum experiments should have inherently higher resolution if the linewidth is due to relaxation, i.e., could be termed 'homogeneous'. The gain in resolution obtained using higher-order MQMAS was found to reduce when the linewidth was 'inhomogeneous'. For example, when there is a distribution of chemical shifts no significant gain in resolution will be observed as this scales with coherence order. Any gain in resolution observed when using higher-order MAS experiments is therefore dependent on the origin of the linewidth. The relative sensitivities of the various MQMAS experiments are widely known to strongly depend on both the quadrupolar coupling constants and strength of the radiofrequency fields used. Therefore, when comparing any two higher-order MQMAS experiments, for example three- and five-quantum, both resolution and sensitivity need to be considered. The spectrum obtained may be of higher resolution using a five-quantum experiment; however it will, typically, be up to five or six times less sensitive than the three-quantum experiment. In past years there has been the development of techniques to try improve the sensitivity of such multiple-quantum experiments, for example the introduction of FAM and SPAM experiments.[186-190] However, in reality, unless there is the necessity for a considerable improvement in resolution it is considered 'convention' to utilise triple-quantum MAS NMR experiments.

2.9.4 Extraction of NMR parameters

It is possible to extract NMR parameters from conventional MAS NMR spectra by computer fitting of the lineshape. One method by which this can be completed is by using the Solids Line Shapes Analysis (SOLA) fitting program (or equivalent) in Topspin 2.1. To demonstrate how this

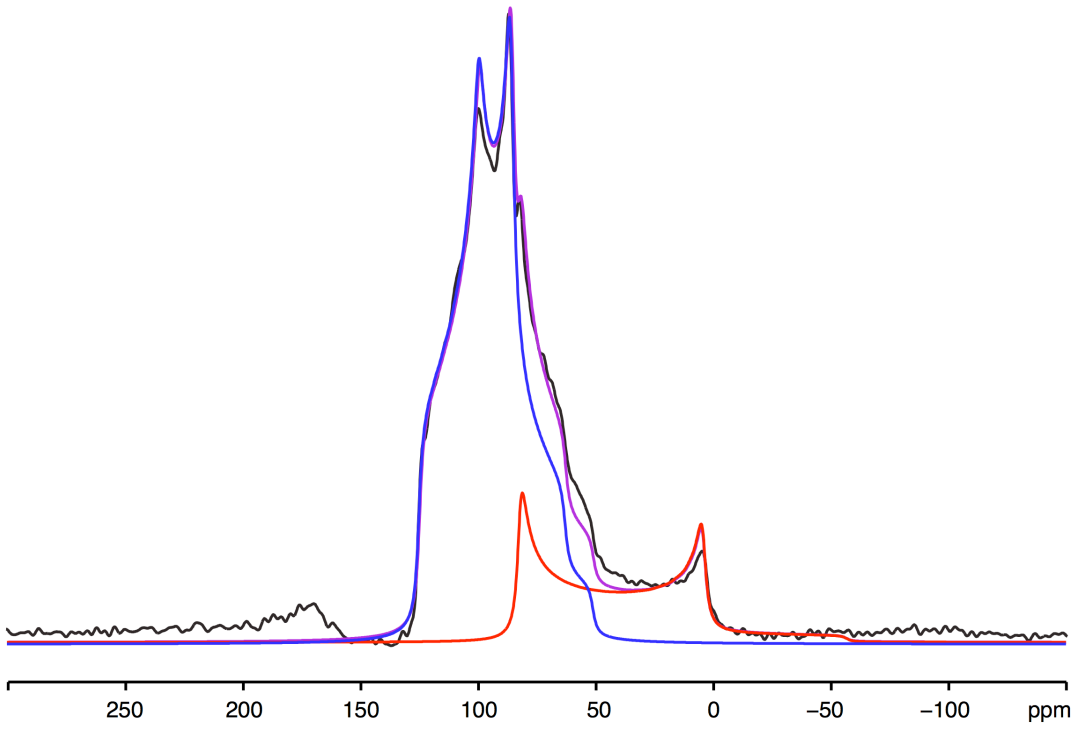

Figure 2.31: Analytical fitting of the ^{45}Sc (14.1 T) MAS NMR spectrum of Sc_2O_3. The experimental spectrum is shown in black, fitted lineshapes for the Sc1 and Sc2 sites are shown by the red and blue lines, respectively, with the summation of the two shown in purple. The spectrum is the result of averaging 512 transients with a recycle interval of 3 s. The MAS rate was 60 kHz. Details of the parameters obtained are given in Table 2.3.

can be achieved a ^{45}Sc (14.1 T) MAS NMR spectrum recorded for Sc_2O_3 has been fitted using SOLA and is shown in Figure 2.31. Sc_2O_3 possesses two crystallographically distinct Sc sites. In Figure 2.31 the experimental spectrum is shown in black with the fitted lineshapes for the Sc1 and Sc2 sites denoted by the red and blue lines respectively. The sum of the two sites is shown in purple. It was possible to extract values for δ_{iso}, C_Q and η_Q for each site. The extracted parameters obtained were in good agreement with the literature and are given in Table 2.3.[191] Whilst this is easy for simple spectra it becomes impractical as the number of sites increases and high-resolution approaches are required.

MQMAS spectra contain a series of ridge lineshapes, each of which corresponds to a different crystallographically-distinct species. Using MQMAS, it is possible to extract information regarding both the

Table 2.3: Experimental ^{45}Sc NMR parameters δ_{iso}, C_Q, η_Q and P_Q for Sc_2O_3 obtained from the MAS spectrum in Figure 2.31.

Site	δ_{iso} (ppm)	P_Q / MHz	C_Q / MHz	η_Q
Sc1	105.8(5)	23.3(1)	23.3(1)	0.0(1)
Sc2	126.6(5)	16.3(1)	15.4(1)	0.6(1)

quadrupolar and chemical shift interactions from spectra. This can be completed in a variety of ways, the most common of which being to obtain the position of the centre of gravity of the ridge lineshape (δ_1, δ_2). This then enables determination of the isotropic chemical shift, δ_{iso}, and the quadrupolar product, P_Q, a combination of the quadrupolar coupling constant, C_Q, and asymmetry, η_Q, given by[192]

$$P_Q = C_Q(1 + \eta_Q^2/3)^{1/2} \quad . \tag{2.57}$$

Alternatively, the parameters δ_{iso}, C_Q and η_Q may be obtained directly by computer fitting of an extracted cross-section along the experimental ridge, parallel to δ_2. However, it must be noted the lineshape obtained in this case can be distorted as a result of non-uniform excitation and conversion of triple-quantum coherences.

To illustrate one method of extracting NMR parameters from an MQMAS spectrum the aluminophosphate AlPO-14 has been used as an example. The aluminophosphates (AlPOs) are an important class of microporous materials with numerous applications in areas such as separation and catalysis. Organic templates, commonly amines or quaternary ammonium salts, are also added during the hydrothermal synthesis of such framework materials. The template molecules are essential in producing the microporous frameworks adopted by aluminophosphates as they are incorporated into the cavities within the structure. Post-synthetic removal of the template can be achieved by conventional calcination methods. Calcined AlPO-14 contains four crystallographically distinct Al sites and the structure is shown in Figure 2.32. ^{27}Al ($I = 5/2$) is a quadrupolar nucleus and commonly displays

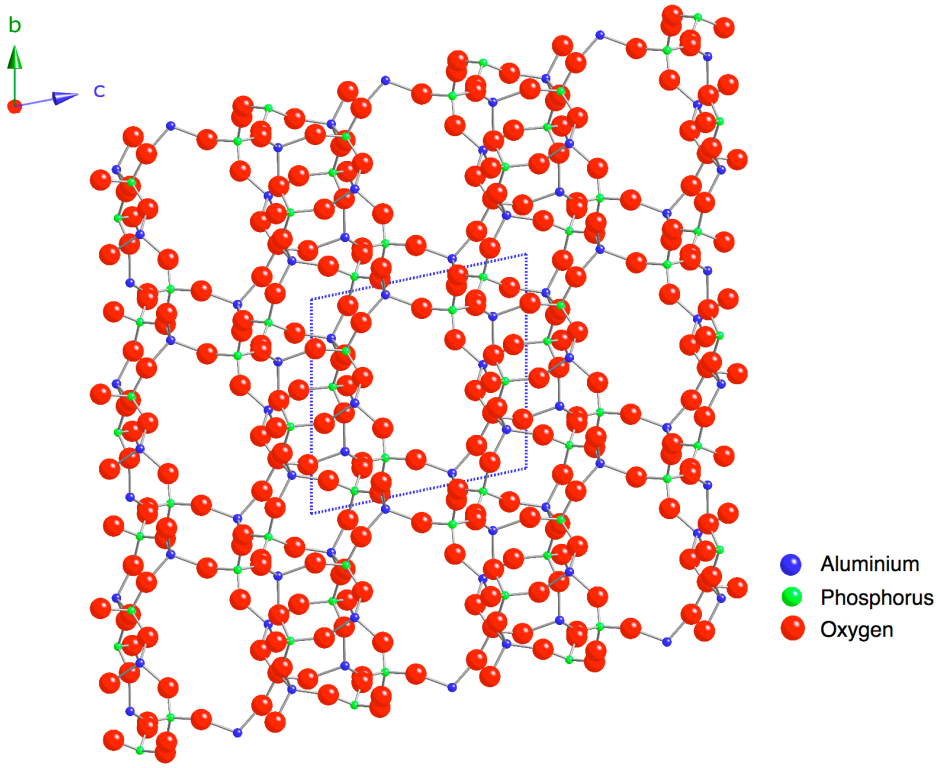

Figure 2.32: Crystal structure of calcined AlPO-14 viewed along the a axis.

broadening as a result of the incomplete removal of second-order quadrupolar interactions. Hence, MQMAS techniques are routinely utilised for materials containing this nucleus. The triple-quantum ^{27}Al MAS NMR spectrum of calcined AlPO-14 is shown in Figure 2.33 and clearly displays four distinct resonances, in good agreement with the literature.[194,195] To determine parameters for each site a cross-section was extracted from each ridge and analysed using SOLA. It was possible to fit each lineshape and obtain values for δ_{iso}, C_Q and η_Q, for each site, all of which are given in Table 2.4. Extracted lineshapes and subsequent fits are also shown in Figure 2.33. It must be noted that it is not always possible to determine quadrupolar parameters for all sites in any two-dimensional spectrum owing to severe line broadening and/or distortion, commonly caused either by non-uniform triple-quantum excitation or possible disorder within the compound. Furthermore, it is often challenging to accurately distinguish between any overlapped sites. In such cases it is often more convenient to quote P_Q values derived from the position of the centre of gravity.

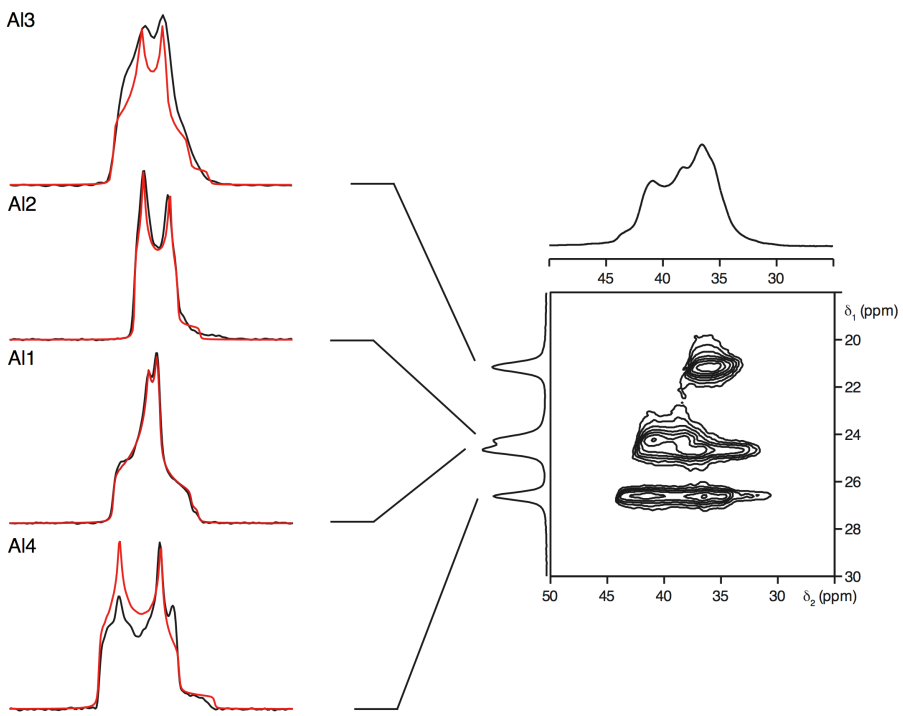

Figure 2.33: Conventional ^{27}Al (14.1 T) MAS NMR spectrum, triple-quantum MAS NMR spectrum, and corresponding isotropic projection. The spectrum was recorded using the phase-modulated split-t_1 shifted echo pulse sequence shown in Figure 2.30 and is the result of averaging 768 transients with a recycle interval of 0.5 s for each of the 256 increments of 129.16 μs. A additional SPAM (soft-pulse added mixing) pulse was added to gain a signal enhancement. The MAS rate was 10 kHz. Also shown (in black) are lineshapes obtained by taking cross sections along ridges parallel to δ_2 corresponding to each site. Each lineshape was subsequently fitted using SOLA, and the fits obtained are also shown in red. The parameters obtained are given in Table 2.4.

2.9.5 MQMAS and Disorder

Disordered materials are a common occurrence throughout solid-state chemistry. Within this particular investigation a variety of perovskite structures have been studied and, like many other materials, they are widely known to exhibit disorder across both the A and B sites. As previously discussed in Chapter 1, there are various synthetic methods that can be utilised to try and promote ordering across these sites.

Table 2.4: Experimental ^{27}Al NMR parameters δ_{iso}, C_Q, η_Q and P_Q for calcined AlPO-14, obtained from the MQMAS spectra in Figure 2.33.

Site	δ_{iso} (ppm)	P_Q / MHz	C_Q / MHz	η_Q
Al1	42.2(5)	4.4(1)	3.9(1)	0.8(1)
Al2	42.5(5)	3.5(1)	3.5(1)	0.2(1)
Al3	37.6(5)	2.7(1)	2.6(1)	0.5(1)
Al4	45.1(5)	5.0(1)	5.0(1)	0.3(1)

However, this is not always successful and, more commonly, a disordered structure will result.

The lineshapes observed for quadrupolar nuclei are commonly broad owing to large quadrupolar interactions. The presence of disorder can produce a substantial effect on the lineshape observed. Therefore, the addition of disorder into any quadrupolar system makes the application of solid-state NMR more challenging. In many quadrupolar spectra the presence of disorder is immediately apparent owing to the observation of 'classic' disordered MAS lineshapes, in which an asymmetric broadening of the central transition is observed with a characteristic 'tail' to lower frequencies. Shown in Figure 2.34 are three different lineshapes which display many of the characteristic features commonly observed in MAS NMR spectra. Figure 2.34(a) displays a quadrupolar lineshape and is representative of a well-ordered crystalline solid. In contrast, Figure 2.34(b) exhibits a broadened lineshape with an asymmetric tail to low frequency. This commonly indicates the presence of a distribution of the quadrupolar interaction. In Figure 2.34(c) a classic 'disordered' lineshape is shown, with no obvious or distinct features. Lineshapes of this type are commonly indicative of a distribution of both quadrupole and chemical shifts. Owing to their broad and often featureless nature it can be difficult to determine the full extent of the disorder exhibited. Therefore, to gain further insight high-resolution two-dimensional techniques such as MQMAS are required. Disorder can result either from a distribution of chemical shifts or a distribution of quadrupolar shifts. However, more commonly, disorder is caused by a combination of the two. The size and shape of the resulting ridge lineshape, in addition to the direction along

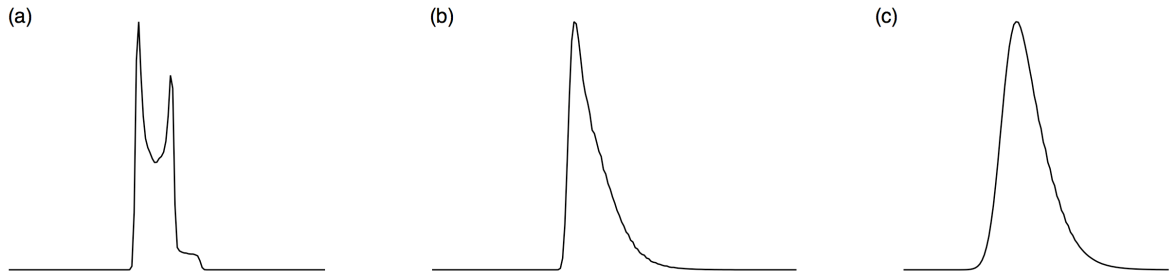

Figure 2.34: Simulated I = 5/2 MAS lineshapes (a) single lineshape with C_Q = 3 MHz, η = 0 and δ_{CS} = 0 ppm, (b) includes a Gaussian distribution of C_Q with a half width at half-height of 0.75 MHz and (c) includes uncorrelated Gaussian distributions of both C_Q (as in (b)) and δ_{CS} (with a half-width at half-height of 2 ppm). All simulations have $\omega_0/2\pi$ = 104.3 MHz.

which each is broadened in any MQMAS spectrum, is highly informative as to the nature of any disorder exhibited. Consider a spin I = 3/2 nucleus, if a single sharp ridge is displayed and aligned along a gradient of −7/9 (the MQMAS ratio, R) no distribution of parameters is present. Hence, the system is well-ordered. However, if the ridge is broadened along a gradient of +3 this is indicative of a distribution of chemical shift environments, $dist_{CS}$. When the ridge is broadened along the ratio $A^0(I,3/2)/A^0(I,1/2)$ this indicates a distribution of quadrupolar contributions, $dist_Q$ is present. Specific values for both $dist_{CS}$ and $dist_Q$ are tabulated in Table 2.5 for half-integer nuclei. When a distribution of both chemical and quadrupolar shifts is exhibited the length and shape of the ridge is altered. Shearing a spectrum also changes the direction along which the ridge is aligned. All values in Table 2.5 are prior to shearing, values post shearing can be found in Appendix I.

To illustrate how different MQMAS spectra of ordered and disordered materials can be, ^{27}Al MQMAS NMR spectra have been recorded and compared for two Al-bearing compounds. Aluminium acetylacetonate, $Al(acac)_3$, is one example of a well ordered material. The ^{27}Al MAS NMR spectrum of $Al(acac)_3$, shown in Figure 2.35(a), displays a single resonance, indicative of a single site. Similarly, the ^{27}Al two-dimensional multiple-quantum MAS NMR spectrum, recorded using a z-

Table 2.5: Values for distribution of chemical shift and quadrupolar shifts for half-integer nuclei.

I	m_I	R	$dist_{CS}$	$dist_Q$
$I = 3/2$	$1/2$			
	$3/2$	$-7/9$	3	-3
$I = 5/2$	$1/2$			
	$3/2$	$19/12$	3	$3/4$
	$5/2$	$-25/12$	5	$-25/4$
$I = 7/2$	$1/2$			
	$3/2$	$101/45$	3	$9/5$
	$5/2$	$11/9$	5	-1
	$7/2$	$-161/45$	7	$-49/5$
$I = 9/2$	$1/2$			
	$3/2$	$91/36$	3	$9/4$
	$5/2$	$95/36$	5	$5/4$
	$7/2$	$7/18$	7	$-7/2$
	$9/2$	$-31/6$	9	$-27/2$

filtered pulse sequence, displays a single narrow ridge aligned along the MQMAS ratio 19/12, thereby confirming there to be no distribution of parameters and hence no disorder (Figure 2.36(a)). In contrast, γ-alumina, γ-Al_2O_3, is a well known example of a disordered material. The ^{27}Al MAS NMR spectrum, shown in Figure 2.35, displays two broad resonances, corresponding to 4 and 6 coordinate Al sites respectively. Both sites display 'disordered' lineshapes with 'tails' to low frequency. The ^{27}Al two-dimensional multiple-quantum MAS NMR spectrum of the 6 coordinate resonance, recorded using a z-filtered pulse sequence, is shown in Figure 2.36(b) and displays a single broad resonance which is suggestive of a distribution of both chemical and quadrupolar shifts. Also shown for completeness in Figure 2.36(c) and (d) are sheared two-dimensional spectra for $Al(acac)_3$ and γ-Al_2O_3 respectively. An extracted cross-section from the $Al(acac)_3$ spectrum in Figure 2.36(a) was fitted using SOLA and the corresponding NMR parameters can be found in Table 2.6. Average chemical shift, $\langle\delta_{iso}\rangle$, and quadrupolar product, $\langle P_Q\rangle$, values

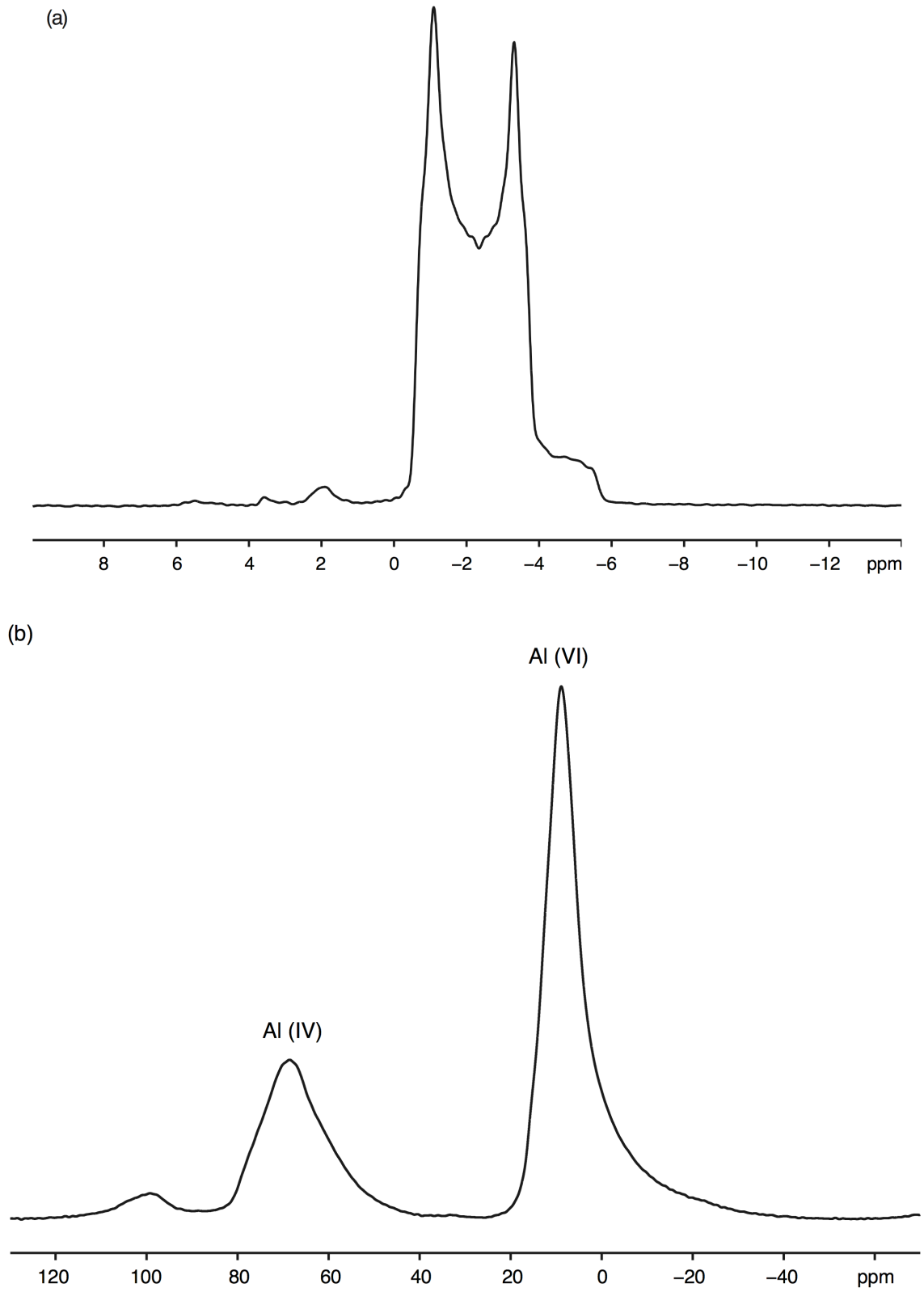

Figure 2.35: Conventional ^{27}Al MAS (14.1 T) NMR spectra for (a) $Al(acac)_3$ and (b) γ-Al_2O_3. Spectra are the result of averaging (a) 64 and (b) 96 transients with a recycle interval of 2 s. The MAS rate was 14 kHz.

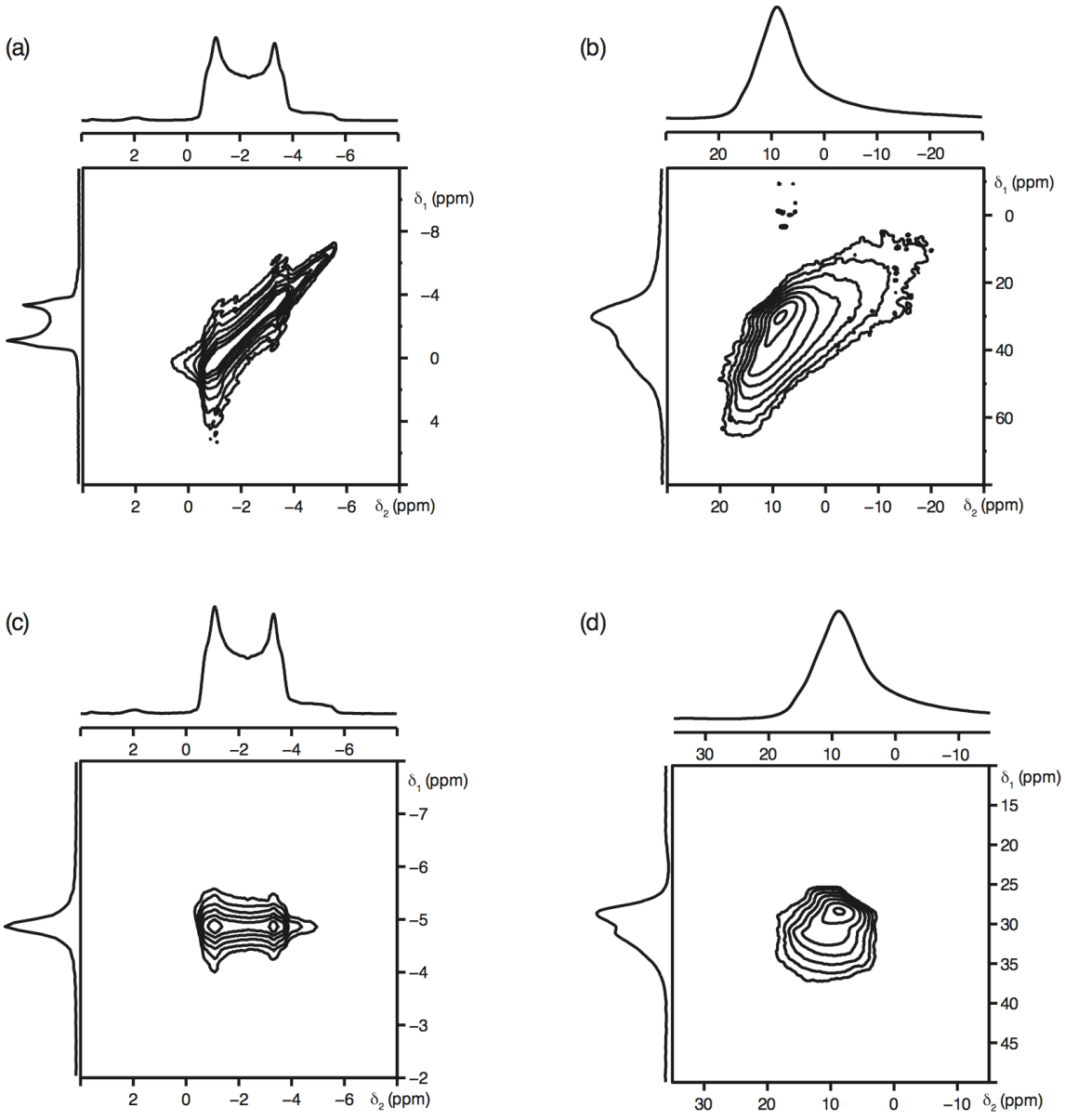

Figure 2.36: Conventional ^{27}Al (14.1 T) MAS NMR spectra and triple-quantum MAS NMR spectra for (a, c) Al(acac)$_3$ and (b, d) γ-Al$_2$O$_3$. The spectra in (a) and (b) were recorded using the z-filtered pulse sequence shown in Figure 2.29 and are the result of averaging 96 transients with a recycle interval of 3 s for each of the (a) 768 and (b) 256 increments of 33.3 μs. The MAS rate was 14 kHz. The ^{27}Al MQMAS spectra and corresponding isotropic projections shown in (c) and (d) are post shearing.

Table 2.6: Experimental ^{27}Al NMR parameters δ_{iso}, C_Q, η_Q and P_Q for Al(acac)$_3$ obtained from the MAS spectrum in Figure 2.35.

Site	δ_{iso} (ppm)	P_Q / MHz	C_Q / MHz	η_Q
Al1	−0.09(5)	3.0(2)	3.0(2)	0.2(1)

Table 2.7: Experimental ^{27}Al NMR parameters $\langle\delta_{iso}\rangle$ and $\langle P_Q\rangle$ C_Q, η_Q and P_Q for γ-Al_2O_3 obtained from the position of the centre of gravity in the MQMAS spectrum in Figure 2.36.

Site	$\langle\delta_{iso}\rangle$ (ppm)	$\langle P_Q\rangle$ / MHz
Al1	−0.09(5)	3.0(2)

obtained for γ-Al_2O_3 from the position of the centre of gravity in the MQMAS spectrum shown in Figure 2.36(b) can be found in Table 2.7. MQMAS NMR spectra can therefore be successfully utilised to gain additional insight into the precise nature of any disorder exhibited in a particular system. Furthermore, when used in conjunction with other structural characterisation techniques such as high-resolution powder diffraction it will aid considerably in both the structural understanding and characterisation of the system under investigation.

2.10 Density Functional Theory (DFT) Calculations

2.10.1 Introduction

The use and practical implementation of first-principles calculations within solid-state chemistry has accelerated in recent years owing to major advancements and modifications of computational codes. Within this particular study first-principles or, more specifically, density functional theory (DFT) calculations have been utilised to calculate NMR parameters, such as the isotropic chemical shift, δ_{iso}, and quadrupolar parameters C_Q and η_Q. DFT methods provide a relatively easy way to

monitor the variation of NMR parameters with changes to local coordination environment and, when used in conjunction with high-resolution NMR data, they provide key assistance in spectral understanding, assignment and interpretation. In addition, DFT calculations aid in linking NMR and diffraction directly as the crystal structures initially used in DFT calculations are commonly obtained from X-ray or neutron diffraction.

In recent years the use of *ab initio* or first-principles calculations has become increasingly important in the field of nuclear magnetic resonance. Parameters obtained by calculation can support those obtained experimentally, where lineshapes may be broadened or distorted as a result of practical imperfections. Furthermore, DFT methods can often provide important additional information regarding anisotropy and tensor orientations, parameters which are often not easy to extract from experiments, particularly under MAS. In some cases the prediction of parameters by calculation can guide experiment and spectral acquisition. For example, a calculation may predict a system to possess a very large CSA or C_Q which cannot, feasibly, be observed experimentally or may require a different practical approach. DFT calculations can also provide insight into the more complex properties of solids, for example disorder or dynamics by comparing experimental data to that calculated for model structures or systems. In general, DFT methods provide a flexible way of studying the dependence of NMR parameters upon structure and local coordination. In turn, they also provide a simple way in which to test various structural models for materials with unknown structures against experimental observables. It must be noted that whilst a full description of DFT is beyond the scope of this thesis some of the methodologies relevant to the calculation of NMR parameters will be discussed in the following sections.

2.10.2 First-Principles Calculations

In principle the energy and properties of a system can be predicted by solving the relevant Schrödinger equation.[196] However, this cannot be

solved exactly for systems with more than one electron, and for larger systems approximations must be made. Consider a single particle that may exist in two quantum mechanical states, 0 and 1, with contributions described by coefficients a and b. The total wavefunction, ψ, can be described by

$$\Psi = (a|0\rangle + b|1\rangle) \quad . \tag{2.58}$$

If this approach is then extended to three particles, each of which may exist in two states, it is entirely plausible to believe ψ may be given by

$$\Psi = (a|0\rangle + b|1\rangle)(c|0\rangle + d|1\rangle)(e|0\rangle + f|1\rangle). \tag{2.59}$$

This expression is, however, incorrect as this approach does not consider the effect of the interactions between the particles. The wavefunction, therefore, needs to be described in terms of all possible combinations of the two states. Hence, the expression for ψ becomes considerably more complex and is given by

$$\Psi = a|000\rangle + b|001\rangle + c|100\rangle + d|010\rangle + e|110\rangle + f|011\rangle + g|101\rangle + h|111\rangle \ , \tag{2.60}$$

where there are contributions from 8 coefficients (a-h) as opposed to 6 in the previous expression. If we then consider *n* particles which can exist in *m* states the number of coefficients required to describe the wavefunction increases as m^n. Whilst for small systems such calculations may appear feasible, for larger molecules or systems this quickly becomes intractable owing to the complexity of the quantum mechanical expression required to describe the total wavefunction. In such cases several approximations need to be made to simplify the problem.

2.10.3 Solving the Schrödinger Equation

To calculate the properties of a system it is necessary to solve the many-particle time-dependent Schrödinger equation, given by

$$-i\hbar\frac{\partial\Psi}{\partial t} = \hat{H}\Psi \quad , \tag{2.61}$$

where the Hamiltonian $\hat{H}$ describes the various electrostatic interactions between particles and is expressed as

$$\hat{H} = \hat{T}_{e,n} + \hat{V}_{e-e} + \hat{V}_{e-n} + \hat{V}_{n-n} \quad , \tag{2.62}$$

where $\hat{T}_{e,n}$ is the kinetic energy between the electrons (e) and nuclei (n) in the system and $\hat{V}$ is the potential energy between the electrons and nuclei in the system. *Ab initio* methods such as Hartree-Fock[197-200] include all terms in the Hamiltonian as far as possible which, in turn, becomes computationally demanding and costly. This method is therefore favoured by small molecular systems where there are fewer atoms. Semi empirical methods, however, use parameters or approximations that compensate for neglecting the more computationally complex terms in the calculation. These parameters are commonly derived either from experiment or *ab initio* calculations completed on model systems. Semi empirical methods can therefore be used for much larger systems. However, it must be noted that such techniques are not always transferable.

2.10.4 The Born-Oppenheimer Approximation

The Born-Oppenheimer approximation[201] exploits the difference in mass between the electrons and the nucleus. Compared to electrons, nuclei are massive and slow. This has two consequences; whenever a nucleus moves, the electrons react so quickly that it may as well be instant, and the wavefunctions for nuclei are zero except in a very small region, hence they contribute only a very small potential. Therefore, only the

effect from the electrons needs to be considered and since they react instantaneously to any change in the position of the nuclei this removes the time dependency of the Schrödinger equation given by

$$\hat{H}\Psi = E\Psi \tag{2.63}$$

where

$$\hat{H} = \hat{T}_e + \hat{V}_{e-e} + \hat{V}_{e-n} \quad . \tag{2.64}$$

The Hamiltonian now depends solely on the quantum mechanics of the electrons. The expression is, however, still relatively complex with two unknown variables; the kinetic energy of the electron, $\hat{T}_e$, and the potential energy between electrons, $\hat{V}_{e-e}$.

2.10.5 Density Functional Theory (DFT)

An alternative approach to this problem was presented in the mid 1960s. Two papers by Hohenberg and Kohn[202] and Kohn and Sham[203] showed that the ground state energy and charge density of interacting electrons in any external potential were equivalent to those of non-interacting electrons in a specially modified potential. Hence, the total ground state energy of the system may be written solely in terms of a functional of the electron density using the Hohenberg-Kohn equation, given by

$$E[\rho] = E_{KE}[\rho] + E_{e-e}[\rho] \tag{2.65}$$

$$E[\rho] = E_{KE}^{non-int}[\rho] + E_{e-e}^{non-int}[\rho] + E_{xc}[\rho] \quad , \tag{2.66}$$

where $E_{KE}^{non-int}[\rho]$ and $E_{e-e}^{non-int}[\rho]$ are the kinetic and potential energy of a system of non-interacting electrons respectively. The extra term in this equation, $E_{xc}[\rho]$, is a functional of the electron density $\rho(r)$ and is called the exchange-correlation functional. This accounts for the quantum mechanical energy not described by the first two terms. The exact form of this term is unknown, but can contribute up to ~10% of the total energy.

To accurately determine its contribution physically motivated approximations need to be made. The simplest and most commonly used approximation is the local density approximation, LDA,[204,205] given by

$$E_{xc}[\rho] = \int \varepsilon_{xc}(\rho)\rho(r)d^3r \ , \qquad (2.67)$$

which uses the local value of the electron density to determine $E_{xc}[\rho]$. It calculates the exchange-correlation density at a given point from that of a uniform electron gas with the same electron density. This approximation is based on a first-principles approach and is routinely used for solid-state systems. LDA works surprisingly well, however, it is widely known to encounter problems regarding the energetics of systems. It has subsequently been shown that for many systems the addition of terms dependent upon the gradient of the density can provide an improvement. This is known as the generalized gradient approximation, GGA,[206,207] and is given by

$$E_{xc}[\rho] = \int \varepsilon_{xc}(\rho, \nabla\rho)\rho(r)d^3r \ . \qquad (2.68)$$

In contrast to LDA, this approximation is routinely used for chemical applications. There are a number of possible methods by which this can be achieved, for example in solid-state NMR calculations the GGA proposed by Perdew, Burke and Ernzerhof (PBE)[208] is routinely used and has been shown to be extremely useful.

2.10.6 Planewaves and Pseudopotentials

Wavefunctions, Ψ, are usually expanded in terms of a linear combination of basis set functions, given by

$$\Psi = \sum_j c_j \psi_j . \qquad (2.69)$$

For molecules the extent of the system is well defined and the atomic or molecular orbitals provide a good basis set. Solids, however, are large

extended systems therefore a suitable method is required to accurately calculate such structures. Traditional computational methods typically use cluster approximations to calculate extended systems. Using this method an 'infinite' solid is approximated around a central atom, and any dangling bonds are appropriately terminated, typically using hydrogen bonds. The size, shape and long-range electrostatics of the cluster are dependent upon the precise position of the termination. Conventionally, atom-based orbitals are the basis set used in cluster approximations. The accuracy of any cluster calculation is therefore dependent upon the size and type of basis set used and the precise point of termination. To obtain accurate results large cluster sizes are typically required which are, computationally, expensive and demanding, and often require large computational resources.

In reality, solids such as zeolites, polymers and glasses are large extended periodic systems and atomic orbitals do not usually provide an adequate basis set. Therefore, a basis set is required that exploits the inherent periodicity of a solid. Bloch's theorem states that if the nuclei are arranged in a periodically repeating pattern their potential acting on the electrons must also be periodic. In addition, the density and the wavefunction, or more specifically its magnitude, must also be periodic. The translational symmetry of solids may therefore be exploited computationally. Three-dimensional periodic boundary conditions can be imposed using the unit cell, enabling long-range effects to be reproduced. Unlike cluster approximations, there are no 'termination' problems when using this method. One basis set which exploits the periodicity of the wavefunctions is planewaves.[209] They form a mathematically simple basis whilst naturally incorporating periodic boundary conditions. Planewave calculations can be taken systematically to convergence as a function of the size of the basis set. There are, however, an infinite number of possible planewaves with increasing energy, and so a cut-off energy, E_{cut}, needs to be defined which results only in planewaves with energy less than this to be included. All calculations must be 'converged' with respect to E_{cut}, i.e., this parameter should be increased until the answer no longer changes within the specified tolerance range. Wavefunctions which

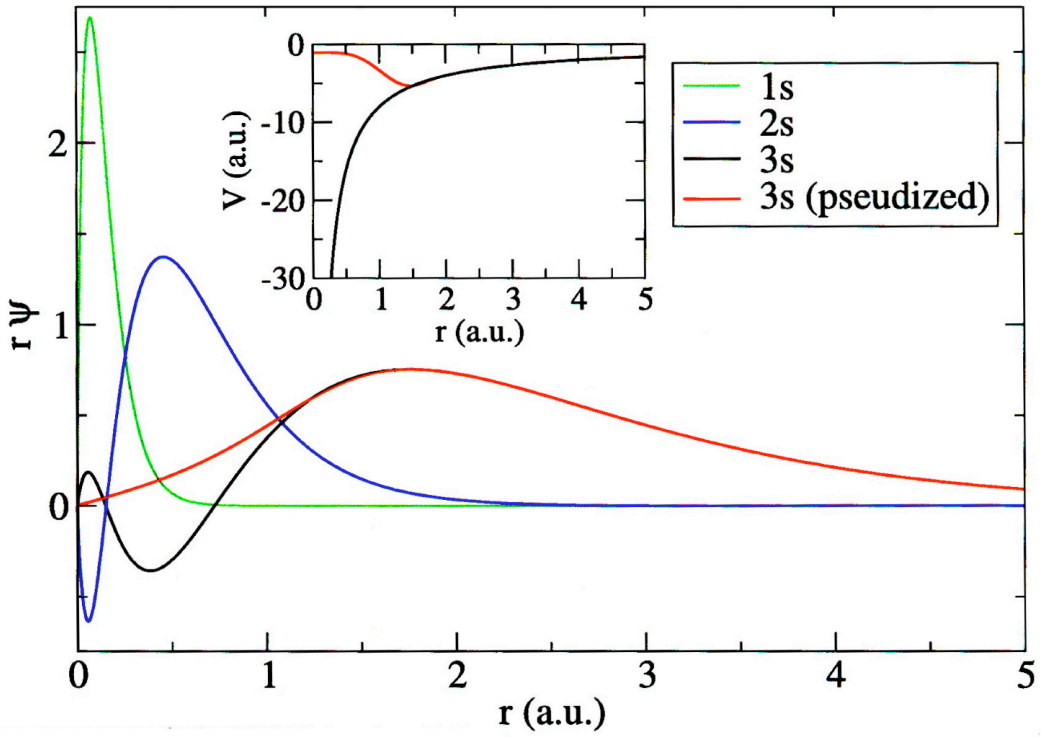

Figure 2.37: Pseudized (red line) and all electron (black line) wavefunction for the 3s valence state of silicon. The two are in good agreement beyond the core radius r_c.

rapidly oscillate require many planewaves to accurately describe them and hence higher cut-off energies.

The use of planewaves is highly advantageous, however, there are some associated technical difficulties. For example, the explicit representation of core and valence electrons near to the nucleus would require too many planewaves. Therefore to ensure the efficiency of all calculations when using planewaves two major approximations must be made; (1) the frozen core approximation and (2) the pseudopotential approximation. The electrons in an atom can be divided broadly into two types, core and valence. The core electrons are tightly bound to the nucleus and are, in turn, not directly involved in bonding, hence they play no part in the interactions between atoms. The core electrons simply provide a shielding or screening of the nuclear charge effect. The frozen core approximation ensures the core electrons are constrained not to differ from their free atomic nature when placed in the molecular or solid-state environment. This approximation reduces the number of electronic degrees of freedom in an all-electron calculation. The pseudopotential

approximation is a different but physically relevant approximation.[210,211] Once the frozen core approximation has been used the valence electron wavefunctions can oscillate rapidly close to the nucleus, thereby requiring many planewaves. Pseudopotentials allow a simplification of the wavefunctions close to the nucleus. The nodal structure of the all-electron wavefunction is replaced by a node-less smooth pseudo wavefunction within the 'core radius', r_c, of the nucleus, as illustrated in Figure 2.37. The pseudo wavefunctions are then used to calculate the resulting pseudopotentials for each atom, each of which is then used in subsequent calculations.

Almost all physical properties depend on the region outside r_c. For core region properties the simplified core region description does not provide accurate results, therefore a true all-electron description of the core region is necessary. This can be achieved using the projector augmented wave (PAW) method, developed by van de Walle and Blöchl.[212] This approach uses the pseudopotential description of the core region and from this the all-electron observables are reconstructed, thereby enabling accurate calculation of the NMR parameters. One major advantage of this method is its ability to compute large systems with high accuracy and low computational cost. The PAW method is, however, not applicable to studying solid systems in a uniform magnetic field. A modification to this method is therefore required. The introduction of an external magnetic field induces a current from both the core and valence electrons and to calculate parameters such as the chemical shift in the presence of a magnetic field this current needs to be accurately calculated. The contribution to the current from the core electrons can be calculated relatively easily. The contribution from the valence electrons, however, is more challenging to calculate as these electrons are described using pseudo wavefunctions in a region close to the nucleus. To accurately calculate the all-electron current in this region an augmentation of the pseudo wavefunction is required. One method for doing this is the Gauge Including Projector Augmented Wave[213] (GIPAW) formalism. This introduces gauge invariance to the PAW method in order to preserve

translational invariance in the magnetic field. This, in turn, enables accurate calculation of chemical shieldings.

2.11 CASTEP

The CASTEP[214-216] code uses first-principles quantum mechanical methods, namely density functional theory, for electronic structure calculations. CASTEP is a planewave DFT code which exploits the inherent periodicity of many solids and enables accurate calculation of NMR parameters from the shielding, quadrupolar and scalar coupling tensors.

2.11.1 Convergence Studies

Once the pseudopotenial has been decided the accuracy of any CASTEP calculation depends on an optimal set of computational parameters, namely the cut-off energy, E_{cut}, of the planewave and the k-point spacing. To accurately determine these optimised values a series of convergence tests are required for individual systems. To do this several calculations must be undertaken with one of the variables fixed whilst the effect on the calculated NMR parameters of varying the other is investigated. These parameters converge to a specific value (within a specified tolerance range) and the point at which convergence is achieved indicates the optimal value for that particular variable. This sequence is then repeated for the other variable. Once completed the optimal cut-off energy and k-point spacing can be used to accurately calculate the NMR parameters for the system of interest. It must be noted that as the specified tolerance limit is increased the answer will become more accurate, however, this accuracy comes at a greater computational cost. Therefore, the exact tolerance used is a compromise between the level of accuracy required and the computational resources available.

Convergence studies were undertaken for the various systems discussed in this work. Detailed below are the convergence tests completed for the Pbcm phase of sodium niobate, $NaNbO_3$.[217] The k-point

spacing in initial tests was fixed at 0.1 $Å^{-1}$. Calculations were then completed using cut-off energies of 30, 40, 50, 60 and 70 Ry respectively. The variation of the isotropic shielding, σ_{iso}, quadrupolar coupling constant, C_Q and asymmetry, η_Q, with cut-off energy for Na1, Na2 and Nb are shown in Figures 2.38, 2.39 and 2.40 respectively. All parameters monitored displayed convergence by 50 Ry, as highlighted in Figures 2.38, 2.39 and 2.40. To ensure complete convergence E_{cut} was fixed at 60 Ry and a series of similar calculations were undertaken to optimise the k-point spacing, testing 0.03, 0.04 and 0.05 $Å^{-1}$ respectively. In a similar manner the variation of σ_{iso}, C_Q and η_Q with k-point spacing were plotted, and convergence occurred at a k-point spacing of k = 0.04 $Å^{-1}$, as shown in Figures 2.41, 2.42 and 2.43. Thus, the optimum k-point spacing and cut-off energy for $NaNbO_3$ were 0.04 $Å^{-1}$ and 60 Ry respectively. All subsequent calculations used these parameters.

2.11.2 Structural Optimisation

DFT calculations are a convenient way of directly linking diffraction and NMR. However, a common problem with such calculations is the quality of the initial crystallographic data used to describe the unit cell. Calculations completed using structures obtained directly from X-ray and neutron powder diffraction commonly possess very high energies and large atomic forces on each atom in the unit cell. In contrast, calculations completed using structures obtained from single crystal diffraction data usually possess very low atomic forces. The high energies and large atomic forces exhibited by many of the structures calculated from powder diffraction data therefore suggest that each structure is not in a local energy minimum and geometry optimisation is required. This process 'relaxes' the structure to a true local minimum by minimising the forces on each of the atoms in the unit cell. During geometry optimisation the energy of the electrons for fixed atomic positions is minimised, the atomic forces are evaluated and the atoms are moved in the direction indicated most favourable by the forces. This process is repeated until the force on each atom is below a specified

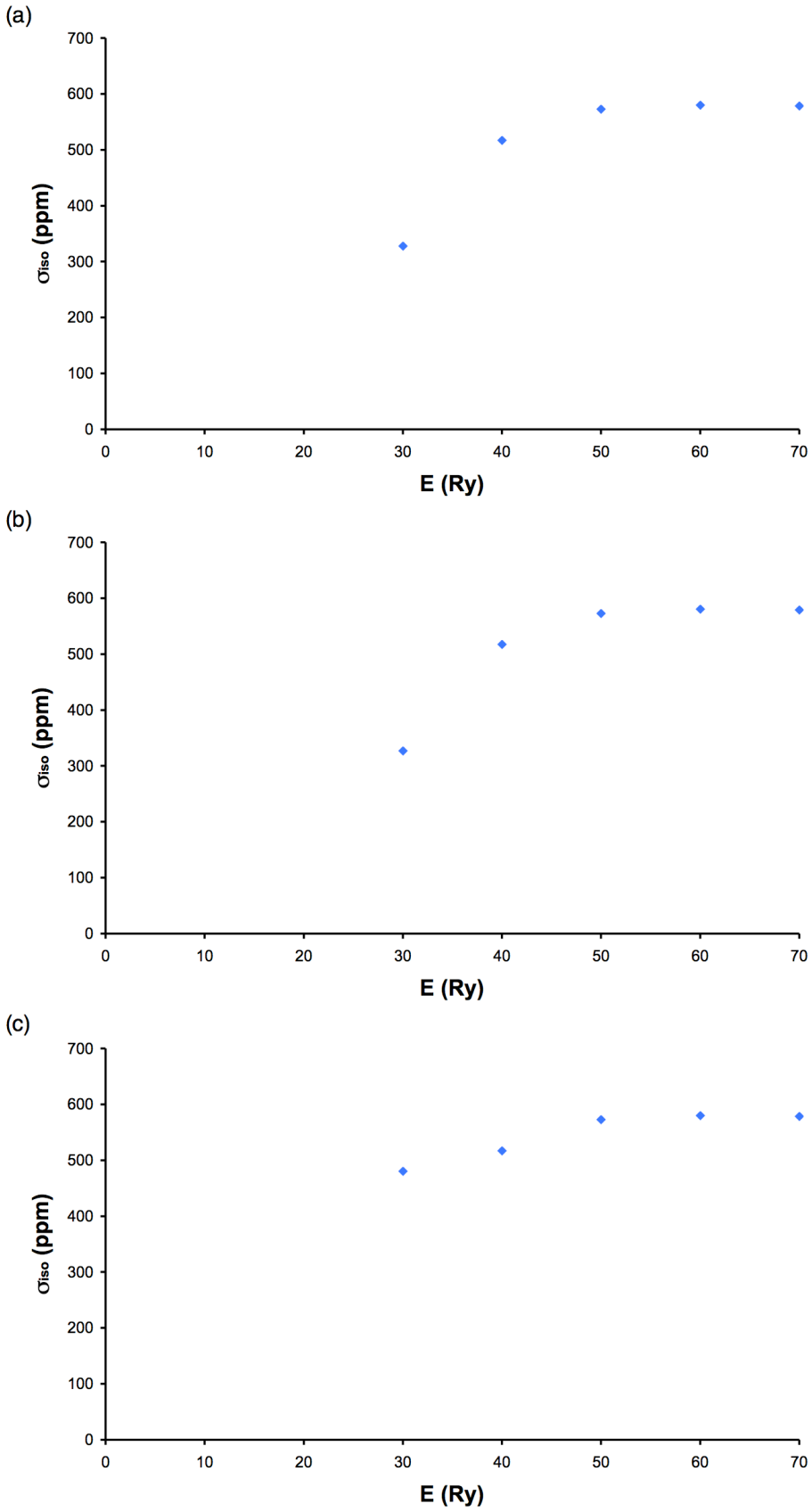

Figure 2.38: Variation of the isotropic shielding, σ_{iso}, with cut-off energy for (a) Na1, (b) Na2 and (c) Nb in $NaNbO_3$.

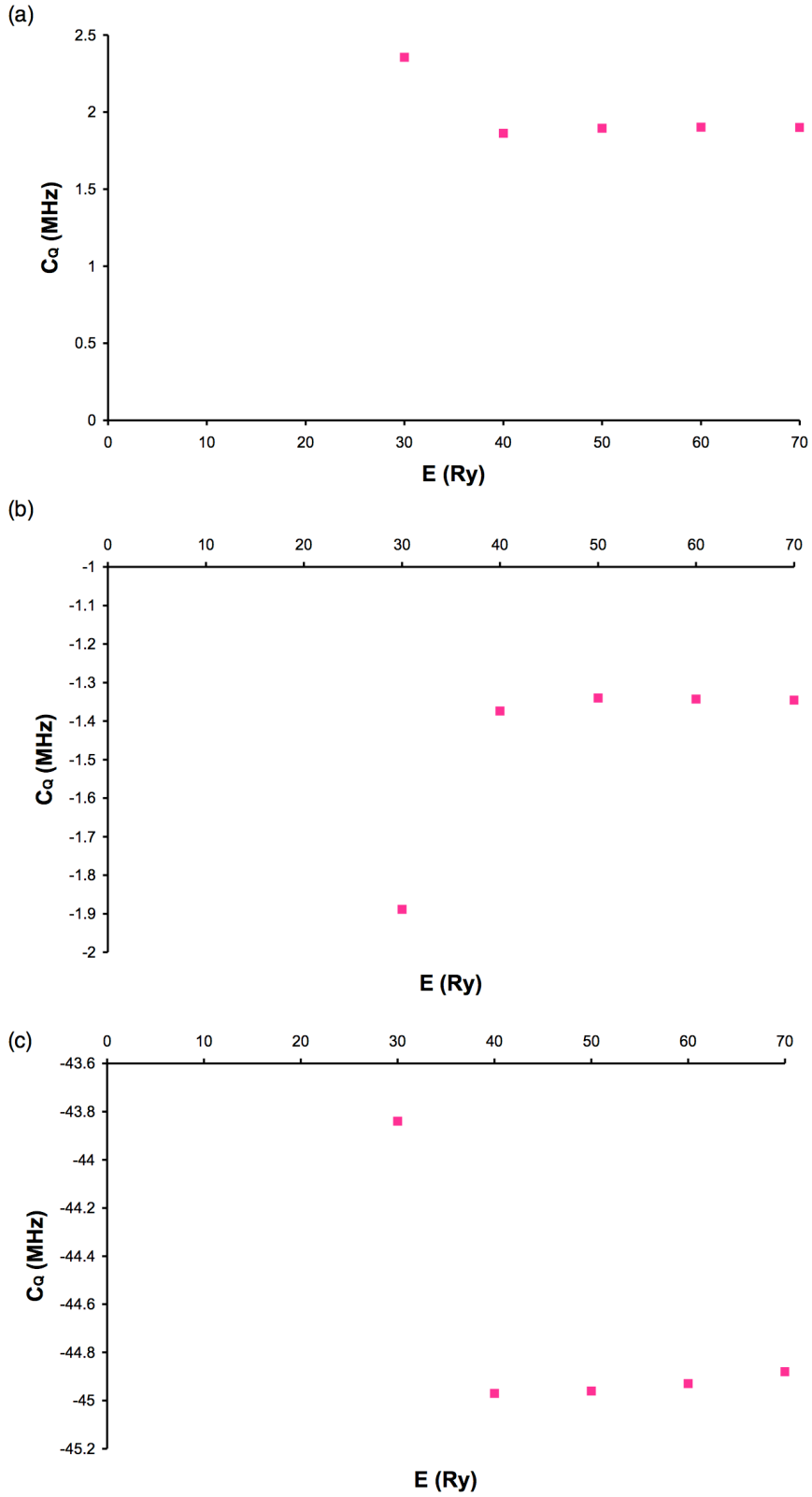

Figure 2.39: Variation of the quadrupolar coupling constant, C_Q, with cut-off energy for (a) Na1, (b) Na2 and (c) Nb in $NaNbO_3$.

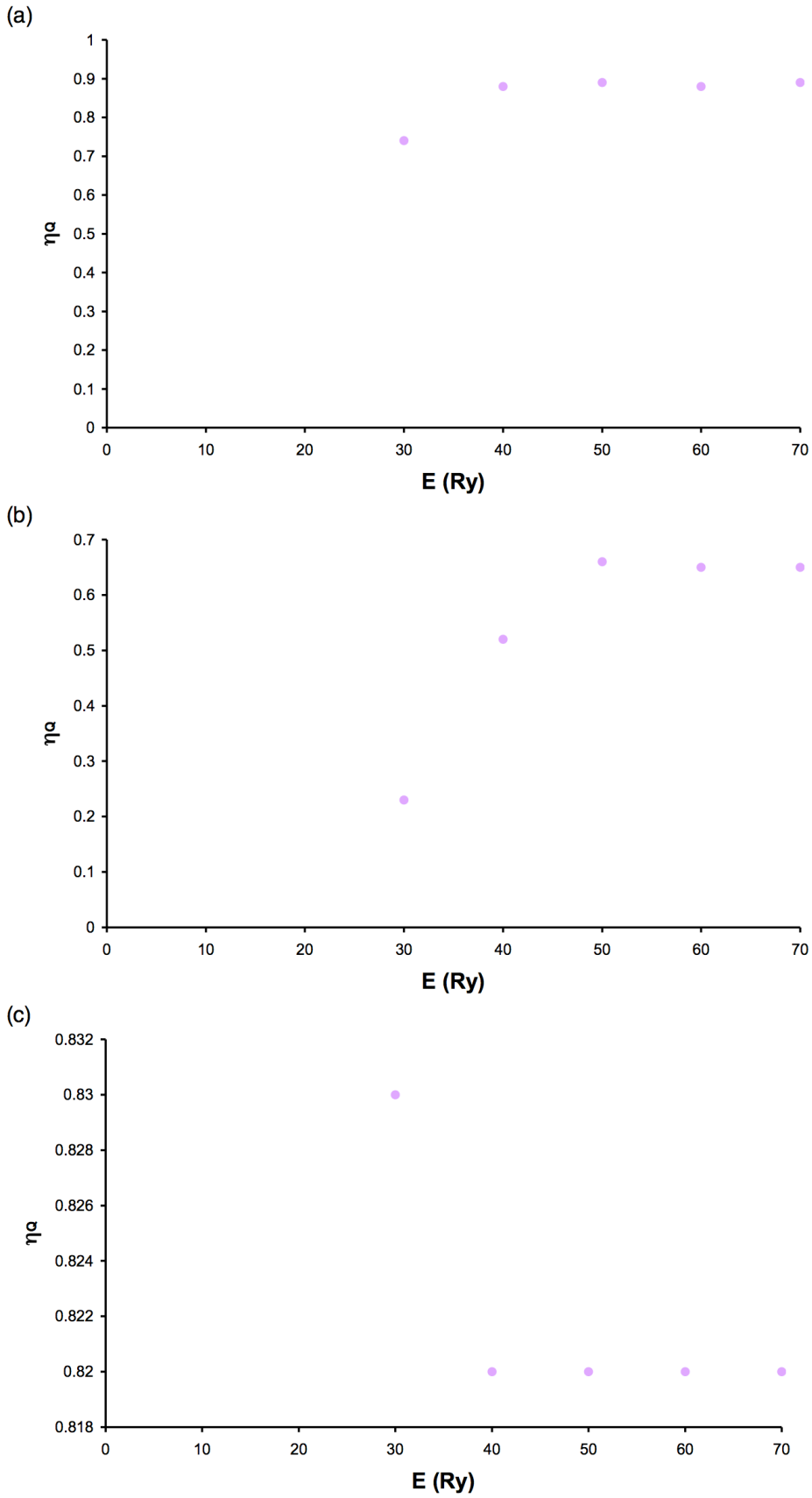

Figure 2.40: Variation of the asymmetry, η_Q, with cut-off energy for (a) Na1, (b) Na2 and (c) Nb in $NaNbO_3$.

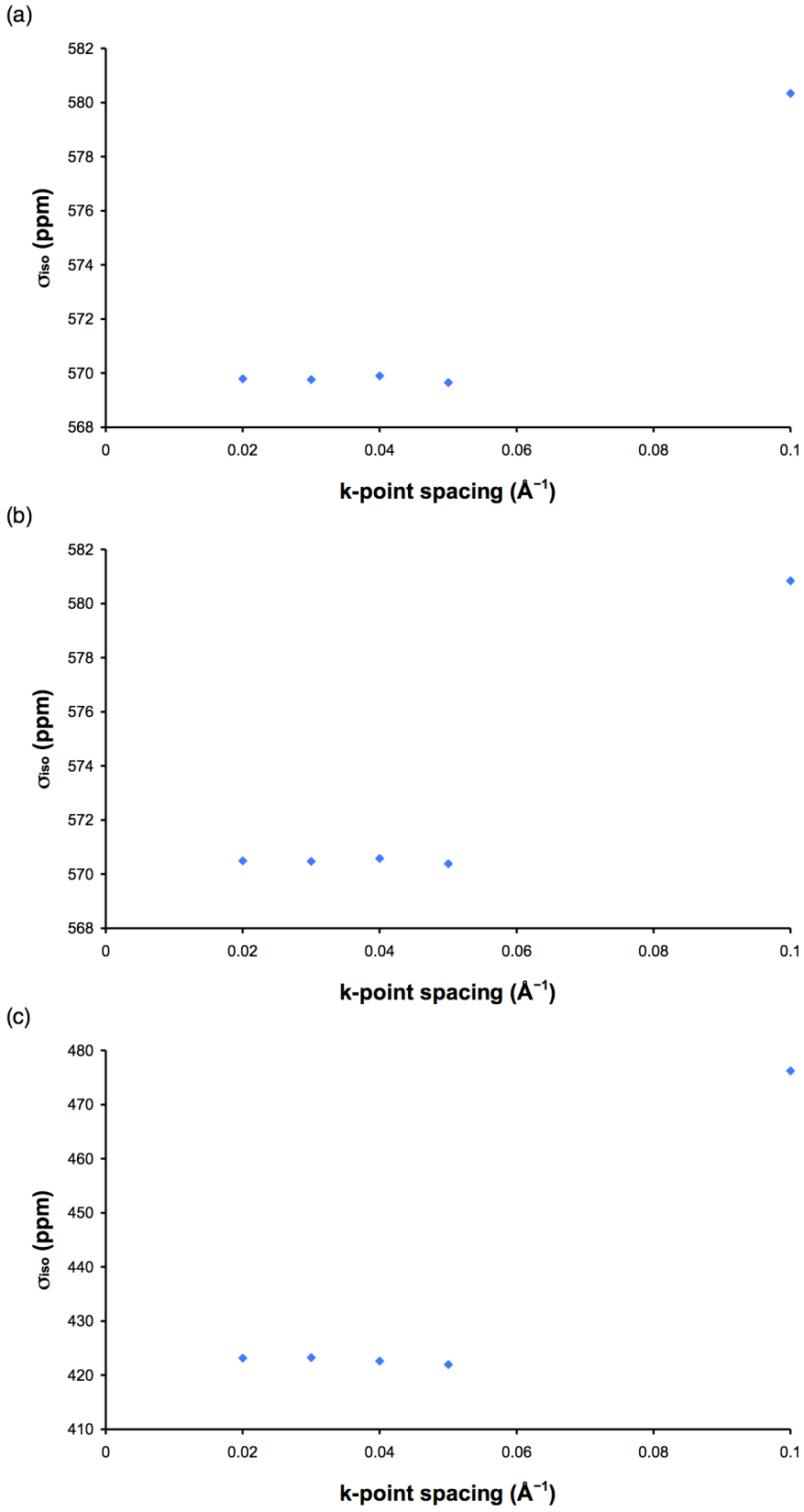

Figure 2.41: Variation of the isotropic shielding, σ_{iso}, with k-point spacing for (a) Na1, (b) Na2 and (c) Nb in $NaNbO_3$.

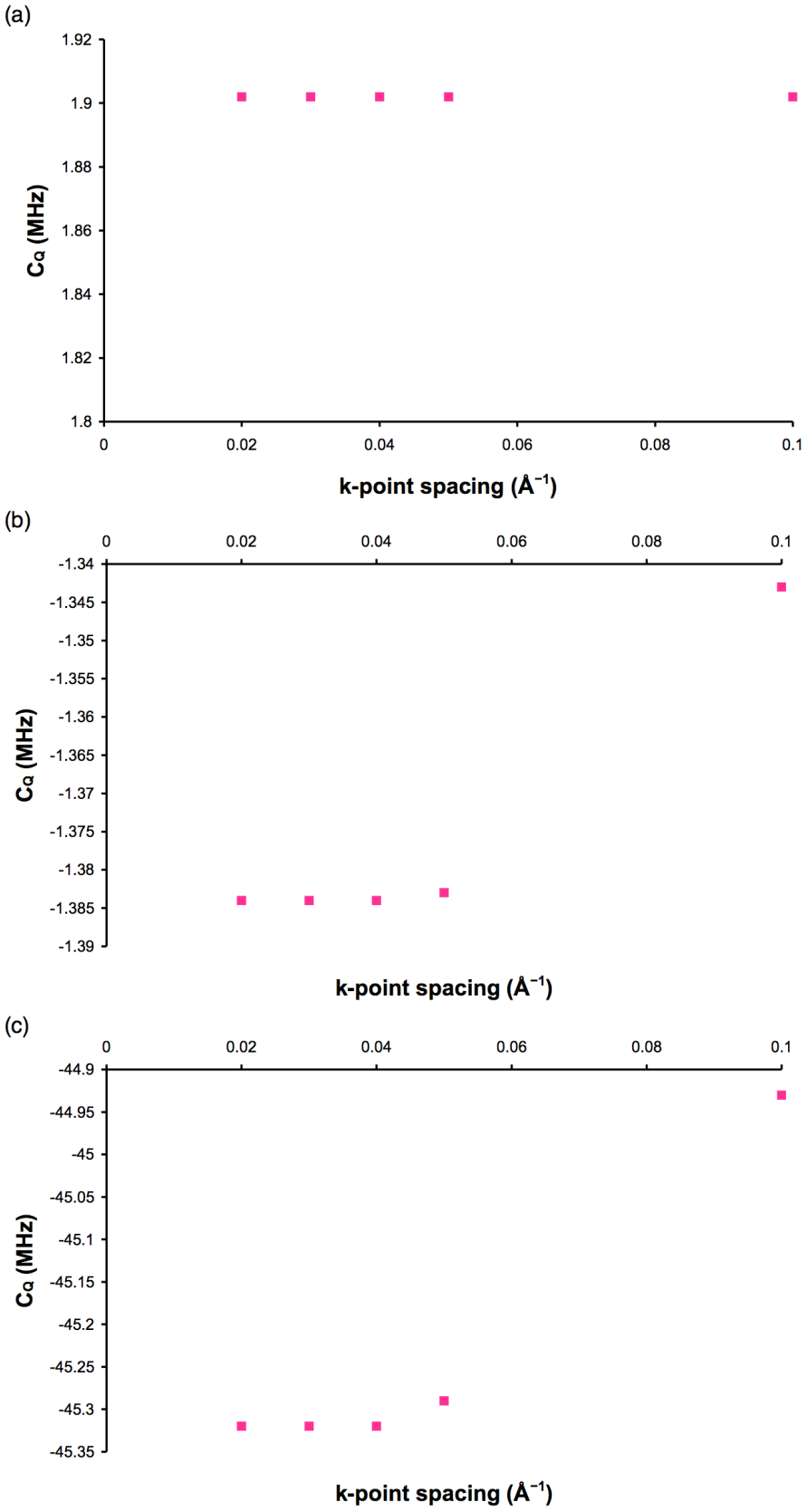

Figure 2.42: Variation of the quadrupolar coupling constant, C_Q, with k-point spacing for (a) Na1, (b) Na2 and (c) Nb in $NaNbO_3$.

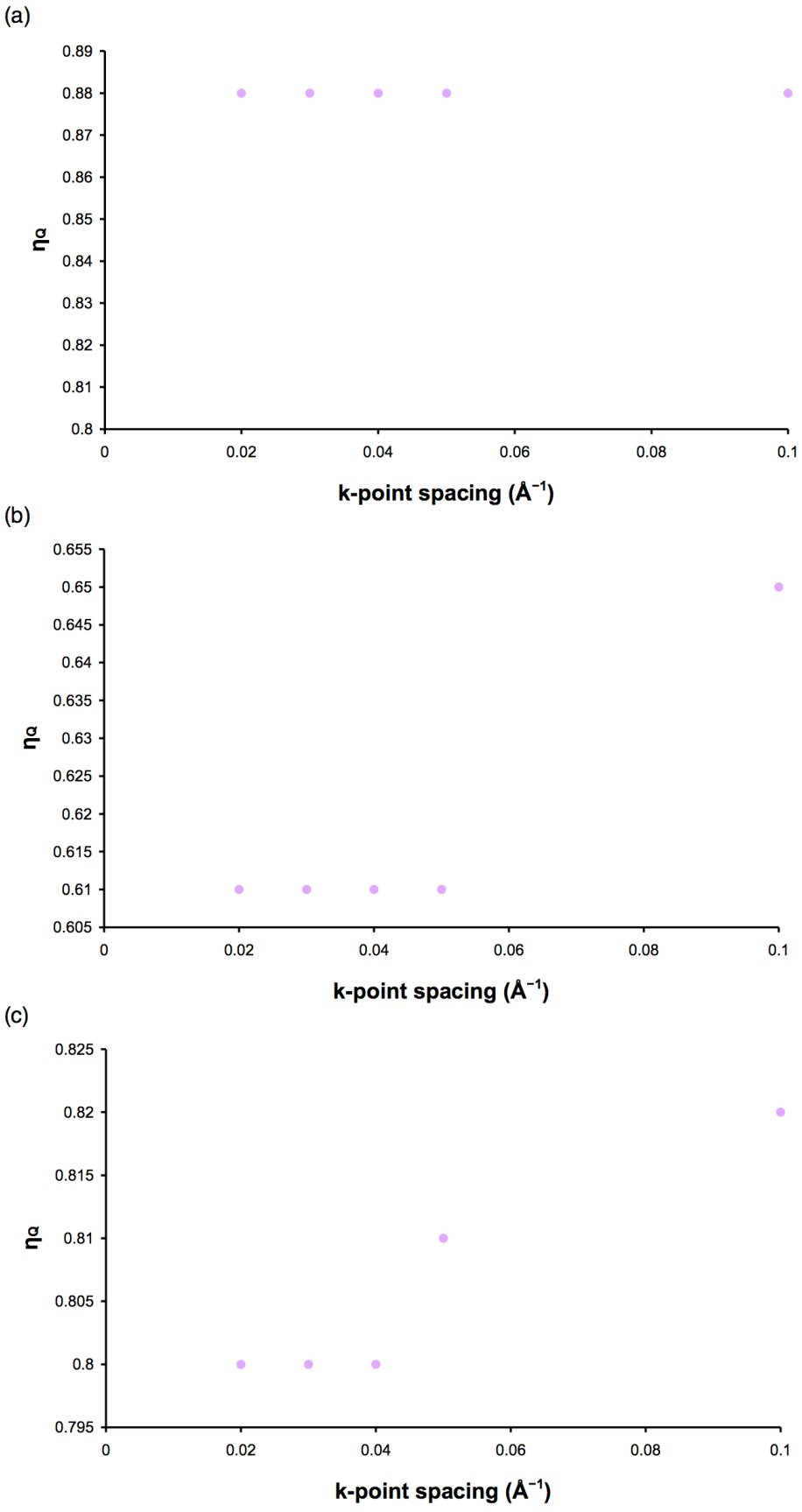

Figure 2.43: Variation of the asymmetry, η_Q, with k-point spacing for (a) Na1, (b) Na2 and (c) Nb in $NaNbO_3$.

tolerance. This then enables the closest local minimum to be found. However, it must be noted that this may not be the global minimum. The structure obtained with the lowest forces is then utilised in subsequent NMR calculations to determine the associated NMR parameters. During a geometry optimisation calculation it is possible to constrain the unit cell parameters (a, b, c, α, β, γ) and allow solely the atomic coordinates to vary. Alternatively all constraints can be removed, enabling both the unit cell and atomic coordinates to vary simultaneously.

Geometry optimisation is an extremely useful method for obtaining the lowest energy structure. However, there is an important issue regarding the accuracy of the structure obtained post optimisation. For example, GGA[206,207] is widely known to overestimate the lattice parameters of a structure during any geometry optimisation whilst LDA[204,205] is known to underestimate the lattice parameters. Therefore, it may be argued that the fully optimised structure is no longer an accurate representation of the initial structure obtained from diffraction. The changes made to the fractional coordinates and/or unit cell are often extremely small, except for atoms that are not initially placed by diffraction, for example protons in microporous materials. NMR parameters are often sensitive to small changes in local structure, hence optimisation is often necessary. There are many associated advantages for relaxing structures prior to calculation of the NMR parameters. For example, within this particular study the greatest degree of correlation between experiment and DFT calculations was generally observed after allowing both the unit cell and atomic coordinates to vary simultaneously. DFT calculations were completed for several different perovskite structures and interestingly, the NMR parameters (δ_{iso}, C_Q and η_Q) calculated for each were found to vary quite considerably depending on whether the structure had been geometry optimised. During any structural optimisation very small adjustments are made to the unit cell and/or atomic coordinates. To highlight how subtle these changes usually are consider the geometry optimisation of $LaScO_3$, an orthorhombic perovskite in space group Pbnm.[218] It must be noted that during optimisation of the structure only the La and O positions are optimised, as the Sc sites are crystallographically fixed on a special

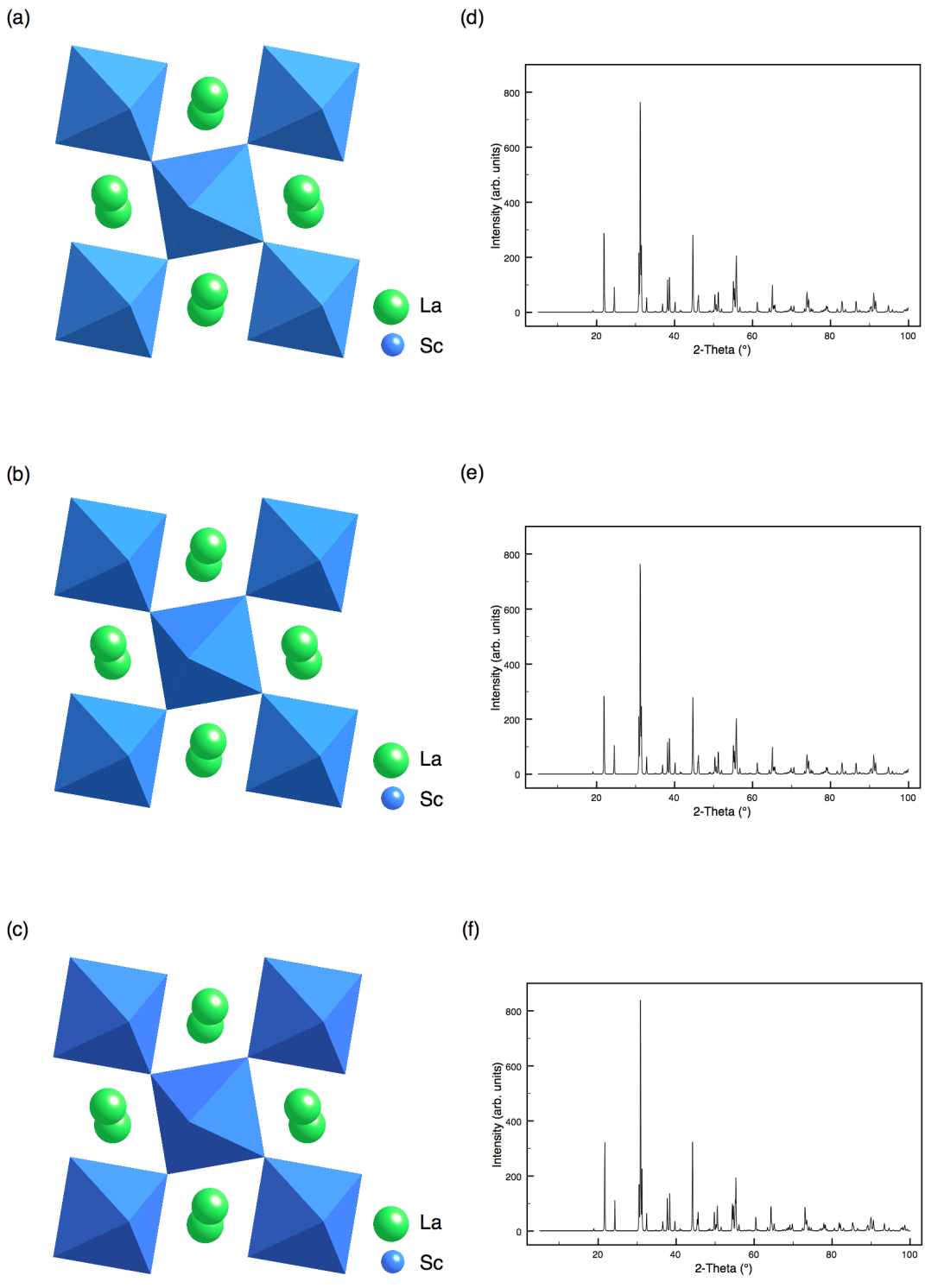

Figure 2.44: The crystal structure of $LaScO_3$ (a) prior to geometry optimisation, (b) post geometry optimisation allowing solely the atomic coordinates to vary, keeping the unit cell fixed and (c) post geometry optimisation allowing both the atomic coordinates and unit cell to vary simultaneously. Also shown in (d-f) are simulated X-ray diffraction patterns for the non-optimised and optimised structures.

Table 2.8: Experimental and calculated (using CASTEP) ^{45}Sc NMR parameters, δ_{iso}, P_Q, C_Q and η_Q, for $LaScO_3$. (a) Experimental parameters for $LaScO_3$ (see Chapter 6), calculated parameters obtained (b) using a structure obtained directly from the literature,[218] (c) post optimisation (fixed unit cell) and (d) post optimisation, allowing both the unit cell and atomic coordinates to vary simultaneously.

	Site	δ_{iso} (ppm)	P_Q / MHz	C_Q / MHz	η_Q
$LaScO_3^{(a)}$	Sc	162.0	4.00	3.90	0.30
$LaScO_3^{(b)}$	Sc	160.9	6.49	5.89	0.80
$LaScO_3^{(c)}$	Sc	161.8	2.80	2.54	0.81
$LaScO_3^{(d)}$	Sc	162.0	3.26	3.05	0.66

position and cannot move. Shown in Figure 2.44(a) is the non-optimised $LaScO_3$ structure (obtained from the literature)[218] and two geometry optimised structures, Figure 2.44(b) and (c), obtained from calculation by (1) fixing the unit cell and enabling solely the atomic coordinates to vary and (2) allowing both the unit cell and atomic coordinates to vary simultaneously. Structurally, all three appear virtually identical; however, the positions of the La and O atoms have been changed in the two optimised structures. (Details of all fractional coordinates prior to and post optimisation can be found in Appendix I). Also shown in Figure 2.44(d-f) are simulated diffraction patterns for each structure. When compared the three patterns appear identical, indicating structural optimisation produces very little effect on the diffraction pattern. The subtle change in atomic position of each atom does, however, produce an associated effect on the calculated NMR parameters. For example, prior optimisation a C_Q = 5.9 MHz was predicted for Sc, however, after optimising both the unit cell and atomic coordinates a considerably smaller value was obtained (C_Q = 3.0 MHz). These differences highlight a very important point regarding structural optimisation. Minor adjustments to both the unit cell and fractional coordinates can produce a

substantial change to the local environment of any nucleus and in such cases parameters sensitive to very local changes, such as C_Q and η_Q, often exhibit large differences in their calculated values. Full details of all NMR parameters calculated for $LaScO_3$, both prior to and post optimisation of the structure, can be found in Table 2.8. Also shown for comparison are the ^{45}Sc (I = 7/2) experimental NMR parameters obtained for $LaScO_3$.

2.11.3 Computational Methods

All calculations were completed using the CASTEP[214] density functional theory code, a planewave pseudopotential method that utilises the gauge-including projector augmented wave (GIPAW) formalism. The CASTEP code enables accurate calculation of quadrupolar and shielding interactions for NMR active nuclei. Calculations used the generalised gradient approximation (GGA) PBE functional with ultrasoft pesudopotentials[219] and periodic boundary conditions, and typical values of the k-point spacing and cut-off energy were 0.04 $Å^{-1}$ and 60 Ry respectively. Calculations were converged as far as possible with respect to the cut-off energy and k-point spacing, as described above.

Crystal structures were obtained from both the Inorganic Crystal Structure Database[140] and Rietveld refinement of high-resolution neutron diffraction experimental data. Where necessary, geometry optimisation of the structure was performed, enabling both the unit cell and atomic positions to vary. Fully optimised structures were then used to calculate NMR parameters. Calculations generate the absolute shielding tensor, $\boldsymbol{\sigma}$, and electric field gradient (EFG) tensor, $\mathbf{V}$, in the crystal frame. From these the isotropic chemical shift, δ_{iso}, is given by

$$\delta_{iso} = -(\sigma_{iso} - \sigma_{ref}) \quad , \qquad (2.)$$

where σ_{iso}, the isotropic shielding, is (1/3) Tr{$\boldsymbol{\sigma}$} and σ_{ref} is a shielding reference determined experimentally. The shielding reference is obtained by setting the calculated isotropic chemical shift equal to that determined experimentally. The magnitude (C_Q) and asymmetry (η_Q) of the

quadrupolar interaction can be generated from the principal components of the EFG tensor (V_{xx}, V_{yy}, V_{zz}) through $C_Q = eQV_{zz}/h$ and $\eta_Q = (V_{xx} - V_{yy})/V_{zz}$. It must be noted that experimentally it is often difficult to determine the sign of C_Q, however, this information is automatically generated by calculation. The signs of all calculated values of C_Q are included in the DFT data presented within this thesis.

Chapter 3

The Polar Phase of $NaNbO_3$: A Combined Study

3.1 Introduction

Sodium niobate, $NaNbO_3$, is a perovskite of significant interest at present owing to recent reports of exceptional piezoelectric responses in $NaNbO_3$-derived ceramics such as the solid-solution $K_xNa_{1-x}NbO_3$ (KNN); these properties have the potential to make KNN-based ceramics a viable lead-free alternative to the most widely used piezoelectric material $Pb(Zr_xTi_{1-x})O_3$ (PZT).[25,26] In recent years research on the KNN system has accelerated, with studies concentrated, in particular, around the x = 0.5 region of the phase diagram at the suggested Morphotropic Phase Boundary (MPB), where the highest piezoelectric responses were initially located. Ultimately, however, to fully understand this system each end-member in the solid-solution requires complete structural characterisation. Whilst the crystal structure of the room temperature form of $KNbO_3$ is widely accepted as orthorhombic, in space group Amm2,[220] with a = 3.971 Å, b = 5.697 Å and c = 5.723 Å, the various polymorphs of $NaNbO_3$ are still a subject of significant discussion. $NaNbO_3$ possesses an extremely complex phase diagram containing a series of complicated and poorly understood phase transitions as a function of temperature.[217,220-224] In more recent work, the existence of several new room temperature polymorph(s) of $NaNbO_3$ has been suggested.[225,226] In the light of these recent findings, in addition to the existing ambiguities regarding the various $NaNbO_3$ polymorphs,[222] the present work concentrates on the synthetic chemistry and structural characterisation of the room temperature polymorphs of $NaNbO_3$.

Published crystallographic data indicates that the most commonly reported room temperature phase of $NaNbO_3$ has an orthorhombic unit cell, space group Pbcm, with a = 5.506 Å, b = 5.566 Å and c = 15.520 Å (Figure 3.1(a)). This phase, first characterised by Sakowski-Cowley *et al.*,[217]

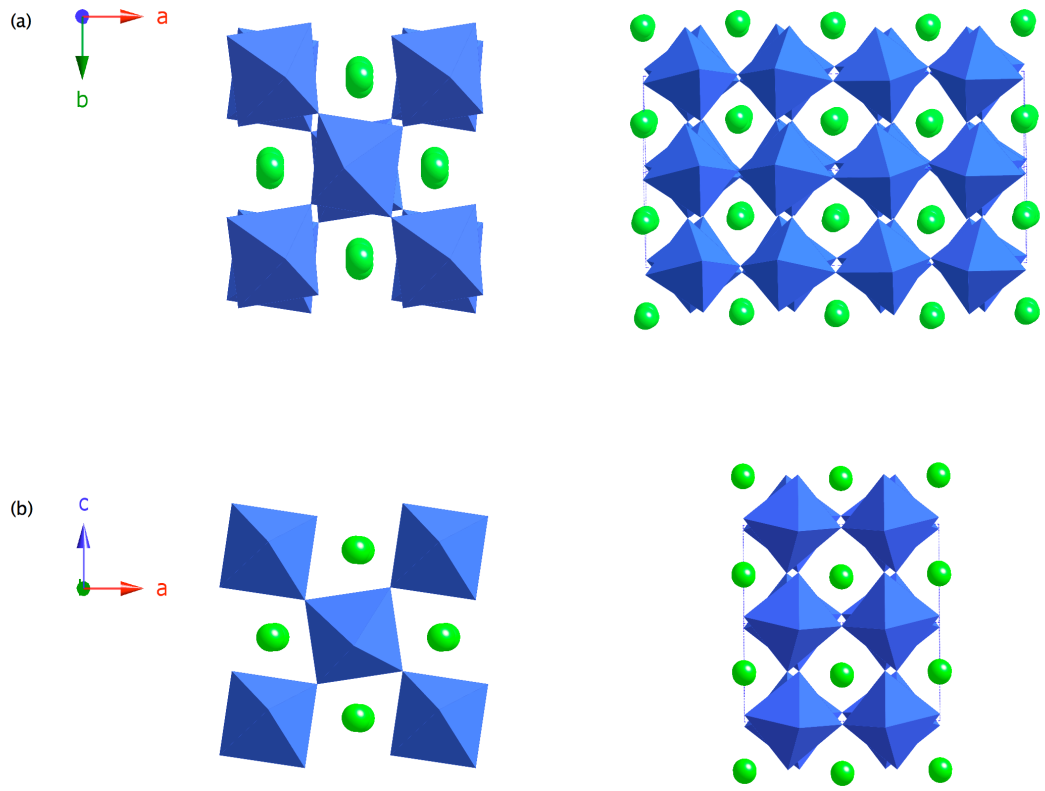

Figure 3.1: Crystal structures reported for the polymorphs (a) Pbcm and (b) $P2_1ma$ of $NaNbO_3$. Green spheres represent the sodium atoms, and the NbO_6 octahedra are shown as enclosed units (blue). Crystallographic data are taken from the literature.[217,228]

displays an unusual 'octahedral tilting' scheme with three independent tilts leading to a $\sqrt{2}a_p \times \sqrt{2}a_p \times 4a_p$ supercell of the basic cubic perovskite subcell, where a_p is the idealised cubic perovskite lattice parameter ~3.9 Å.[227] This structure possesses two crystallographically distinct Na sites. However, on the basis of peak broadenings observed using high-resolution neutron powder diffraction, Darlington and Knight suggest this phase is actually monoclinic, with $\gamma = 89.94°$.[222] Despite such structural confusion $NaNbO_3$ is well documented as being antiferroelectric at room temperature and, as a result of work presented by Shuvaeva *et al.*, it is known to undergo an electric field induced phase transition to a ferroelectric phase, in the polar space group $P2_1ma$, with unit cell dimensions a = 5.569 Å, b = 7.790 Å and c = 5.518 Å.[228] In contrast to the Pbcm polymorph, the $P2_1ma$ polymorph exhibits a simpler octahedral tilt system leading to a smaller unit cell described by $\sqrt{2}a_p \times \sqrt{2}a_p \times 2a_p$, as

shown in Figure 3.1(b). This phase results from the polarisation of single crystals of $NaNbO_3$.

Amongst the various structural studies undertaken on polycrystalline samples, submicron powders and single crystals of $NaNbO_3$, Waser and co-workers[226,227] have suggested, based on X-ray powder diffraction and Raman spectroscopy, that samples of $NaNbO_3$ reveal a number of structural phase transitions as a function of particle size. One of the most interesting proposals is that $NaNbO_3$ crystallises in the polar (and hence potentially ferroelectric) space group $Pmc2_1$ (alternative setting $P2_1ma$) at submicron particle sizes. This phase apparently corresponds to the 'field-induced' phase of Shuvaeva.[228] Many of the ambiguities in determining the exact nature of the various $NaNbO_3$ polymorphs arise from the subtleties in the different octahedral tilting schemes well-known in perovskites. Octahedral tilting is an intrinsic property of perovskites and is a direct consequence of the relative sizes and nature of the A- and B-site cations. As previously discussed in Chapter 1 section 1.3, Glazer developed a convenient notation to describe the most commonly encountered tilt systems.[16,20] Owing to the ambiguities regarding the correct structural models for the various polymorphs of $NaNbO_3$ a variety of Glazer systems have been proposed. Subtle changes of this nature can be extremely difficult to detect using diffraction methods alone, and for this reason techniques that probe short-range order are highly beneficial as they enable local changes in the cation environments, particularly the A-sites, to be monitored closely. Moreover, given the confusion and apparent complexity surrounding the proposed ambient temperature polymorphs of $NaNbO_3$ it is essential to employ a variety of complementary techniques in order to establish their nature and how their occurrence depends on synthetic variables, particle size, temperature and other intrinsic and extrinsic effects.

Here we present a comprehensive structural study of $NaNbO_3$ at room temperature using a variety of complementary techniques, including high-resolution X-ray (PXRD) and neutron powder diffraction (NPD), high-resolution solid-state ^{23}Na and ^{93}Nb magic-angle spinning (MAS) NMR, density functional theory (DFT) calculations, scanning electron

microscopy (SEM) and second harmonic generation (SHG) measurements. Previous studies of $NaNbO_3$ have often focused primarily on the use of PXRD and NPD as methods for structural characterisation. In contrast, there have been relatively few investigations using solid-state NMR,[230,231] the most detailed of which was by Ashbrook *et al*.[231] There has been a growing interest in the use of DFT calculations to aid assignment and interpretation of NMR spectra, that has accelerated in recent years owing to the advancement and modification of computational codes. In particular, the introduction of codes which exploit the inherent periodicity and translational symmetry of solids has made them an integral addition to the solid-state NMR community, and a variety of applications investigating structure, order and dynamics in a range of materials have been demonstrated.[232-239] Calculations provide a relatively easy way to monitor the variation of the NMR parameters with changes to local coordination environment, providing key assistance in the structural characterisation of many solids, in this case $NaNbO_3$. In an effort to gain an understanding of the relationship between structure and synthetic route a variety of different synthesis methods have also been heavily investigated. Within this chapter conventional solid-state synthetic techniques[240,241] are compared with molten salt[242] and sol-gel[243] approaches and significant differences are observed in the relative phases formed, as well as in both crystallinity and crystal morphology, thereby implying synthesis route heavily influences both crystal structure and microstructure.

3.2 Experimental

3.2.1 Synthesis

A sample of $NaNbO_3$ was purchased from Sigma-Aldrich (99.9%) and used without further purification. All other $NaNbO_3$ samples were synthesised using conventional solid-state, molten salt and sol-gel methods. Using a solid-state approach stoichiometric amounts of purchased Na_2CO_3 (Fisher Scientific, 99.5%) and Nb_2O_5 (Sigma-Aldrich, 99.99%) were mixed and ground in an agate mortar and pestle. Samples

were pressed into 1 cm diameter pellets, using a pressure of 10 tons cm^{-2}, and sintered at temperatures ranging from 450 °C to 950 °C for up to 48 hours (Solid-State Samples A and B).[240,241] Excess Na_2CO_3 (~1-10%) was also added to a number of the solid-state reactions in an attempt to reduce the volatilisation of the Na (Solid-State Sample C). In addition, different cooling rates were tested: slow cooling and quenching techniques were compared. Using the molten salt method stoichiometric amounts of purchased Na_2O (Sigma-Aldrich, 80%) and Nb_2O_5 were ground and mixed with a quantity of NaCl equal to the total amount of reagents added and annealed at temperatures ranging from 850 °C to 1100 °C for between 3 and 48 hours. Once fully cooled, samples were washed in distilled H_2O, filtered and allowed to air dry at room temperature.[242] Using a sol-gel process sodium ethoxide (3.67 mmol) and niobium (V) ethoxide (2.99 mmol) were dissolved in 2-methoxyethanol (10 ml) and refluxed at 80 °C for 90 minutes then at 120 °C for an additional 90 minutes. Once fully heated, the solution was allowed to cool and the resultant product was sintered at 950 °C for 12 hours.[243] Post-synthetic ^{17}O enrichment of selected solid-state and molten salt samples was performed by heating each sample under 50% ^{17}O enriched O_2 gas (Isotec, 99% ^{17}O) for 7 days at 950 °C. All enrichments were completed in collaboration with Professor Clare Grey and Dr Frédéric Blanc at the State University of New York, Stony Brook.

3.2.2 X-ray and Neutron Powder Diffraction

Room temperature "laboratory" powder X-ray diffraction (l-PXRD) experiments were carried out on a Stoe STADI-P X-ray diffractometer using Cu $K_{\alpha 1}$ (λ = 1.54056 Å) radiation. Using Beamline I11 at the Diamond Light Source Synchrotron (λ = 0.827267 Å) high-resolution room temperature powder X-ray diffraction (s-PXRD) experiments were conducted.[122,123] Room temperature time-of-flight neutron powder diffraction (NPD) experiments were completed using the High Resolution Powder Diffractometer (HRPD) at the ISIS neutron spallation source, Rutherford-Appleton Laboratories. All diffraction data were analysed by

Rietveld refinement using the General Structure Analysis System (GSAS) software package.[125] Parameters refined included background coefficients, detector zero point, instrumental parameters, lattice parameters, profile coefficients, isotropic thermal factors and atomic positional coordinates. An absorption correction was also applied to the neutron diffraction data.

3.2.3 NMR Spectroscopy

Solid-state NMR spectra were acquired using either Bruker 400, 600 or 850 Avance III spectrometers, equipped with wide-bore 9.4 T, 14.1 T and 20 T magnets, respectively, using Larmor frequencies of 105.8 MHz, 158.75 MHz and 224.88 MHz for ^{23}Na (I = 3/2), 97.94 MHz, 146.89 MHz and 208.08 MHz for ^{93}Nb (I = 9/2) and 81.36 MHz for ^{17}O (I = 5/2). The finely powdered samples were tightly packed into conventional 4-, 3.2- and 2.5-mm ZrO_2 rotors and magic-angle spinning (MAS) rates of 14 kHz and 30 kHz respectively were employed. Chemical shifts were referenced to 1 M NaCl (aq), a saturated solution of $K[NbCl_6]$ in acetonitrile and H_2O (aq), using NaCl (s) (δ_{iso} = 7.8 ppm), $LiNbO_3$ (s) (centre of gravity of MAS lineshape at δ = –1036.4 ppm at 14.1 T) and 35% ^{17}O enriched clinohumite $4Mg_2SiO_4.Mg(OH)_2$ (δ = 57.0 ppm) as secondary references. Conventional ^{23}Na MAS NMR spectra were obtained using single pulse experiments at 9.4 T, 14.1 T and 20 T with typical (central-transition selective) pulse lengths of 0.9 μs, 1.1 μs and 1.1 μs respectively. Conventional ^{93}Nb and ^{17}O MAS NMR spectra were also obtained using single pulse experiments at 14.1 T with typical (central-transition selective) pulse lengths of 0.65 μs and 1.5 μs. Optimised recycle intervals for ^{23}Na, ^{93}Nb and ^{17}O were 3 s, 0.5 s and 20 s. Typical radiofrequency field strengths employed were between 100-170 kHz. Two-dimensional triple-quantum MAS NMR experiments were recorded at 9.4 T and 14.1 T using a phase-modulated rotor-synchronised split-t_1 shifted echo pulse sequence.[181] At 9.4 T spectra result from the averaging of 192 transients with a recycle interval of 3 s for each of the 98 t_1 increments of 126.98 μs, whilst at 14.1 T spectra result from the averaging of 96 transients with a recycle interval of 3 s for each of the 128 t_1 increments. ^{93}Nb MQMAS NMR spectra result from the

averaging of 1440 transients with a recycle interval of 0.5 s for each of the 48 t_1 increments of 117.6 μs, and an additional SPAM (soft-pulse added mixing)[189,190] pulse was added (resulting in a signal enhancement of ~40%). Static wideline ^{93}Nb spectra were recorded at 9.4 T, 14.1 T and 20 T using a spin-echo pulse sequence with central-transition selective pulses and a τ interval of 20 μs. A half-echo was recorded and the FID was left shifted prior to Fourier transformation. Conventional ^{17}O MAS NMR spectra were obtained using a spin-echo pulse sequence with a rotor synchronized τ interval of 64.04 μs. A half-echo was recorded and the FID was left shifted prior to Fourier transformation. Chemical shift scales are referenced according to the convention in Reference 185. Further experimental details can be found in the relevant figure captions. Spectral analysis and fitting was performed within Topspin 2.1.

3.2.4 Calculations

^{23}Na, ^{93}Nb and ^{17}O density functional theory (DFT) calculations were completed using the CASTEP[214] code. Calculations were converged as far as possible with respect to k-point spacing and cut-off energy, with typical values of 0.04 $Å^{-1}$ and 60 Ry, respectively. Crystal structures were obtained from both the Inorganic Crystal Structure Database and Rietveld refinement of experimental data. Where necessary, geometry optimisation of the structure was performed prior to calculation of the NMR parameters. The isotropic chemical shift, δ_{iso}, in each was obtained from the isotropic shielding, σ_{iso}, using $\delta_{iso} = -(\sigma_{iso} - \sigma_{ref})$, where σ_{ref} is the isotropic shielding (565.84 ppm for ^{23}Na, −648.12 ppm for ^{93}Nb and 253.70 ppm for ^{17}O), determined from calculations on the ilmenite polymorph of $NaNbO_3$,[225] $LiNbO_3$ and Mg_2SiO_4 respectively. Typical calculation times were up to 24 hours using 12 cores. All structure searching calculations utilised the *Ab Initio* Random Structure Searching[244-247] (AIRSS) algorithm and were completed using the CASTEP code with a planewave cut-off energy of 27 Ry and a Brillouin zone sampling grid spacing of 0.07 $Å^{-1}$. The lowest energy phases were then selected and their energies and properties were recalculated at a higher level of accuracy using a

planewave cut-off energy of 60 Ry and a grid spacing of 0.07 $Å^{-1}$. Refer to section 3.6 for specific details regarding the strategy utilised to structure search. All structure searching has been completed in collaboration with Professor Chris J. Pickard and Dr Maria Baias, University College London, UK.

3.2.5 Second Harmonic Generation (SHG)

Nonlinear Optic (NLO) properties were studied using powder Second Harmonic Generation (SHG) techniques. Samples were pressed between two microscope slides and analysed using a Nd vanadate pulsed laser. Each pulse had a typical duration of 12 ps. Pulses typically came in bundles of 2-5 and at a rate of 1 kHz. The beam diameter was 5 mm and the power used varied between 1 and 2.5 W.

3.2.6 Scanning Electron Microscopy (SEM)

The crystal morphology of each sample was examined using scanning electron microscopy (SEM) on a Jeol JSM-5600 microscope operating at 20-30 kV equipped with an Oxford INCA system for energy-dispersive X-ray spectroscopy (EDX).

3.3 Experimental Results

3.3.1 Commercial Sample

Initial investigations concentrated on $NaNbO_3$ purchased commercially (Sigma-Aldrich). Structure and phase purity were initially verified using l-PXRD and subsequently s-PXRD, both of which displayed excellent agreement with the orthorhombic structure reported in the literature (Pbcm).[248] The Rietveld refinement using the s-PXRD data is shown in Figure 3.2(a), and full refinement details can be found in Table 3.1. All bond lengths obtained from refinement are given in Appendix II. The ^{23}Na MAS NMR spectrum (Figure 3.2(b)) contains a broadened lineshape, hindering the extraction of information regarding the number

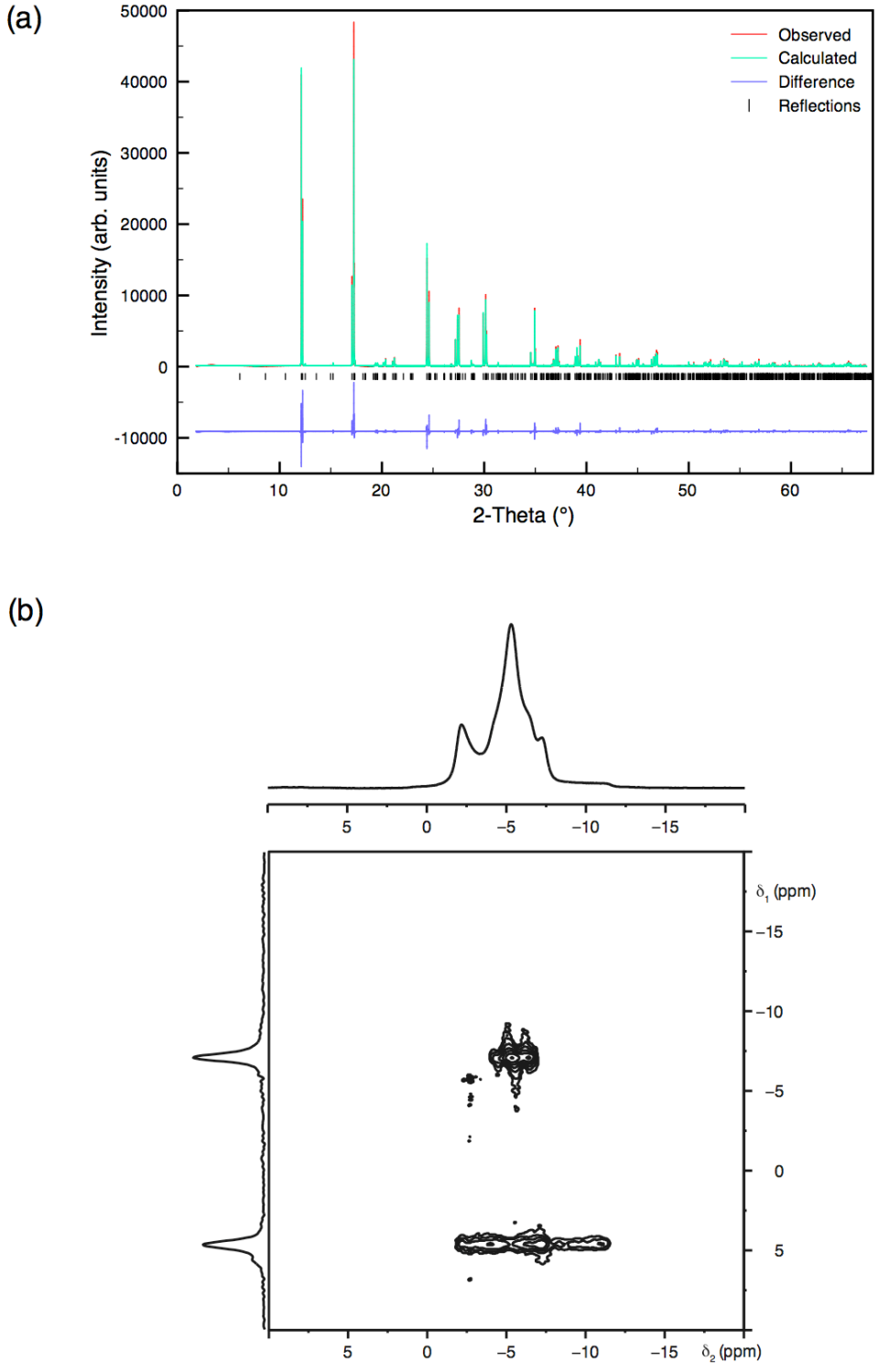

Figure 3.2: Commercial $NaNbO_3$ (Aldrich) (a) Rietveld profile (Pbcm model) of s-PXRD data and (b) conventional ^{23}Na (14.1 T) MAS NMR spectrum, triple-quantum MAS NMR spectrum and corresponding isotropic projection. The MAS rate was 14 kHz.

Table 3.1: Structural parameters for $NaNbO_3$ (Aldrich) from s-PXRD data using isotropic thermal factors. Space group Pbcm, a = 5.50398(1) Å, b = 5.56950(1) Å, c = 15.51647(1) Å and V = 475.648(1) Å^3. $\chi^2 = 7.9$, $wR_p = 14.6\%$ and $R_p = 10.9\%$.

Atom	Site	x	y	z	U(iso) × 100 / Å^2
Na	4c	0.2288(5)	0.25	0	1.62(9)
Na	4d	0.2296(5)	0.2243(3)	0.25	0.99(8)
Nb	8e	0.2525(1)	0.7316(1)	0.1250(1)	0.84(1)
O1	4c	0.6886(10)	0.25	0	0.61(16)
O2	4d	0.1846(10)	0.7541(6)	0.25	1.19(17)
O3	8e	0.4743(4)	0.4653(5)	0.1418(3)	2.43(9)
O4	8e	0.0330(4)	0.0292(4)	0.1108(3)	1.52(8)

of crystallographically distinct Na sites present. ^{23}Na (I = 3/2) is a quadrupolar nucleus and under conventional MAS ^{23}Na lineshapes commonly exhibit broadening as a result of the inefficient removal of second-order quadrupolar interactions. For this reason high-resolution NMR techniques such as multiple-quantum MAS[171] (MQMAS) are required to fully remove inhomogeneous second-order quadrupolar broadenings and resolve distinct sites. The ^{23}Na triple-quantum MAS spectrum of $NaNbO_3$, shown in Figure 3.2(b), clearly displays two distinct Na resonances, in agreement with the reported crystal structure for Pbcm $NaNbO_3$.[248] The projection of the spectrum onto the δ_1 axis also exhibits two sharp isotropic peaks, again highlighting the presence of two distinct Na environments. The NMR parameters extracted from the position of the centre of gravity from the spectrum in Figure 3.2(b) are given in Table 3.2. The upper, and notably narrower of the two ridges in the two-dimensional spectrum, with $\delta_{iso} = -4.2$ ppm, has $P_Q = 1.2$ MHz, whilst the lower ridge, with $\delta_{iso} = -0.6$ ppm, has a considerably larger quadrupolar contribution, $P_Q = 2.2$ MHz. It is possible to confirm the accuracy of the parameters extracted by simulating the MAS spectrum which would result. This is shown in Figure 3.3 and is in good agreement with that obtained experimentally.

Table 3.2: ^{23}Na NMR parameters, δ_{iso}, P_Q, C_Q and η_Q, for commercially purchased $NaNbO_3$ (Aldrich), Solid-State Sample A $NaNbO_3$ and sol-gel $NaNbO_3$ sample, obtained from the MAS and MQMAS spectra in Figures 3.2(b), 3.6(a-b) and 3.28(c) respectively.

	Site	δ_{iso} (ppm)	P_Q / MHz	C_Q / MHz	η_Q
Commercial Sample (Aldrich)					
Pbcm	Na1	−0.6(5)	2.2(1)	-	-
	Na2	−4.2(5)	1.2(2)	-	-
Solid-State Sample A (14.1 T)					
Pbcm	Na1	−0.7(5)	2.2(1)	-	-
	Na2	−4.4(5)	1.2(2)	-	-
"$P2_1ma$"	Na1	−5.1(5)	1.1(2)	-	-
Solid-State Sample A (9.4 T)					
Pbcm	Na1	−0.5(5)	2.1(1)	2.1(1)	0.0(1)
	Na2	−4.2(5)	1.2(2)	1.0(2)	0.8(1)
"$P2_1ma$"	Na1	−1.4(5)	2.4(1)	2.1(1)	0.9(1)
	Na2	−5.1(5)	1.2(2)	1.1(2)	0.7(1)
Sol-gel Sample					
"$P2_1ma$"	Na1	−1.5(5)	2.4(1)	-	-
	Na2	−5.1(5)	1.2(2)	-	-

3.3.2 Solid-State Preparation

$NaNbO_3$ was also synthesised using conventional solid-state techniques (Solid-State Sample A). Phase purity was examined using l-PXRD and displayed good agreement with the literature, initially suggesting the presence of single-phase Pbcm $NaNbO_3$, as shown in Figure 3.4(a). However, under MAS the ^{23}Na NMR spectrum appears different in comparison to that obtained for the commercially purchased sample, as shown in Figures 3.5(a) and (b). In addition, the crystallinity

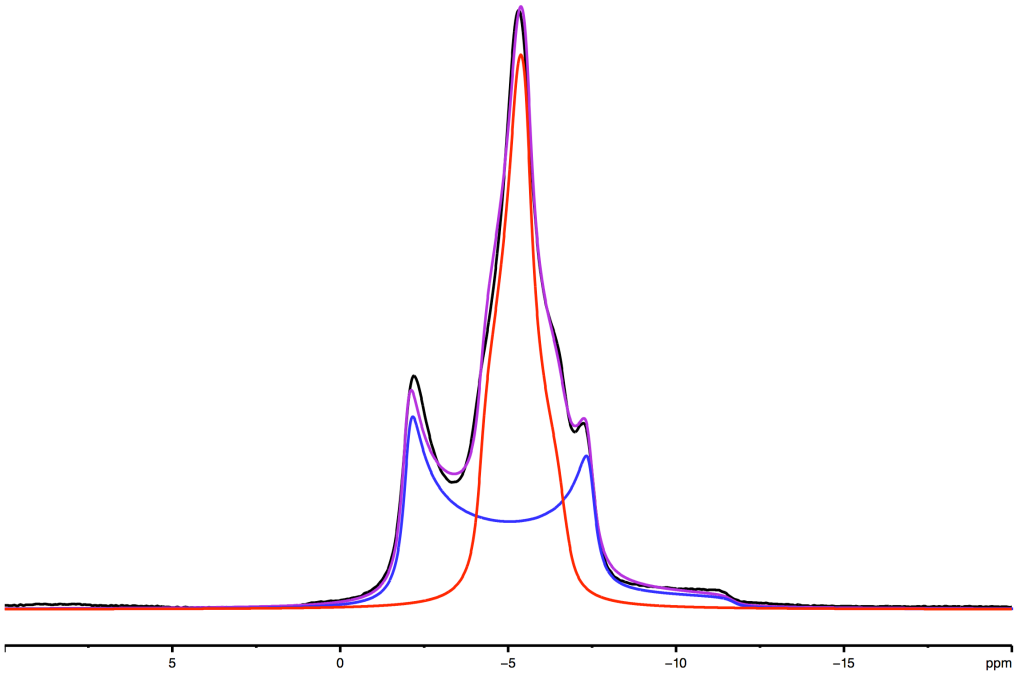

Figure 3.3: Analytical fitting of the ^{23}Na (14.1 T) MAS NMR spectrum of commercially-purchased (Aldrich) $NaNbO_3$. The experimental spectrum is shown in black, fitted lineshapes for the Na1 and Na2 sites are shown by the blue and red lines, respectively, with the summation of the two sites shown in purple.

and microstructure displayed visible differences (Figures 3.5(g) and (h)). Using ^{23}Na MQMAS NMR, however, it was evident a second Na-containing phase was present in Solid-State Sample A. At 14.1 T an additional resonance was clearly observed at $\delta_1 = -9.3$ ppm, as shown in Figure 3.6(a). In addition, the resonance at $\delta_1 = 4.3$ ppm covers a wider δ_2 shift range, suggesting the potential overlap of two resonances here also. This is highlighted in the overlay of the ^{23}Na MQMAS NMR spectra for this sample and that of the commercial material shown in Figure 3.7. Therefore, in an attempt to resolve any overlapped sites an MQMAS spectrum was recorded at 9.4 T. The position of resonance in an isotropic MQMAS spectrum depends not only upon the chemical shift but also on the quadrupolar interaction, and owing to the differing field dependences of these interactions (proportional to B_0 and B_0^{-1}, respectively) resolution may be improved both at lower and higher magnetic field strength. As shown in Figure 3.6(b) four crystallographically distinct Na sites are clearly observed, suggesting the presence of a second Na-containing

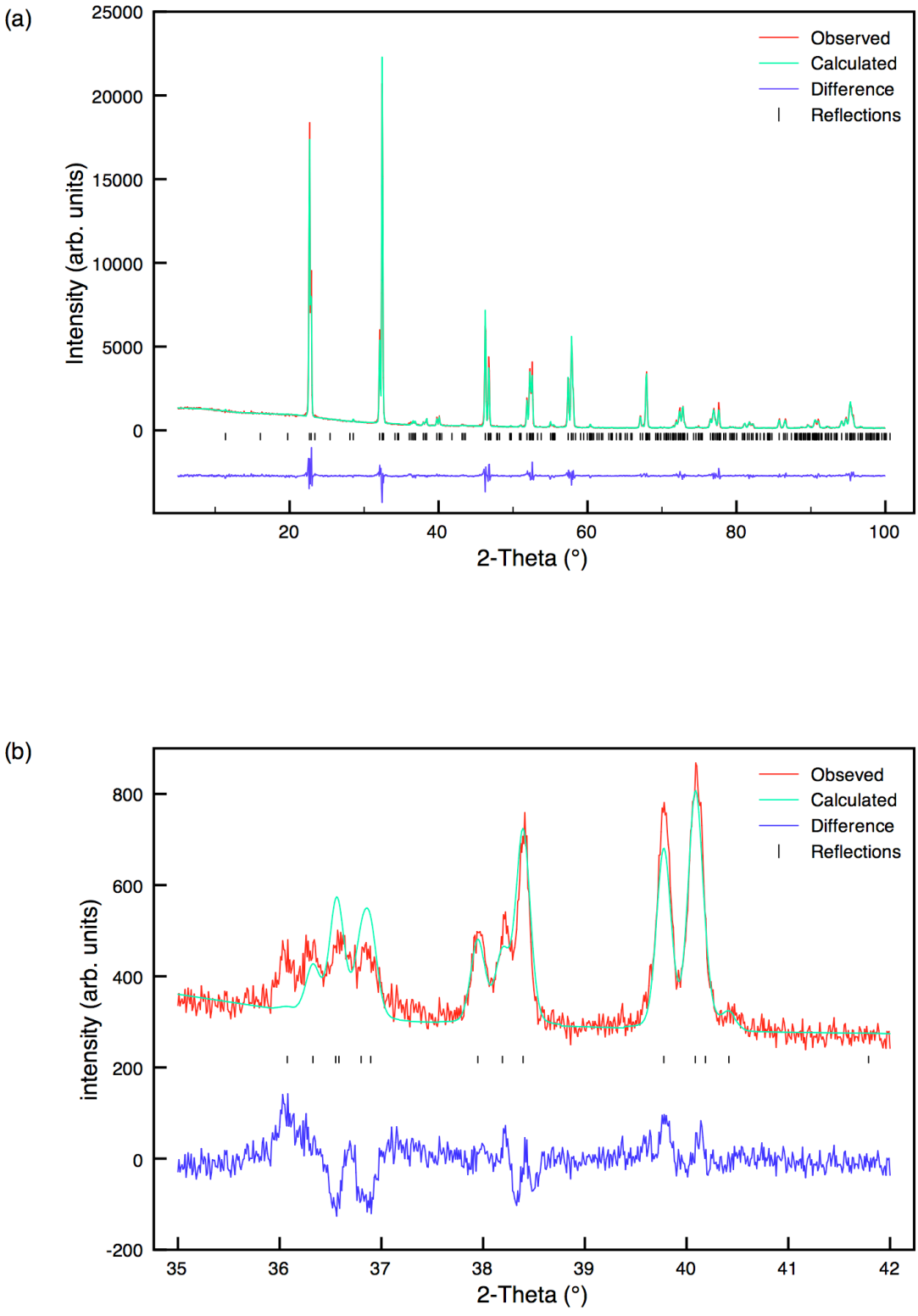

Figure 3.4: (a) Rietveld profile for Solid-State Sample A $NaNbO_3$ using l-PXRD data and Pbcm model, and (b) expansion of the superstructure region 2θ = 34° – 42°.

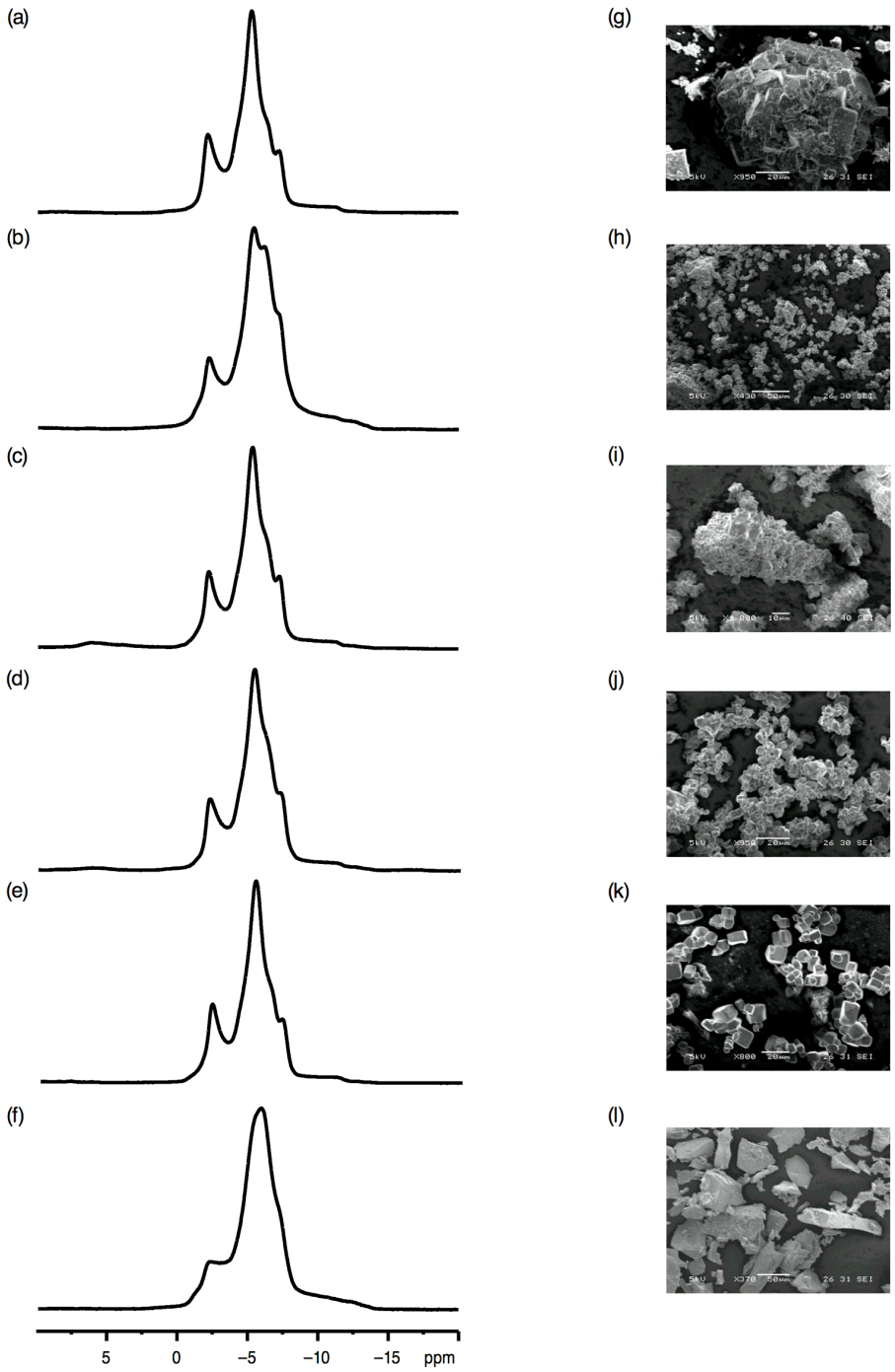

Figure 3.5: Comparison of (a-f) ^{23}Na (14.1 T) MAS NMR spectra and (g-l) Scanning Electron Microscopy (SEM) images of (a, g) commercially purchased $NaNbO_3$ (Aldrich), (b, h) Solid-State Sample A $NaNbO_3$, (c, i) Solid-State Sample B $NaNbO_3$, (d, j) Solid-State Sample C $NaNbO_3$, (e, k) molten salt $NaNbO_3$ (850°C for 24 hours) and (f, l) sol-gel $NaNbO_3$.

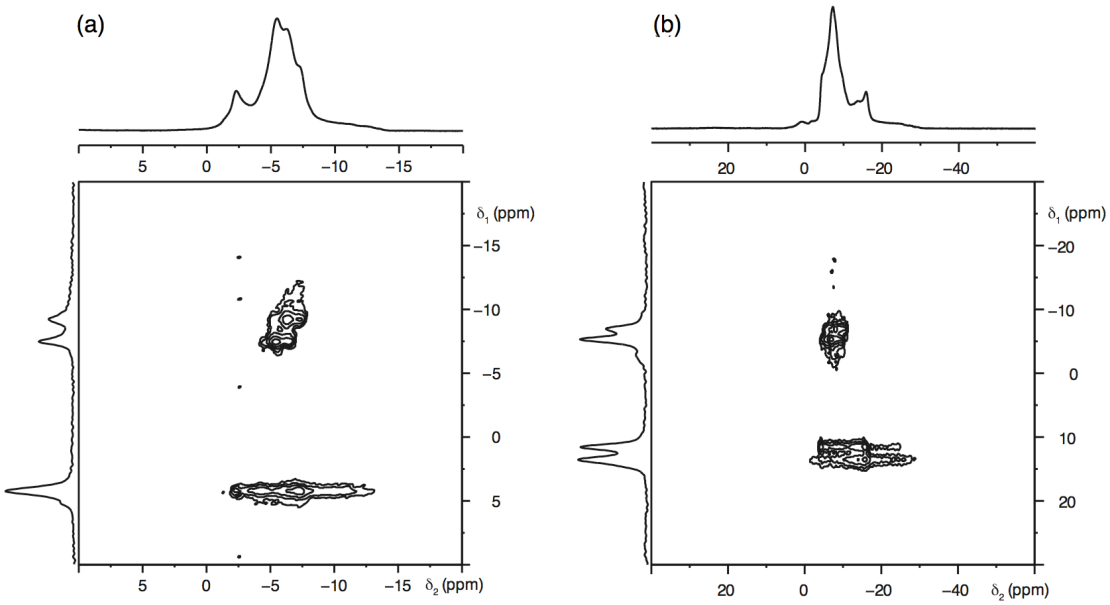

Figure 3.6: ^{23}Na MAS NMR spectra, triple-quantum MAS NMR spectra and corresponding isotropic projections for Solid-State Sample A $NaNbO_3$ at (a) 14.1 T and (b) 9.4 T. The MAS rate was 14 kHz.

phase, with two Na species. Although the intensity of resonances in MQMAS spectra is in general non-quantitative (i.e., does not accurately reflect the proportions of different phases), for species with very similar quadrupolar interactions it is possible to interpret spectral intensities in a quantitative way. The two peaks at δ_1 = –9.3 ppm and –7.5 ppm, suggest that the second phase accounts for ~40% of the material synthesised in this case. NMR parameters extracted for each phase at both 14.1 T and 9.4 T are given in Table 3.2. Accurate quadrupolar parameters could not be extracted for all sites owing to spectral overlap and significant line broadening and distortion, potentially caused by non-uniform triple-quantum excitation. Therefore, P_Q values derived from the position of the centre of gravity have been quoted for these sites. To confirm that the additional resonances observed were not unreacted Na-based starting reagents various anhydrous and hydrous samples of the starting reagent Na_2CO_3 were analysed using ^{23}Na MAS NMR. Two-dimensional ^{23}Na MQMAS spectra were recorded for two commercially purchased samples of anhydrous Na_2CO_3 (Sigma-Aldrich and Fisher Scientific), monohydrate Na_2CO_3 (Sigma-Aldrich) and sodium bicarbonate, $NaHCO_3$ (Sigma-

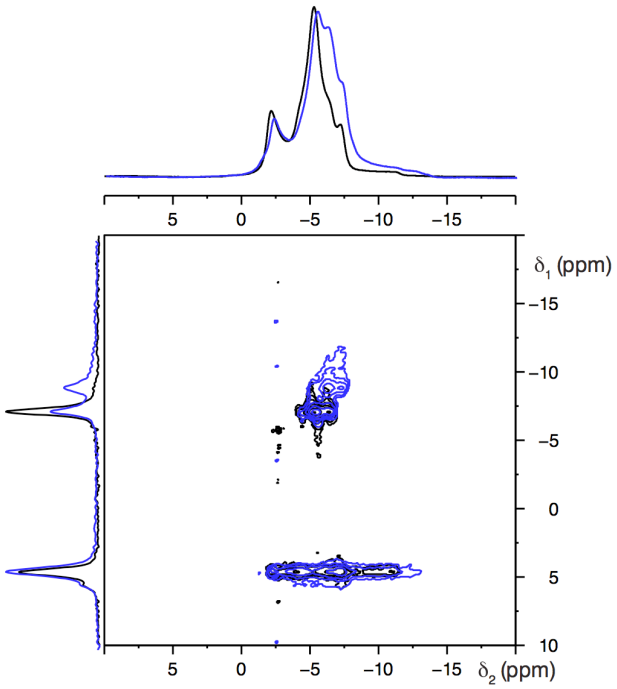

Figure 3.7: ^{23}Na (14.1 T) MAS NMR spectra, two-dimensional triple-quantum MAS NMR spectra and corresponding isotropic projections of phase pure commercially-purchased Pbcm $NaNbO_3$ (shown in black) and Solid-State Sample A $NaNbO_3$ (shown in blue). The MAS rate was 14 kHz.

Aldrich). Each spectrum confirmed that the additional resonance present in Solid-State Sample A did not correlate with any of the anhydrous or hydrous forms of the starting reagent Na_2CO_3. All two-dimensional spectra recorded are shown in Appendix II.

Using solid-state techniques several additional samples were synthesised to determine whether the extra phase identified in Solid-State Sample A was consistently and repeatably produced in all samples synthesised using solid-state methods. Various experimental conditions were thoroughly investigated, including annealing temperature and time, the effects of different cooling rates (e.g., quenching vs. slow cooling) as well as the effect of addition of an excess (1-10%) of the primary starting reagent, Na_2CO_3. An excess was added in order to compensate for the volatile nature of the Na-based starting reagents. Using solely l-PXRD Rietveld refinements were completed for all samples and initially suggested the presence of a single-phase perovskite in space group Pbcm.

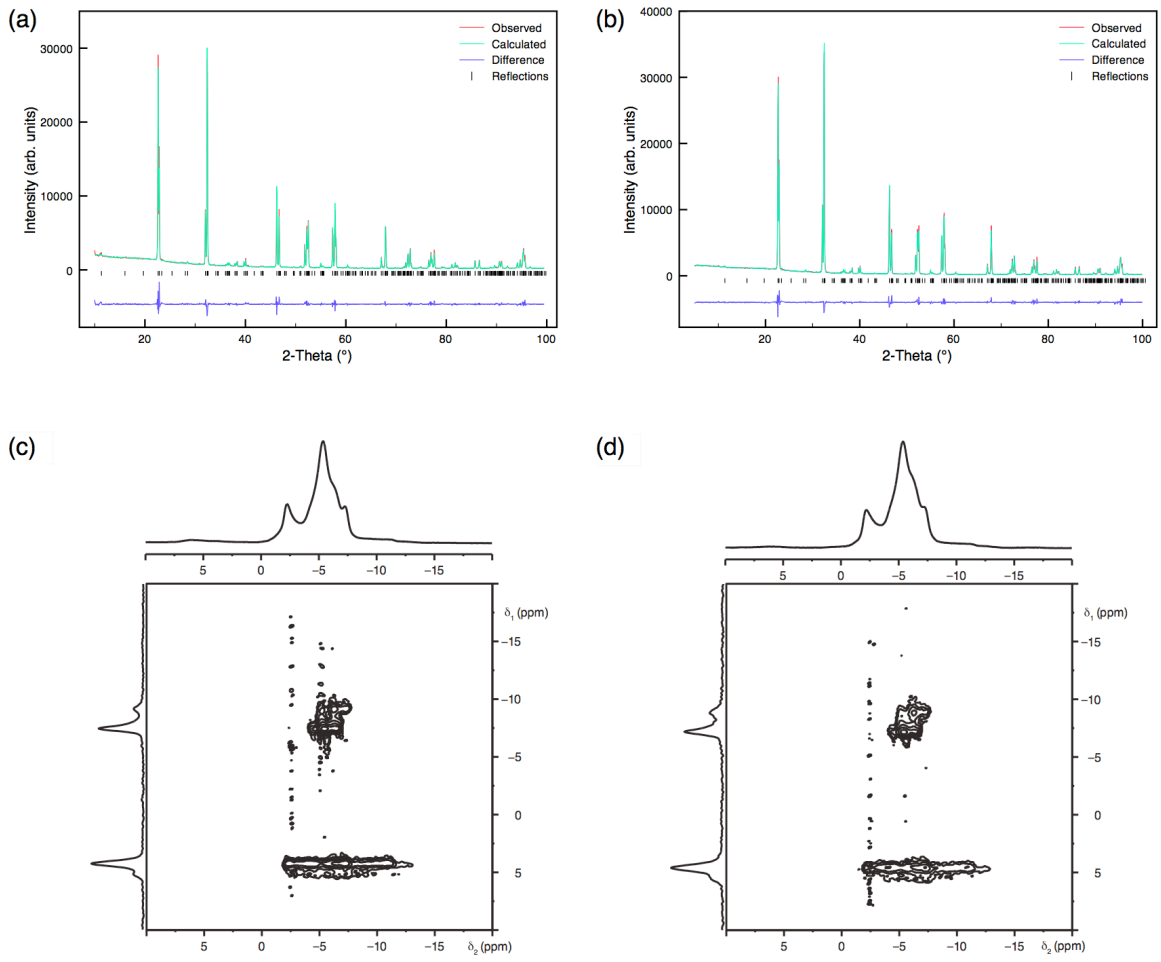

Figure 3.8: Rietveld profiles of l-PXRD data using Pbcm model for (a) Solid-State Sample B $NaNbO_3$ and (b) Solid-State Sample C $NaNbO_3$. Refined lattice parameters for each are located in Table 3.3. Conventional ^{23}Na (14.1 T) MAS NMR spectra, triple-quantum MAS NMR spectra and corresponding isotropic projections for (c) Solid-State Sample B $NaNbO_3$ and (d) Solid-State Sample C $NaNbO_3$.

Full Rietveld refinements for Solid-State Samples B and C are shown in Figures 3.8(a) and (b). The refined lattice parameter values from each refinement are given in Table 3.3. Again, using ^{23}Na MAS NMR the lineshapes obtained for Solid-State Samples B and C displayed subtle variations when compared with the commercially purchased sample, suggesting a different composition within each (Figures 3.5(a), (c) and (d)). This is perhaps more easily seen when the lineshapes for these different phases are superimposed, as shown in Figure 3.9. Upon closer inspection using two-dimensional ^{23}Na MQMAS NMR it was evident the same secondary phase was consistently present, with two additional Na sites.

Table 3.3: Refined lattice parameters, χ^2, wRp and Rp values for (a) Solid-State Sample B and (b) Solid-State Sample C, both from l-PXRD data. All refinements were completed using the Pbcm model by Chizhova *et al.*[248]

	a (Å)	b (Å)	c (Å)	V (Å^3)	χ^2	wR_p (%)	R_p (%)
(a)	5.50746(4)	5.57290(4)	15.52295(10)	476.438(7)	5.0	7.5	5.5
(b)	5.51131(5)	5.57569(4)	15.53211(11)	477.291(8)	6.0	8.4	6.0

Interestingly, Solid-State Samples A and B were synthesised using exactly the same reaction conditions. However, the two possess very different ratios of the two phases, as shown in Figure 3.8. Using variations of the original solid-state synthesis it was possible to vary the quantities of each phase significantly, from as little as a few percent to almost a 50% mix of the two; however the Pbcm phase was consistently present in abundance, suggesting it to be the more thermodynamically stable of the two. It was possible to slightly reduce the quantity of second phase by addition of a small excess of Na_2CO_3, as in Solid-State Sample C; however it was never possible to fully eradicate it using such methods.

Systematic studies of both annealing temperature and time were completed to accurately determine the effect on quantity of second phase produced. Initially, the annealing temperature was fixed at 850 °C and reaction times were varied between 3 and 72 hours. All l-PXRD data for each of the samples in this series refined well to the orthorhombic Pbcm model,[248] with no obvious additional peaks. This therefore suggested the presence of a single phase perovskite. The Rietveld refinements completed for each sample in this series are shown in Figures 3.10(a-g). However, two-dimensional ^{23}Na MAS NMR spectra indicated the presence of an additional Na-bearing phase, clearly visible in Figures 3.11(a-g). The same second phase was consistently produced in all samples; however, the quantities exhibited varied considerably. This variation is easily observed in the isotropic projections obtained from each two-dimensional spectrum, as shown in Figure 3.12(a). It must be noted that the sample annealed at 850 °C for 36 hours exhibits two considerably

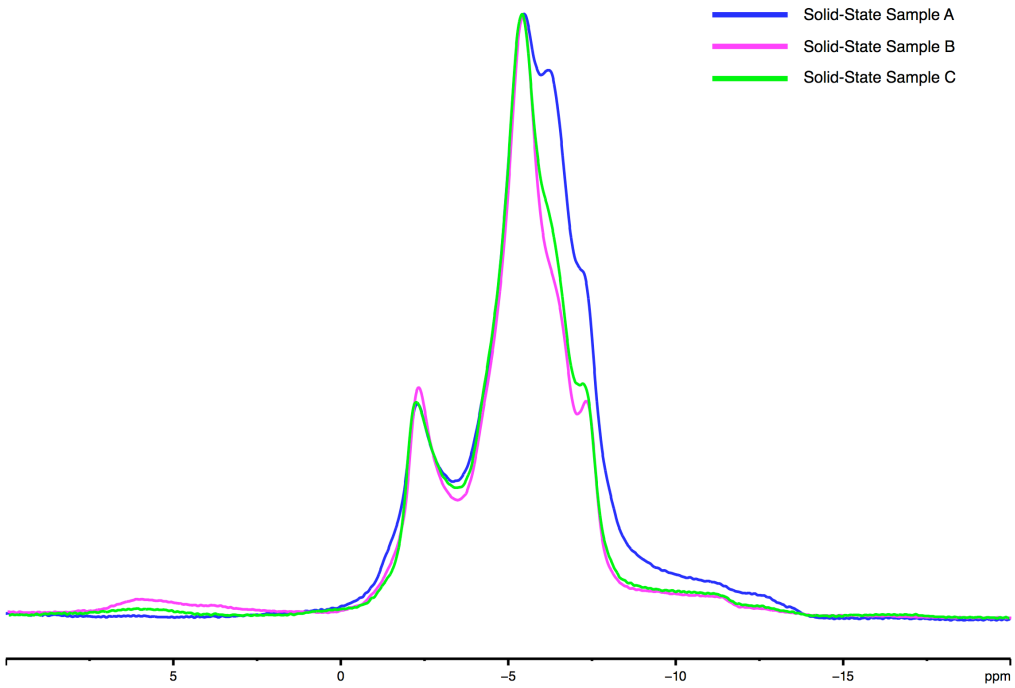

Figure 3.9: Overlay of ^{23}Na (14.1 T) MAS NMR spectra for Solid-State Samples A, B and C $NaNbO_3$.

broader isotropic peaks when compared with all other samples in this series, most probably owing to poor crystallinity. A second heating series was also completed in which the annealing temperature remained constant at 950 °C and reaction time was again varied. In this particular series, relatively short annealing times were investigated, from 15 minutes to 5 hours and in a similar manner to the earlier series all l-PXRD data refined to the orthorhombic Pbcm model,[248] suggesting each to be single phase. All Rietveld refinements completed for this series are shown in Figures 3.13(a-h). Refined lattice parameters obtained from each refinement are given in Appendix II. However, the two-dimensional ^{23}Na MQMAS NMR spectra recorded for each highlights the presence of the same secondary phase previously identified, indicating it is consistently synthesised in all solid-state samples, irrespective of annealing temperature or time. All ^{23}Na MQMAS spectra recorded in this series are shown in Figures 3.14(a-h). Only the relative quantities of the additional phase appeared to vary depending on the specific synthesis conditions

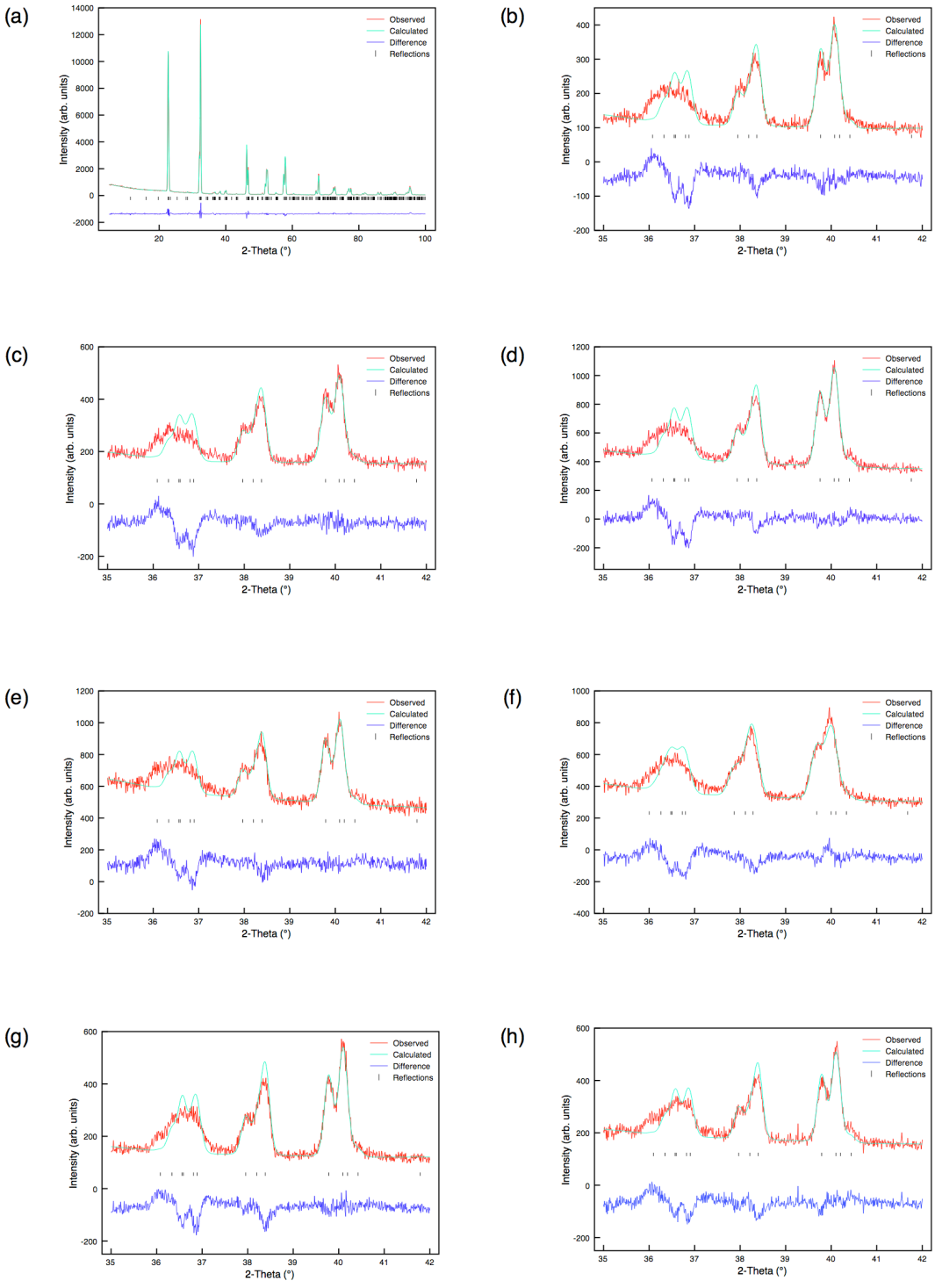

Figure 3.10: Rietveld profiles of l-PXRD data for samples of $NaNbO_3$ prepared in the solid-state heating series where annealing time was varied using (a) 3 hours, (c) 6 hours, (d) 12 hours, (e) 24 hours, (f) 36 hours, (g) 48 hours and (h) 72 hours. In each, the annealing temperature was fixed at 850 °C. Full Rietveld profiles for all samples are given in Appendix II.

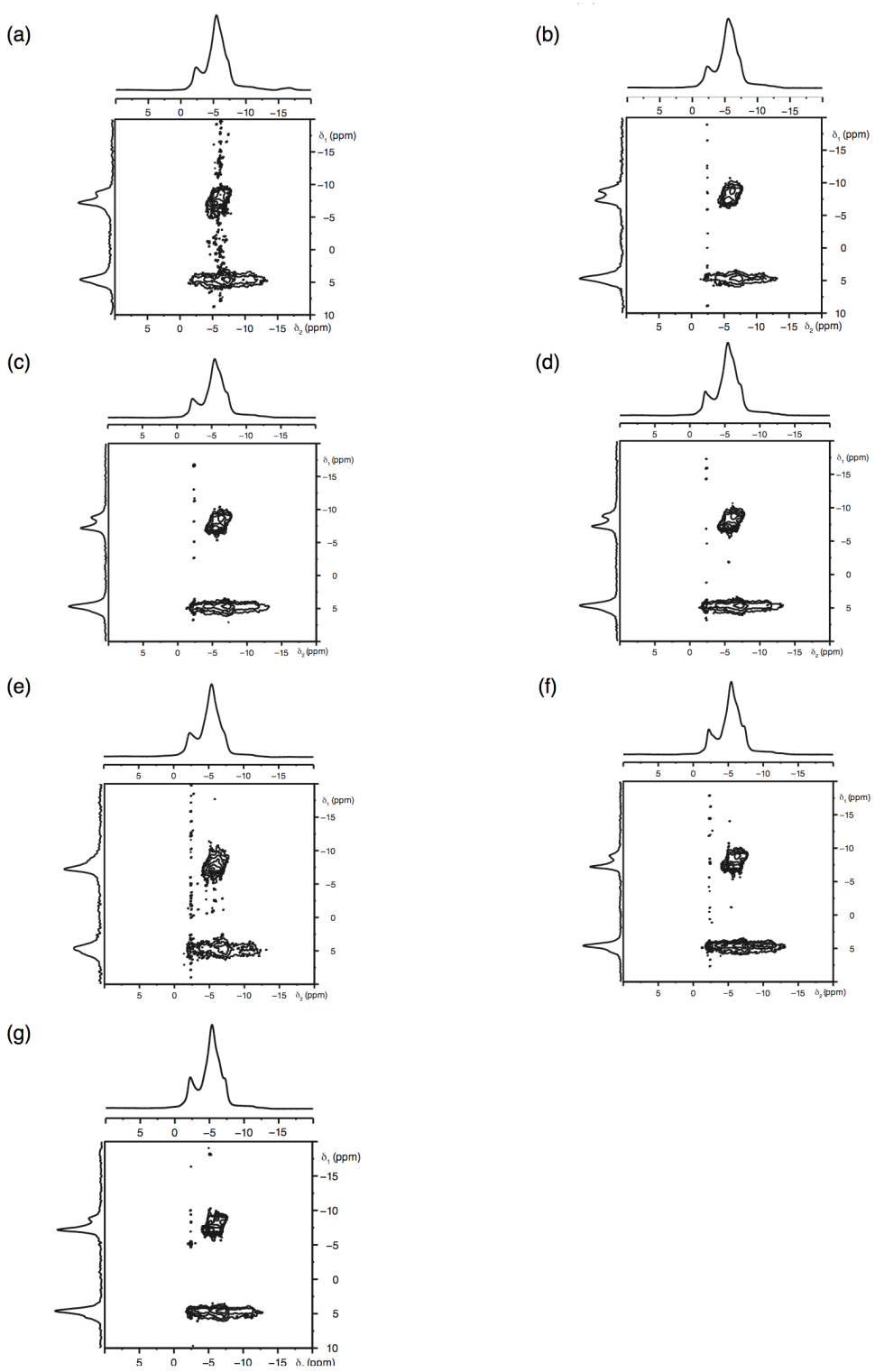

Figure 3.11: Conventional ^{23}Na (14.1 T) MAS NMR spectra, triple-quantum ^{23}Na MAS NMR spectra and corresponding isotropic projections, for solid-state samples of $NaNbO_3$ prepared using annealing times of (a) 3 hours, (b) 6 hours, (c) 12 hours, (d) 24 hours, (e) 36 hours and (f) 48 hours. In each case the annealing temperature was fixed at 850 °C.

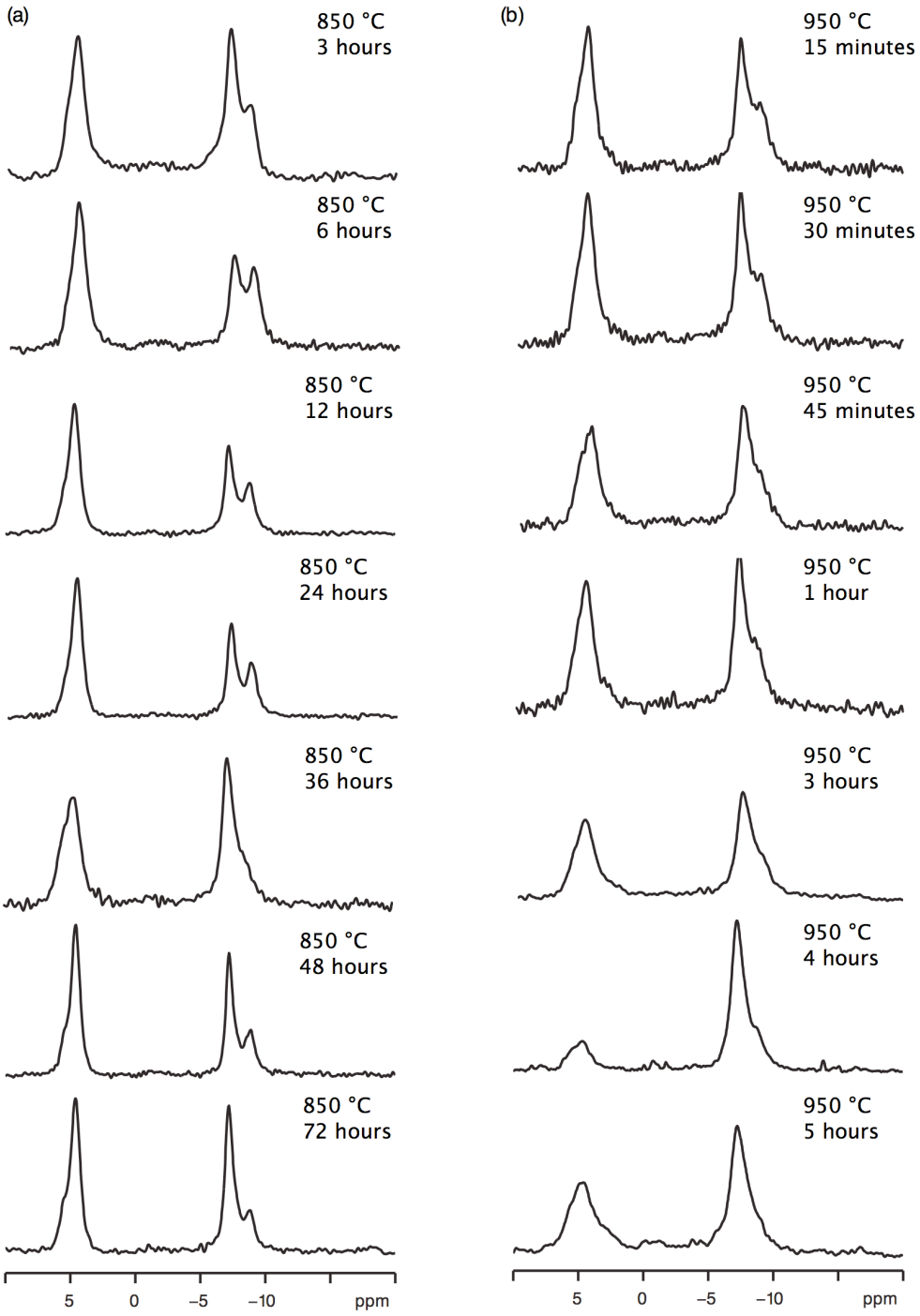

Figure 3.12: Isotropic projections obtained from triple-quantum ^{23}Na (14.1 T) MAS NMR spectra of solid-state samples of $NaNbO_3$. In (a), annealing time was varied between 3 and 48 hours, with a fixed annealing temperature of 850 °C. In (b), the annealing time was varied from 15 minutes to 6 hours, with a fixed annealing temperature of 950 °C.

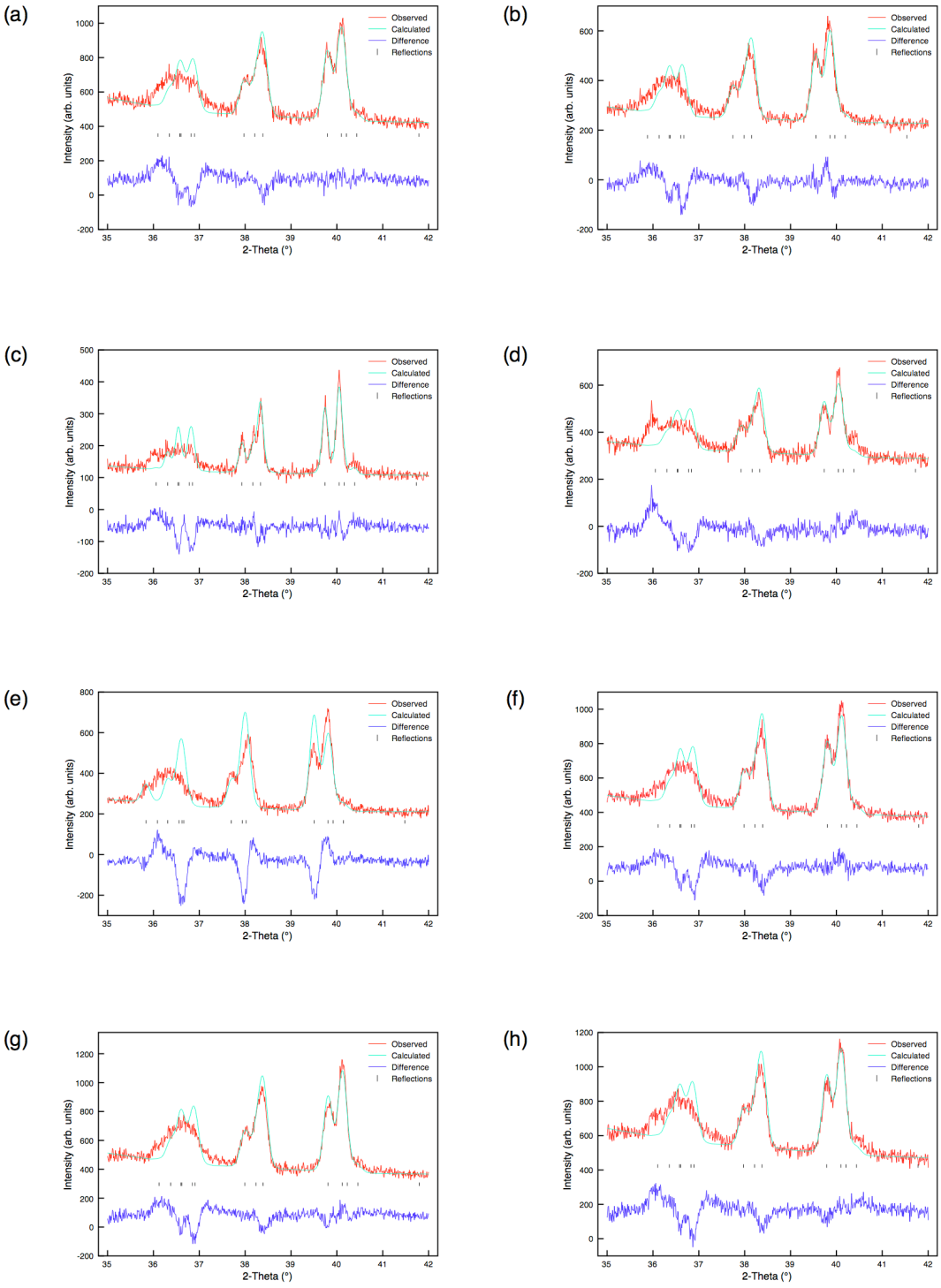

Figure 3.13: Rietveld profiles of l-PXRD data for samples of $NaNbO_3$ prepared in the solid-state heating series where annealing time was varied using (a) 15 minutes, (b) 30 minutes, (c) 45 minutes, (d) 1 hour, (e) 3 hours, (f) 4 hours, (g) 5 hours and (h) 6 hours. In each, the annealing temperature was fixed at 950 °C. Full Rietveld profiles can be found in Appendix II.

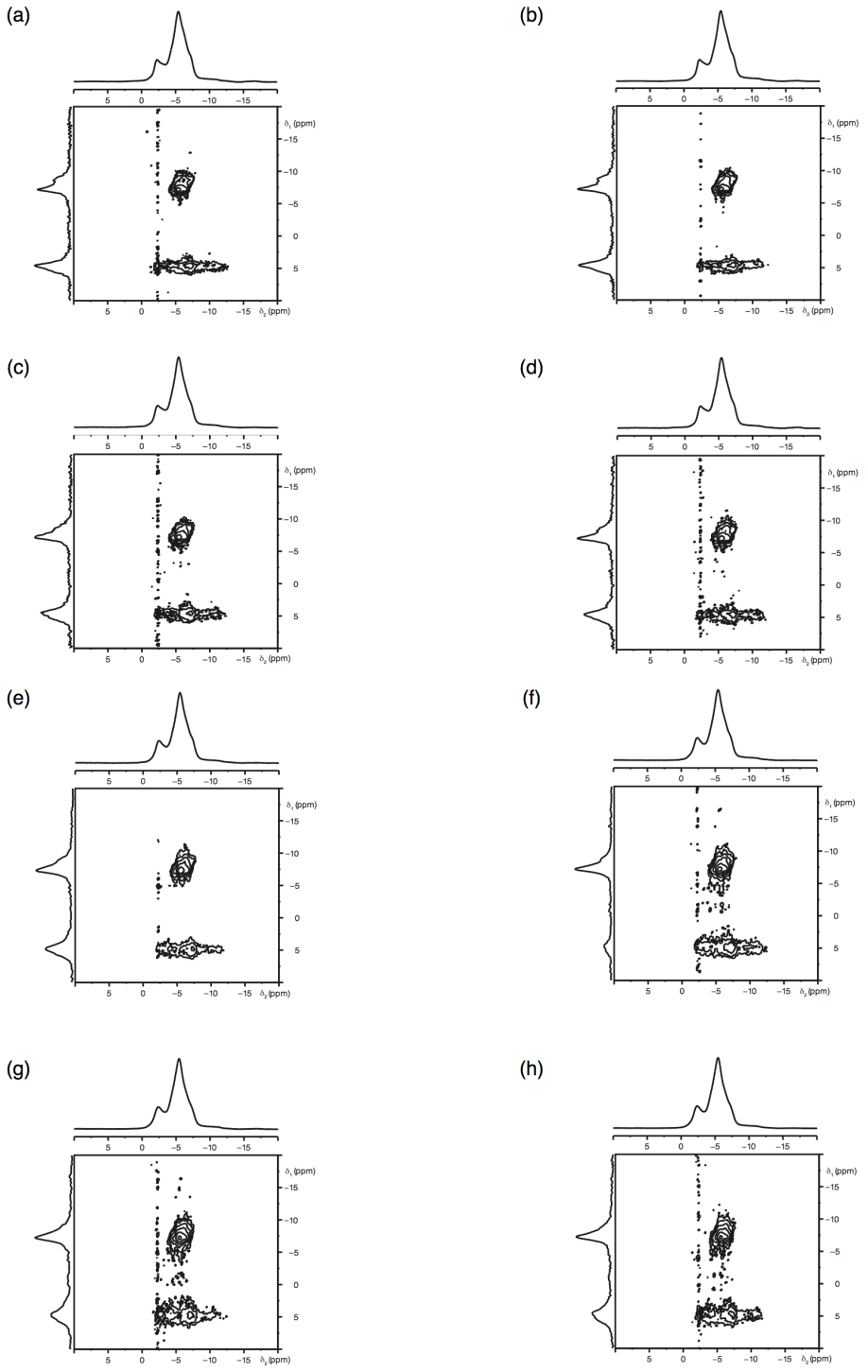

Figure 3.14: Conventional ^{23}Na (14.1 T) MAS NMR spectra, triple-quantum ^{23}Na MAS NMR spectra and corresponding isotropic projections, for solid-state samples of $NaNbO_3$ prepared using annealing times of (a) 15 minutes, (b) 30 minutes, (c) 45 minutes, (d) 1 hour, (e) 3 hours, (f) 4 hours, (g) 5 hours and (i) 6 hours. In each case the annealing temperature was fixed at 950 °C.

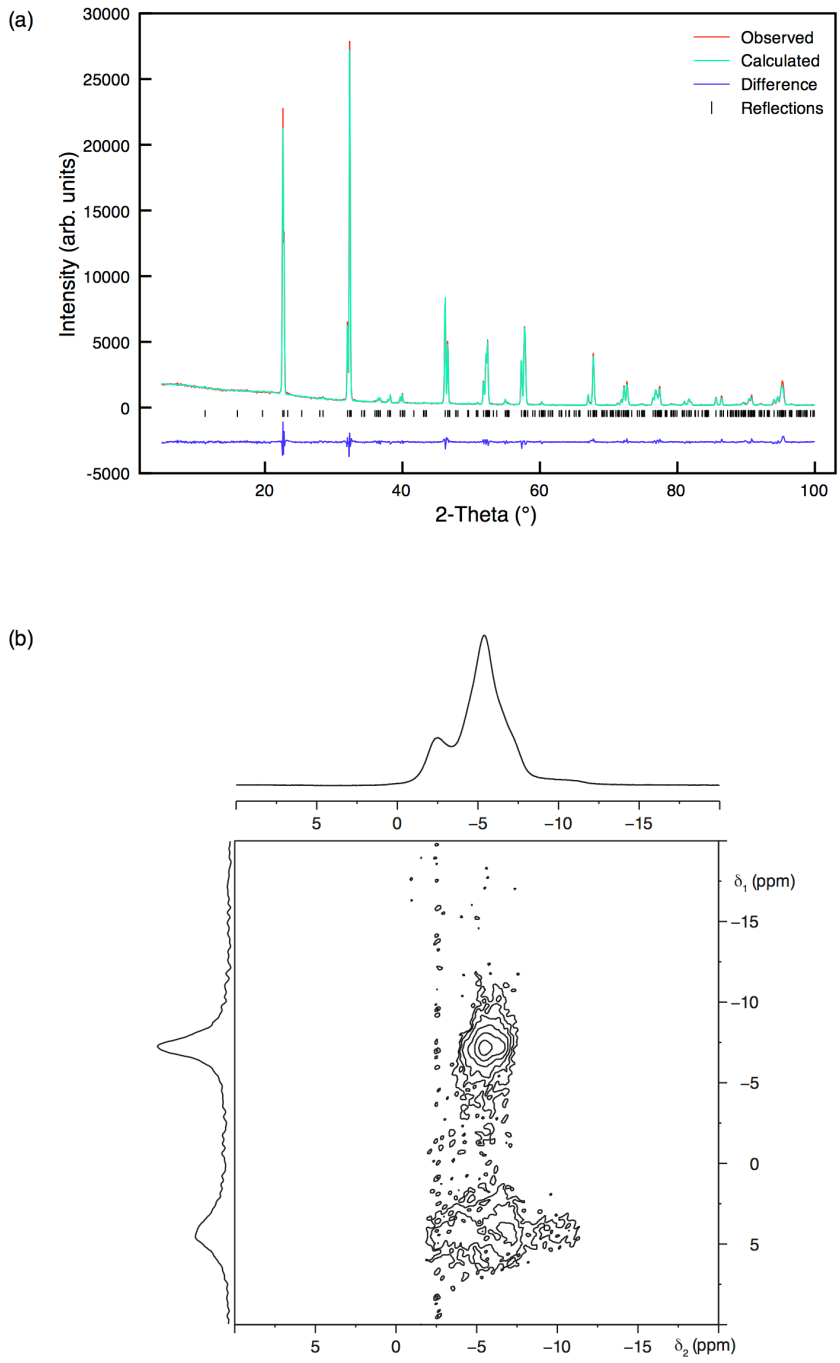

Figure 3.15: (a) Rietveld profile and (b) conventional ^{23}Na (9.4 T) MAS NMR spectrum, triple-quantum MAS NMR spectrum and corresponding isotropic projection for solid-state sample of $NaNbO_3$ prepared using an annealing temperature of 1000 °C for 24 hours.

used. The isotropic projections obtained from each two-dimensional spectrum displayed severe peak broadening (Figure 3.12(b)), suggesting all samples in this series to possess relatively poor crystallinity.

In such cases it is difficult to quantitatively measure the amount of second phase in each sample. This reduction in crystallinity is, most probably, as a result of the use of both relatively short reaction times and high annealing temperatures. Fast reaction rates commonly produce samples with low crystallinity. A sample of $NaNbO_3$ was also synthesised using 1000 °C for 24 hours to determine the effect of higher annealing temperature on sample crystallinity. Using l-PXRD the sample refined well the Pbcm phase of $NaNbO_3$, suggesting a single phase perovskite. The ^{23}Na MQMAS spectrum displayed two broad resonances, as shown in Figure 3.15(b). The spectrum exhibited considerable peak broadening when compared with other samples of $NaNbO_3$. The broadening exhibited is believed to be owing to a reduction in crystallinity in the sample. This, therefore, suggests that to successfully synthesise samples of $NaNbO_3$ with good crystallinity lower annealing temperatures are required. For example, samples synthesised using 850 °C appear to possess very good crystallinity, therefore, temperatures close to this should be utilised to synthesise samples of reasonably high crystallinity.

The systematic studies completed appear to suggest that there is no obvious correlation between the conditions of the solid-state synthesis and the quantity of the second phase produced. All solid-state experimental conditions were tested multiple times to establish the feasibility of achieving reproducible results, each of which confirmed it was not possible to routinely synthesise samples with identical ratios of the two phases. This is perhaps more easily observed in Figures 3.12(a) and (b) where the isotropic projections obtained from each two-dimensional spectrum for both heating series have been overlaid and compared. This suggests solid-state synthesis is not an easily controlled experimental method and, in this particular case, it is presumably owing to the volatile nature of the Na-based starting reagents. Working with highly volatile materials can lead to a non-stoichiometric reaction mixture, resulting in incomplete reaction or, more commonly, the formation of unknown intermediate phases. It is also extremely difficult to ensure complete mixing of the powdered starting reagents; therefore, to overcome this, the precursors are often mixed in a solvent (commonly

acetone or ethanol) prior to reaction at high annealing temperatures. This reduces particle size and ensures complete mixing of the powders. In contrast to sol-gel techniques, solid-state methods commonly produce samples with reasonably good crystallinity. This is highlighted in Figures 3.5(h-j) in which partially formed cube-like microstructures are observed for Solid-State Samples A and C. To obtain highly crystalline samples a relatively slow rate of reaction is required.

The sample containing the largest quantity of the second phase (~50%), Solid-State Sample A, was analysed in more detail. Using l-PXRD it was virtually impossible to identify any significant differences between this and that of phase pure Pbcm $NaNbO_3$, indicating the two phases must be, structurally, very closely related. X-ray diffraction principally examines the long-range order within a material whereas solid-state NMR investigates more local, short-range effects. The two techniques are therefore highly complementary to one another and enable enhanced structural characterisation of many complex solids. For the case of $NaNbO_3$, solid-state NMR provides more detailed information regarding the number of crystallographically distinct Na sites present and, in turn, the number of phases. NMR identifies the presence of two highly crystalline phases, confirming that X-ray diffraction is not simply missing the identification of an amorphous phase. This, in turn, provides confirmation that both phases diffract in a similar manner producing peaks that essentially overlap, thereby suggesting the second phase to be a polymorph of $NaNbO_3$ rather than an impurity phase. Without high-resolution diffraction data, it is extremely challenging to distinguish between the two; with the only subtle visible discrepancies occurring in the superstructure peaks ($2\theta = 34° - 42°$), as shown in Figure 3.4(b). However, solid-state NMR generally does not provide detailed information regarding the symmetry adopted within a structure or the precise location of the oxygen or sodium positions. To obtain this detailed information, diffraction is a necessity. Neutron diffraction is therefore essential for the study of $NaNbO_3$ as it enhances superstructure peaks and enables accurate location of the oxygen atoms, which ultimately aids in structural refinement and, in turn, spectral interpretation. Hence, both

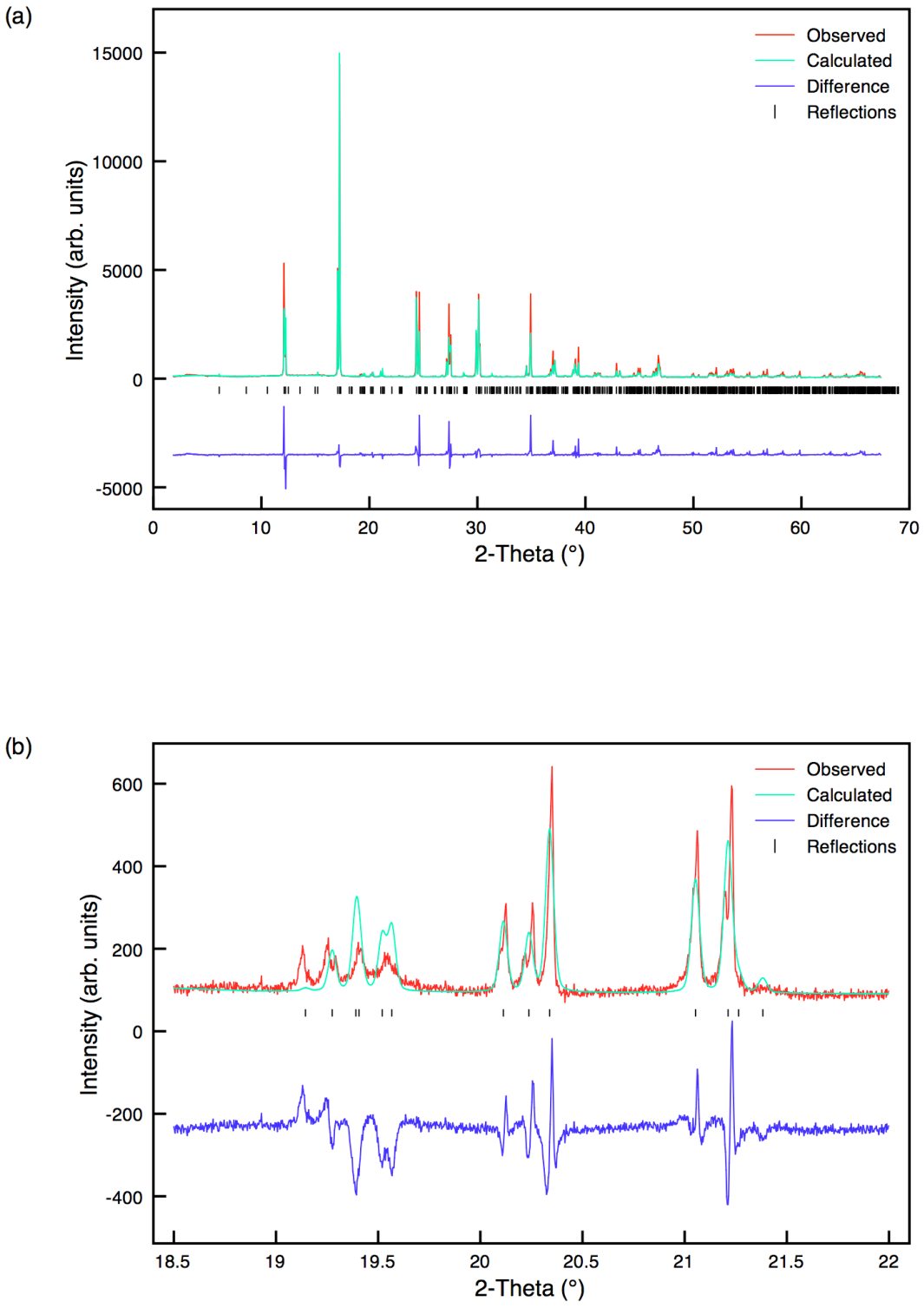

Figure 3.16: (a) Rietveld profile of s-PXRD data using Pbcm model for Solid-State Sample A $NaNbO_3$, (b) expansion of the corresponding superstructure peaks, 2θ = 18.5° – 22°.

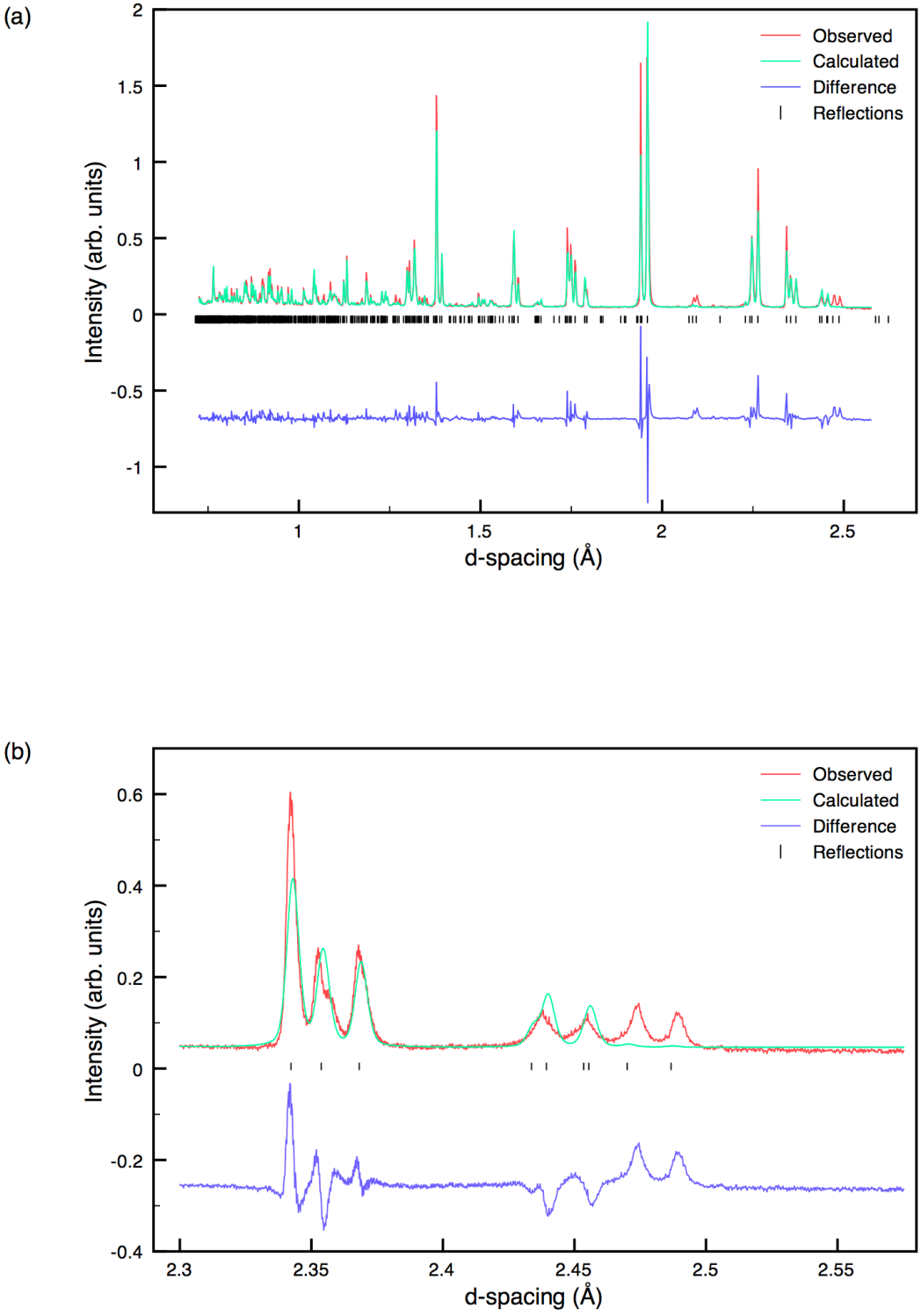

Figure 3.17: (a) Rietveld profile of NPD data using Pbcm model for Solid-State Sample A $NaNbO_3$, (b) expansion of the corresponding superstructure peaks, d = 2.3 Å – 2.55 Å.

Table 3.4: Structural parameters for Solid-State Sample A $NaNbO_3$ from s-PXRD data using isotropic thermal factors. Space group Pbcm, a = 5.51010(4) Å, b = 5.57279(3) Å, c = 15.52287(6) Å and V = 476.655(3) Å^3. χ^2 = 23.0, wR_p = 24.5% and R_p = 17.6%.

Atom	Site	x	y	z	U(iso) × 100 / Å^2
Na1	4c	0.2455(12)	0.25	0	2.00(5)
Na2	4d	0.2426(11)	0.2227(15)	0.25	0.40(4)
Nb1	8e	0.2577(2)	0.7412(2)	0.1251(4)	0.83(1)
O1	4c	0.6804(20)	0.25	0	3.49(10)
O2	4d	0.1817(21)	0.7725(28)	0.25	3.49(10)
O3	8e	0.4981(17)	0.4428(13)	0.1414(8)	3.49(10)
O4	8e	0.0159(21)	0.0075(19)	0.1100(8)	3.49(10)

Table 3.5: Structural parameters for Solid-State Sample A $NaNbO_3$ from NPD data using isotropic thermal factors. Space group Pbcm, a = 5.51088(7) Å, b = 5.57325(6) Å, c = 15.52551(17) Å and V = 476.843(7) Å^3. χ^2 = 61.1, wR_p = 13.8% and R_p = 13.6%.

Atom	Site	x	y	z	U(iso) × 100 / Å^2
Na1	4c	0.2585(14)	0.25	0	3.5(2)
Na2	4d	0.2606(10)	0.2298(10)	0.25	0.92(12)
Nb1	8e	0.2511(4)	0.7408(4)	0.1256(2)	1.19(5)
O1	4c	0.6956(8)	0.25	0	2.85(12)
O2	4d	0.1796(6)	0.7670(6)	0.25	0.08(6)
O3	8e	0.4619(6)	0.4513(5)	0.1417(3)	3.32(9)
O4	8e	0.0200(5)	0.0163(5)	0.1094(2)	1.62(6)

high-resolution synchrotron X-ray and neutron powder diffraction were undertaken on Solid-State Sample A.

The high-resolution diffraction data collected for Solid-State Sample A were analysed in significant detail and single phase refinements were completed for both datasets using the Pbcm model[248] and are shown in Figures 3.16(a) and 3.17(a). Full refinement details including structural parameters are given in Tables 3.4 and 3.5, respectively. It was immediately apparent in both datasets that a single model was insufficient owing to considerable discrepancies between the theoretical model and experimental data. The Rietveld refinement completed using the s-PXRD data highlighted regions in which shoulders and/or peaks were unaccounted for, as shown in Figure 3.16(b). Upon closer inspection it was evident split peaks were not indexed by the model and the lattice parameters considered them as simply single peaks. In addition, a number of the most intense peaks were not allocated sufficient intensity by the model, leading to relatively poor agreement factor, wR_p (24.5%) and χ^2 (23.0) values. The Rietveld refinement completed using the NPD data was significantly more informative, and is shown in Figure 3.17(a). Neutron diffraction enhances superstructure peaks therefore the small discrepancies initially identified by l-PXRD were magnified considerably by neutrons. The quality of refinement produced using solely the conventional Pbcm model was relatively poor (wR_p = 13.8% and χ^2 = 61.1), in particular over lower d-spacings. More specifically, two peaks in the experimental data at 2.47 Å and 2.49 Å were not accounted for in the model, suggesting they were associated with the additional polymorph present. These peaks are highlighted in Figure 3.17(b). Using this in conjunction with the ^{23}Na NMR data it was obvious a second phase very closely related to the orthorhombic Pbcm phase was present. A more detailed discussion of the possibility of multiphase refinements for Solid-State Sample A is given later.

3.3.3 Molten Salt Preparation

Initially, the precise experimental conditions required to synthesise a sample of $NaNbO_3$ using molten salt techniques were unknown therefore several 'test' reactions were undertaken to establish feasible reaction conditions. Using an annealing temperature of 850 °C for 24 hours a sample of $NaNbO_3$ was synthesised. Phase purity was verified using PXRD, and Rietveld refinement confirmed the sample refined well to the orthorhombic structure, Pbcm, as shown in Figure 3.18(a). EDX analysis revealed no presence of residual Cl^- from the synthesis. These spectra are given in Figure 3.19. The ^{23}Na MAS NMR spectrum recorded produced a broadened lineshape which appeared subtly different from the commercially purchased sample (Figures 3.5(a) and (e)). An overlay of these lineshapes is also shown in Figure 3.20. The conventional ^{23}Na MAS NMR spectrum failed to provide adequate information regarding both the composition of the sample and number of crystallographically distinct Na sites present; hence MQMAS techniques were utilised. The triple-quantum ^{23}Na MQMAS spectrum, as shown in Figure 3.21(a), indicated the presence of a second Na-containing phase, as observed for materials synthesised using solid-state methods (see Figures 3.6, 3.11 and 3.14). The isotropic spectrum indicated the quantity of this phase to be considerably reduced (to ~1-5%) when compared with the samples prepared using solid-state synthesis. Such a result suggested this synthetic method to be the most promising way of significantly reducing the phase or even eradicating it completely. Therefore, using this approach a systematic study of annealing temperature and time was completed to determine the effect on the quantity of second phase produced. Samples synthesised using this method possessed morphological uniformity, most probably owing to intimate mixing of the starting reagents due to reaction in a liquid medium. In particular, samples synthesised using an annealing temperature of 1000 °C for 24 hours produced crystallites with almost fully formed cube-like microstructures, shown in Figure 3.5(k). This cube-like microstructure was consistently produced for each sample synthesised using molten salt methods. To emphasise the regularity of the

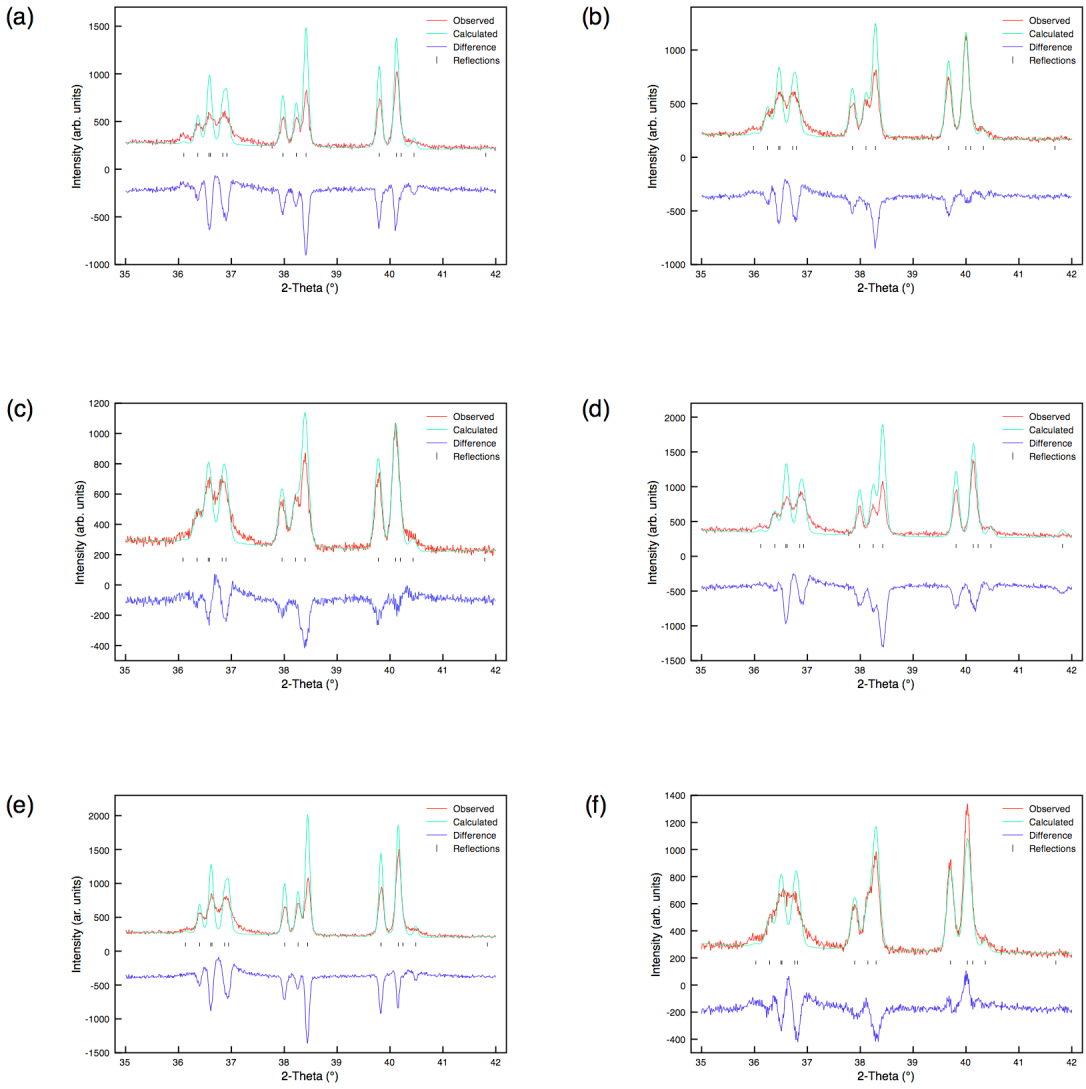

Figure 3.18: Rietveld profiles of l-PXRD data for molten salt $NaNbO_3$ with annealing temperatures of (a) 850 °C, (b) 900 °C, (c) 950 °C, (d) 1000 °C, (e) 1050 °C and (f) 1100 °C. In each case, the annealing time was fixed at 24 hours. Each refinement is consistent with the presence of single phase Pbcm $NaNbO_3$.

microstructure observed in each of the samples synthesised using molten salt methods an expansion of an SEM image is shown in Figure 3.22. The image clearly displays well-defined cubes and further highlights the exceptionally high crystallinity observed in each sample. Initially temperature was the sole variable in the systematic study completed, investigating the range between 850 °C and 1100 °C with annealing times fixed at 24 hours. Using Rietveld refinement all l-PXRD data in this range

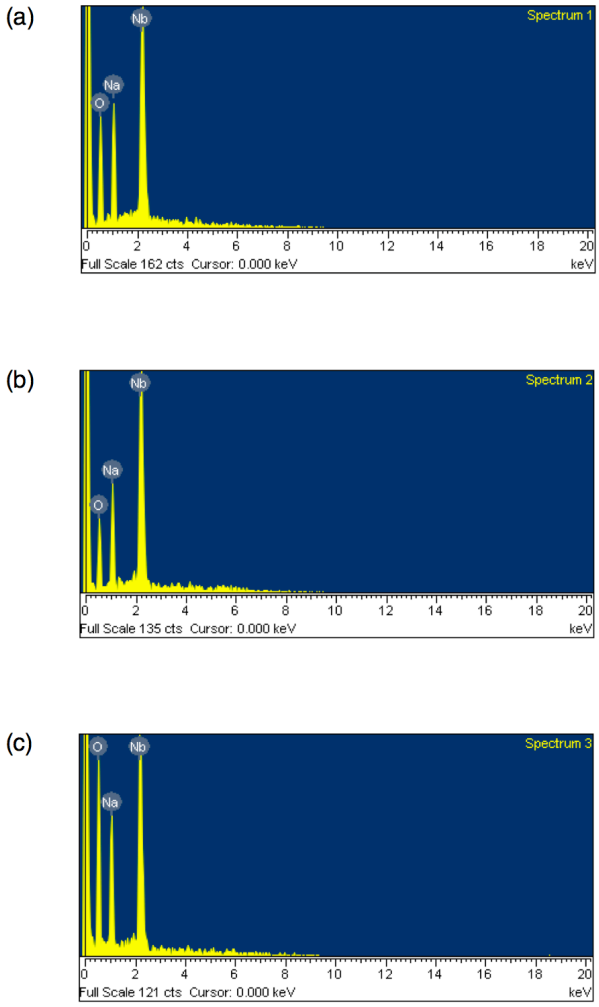

Figure 3.19: EDX spectra obtained for molten salt $NaNbO_3$ (synthesised using 1000 °C for 24 hours). All spectra indicate there is no residual Cl^- present from the molten salt synthesis process.

refined well to the Pbcm model. All Rietveld refinements completed for each sample in this heating series are shown in Figure 3.18(a-f). However, two-dimensional ^{23}Na NMR data highlighted the presence of an additional phase which consistently correlated with that identified in the initial molten salt sample synthesised. Via a systematic temperature study it was possible to eliminate this secondary phase entirely using a temperature of 1000 °C, as shown in Figure 3.21(d). However, at higher temperatures a reduction in crystallinity was observed. This is perhaps clearer to see in Figure 3.23 where the isotropic projections from each two-dimensional spectrum are compared. All two-dimensional ^{23}Na MQMAS NMR spectra

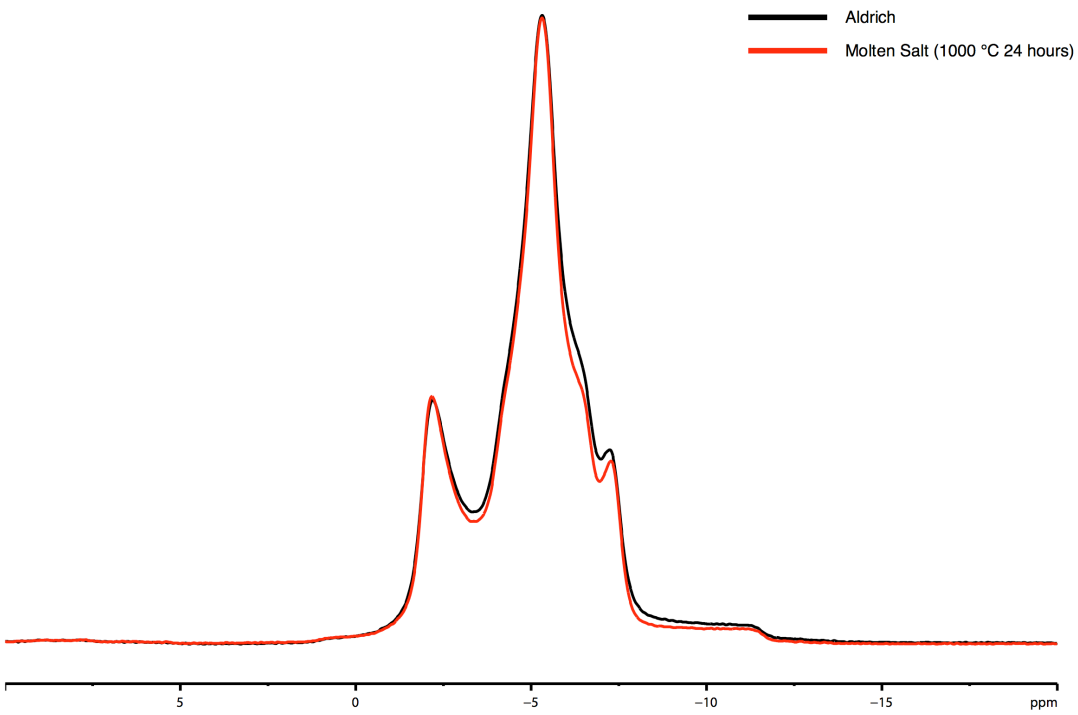

Figure 3.20: Overlay of ^{23}Na (14.1 T) MAS NMR spectra for phase pure sample $NaNbO_3$ (Aldrich) and a molten salt sample of $NaNbO_3$.

recorded for each sample in this series are shown in Figures 3.21(a-f). In addition, heating times between 3 and 48 hours were tested on reactions using 1000 °C. Rietveld refinement of all data in this series indicated excellent agreement with the literature, again suggesting the presence of single phase Pbcm $NaNbO_3$, and once again it was not possible to trace either the presence or quantity of any impurity phase using solely diffraction. All Rietveld refinements completed for each sample in this particular series are shown in Figures 3.24(a-f). Samples prepared using shorter reaction times displayed an abundance of the second phase previously identified in the temperature-dependent study. However, it was possible to eradicate the phase after 24 hours of heating to leave solely the Pbcm phase of $NaNbO_3$. Samples with longer annealing times confirmed this trend, indicating the second phase did not return to the sample and the phase produced was thermodynamically stable. Using ^{23}Na MQMAS the presence and relative quantities of second phase were

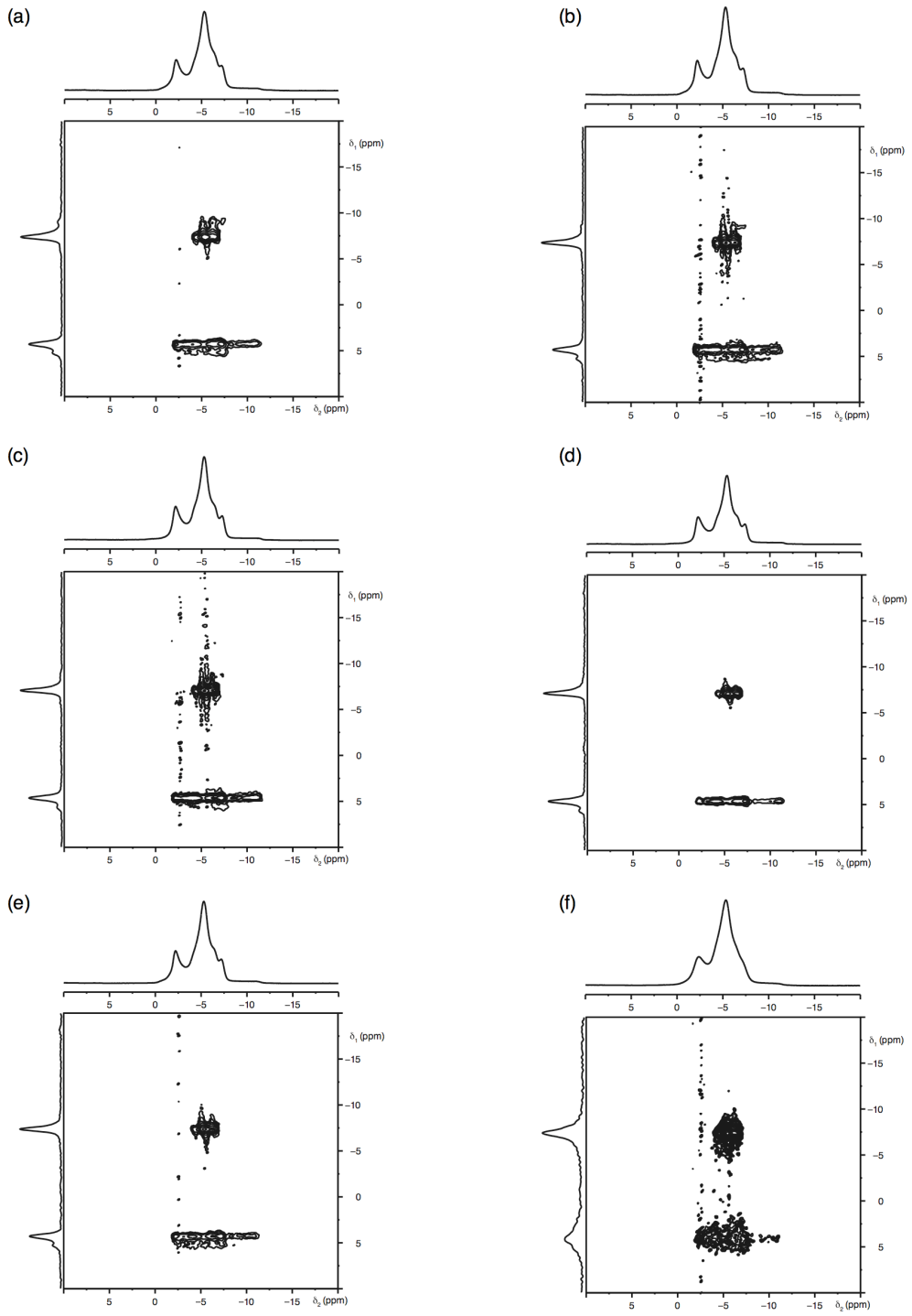

Figure 3.21: Conventional ^{23}Na (14.1 T) MAS NMR spectra, triple-quantum ^{23}Na MAS NMR spectra and corresponding isotropic projections, for molten salt $NaNbO_3$ with annealing temperatures of (a) 850 °C, (b) 900 °C, (c) 950 °C, (d) 1000 °C, (e) 1050 °C and (f) 1100 °C. In each case the annealing time was fixed at 24 hours. Small quantities of the secondary phase are observed in (a-c). This phase is fully removed in (d-f) however poor crystallinity is observed in (f) owing to high reaction temperatures and fast precipitation rates.

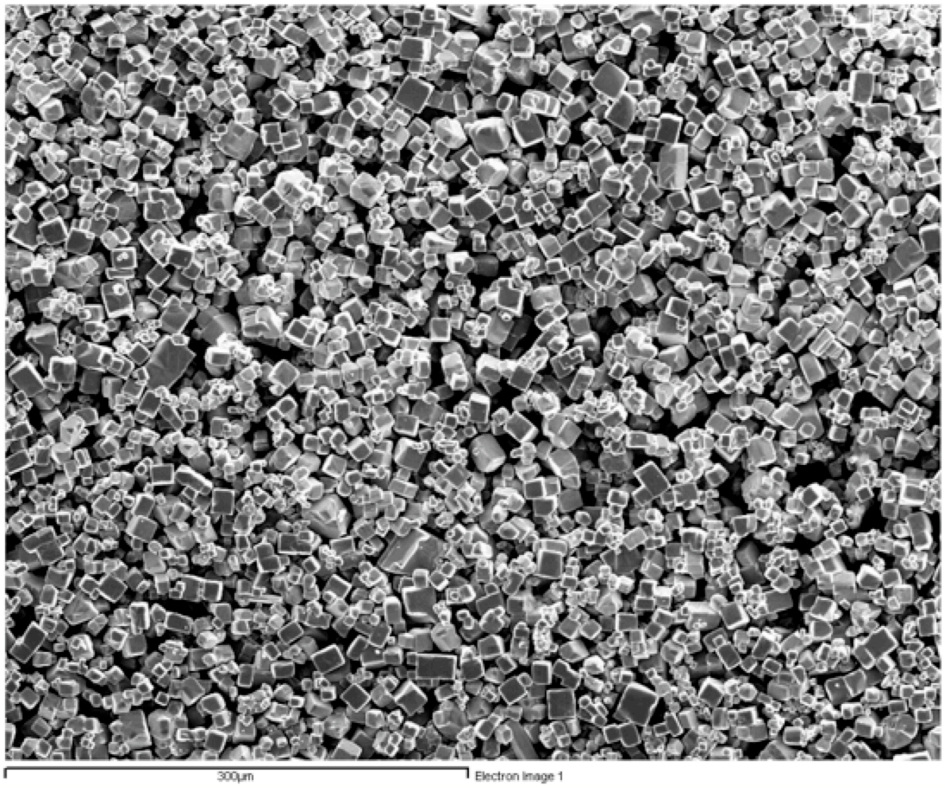

Figure 3.22: An expansion of an SEM image of a molten salt sample of $NaNbO_3$. This highlights the cube-like microstructure adopted by samples synthesised using these methods.

clearly visible, as shown in Figure 3.25. This is perhaps more easily observed by inspection of the isotropic projections shown in Figure 3.23(b). Full refinement details for both heating series are given in Appendix II.

Two phases were consistently synthesised using molten salt techniques, however both temperature and time appeared to affect the formation of the second phase. In the case of our molten salt reactions it was possible to determine the exact temperature and time of reaction required to fully eradicate the second phase. For solid-state reactions, however, this does not appear to be the case. The synthetic conditions alter the proportions of the two phases present, but it is not possible to remove either entirely. Even when reactions were carried out with

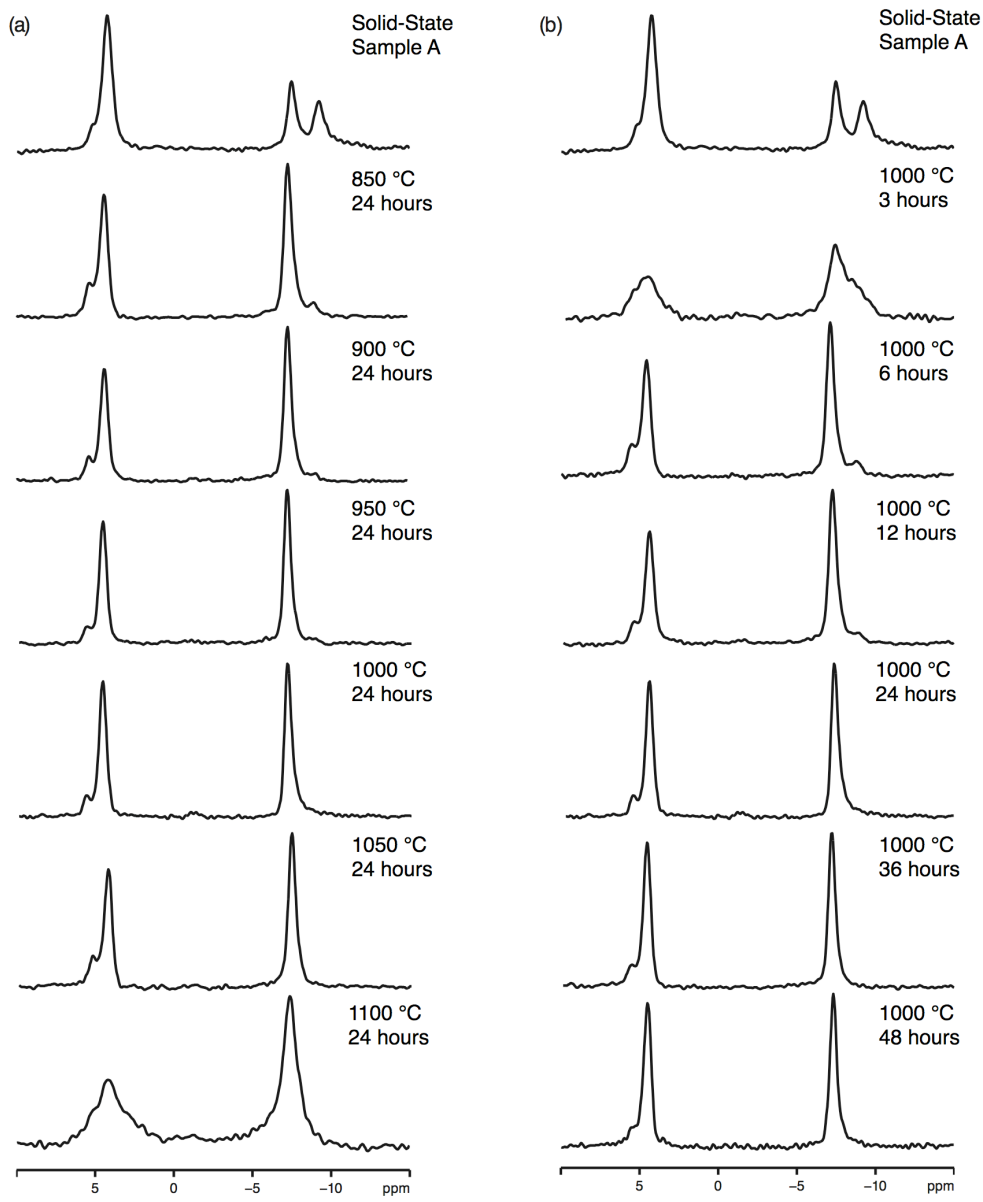

Figure 3.23: Isotropic projections obtained from triple-quantum ^{23}Na (14.1 T) MAS NMR spectra of molten salt samples of $NaNbO_3$. In (a), annealing temperature was varied from 850 °C to 1100 °C, with a fixed annealing time of 24 hours. In (b), the annealing time was varied from 3 to 48 hours, with a fixed annealing temperature of 1000 °C. For comparison the isotropic projection for Solid-State Sample A of $NaNbO_3$ is also shown.

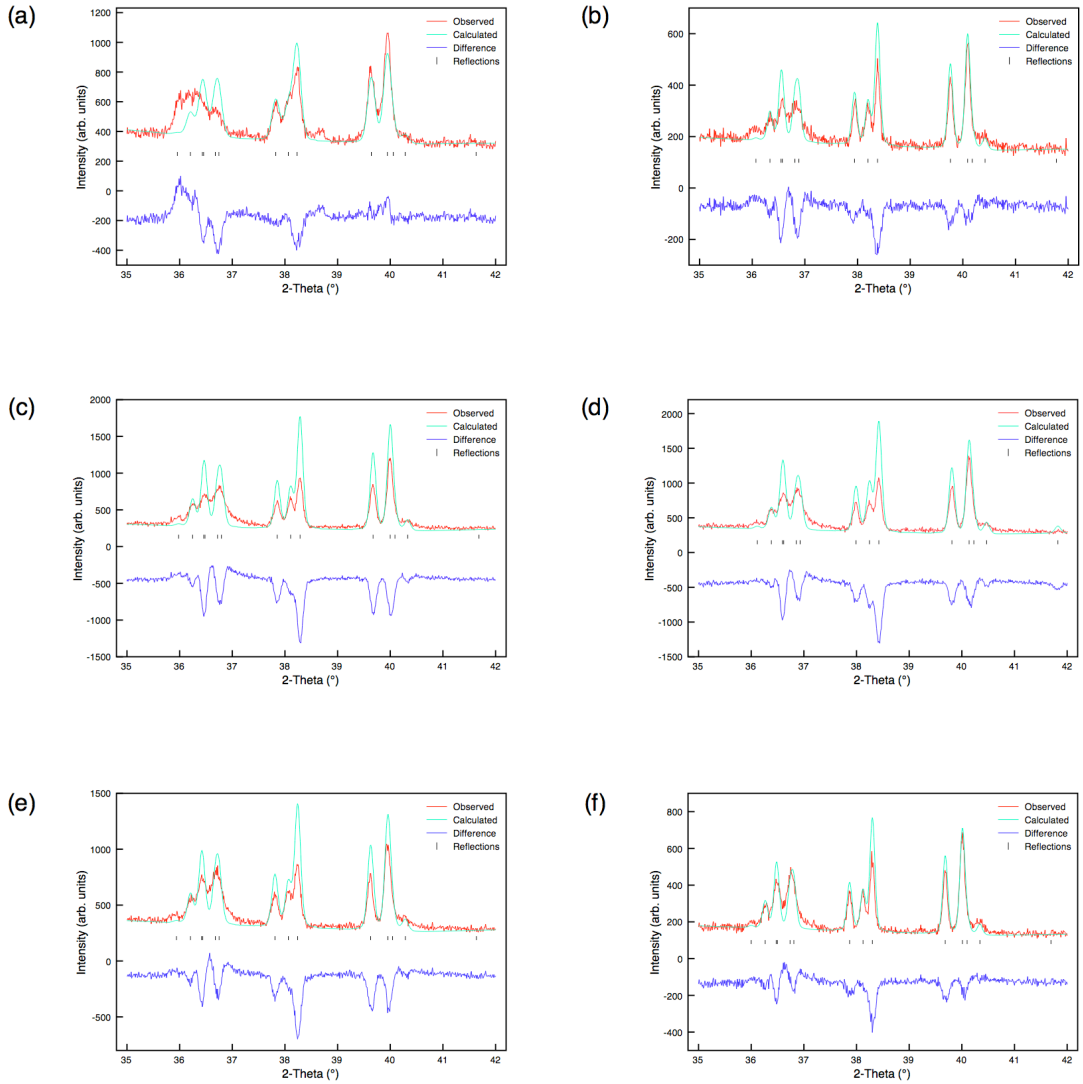

Figure 3.24: Rietveld profiles of l-PXRD data for molten salt $NaNbO_3$ with annealing times of (a) 3 hours, (b) 6 hours, (c) 12 hours, (d) 24 hours, (e) 36 hours and (f) 48 hours. In each case the annealing temperature was fixed at 1000 °C. Each refinement is consistent with the presence of single phase Pbcm $NaNbO_3$.

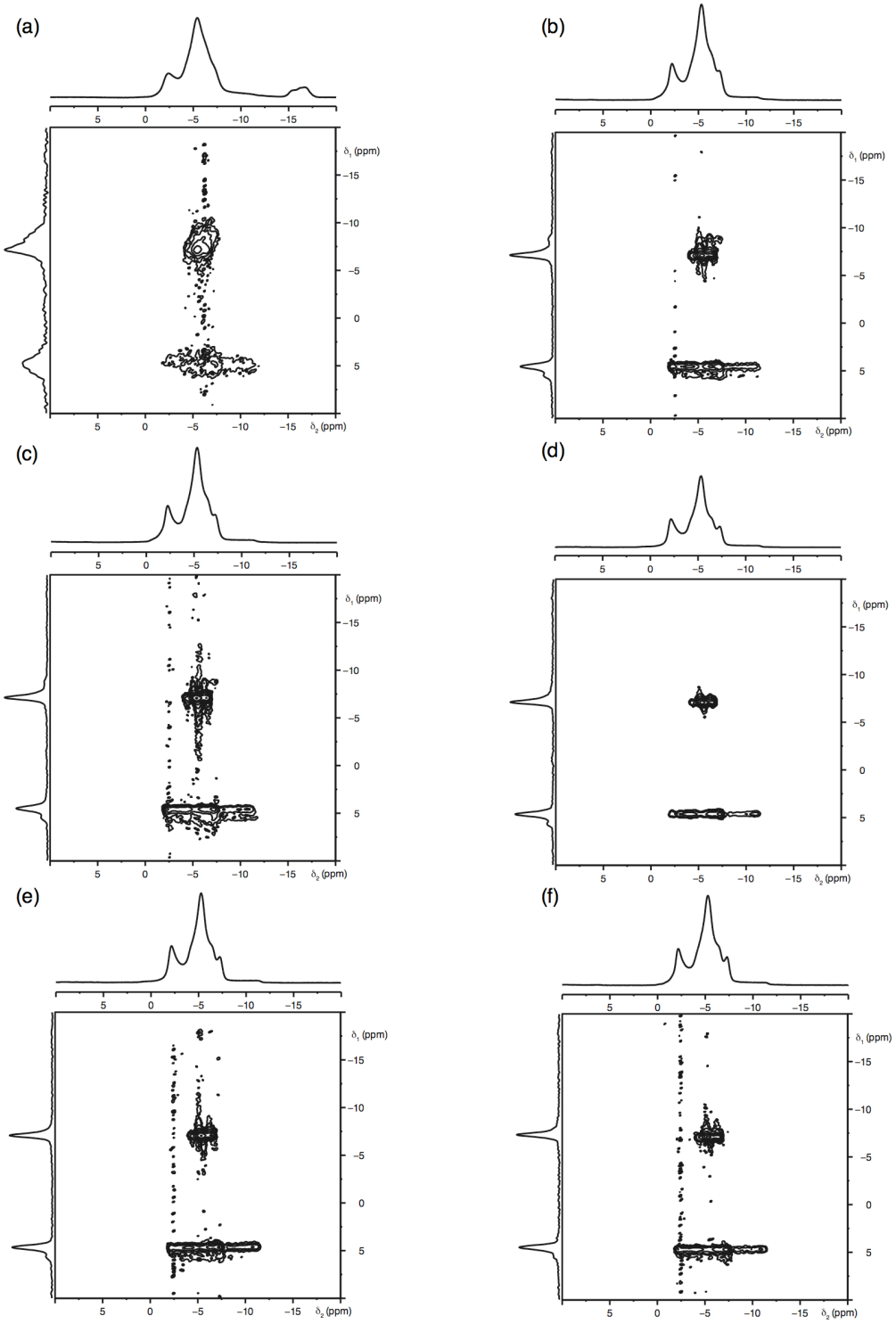

Figure 3.25: Conventional ^{23}Na (14.1 T) MAS NMR spectra, triple-quantum ^{23}Na MAS NMR spectra and corresponding isotropic projections for molten salt $NaNbO_3$, with annealing times of (a) 3 hours, (b) 6 hours, (c) 12 hours, (d) 24 hours, (e) 36 hours and (f) 48 hours. In each the annealing temperature was fixed at 1000 °C. Small quantities of the secondary phase are observed in (a-c) however this phase is fully removed in (d-f).

apparently similar conditions the proportions of the two phases obtained varied. In both solid-state and molten salt reactions the major polymorph formed was the Pbcm phase, although the proportion of the second phase was as high as ~50% in some solid-state syntheses. However, by means of a molten salt approach it was possible to synthesise phase pure Pbcm $NaNbO_3$. Unfortunately, this provides little or no assistance in determining the precise nature of the second phase, although it does, however, provide valuable information regarding reaction mechanism.

3.3.4 Sol-Gel Preparation

In order to use a diverse range of synthetic routes, and to clarify the nature of the second polymorph present in the solid-state preparations, a sol-gel approach was also utilised. In a similar manner to molten salt techniques this allows intimate mixing and reaction of the starting reagents. Conventionally, solid-state methods are adopted over sol-gel processes for the synthesis of perovskites owing, principally, to the simplicity of the reaction. However, occasionally sol-gel methods are favoured as they can enable alternative phases to form which are not commonly observed within solid-state reactions. In contrast to solid-state methods, sol-gel techniques utilise considerably lower temperatures during synthesis. However, an associated disadvantage of these processes, particularly in the case of $NaNbO_3$, is the severe lack of control and reproducibility.

Using a basic sol-gel approach a sample of $NaNbO_3$ was synthesised and structure and phase purity were studied using PXRD. It was immediately apparent a different polymorph of $NaNbO_3$ had been synthesised than the commonly formed orthorhombic Pbcm phase. Rietveld refinement of l-PXRD data (Figure 3.26(a)) highlighted differences in the superstructure peaks ($2\theta = 34° – 42°$), as shown in Figure 3.26(b), in which the theoretical model (Pbcm) placed intensity where no observed experimental data appeared. The presence of a different polymorphic form of $NaNbO_3$ was confirmed using s-PXRD and NPD. Close examination of the high-resolution diffraction data revealed the

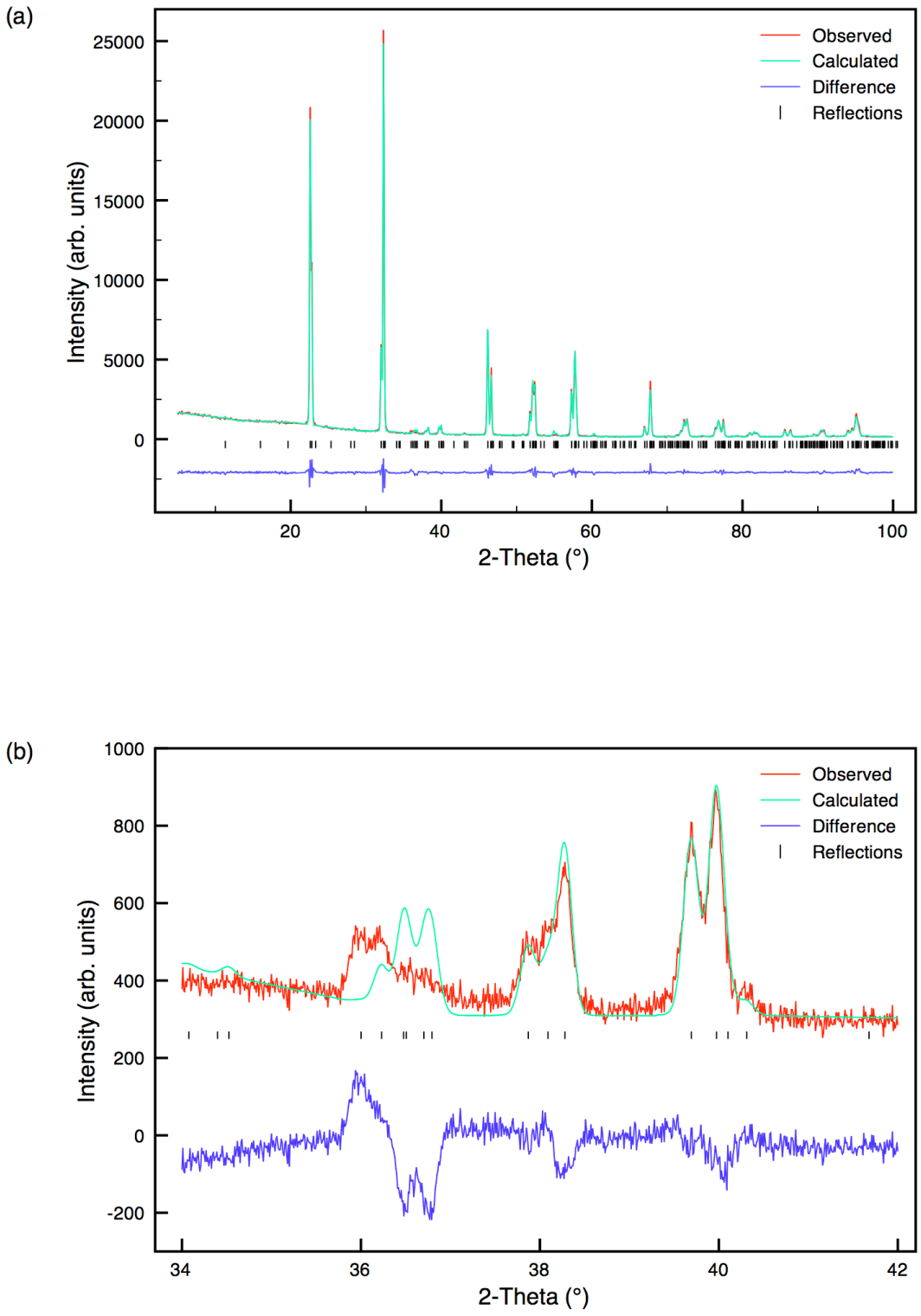

Figure 3.26: Sol-gel $NaNbO_3$ (a) Rietveld profile (Pbcm model) of l-PXRD data and (b) corresponding expansion of the superstructure peaks (2θ = 35° – 45°) highlighting areas of discrepancy.

disappearance of the peaks due to the $4a_p$ superlattice, thereby indicating the phase present did not require additional doubling of the unit cell, as in Pbcm, merely the $\sqrt{2}a_p \times \sqrt{2}a_p \times 2a_p$ cell. This type of distortion in perovskites is well known (in fact it corresponds to the most common tilt system $a^-a^-b^+$). A standard structural model for the centrosymmetric orthorhombic space group Pnma was sufficient to index all peaks, and each dataset refined reasonably well to this model, as shown in Figure 3.27. Refinement details for the NPD data (using both isotropic and anisotropic temperature factors) can be found in Tables 3.6 and 3.7. The Rietveld refinement completed using the s-PXRD data is shown in Figure 3.27(b). Full refinement details are given in Appendix II.

Using conventional ^{23}Na MAS NMR a different and broadened lineshape was observed, which appeared to have lost many of the sharp, distinct features previously identified in the commercially purchased sample. This can be seen in Figures 3.5(a) and (f), where the two lineshapes are compared. To further highlight the differences in lineshape exhibited as a function of synthesis method a comparison of all ^{23}Na MAS NMR spectra recorded at varying fieldstrengths (9.4 T, 14.1 T and 20 T) is shown in Figure 3.28. The two-dimensional ^{23}Na MQMAS NMR spectrum recorded for the sol-gel sample also confirmed the presence of a different phase of $NaNbO_3$ in addition to a small percentage (~10%) of the Pbcm phase (Figure 3.29). It was evident this new phase contained two crystallographically distinct Na sites with δ_1 values of −7.1 ppm and 13.5 ppm, thereby contradicting the conclusions initially drawn from diffraction data alone. The NMR parameters extracted from this spectrum are given in Table 3.2. Although providing an adequate refinement to both the synchrotron and neutron data, the presence of only a single distinct Na species for Pnma reveals it would not appear to be the correct model. In addition, when refined anisotropically the oxygen atom O1 did not have a positive definite thermal displacement factor, thereby indicating this model to be incorrect, as highlighted in Table 3.7.

Perovskites frequently favour centrosymmetric structures except when ferroelectric ions are present. Of the many reported polymorphs of $NaNbO_3$ the majority are centrosymmetric with only one confirmed report

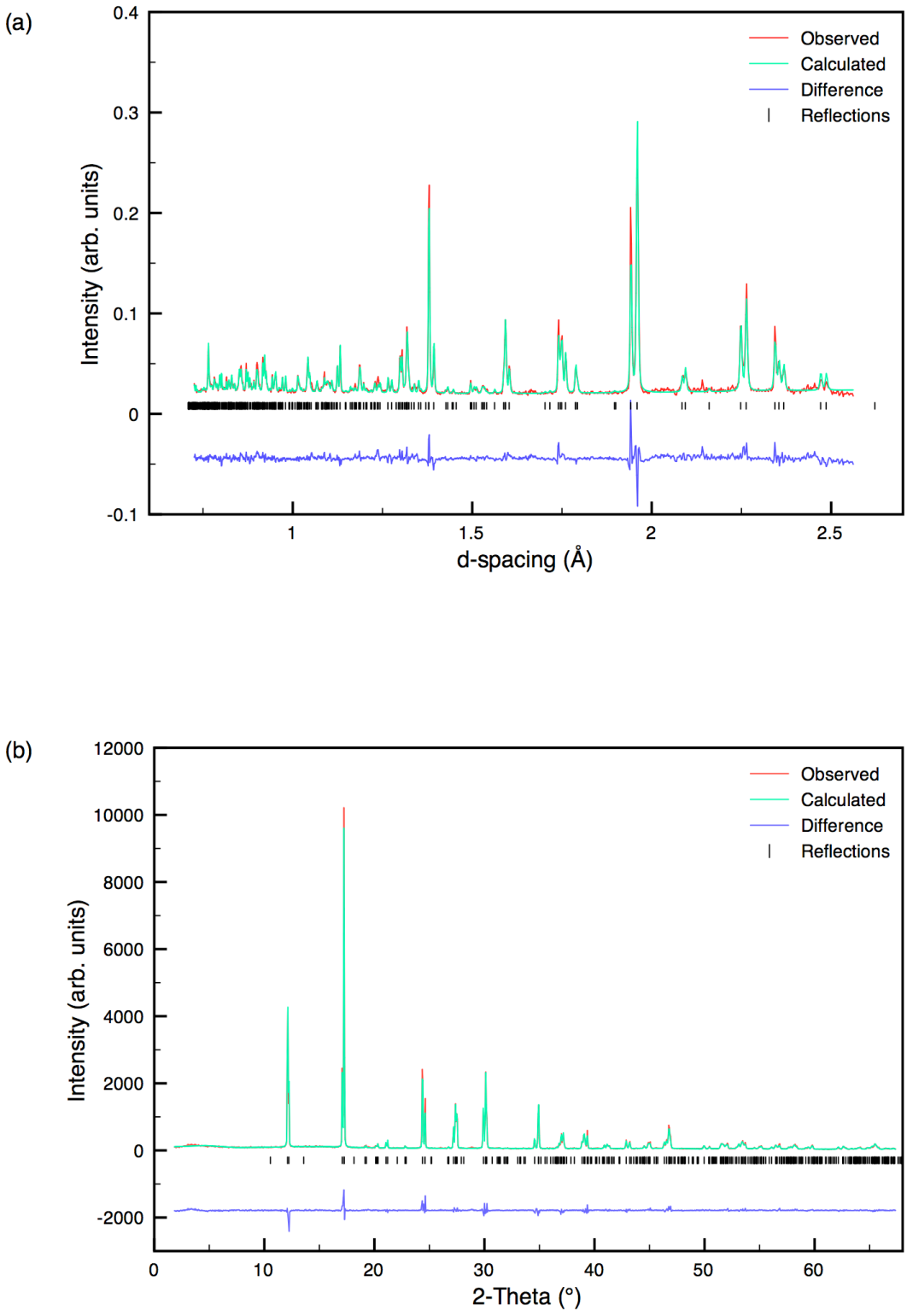

Figure 3.27: Rietveld profiles of (a) NPD and (b) s-PXRD data for sol-gel $NaNbO_3$ using the structural model Pnma. Isotropic thermal parameters were used during refinement of the NPD data.

Table 3.6: Structural parameters for sol-gel $NaNbO_3$ from NPD data, using isotropic thermal factors. Space group Pnma, a = 5.57068(10) Å, b = 7.76621(14) Å, c = 5.51329(10) Å and V = 238.522(11) Å^3. χ^2 = 5.8, wR_p = 7.3% and R_p = 6.6%.

Atom	Site	x	y	z	U(iso) × 100 / Å^2
Na1	4c	0.4958(8)	0.25	0.0026(7)	1.64(5)
Nb1	4a	0	0	0	0.31(4)
O1	4c	0.5111(4)	0.25	0.5619(3)	0.57(4)
O2	8d	0.2158(2)	0.0308(1)	0.2817(2)	1.46(4)

of a non-centrosymmetric structure, that by Shuvaeva *et al.*,[228] obtained from single crystal diffraction. Both the neutron and ^{23}Na NMR data presented suggested the newly synthesised polymorph of $NaNbO_3$ had undergone a reduction in symmetry from the centrosymmetric space group Pnma to a non-centrosymmetric structure. Therefore, to provide further support for this, the nonlinear optic (NLO) properties of selected $NaNbO_3$ samples were tested. Second Harmonic Generation (SHG) experiments are a relatively simple and effective way of identifying whether a structure is centrosymmetric or non-centrosymmetric. SHG measurements were conducted on both the sol-gel sample and a phase pure sample of $NaNbO_3$ (synthesised using molten salt techniques). No response was detected from the phase pure $NaNbO_3$ sample, as shown in Figure 3.30(a). The sol-gel sample displayed an intense SHG active (green) signal, Figure 3.30(b), indicating it to be non-centrosymmetic. This, in conjunction with the ^{23}Na NMR data, provided a significant step towards structural characterisation and allowed identification of three potential non-centrosymmetric subgroups of Pnma; $P2_1ma$, $Pn2_1a$ and $Pnm2_1$. Rietveld refinements were completed for each potential space group using the NPD data collected, although it should be noted that the $Pn2_1a$ model also possesses only a single Na site. Interestingly, the work by Shuvaeva and co-workers was the result of an electric field induced phase transition from Pbcm to $P2_1ma$ in a single crystal of $NaNbO_3$. This polymorph was also recently reported by Waser *et al.*,[226,229] as existing in submicron powders of $NaNbO_3$. Their work suggests $NaNbO_3$ undergoes

Table 3.7: Structural parameters for sol-gel $NaNbO_3$ from NPD data using anisotropic thermal factors. Space group Pnma, a = 5.57067(10) Å, b = 7.76626(12) Å, c = 5.51354(9) Å and V = 238.534(10) Å^3. $\chi^2 = 4.6$, $wR_p = 6.5\%$ and $R_p = 6.2\%$.

Atom	Site	x	y	z	$U_{11} \times 100/Å^2$	$U_{22} \times 100/Å^2$	$U_{33} \times 100/Å^2$
Na1	4c	0.4973(9)	0.25	0.0025(7)	2.94(11)	1.02(9)	2.12(12)
Nb1	4a	0	0	0	0.90(5)	0.39(6)	0.48(6)
O1	4c	0.5091(5)	0.25	0.5600(3)	2.60(9)	−0.11(6)	0.98(7)
O2	8d	0.2172(2)	0.0301(1)	0.2838(2)	2.72(7)	0.93(6)	2.18(7)

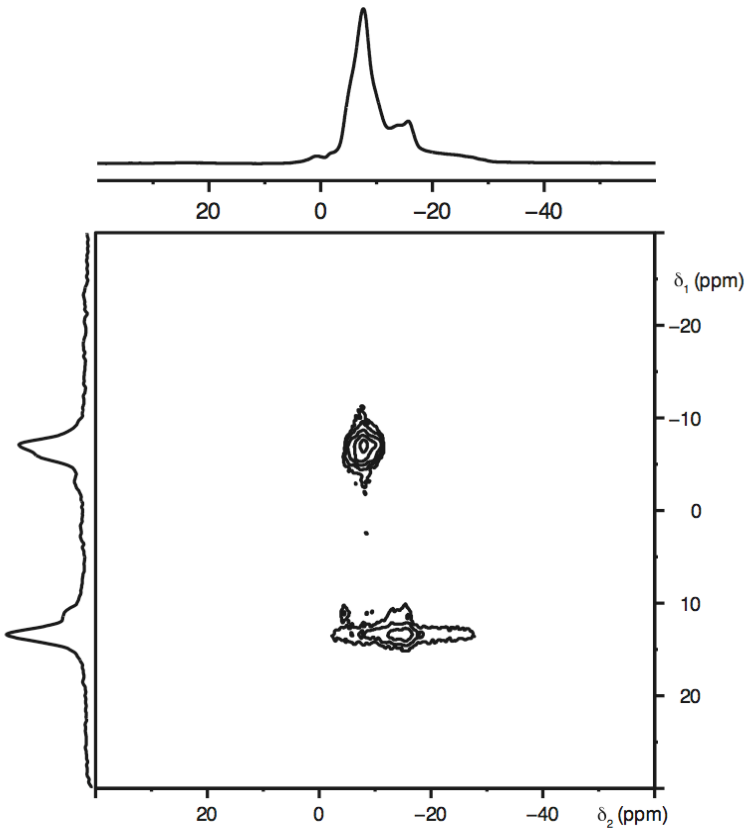

Figure 3.28: Conventional ^{23}Na (9.4 T) MAS NMR spectrum, triple-quantum MAS NMR spectrum, and corresponding isotropic projection for sol-gel sample of $NaNbO_3$.

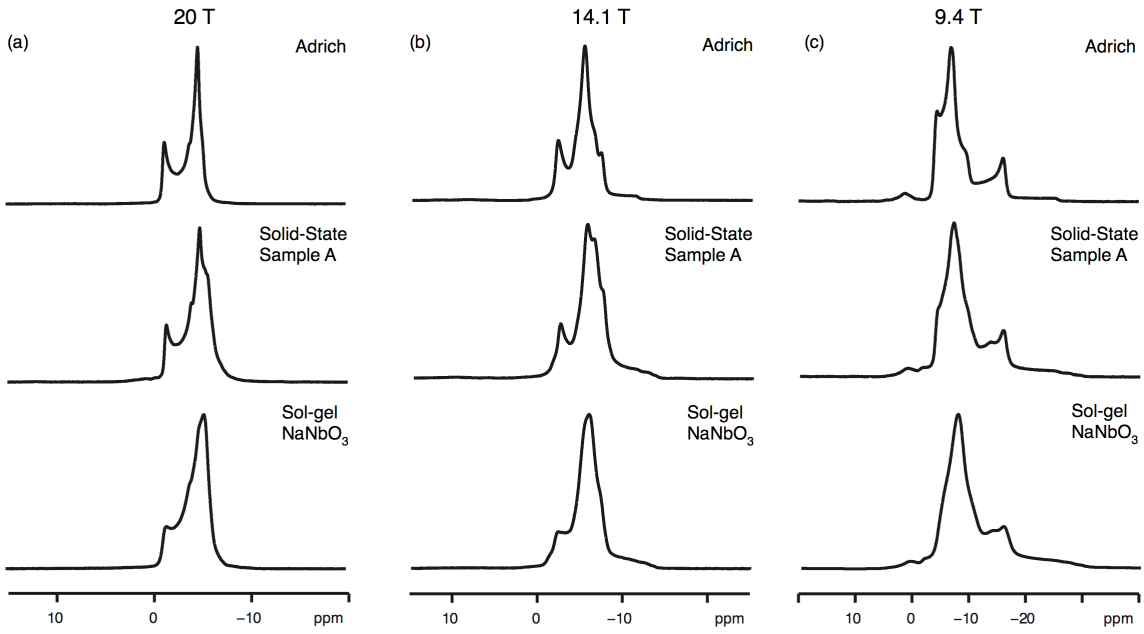

Figure 3.29: Comparison of conventional ^{23}Na MAS NMR spectra for commercial $NaNbO_3$ (Aldrich), Solid-State Sample A $NaNbO_3$ and sol-gel $NaNbO_3$ recorded at (a) 20 T, (b) 14.1 T and (c) 9.4 T. This highlights the change in lineshape observed with varying fieldstrength. The MAS rate was 14 kHz.

a particle size induced phase transition from Pbcm to Pmma via the orthorhombic phase $Pmc2_1$ (alternative setting $P2_1ma$). Using microemulsion-mediated synthetic techniques nanosized powders were synthesised and annealed at various temperatures, producing a range of micron, submicron and nano-ordered powders. In a later publication Waser *et al.*, investigated similar temperature and pressure induced phase transitions for submicron powders of $NaNbO_3$ and identified a similar submicron sample to that previously synthesised. Using piezoresponse force microscopy (PFM) the sample was confirmed to be noncentrosymmetric and, in turn, suggested the presence of the $Pmc2_1$ polymorph of $NaNbO_3$.[249] Waser concluded that enhanced piezoelectric behaviour was observed for submicron powders, in contrast to much weaker activity observed in micron powders. To date there are no reports of this phase existing in powders of $NaNbO_3$ with a larger average particle size distribution.

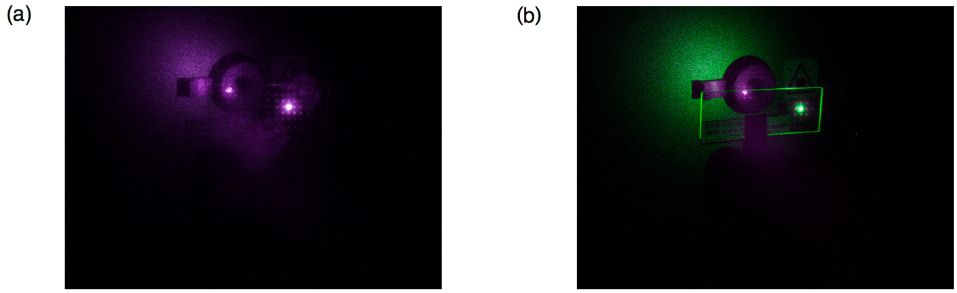

Figure 3.30: Second Harmonic Generation (SHG) measurements for (a) a phase pure sample of Pbcm $NaNbO_3$ synthesised using molten salt techniques (1000 °C for 24 hours) and (b) sol-gel $NaNbO_3$.

Rietveld refinement of the model in space group $P2_1ma$ was undertaken using the model of Shuvaeva.[228] However, structural models for $NaNbO_3$ in space groups $Pn2_1a$ and $Pnm2_1$ were not available in the literature so these were obtained by reduction down in symmetry to the respective space group from Pnma.[107] Rietveld refinement using the space group $P2_1ma$ produced a better fit when compared with $Pn2_1a$ and $Pnm2_1$. All Rietveld refinements can be found in Figures 3.31 – 3.33. Corresponding χ^2 values for the Pnma, $P2_1ma$, $Pn2_1a$ and $Pnm2_1$ Rietveld refinements are 5.8, 4.8, 5.6 and 7.9 respectively. The $Pn2_1a$ model possesses only a single Na site and can therefore be excluded. All structural parameters obtained from each refinement are given in Tables 3.8 - 3.10. Corresponding bond lengths are given in Appendix II. When refined in $Pnm2_1$ extremely high isotropic thermal parameters were obtained, thereby clearly indicating this not to be the correct structure. $P2_1ma$ provides the best agreement with the experimental data.

At no stage in this investigation was the sol-gel sample exposed to an electric field, confirming it is feasible to directly synthesise a non-centrosymmetric, polar phase of $NaNbO_3$; however it is extremely difficult to produce a phase pure sample. The Pbcm phase of $NaNbO_3$ is consistently formed within the reaction owing, presumably, to its relative thermodynamic stability. The crystallinity of the sample was also severely reduced when compared with that produced using molten salt and solid-state techniques. The microstructure adopted displayed no regularity,

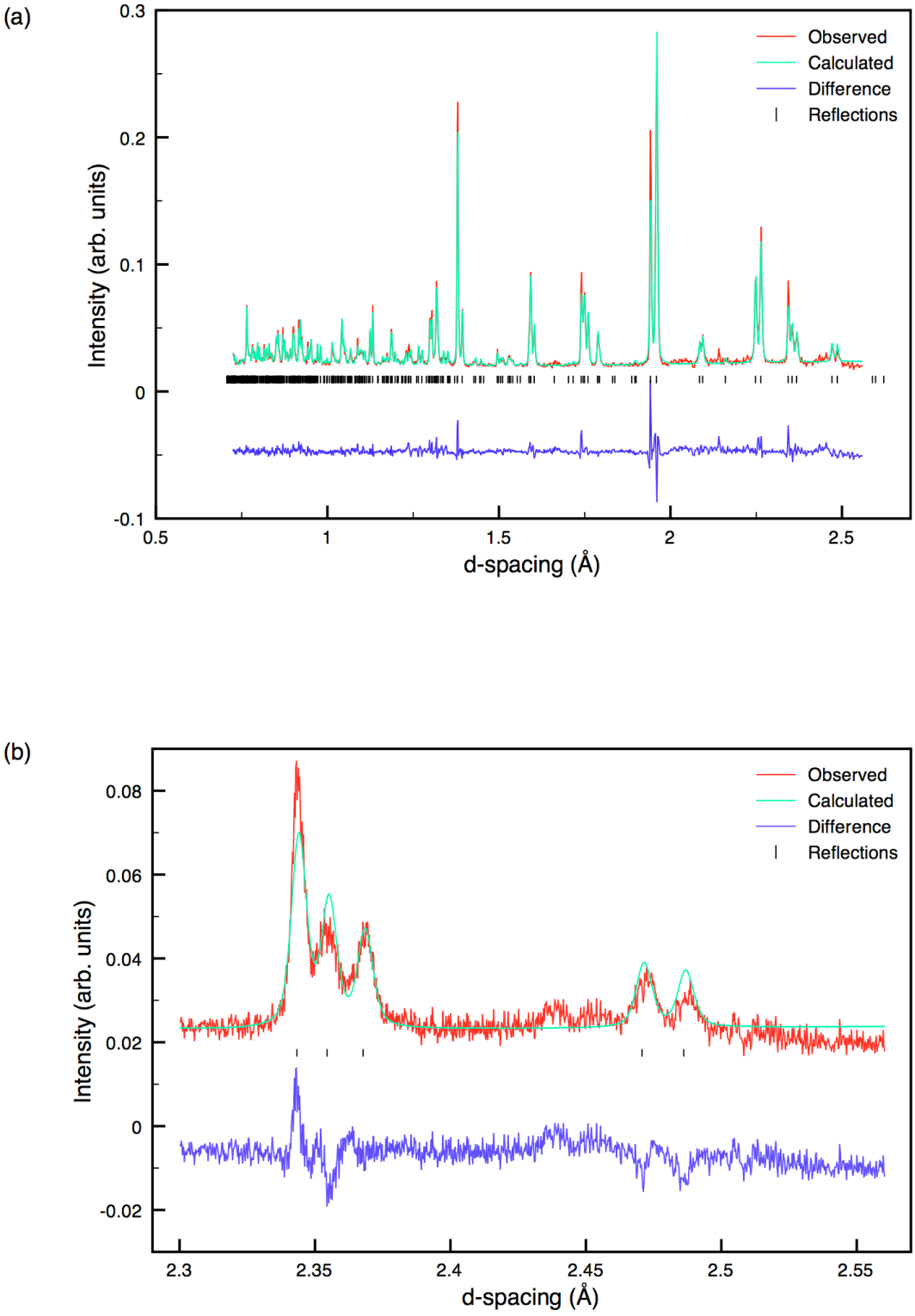

Figure 3.31: Rietveld profile of NPD data for sol-gel $NaNbO_3$ using structural model $P2_1ma$. Also shown is a corresponding expansion of the superstructure peaks (2.3 Å – 2.55 Å). Isotropic thermal parameters were used during the Rietveld refinement.

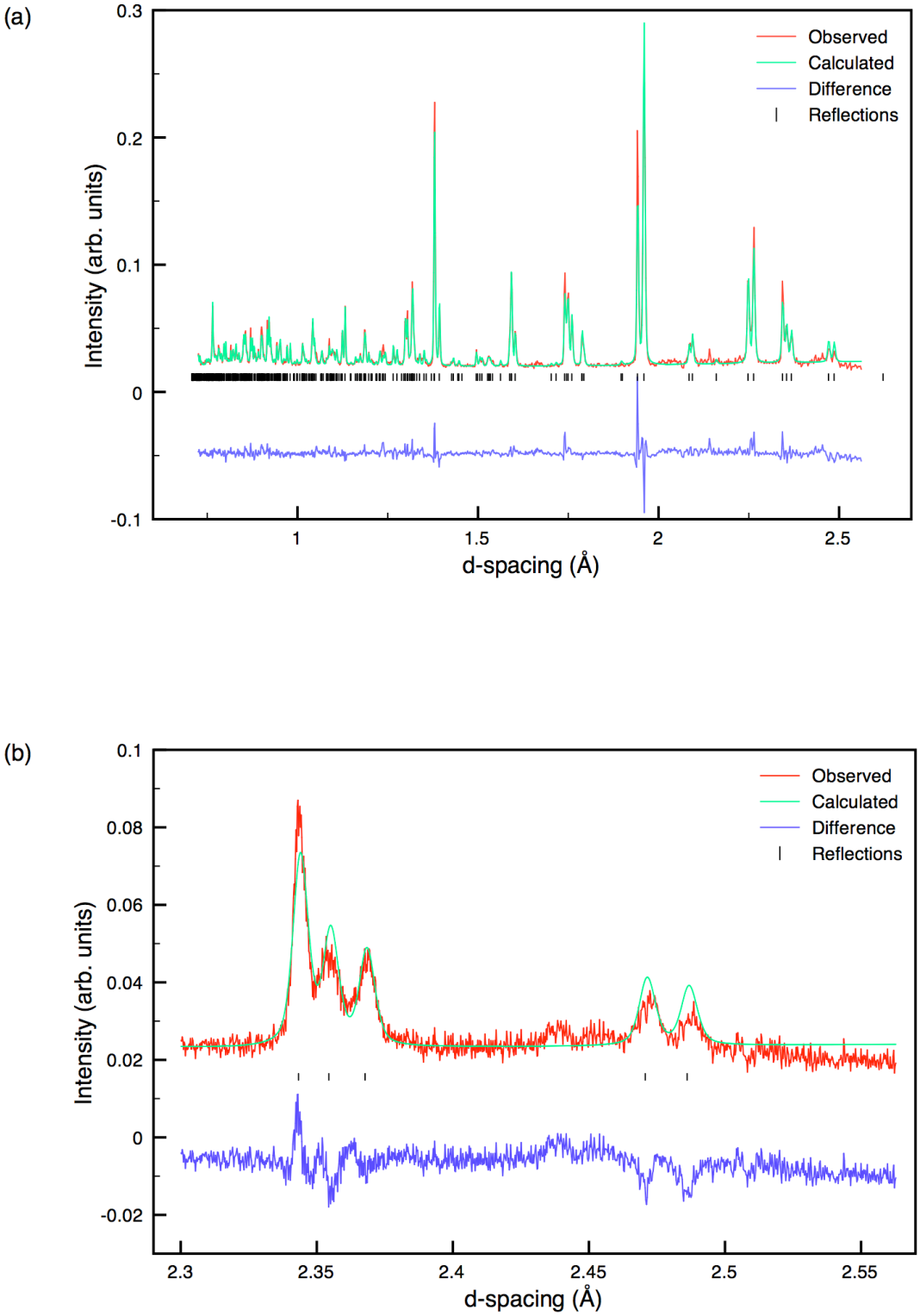

Figure 3.32: Rietveld profile of NPD data for sol-gel $NaNbO_3$ using structural model $Pn2_1a$. Also shown is a corresponding expansion of the superstructure peaks (2.3 Å – 2.55 Å). Isotropic thermal parameters were used during the Rietveld refinement.

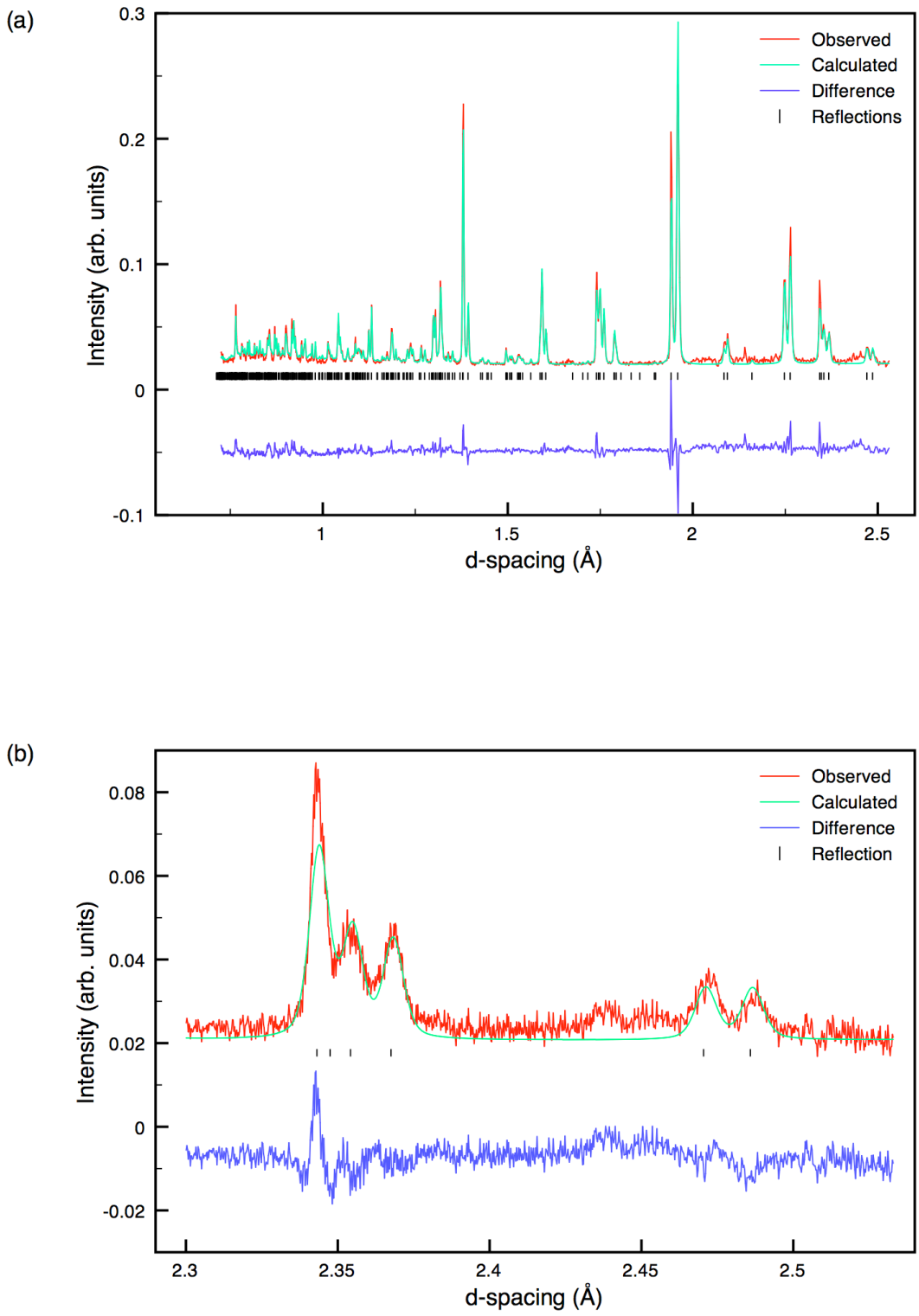

Figure 3.33: Rietveld profile of NPD data for sol-gel $NaNbO_3$ using structural model $Pnm2_1$. Also shown is a corresponding expansion of the superstructure peaks (2.3 Å – 2.55 Å). Isotropic thermal parameters were used during the Rietveld refinement.

Table 3.8: Structural parameters for sol-gel $NaNbO_3$ from NPD data, using isotropic thermal factors. Space group $P2_1ma$, a = 5.57070(9) Å, b = 7.76623(12) Å, c = 5.51331(9) Å and V = 238.524(10) Å^3. χ^2 = 4.8, wRp = 6.6% and Rp = 6.2%.

Atom	Site	x	y	z	U(iso) × 100 / Å^2
Na1	2a	0.2596(11)	0	0.7481(10)	0.50(10)
Na2	2b	0.2915(12)	0.5	0.7327(11)	2.24(15)
Nb1	4c	0.2625	0.2500(5)	0.2466(5)	0.20(4)
O1	2a	0.2409(6)	0	0.3124(11)	0.53(13)
O2	2b	0.2257(5)	0.5	0.1928(11)	0.37(12)
O3	4c	0.0131(7)	0.2790(6)	0.5272(7)	1.84(9)
O4	4c	−0.0490(6)	0.2197(5)	0.0360(6)	0.61(7)

Table 3.9: Structural parameters for sol-gel $NaNbO_3$ from NPD data using isotropic thermal factors. Space group $Pn2_1a$, a = 5.57069(10) Å, b = 7.76625(14) Å, c = 5.51334(10) Å and V = 238.526(11) Å^3. χ^2 = 5.6, wR_p = 7.2% and R_p = 6.6%.

Atom	Site	x	y	z	U(iso) × 100 / Å^2
Na1	4a	0.4952(8)	0.2487(8)	0.0031(7)	1.57(6)
Nb1	4a	0.0022(8)	0.0107(4)	−0.0045(7)	0.23(4)
O1	4a	0.5119(4)	0.2512(6)	0.5609(3)	0.78(5)
O2	4a	0.2044(5)	0.0317(6)	0.2855(8)	1.20(8)
O3	4a	−0.2276(6)	−0.0304(5)	−0.2777(9)	1.44(9)

Table 3.10: Structural parameters for sol-gel $NaNbO_3$ from NPD data using isotropic thermal factors. Space group $Pnm2_1$, a = 5.57022(13) Å, b = 7.76573(17) Å, c = 5.51272(13) Å and V = 238.463(14) Å^3. $\chi^2 = 7.9$, $wR_p = 8.5\%$ and $R_p = 7.8\%$.

Atom	Site	x	y	z	U(iso) × 100 / Å^2
Na1	2a	0.7550(13)	0.5	0.0015(11)	0.34(9)
Na2	2a	−0.226(3)	0	−0.005(3)	7.0(3)
Nb1	4b	0.2462(8)	0.2513(5)	−0.0015(13)	2.02(6)
O1	2a	0.7724(15)	0.5	0.5516(16)	4.8(2)
O2	2a	−0.2528(10)	0	−0.5666(10)	0.91(8)
O3	4b	0.4572(7)	0.2802(6)	0.2927(9)	2.40(9)
O4	4b	0.0178(9)	0.2198(8)	−0.2626(10)	4.74(17)

with a variety of different crystal sizes and morphologies adopted throughout, as illustrated in Figure 3.5(l), in contrast to the regularly repeating cube-like microstructure adopted in the molten salt samples. The reduction in crystallinity is also highlighted by broadening of the ridges observed in the ^{23}Na MQMAS NMR spectrum, Figure 3.28, and in all diffraction patterns collected.

3.3.5 ^{93}Nb MAS NMR

To date the data presented suggests that the ^{23}Na NMR parameters are sensitive to small structural changes. $NaNbO_3$ does, however, possess two additional NMR active nuclei, ^{93}Nb (I = 9/2) and ^{17}O (I = 5/2). The Nb environment in $NaNbO_3$ could potentially provide additional information regarding the different phases present in each sample. Therefore, in an attempt to establish the differences between the two phases the Nb environment of each sample was investigated using ^{93}Nb NMR. ^{93}Nb is a quadrupolar nucleus and, as observed for ^{23}Na, lineshapes commonly exhibit broadening as a result of inefficient removal of the quadrupolar interaction. Niobium-based compounds are known to exhibit large

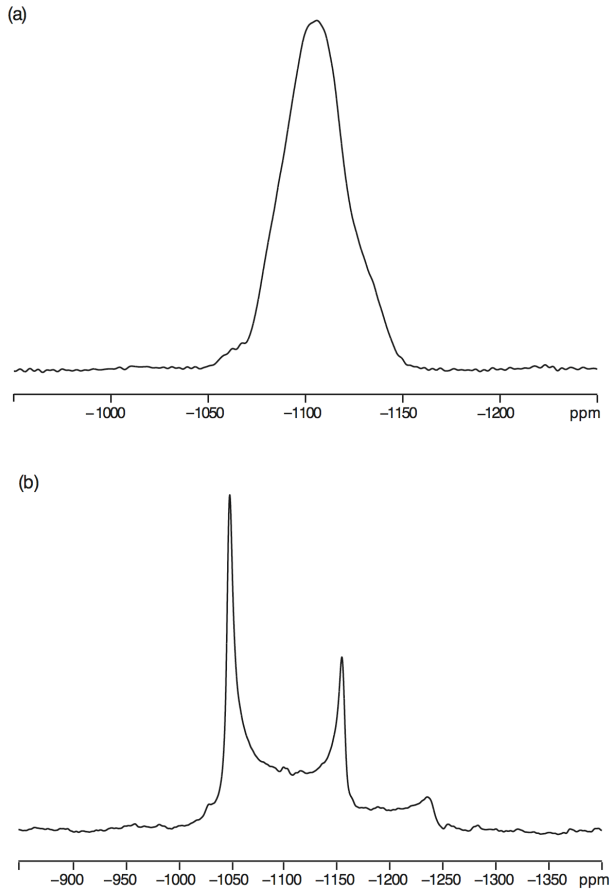

Figure 3.34: Conventional ^{93}Nb (14.1 T) MAS NMR spectra for (a) commercial $NaNbO_3$ (Aldrich) and (b) the ilmenite[225] polymorph of $NaNbO_3$. The MAS rate was 30 kHz.

quadrupolar interactions, commonly on the order of many megahertz and in order to adequately suppress this interaction high-resolution two-dimensional techniques such as MQMAS are required.

The sample purchased commercially (Sigma-Aldrich) was initially investigated and under MAS a broadened lineshape was observed, characteristic of second-order quadrupolar broadening. The MAS spectrum displayed additional broadening of the main features of the lineshape, suggesting the possible presence of disorder within the sample, as shown in Figure 3.34(a). In contrast, the ^{93}Nb MAS NMR spectrum for the ilmenite[225] polymorph of $NaNbO_3$ produces a quadrupolar lineshape characteristic of an ordered Nb environment, as shown in Figure 3.34(b). The two-dimensional ^{93}Nb MQMAS spectrum for the Aldrich sample of $NaNbO_3$ is shown in Figure 3.35(a) and confirms the presence of a single broadened resonance, in good agreement with the literature.[250,251] Full

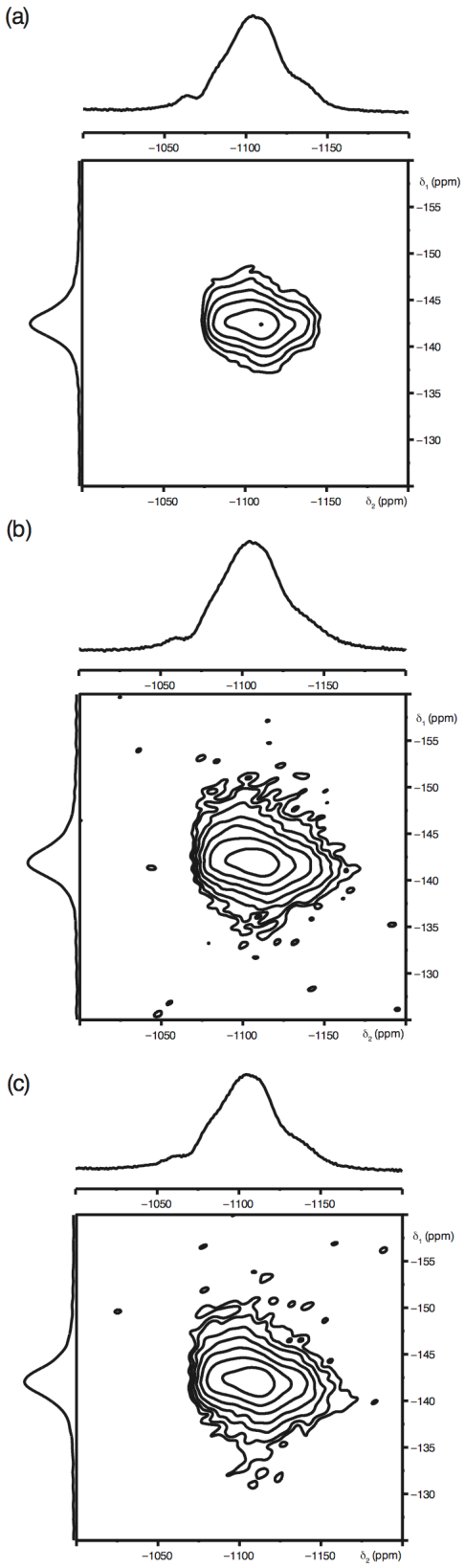

Figure 3.35: Conventional ^{93}Nb (14.1 T) MAS NMR spectrum, triple-quantum MAS NMR spectrum, and corresponding projections for (a) commercial $NaNbO_3$ (Aldrich), (b) Solid-State Sample A $NaNbO_3$ and (c) sol-gel $NaNbO_3$. The MAS rate was 30 kHz.

details of the ^{93}Nb quadrupolar parameters for this sample can be found in Table 3.11. According to diffraction, in single phase Pbcm $NaNbO_3$ the Nb 'on average' lie approximately centrosymmetrically within the octahedra. The ^{93}Nb MAS NMR spectrum however suggests the Nb^{5+} cations exhibit, to some extent, positional disorder, i.e., each Nb is marginally displaced from the centre of the octahedron. This displacement is not detected using diffraction as only the long-range order of a material is examined using diffraction and any subtle movement of the Nb is averaged over this range.

Samples from each of the synthetic methods investigated were also studied using ^{93}Nb MAS and MQMAS NMR, each of which produced similar findings to those for the Aldrich sample. Under MAS each displayed a single broad resonance, indicative of a large second-order quadrupolar broadening. In a similar manner to the Aldrich sample additional broadening of the lineshape was observed in each, again suggesting the presence of positional disorder of the Nb^{5+} cation. The ^{93}Nb MQMAS spectra recorded for the sol-gel sample of $NaNbO_3$ and Solid-State Sample A are shown in Figures 3.35(b) and (c) respectively. Interestingly, when spectra from each were overlaid it became apparent subtle changes were displayed in each depending on synthetic method used, as shown in Figure 3.36. The single resonance observed in phase pure Pbcm $NaNbO_3$ consistently covered a narrow δ_2 shift range when compared with Solid-State Sample A and the sol-gel sample of $NaNbO_3$. There are many possible reasons for this, namely crystallite size, shape, structural stress, strain and other such sample dependent effects.

Using two-dimensional ^{23}Na MAS NMR it was possible to identify the presence of two different phases of $NaNbO_3$ in Solid-State Sample A, believed to be two structurally very closely related polymorphs of $NaNbO_3$. The ^{93}Nb NMR findings presented suggest that it is not possible to distinguish between distinct phases or polymorphs of $NaNbO_3$ using ^{93}Nb MQMAS techniques. This, as a result, suggests the local environment of the Na^+ cation is more sensitive to the subtle structural changes observed in $NaNbO_3$. Close examination of the $NaNbO_3$ structure reveals the Nb is enclosed in NbO_6 units and only marginal movement of the Nb

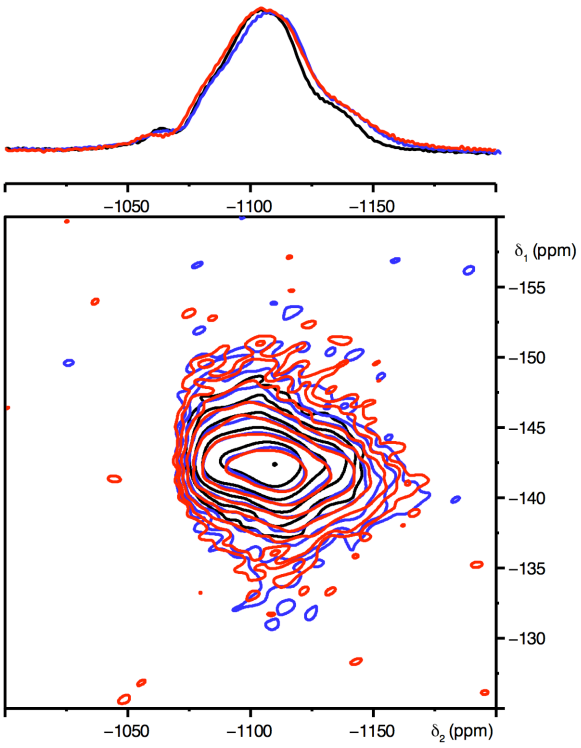

Figure 3.36: ^{93}**Nb (14.1 T) MAS NMR spectra, two-dimensional triple-quantum MAS NMR spectra and corresponding isotropic projections of phase pure commercially-purchased $NaNbO_3$ (shown in black), Solid-State Sample A $NaNbO_3$ (shown in blue) and sol-gel $NaNbO_3$ (shown in red).**

Table 3.11: ^{93}**Nb NMR parameters, δ_{iso}, P_Q, C_Q and η_Q, for commercially purchased $NaNbO_3$ (Aldrich), Solid-State Sample A $NaNbO_3$ and sol-gel $NaNbO_3$ sample, obtained from the MQMAS spectra in Figure 3.35.**

	Site	δ_{iso} (ppm)	P_Q / MHz	C_Q / MHz	η_Q
Commercial Sample (Aldrich)					
Pbcm	Nb	−1078.3(5)	21.2(2)	19.6(2)	0.7(1)
Solid-State Sample A					
Pbcm	Nb	−1077.2(5)	21.9(2)	20.3(2)	0.7(1)
Sol-gel Sample					
"$P2_1ma$"	Nb	−1076.6(5)	22.2(2)	20.8(2)	0.6(1)

is possible from the centre of the octahedron. The Na^+ cations, however, possess a considerably greater degree of positional freedom which, presumably, plays a more influential role in the phases of $NaNbO_3$ formed. In addition, the tilting and/or rotation exhibited by the NbO_6 octahedra will also affect the position of the Na^+ cation in the structure and therefore influence the phase(s) produced. The broadened ^{93}Nb MAS lineshapes obtained for each sample hinders the extraction of valuable structural information. Therefore, to aid in obtaining such information static ^{93}Nb NMR spectra were also recorded for each sample using a central-transition selective spin-echo pulse sequence.

3.3.6 Static ^{93}Nb NMR Spectra

Due to the broad nature of quadrupolar lineshapes the time-domain FID is extremely short. Much of the FID is therefore lost during the 'dead time', i.e., the time between the pulse and acquisition. Therefore, to address this problem a 180° pulse is often applied a short time, τ, after the initial pulse. This pulse refocuses evolutions due to all terms that act as offsets, for example chemical shift, dipolar and second-order quadrupolar interactions. At a time τ after the 180° pulse the signal is refocused and acquisition of the whole FID is possible, producing a spectrum free from distortions owing to dead time effects. A schematic representation of a spin-echo pulse sequence (90 - τ - 180) is shown in Figure 3.37.

Under static conditions both the quadrupolar interaction and chemical shift anisotropy are present. Each interaction contributes to the observed lineshape and, when fitted, each can provide valuable information. However, it is often difficult to deconvolute the lineshape and determine the contribution from each of the different sites present. The two interactions are however field dependent. The CSA and quadrupolar interactions are proportional to B_0 and B_0^{-1} respectively. Therefore, resolution may be improved at both higher and lower magnetic fieldstrength. To illustrate the dependency of each interaction with field several lineshapes with different CSA and quadrupolar contributions have

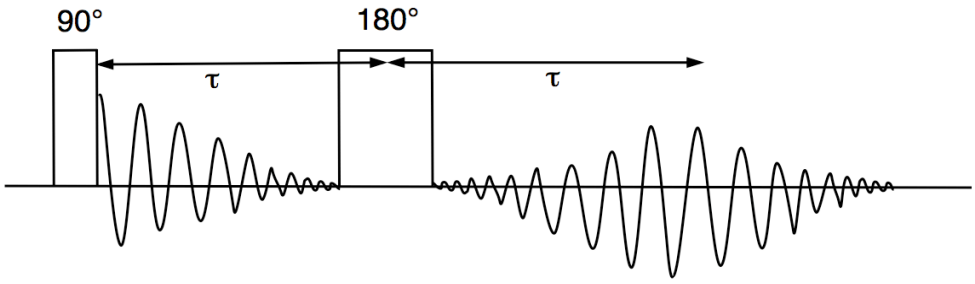

Figure 3.37: Schematic representation of a spin-echo pulse sequence (90 - τ - 180).

been simulated under static conditions at 7 T, 9.4 T, 14.1 T and 20 T using SIMPSON.[252] Figure 3.38(a) exhibits CSA lineshapes possessing $\Delta\sigma_{CS}$ = 75 ppm and η_{CS} = 0 at varying fieldstrengths. The lineshape at 20 T is considerably broadened when compared with that at 7 T. This confirms that the CSA dominates at high field and scales with B_0. In contrast, Figure 3.38(b) displays a quadrupolar lineshape with C_Q = 3 MHz and η_Q = 0. At high field the spectrum is relatively narrow and at low field a much broader resonance is observed. Such behaviour highlights the dominance of the quadrupolar interaction at low field and confirms the interaction is inversely proportional to the field. However, in reality the resonances observed in any solid-state NMR spectrum will possess both a CSA and quadrupolar contribution. Hence, the lineshape observed will depend on the contribution of each interaction to the sample, the fieldstrength used and the relative orientation of the two tensors. In such cases it can be extremely difficult to accurately determine the contribution from each interaction. To highlight how challenging this can be a spectrum possessing C_Q = 3 MHz, η_Q = 0, $\Delta\sigma_{CS}$ = 75 ppm and η_{CS} = 0 has been simulated at varying fieldstrengths and is shown in Figure 3.39. The spectra observed at 7 T and 20 T appear very different owing to the presence of both interactions. For example, the spectrum at low field possesses an obvious quadrupolar lineshape, whereas at high field the lineshape exhibits features characteristic of the CSA. The spectra shown indicate how challenging it would be to accurately determine the values of C_Q and $\Delta\sigma_{CS}$. It is for this reason that spectra are commonly recorded under static conditions at multiple fieldstrengths, as the field dependency of each interaction enables accurate values of each to be obtained. This

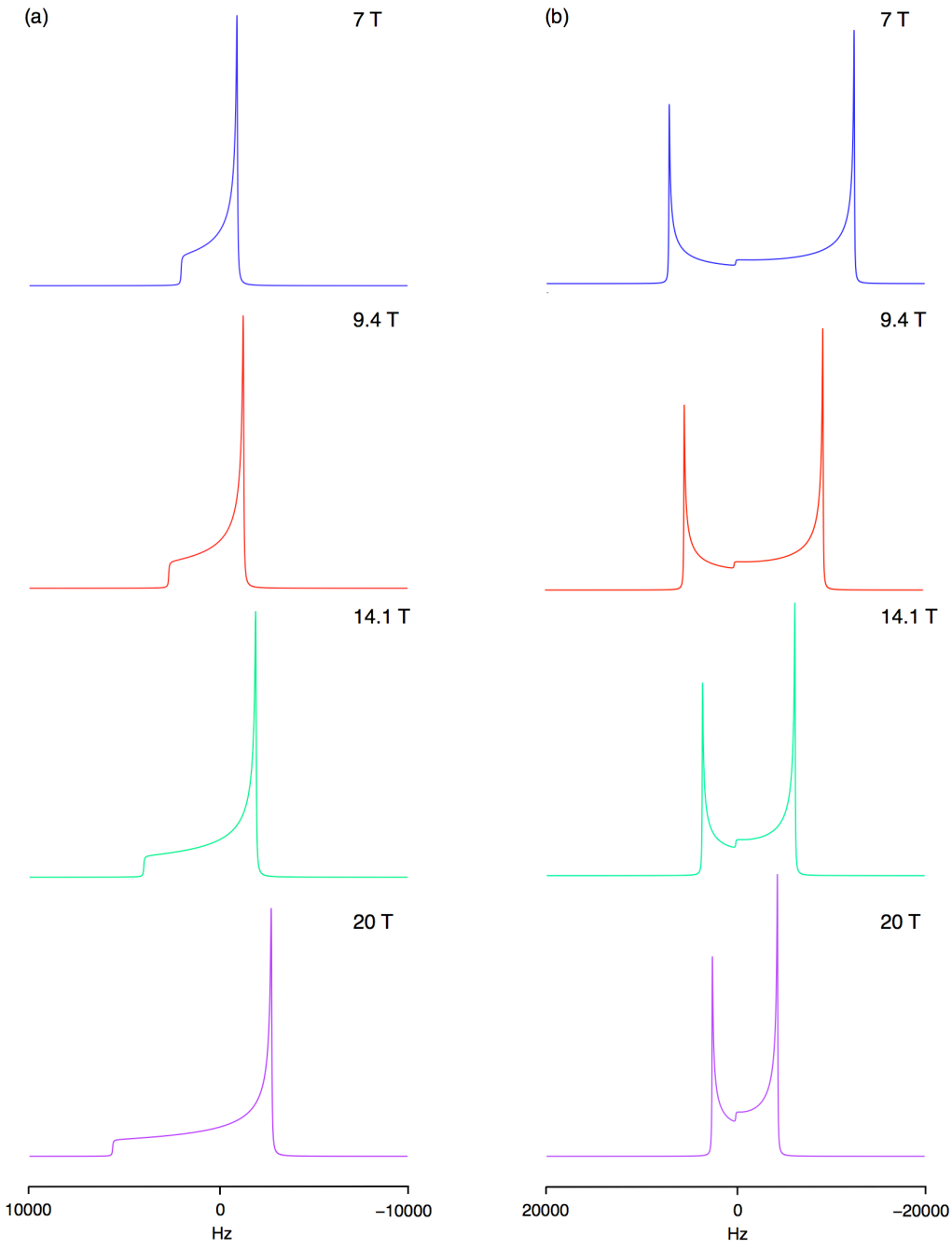

Figure 3.38: Simulated static (a) CSA and (b) second-order quadrupolar lineshapes with varying B_0 fieldstrength. Simulation parameters include (a) $\delta_{iso} = 0$, $\Delta\sigma_{CS} = 75$ ppm, $\eta_{CS} = 0$ and (b) $C_Q = 3$ MHz and $\eta_Q = 0$.

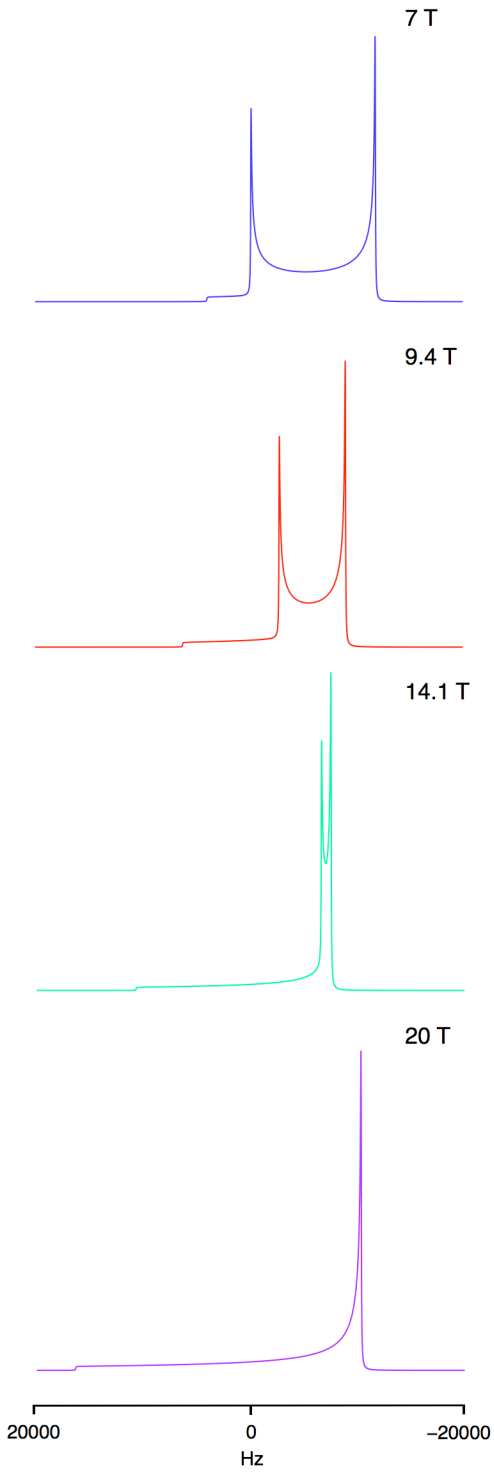

Figure 3.39: Simulated static lineshapes exhibiting contributions from both CSA and second-order quadrupolar interactions at varying B_0 fieldstrengths. Simulation parameters include $\delta_{iso} = 0$, $\Delta\sigma_{CS} = 75$ ppm, $\eta_{CS} = 0$, $C_Q = 3$ MHz and $\eta_Q = 0$.

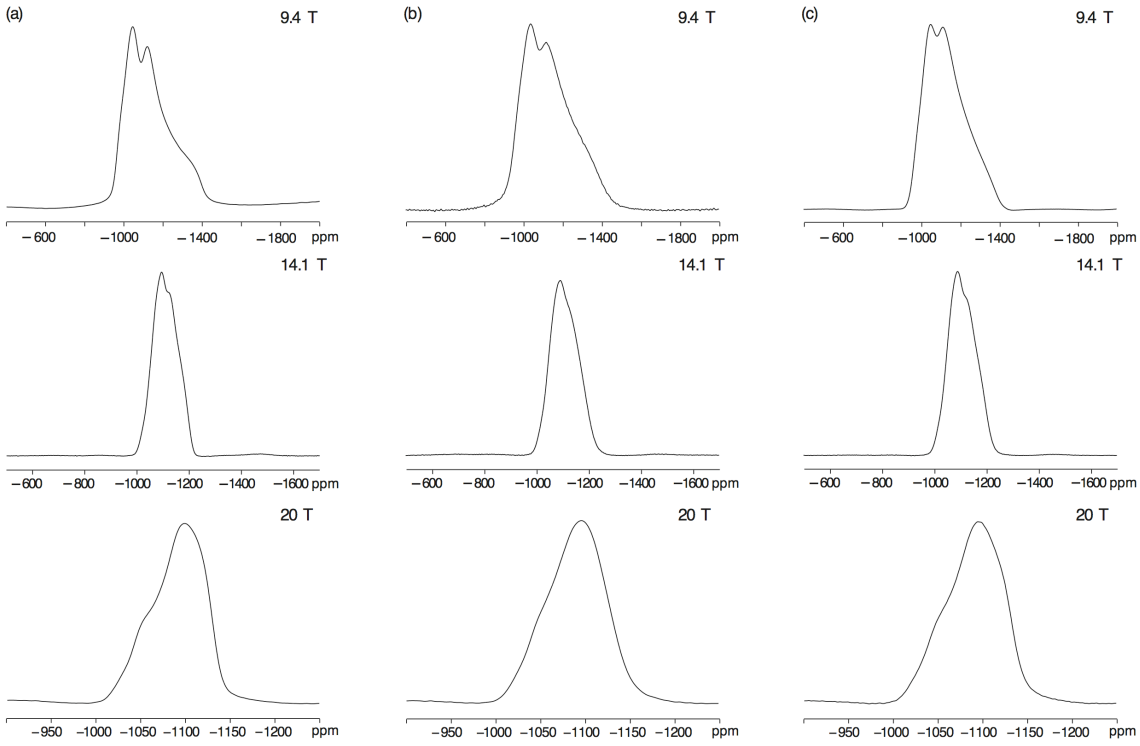

Figure 3.40: Static ^{93}Nb NMR spectra recorded for (a) commercial $NaNbO_3$ (Aldrich), (b) sol-gel $NaNbO_3$ and (c) Solid-State Sample A $NaNbO_3$ recorded at 9.4 T, 14.1 T and 20 T.

can then aid considerably in the understanding and interpretation of complex NMR spectra. Static spectra were therefore recorded for a phase pure sample of Pbcm $NaNbO_3$, Solid-State Sample A $NaNbO_3$ and the sol-gel $NaNbO_3$ sample at 9.4 T, 14.1 T and 20 T using a central-transition selective 90 - τ - 180 spin-echo pulse sequence.

All spectra recorded at 9.4 T were broad owing to the dominance of the quadrupolar interaction. However, unlike the lineshapes observed under MAS, there were distinct features present in each. This is highlighted in Figures 3.40(a), (b) and (c), where static ^{93}Nb NMR spectra for the Aldrich sample of $NaNbO_3$, the sol-gel sample of $NaNbO_3$ and Solid-State Sample A are compared. Interestingly, the commercially purchased sample of Pbcm $NaNbO_3$ and the sol-gel sample, believed to be composed of largely the $P2_1ma$ polymorph of $NaNbO_3$, produced very similar lineshapes, suggesting the Nb environments to be very similar in each. Solid-State Sample A is known to contain the Pbcm phase of

$NaNbO_3$ and a second very similar polymorph. The static ^{93}Nb NMR spectrum recorded for Solid-State Sample A (Figure 3.40(c)) appeared similar to both the phase pure sample of Pbcm $NaNbO_3$ and the sol-gel sample of $NaNbO_3$ with distinct features observed in the lineshape. Broad resonances were also observed for each sample using 14.1 T. However, it must be noted that the features previously identified in each lineshape began to diminish with increasing fieldstrength, also highlighted in Figure 3.40. This is most probably owing to the increasing dominance of the CSA. At 14.1 T each lineshape appeared very similar, with only slight differences observed. This therefore confirms that the two phases present in many of the samples of $NaNbO_3$ synthesised are extremely similar and also suggests that it may not be possible to accurately distinguish between the two using ^{93}Nb NMR. At 20 T the CSA is the more dominant interaction and, as a result, the lineshapes observed for both the phase pure Pbcm $NaNbO_3$ (Aldrich) and $P2_1ma$ $NaNbO_3$ were relatively broad, as shown in Figures 3.40(a) and (b). It must be noted that the quadrupolar features previously identified at lower fields were not present at 20 T owing to the dominance of the CSA.

The findings presented appear to suggest it is not possible to distinguish between different phases of $NaNbO_3$ using ^{93}Nb NMR. This therefore confirms earlier conclusions regarding the very similar nature of the different polymorphs present. Given the obvious similarities of the two phases it would be extremely challenging to obtain accurate ^{93}Nb NMR parameters for each phase. At present, it does not appear to be possible to determine the contribution of each phase to the observed lineshape. Recent work by Hanna *et al.*[251] suggests using DFT calculations, in conjunction with experiment, can aid in the understanding and interpretation of static ^{93}Nb NMR spectra. A detailed discussion regarding the possibility of ^{93}Nb DFT calculations within this particular investigation is given in section 3.4.

3.3.7 ^{17}O Enrichment of $NaNbO_3$

To complete a comprehensive structural investigation of $NaNbO_3$ several samples synthesised were post-synthetically enriched with $^{17}O_2$. This procedure is very costly (~$3,500 for 3 L 50% ^{17}O enriched O_2 gas). Successful enrichment is commonly achieved using either ^{17}O enriched water or gas and the method utilised is often sample dependent. To date, little work has been completed on the enrichment of dense perovskite-based materials using $^{17}O_2$. Work has, instead, concentrated on perovskites exhibiting conduction properties. This class of material has been shown to aid in the enrichment process. [253,254]

^{17}O enrichment is often highly informative and can aid considerably in the structural characterisation of complex materials. To date the experimental results presented have highlighted the structural confusion surrounding $NaNbO_3$. Both high-resolution powder diffraction and ^{23}Na MAS NMR confirm the presence of two very similar phases in many of the samples synthesised. Using ^{93}Nb NMR we have also shown that it is impossible to accurately distinguish between the two phases owing to virtually identical Nb environments in each. Both the nature and degree of tilting exhibited by the NbO_6 octahedra in each phase are key in the understanding of precisely how the two phases present differ. In addition, the position of the Na^+ cation in the $NaNbO_3$ structure is also affected by the tilt exhibited. Therefore, to understand the differences in tilting mechanism exhibited by each phase various samples of $NaNbO_3$ were enriched with ^{17}O. Using $^{17}O_2$ gas a molten salt sample of phase pure Pbcm $NaNbO_3$ (synthesised at 1000 °C for 24 hours) and Solid-State Sample D (synthesised using 450 °C for 24 hours and 850 °C for an additional 24 hours) were enriched.

The ^{17}O MAS NMR spectra recorded for both the phase pure sample of Pbcm $NaNbO_3$ and Solid-State Sample D appeared to display large CSA contributions, as shown in Figures 3.41(a) and (b). Therefore, to remove the effect of the CSA faster MAS were used and spectra were recorded using an MAS rate of 30 kHz. The ^{17}O MAS NMR spectrum recorded for phase pure Pbcm $NaNbO_3$ is shown in Figure 3.42(a). An

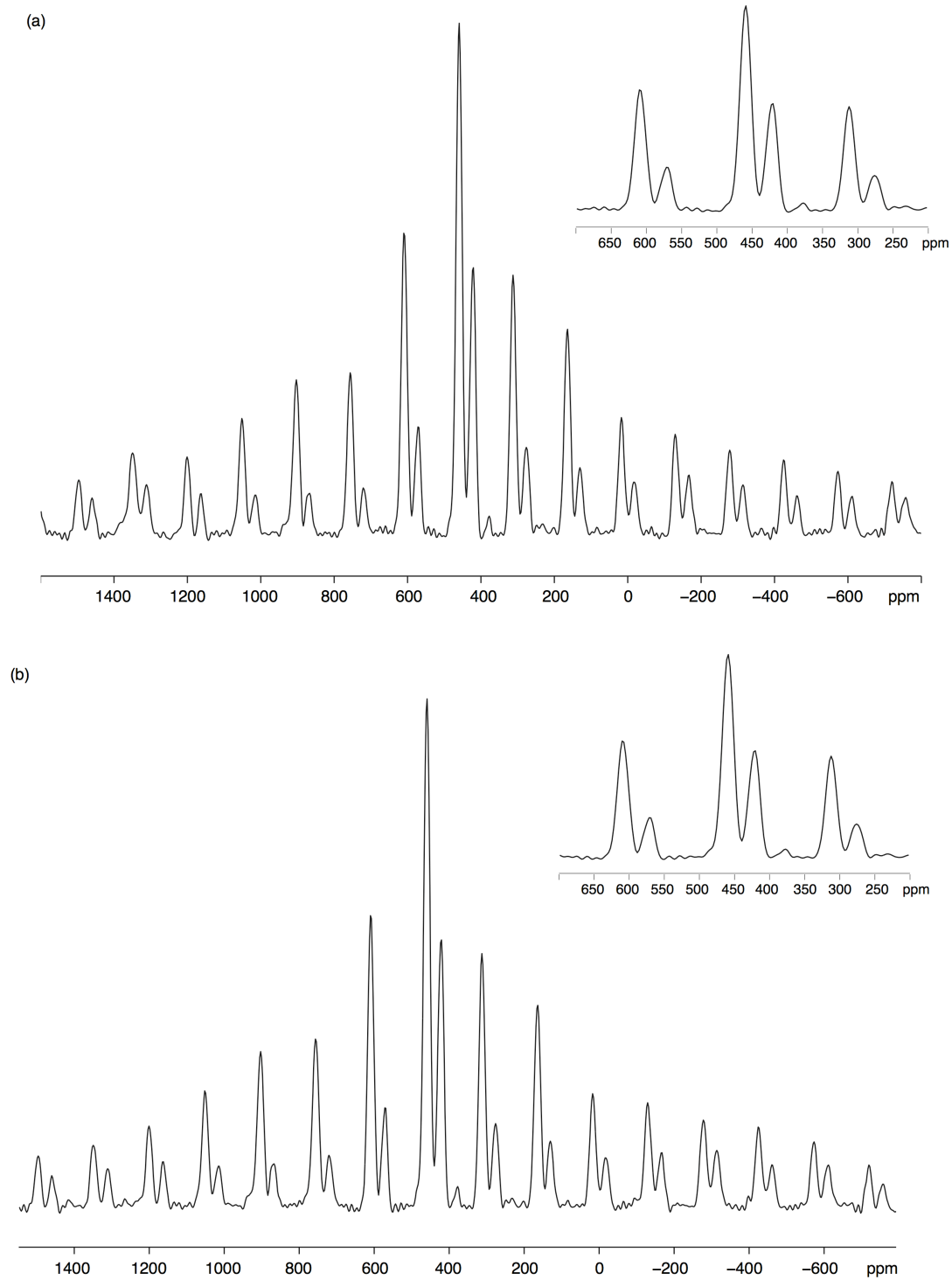

Figure 3.41: ^{17}O (14.1 T) MAS NMR spectra for (a) phase pure molten salt sample of Pbcm $NaNbO_3$ (synthesised using 1000 °C and 24 hours) and (b) Solid-State Sample D $NaNbO_3$ (synthesised using 450 °C for 24 hours and 850 °C for an additional 24 hours). Also shown in (a) and (b) are expansions of the central transition in each spectrum. The MAS rate was 14 kHz.

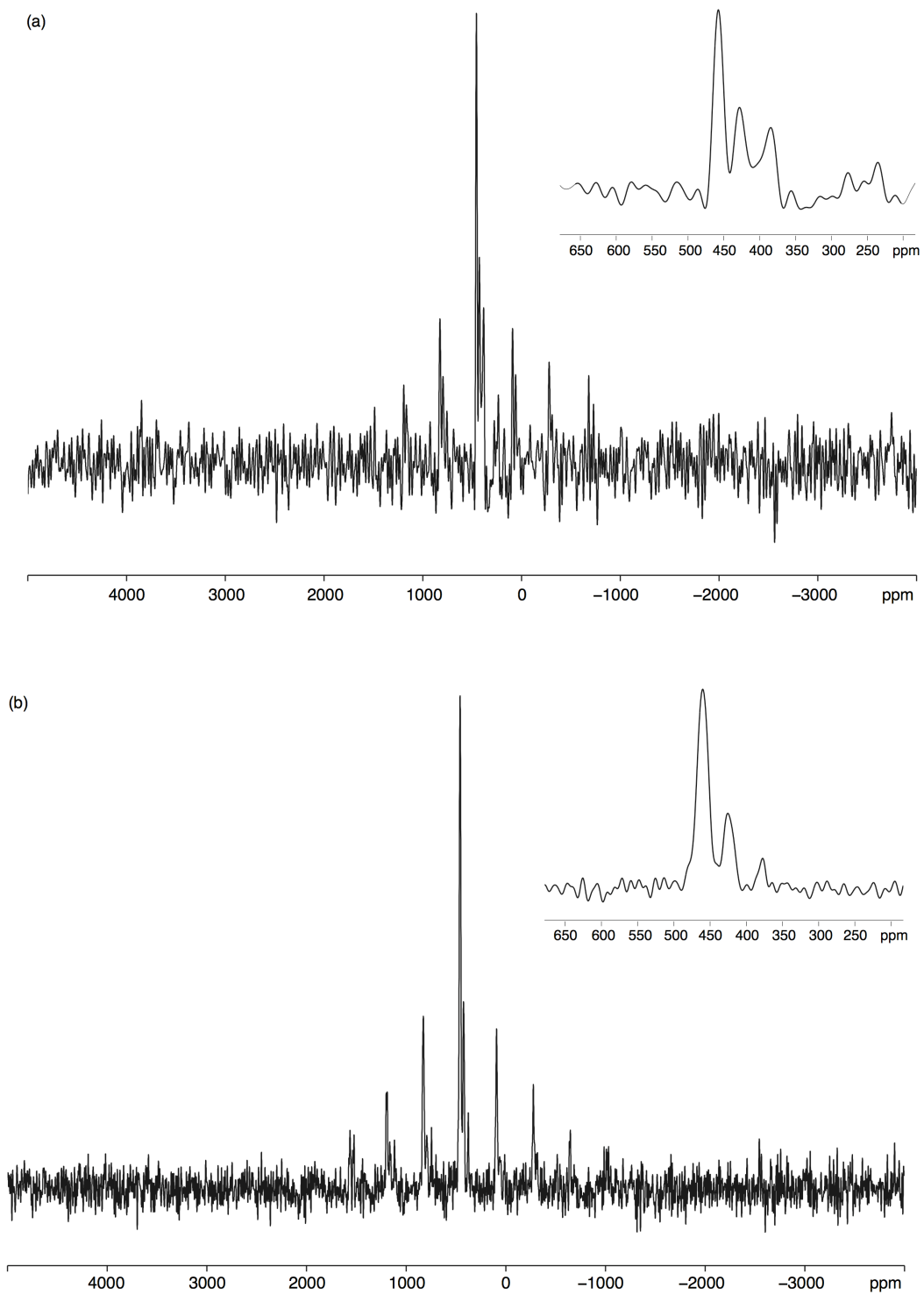

Figure 3.42: ^{17}O (14.1 T) MAS NMR spectra for (a) phase pure molten salt sample of Pbcm $NaNbO_3$ (synthesised using 1000 °C and 24 hours) and (b) Solid-State Sample D $NaNbO_3$ (synthesised using 450 °C for 24 hours and 850 °C for an additional 24 hours). Also shown in (a) and (b) are expansions of the central transition in each spectrum. The MAS rate was 30 kHz.

expansion of the central transition region of this spectrum is also shown as an inset in Figure 3.42(a). The ^{17}O MAS NMR spectrum displays three distinct oxygen resonances, with δ = 458.2 ppm, 428.5 ppm and 384.3 ppm. Published crystallographic data for Pbcm $NaNbO_3$ indicates the presence of four different oxygen environments. Hence there appeared to be a discrepancy between the NMR data presented and the known diffraction data. The resonance at δ = 384.3 ppm is believed to correspond to naturally occurring ^{17}O from ZrO_2 in the MAS rotor.[255] Therefore, only two peaks remained in the ^{17}O MAS NMR spectrum recorded for phase pure Pbcm $NaNbO_3$ and the four crystallographically distinct oxygen sites identified by diffraction must reside under the two observed resonances. The spectral overlap observed in the ^{17}O MAS NMR spectrum for phase pure Pbcm $NaNbO_3$ suggests that each of the four oxygen environments present in the structure are extremely similar and, as a result, it is very difficult to accurately assign each oxygen site. The ratio of the two resonances observed is 2:1, indicating there to be a greater number of oxygen sites under the resonance at δ = 458.2 ppm. The published crystallographic data for Pbcm $NaNbO_3$ indicates that there are eight O3 and O4 sites per unit cell and four O1 and O2 sites. This enabled us to assign the resonances at δ = 458.2 ppm and δ = 428.5 ppm to sites O3 and O4 and sites O1 and O2 respectively. However, owing to severe spectral overlap it was not possible to distinguish peaks belonging to each of the oxygen sites. The spectral overlap observed indicates just how similar each of the oxygen environments are in Pbcm $NaNbO_3$. In addition, each of the observed resonances appears to possess a relatively small quadrupolar interaction. The presence of such small quadrupolar interactions suggests that each of the oxygen environments in $NaNbO_3$ is highly symmetrical and relatively undistorted. To highlight how similar the four environments are in the Pbcm phase of $NaNbO_3$ each has been isolated and is shown in Figure 3.43(a-d). In addition, this provides a possible reason for the significant spectral overlap observed.

The ^{17}O MAS NMR spectrum recorded for Solid-State Sample D is shown in Figure 3.42 and, as for phase pure Pbcm $NaNbO_3$, it also displays three distinct resonances, δ = 460.3 ppm, 425.9 ppm and 379.0

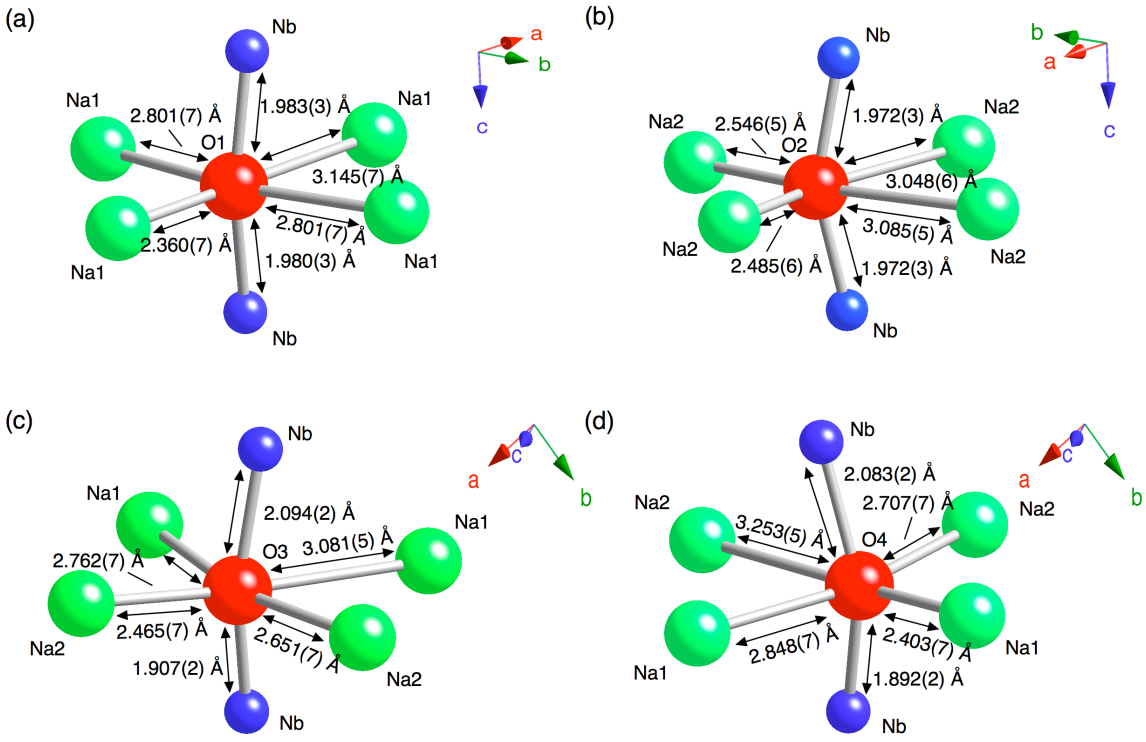

Figure 3.43: The coordination environments for sites (a) O1, (b) O2, (c) O3 and (d) O4 in Pbcm $NaNbO_3$, obtained from Rietveld refinement.

ppm. The resonance at δ = 379 ppm was assigned to ^{17}O signal from ZrO_2 in the MAS rotor. The two remaining sites are believed to correspond to the observed oxygen environments. Solid-State Sample D was synthesised using identical solid-state reaction conditions to Solid-State Sample A and using diffraction techniques the sample has been shown to contain the same two polymorphs as those present in Solid-State Sample A. Despite containing an additional polymorph the ^{17}O MAS NMR spectrum does not appear to contain any additional peaks. This therefore suggests that peaks belonging to both polymorphs reside under the two resonances observed in the MAS spectrum. Hence, this again highlights the very similar nature of the two polymorphs present in the sample and it appears to be virtually impossible to accurately distinguish peaks belonging to the respective phases using ^{17}O MAS NMR owing to their extreme similarities. The ratio of the resonances observed in the spectrum was the same as observed for phase pure Pbcm $NaNbO_3$, 2:1. Again, this indicated that a greater number of oxygen sites were under the resonance

at δ = 460.3 ppm. However, the exact nature of the second polymorph present in the sample was unknown, therefore it is difficult to identify the number of oxygen sites under this peak.

^{17}O enrichment of $NaNbO_3$ has therefore aided in confirming previous conclusions regarding the extreme similarities of the two phases of $NaNbO_3$ routinely synthesised in many samples. The ^{17}O MAS NMR spectrum recorded for phase pure Pbcm $NaNbO_3$ has shown that there is considerable spectral overlap of sites O1 and O2 and sites O3 and O4. When directly compared, as in Figure 3.43, it is clear to see why sites O1 and O2, and sites O3 and O4 are overlapped in the ^{17}O MAS NMR spectrum. Using crystallographic data obtained from diffraction it was possible to tentatively assign where each site lay in the spectrum. The ^{17}O MAS NMR spectrum recorded for Solid-State Sample D has shown that it is not possible to differentiate between the different polymorphs of $NaNbO_3$ present in many solid-state, molten salt and sol-gel samples of $NaNbO_3$ owing to considerable spectral overlap. The results presented therefore confirm that, experimentally, the easiest and most convenient way of distinguishing between the different polymorphs of $NaNbO_3$ is to use two-dimensional ^{23}Na MQMAS NMR techniques.

3.4 DFT Calculations

In conjunction with experiment, ^{23}Na, ^{93}Nb and ^{17}O density functional theory (DFT) calculations were completed to aid with spectral interpretation. Using the CASTEP[214] code it was possible to predict the NMR parameters δ_{iso}, C_Q and η_Q for any structural model and compare with the experimental values obtained. Initially, structures reported within the literature were calculated in order to establish the feasibility and accuracy of the calculations for $NaNbO_3$. Similar calculations were completed by Ashbrook *et al.*,[231] using both CASTEP and WIEN2k and our results were in good agreement.

^{23}Na NMR parameters were calculated for several $NaNbO_3$ phases suggested in the literature,[140] each of which was then compared with the experimental NMR parameters obtained. Two structures in particular,

Table 3.12: Calculated (using CASTEP) ^{23}Na NMR parameters, δ_{iso}, P_Q, C_Q and η_Q, post optimisation, for selected room temperature phases of $NaNbO_3$, obtained from both literature and Rietveld refinement.

Phase	Site	δ_{iso} (ppm)	P_Q / MHz	C_Q / MHz	η_Q
Literature					
Pbcm[217]	Na1	−4.8	2.23	2.22	0.17
	Na2	−9.0	0.96	0.87	0.79
$P2_1ma$[228]	Na1	−4.9	2.52	2.33	0.71
	Na2	−9.5	1.11	1.01	0.8
Pmma[226]	Na1	−9.4	−1.25	−1.25	0.07
	Na2	−9.4	−1.19	−1.19	0.06
Refinement					
Pbcm	Na1	−4.8	2.27	2.27	0.07
	Na2	−8.9	0.96	0.89	0.71
$P2_1ma$	Na1	−5.7	2.47	2.22	0.85
	Na2	−9.9	−0.89	−0.80	0.82
$Pnm2_1$	Na1	−8.4	1.61	1.61	0.13
	Na2	−7.3	−2.04	−1.88	0.74
Pnma	Na1	−7.7	1.60	1.28	0.86
$Pn2_1a$	Na1	−7.7	1.43	1.25	0.98

namely Pbcm and $P2_1ma$, displayed good correlation with experiment after geometry optimisation (allowing both the unit cell and atomic positions to vary), suggesting the structure was perhaps not an energy minimum initially. All ^{23}Na NMR parameters calculated for literature phases of $NaNbO_3$ (post optimisation) are listed in Table 3.12. Parameters were also calculated using structures obtained from Rietveld refinement of our NPD data, post optimisation values are also listed in Table 3.12. For completeness phases containing a single Na site, namely Pnma and $Pn2_1a$, were also calculated which aided further in eliminating them from our investigation as plausible secondary phases. All ^{23}Na parameters calculated for each phase prior to optimisation can be found in Table 3.13.

Table 3.13: Calculated (using CASTEP) ^{23}Na NMR parameters, δ_{iso}, P_Q, C_Q and η_Q, prior to optimisation, for selected room temperature phases of $NaNbO_3$, obtained from both literature and Rietveld refinement.

Phase	Site	δ_{iso} (ppm)	P_Q / MHz	C_Q / MHz	η_Q
Literature					
Pbcm[217]	Na1	−4.9	2.17	1.98	0.77
	Na2	−8.0	1.09	1.03	0.58
$P2_1ma$[228]	Na1	−3.9	2.42	2.20	0.80
	Na2	−7.5	1.22	1.13	0.72
Pmma[226]	Na1	−4.5	−2.50	−2.50	0.05
	Na2	−12.5	−0.20	−0.20	0.35
Refinement					
Pbcm	Na1	−3.7	2.22	2.22	0.02
	Na2	−6.6	1.19	1.16	0.38
$P2_1ma$	Na1	−2.8	2.50	2.39	0.54
	Na2	−7.9	0.72	0.69	0.48
$Pnm2_1$	Na1	−9.2	2.00	1.92	0.49
	Na2	−5.5	1.66	1.60	0.48
Pnma	Na1	−6.0	1.83	1.73	0.59
$Pn2_1a$	Na1	−5.7	2.13	1.88	0.92

^{23}Na DFT calculations were also completed using a fixed cell during the geometry optimisation of the structure and the calculated parameters can be found in Appendix II. Once optimised the atomic forces were closely examined and found to be considerably lower than those observed for the initial structure obtained from diffraction. This therefore indicated that the structure had been successfully optimised into a local energy minimum. Consistently the phases Pbcm and $P2_1ma$ provided the best agreement with experiment (both from the literature and Rietveld refinement), as they appeared to correlate with each of the phases identified. In particular the C_Q values obtained for ^{23}Na were in reasonable agreement, as highlighted by comparison of the solid-state

NMR (9.4 T) data in Table 3.2 and the calculated parameters for Pbcm and $P2_1ma$ (Table 3.12). Note that the sign of C_Q, although displayed for calculated values, is not determined by experiment. The asymmetry parameter, η_Q, displayed the greatest degree of discrepancy with experiment however this was a consistent finding with all structures calculated. This poor agreement has been observed previously, for example in the aluminophosphate framework AlPO-14.[195] It should be noted that C_Q depends upon one principal tensor component, V_{ZZ}, whereas η_Q depends upon all three. Similar differences were also found in the WIEN2k calculations completed by Ashbrook *at al*.[231]

Similarly, ^{93}Nb DFT calculations were completed for several of the $NaNbO_3$ phases suggested in the literature[140] and the calculated parameters were compared with the experimental results obtained. Using ^{93}Nb MAS NMR the lineshapes observed for the Pbcm and $P2_1ma$ phases of $NaNbO_3$ appeared very similar, suggesting it was not feasible to distinguish between different phases of $NaNbO_3$ using ^{93}Nb NMR. The calculated ^{93}Nb NMR parameters obtained, post optimisation of each phase of $NaNbO_3$ are shown in Table 3.14, where many of the phases calculated exhibit very similar values of C_Q and η_Q. Two of the phases, namely Pmma and Pnma, possessed considerably smaller values of C_Q (~3-4 MHz) that did not appear to correlate with any of the parameters observed experimentally, therefore suggesting that neither of these phases are present in any of the $NaNbO_3$ samples investigated. The calculated parameters obtained for the Pbcm and $P2_1ma$ phases of $NaNbO_3$ were extremely similar and both displayed the greatest degree of agreement with the observed experimental findings. This was true for structures obtained both directly from the literature and Rietveld refinement of the NPD data. The similarities observed in the calculated ^{93}Nb parameters for the Pbcm and $P2_1ma$ phases suggests that the Nb environment in each is extremely similar and it would therefore be virtually impossible to distinguish between the two using ^{93}Nb MAS NMR. These findings are again in good agreement with experiment. Recent work by Hanna *et al.*[251] suggests it is possible to distinguish between different phases of $NaNbO_3$ using ^{93}Nb DFT calculations. Their work concentrated on calculating the

Table 3.14: Calculated (using CASTEP) ^{93}Nb NMR parameters, δ_{iso}, P_Q, C_Q and η_Q, post optimisation, for selected room temperature phases of $NaNbO_3$, obtained from both literature and Rietveld refinement.

Phase	Site	δ_{iso} (ppm)	P_Q / MHz	C_Q / MHz	η_Q
Literature					
Pbcm[217]	Nb	−1057.0	29.28	25.61	0.96
$P2_1ma$[228]	Nb	−1055.1	−28.51	−25.24	0.91
Pmma[226]	Nb	−1069.5	2.76	2.45	0.90
Refinement					
Pbcm	Nb	−1057.9	31.10	27.00	0.99
$P2_1ma$	Nb	−1055.4	−29.99	−26.49	0.92
$Pnm2_1$	Nb	−1058.6	29.38	26.19	0.88
Pnma	Nb	−1060.6	−4.05	−3.80	0.64
$Pn2_1a$	Nb	−1053.8	−27.70	−26.69	0.48

Table 3.15: Calculated (using CASTEP) ^{93}Nb NMR parameters, δ_{iso}, P_Q, C_Q and η_Q, prior to optimisation, for selected room temperature phases of $NaNbO_3$, obtained from both literature and Rietveld refinement.

Phase	Site	δ_{iso} (ppm)	P_Q / MHz	C_Q / MHz	η_Q
Literature					
Pbcm[217]	Nb	−1098.8	−20.97	−20.80	0.22
$P2_1ma$[228]	Nb	−1077.4	−15.29	−15.11	0.27
Pmma[226]	Nb	−1076.0	−92.40	−88.50	0.52
Refinement					
Pbcm	Nb	−1089.0	−16.97	−14.84	0.96
$P2_1ma$	Nb	−1090.4	−20.14	−19.26	0.53
$Pnm2_1$	Nb	−1105.8	−33.84	−31.50	0.68
Pnma	Nb	−1084.5	−25.57	−25.17	0.31
$Pn2_1a$	Nb	−1072.1	25.49	23.77	0.67

NMR parameters for three of the most commonly reported phases of $NaNbO_3$; Pbcm, $P2_1ma$ and Pbma. Using powder X-ray diffraction their sample displayed good agreement with the Sakowski-Cowley[217] Pbcm model and of the three phases calculated the Pbcm phase displayed the greatest degree of agreement with their experimental ^{93}Nb (wideline) NMR spectra recorded. Within this particular investigation both the Pbcm and $P2_1ma$ structures obtained directly from the literature[140] were calculated and the NMR parameters obtained for each phase prior to optimisation were very different, as shown in Table 3.15. These appear to be in very good agreement with those reported by Hanna *et al*. Structures obtained directly from the crystal structure database or Rietveld refinement are, quite often, not in a local energy minimum and geometry optimisation is required. Within this investigation the Pbcm and $P2_1ma$ phases were geometry optimised and the calculated values obtained for each appeared to be very similar, as highlighted in Table 3.14. Therefore, the ^{93}Nb DFT calculations performed by Hanna *et al*. appear to be in very good agreement with our non-optimised values, suggesting that no structural optimisation had been performed and the structures calculated were either directly from the ICSD or refinement. We have shown that post optimisation the Pbcm and $P2_1ma$ phases produce virtually identical NMR parameters, making it difficult to distinguish between the two, as shown experimentally.

The ^{93}Nb DFT calculations completed within this investigation have aided in eliminating several phases as plausible secondary phases and appear to have confirmed initial experimental findings that it is not possible to distinguish between the different phases of $NaNbO_3$ using ^{93}Nb MAS NMR. We have also highlighted an important point regarding structural optimisation. For systems such as $NaNbO_3$ geometry optimisation is essential as often the initial structure is not in a local energy minimum. One possible reason for this is the presence of more than one polymorph in many samples. For $NaNbO_3$ better correlation with experiment was observed post geometry optimisation. All ^{93}Nb parameters calculated for each of the phases post optimisation using a fixed cell can be found in Appendix II.

^{17}O DFT calculations were also completed for the various phases of $NaNbO_3$ obtained from the literature and Rietveld refinement.[140] The ^{17}O NMR parameters obtained post optimisation of each structure are given in Table 3.16. All ^{17}O parameters calculated prior to optimisation and using a fixed unit cell are given in Appendix II. Experimentally, two oxygen resonances were observed in the ^{17}O MAS NMR spectra obtained for both phase pure Pbcm $NaNbO_3$ and Solid-State Sample D. Tentative assignments of the two peaks observed in each spectrum were initially made using published crystallographic data. However, it was hoped that the ^{17}O parameters calculated would provide additional assistance with spectral assignment. Each of the phases calculated predicted very small values of C_Q for each of the crystallographically distinct oxygen sites, as shown in Table 3.16. These values suggest that each oxygen is in a symmetrical local environment, in good agreement with the observed experimental findings. In addition, for several of the phases calculated the chemical shifts of sites O1 and O2, and O3 and O4 were very similar, suggesting the potential overlap of these sites experimentally. Consistently in each of the DFT calculations completed the Pbcm and $P2_1ma$ phases of $NaNbO_3$ displayed similar parameters. This was also true for the ^{17}O NMR parameters calculated for the two phases. The four oxygen environments in the $P2_1ma$ phase of $NaNbO_3$ have been isolated and are shown in Figure 3.44(a-d). As observed for the Pbcm phase the four sites appear very similar. In addition, when compared with Figure 3.43 it is clear to see how subtly different the two polymorphs of $NaNbO_3$ are. This therefore aids in confirming the similarities observed in the NMR parameters calculated. The calculated ^{17}O NMR parameters therefore provide a possible reason as to why it is so challenging to distinguish between the various different phases of $NaNbO_3$ experimentally using ^{17}O NMR. The combined effect of very similar chemical shifts and very small values of C_Q indicates that peaks corresponding to each site will lie almost directly on top of one another, making it impossible to distinguish between very similar phases. To confirm the number of sites under each resonance higher-resolution approaches such as DOR and MQMAS could be utilised. However, the

Table 3.16: Calculated (using CASTEP) ^{17}O NMR parameters, δ_{iso}, P_Q, C_Q and η_Q, post optimisation, for selected room temperature phases of $NaNbO_3$, obtained from both literature and Rietveld refinement.

Phase	Site	δ_{iso} (ppm)	P_Q / MHz	C_Q / MHz	η_Q
Literature					
Pbcm[217]	O1	445.1	−1.38	−1.38	0.08
	O2	458.2	−1.18	−1.12	0.55
	O3	489.4	−0.48	−0.46	0.47
	O4	495.3	0.90	0.78	0.99
$P2_1ma$[228]	O1	447.0	−1.22	−1.20	0.33
	O2	452.7	−1.28	−1.23	0.50
	O3	488.1	−0.44	−0.43	0.33
	O4	496.3	0.88	0.77	0.98
Pmma[226]	O1	493.7	−0.51	−0.48	0.60
	O2	493.9	−0.51	−0.48	0.58
	O3	490.3	−0.47	−0.47	0.23
	O4	490.3	−0.47	−0.47	0.23
Refinement					
Pbcm	O1	443.5	−1.38	−1.38	0.11
	O2	460.3	−1.14	−1.08	0.56
	O3	488.5	−0.50	−0.48	0.46
	O4	494.6	−0.89	−0.78	0.94
$P2_1ma$	O1	445.6	−1.27	−1.25	0.32
	O2	453.1	−1.33	−1.28	0.50
	O3	488.6	−0.46	−0.45	0.31
	O4	496.0	0.87	0.75	1.00
$Pnm2_1$	O1	446.7	−0.82	−0.80	0.37
	O2	457.2	−1.40	−1.36	0.43
	O3	487.1	−0.49	−0.48	0.33
	O4	493.8	−0.84	−0.75	0.85
Pnma	O1	492.4	−0.50	−0.48	0.52
	O2	490.6	−0.51	−0.49	0.54

$Pn2_1a$	O1	506.0	0.54	0.49	0.78
	O2	463.6	−0.96	−0.94	0.37
	O3	466.2	−1.18	−1.10	0.67

exact level of ^{17}O enrichment obtained for each sample of $NaNbO_3$ is unknown. It is anticipated that the level of enrichment will be relatively low, therefore an MQMAS experiement would take a considerable amount of time to obtain. In samples containing a mix of two phases it would be considerably more informative to determine which oxygen environments are connected to one another in the structure. To do this a two-dimensional NOESY-like correlation experiment is required that can detect the transfer of magnetization through dipolar couplings. This would enable us to obtain additional information regarding the composition of each sample and possible connectivity within the sample. The presence of cross peaks in the NOESY-type experiment would indicate magnetization had been transferred from one oxygen site to another, thereby indicating the nuclei are spatially in bonding proximity and able to transfer magnetization between one another.

3.5 Discussion

Overlaid two-dimensional ^{23}Na NMR spectra for Solid-State Sample A, molten salt and sol-gel samples are shown in Figure 3.45(a). Expansions of the upper and lower sets of ridges are also shown in Figures 3.45(b) and (c) respectively. All four distinct Na sites present in Solid-State Sample A correlate with those present in the sol-gel sample. In particular, the two Na sites with $\delta_1 = -7.1$ ppm and 13.5 ppm in the sol-gel sample align exactly with the second phase consistently found in all solid-state and molten salt samples, as illustrated in the overlaid isotropic projections in Figure 3.45(b). This, therefore, suggests that the major phase produced by sol-gel synthesis is consistently present in all samples, irrespective of synthesis route. The quantity of this phase produced, however, varies significantly depending upon synthesis method.

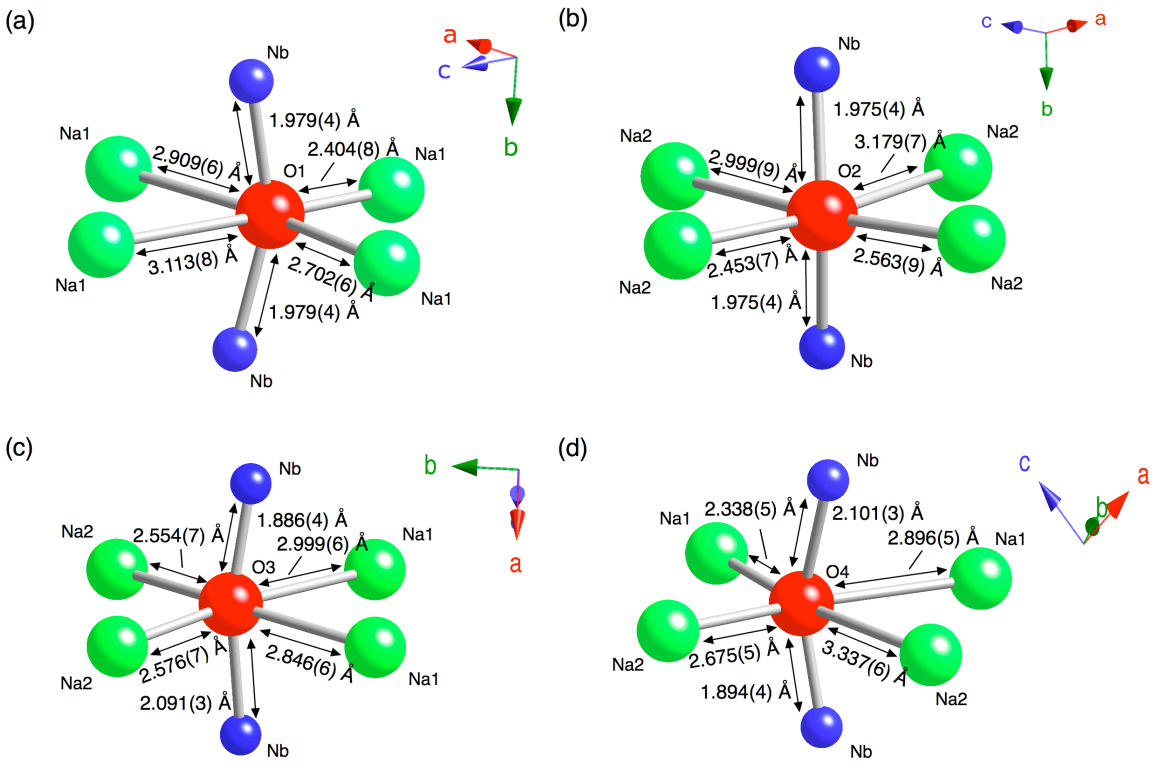

Figure 3.44: The coordination environments for sites (a) O1, (b) O2, (c) O3 and (d) O4 for the P2$_1$ma polymorph of NaNbO$_3$ obtained from Rietveld refinement.

In a similar manner to solid-state reactions sol-gel methods can be difficult to control. It is often challenging to accurately monitor reaction temperatures during the reflux stage of the sol-gel synthesis owing to differences between internal and external vessel temperatures. In addition, for $NaNbO_3$ it is difficult to synthesise samples free from impurities using sol-gel reactions. For example, within our reactions the compound $Na_2Nb_4O_{11}$ was consistently formed.[256] There are, therefore, several contributing factors within the sol-gel reaction that aid in determining the exact polymorphs of $NaNbO_3$ produced.

Conclusions drawn from detailed comparison of the ^{23}Na NMR data aided considerably in the interpretation and structural refinement of both the s-PXRD and NPD data for Solid-State Sample A. Prior to such conclusions a variety of potential orthorhombic structures similar to Pbcm were tested using multiphase refinements, with little success. The potential identification of the P2$_1$ma polymorph of $NaNbO_3$ by NMR in both the solid-state and molten salt samples provided a plausible structure

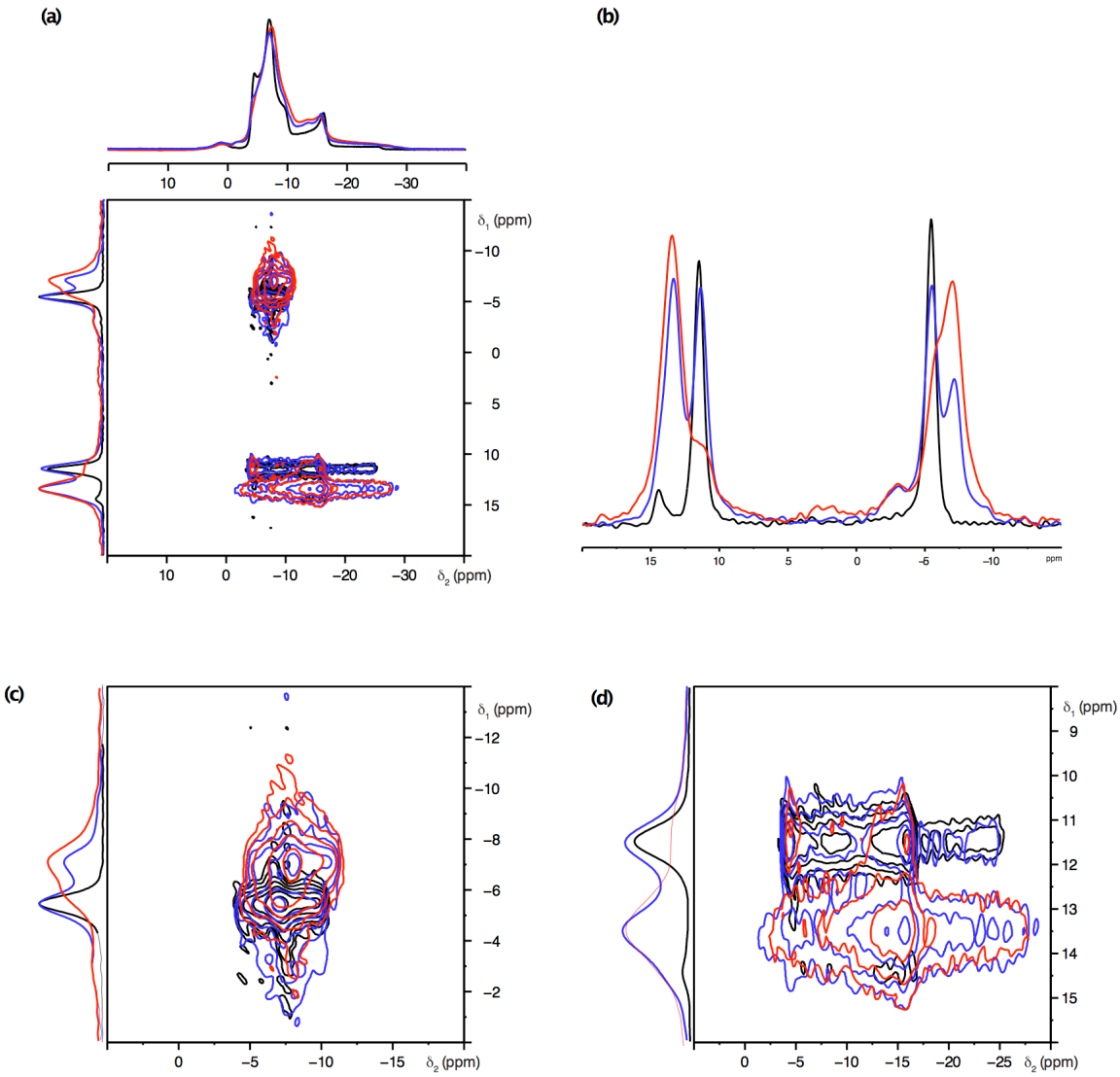

Figure 3.45: **^{23}Na (9.4 T) NMR of phase pure Pbcm $NaNbO_3$ (shown in black and synthesised using molten salt methods, 1000°C for 24 hours), Solid-State Sample A $NaNbO_3$ (shown in blue) and sol-gel $NaNbO_3$ (shown in red). (a) Conventional MAS and triple-quantum MAS NMR spectra, (b) corresponding isotropic projections and (c, d) expansions showing the upper (δ_{iso} = −5.08 ppm and δ_{iso} = −4.24 ppm) and lower (δ_{iso} = −0.51 ppm and δ_{iso} = 1.44 ppm) ridges.**

to test by Rietveld refinement. Therefore, multiphase refinements were completed on both the s-PXRD and NPD data obtained for Solid-State Sample A using the previously obtained Pbcm and $P2_1ma$ models, and are shown in Figures 3.46 and 3.47, respectively. These models were fixed, with only lattice parameters and phase fractions being refined. Upon the

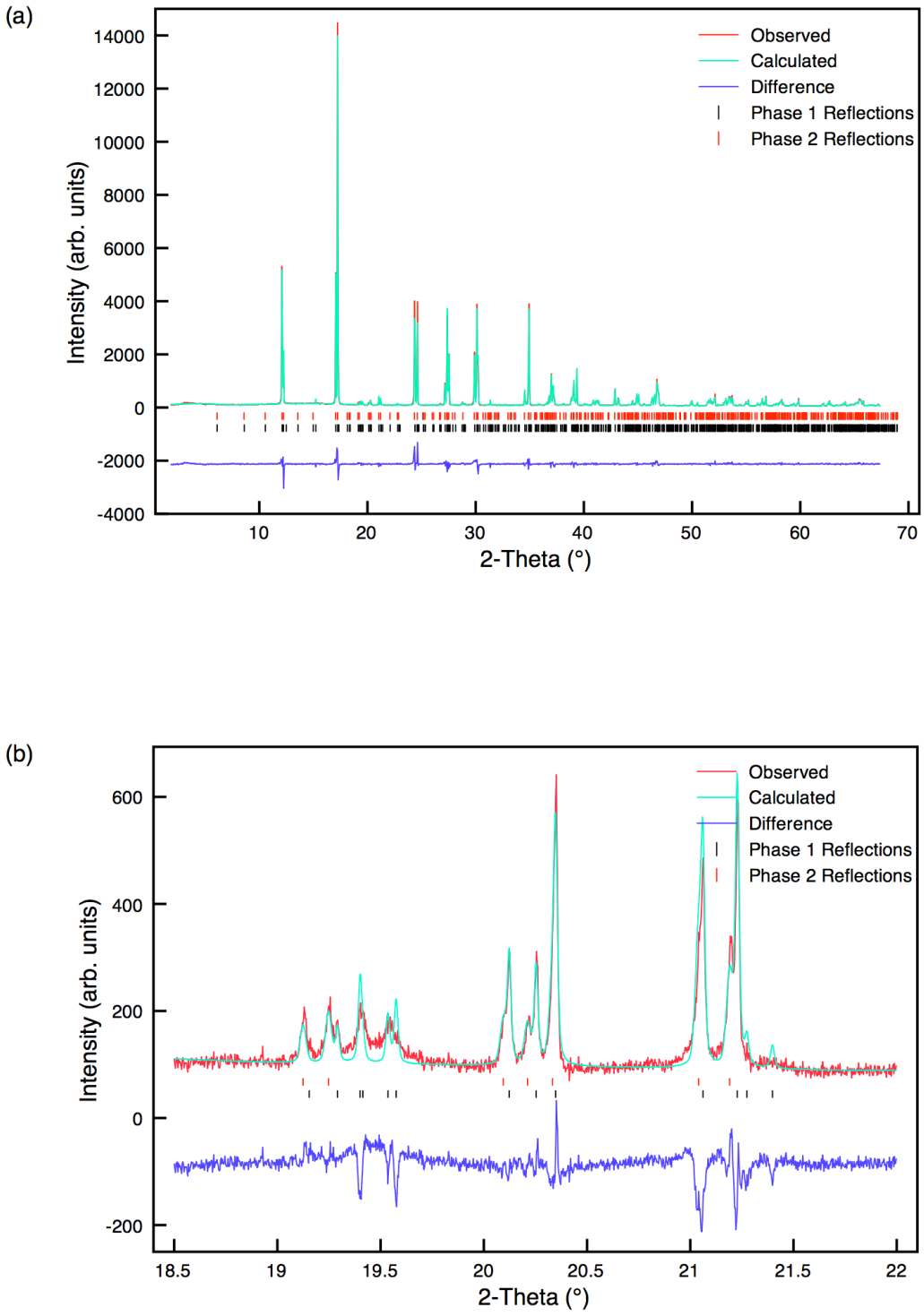

Figure 3.46: Multiphase Rietveld profiles for Solid-State Sample A $NaNbO_3$ using structural models Pbcm and $P2_1ma$ for s-PXRD data. Expansions of the corresponding superstructure peaks are shown in (b) 2θ = 18.5° - 22°.

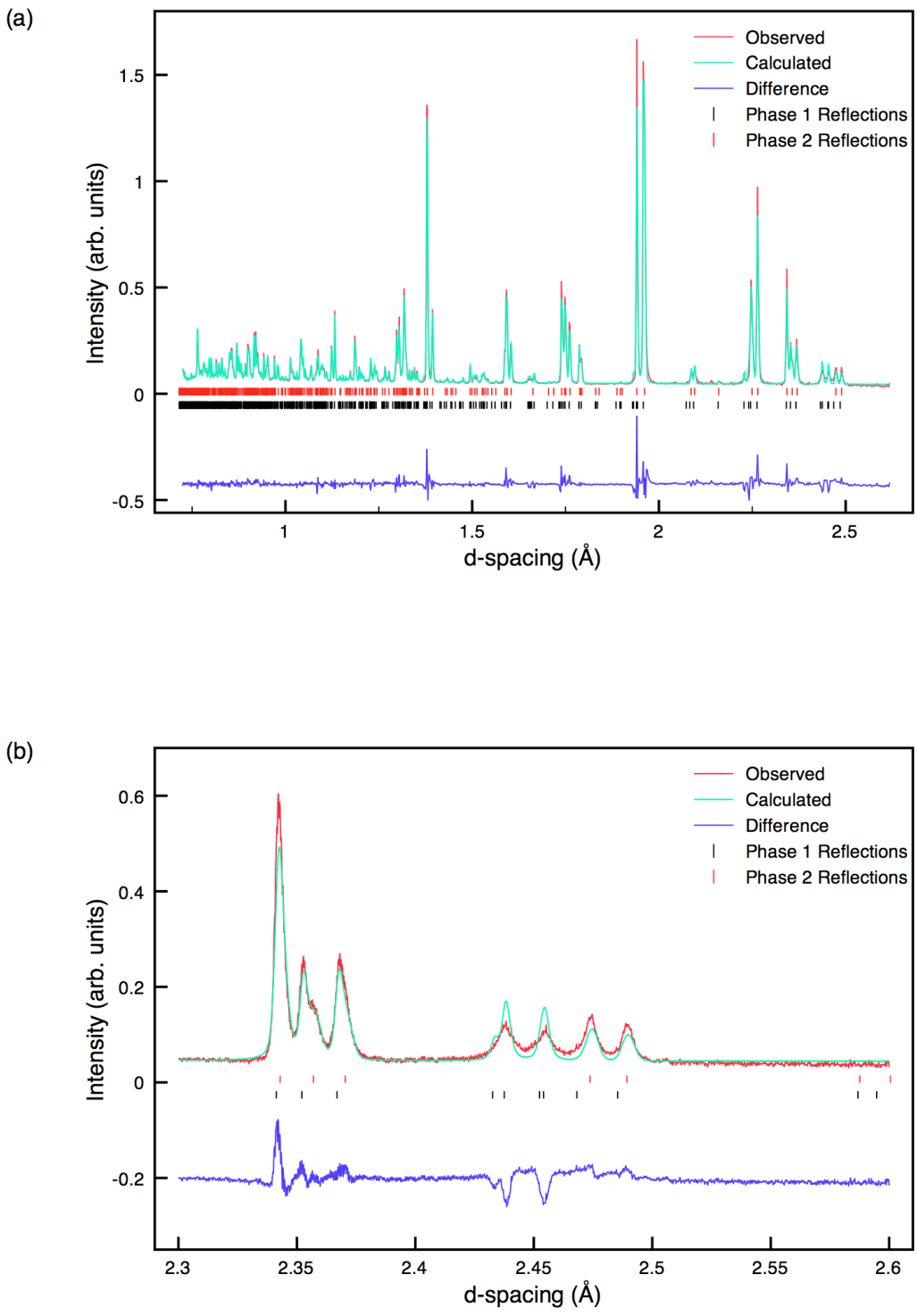

Figure 3.47: Multiphase Rietveld profiles for Solid-State Sample A $NaNbO_3$ using structural models Pbcm and $P2_1ma$ for NPD data. Expansions of the corresponding superstructure peaks are shown in (b) d = 2.3 Å – 2.6 Å.

Table 3.17: Monoclinic structural model used for refinement of NPD data for sol-gel $NaNbO_3$. Space group Pm, a = 5.57073(5) Å, b = 7.76625(6) Å, c = 5.51338(5) Å, β = 90.084(1)° and V = 238.529(3) Å^3. χ^2 = 4.2, wR_p = 6.2% and R_p = 5.7%.

Atom	Site	x	y	z	U(iso) × 100 / Å^2
Nb1(a)	2c	0.26246	0.25	0.2466	0.20
Nb1(b)	2c	0.76246	−0.25	−0.2466	0.20
Na1(a)	1a	0.2596	0	0.7481	0.50
Na1(b)	1a	0.7596	0	−0.7481	0.50
Na2(a)	1b	0.2915	0.5	0.7327	2.24
Na2(b)	1b	0.7915	−0.5	−0.7327	2.24
O1(a)	1a	0.2409	0	0.3124	0.53
O1(b)	1a	0.7409	0	−0.3124	0.53
O2(a)	1b	0.2257	0.5	0.1928	0.37
O2(b)	1b	0.7257	−0.5	−0.1928	0.37
O3(a)	2c	0.0131	0.279	0.5272	1.84
O3(b)	2c	0.5131	−0.279	−0.5272	1.84
O4(a)	2c	−0.049	0.2197	0.036	0.61
O4(b)	2c	0.451	−0.2197	−0.036	0.61

addition of the $P2_1ma$ phase the quality of refinement improved considerably for both datasets. Subtle peak splittings previously treated as single phase in the s-PXRD data were now accounted for and indexed which, in turn, assisted in the accurate modelling of both the profile parameters and peak intensities. An expansion of the superstructure region 18.5° – 22° is shown in Figure 3.46(b). Considerably better wR_p (14.2%) and χ^2 (7.6) values were obtained, with refined phase fractions of 60(2)% and 40(2)% for the Pbcm and $P2_1ma$ phases, respectively. A similar two-phase refinement of the NPD data considerably improved the quality of the fit at low d-spacing, in comparison to the single phase refinements previously discussed, leading to better wR_p (8.4%) and χ^2 (22.7) values, with refined phase fractions of 57(2)% and 43(2)% for the Pbcm and $P2_1ma$ phases, respectively. The phase fractions obtained from refinement are in

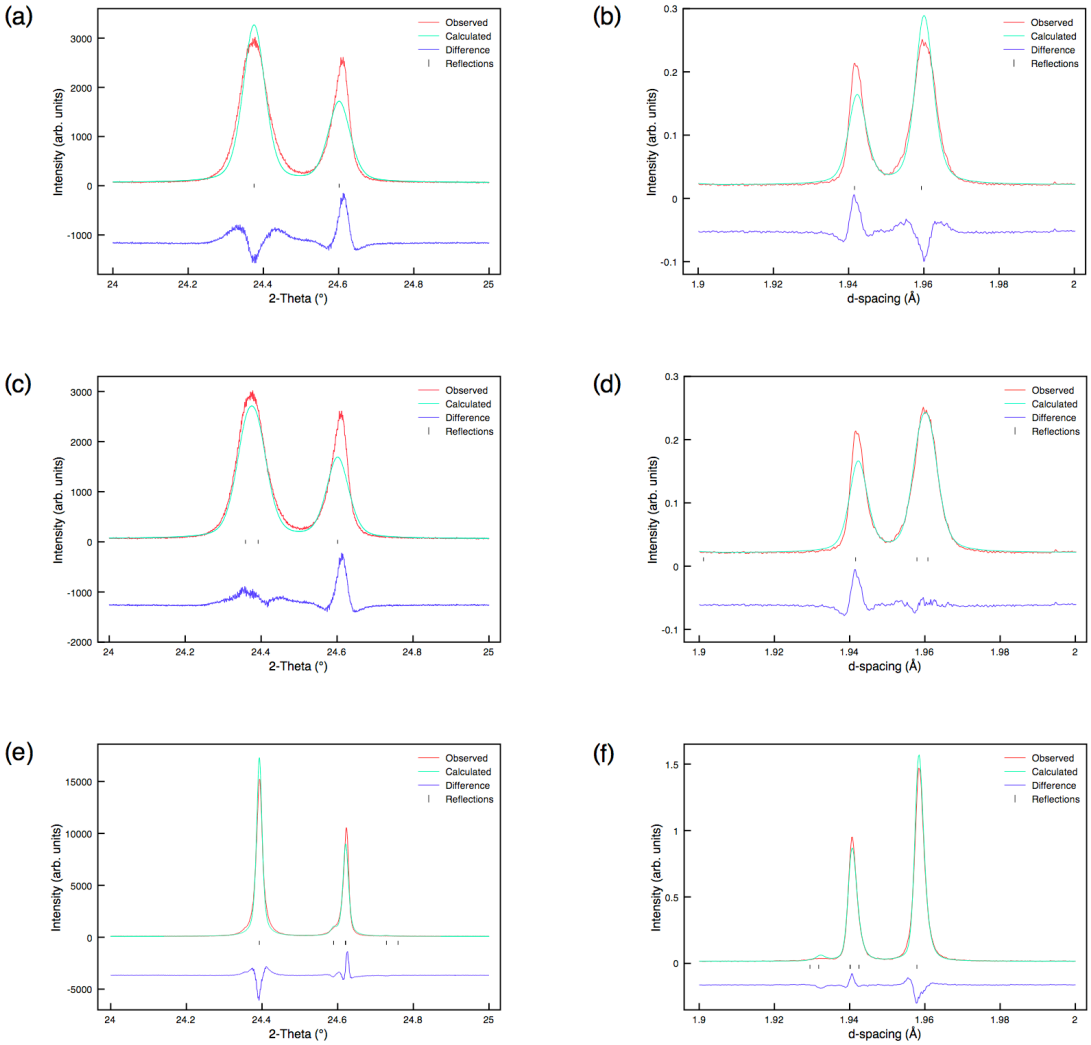

Figure 3.48: Rietveld profiles of (a, c) s-PXRD data (2θ = 24° - 25°) and (b, d) NPD data (d = 1.9 Å – 2 Å) for sol-gel $NaNbO_3$ using structural models (a, b) $P2_1ma$ and (c, d) Pm. Plots (e) and (f) show the corresponding regions for the refinement of commercial $NaNbO_3$ (Aldrich) using the Pbcm model, suggesting that this phase is truly orthorhombic, and does not have the monoclinic distortion previously suggested.

agreement with those from NMR (estimated to be ~60% and ~40%) from the MQMAS spectrum in Figure 3.6. In particular, the additional peaks previously highlighted in the single phase refinement at 2.47 Å and 2.49 Å were now adequately modelled, as shown in Figure 3.47(b).

On closer inspection of the refinements involving the suggested $P2_1ma$ phase it is apparent that subtle peak broadenings exist which are compatible with a symmetry-lowering to monoclinic ($\beta \neq 90°$). Such a

Table 3.18: Refined lattice parameters from multiphase refinement of Solid-State Sample A $NaNbO_3$ for the s-PXRD (χ^2 = 7.6, wR_p = 14.2% and R_p = 10.0%) and NPD data (χ^2 = 22.7, wR_p = 8.4% and R_p = 7.7%), using structural models Pbcm and $P2_1ma$.

		a (Å)	b (Å)	c (Å)	V (Å^3)
s-PXRD	Pbcm	5.50490(1)	5.56973(1)	15.51753(4)	475.780(2)
	"$P2_1ma$"	5.57667(3)	7.76157(4)	5.51774(3)	238.828(2)
NPD	Pbcm	5.50641(7)	5.57068(7)	15.52364(2)	476.179(14)
	"$P2_1ma$"	5.57734(8)	7.76281(16)	5.51986(9)	238.987(8)

symmetry-lowering has previously been observed in the KNN solid-solution at low potassium content.[257] Rietveld refinements were completed for both the s-PXRD and NPD data for the sol-gel $NaNbO_3$ sample using the monoclinic model Pm. Expansions of the regions 2θ = 24° - 25° in the s-PXRD data and d = 1.9 Å – 2 Å in the NPD data are shown in Figure 3.48. Also shown for comparison are the Rietveld refinements completed using the "$P2_1ma$" model. The quality of refinement for these particular regions in both datasets is improved using the structural model for a monoclinic cell, suggesting there may be a monoclinic distortion present in the sol-gel $NaNbO_3$ sample. The model used is given in Table 3.17. This model was derived from the $P2_1ma$ model by reducing the symmetry to monoclinic, Pm, but imposing strict "$P2_1ma$" constraints on all the structural parameters, and keeping these fixed. The only additionally refined structural parameter was therefore the β angle, which refines to 90.084(1)°. We stress that this refinement merely demonstrates that this phase may well be monoclinic and does not refine the true space group or the nature or driving force of the monoclinic distortion. The allowed non-centrosymmetric monoclinic subgroups of Pnma are Pm and $P2_1$, both of which are possibilities (also both are polar). Pm gives 4 Na sites whereas $P2_1$ gives only 2, which is perhaps more compatible with the NMR data. The precise nature of this monoclinic phase (and that of the analogous K-doped $NaNbO_3$[222]) has yet to be determined. The plots shown in Figures 3.48(e) and (f) show the

corresponding regions for the refinement of commercial $NaNbO_3$ (Aldrich) using the Pbcm model, suggesting that this phase is truly orthorhombic, and does not have the monoclinic distortion previously suggested.[222] The previous suggestion by Darlington and Knight[222] is now believed to be owing to the presence of the $P2_1ma$ phase which lay undetected in their sample. Therefore, we shall now refer to this phase as "$P2_1ma$", on the understanding that it appears very subtly monoclinic. Refined lattice parameters for multiphase refinement of Solid-State Sample A using both s-PXRD and NPD data are given in Table 3.18.

The space group $P2_1ma$ was a tentative suggestion by Ashbrook *et al.*,[231] for the nature of the unknown phase within their sample, made purely by a preliminary examination of the additional peaks in their l-PXRD pattern. Although high-resolution data is usually required to draw such conclusions, in this particular case their tentative suggestion appears to have been borne out. Their explanation as to why the "$P2_1ma$" polymorph is formed perhaps relates to their use of a low temperature synthetic route (hydrothermal methods using 200 °C) as opposed to conventional solid-state methods using temperatures in excess of 1000 °C. We have shown, using a variety of techniques, that this "$P2_1ma$" polymorph is consistently formed, regardless of specific experimental conditions. Their suggestion as to why is also consistent with our findings; temperature plays a prominent role in the phases of $NaNbO_3$ synthesised and their relative quantities.

The two polymorphic phases of $NaNbO_3$, Pbcm and "$P2_1ma$", routinely coexist in many samples irrespective of synthesis route and are seen, from both diffraction and solid-state NMR, to be structurally similar. However, crystallographic examination shows that the two adopt subtly different octahedral tilt systems. This cooperates with local Na^+ cation displacements to produce both a centrosymmetric and a polar phase of similar stability. In the Pbcm phase the Na displacements are out-of-phase with one another leading to the longer periodicity of the c-axis ($4a_p$ or about 15.5 Å), as shown in Figure 3.1(a). The mechanism of octahedral tilting within the Pbcm structure is effectively a 'twinning' operation when compared with $P2_1ma$ (or, more strictly the parent Pnma). Hence

the standard $a^-a^-b^+$ system in $P2_1ma$ becomes [$a^-a^-b^+$ / $a^-a^-b^-$ / $a^-a^-b^+$] *via* an inversion about the central block (equivalent to an additional out-of-phase tilt between blocks 2 and 3 along the c-axis). It is perhaps therefore little surprise that two polymorphs based on these very similar tilt systems can compete, depending on synthetic variables, and also no surprise that their diffraction patterns are so similar. In fact, a further manifestation of the similarity of the two structures can be seen in the NPD data (Figure 3.47), where the additional superlattice peaks due to the $4a_p$ supercell in the Pbcm phase (i.e., the l-odd reflections) are noticeably broader than the subcell peaks, suggesting that long-range registry of the additional out-of-phase tilt is weak.

The subtle effects that drive the appearance of both polymorphs are currently unknown, but the influence of the 'ferroelectrically–active' Nb^{5+} cation on the B-site must be considered. In the case of $NaNbO_3$ diffraction indicates that in the Pbcm phase Nb 'on average' lies approximately centrosymmetrically within the octahedra. However, the local environment probe, solid-state NMR, suggests it may be disordered in some manner. The ^{93}Nb MQMAS NMR spectrum recorded for the commercially purchased sample (Figure 3.35) displays a degree of additional broadening, suggesting Nb may exhibit some positional disorder. In the "$P2_1ma$" polymorph the Nb^{5+} cation lies significantly off-centre (towards an edge of the octahedron). All bond lengths obtained from the Rietveld refinement are given in Appendix II.

Ultimately, the use of several complementary techniques within this investigation has led to the accurate structural identification of two polymorphic room temperature phases of $NaNbO_3$ present in a variety of samples synthesised by various synthetic routes. Previous studies have often concentrated solely on one particular characterisation technique. However, as presented within this particular study, it can be extremely challenging, and dangerous, to rely on such an approach. Using diffraction alone for example, it can be difficult to identify and correctly model weak superlattice peaks and peak splittings or broadenings. In such cases it is vital to utilise a number of different techniques in order to ensure an accurate and robust structural characterisation.

3.6 Prediction of Perovskites using *Ab Initio* Random Structure Searching (AIRSS)

3.6.1 Introduction to AIRSS

The theoretical prediction of crystal structures is highly desirable. However, in reality it is extremely complex and challenging. In recent years computational codes capable of finding new phases and structures have been successfully developed. One such method is *ab initio* random structure searching (AIRSS), a first-principles DFT approach.[244-247] This particular method of structure searching works by relaxing many random structures to their enthalpy minimum at fixed pressures. It is important to note that this method does not rely on any previous theoretical or experimental results. To date, AIRSS has successfully predicted high-pressure phases of materials such as silane,[244] aluminium hydride[246] and ammonia.[247] This particular method of structure searching has also been used for pure elements such as hydrogen,[245] nitrogen,[258] lithium[259] and iron.[260] More recently AIRSS has been successfully used to investigate defect complexes in silica[261,262] and, at present, there is considerable interest in determining whether AIRSS may be extended to other structurally complex materials, for example perovskites. AIRSS is a DFT approach, and an important limitation of this method is the number of atoms per unit cell. As a result, it is often challenging to implement structure searching methods on systems with a large number of atoms per unit cell. In many cases, however, this can be overcome by the application of sensible constraints to a system, such as cell volume, bond distances, number of symmetry operations or coordination number.

As stated previously, perovskites are currently one of the most widely studied areas of solid-state chemistry, with numerous applications to a variety of materials and devices. Hence, a technique capable of predicting complex perovskite structures would be extremely useful to many solid-state chemists. Within this particular investigation structure searching techniques have been used in conjunction with experimental methods and initial DFT calculations. Structure prediction has been

attempted for $NaNbO_3$ to determine whether any alternative phases of $NaNbO_3$ exist which differ from those found experimentally.

3.6.2 AIRSS Computational Details

The following procedure was used for the prediction of perovskite structures using AIRSS. Perovskites are composed of ABO_3 units, commonly referred to as formula units (f.u.). A specific number of f.u., usually 2, 4, 6 or 8, are randomly placed into a unit cell where the starting structure is a simple cubic perovskite. The lattice parameters are then redefined to produce a new structure corresponding to the number of $NaNbO_3$ units placed into the cell. Structures are then generated by randomising the positions of the atoms to within 0.5 Å about their initial position. Each of these configurations is then relaxed to a minimum in enthalpy. This search is then continued until the lowest enthalpy structures are consistently found. In this particular investigation it was possible to search for different phases of $NaNbO_3$ with up to 40 atoms per unit cell. This was possible owing to the application of carefully selected constraints.

3.6.3 Structure Searching $NaNbO_3$

Structure searching for $NaNbO_3$ was completed using 2, 4, 6 and 8 formula units (f.u.) as the initial configurations. During each search the known low temperature phase of $NaNbO_3$, R3c, was consistently found as the lowest energy structure. The R3c phase was therefore identified as the most thermodynamically stable polymorph of $NaNbO_3$. All DFT calculations were completed at 0 K and therefore it is of little surprise a low temperature phase was identified as the most stable. During each search many other phases were also found, the results of which will be discussed in the following section.

Initial searches for $NaNbO_3$ were completed using 2 $NaNbO_3$ formula units. This search produced 219 structures, the most stable of which was the orthorhombic $Pmc2_1$ phase (alternative setting $P2_1ma$),

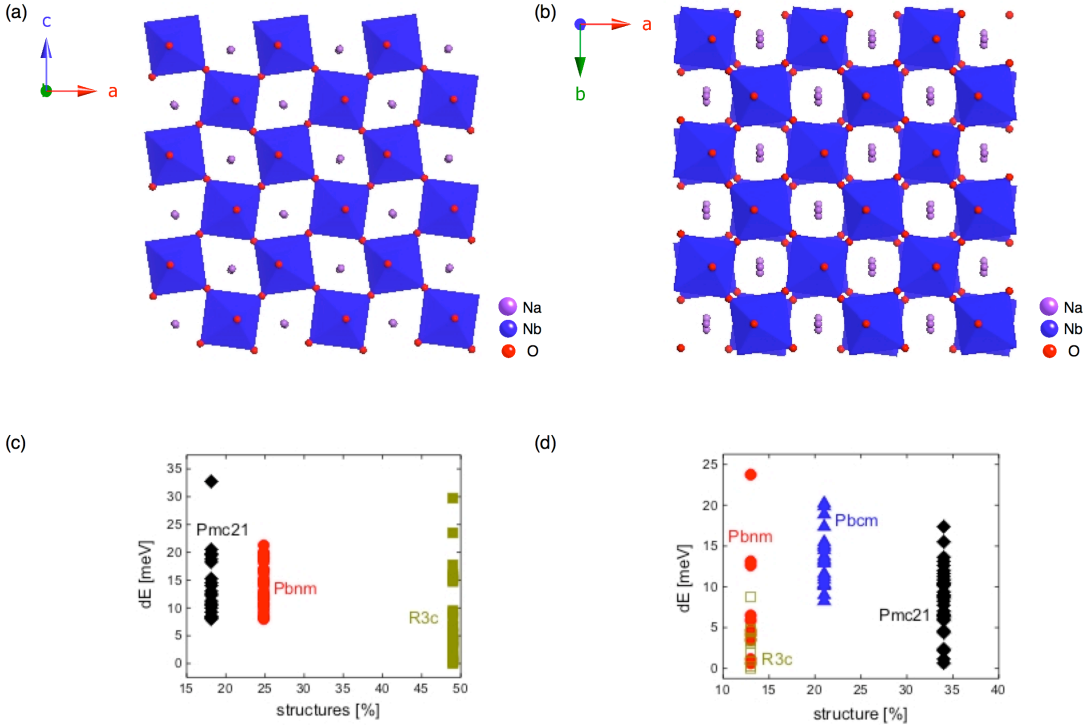

Figure 3.49: The (a) $Pmc2_1$ and (b) Pbcm structure of $NaNbO_3$ found using AIRSS. (c, d) Plots showing the relative energies of the phases found during the 4 f.u. and 8 f.u. searches, respectively.

shown in Figure 3.49(a). Searches completed using 4 f.u. produced 149 structures. The low temperature R3c phase of $NaNbO_3$ was again identified as the most stable, with 49% of all structures found being this phase. After the R3c phase, the most frequently found structures with the lowest energies were the Pbnm (24.8%) and $Pmc2_1$ (18.1%) phases. All of the phases discovered during the 4 f.u. search and their relative percentages are shown in Figure 3.49(c). Redefining the lattice parameters in the 4 f.u. search in an alternative manner produced a 2 × 2 × 1 4 f.u. perovskite. This search produced 141 structures and, as previously observed in the 2 f.u. searches, the $Pmc2_1$ phase was found to be the most stable. Of the lowest energy structures obtained 69.5% were this phase, as shown in Figure 3.49(c). Interestingly, a different structure type belonging to space group Amm2 was also found in this search. As previously stated, the $KNbO_3$ structure is widely accepted as an orthorhombic structure in space group Amm2. The identification of this particular phase of $NaNbO_3$

suggests it is possible for $NaNbO_3$ to adopt a structure-type similar to $KNbO_3$. However, despite being discovered in 29.8% of cases the high energy of this phase indicates that, experimentally, it is unlikely to be observed as there are phases with considerably lower energies that can be more feasibly observed.

Using 6 f.u. 102 structures were found and, as in the 4 f.u. search, consistently the lowest energy structure was the $Pmc2_1$ phase (68.6%). Searches completed using 8 f.u. produced 100 structures, 13% of which were the lowest energy R3c phase. In this search 13% of the structures found were a Pbnm phase, however, these were at relatively high energies. Therefore, in the 8 f.u. search the most energetically stable structures of $NaNbO_3$ were the $Pmc2_1$ (34%) and Pbcm (shown in Figure 3.49(b)) (21%) phases respectively. A plot of the relative percentages of each phase found for all 8 f.u. searches is shown in Figure 3.49(d). When symmetry checks were completed for each of the structures found using 8 f.u. the most stable $Pmc2_1$ phases were discovered to transform into 4 f.u. $Pmc2_1$ structures, whilst the higher energy $Pmc2_1$ phases yielded 8 formula units per unit cell. It must be noted that when the $Pmc2_1$ and Pbcm phases of $NaNbO_3$ found using AIRSS were compared with those found experimentally there were subtle differences in the position of the Na. It is possible that slight differences in the Na positions within each phase could be responsible for the phases observed experimentally. Very subtle changes of this type to the position of the Na is not likely to be observed using diffraction techniques as diffraction will only observe the average position of the Na.

Shown in Figure 3.50 is an energy plot displaying the phases of $NaNbO_3$ found using structure searching methods and their relative energies. Consistently the most thermodynamically stable phases of $NaNbO_3$ identified were the low temperature R3c phase, followed by both the $Pmc2_1$ and Pbcm phases. However, Figure 3.50(a) highlights an important point regarding the energy difference observed between the very similar $Pmc2_1$ and Pbcm phases. The difference observed between the two is extremely small. This therefore suggests that, experimentally, it would be very difficult to distinguish between the two phases owing to

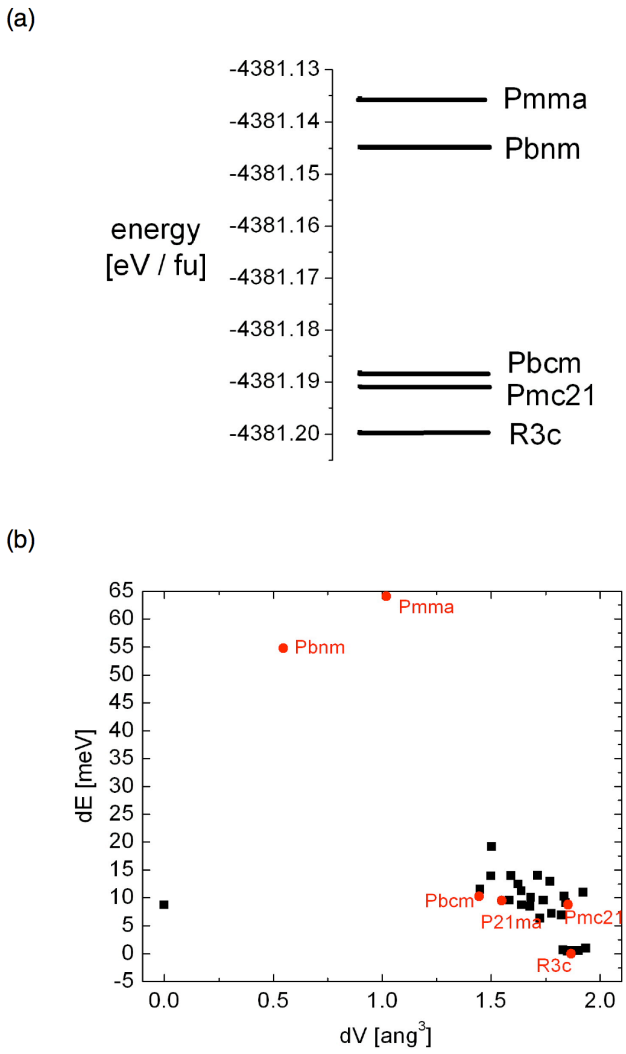

Figure 3.50: (a) Plot showing the relative energies of all phases of $NaNbO_3$ found during the structure search using AIRSS. (b) Plot displaying the experimental (red) and predicted (black) phases of $NaNbO_3$ and their relative energies as a function of cell volume.

their very similar energies. This, to some extent, confirms many of the experimental findings presented within this work. Experimentally, samples of $NaNbO_3$ are composed of two structurally very similar phases, Pbcm and $P2_1ma$, the quantities of which have been shown to vary depending on the precise reaction conditions used. It is therefore extremely challenging to routinely synthesise samples of $NaNbO_3$ with identical ratios of the two phases. The results obtained using structure prediction methods highlight a possible reason for such behaviour. The energies of the two phases have been shown to be extremely similar,

suggesting factors such as annealing temperature and/or time may affect the phases that form experimentally. For example, marginally higher or lower reaction temperatures could potentially cause one phase to preferentially form over the other. In addition, the particle size, stress and strain exhibited by the structure may also play a vital role in determining the phases observed experimentally. Also shown in Figure 3.50(b) is a plot displaying each of the phases found experimentally, denoted in red, and the optimised structures obtained using AIRSS, denoted in black. Using this plot it is clear to see that the phases found using structure searching correlate with the major phases of $NaNbO_3$ obtained experimentally within this investigation.

The major phases of $NaNbO_3$ predicted using AIRSS were the Pbcm and $P2_1ma$ phases, and this is in good agreement with those observed experimentally. The low temperature R3c phase of $NaNbO_3$ was also consistently found using AIRSS owing to the calculations being completed at 0 K. It must be noted that several of the additional phases of $NaNbO_3$ found using AIRSS, namely Pbnm and Pmma, exhibit no real agreement with those observed experimentally. For example, the Pbnm phase possesses only a single Na site and therefore bears no correlation with the high-resolution ^{23}Na MQMAS data obtained. The Pmma phase was relatively high in energy when compared with all other phases of $NaNbO_3$ found. Therefore, experimentally, it is highly unlikely this high energy phase would form under ambient temperature and pressure conditions.

The identification of the Pbcm and $Pmc2_1$ polymorphs of $NaNbO_3$ by structure searching is both an interesting and surprising result. Starting from a random arrangement of $NaNbO_3$ units in a unit cell it was possible to match experimental findings. $NaNbO_3$ is an extremely complex perovskite and for many years there has been considerable dispute regarding the phases of $NaNbO_3$ formed. Therefore, the identification of the same two phases consistently observed experimentally using computational methods is extremely encouraging. This, in turn, suggests that structure searching using AIRSS could be successfully applied to many other perovskite-based compounds. It is therefore hoped that these methods will be extended to other complex

solid-state systems in the future and that structure predicting techniques could aid many solid-state chemists.

3.7 A Third Polymorph?

The ^{23}Na MQMAS spectra presented in this chapter have shown almost all samples of $NaNbO_3$ to comprise of two very similar phases, now known to be the Pbcm and $P2_1ma$ polymorphs. However, consistently in each two-dimensional ^{23}Na MAS NMR spectrum recorded, including that of the commercially purchased sample of $NaNbO_3$, an additional resonance was observed that did not appear to correlate with either the Pbcm or $P2_1ma$ phases of $NaNbO_3$. Initially signal corresponding to this extra site was attributed to 'noise' in the MQMAS spectrum. However, upon closer inspection and calculation of the isotropic projections onto the δ_1 axis it became apparent that this signal produced a corresponding peak in the isotropic spectrum. This, therefore, suggested the presence of a third phase. The peak was consistently present in spectra recorded at both 9.4 T and 14.1 T and, as with the Pbcm and $P2_1ma$ polymorphs of $NaNbO_3$, the quantity of this phase present in each spectrum appeared to vary depending on the precise reaction conditions used. In addition, there did not appear to be any direct correlation between the synthesis method used and the quantity of this phase produced. Consistently, only very small percentages of this phase were present in each sample, i.e., ~1-2%. Therefore, it was very difficult to detect its presence by MAS NMR. The ^{23}Na MQMAS (14.1 T) NMR spectrum shown in Figure 3.51 contains the greatest quantities of this third phase and it is clear to see how small the quantity of this phase is. In addition, the position of this resonance, δ_1 = 5.47 ppm, is very close to the overlapped Na1 sites of the Pbcm and $P2_1ma$ polymorphs in spectra recorded at 14.1 T. To highlight how the quantity of this phase varies from sample to sample and depends on the synthesis method, several isotropic projections obtained from MQMAS spectra are shown in Figure 3.52.

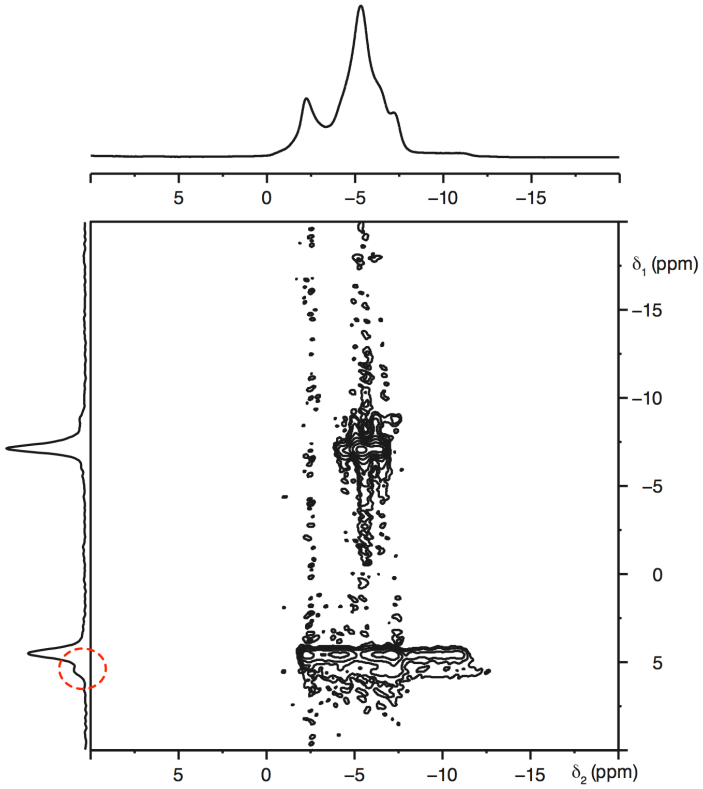

Figure 3.51: Conventional ^{23}Na (14.1 T) MAS NMR spectrum, triple-quantum MAS NMR spectrum, and corresponding projection for a molten salt sample of $NaNbO_3$ synthesised using 1000 °C for 12 hours. The region highlighted indicates the possible presence of a third polymorph of $NaNbO_3$. The MAS rate was 14 kHz.

At present, it is only possible to identify the presence of this phase using ^{23}Na MQMAS techniques. The high-resolution diffraction patterns obtained for each of the samples investigated do not appear to possess any additional peaks. Given the exceptionally small quantities of this phase present in each sample it is likely that peaks belonging to this phase lie in the background of any diffraction pattern. This will therefore make it very difficult to accurately identify and structurally characterise this phase. If this phase is a different polymorph of $NaNbO_3$ it is highly likely that the most intense peaks in the diffraction pattern will reside under those belonging to the Pbcm and/or $P2_1ma$ polymorphs already present in the sample. This would, in turn, make it impractical to identify peaks belonging to this phase and structurally characterise the phase. We are confident that this resonance is not related to either the Pbcm or $P2_1ma$

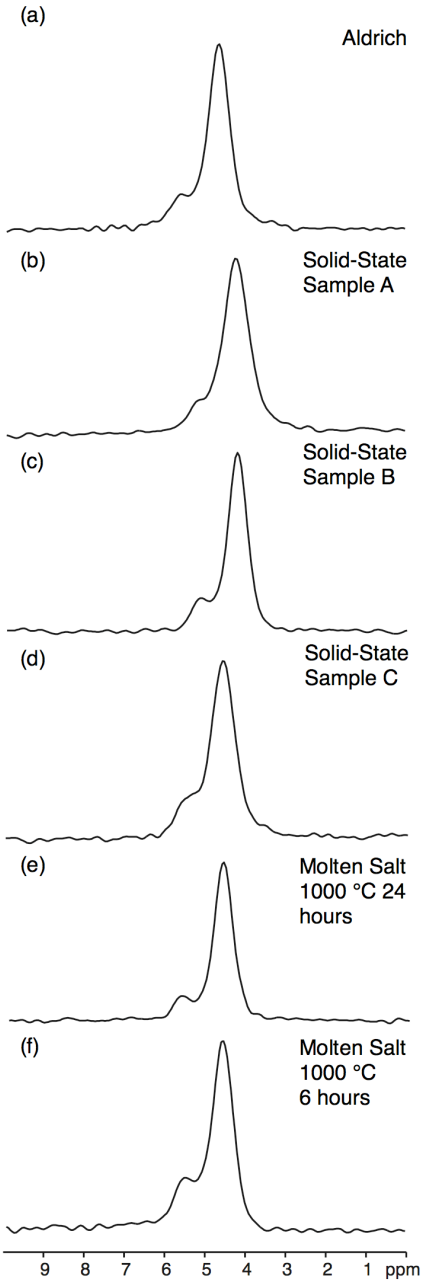

Figure 3.52: Isotropic projections obtained from triple-quantum ^{23}Na (14.1 T) MAS NMR spectra of (a) Solid-State Sample A, (b) Solid-State Sample B, (c) Solid-State Sample C and (d, e) molten salt samples of $NaNbO_3$ synthesised at 1000 °C for 24 hours and 6 hours, respectively.

polymorphs of $NaNbO_3$. Therefore, we believe that this phase is either a different polymorph of $NaNbO_3$ or an unrelated Na-bearing phase. At present there is no evidence to suggest that the quantity of this phase correlates with the ratio of the Pbcm/$P2_1ma$ phases present in each sample, i.e., it does not increase or decrease with the changing ratios of the

Pbcm and $P2_1ma$ phases. It must be noted that there may be other additional sites relating to this unknown phase present in the MQMAS spectrum. However, given the relative quantities of this phase it is likely that signal corresponding to these sites is heavily masked by noise and/or the other Na sites belonging to the Pbcm and $P2_1ma$ polymorphs. The only feasible way of characterising this phase is to synthesise a sample with much greater quantities, as peaks corresponding to this phase would then appear in the diffraction pattern. However, at present the precise reaction conditions required to synthesise a sample containing greater quantities of this particular phase are unknown. Therefore, in order to establish the necessary conditions a systematic study of synthetic method is needed. A considerable amount of work is therefore required before any accurate conclusions may be drawn regarding the exact nature of this third phase.

3.8 Conclusions

In summary, we have confirmed it is possible to synthesise a polar phase (probably monoclinic, but of symmetry very close to orthorhombic, space group $P2_1ma$) of $NaNbO_3$ using sol-gel techniques. We have also shown, by means of a systematic study, that synthetic method affects the polymorphic forms of $NaNbO_3$ produced in any one reaction. It is possible to isolate a pure sample of the Pbcm polymorph, and high-resolution powder diffraction studies confirm that this is indeed a correct space group assignment for this phase: previous confusion regarding the possibility of a symmetry-lowering to monoclinic might be explained by the occurrence of a significant "$P2_1ma$" phase impurity in the sample studied by Darlington and Knight.[222] Routinely the phases Pbcm and "$P2_1ma$" coexist as the two major room temperature polymorphs of $NaNbO_3$. The thermodynamic stabilities of the two phases are believed to be extremely similar, therefore slight variations in the reaction conditions force one to preferentially form over the other. Consistently, the Pbcm polymorph forms more readily, suggesting it to be the more thermodynamically stable of the two. The identification of the Pbcm and

$P2_1ma$ phases is also consistent with initial DFT calculations and preliminary structure searching results. Using AIRSS the R3c, $Pmc2_1$ and Pbcm phases were routinely found to be the most thermodynamically stable phases of $NaNbO_3$. Very little difference in energy was identified between the $Pmc2_1$ and Pbcm phases, highlighting once again how similar the two phases are. The possible occurrence of a third polymorph of $NaNbO_3$ was also suggested using ^{23}Na MQMAS NMR techniques. The quantities of this phase were extremely low (~1-2%) which made it impossible to successfully identify and/or characterise the phase. Further work is therefore needed to determine whether this corresponds to a different polymorphic form of $NaNbO_3$. It is therefore important to emphasise that it is essential to be aware of this subtle polymorphism in $NaNbO_3$, its occurrence as a function of preparative method, and how to identify it from both diffraction and NMR data; much of the earlier work regarding $NaNbO_3$ and its phase diagram should be treated with some degree of caution in light of our findings. Furthermore, these findings have implications for the present and future study of the KNN solid-solution and its piezoelectric behaviour.

Chapter 4

Synthesis and Characterisation of $NaNbO_3$-based Solid-Solutions

4.1 Introduction

Sodium niobate, $NaNbO_3$, is an extremely complex perovskite that has been studied extensively for many years.[222,223,263-266] The comprehensive structural study completed in the previous chapter employed a variety of complementary techniques to characterise room temperature $NaNbO_3$ and samples were found to routinely comprise of two structurally very similar orthorhombic phases; the centrosymmetric Pbcm and polar $P2_1ma$ polymorphs. The quantities of the two phases present are now known to vary considerably depending on the precise synthesis method used.

Lead zirconium titanate, $Pb(Zr_xTi_{1-x})O_3$ (PZT), is currently the most widely used piezoelectric material, with numerous applications to a variety of materials and devices. There is, however, considerable motivation to establish lead-free alternatives capable of achieving responses equal to or superior to PZT. Several recent high profile publications within the literature suggest $NaNbO_3$-based ceramics are capable of achieving such responses.[25,26] In particular the solid-solution $K_xNa_{1-x}NbO_3$ (KNN) has been shown to produce exceptional piezoelectric responses at compositions close to $x = 0.5$.[25,26] This has, in turn, accelerated the alkaline niobates to the forefront of the search for suitable lead-free piezoelectric ceramics. The room temperature phase diagram of KNN, initially published by Athee and Glazer,[267] suggests the presence of three phase boundaries; $x = 0.17$, $x = 0.3$ and $x = 0.5$. Whilst there is confusion regarding the Na-rich region of the phase diagram the crystal structure of the other end-member $KNbO_3$ is widely known as being orthorhombic, in space group Amm2.[220] To date, several structural studies have been completed for many compositions in the KNN series.[268,269] This particular series is widely known to exhibit the highest dielectric and piezoelectric responses at $x = 0.5$, near to the suggested morphotropic phase boundary

(MPB) at x = 0.45.[270,272] Hence, many investigations have concentrated in this region.[273-276] It must be noted that, at present, despite considerable research in this field no effective alternative to PZT has yet been found. The KNN series is therefore still the focus of many important structural investigations throughout the world.

The $NaNbO_3$ literature is extensive and largely dominated by KNN, and in particular x = 0.5. Detailed investigations are currently being undertaken for polycrystalline, nanocrystalline and submicron powders to determine whether enhanced piezoelectric responses are also observed in samples with varying particle size distributions. To date, however, relatively little work has been completed on the other predicted phase boundaries in the KNN phase diagram, namely x = 0.17 and x = 0.3. It is possible such areas may also exhibit MPBs and, in turn, may be potential 'green' replacements for PZT. Comprehensive studies have recently been completed by Baker *et al*.[277] and Zhang *et al*.[257] for compositions close to x = 0.3. The first of these concluded that samples with composition x = 0.3 refined well to the monoclinic space group Pm at room temperature and the tetragonal space group P4mm at 523 K. This work also highlighted a region of phase coexistence between the monoclinic and tetragonal phases, consistent with a first-order phase boundary. Zhang and co-workers conducted a similar structural study at low temperatures for compositions x = 0.05 and x = 0.3, both of which were found to be rhombohedral, in space group R3c. In a similar manner to the work by Baker *et al*., a region of phase coexistence was found close to room temperature between the rhombohedral and monoclinic phases, indicating the presence of a phase boundary. This was in good agreement with earlier suggestions by Ahtee and Glazer.[267] Interestingly, both publications suggested a lowering in symmetry to a monoclinic phase was observed when 30% K was doped into the $NaNbO_3$ structure at room temperature. As discussed in the previous chapter, many of our $NaNbO_3$ samples exhibited two phases, the orthorhombic structure Pbcm and a polar phase labelled '$P2_1ma$'. This, to date, is the most appropriate space group allocation for the polar phase, as it provides the greatest agreement with the experimental data presented. However, it must be noted that a

lowering of symmetry to monoclinic space group Pm for the '$P2_1ma$' phase cannot be ruled out. During the room temperature structural characterisation of $NaNbO_3$ the sol-gel sample, composed of principally the $P2_1ma$ phase, was also refined using the monoclinic space group Pm and the deviation observed in the monoclinic angle was extremely subtle, 90.084(1)°. Similarly, the monoclinic angle suggested by Baker *et al.* was extremely small, $\beta = 89.914°$. Such distortions are commonly proposed owing to subtle peak splittings and/or broadenings identified in high-resolution diffraction data. The broadenings observed can, however, be the result of many different effects, for example crystallite size and shape, strain and grain boundaries. Therefore, the contribution from all such effects needs to be considered when establishing whether a real monoclinic distortion is observed.

The structural challenges faced in the KNN series appear to be mirrored in other related $NaNbO_3$ solid-solutions, for example the $Li_xNa_{1-x}NbO_3$ (LNN) and $Na_{1-x}Sr_{x/2}\square_{x/2}NbO_3$ (SNN) series, where □ denotes a vacancy. Although the LNN series has been investigated numerous times, the phase diagram is still a subject of considerable confusion.[278-282] The Na-rich region of the phase diagram is believed to contain classic perovskite-type structures with corner-linked NbO_6 octahedra. Li-rich compositions, however, are believed to exhibit structures composed of face sharing ocatahedra along the threefold axis. To date, literature regarding low level Li doping ($x < 0.15$) is considered controversial, with several contradictory reports of observed phase transitions occurring at various different Li compositions. Yuzyuk *et al.*,[283] investigated very low percentage Li doping, $0 \leq x \leq 0.145$ using high-resolution powder diffraction and Raman spectroscopy. Their findings confirmed previous reports of a phase transition from the orthorhombic Pbma structure to a polar orthorhombic phase, in space group $P2_1ma$. This transition was observed at extremely low doping levels ($0.02 \leq x \leq 0.03$). Furthermore, the polar $P2_1ma$ phase was found to be stable up to $x = 0.145$. Interestingly, samples with composition $x = 0.12$ were found to exhibit a two phase region of coexistence between a rhombohedral phase, R3c, and the previously recognised polar $P2_1ma$ phase.

The $NaNbO_3$-$Sr_{0.5}NbO_3$ system was first studied by Mori *et al.*,[284] who established the formation of two solid-solutions $Na_{1-x}Sr_{x/2}\square_{x/2}NbO_3$ (SNN) in the compositional ranges $0 \leq x \leq 0.03$ and $0.14 \leq x \leq 0.5$. Interestingly, in the intermediate range a region of coexistence was observed between the two. The first of these solid-solutions, in the range $0 \leq x \leq 0.03$, produced antiferroelectric compounds, whereas the second produced ferroelectric materials. However, no specific role was assigned by Mori *et al.* for the A site vacancies or their influence on the dielectric properties exhibited. It was not until much later that the room temperature ferroelectric behaviour exhibited in the SNN system was found to exist through the introduction of the cation vacancies.[285] Changing the chemical composition caused a structural change which, in turn, modified the dielectric behaviour of the system. Using room temperature X-ray diffraction, samples with compositions $x = 0.1$ and 0.2 were found to be isostructural with the $P2_1ma$ phase of $NaNbO_3$. The identification of this phase suggests the introduction of Sr into the structure favours a polar, ferroelectric phase. However, using transmission electron microscopy (TEM) a region of phase coexistence was found for the $x = 0.1$ composition, with intergrowths from two orthorhombic perovskite phases; $P2_1ma$ and $Pbma$. Previous studies also observed similar regions of phase coexistence, however, they were reported as being restricted to the compositional range $0.022 \leq x \leq 0.05$. No two phase regions were identified in samples with $x = 0.2$ and electrical measurements completed by Torres-Pardo *et al.*,[285] suggest a pure ferroelectric material at this composition.

Evidence obtained from recent literature studies suggests doping the $NaNbO_3$ structure with cations such as Li or Sr results in the formation of the same polar $P2_1ma$ phase of $NaNbO_3$ identified earlier in this work. Hence, within this chapter a variety of $NaNbO_3$-based solid-solutions will be investigated, in particular $K_xNa_{1-x}NbO_3$ ($0.01 \leq x \leq 0.05$), $Li_xNa_{1-x}NbO_3$ ($0.01 \leq x \leq 0.1$) and $Na_{1-x}Sr_{x/2}\square_{x/2}NbO_3$ ($0.1 \leq x \leq 0.4$), to determine whether the $P2_1ma$ phase is formed. Both high-resolution powder diffraction and solid-state NMR data is presented and discussed.

4.2 Experimental

4.2.1 Synthesis

All samples in the $K_xNa_{1-x}NbO_3$ (KNN), $Li_xNa_{1-x}NbO_3$ (LNN) and $Na_{1-x}Sr_{x/2}\square_{x/2}NbO_3$ series were synthesised using conventional solid-state methods. Stoichiometric amounts of Na_2CO_3 (Fisher Scientific, 99.5%), K_2CO_3 (Fisher Scientific, 99%), Li_2CO_3 (Sigma-Aldrich, 99%), $SrCO_3$ (Sigma-Aldrich, 99.9%) and Nb_2O_5 (Sigma-Aldrich, 99.99%) were mixed and ground in an agate mortar and pestle. Samples were pressed into 1 cm pellets, using a pressure of 10 tons cm^{-2}. All samples in the KNN and LNN series were prepared using an annealing temperature of 850 °C. For compositions $0.03 \leq x \leq 0.05$ in the KNN series an annealing time of 48 hours was utilised, with an intermediate regrind occurring after 24 hours of heating. All samples in the LNN series, in addition to $x = 0.01$ and 0.02 in the KNN series, utilised an annealing time of 10 hours, with an intermediate regrind.[282] All $Na_{1-x}Sr_{x/2}\square_{x/2}NbO_3$ samples were synthesised using an annealing temperature of 1300 °C for 24 hours.[285]

4.2.2 X-ray and Neutron Powder Diffraction

Using Beamline Ill at the Diamond Light Source Synchrotron (λ = 0.827267 Å) high-resolution room temperature PXRD experiments were conducted for all samples in the KNN, LNN and $Na_{1-x}Sr_{x/2}\square_{x/2}NbO_3$ series.[122,123] Room temperature time-of-flight neutron powder diffraction experiments were completed for the KNN and LNN series using HRPD[134,135] at the ISIS neutron spallation source, Rutherford-Appleton Laboratories. All diffraction data were analysed using the GSAS software package.[125]

4.2.3 NMR Spectroscopy

Solid-state NMR spectra were acquired using a Bruker 600 Avance III spectrometer, equipped with a wide-bore 14.1 T magnet using a Larmor frequency of 158.75 MHz. The finely powdered samples were tightly

packed into conventional 4-mm ZrO_2 rotors and a MAS rate of 14 kHz was employed. Chemical shifts were reference to 1 M NaCl (aq), using NaCl (s) as a secondary reference at 7.8 ppm.

Conventional ^{23}Na MAS NMR spectra were obtained using single pulse experiments with a typical pulse length of 1.1 μs. The optimised recycle interval for ^{23}Na was 3 s and a typical radiofrequency field strength of between 100 and 170 kHz was employed. Two-dimensional MAS NMR experiments were recorded using a phase-modulated rotor-synchronised split-t_1 shifted-echo pulse sequence.[181] Spectra result from the averaging of 96 transients with a recycle interval of 3 s for each of the 128 t_1 increments. Additional experimental information can be found in the relevant figure captions.

4.3 Results and Discussion

4.3.1 Low Percentage K doping

4.3.1.1 $K_{0.01}Na_{0.99}NbO_3$

Initial investigations concentrated on low percentage doping of K into the $NaNbO_3$ structure. Samples in the range $0.01 \leq x \leq 0.05$ were synthesised with structure and phase purity examined using l-PXRD. To gain accurate structural information high-resolution NPD and s-PXRD experiments were also conducted for each sample. Rietveld refinement of the $x = 0.01$ sample using the NPD data was initially completed using the Pbcm structural model.[248] However, the level of fit obtained was relatively poor, with $wR_p = 13.7\%$ and $\chi^2 = 19.3$, as shown in Figure 4.1(a). Several additional peaks were present in the diffraction pattern that were not indexed by the Pbcm model. This, in turn, suggested the possible presence of a different phase of $NaNbO_3$. An expansion of the superstructure peaks, 2.3 Å – 2.55 Å, is shown in Figure 4.1(b) and highlights the four major peaks in the pattern not fitted by the Pbcm model. Interestingly, the two peaks at ~2.47 Å and ~2.49 Å appeared to correlate with those previously identified in the $P2_1ma$ phase of $NaNbO_3$ discussed in the previous chapter. The identification of these peaks suggested the $P2_1ma$ polymorph of $NaNbO_3$ to also be present in the

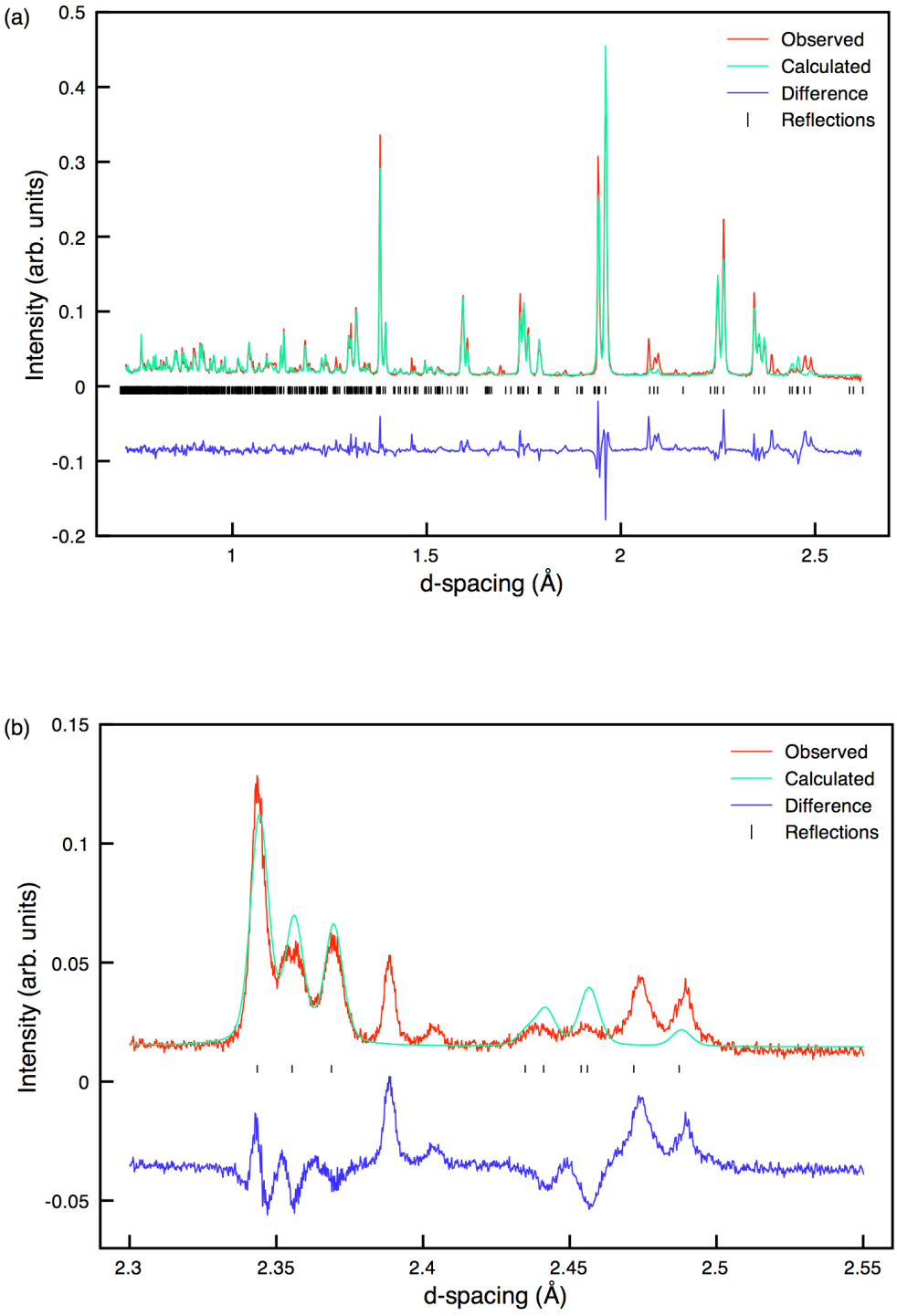

Figure 4.1: (a) Single phase Rietveld refinement of the NPD for $K_{0.01}Na_{0.99}NbO_3$ using the Pbcm structural model and (b) an expansion of the superstructure region of the refinement, 2.3 Å – 2.55 Å, highlighting the poor level of fit.

Table 4.1: Structural parameters for $K_{0.01}Na_{0.99}NbO_3$ from NPD data, using isotropic thermal factors. Space group Pbcm, a = 5.51575(15) Å, b = 5.57350(15) Å, c = 15.5328(4) Å and V = 477.51(3) Å^3. χ^2 = 19.3, wR_p = 13.7% and R_p = 12.6%.

Atom	Site	x	y	z	U(iso) × 100 / Å^2
Na1*	4c	0.2569(15)	0.25	0	1.9(2)
Na2	4d	0.2554(12)	0.2288(13)	0.25	0.36(17)
Nb1	8e	0.2659(14)	0.7483(6)	0.1227(2)	1.13(3)
O1	4c	0.6901(9)	0.25	0	1.04(3)
O2	4d	0.1784(9)	0.7653(10)	0.25	1.04(3)
O3	8e	0.4699(6)	0.4444(4)	0.1403(3)	1.04(3)
O4	8e	0.0102(8)	0.0035(8)	0.1094(2)	1.04(3)
*Na 0.99, K 0.01					

sample. Therefore, a multiphase Rietveld refinement was completed using both the $P2_1ma$[228] and Pbcm[248] polymorphs of $NaNbO_3$ as shown in Figure 4.2(a). The quality of refinement improved upon the addition of the two models (wR_p = 8.9% and χ^2 = 8.1%) and the refined phase fractions obtained suggested an almost 50% mix of the two phases in the sample, with 52.8(2)% and 47.2(2)% of the Pbcm and $P2_1ma$ phases, respectively. The four superstructure peaks initially identified in the region 2.3 Å – 2.55 Å were now accurately modelled using the two phases, as shown in Figure 4.2(b). It must be noted that several other additional peaks were also present in the NPD data for the x = 0.01 sample which could not be correctly modelled by either the Pbcm or $P2_1ma$ phases. These additional peaks indicated the presence of an unknown third phase, believed to be either unreacted metal oxides and/or carbonates or a non-stoichiometric mix of reagents. This phase was not considered to be a different polymorphic form of $NaNbO_3$ as peaks belonging to this phase did not appear to correlate with any of the known polymorphs of $NaNbO_3$. Similarly, these peaks were not considered as being related to the other end-member in the KNN series, $KNbO_3$. Full refinement details obtained

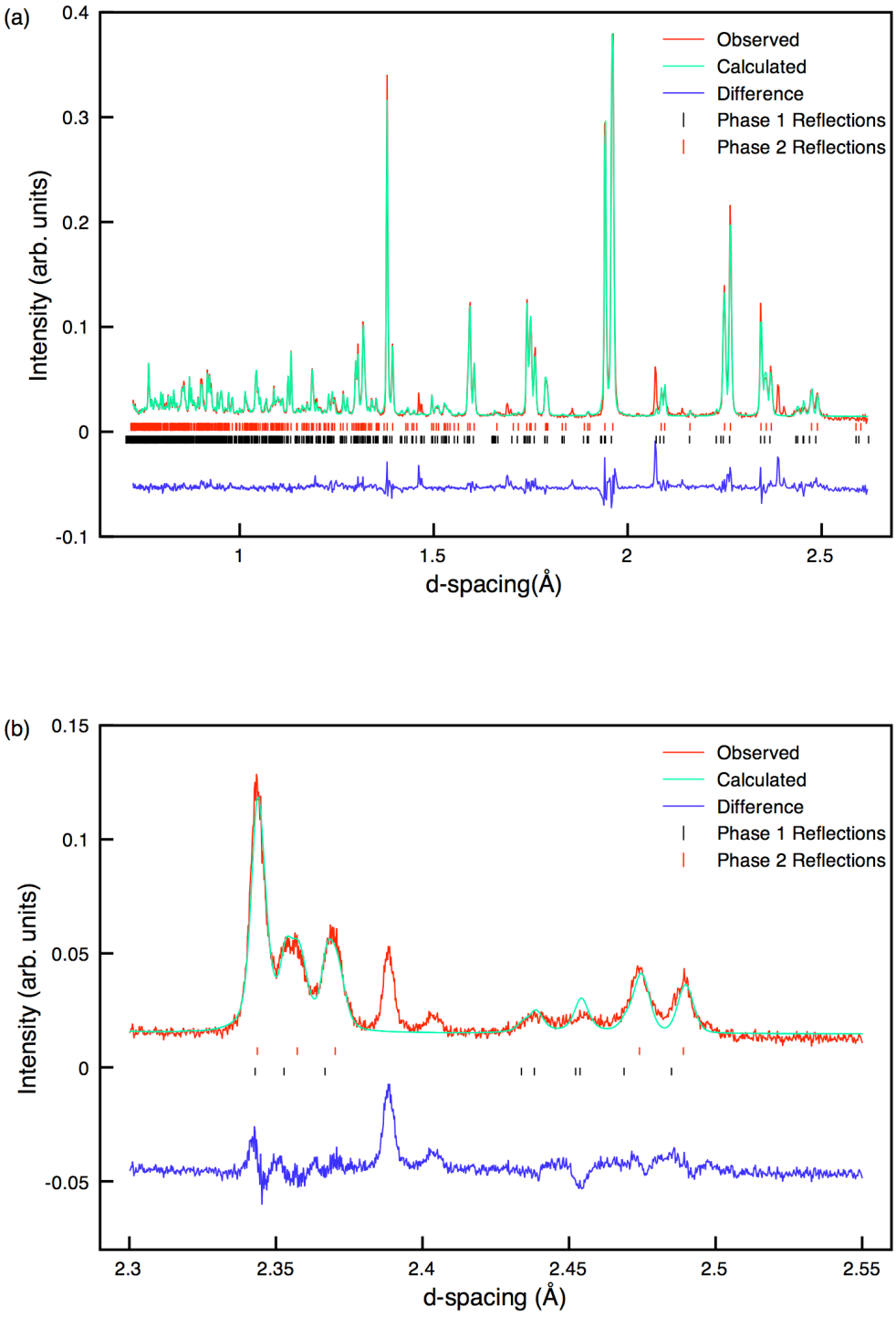

Figure 4.2: (a) Multiphase Rietveld refinement of the NPD data for $K_{0.01}Na_{0.99}NbO_3$ using structural models Pbcm and $P2_1ma$, (b) an expansion of the superstructure region of the refinement, 2.3 Å – 2.55 Å, highlighting the better quality of fit obtained using two structural models.

Table 4.2: Structural parameters for $K_{0.01}Na_{0.99}NbO_3$ from NPD data, using isotropic thermal factors. Space group Pbcm, a = 5.50818(11) Å, b = 5.56847(10) Å, c = 15.5321(5) Å and V = 476.403(15) Å^3. Space group $P2_1ma$, a = 5.57652(8) Å, b = 7.76508(17) Å, c = 5.52056(9) Å and V = 239.052(6) Å^3. χ^2 = 8.10, wR_p = 8.9% and R_p = 7.8%.

Phase	Atom	Site	x	y	z	U(iso) × 100 / Å^2
Pbcm	Na1*	4c	0.250(3)	0.25	0	1.70(4)
	Na2	4d	0.248(3)	0.220(3)	0.25	2.90(5)
	Nb1	8e	0.2420(11)	0.7513(8)	0.1250(7)	1.43(9)
	O1	4c	0.688(2)	0.25	0	3.3(3)
	O2	4d	0.1818(18)	0.7613(3)	0.25	1.02(19)
	O3	8e	0.4707(9)	0.4549(10)	0.1409(5)	1.99(12)
	O4	8e	0.0174(12)	0.0113(13)	0.1062(5)	3.3(2)
	*Na 0.99, K 0.01					
$P2_1ma$	Na1	2a	0.2478(16)	0	0.743(2)	2.00(4)
	Na2	2b	0.2719(17)	0.5	0.7326(16)	1.2(3)
	Nb1	4c	0.2647(6)	0.2497(7)	0.2463(6)	0.11(5)
	O1	2a	0.2351(7)	0	0.3108(15)	0.32(19)
	O2	2b	0.2179(8)	0.5	0.2013(15)	0.34(19)
	O3	4c	0.0197(8)	0.2749(9)	0.5349(9)	1.09(10)
	O4	4c	−0.0527(7)	0.2211(7)	0.0413(8)	0.09(8)

from the NPD data for both the single phase and multiphase refinements of the x = 0.01 sample can be found in Tables 4.1 and 4.2, respectively. All associated bond lengths are given in Appendix III.

As a direct result of the initial findings obtained from the NPD data a multiphase Rietveld refinement was also completed for the s-PXRD data and, in a similar manner, a two phase coexistence was observed between the Pbcm and $P2_1ma$ phases. The multiphase Rietveld refinement of the s-PXRD data is shown in Figure 4.3(a) with an expansion of the superstructure peaks, 18.5° - 22°, also shown in Figure 4.3(b). The refined

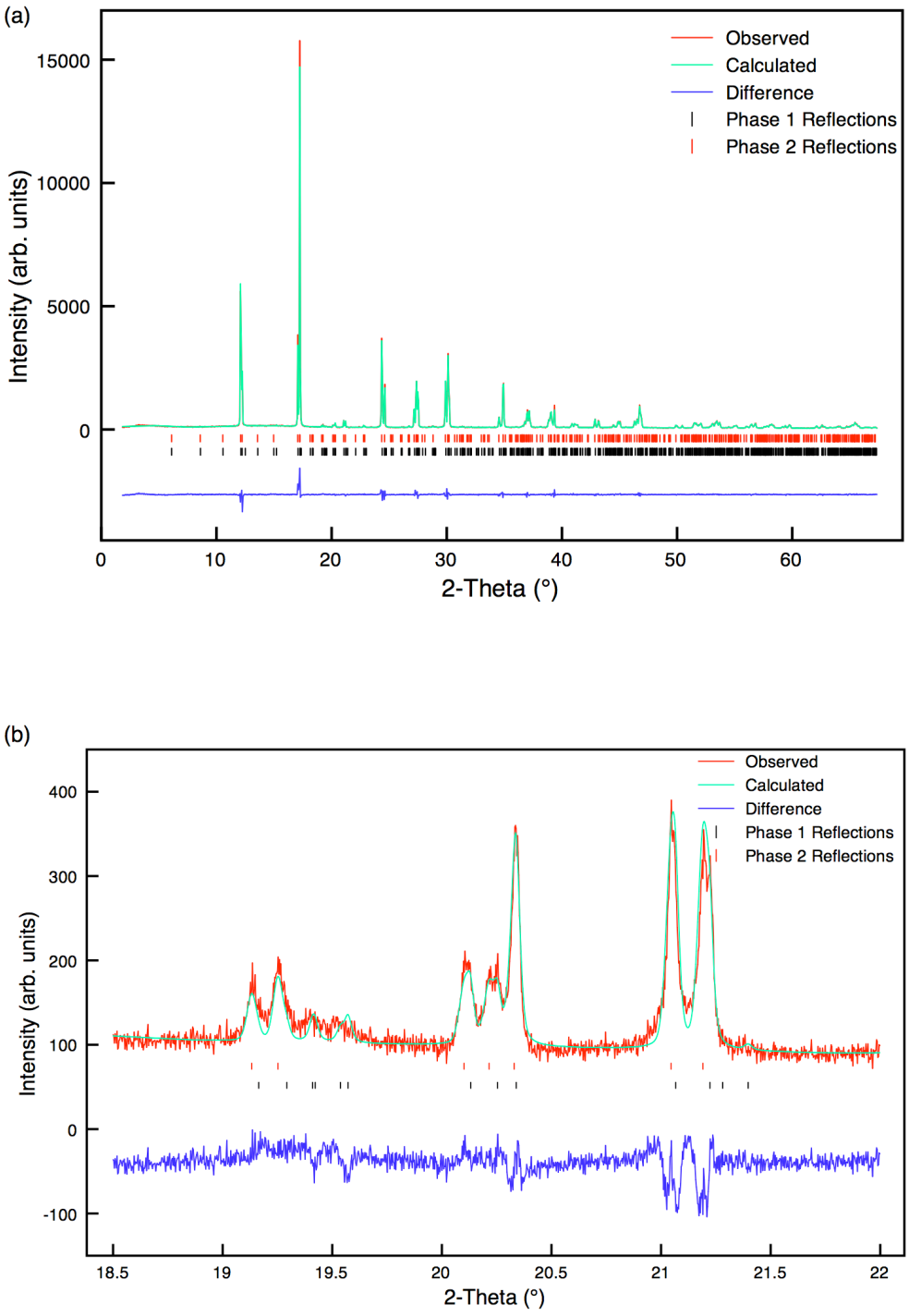

Figure 4.3: (a) Multiphase Rietveld refinement of the s-PXRD data for $K_{0.01}Na_{0.99}NbO_3$ using structural models Pbcm and $P2_1ma$, (b) an expansion of the superstructure region of the refinement, 18.5° – 22°, indicating a good level of fit using the two orthorhombic models.

Table 4.3: Structural parameters for $K_{0.01}Na_{0.99}NbO_3$ from s-PXRD data, using isotropic thermal factors. Space group Pbcm, a = 5.50593(3) Å, b = 5.66902(3) Å, c = 15.52649(8) Å and V = 475.902(3) Å^3. Space group $P2_1ma$, a = 5.57519(2) Å, b = 7.76397(3) Å, c = 5.51813(2) Å and V = 238.855(1) Å^3. χ^2 = 2.1, wR_p = 10.7% and R_p = 7.9%.

Phase	Atom	Site	x	y	z	U(iso) × 100 / Å^2
Pbcm	Na1*	4c	0.2280(12)	0.25	0	0.9(2)
	Na2	4d	0.2315(13)	0.2163(9)	0.25	0.9(2)
	Nb1	8e	0.2530(3)	0.7387(2)		0.76(1)
	O1	4c	0.683(3)	0.25	0	0.86(8)
	O2	4d	0.204(3)	0.7366(18)	0.25	0.86(8)
	O3	8e	0.4752(12)	0.4363(13)	0.1427(7)	0.86(8)
	O4	8e	0.0137(15)	−0.027(2)	0.1062(6)	0.86(8)
	*Na 0.99, K 0.01					
$P2_1ma$	Na1	2a	0.266(2)	0	0.7403(10)	1.20(4)
	Na2	2b	0.2736(13)	0.5	0.7418(10)	1.10(4)
	Nb1	4c	0.2532(5)	0.2499(7)	0.2446(1)	0.85(1)
	O1	2a	0.237(2)	0	0.3086(16)	0.40(5)
	O2	2b	0.2168(16)	0.5	0.192(2)	2.17(5)
	O3	4c	0.032(2)	0.2787(17)	0.5332(16)	0.76(5)
	O4	4c	−0.038(2)	0.222(2)	0.0322(19)	2.26(5)

phase fractions obtained from the multiphase refinement of the s-PXRD data suggested the $P2_1ma$ phase to be slightly more abundant, with 62.8(2)% and 37.2(2)% of the $P2_1ma$ and Pbcm phases, respectively. This was in contrast to the phase fractions obtained from the NPD data, which suggested there to be very similar quantities of the two phases present in the x = 0.01 sample. There are many possible reasons for this discrepancy. It is possible such a difference could be owing to disorder in the sample. The addition of small quantities of K into the $NaNbO_3$ structure is most

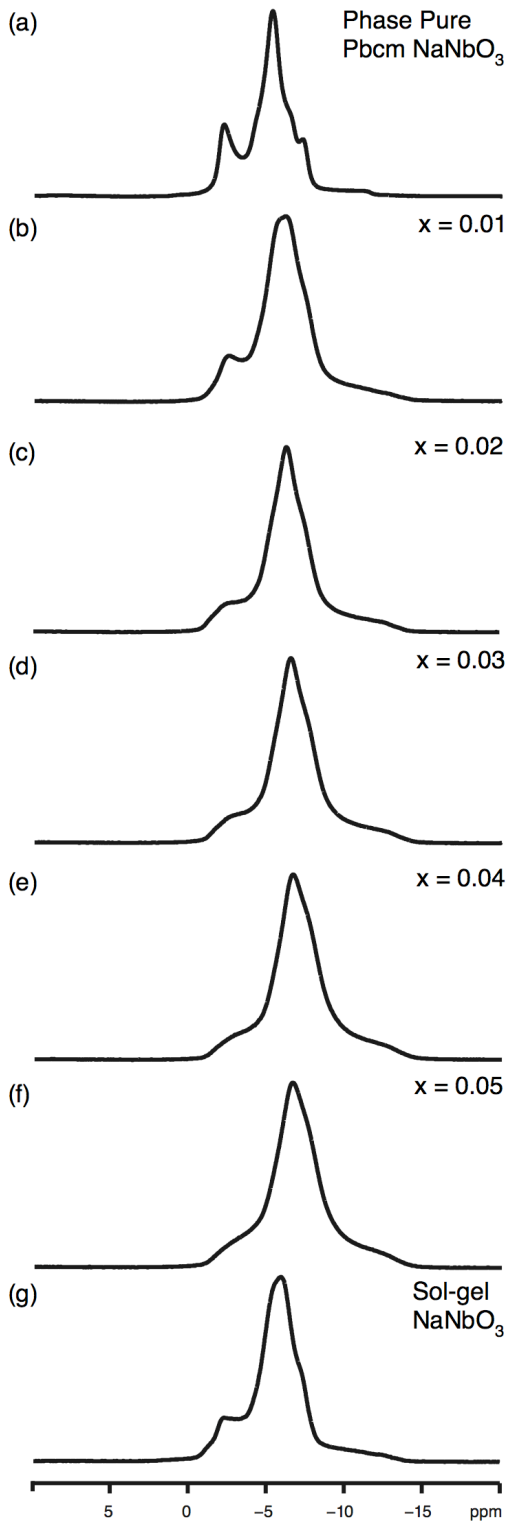

Figure 4.4: Comparison of ^{23}Na (14.1 T) MAS NMR spectra obtained for the $K_xNa_{1-x}NbO_3$ series. Also shown in (a) and (g) for comparison are phase pure Pbcm $NaNbO_3$ (synthesised using molten salt techniques) and the sol-gel sample of $NaNbO_3$ composed of ~90% of the $P2_1ma$ and ~10% of the Pbcm polymorphs of $NaNbO_3$.

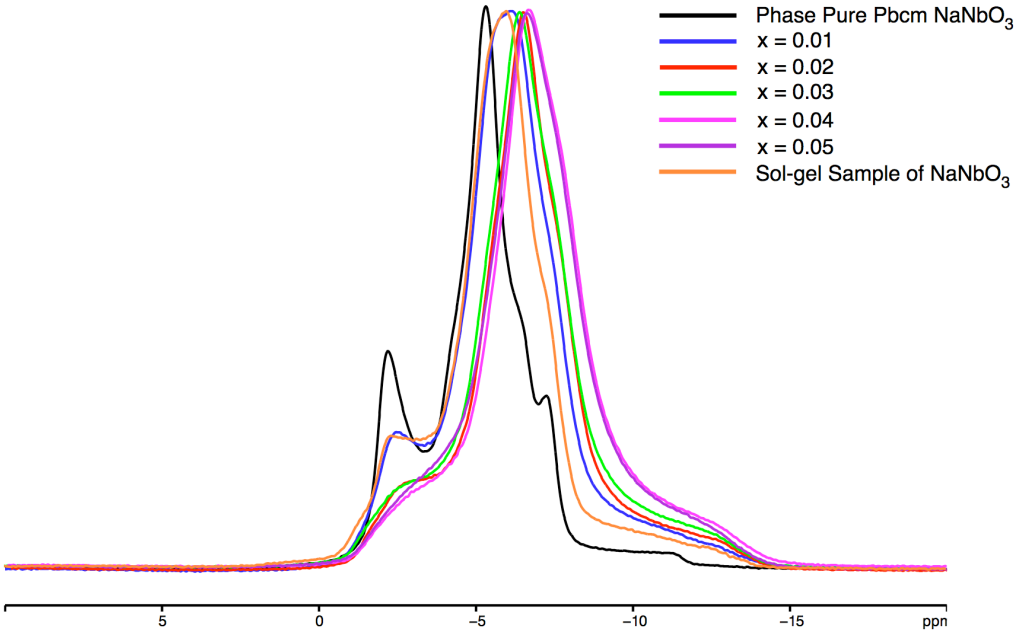

Figure 4.5: Overlay of all ^{23}Na (14.1 T) MAS NMR spectra obtained for the $K_xNa_{1-x}NbO_3$ series. Also shown for comparison are phase pure Pbcm $NaNbO_3$ (synthesised using molten salt techniques) and the sol-gel sample of $NaNbO_3$ composed of ~90% of the $P2_1ma$ and ~10% of the Pbcm polymorphs of $NaNbO_3$.

likely to occur in a disordered manner. As a result this can often lead to broadening of the peaks in the diffraction patterns obtained. It was shown earlier in Chapter 3 that in all X-ray diffraction patterns peaks belonging to the $P2_1ma$ and Pbcm phases were severely overlapped and the only observable discrepancies occurred in the superstructure peaks. Therefore, given the obvious difficulties in distinguishing between the two phases it is possible that with additional peak broadening it is much harder to accurately determine the quantities of each phase present in each diffraction pattern. This is, however, only one of the possible reasons for the discrepancy observed in the phase fractions obtained in the NPD and s-PXRD data for the x = 0.01 sample. Full refinement details obtained from the multiphase Rietveld refinement of the s-PXRD data can be found in Table 4.3 and all associated bond lengths are given in Appendix III.

The ^{23}Na MAS NMR spectrum recorded for $K_{0.01}Na_{0.99}NbO_3$ appeared broadened and subtly different when compared with single phase Pbcm $NaNbO_3$. This is highlighted in Figures 4.4(a) and (b) where

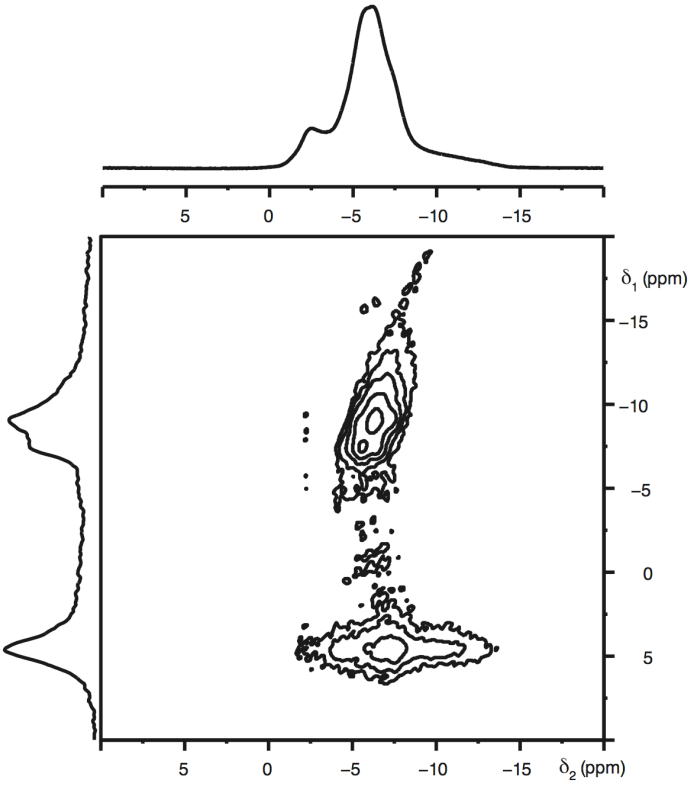

Figure 4.6: The conventional ^{23}Na (14.1 T) MAS NMR spectrum, triple-quantum MAS NMR spectrum, and corresponding isotropic projections for the $K_{0.01}Na_{0.99}NbO_3$ sample. The MAS rate was 14 kHz.

the two lineshapes are compared. Most notably, the lineshape obtained for the x = 0.01 sample appeared to have lost several of the distinct features previously identified in phase pure Pbcm $NaNbO_3$. Also shown for comparison in Figure 4.4(g) is the ^{23}Na MAS NMR spectrum recorded for the sol-gel sample of $NaNbO_3$, composed of ~90% of the $P2_1ma$ polymorph of $NaNbO_3$. When Figures 4.4(b) and (g) are compared they appear very similar, thereby confirming the possible presence of the $P2_1ma$ polymorph in the x = 0.01 sample. This is perhaps clearer to observe in Figure 4.5 where the two are directly overlaid. Many of the lineshape features appear considerably broadened owing, most probably, to the presence of two different phases and different crystallite sizes. It is not possible to accurately determine precisely which phases are present and in which quantities by solely inspection of the MAS spectrum, therefore two-dimensional techniques are required. In general, solid-

Table 4.4: ^{23}Na (14.1 T) MAS NMR parameters obtained for the series $K_{1-x}Na_xNbO_3$, where $0.01 \leq x \leq 0.05$. All parameters were obtained from the position of the centre of gravity (δ_1, δ_2) of the resonance.

x	$\langle\delta_1\rangle$ (ppm)	$\langle\delta_{iso}\rangle$ (ppm)	$\langle P_Q\rangle$ / MHz
0.01	−9.0	−5.1(5)	1.2(2)
	−7.4	−4.4(5)	1.2(2)
	4.7	−1.3(5)	2.3(2)
0.02	−9.0	−5.1(5)	1.2(2)
	4.6	−1.3(5)	2.4(2)
0.03	−10.2	−5.6(5)	1.2(2)
	4.5	−1.4(5)	2.4(2)
0.04	−11.7	−6.2(5)	1.1(2)
	4.3	−1.5(5)	2.4(2)
0.05	−11.4	−6.1(5)	1.1(2)
	3.9	−1.5(5)	2.4(2)

solutions exhibit some degree of disorder owing to the substitution of cations onto the A and/or B sites in a 'random' or disordered manner. However, it is often difficult to determine the precise nature and full extent of the disorder exhibited using diffraction techniques alone. Therefore, in an attempt to establish the extent of disorder exhibited in the $K_{0.01}Na_{0.99}NbO_3$ system MQMAS techniques were also used. The triple-quantum ^{23}Na MQMAS spectrum, shown in Figure 4.6, displayed three distinct Na resonances. The upper of the three ridges, with $\langle\delta_1\rangle$ = −9.0 ppm and $\langle P_Q\rangle$ = 1.2 MHz was in good agreement with that observed for the $P2_1ma$ phase of $NaNbO_3$ accurately assigned earlier in this work (Chapter 3, section 3.3.4). The ridge below, with $\langle\delta_1\rangle$ = −7.4 ppm and $\langle P_Q\rangle$ = 1.2 MHz was also in good agreement with Na2 in the Pbcm phase of $NaNbO_3$. The third ridge, with $\langle\delta_1\rangle$ = 4.7 ppm, possessed a considerably

larger quadrupolar contribution, $\langle P_Q \rangle$ = 2.5 MHz. It was shown earlier that spectra recorded using 14.1 T for samples comprising a mix of the Pbcm and $P2_1ma$ phases possessed two overlapped resonances at $\langle \delta_1 \rangle$ = 4.3 ppm and in order to accurately distinguish the two, multi-field two-dimensional ^{23}Na NMR techniques were required. The three sites identified in the x = 0.01 sample suggested it contained the same two polymorphs previously identified in samples of $NaNbO_3$ synthesised using solid-state, molten salt and sol-gel methods. Hence, it is suggested that two extremely similar resonances reside under the site at $\langle \delta_1 \rangle$ = 4.7 ppm. The presence of disorder results in broader lineshapes and a distribution of parameters. Therefore, in such cases it is only possible to extract average values for the isotropic chemical shift, $\langle \delta_{iso} \rangle$, and the quadrupolar product, $\langle P_Q \rangle$. The NMR parameters obtained from the MQMAS spectrum shown in Figure 4.6 and can be found in Table 4.4. The site at $\langle \delta_1 \rangle$ = −9.0 ppm appears to be aligned along a gradient of +2.125, suggesting there to be a distribution of chemical shifts. Interestingly, the site at $\langle \delta_1 \rangle$ = 4.7 ppm does not appear to exhibit the same alignment along +2.125. This suggests that this particular Na site is less affected by the distribution of chemical shifts. The ^{23}Na MQMAS spectrum for the x = 0.01 sample therefore appears to be dominated largely by a distribution of chemical shifts. In contrast, the contribution from a distribution of quadrupoles is thought to be relatively small in this particular sample. The relative ratios of the two peaks in the isotropic projection for the x = 0.01 sample perhaps suggest the $P2_1ma$ polymorph to be the more abundant of the two, however, no quantitative measurement of the phase fractions could be obtained owing to the extent of peak broadening exhibited in the isotropic projection.

Using high-resolution powder diffraction and ^{23}Na MQMAS techniques, the $K_{0.01}Na_{0.99}NbO_3$ sample was found to comprise of a mix of two phases, believed to be the antiferroelectric Pbcm and polar $P2_1ma$ polymorphs. An additional phase, believed to be a mixed metal oxide and/or carbonate phase was also identified using diffraction methods. However, the exact composition and quantity of this phase are, at present, unknown. No traces of this third phase were present in the ^{23}Na MQMAS

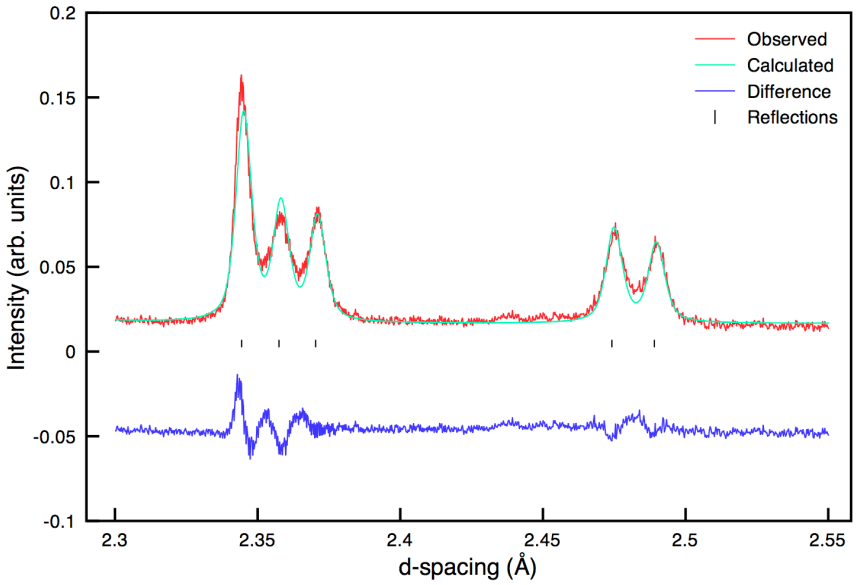

Figure 4.7: An expansion of the superstructure region, 2.3 Å – 2.55 Å, of the Rietveld refinement completed using the NPD data for the $K_{0.02}Na_{0.98}NbO_3$ sample. The refinement was completed using the $P2_1ma$ structural model and, as shown, a good level of fit was obtained.

spectrum, suggesting this additional phase is either below the level of detection or not Na-based.

4.3.1.2 Higher Percentage Doping ($0.02 \leq x \leq 0.05$)

Structure and phase purity of all remaining samples synthesised in the $K_xNa_{1-x}NbO_3$ series (x = 0.02, 0.03, 0.04 and 0.05) were also verified using high-resolution NPD and s-PXRD. Rietveld refinement of each sample suggested the presence of a single phase perovskite and consistently, all samples refined well to the polar orthorhombic $P2_1ma$ structure, suggesting the complete removal of the Pbcm phase from each sample. An expansion of the superstructure peaks, 2.3 Å – 2.55 Å, in the NPD data for the x = 0.02 sample is shown in Figure 4.7. The peaks previously identified in the x = 0.01 sample as belonging to the Pbcm polymorph of $NaNbO_3$ (~2.44 Å and ~2.46 Å) appeared to have been removed completely, confirming the presence of a single phase perovskite in space group $P2_1ma$. All Rietveld refinements completed using the NPD

data in the range $0.02 \leq x \leq 0.05$ are shown in Figures 4.8 and 4.9. Corresponding χ^2 values obtained for x = 0.02, 0.03, 0.04 and 0.05 were 6.9, 7.5, 6.2 and 5.4, respectively. The quality of refinement appeared to improve as greater quantities of K were introduced to the system. This therefore suggested that the introduction of K to the structure favours the formation of the $P2_1ma$ phase and perhaps stabilises this particular polymorph. All structural parameters obtained from each refinement can be found in Tables 4.5 - 4.8. All corresponding bond lengths obtained from each refinement are given in Appendix III. In a similar manner, Rietveld refinement of the s-PXRD data also suggested the presence of a single phase perovskite and each sample in this series refined well to the polar orthorhombic $P2_1ma$ phase. All Rietveld refinements completed using the s-PXRD data are shown in Figures 4.10 and 4.11. Corresponding χ^2 values obtained for x = 0.02, 0.03, 0.04 and 0.05 were 9.5, 3.8, 1.7 and 1.6 respectively. In a similar manner to the NPD data, the quality of the refinement appeared to improve with increasing x. All associated structural parameters obtained from each refinement using the s-PXRD data, including corresponding bond lengths, can be found in Appendix III.

The substitution of K into the $NaNbO_3$ structure produced a corresponding change in both the lattice parameters and unit cell volume. As x was increased a gradual increase in the unit cell parameters and cell volume was observed for both the NPD and s-PXRD data. The variation of each parameter with increasing K content is shown in Figures 4.12, 4.13, 4.14 and 4.15, respectively. Potassium possesses a larger ionic radius (1.51 Å)[4] than Na (1.02 Å),[4] and so, as K is introduced into the structure it will result in an expansion of the unit cell. This hypothesis is in good agreement with the findings presented. A near linear correlation was observed with increasing x for each parameter.

As observed for the x = 0.01 sample, the ^{23}Na MAS NMR spectra recorded for each composition appeared subtly different. All ^{23}Na MAS NMR spectra recorded in this series are compared in Figure 4.4 and overlaid in Figure 4.5. Consistently, each lineshape appeared broadened relative to phase pure Pbcm $NaNbO_3$ and as x was increased many of the

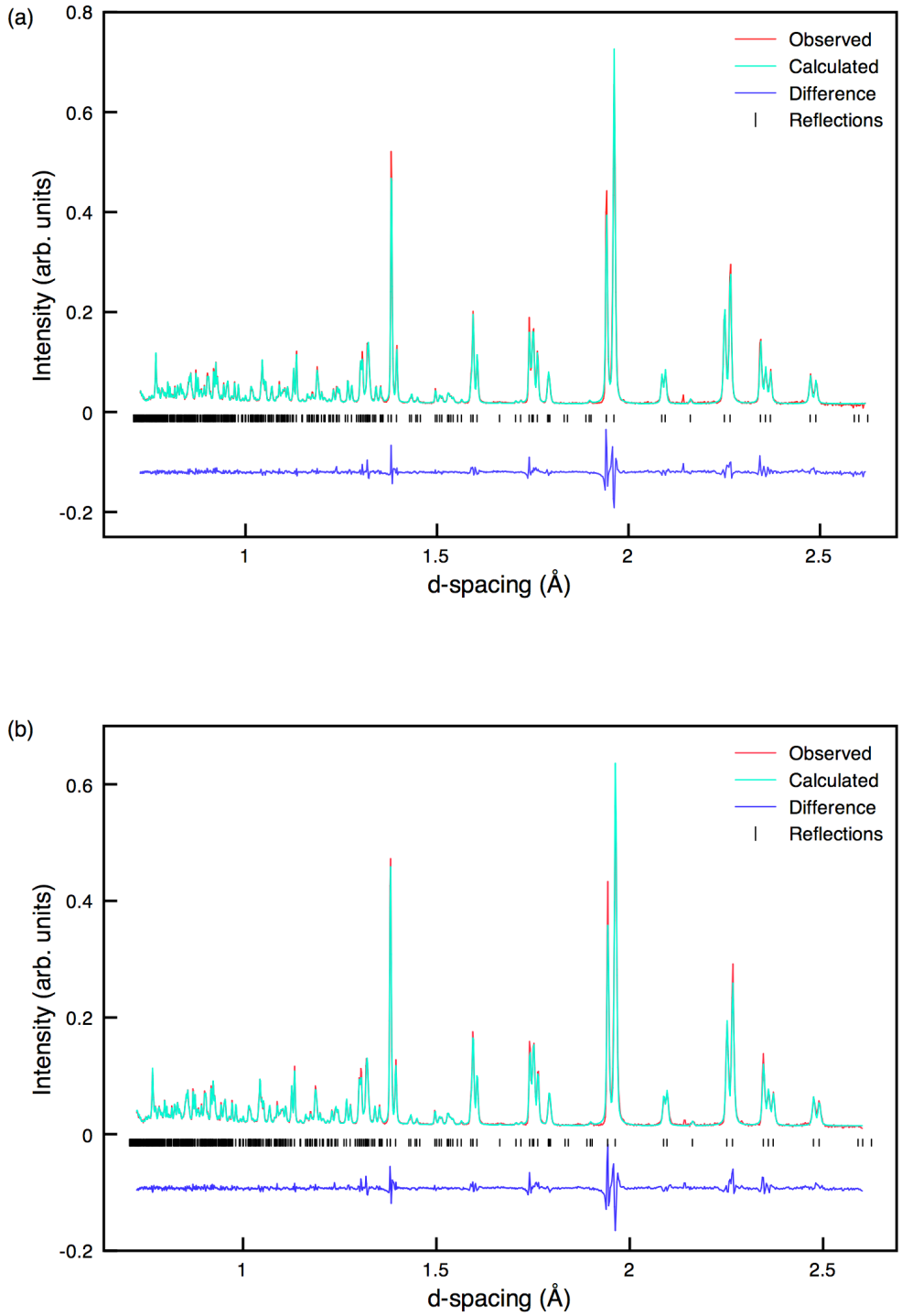

Figure 4.8: Single phase Rietveld refinements of the NPD for (a) $K_{0.02}Na_{0.98}NbO_3$ and (b) $K_{0.03}Na_{0.97}NbO_3$ using the $P2_1ma$ structural model. Both refinements indicate a good level of fit.

Table 4.5: Structural parameters for $K_{0.02}Na_{0.98}NbO_3$ from NPD data, using isotropic thermal factors. Space group $P2_1ma$, a = 5.57687(6) Å, b = 7.76821(8) Å, c = 5.52147(6) Å and V = 239.203(7) Å^3. $\chi^2 = 6.9$, $wR_p = 7.1\%$ and $R_p = 6.8\%$.

Atom	Site	x	y	z	U(iso) × 100 / Å^2
Na1*	2a	0.2648(9)	0	0.7410(7)	1.77(13)
Na2	2b	0.2817(9)	0.5	0.7369(7)	1.65(12)
Nb1	4c	0.2696	0.2494(3)	0.2454(3)	0.35(3)
O1	2a	0.2411(3)	0	0.3099(9)	0.94(10)
O2	2b	0.2264(3)	0.5	0.1966(9)	0.70(8)
O3	4c	0.0224(4)	0.2787(4)	0.5332(4)	1.42(5)
O4	4c	−0.0450(4)	0.2210(4)	0.0375(4)	0.95(5)
*Na 0.98, K 0.02					

Table 4.6: Structural parameters for $K_{0.03}Na_{0.97}NbO_3$ from NPD data, using isotropic thermal factors. Space group $P2_1ma$, a = 5.57761(4) Å, b = 7.77092(5) Å, c = 5.52332(4) Å and V = 239.398(2) Å^3. $\chi^2 = 7.5$, $wR_p = 7.5\%$ and $R_p = 7.1\%$.

Atom	Site	x	y	z	U(iso) × 100 / Å^2
Na1*	2a	0.2660(10)	0	0.7408(8)	1.78(14)
Na2	2b	0.2791(10)	0.5	0.7368(7)	1.41(12)
Nb1	4c	0.2694	0.2494(3)	0.2453(3)	0.25(2)
O1	2a	0.2404(4)	0	0.3085(10)	0.79(10)
O2	2b	0.2263(3)	0.5	0.1971(10)	0.69(9)
O3	4c	0.0217(4)	0.2786(4)	0.5332(4)	1.22(5)
O4	4c	−0.0454(4)	0.2219(4)	0.0376(4)	0.84(4)
*Na 0.97, K 0.03					

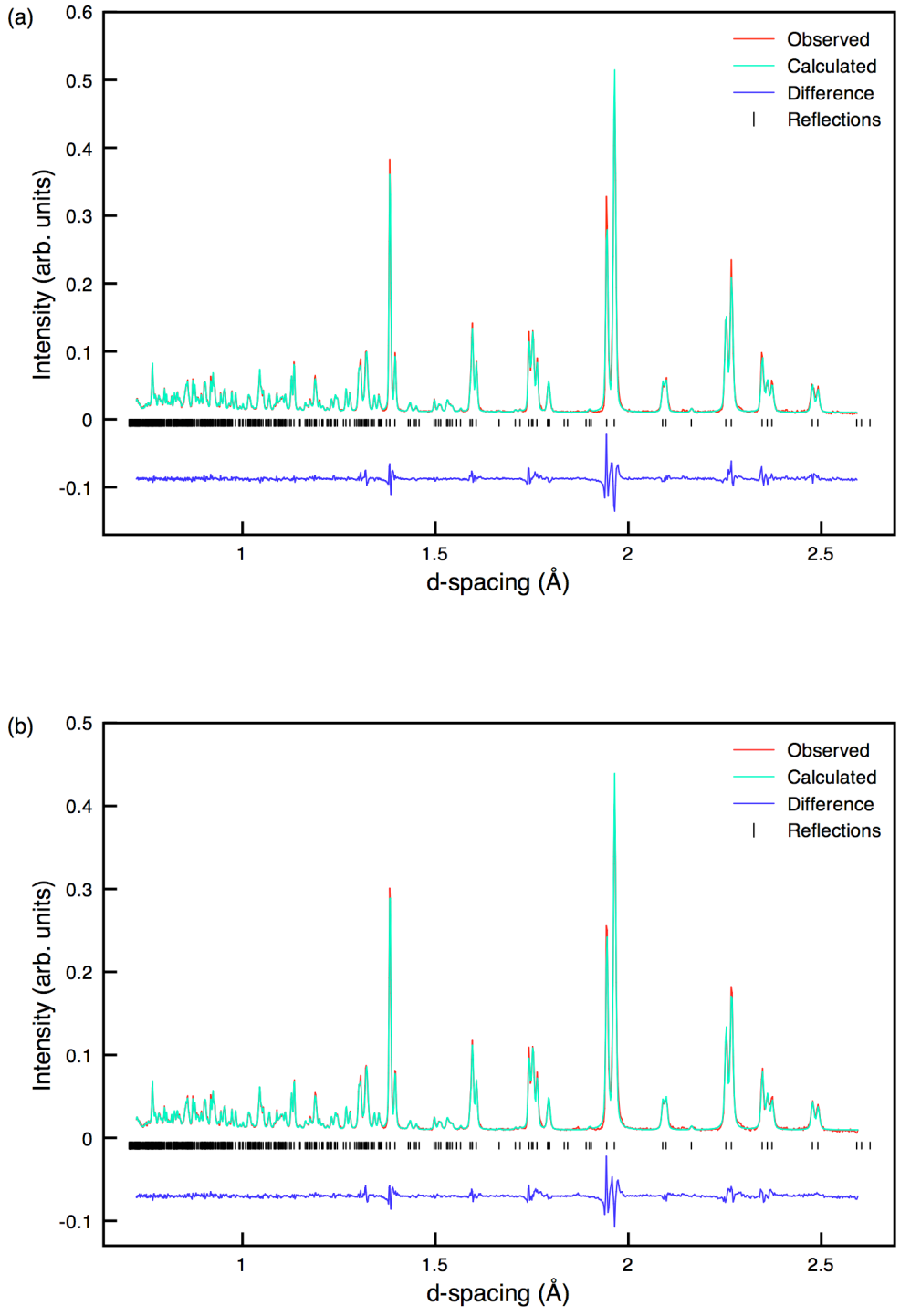

Figure 4.9: Single phase Rietveld refinements of the NPD for (a) $K_{0.04}Na_{0.96}NbO_3$ and (b) $K_{0.05}Na_{0.95}NbO_3$ using the $P2_1ma$ structural model. Both refinements indicate a good level of fit.

Table 4.7: Structural parameters for $K_{0.04}Na_{0.96}NbO_3$ from NPD data, using isotropic thermal factors. Space group $P2_1ma$, a = 5.58003(8) Å, b = 7.77488(10) Å, c = 5.52736(8) Å and V = 239.799(9) Å^3. $\chi^2 = 6.2$, $wR_p = 7.7\%$ and $R_p = 7.1\%$.

Atom	Site	x	y	z	U(iso) × 100 / Å^2
Na1*	2a	0.2657(10)	0	0.7404(8)	1.72(14)
Na2	2b	0.2749(10)	0.5	0.7374(7)	1.58(13)
Nb1	4c	0.2688	0.2494(3)	0.2458(3)	0.39(3)
O1	2a	0.2386(4)	0.	0.3083(8)	0.85(10)
O2	2b	0.2250(4)	0.5	0.2003(8)	0.88(10)
O3	4c	0.0218(4)	0.2777(4)	0.5333(4)	1.21(5)
O4	4c	−0.0453(4)	0.2225(4)	0.0386(4)	1.00(5)
*Na 0.96, K 0.04					

Table 4.8: Structural parameters for $K_{0.05}Na_{0.95}NbO_3$ from NPD data, using isotropic thermal factors. Space group $P2_1ma$, a = 5.58067(8) Å, b = 7.77549(11) Å, c = 5.52787(8) Å and V = 239.868(9) Å^3. $\chi^2 = 5.4$, $wR_p = 7.7\%$ and $R_p = 7.2\%$.

Atom	Site	x	y	z	U(iso) × 100 / Å^2
Na1*	2a	0.2670(11)	0	0.7411(8)	1.77(16)
Na2	2b	0.2756(11)	0.5	0.7354(8)	1.66(15)
Nb1	4c	0.2688	0.2495(3)	0.2462(3)	0.43(3)
O1	2a	0.2394(4)	0	0.3086(10)	0.92(11)
O2	2b	0.2259(4)	0.5	0.1987(10)	0.82(10)
O3	4c	0.0216(4)	0.2786(4)	0.5331(4)	1.24(5)
O4	4c	−0.0442(4)	0.2232(4)	0.0375(4)	1.07(5)
*Na 0.95, K 0.05					

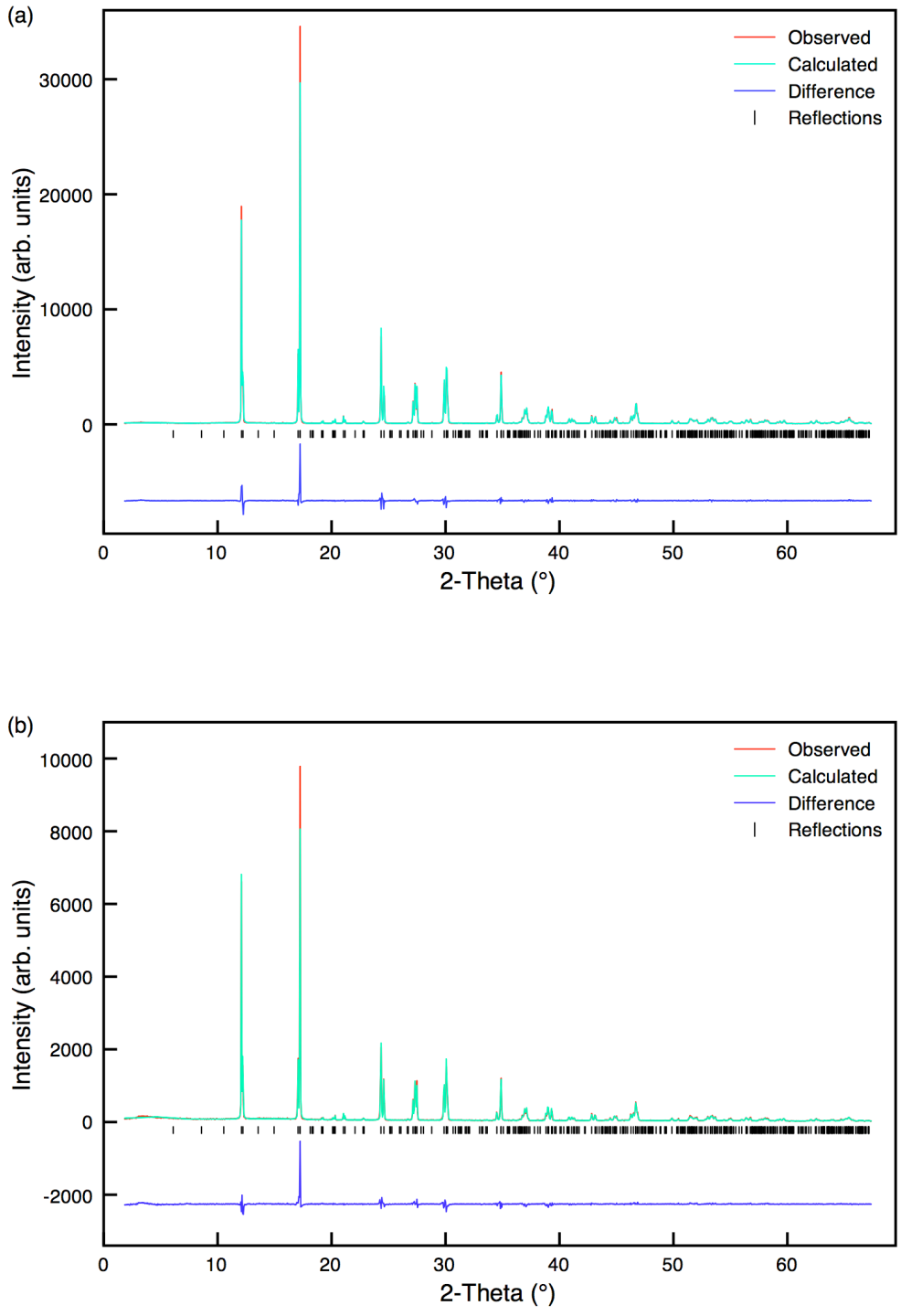

Figure 4.10: Single phase Rietveld refinements of the s-PXRD data for (a) $K_{0.02}Na_{0.98}NbO_3$ and (b) $K_{0.03}Na_{0.97}NbO_3$ using the $P2_1ma$ structural model. Both refinements indicate a good level of fit.

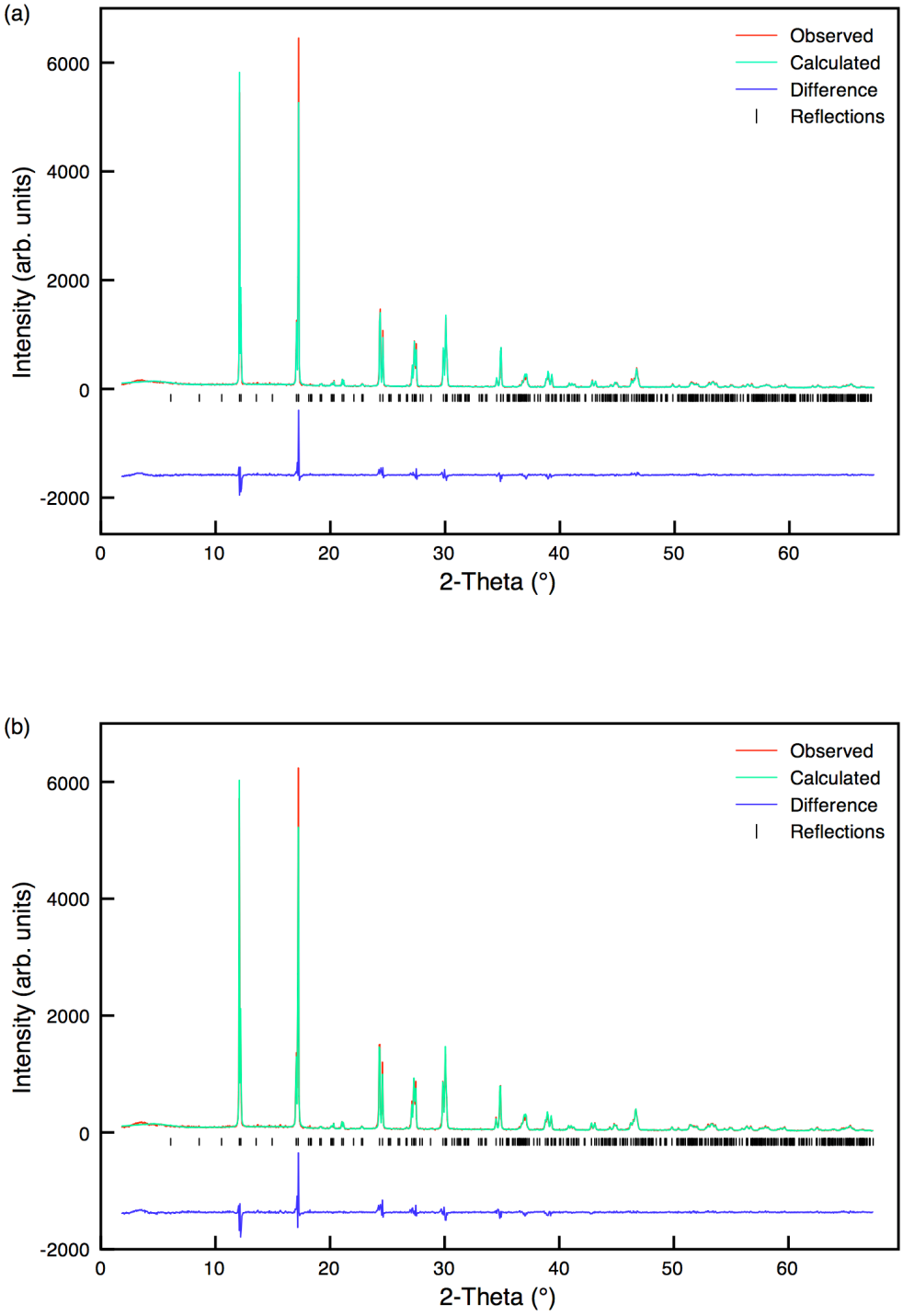

Figure 4.11: Single phase Rietveld refinements of the s-PXRD data for (a) $K_{0.04}Na_{0.96}NbO_3$ and (b) $K_{0.05}Na_{0.95}NbO_3$ using the $P2_1ma$ structural model. Both refinements indicate a good level of fit.

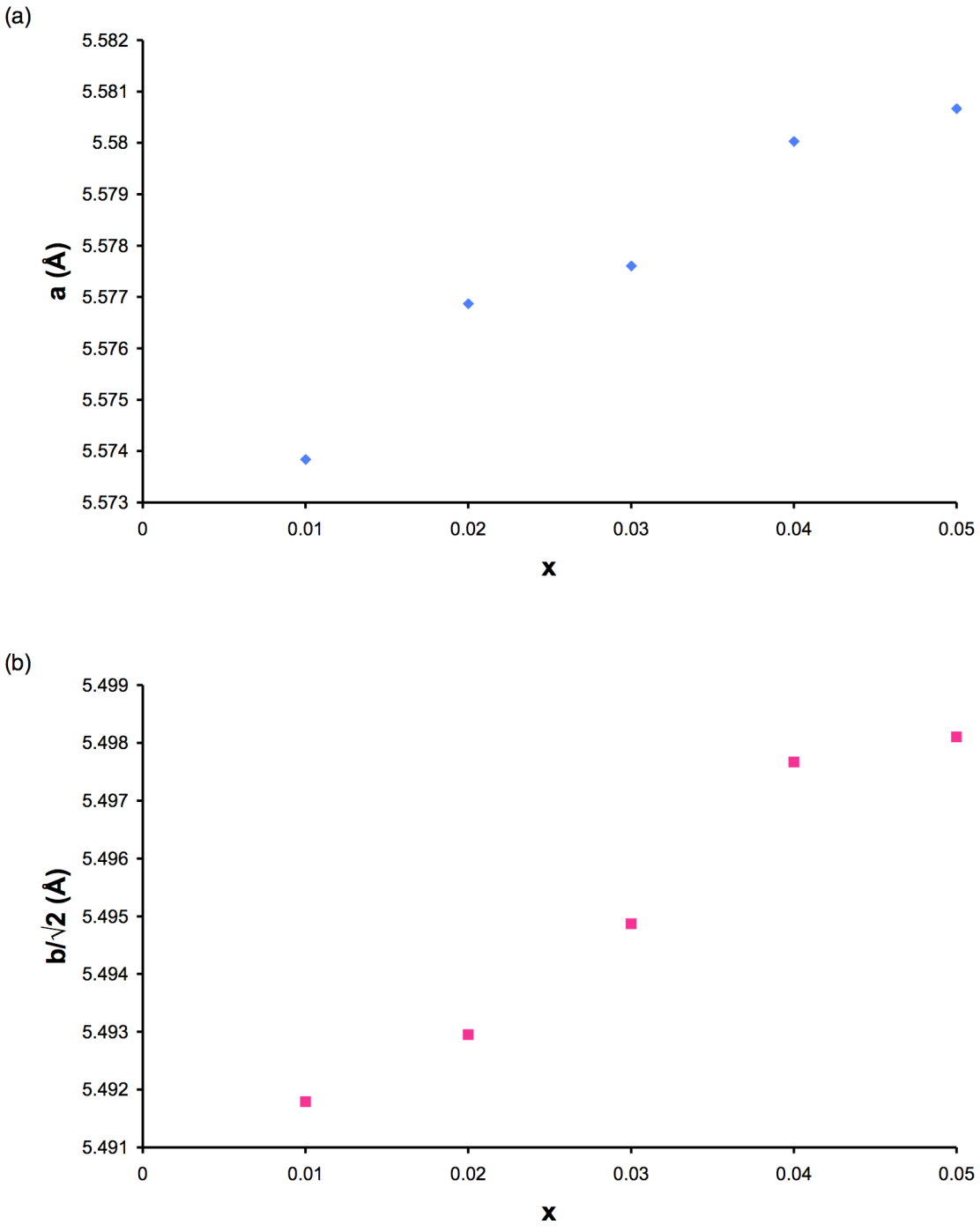

Figure 4.12: Variation observed in the unit cell parameters (a) a and (b) b with increasing x in the solid-solution $K_xNa_{1-x}NbO_3$ using the NPD data. Note that for ease of comparison with unit cell parameters a and c, the b parameter has been divided by √2. The estimated error bars are smaller than the symbols used and are therefore not shown.

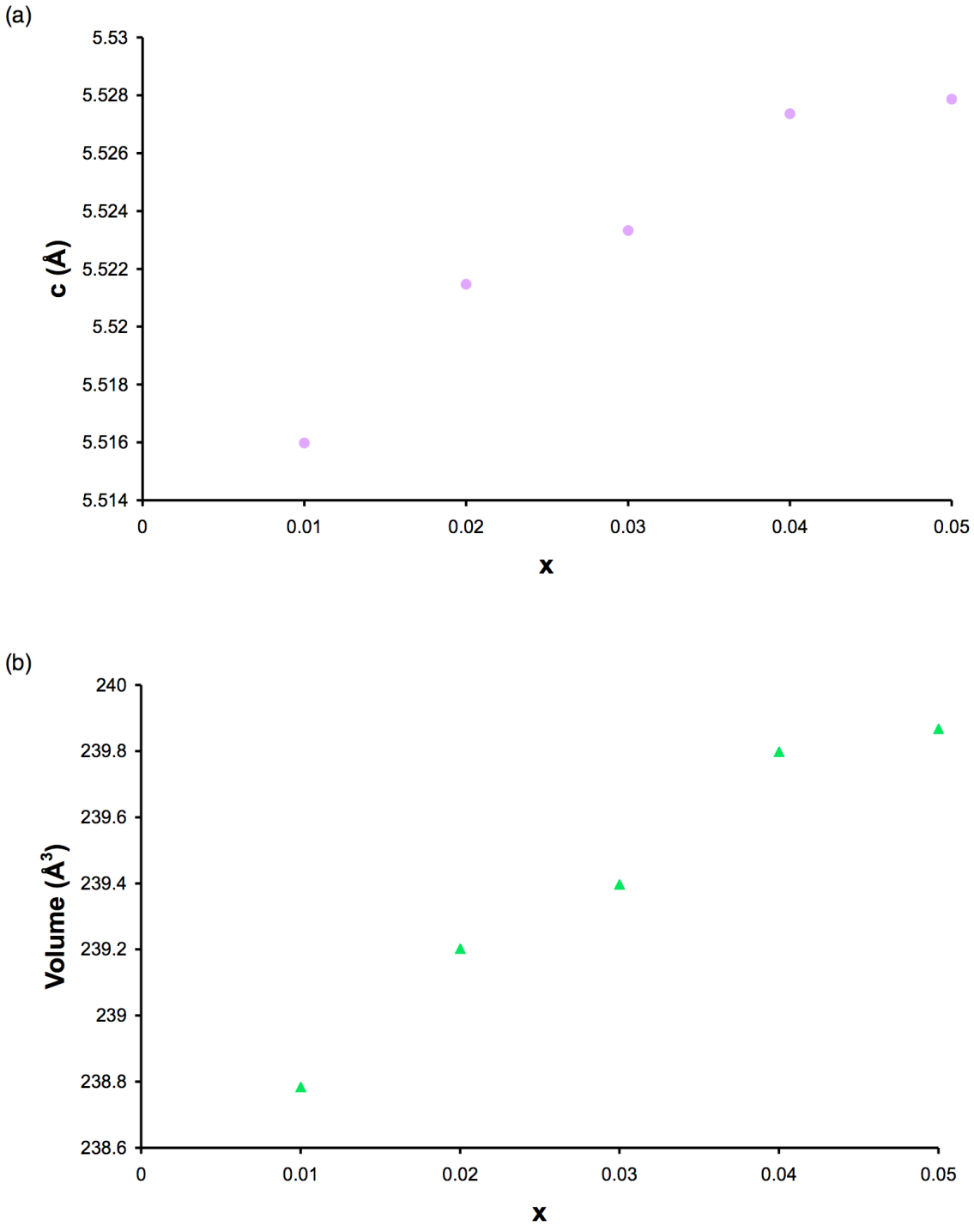

Figure 4.13: Variation observed in (a) the unit cell parameter c and (b) the unit cell volume with increasing x for $K_xNa_{1-x}NbO_3$ using the NPD data. The estimated error bars are smaller than the symbols used and are therefore not shown.

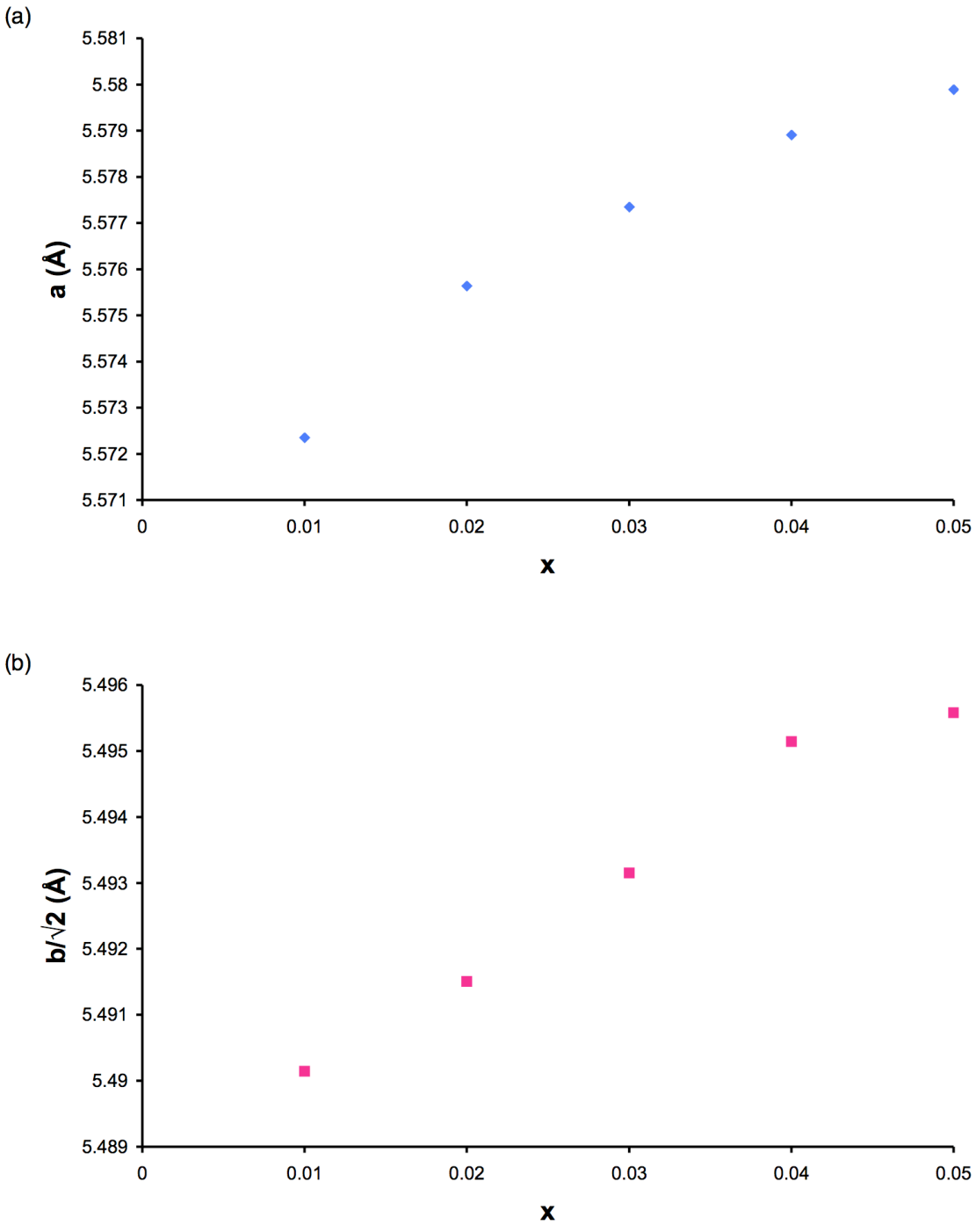

Figure 4.14: Variation observed in the unit cell parameters (a) a and (b) b with increasing x in the solid-solution $K_xNa_{1-x}NbO_3$ using the s-PXRD data. Note that for ease of comparison with unit cell parameters a and c, the b parameter has been divided by √2. The estimated error bars are smaller than the symbols used and are therefore not shown.

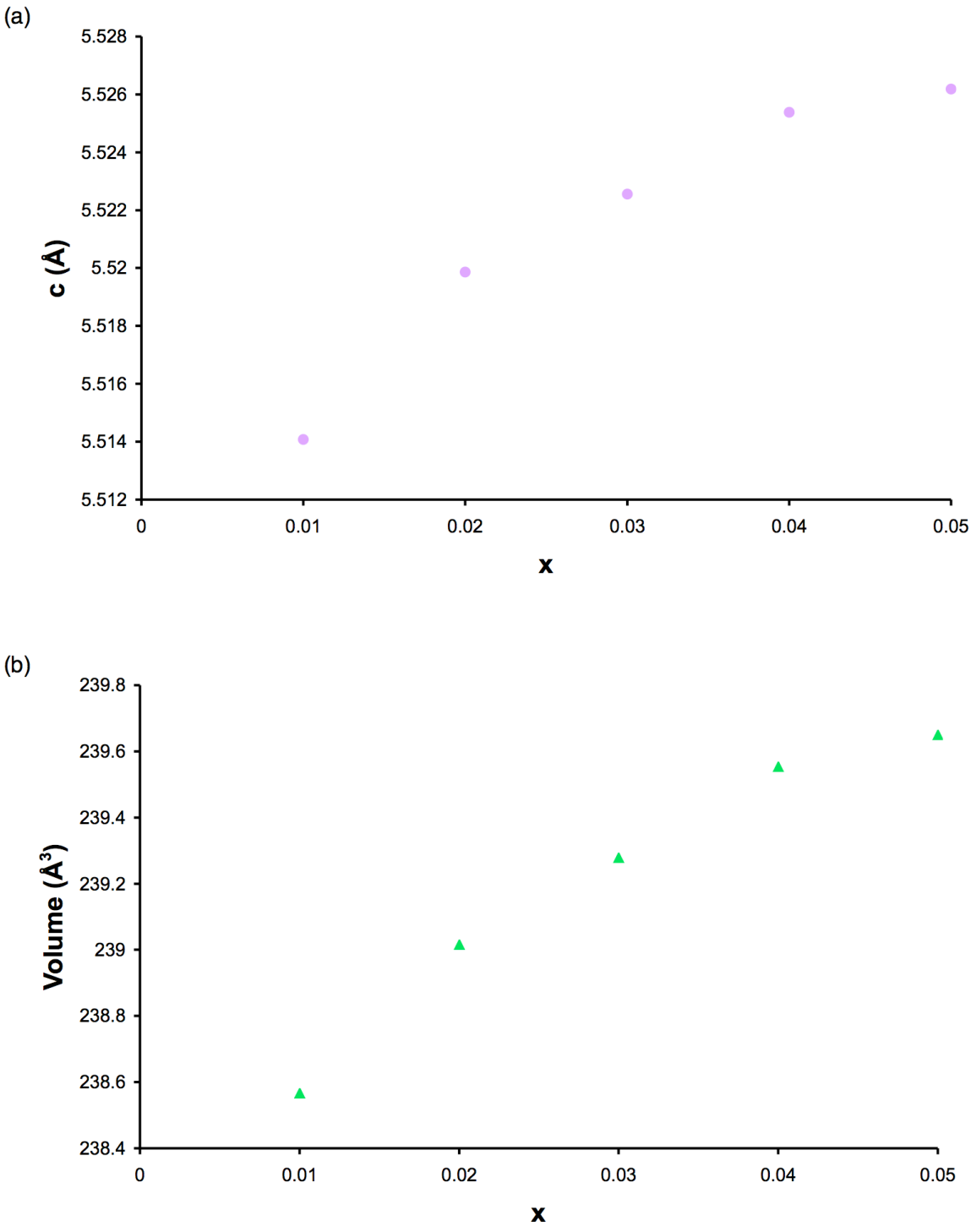

Figure 4.15: Variation observed in (a) the unit cell parameter c and (b) the unit cell volume with increasing x for $K_xNa_{1-x}NbO_3$ using the s-PXRD data. The estimated error bars are smaller than the symbols used and are therefore not shown.

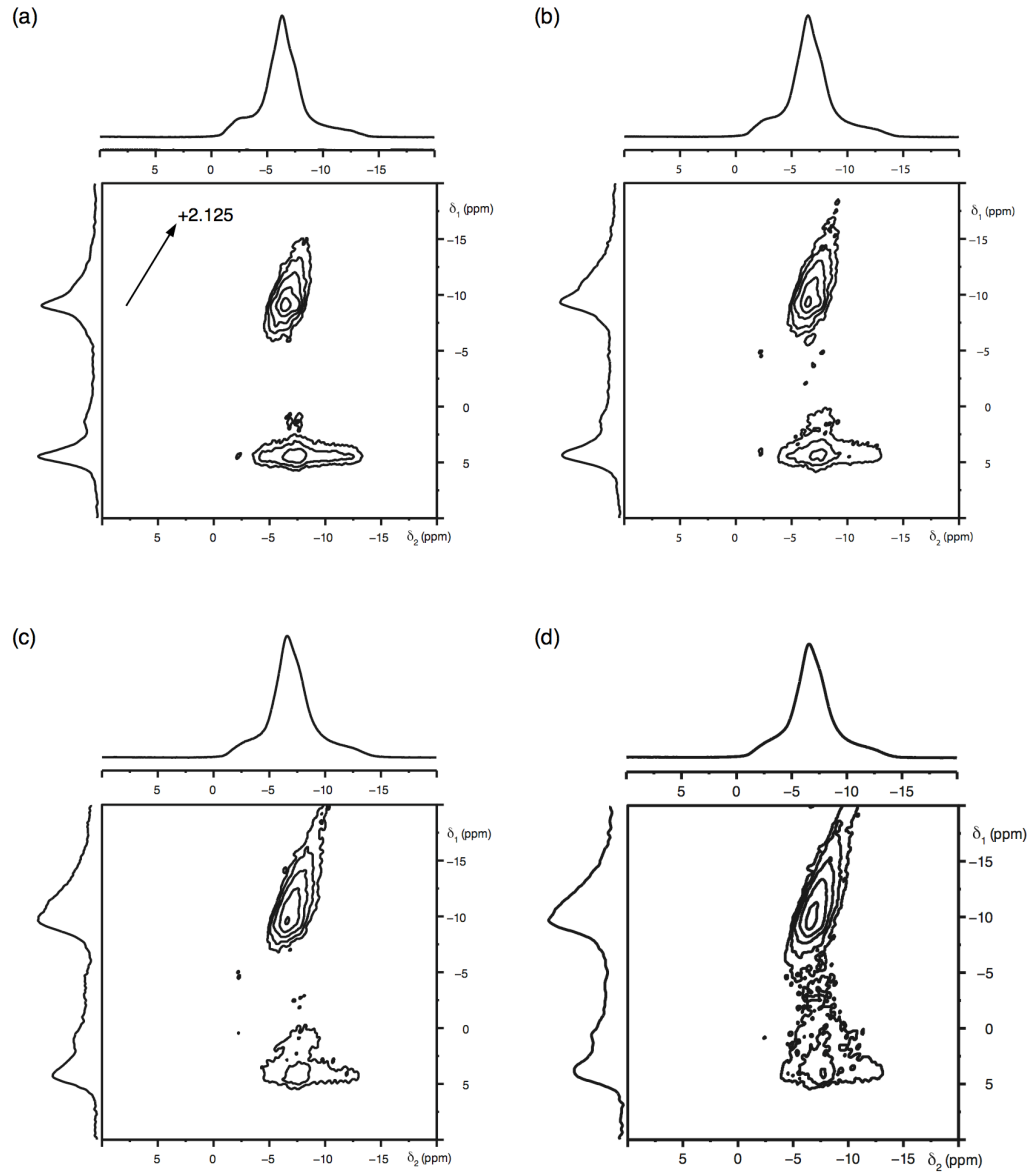

Figure 4.16: ^{23}Na MAS NMR spectra, triple-quantum MAS NMR spectra, and corresponding isotropic projections for (a) $K_{0.02}Na_{0.98}NbO_3$, (b) $K_{0.03}Na_{0.97}NbO_3$, (c) $K_{0.04}Na_{0.96}NbO_3$ and (d) $K_{0.05}Na_{0.95}NbO_3$. The spectral broadening observed increases with increasing x, indicating the presence of disorder. Also shown is an axis along +2.125 denoting the direction along which a distribution of chemical shifts would lie.

distinct features previously observed were gradually lost as the extent of broadening exhibited in each increased. Each lineshape therefore bore more resemblance to the $P2_1ma$ polymorph of $NaNbO_3$ and, as a result, appeared in good agreement with the diffraction data presented. Broadening of the MAS spectrum, in this particular case, is presumably

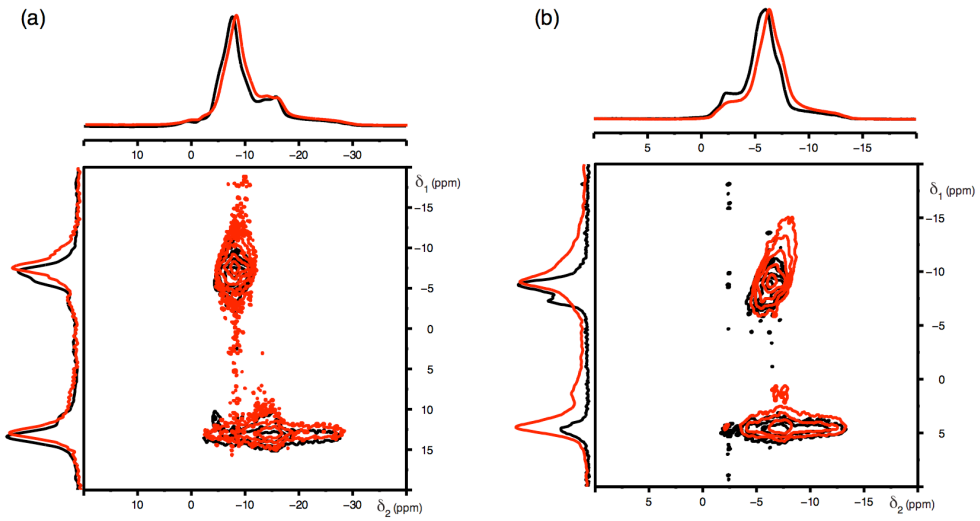

Figure 4.17: An overlay of the ^{23}Na MAS NMR spectra, triple-quantum MAS NMR spectra, and corresponding isotropic projections for sol-gel $NaNbO_3$ (shown in black) and $K_{0.02}Na_{0.98}NbO_3$ (shown in red) at (a) 9.4 T and (b) 14.1 T.

owing to both the inefficient removal of the quadrupolar interaction and disorder. Hence, to accurately determine the number of crystallographically distinct Na sites present in each sample MQMAS techniques were also used. The ^{23}Na MQMAS NMR spectra recorded for each composition are shown in Figures 4.16(a-d). Each spectrum displays two broadened Na sites. The extent of broadening observed in each does, however, make it difficult to detect the presence of very small amounts of the Pbcm phase. The δ_1 position of each site was the same as the $P2_1ma$ polymorph, and at a lower shift than that expected for Pbcm. The spectra (9.4 T and 14. 1 T) for sol-gel $NaNbO_3$ (~90% $P2_1ma$ and ~10% Pbcm phases) and $K_{0.02}Na_{0.98}NbO_3$ have been overlaid and are shown in Figures 4.17(a) and (b), respectively. The two sites in each spectrum appear to align, indicating good agreement between the two, confirming the presence of the $P2_1ma$ polymorph. Note that the extent of broadening exhibited in each spectrum in the KNN series is consistent with the presence of disorder and this is most probably owing to disorder across the A site. The spectral broadening exhibited increases with increasing x and, as observed for the x = 0.01 sample, each spectrum appears to be

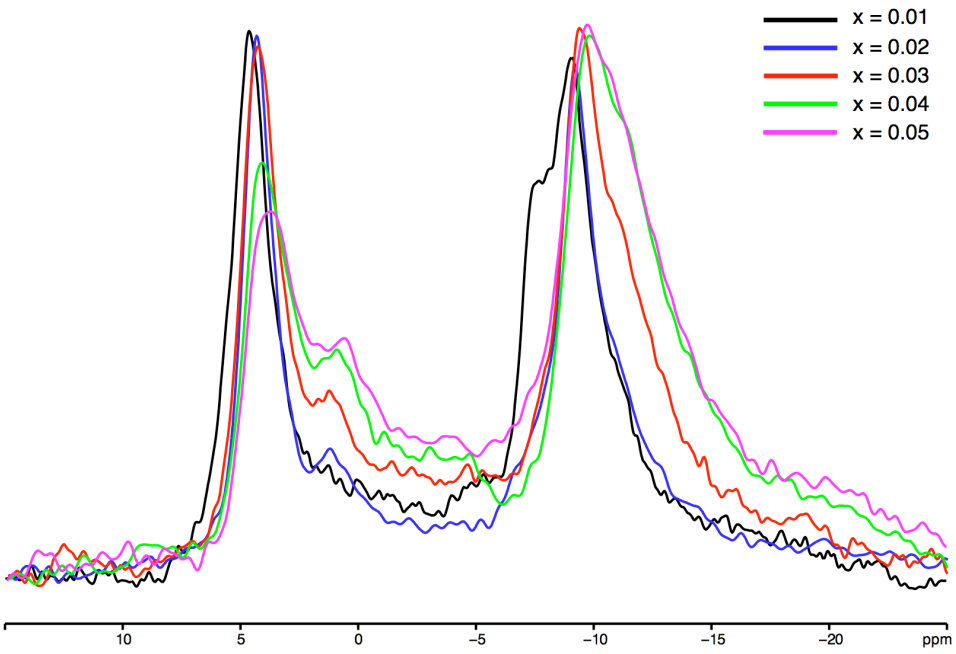

Figure 4.18: An overlay of the isotropic projections obtained from all two-dimensional ^{23}Na MQMAS NMR spectra recorded in the KNN series.

dominated by a distribution of chemical shifts. Again the contribution from a distribution of quadrupoles is thought to be relatively small in each sample. To highlight the extent of broadening exhibited in each spectrum the isotropic projections obtained from each have been overlaid and compared, as shown in Figure 4.18. In addition, the variation in linewidth, i.e., the full width half maximum ($\Delta\upsilon_{1/2}$) of each projection with increasing x has been plotted and is shown in Figure 4.19(a) and (b). The trend observed suggests that the line broadening increases in a non-linear manner with increasing x. Owing to the presence of disorder and hence a distribution of parameters, $\langle\delta_{iso}\rangle$ and $\langle P_Q\rangle$ values were extracted from each spectrum and are given in Table 4.4.

The results obtained for the compositional range, $0.01 \leq x \leq 0.05$, in the KNN series suggest low percentage doping of K into the $NaNbO_3$ structure produces the polar orthorhombic $P2_1ma$ polymorph. In a similar manner, Schuvaeva *et al.*[228] suggested samples with composition $K_{0.025}Na_{0.975}NbO_3$ possessed a structure type similar to that of the field induced ferroelectric $P2_1ma$ phase identified in their work. The only major difference observed between the two phases was a more

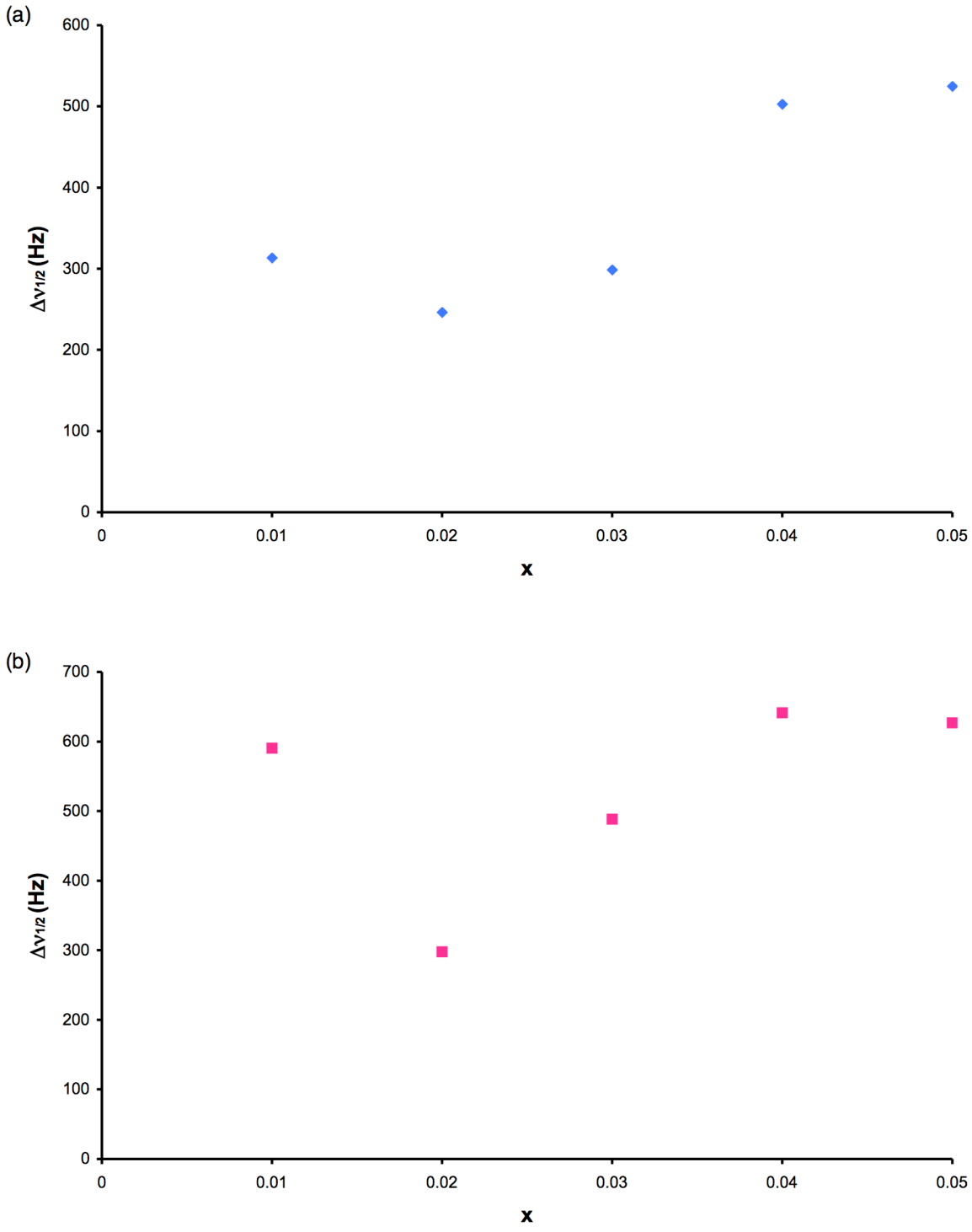

Figure 4.19: Variation in δ_1 linewidth of the resonances corresponding to the two Na sites (a) $\langle\delta_1\rangle \approx 4.7$ ppm and (b) $\langle\delta_1\rangle \approx -9.0$ ppm extracted from the spectra of $K_xNa_{1-x}NbO_3$ with increasing x in Figure 4.16.

pronounced tilting of the NbO_6 octahedra around the [010] axis in the electric field induced phase. The presence of the $P2_1ma$ phase in their work is in good agreement with the findings presented in this investigation. One possible reason for the formation of the $P2_1ma$ polymorph is a 'stabilisation' effect, i.e., the introduction of K into the $NaNbO_3$ structure stabilises this particular polymorph. There are many possible reasons for such an effect, including cation size, structural stress and strain. Athee and Hewat[268] found that compositions x = 0.01 and x = 0.02 in the KNN series could be refined using monoclinic symmetry. However, they also discovered the differences exhibited between monoclinic and orthorhombic structures was extremely small and often difficult to detect. Within this investigation we have shown that compositions x = 0.02, 0.03, 0.04 and 0.05 refine well to the polar orthorhombic $P2_1ma$ structure previously identified in the room temperature structural characterisation of $NaNbO_3$. However, it must be noted that a lowering of symmetry to monoclinic cannot be ruled out. At present it is, therefore, believed that in the case of both $NaNbO_3$ and the KNN series the structural differences exhibited between the orthorhombic and monoclinic structures are too subtle to be accurately characterised, using even the highest resolution diffraction data available.

Using high-resolution powder diffraction and ^{23}Na solid-state NMR we have therefore confirmed that the polar, and potentially ferroelectric, $P2_1ma$ phase of $NaNbO_3$ can be produced with relative ease by doping small quantities of K into the $NaNbO_3$ structure. We believe that the formation of this phase is owing to a stabilisation effect, most probably due to factors such as cation size and structural stress/strain. No additional phase transitions were observed for any of the compositions investigated in this particular study. As x was increased the ^{23}Na MQMAS spectra were severely broadened owing to the presence of disorder in the system, thereby preventing any more detailed structural information being gained.

The findings presented in Chapter 3 indicated that phase pure samples of Pbcm $NaNbO_3$ could be synthesised using molten salt methods. This particular synthesis method was also attempted for

$KNbO_3$. However, this proved unsuccessful as each sample contained a mix of the initial starting reagents, K_2CO_3 and Nb_2O_5. Several different reaction conditions were attempted varying annealing temperature and time. However, it appeared that $KNbO_3$ could not be synthesised using this method. Therefore, molten salt techniques were not used to synthesise samples in the KNN series. Similarly, sol-gel methods were not used to synthesise any samples in the KNN series. Each of these methods are, however, possible areas for future investigation. A systematic study of synthesis method for the KNN series could be completed to determine whether any additional polymorphs of $NaNbO_3$ can be produced. The findings presented concentrated solely on characterising the Na environment of each sample in the KNN series. There are, however, two other NMR active nuclei in each sample, ^{39}K (I = 3/2) and ^{17}O (I = 5/2). It would be interesting to investigate the K environment of each sample in the KNN series as it is hoped that this will provide additional detail regarding how K is substituted onto the A site in the $NaNbO_3$ structure. Similarly, it would also be of interest to probe the oxygen environment in each sample. However, to do so post-synthetic enrichment of each sample in the KNN series would be required using ^{17}O enriched O_2 gas. Once completed this would enable the oxygen environments to be investigated in detail and provide information regarding the tilting mechanisms observed in each structure. Therefore, several additional areas of investigation still remain.

4.3.2 Low Percentage Li Doping ($Li_xNa_{1-x}NbO_3$)

In a similar manner to the KNN series, this investigation concentrated on low percentage doping of Li into the $NaNbO_3$ structure. Structure and phase purity were initially verified using l-PXRD, which suggested the presence of a single phase perovskite. All samples were subsequently analysed using high-resolution NPD and s-PXRD. A Rietveld refinement of the x = 0.01 sample using the NPD data was initially completed using the Pbcm structural model[248] for $NaNbO_3$ and is shown in Figure 4.20(a). The quality of fit obtained was relatively poor,

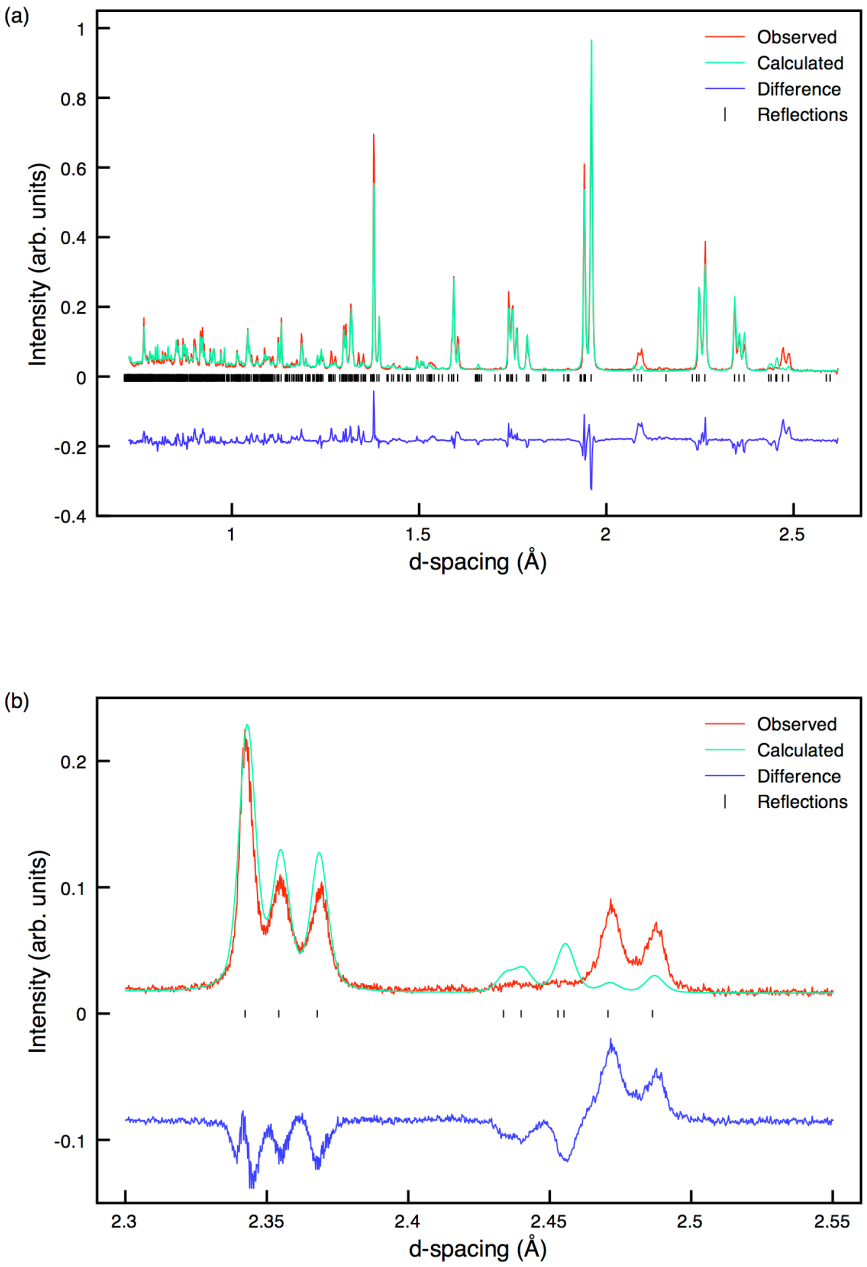

Figure 4.20: (a) Single phase Rietveld refinement of the NPD for $Li_{0.01}Na_{0.99}NbO_3$ using the Pbcm structural model and (b) an expansion of the superstructure region of the refinement, 2.3 Å – 2.55 Å, highlighting the poor level of fit obtained.

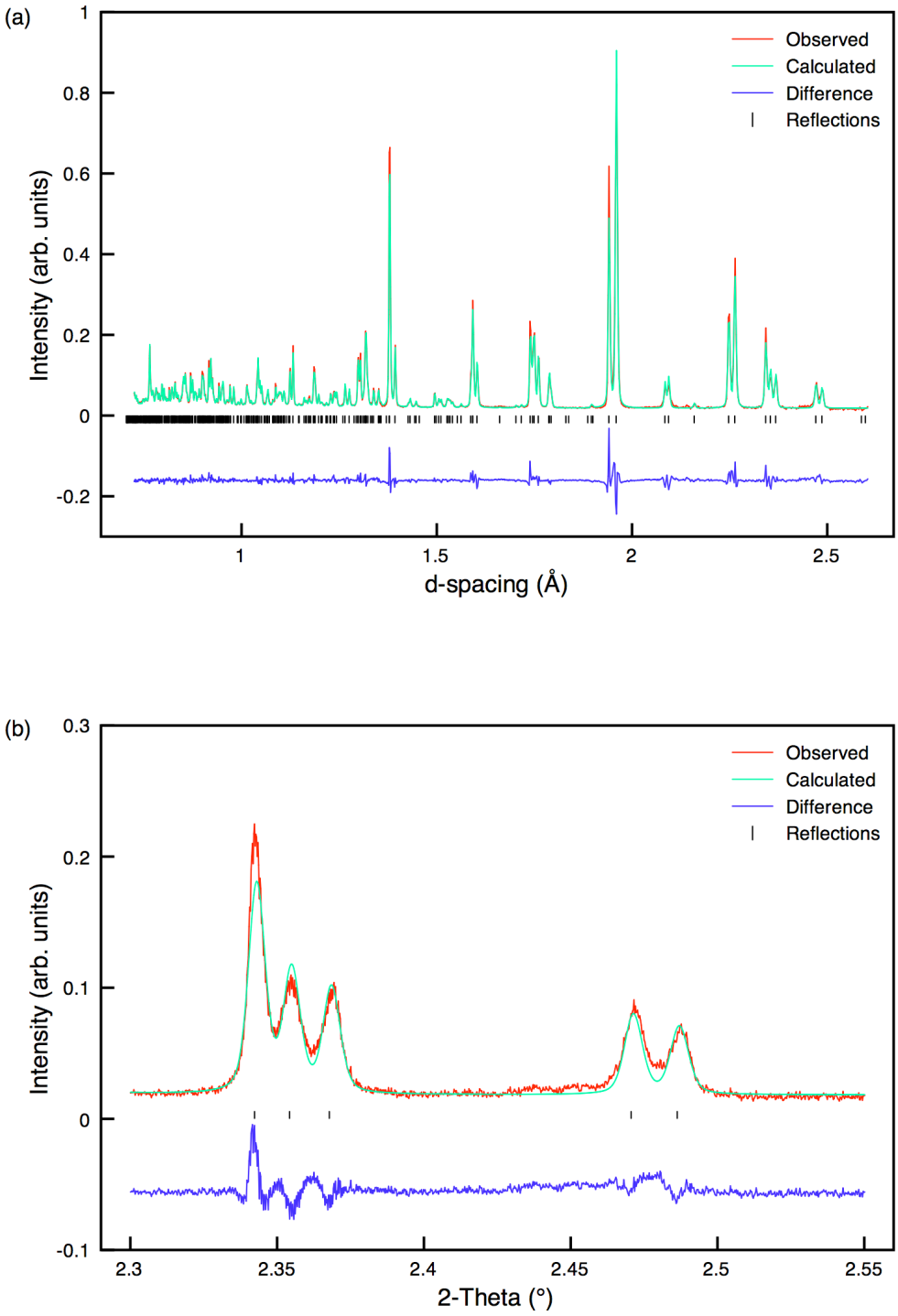

Figure 4.21: (a) Single phase Rietveld refinement of the NPD for $Li_{0.01}Na_{0.99}NbO_3$ using the $P2_1ma$ structural model and (b) an expansion of the superstructure region of the refinement, 2.3 Å – 2.55 Å, highlighting the considerably better level of fit obtained.

Table 4.9: Structural parameters for $Li_{0.01}Na_{0.99}NbO_3$ from NPD data, using isotropic thermal factors. Space group $P2_1ma$, a = 5.57134(6) Å, b = 7.76245(9) Å, c = 5.51288(7) Å and V = 238.417(7) Å^3. χ^2 = 10.9, wR_p = 8.1% and R_p = 7.8%.

Atom	Site	x	y	z	U(iso) × 100 / Å^2
Na1*	2a	0.2643(9)	0	0.7443(8)	1.22(12)
Na2	2b	0.2848(10)	0.5	0.7366(7)	1.69(13)
Nb1	4c	0.2677(4)	0.2497(3)	0.2463(3)	0.12(3)
O1	2a	0.2433(5)	0	0.3126(10)	0.68(10)
O2	2b	0.2283(5)	0.5	0.1923(10)	0.33(9)
O3	4c	0.0205(3)	0.2803(4)	0.5306(5)	1.47(6)
O4	4c	−0.0453(3)	0.2202(4)	0.0371(5)	0.56(5)
*Na 0.99, Li 0.01					

with wR_p = 17.9% and χ^2 = 53.1. Full refinement details for this single phase refinement are given in Appendix III. Most notably the superstructure peaks at ~2.47 Å and ~2.49 Å were not indexed correctly or allocated sufficient intensity using this model. This therefore suggested a different phase of $NaNbO_3$ to be present. It must be noted that $LiNbO_3$[286] possesses a different structure when compared with the orthorhombic phases of $NaNbO_3$. Interestingly, $LiNbO_3$ and the Ilmenite[225] polymorph of $NaNbO_3$ are very similar. The only major difference between the two structures is the presence of cation ordering in $LiNbO_3$. The additional peaks identified in the diffraction pattern did not appear to correlate with this particular phase. This therefore confirmed that the $LiNbO_3$ structure was not adopted at very low percentage doping in the LNN series. The peaks identified did, however, appear to correlate with those highlighted earlier in the KNN series as belonging to the $P2_1ma$ phase of $NaNbO_3$. Therefore, it appeared the $P2_1ma$ polymorph of $NaNbO_3$ was formed upon the addition of very small quantities of Li into the structure. Unlike the $K_{0.01}Na_{0.99}NbO_3$ sample, no additional peaks corresponding to unreacted metal oxides and/or carbonates appeared to be present in the diffraction pattern, suggesting the sample to be a single phase perovskite. Close inspection of the superstructure peaks in the diffraction pattern obtained

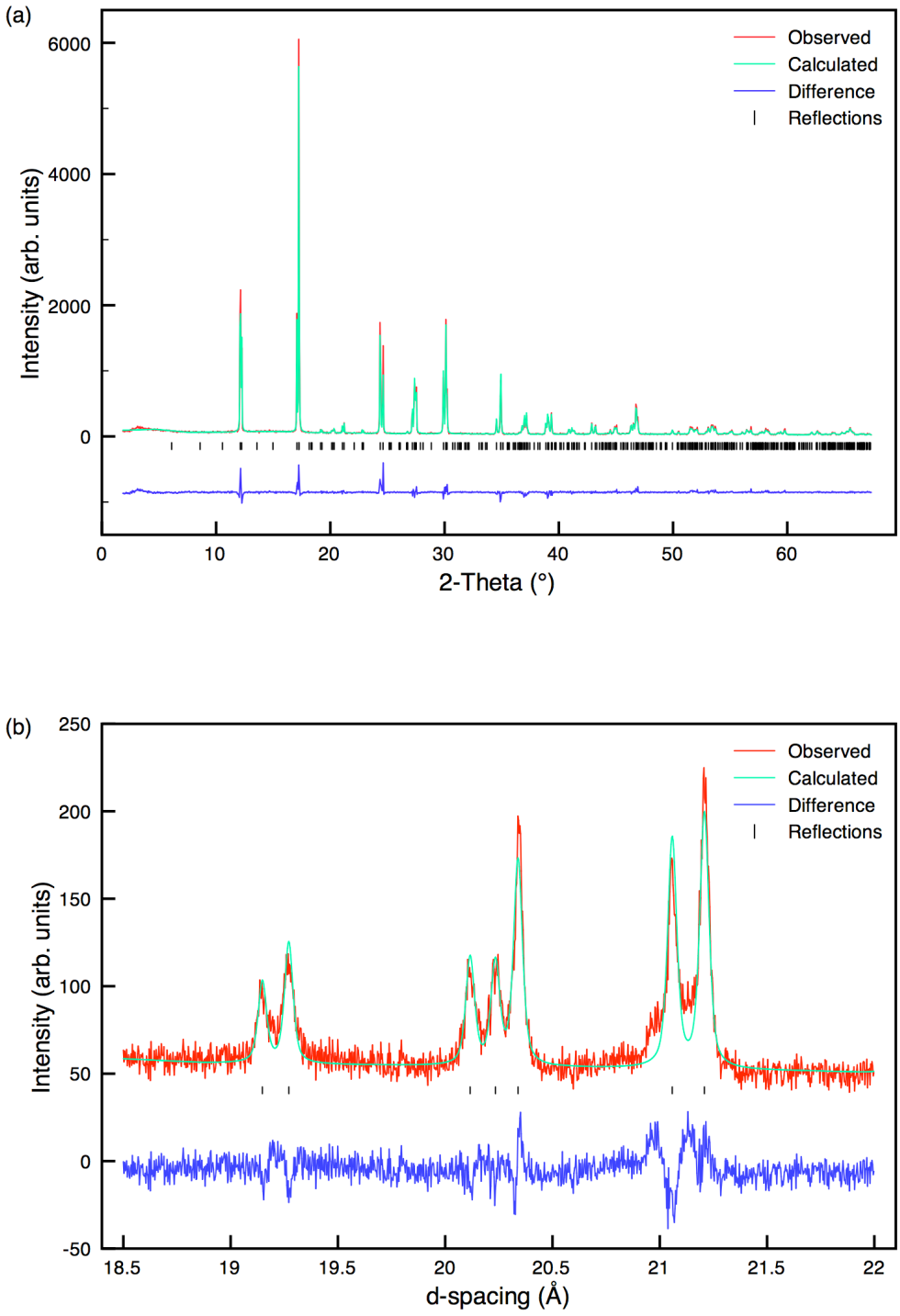

Figure 4.22: (a) Single phase Rietveld refinement of the s-PXRD for $Li_{0.01}Na_{0.99}NbO_3$ using the $P2_1ma$ structural model and (b) an expansion of the superstructure region of the refinement, 2.3 Å – 2.55 Å, highlighting a good level of fit.

Table 4.10: Structural parameters for $Li_{0.01}Na_{0.99}NbO_3$ from s-PXRD data, using isotropic thermal factors. Space group $P2_1ma$, a = 5.57112(3) Å, b = 7.76115(3) Å, c = 5.51243(3) Å and V = 238.348(2) Å^3. χ^2 = 3.3, wR_p = 13.6% and R_p = 10.7%.

Atom	Site	x	y	z	U(iso) × 100 / Å^2
Na1*	2a	0.2483(8)	0	0.7420(10)	1.10(4)
Na2	2b	0.2618(15)	0.5	0.7438(10)	1.40(4)
Nb1	4c	0.2698	0.2500(6)	0.2455(2)	0.97(1)
O1	2a	0.2550(19)	0	0.312(2)	1.57(4)
O2	2b	0.2309(12)	0.5	0.191(2)	1.57(4)
O3	4c	0.0542(14)	0.2764(11)	0.5225(12)	1.57(4)
O4	4c	−0.0175(13)	0.2136(11)	0.0522(12)	1.57(4)
*Na 0.99, Li 0.01					

for the $Li_{0.01}Na_{0.99}NbO_3$ sample revealed the presence of solely the $P2_1ma$ polymorph, as shown in Figure 4.20(b). This was in contrast to the $K_{0.01}Na_{0.99}NbO_3$ sample in the KNN series where small quantities of the Pbcm phase were found. A Rietveld refinement was therefore completed for the NPD data using solely the $P2_1ma$ structural model.[228] This produced a considerably better quality of fit, with wR_p = 8.1% and χ^2 = 10.9, as shown in Figure 4.21(a). Using the $P2_1ma$ model the peaks previously identified at ~2.47 Å and ~2.49 Å as being incorrectly modelled using the Pbcm phase were subsequently fitted. This is shown in the expansion of the region 2.3 Å – 2.55 Å shown in Figure 4.21(b). Full refinement details can be found in Table 4.9. Corresponding bond distances are given in Appendix III.

The superstructure peaks present in diffraction patterns are well known to be magnified by neutrons, and so the interpretation of even the subtlest of changes in this region is considerably easier when using NPD data. Such distinctions are, however, considerably harder to make using s-PXRD data as the superstructure peaks are, typically, of much lower intensity, making it extremely challenging to detect subtle changes to the superstructure. In many cases it is often very difficult to successfully distinguish these peaks from the background, owing to their very low

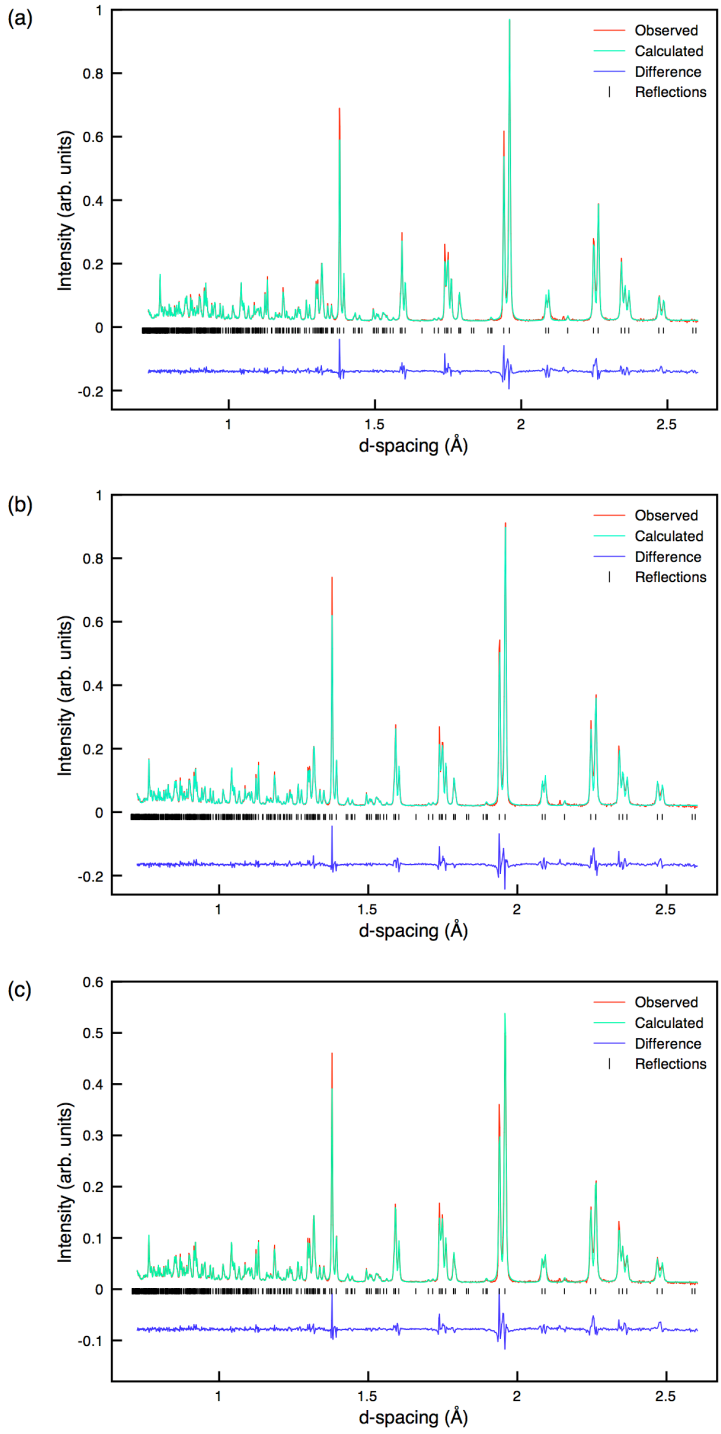

Figure 4.23: (a) Single phase Rietveld refinements completed using the NPD and $P2_1ma$ structural model for (a) $Li_{0.02}Na_{0.98}NbO_3$, (b) $Li_{0.03}Na_{0.97}NbO_3$ and (c) $Li_{0.04}Na_{0.96}NbO_3$.

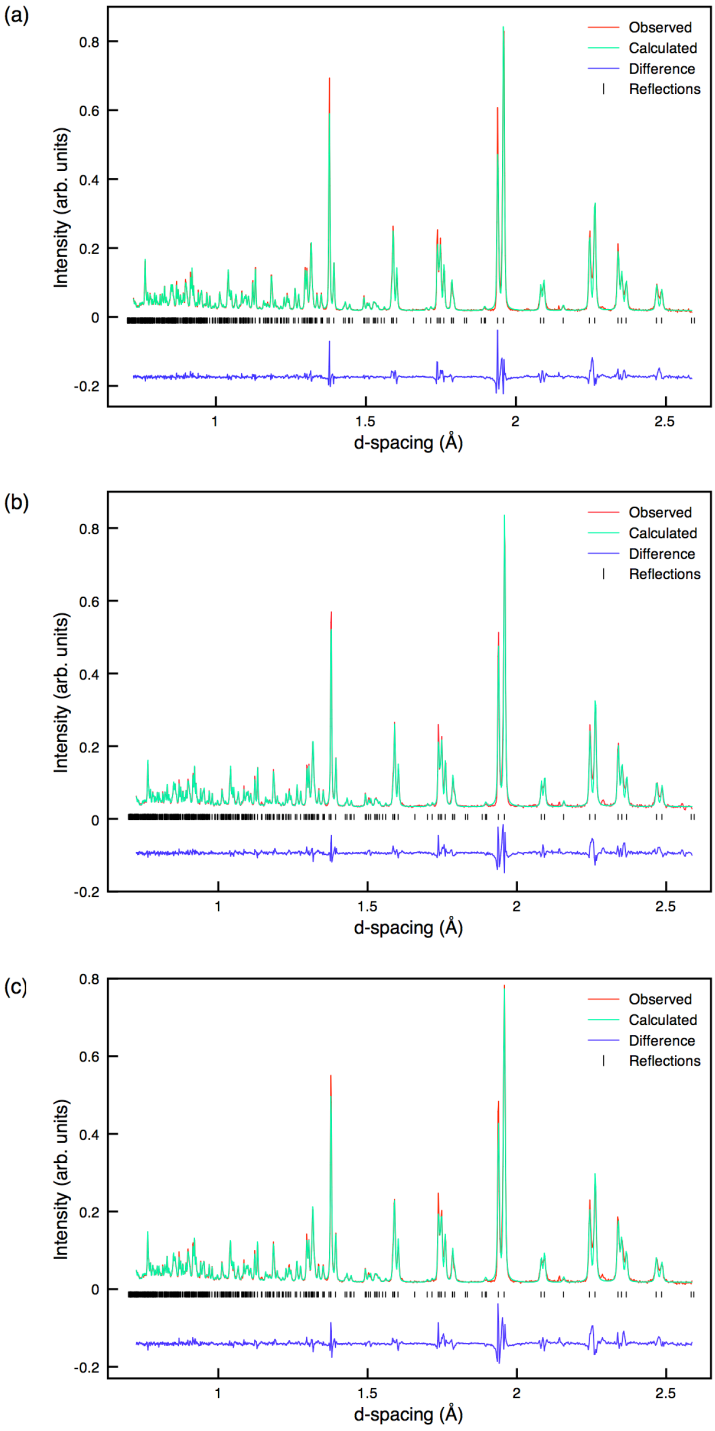

Figure 4.24: (a) Single phase Rietveld refinements completed using the NPD and $P2_1ma$ structural model for (a) $Li_{0.05}Na_{0.95}NbO_3$, (b) $Li_{0.06}Na_{0.94}NbO_3$ and (c) $Li_{0.07}Na_{0.93}NbO_3$.

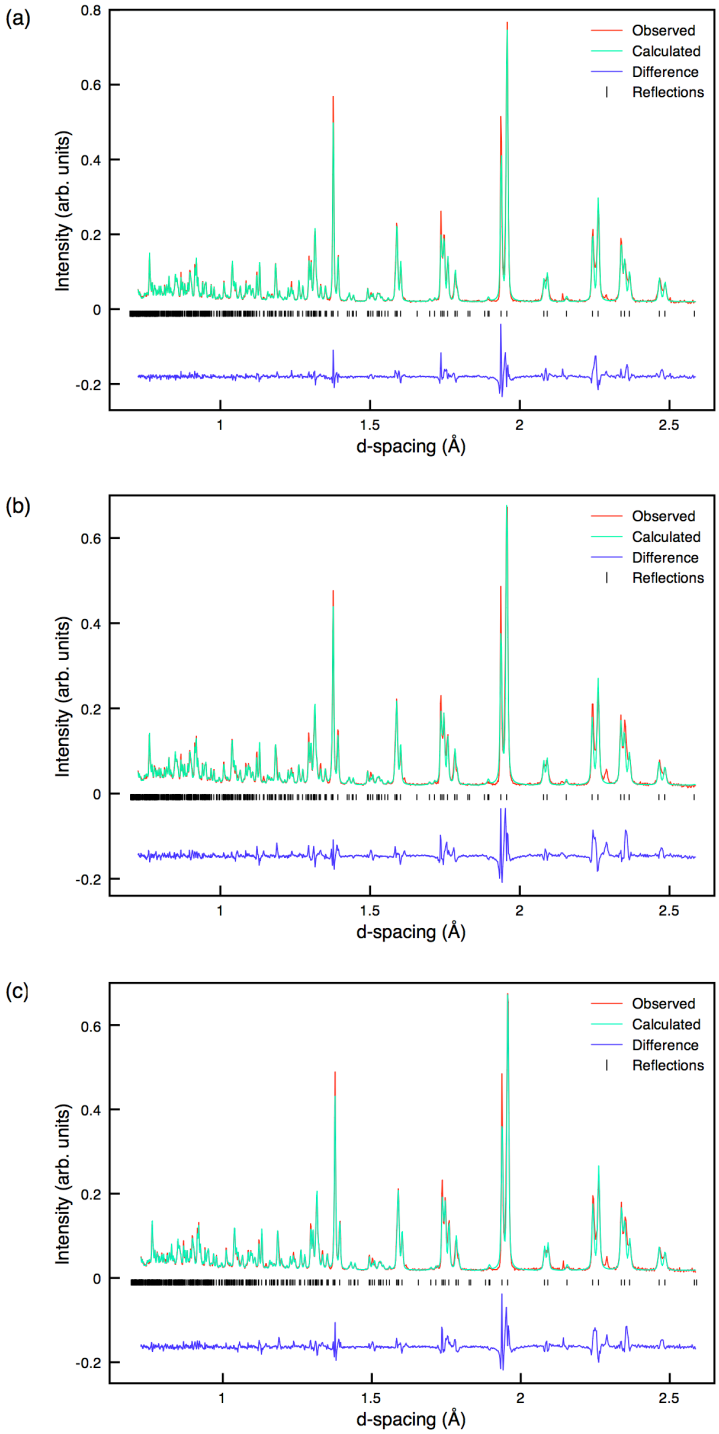

Figure 4.25: (a) Single phase Rietveld refinements completed using the NPD and $P2_1ma$ structural model for (a) $Li_{0.08}Na_{0.92}NbO_3$, (b) $Li_{0.09}Na_{0.91}NbO_3$ and (c) $Li_{0.10}Na_{0.90}NbO_3$.

Table 4.11: Structural parameters for $Li_{0.02}Na_{0.98}NbO_3$ from NPD data, using isotropic thermal factors. Space group $P2_1ma$, a = 5.57198(6) Å, b = 7.76086(8) Å, c = 5.51281(6) Å and V = 238.392(7) Å^3. $\chi^2 = 14.9$, $wR_p = 7.5\%$ and $R_p = 7.1\%$.

Atom	Site	x	y	z	U(iso) × 100 / Å^2
Na1*	2a	0.2606(8)	0	0.7432(7)	1.21(12)
Na2	2b	0.2841(9)	0.5	0.7357(7)	1.54(11)
Nb1	4c	0.2682	0.2497(3)	0.2455(3)	0.06(2)
O1	2a	0.2408(3)	0	0.3126(9)	0.66(9)
O2	2b	0.2249(3)	0.5	0.1929(9)	0.40(8)
O3	4c	0.0226(4)	0.2809(4)	0.5353(4)	1.04(5)
O4	4c	−0.0465(4)	0.2209(3)	0.0363(4)	0.58(5)

*Na 0.98, Li 0.02

Table 4.12: Structural parameters for $Li_{0.06}Na_{0.94}NbO_3$ from NPD data, using isotropic thermal factors. Space group $P2_1ma$, a = 5.57196(7) Å, b = 7.75106(10) Å, c = 5.50466(7) Å and V = 237.738(8) Å^3. $\chi^2 = 15.4$, $wR_p = 6.8\%$ and $R_p = 6.6\%$.

Atom	Site	x	y	z	U(iso) × 100 / Å^2
Na1*	2a	0.2552(9)	0	0.7536(9)	0.82(13)
Na2	2b	0.2869(10)	0.5	0.7322(9)	1.95(13)
Nb1	4c	0.2679	0.2501(3)	0.2441(3)	0.06(3)
O1	2a	0.2385(4)	0	0.3161(9)	0.63(10)
O2	2b	0.2225(4)	0.5	0.1886(9)	0.48(9)
O3	4c	0.0221(5)	0.2831(4)	0.5377(4)	0.85(5)
O4	4c	−0.0471(4)	0.2202(4)	0.0347(5)	0.95(5)

*Na 0.94, Li 0.06

Table 4.13: Structural parameters for $Li_{0.08}Na_{0.92}NbO_3$ from NPD data, using isotropic thermal factors. Space group $P2_1ma$, a = 5.56963(9) Å, b = 7.74910(12) Å, c = 5.49995(9) Å and V = 237.376(10) Å^3. χ^2 = 21.4, wR_p = 8.9% and R_p = 8.6%.

Atom	Site	x	y	z	U(iso) × 100 / Å^2
Na1	2a	0.2557(10)	0	0.7522(11)	0.88(15)
Na2	2b	0.2829(12)	0.5	0.7322(10)	2.18(16)
Nb1	4c	0.2680	0.2500(3)	0.2441(4)	0.08(3)
O1	2a	0.2387(4)	0	0.3171(10)	0.71(11)
O2	2b	0.2228(4)	0.5	0.1873(10)	0.50(9)
O3	4c	0.0230(5)	0.2838(4)	0.5378(5)	0.97(6)
O4	4c	−0.0468(5)	0.2198(4)	0.0349(5)	0.94(6)
*Na 0.92, Li 0.08					

intensity. The accurate assignment of the superstructure peaks in the NPD data therefore enabled an accurate single phase Rietveld refinement to be completed for the x = 0.01 sample using the s-PXRD data. The quality of refinement obtained was relatively good, with wR_p = 13.6% and χ^2 = 3.3. The full Rietveld refinement is shown in Figure 4.22(a), with a corresponding expansion of the superstructure peaks, 18.5° - 22°, also shown in Figure 4.22(b). The two peaks previously identified as belonging to the $P2_1ma$ phase in the s-PXRD data, 19.2° and 19.3°, were well fitted and in good agreement with the NPD findings. Full refinement details can be found in Table 4.10. All associated bond distances obtained from this refinement can be found in Appendix III.

Given the obvious presence of the $P2_1ma$ phase in the x = 0.01 sample similar single phase Rietveld refinements were completed using the $P2_1ma$ model[228] for all remaining samples in the LNN series. Each sample displayed good agreement with the presence of the polar $P2_1ma$ phase. All Rietveld refinements completed using the NPD data for all compositions can be found in Figures 4.23, 4.24 and 4.25 respectively. Full refinement details for x = 0.02, 0.06 and 0.08 can be found in Tables 4.11 - 4.13, with all corresponding wR_p and χ^2 values. All Rietveld refinement details for all remaining samples in this LNN series can be found in

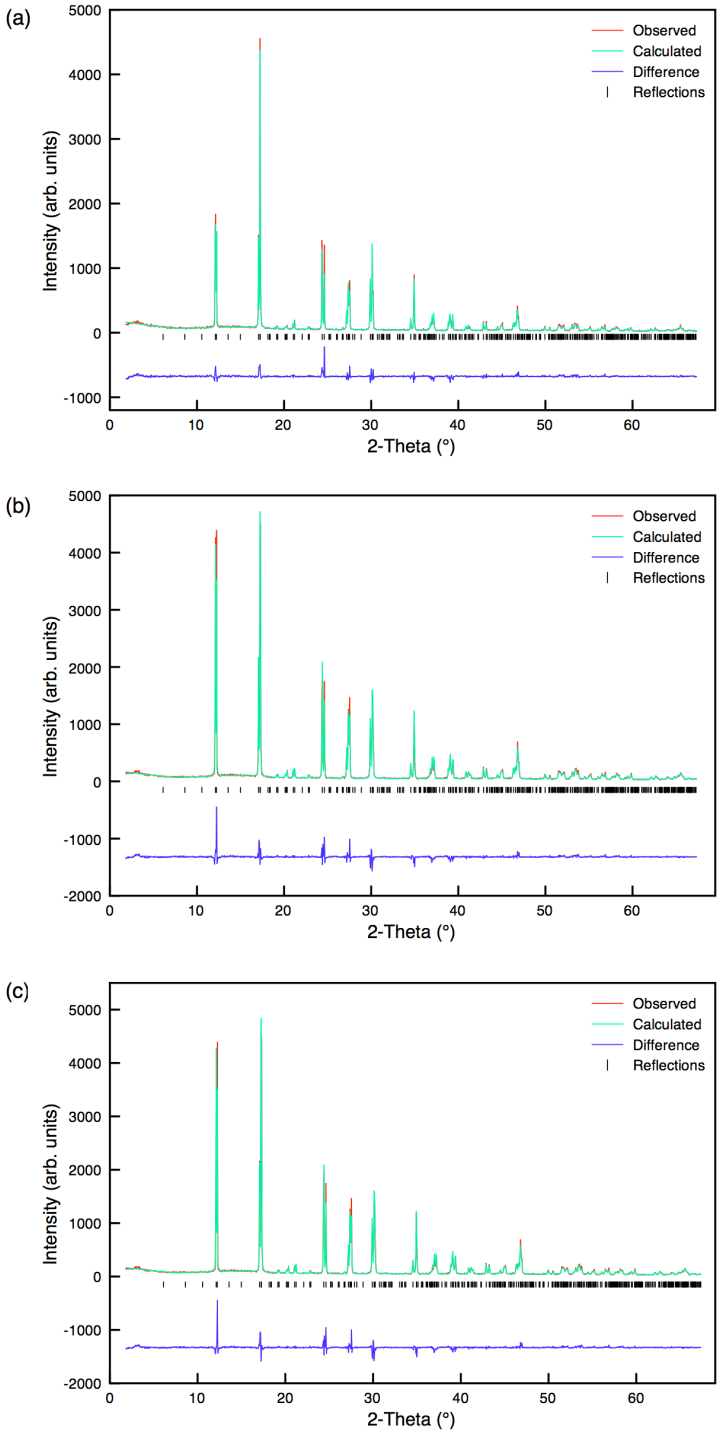

Figure 4.26: (a) Single phase Rietveld refinements completed using the s-PXRD and $P2_1ma$ structural model for (a) $Li_{0.02}Na_{0.98}NbO_3$, (b) $Li_{0.03}Na_{0.97}NbO_3$ and (c) $Li_{0.04}Na_{0.96}NbO_3$.

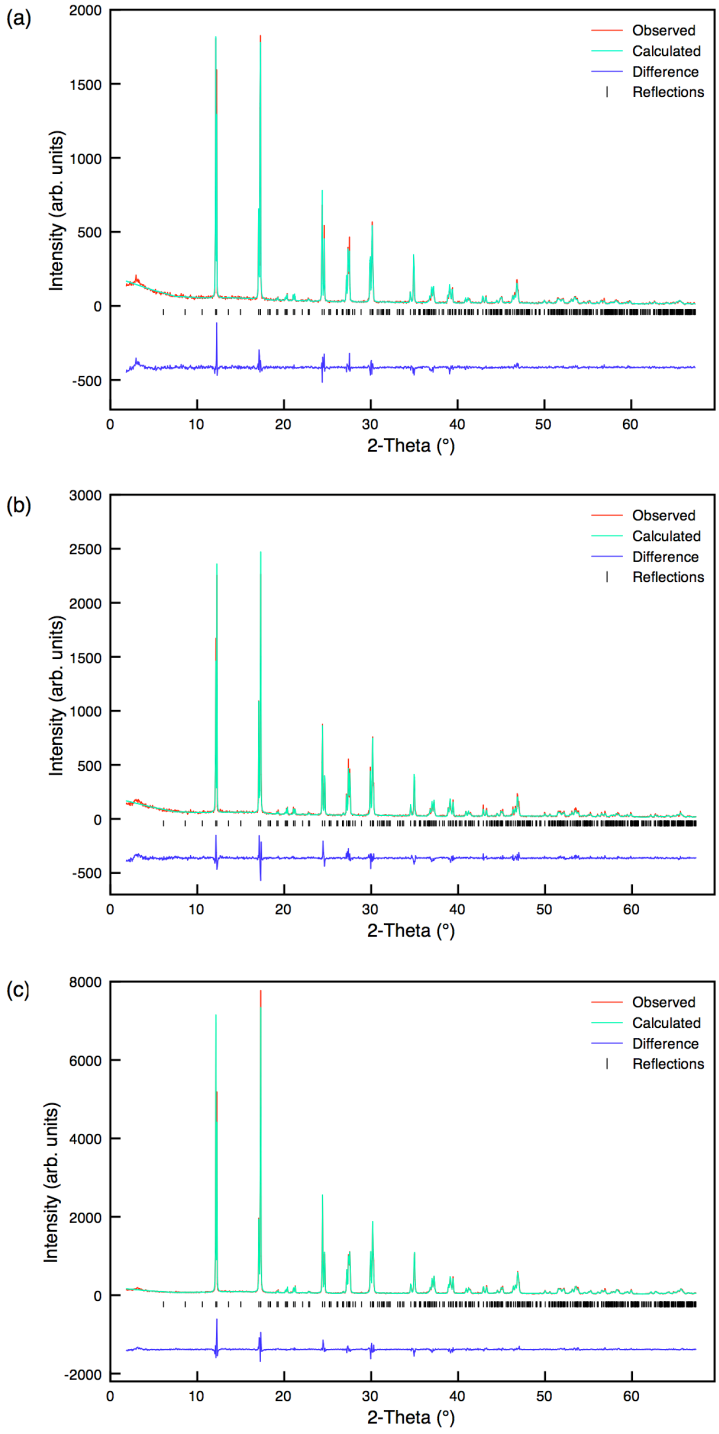

Figure 4.27: (a) Single phase Rietveld refinements completed using the s-PXRD and $P2_1ma$ structural model for (a) $Li_{0.05}Na_{0.95}NbO_3$, (b) $Li_{0.06}Na_{0.94}NbO_3$ and (c) $Li_{0.07}Na_{0.93}NbO_3$.

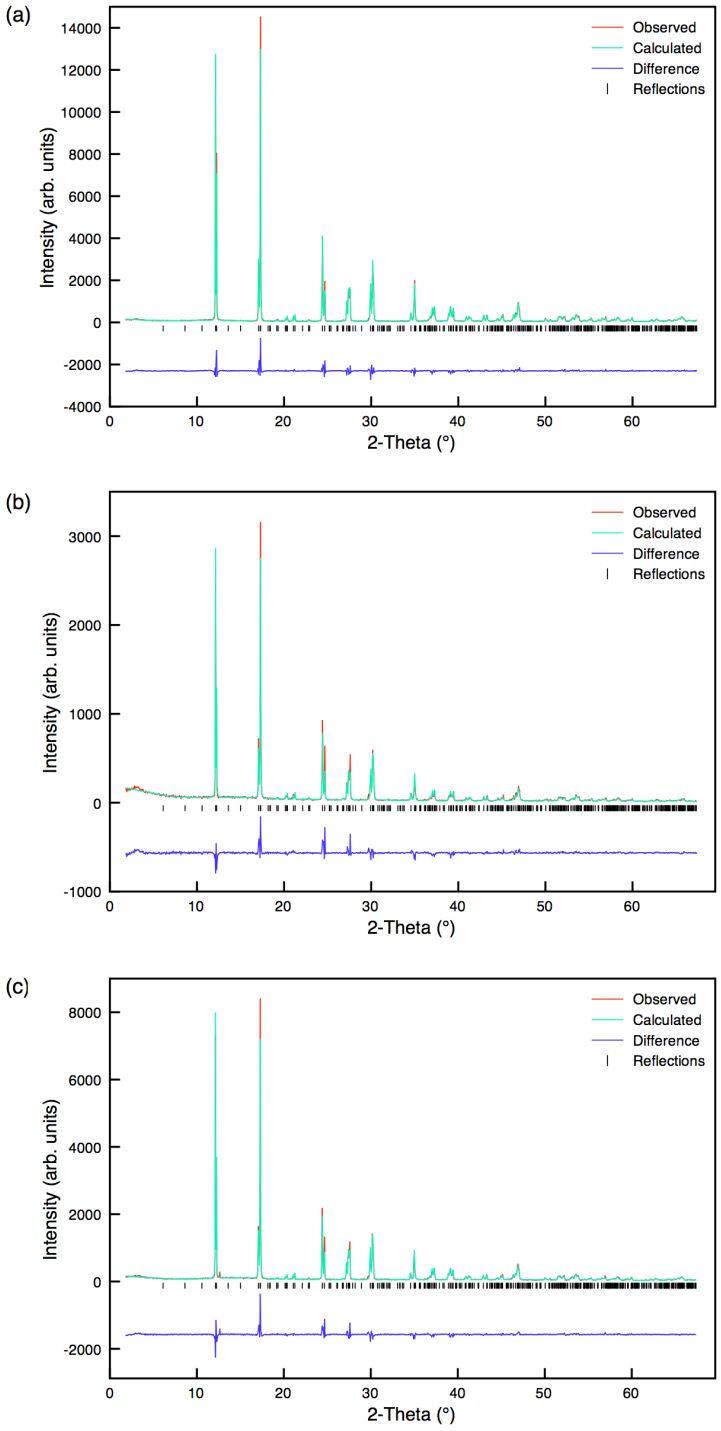

Figure 4.28: (a) Single phase Rietveld refinements completed using the s-PXRD and $P2_1ma$ structural model for (a) $Li_{0.08}Na_{0.92}NbO_3$, (b) $Li_{0.09}Na_{0.91}NbO_3$ and (c) $Li_{0.10}Na_{0.90}NbO_3$.

Table 4.14: Structural parameters for $Li_{0.02}Na_{0.98}NbO_3$ from s-PXRD data, using isotropic thermal factors. Space group $P2_1ma$, a = 5.57141(3) Å, b = 7.75924(4) Å, c = 5.51211(3) Å and V = 238.288(3) Å^3. $\chi^2 = 2.9$, $wR_p = 12.9\%$ and $R_p = 9.9\%$.

Atom	Site	x	y	z	U(iso) × 100 / Å^2
Na1*	2a	0.266(2)	0	0.7420(11)	1.72(5)
Na2	2b	0.2915(12)	0.5	0.7433(11)	1.19(9)
Nb1	4c	0.2719	0.2496(2)	0.2454(2)	1.02(1)
O1	2a	0.2463(19)	0	0.3119(18)	1.70(5)
O2	2b	0.2243(13)	0.5	0.191(3)	1.70(5)
O3	4c	0.0433(15)	0.2822(16)	0.5492(12)	1.70(5)
O4	4c	−0.0252(11)	0.2207(16)	0.0248(15)	1.70(5)

*Na 0.98, Li 0.02

Table 4.15: Structural parameters for $Li_{0.06}Na_{0.94}NbO_3$ from s-PXRD data, using isotropic thermal factors. Space group $P2_1ma$, a = 5.57290(3) Å, b = 7.74826(4) Å, c = 5.50523(4) Å and V = 237.717(3) Å^3. $\chi^2 = 2.7$, $wR_p = 14.9\%$ and $R_p = 11.2\%$.

Atom	Site	x	y	z	U(iso) × 100 / Å^2
Na1*	2a	0.268(3)	0	0.7531(13)	2.30(4)
Na2	2b	0.2947(11)	0.5	0.7355(10)	1.1(3)
Nb1	4c	0.2721	0.2503(4)	0.2437(2)	1.28(9)
O1	2a	0.262(3)	0	0.318(2)	2.11(6)
O2	2b	0.251(2)	0.5	0.186(2)	2.11(6)
O3	4c	0.0195(14)	0.2760(8)	0.5359(12)	2.11(6)
O4	4c	−0.0424(8)	0.2005(8)	0.0342(15)	2.11(6)

*Na 0.94, Li 0.06

Table 4.16: Structural parameters for $Li_{0.08}Na_{0.92}NbO_3$ from s-PXRD data, using isotropic thermal factors. Space group $P2_1ma$, a = 5.56853(3) Å, b = 7.74747(4) Å, c = 5.49902(4) Å and V = 237.239(1) Å^3. $\chi^2 = 4.4$, $wR_p = 13.5\%$ and $R_p = 10.3\%$.

Atom	Site	x	y	z	U(iso) × 100 / Å^2
Na1*	2a	0.2772(14)	0	0.7495(8)	0.9(2)
Na2	2b	0.2994(10)	0.5	0.7383(8)	1.7(2)
Nb1	4c	0.2704	0.2501	0.2434(1)	0.54(1)
O1	2a	0.2523(17)	0	0.3196(11)	2.06(7)
O2	2b	0.2399(14)	0.5	0.1891(12)	2.06(7)
O3	4c	0.0256(11)	0.2788(8)	0.5440(9)	2.06(7)
O4	4c	−0.0399(7)	0.2095(7)	0.0016(12)	2.06(7)

*Na 0.92, Li 0.08

Appendix III. Similarly, all associated bond lengths obtained from each refinement are also given in Appendix III. Single phase Rietveld refinements (using the $P2_1ma$ model[228]) were also completed using s-PXRD data for all samples in the range $0.02 \leq x \leq 0.1$ and, as observed for NPD, a good level of fit was obtained in each case. All Rietveld refinements completed using s-PXRD data are shown in Figures 4.26, 4.27 and 4.28. Structural parameters obtained for compositions x = 0.02, 0.06 and 0.08 can be found in Tables 4.14 – 4.16 respectively. Full refinement details obtained for all remaining samples in this series and corresponding structural parameters, such as bond distances, can be found in Appendix III. It must be noted that as x was increased an increase in peak broadening was observed in both the NPD and s-PXRD data. The peak broadening indicates the gradual introduction of disorder to the LNN system, as expected. Cation ordering across the A site is considerably harder to achieve when compared with B-site cation ordering. It is commonly only observed in anion deficient or double perovskites and therefore the likelihood of achieving A-site cation ordering in the $Li_xNa_{1-x}NbO_3$ solid-solution is extremely low as it does not meet the strict requirements previously detailed in Chapter 1. It is, therefore, of little surprise that the substitution of Li into the $NaNbO_3$ structure produces a

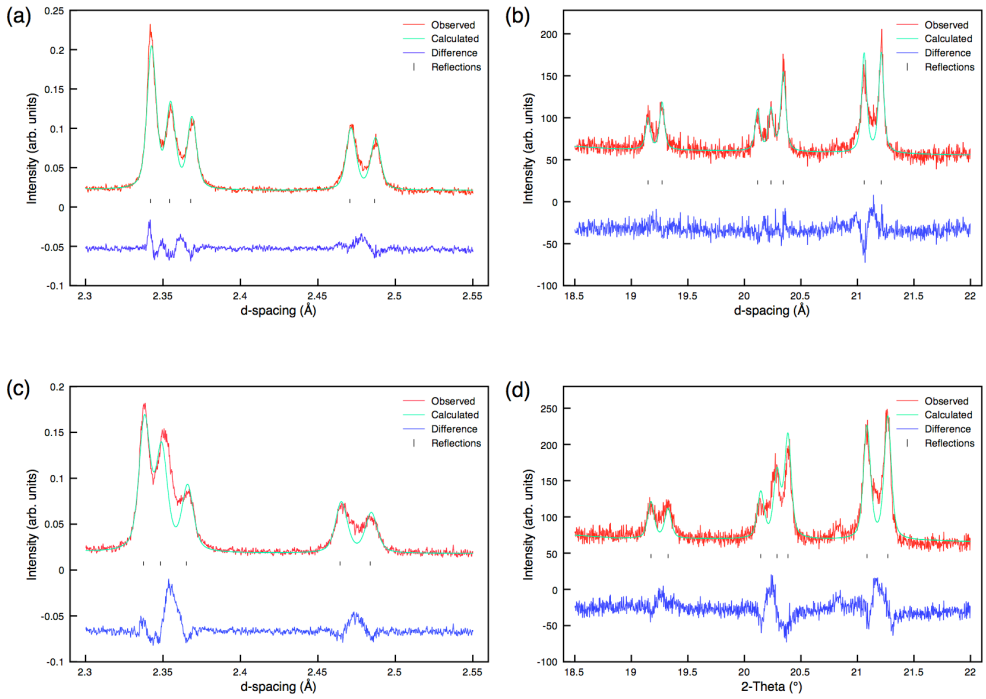

Figure 4.29: Expansions of the superstructure peaks obtained from Rietveld refinement of NPD and s-PXRD data for (a,b) $Li_{0.02}Na_{0.98}NbO_3$ and (c,d) $Li_{0.10}Na_{0.90}NbO_3$ highlighting the extent of peak broadening exhibited with increasing Li content in the LNN solid-solution.

series of disordered compounds. To highlight the extent of peak broadening exhibited in both the NPD and s-PXRD data an expansion of the superstructure peaks in the x = 0.02 and x = 0.1 samples are shown and compared in Figure 4.29(a-d) for both the NPD and s-PXRD datasets obtained. The significant loss in resolution of the observed peaks is clear. This highlights the effect disorder can produce on even the highest resolution diffraction data.

As expected, the substitution of Li into $NaNbO_3$ produced an associated change in both the lattice parameters and unit cell volume. As x was increased a decrease in the lattice parameters a, b and c was observed and, as a direct result, a corresponding decrease in the unit cell volume was also observed. Identical behaviour was exhibited in both the NPD and s-PXRD data and the variation of each parameter with x for each dataset is shown in Figures 4.30, 4.31, 4.32 and 4.33, respectively. As Li^+

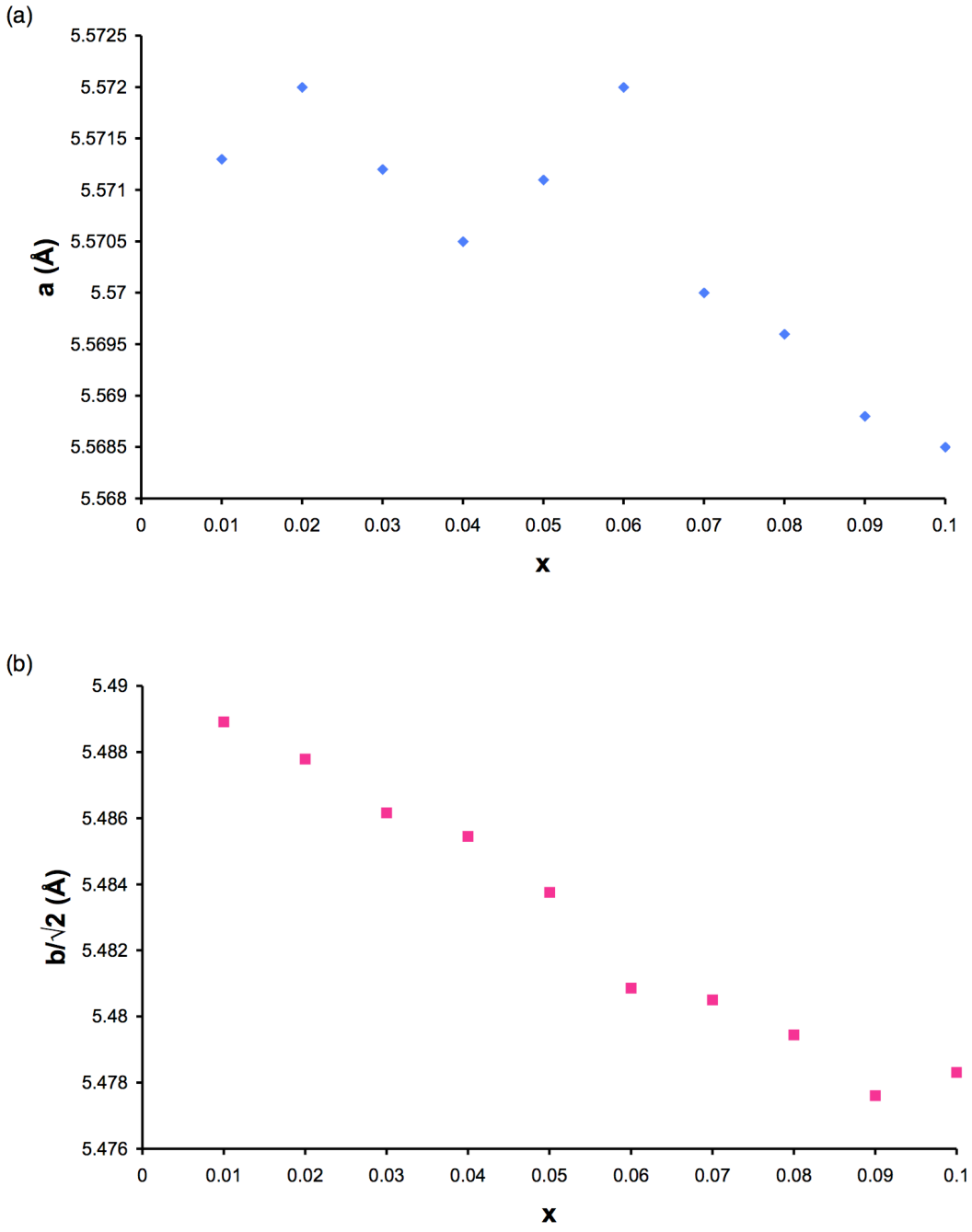

Figure 4.30: Variation observed in the unit cell parameters (a) a and (b) b with increasing x for $Li_xNa_{1-x}NbO_3$ using the NPD data. Note that for ease of comparison with unit cell parameters a and c, the b parameter has been divided by √2. The estimated error bars are smaller than the symbols used and are therefore not shown.

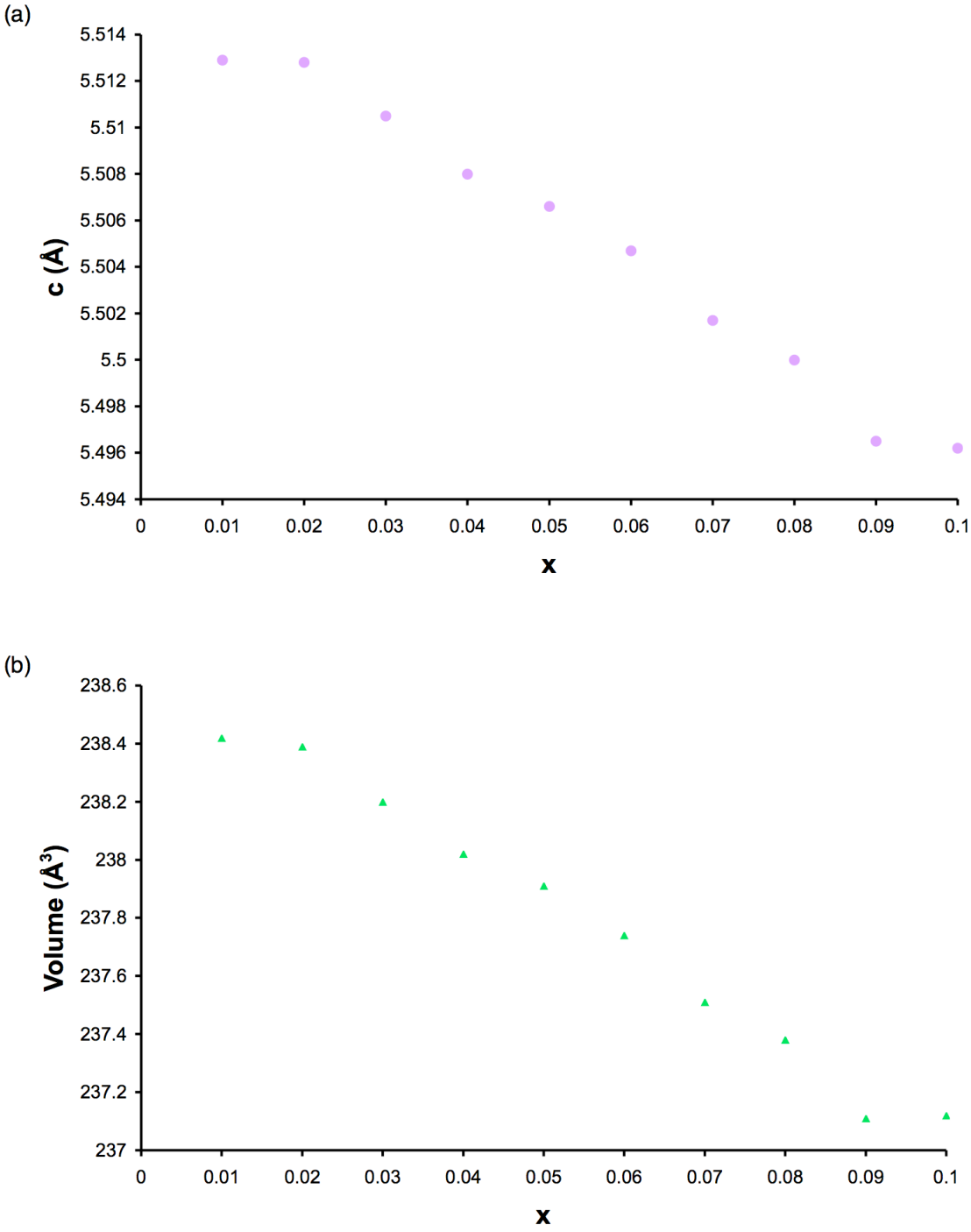

Figure 4.31: Variation observed in (a) the unit cell parameter c and (b) the unit cell volume with increasing x for $Li_xNa_{1-x}NbO_3$ using the NPD data. The estimated error bars are smaller then the symbols used and are therefore not shown.

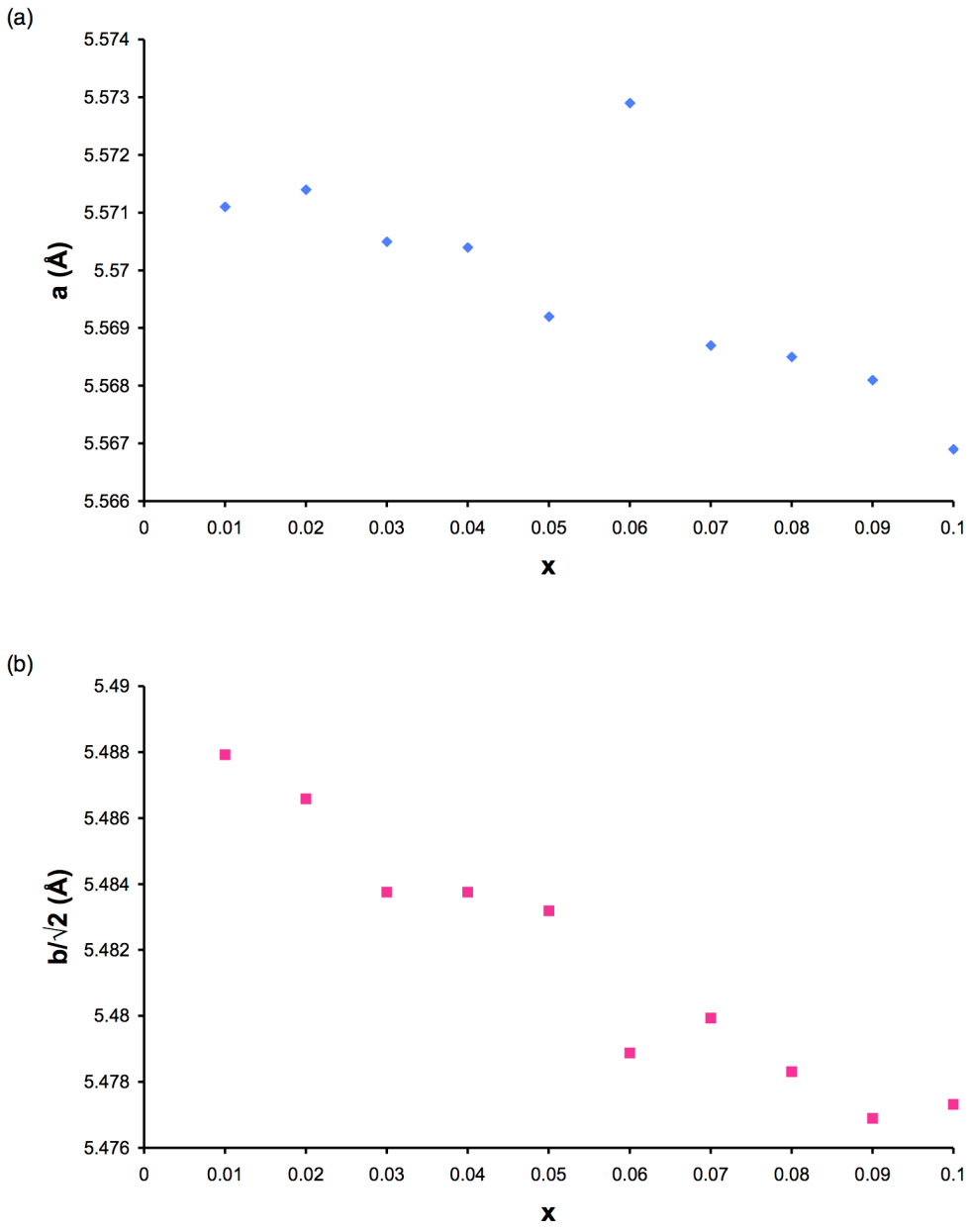

Figure 4.32: Variation observed in the unit cell parameters (a) a and (b) b with increasing x for $Li_xNa_{1-x}NbO_3$ using the s-PXRD data. Note that for ease of comparison with unit cell parameters a and c, the b parameter has been divided by √2. The estimated error bars are smaller than the symbols used and are therefore not shown.

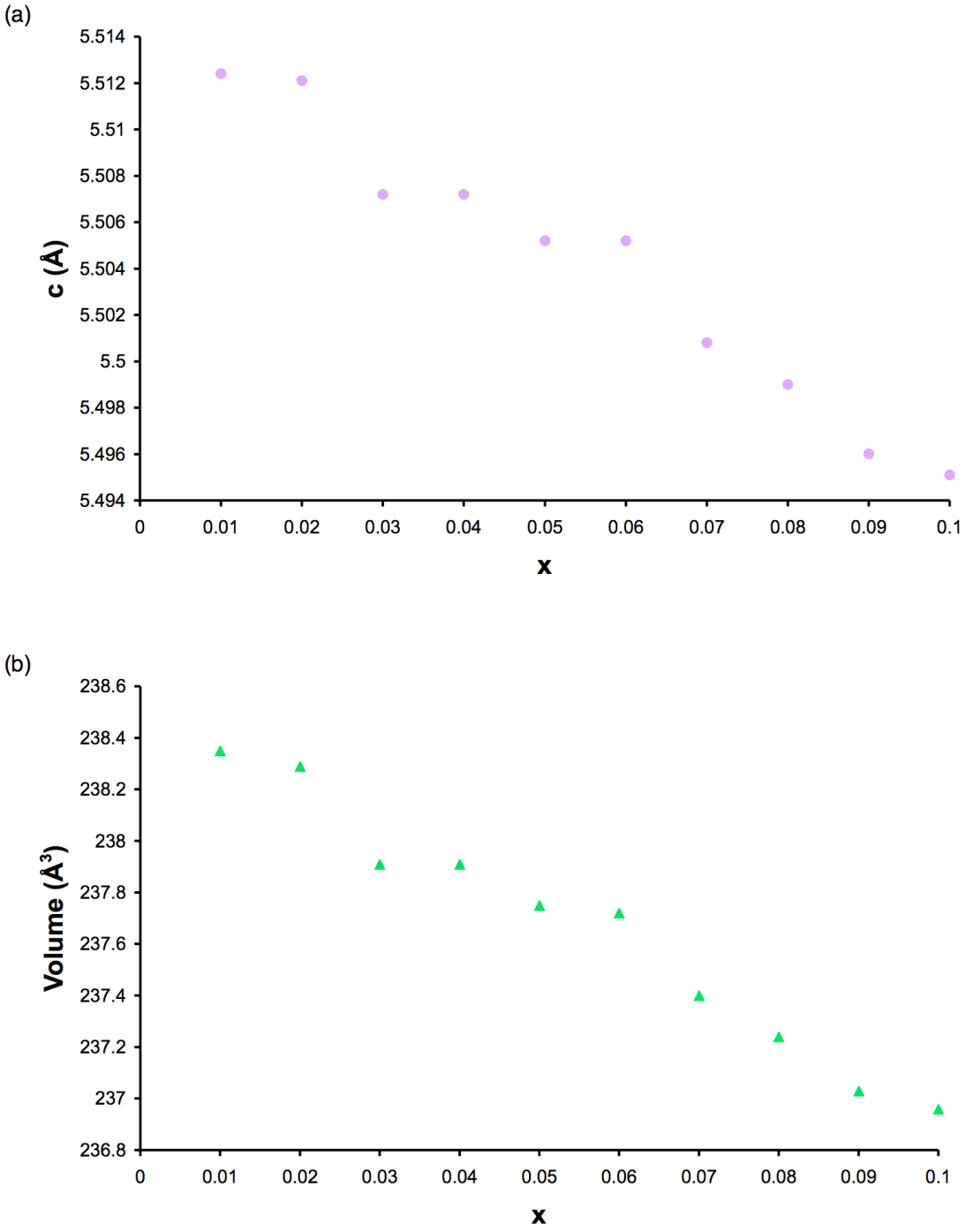

Figure 4.33: Variation observed in (a) the unit cell parameter c and (b) the unit cell volume with increasing x for $Li_xNa_{1-x}NbO_3$ using the s-PXRD data. The estimated error bars are smaller than the symbols used and are therefore not shown.

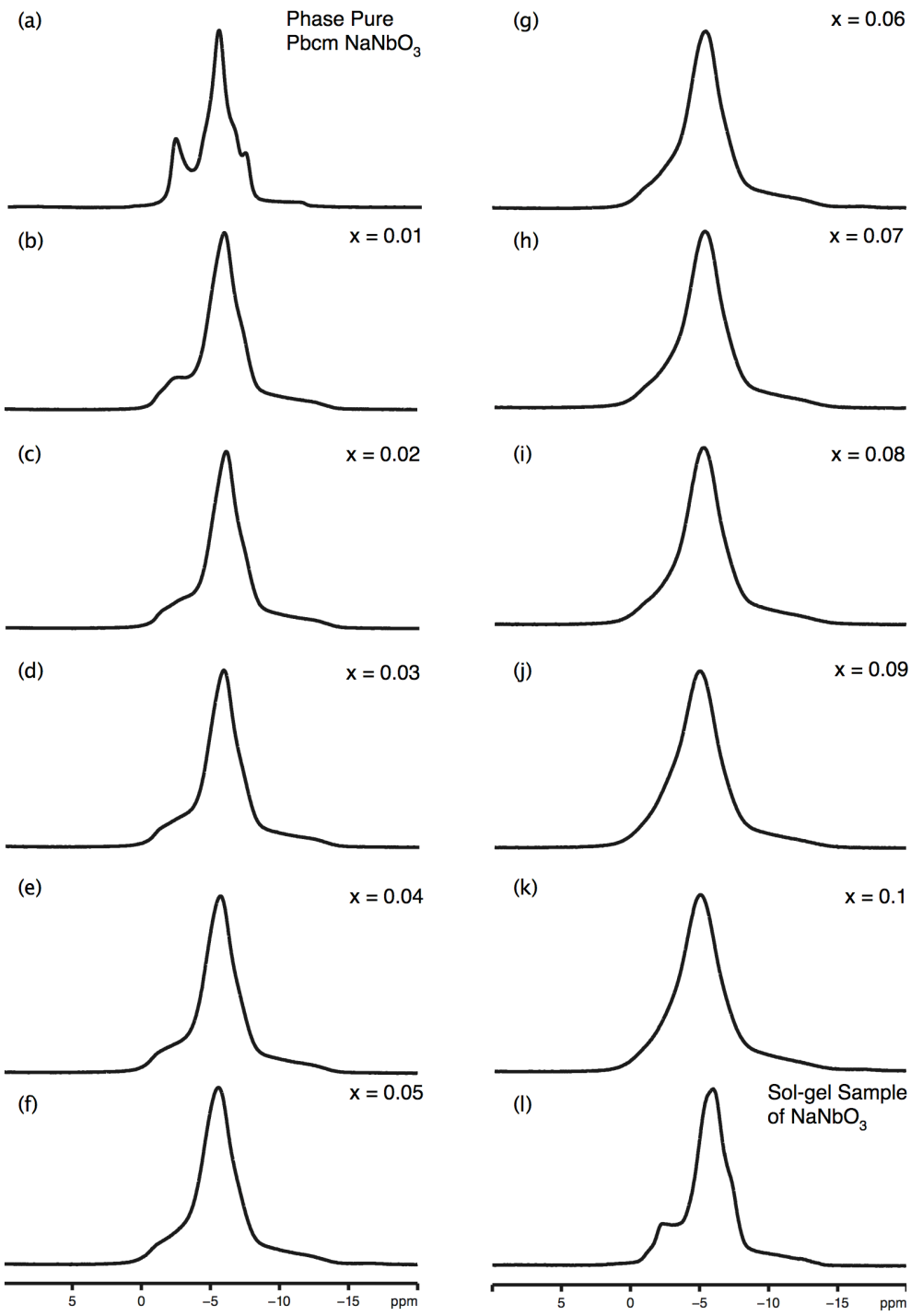

Figure 4.34: Comparison of ^{23}Na (14.1 T) MAS NMR spectra obtained for the LNN series. Also shown in (a) and (l) for comparison are phase pure Pbcm $NaNbO_3$ (synthesised using molten salt techniques) and the sol-gel sample of $NaNbO_3$ composed of ~90% of the $P2_1ma$ and ~10% of the Pbcm polymorphs of $NaNbO_3$.

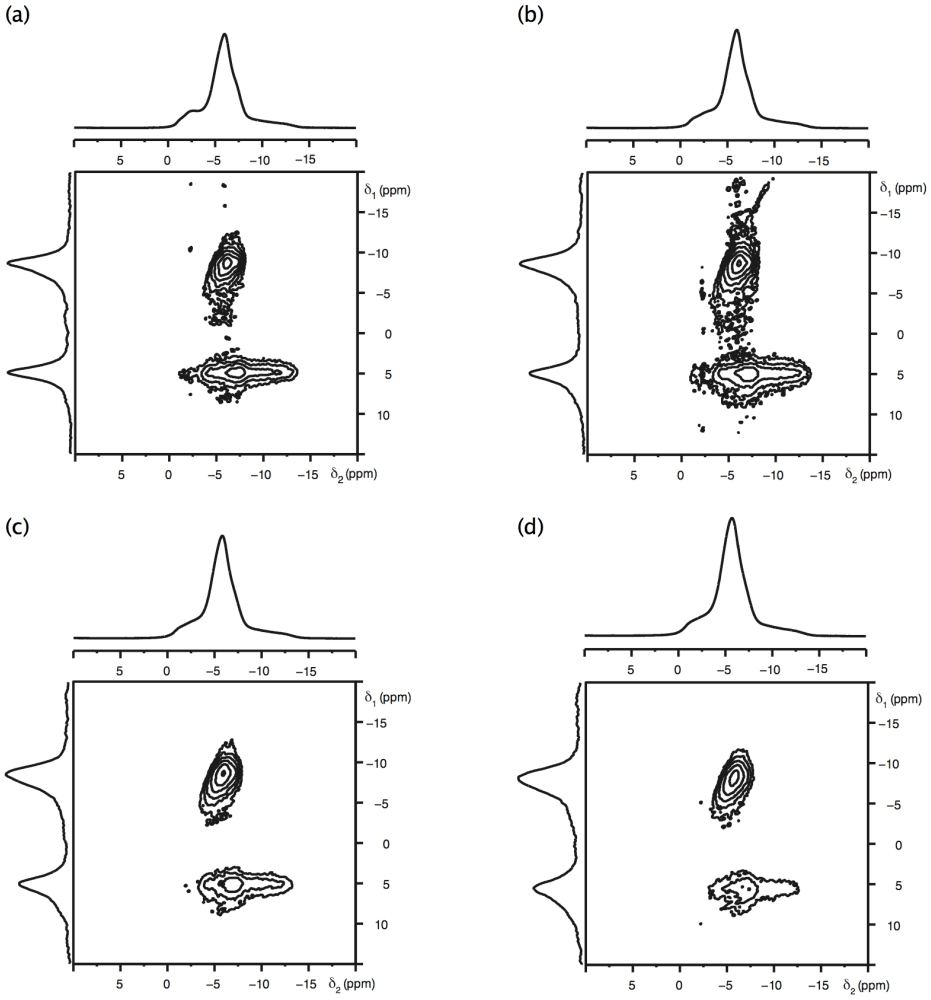

Figure 4.35: ^{23}Na MAS NMR spectra, triple-quantum MAS NMR spectra (14.1 T), and corresponding isotropic projections for (a) $Li_{0.01}Na_{0.99}NbO_3$, (b) $Li_{0.02}Na_{0.98}NbO_3$, (c) $Li_{0.03}Na_{0.97}NbO_3$ and (d) $Li_{0.04}Na_{0.96}NbO_3$. The extent of spectral broadening increases with increasing x, indicating the presence of disorder.

(0.76 Å) is substituted into the structure it would be expected to cause the unit cell to contract, in good agreement with the findings presented.

A ^{23}Na MAS NMR spectrum was recorded for each composition in the LNN series and, as observed for the KNN series, each appeared subtly different. These differences are highlighted in Figures 4.34(b-k) where all MAS spectra recorded in this series are compared. Each lineshape appears broadened relative to phase pure Pbcm (Figure 4.34(a)), with many of the distinct features lost owing to line broadening. Again, the broadening exhibited is characteristic of both inefficient removal of the

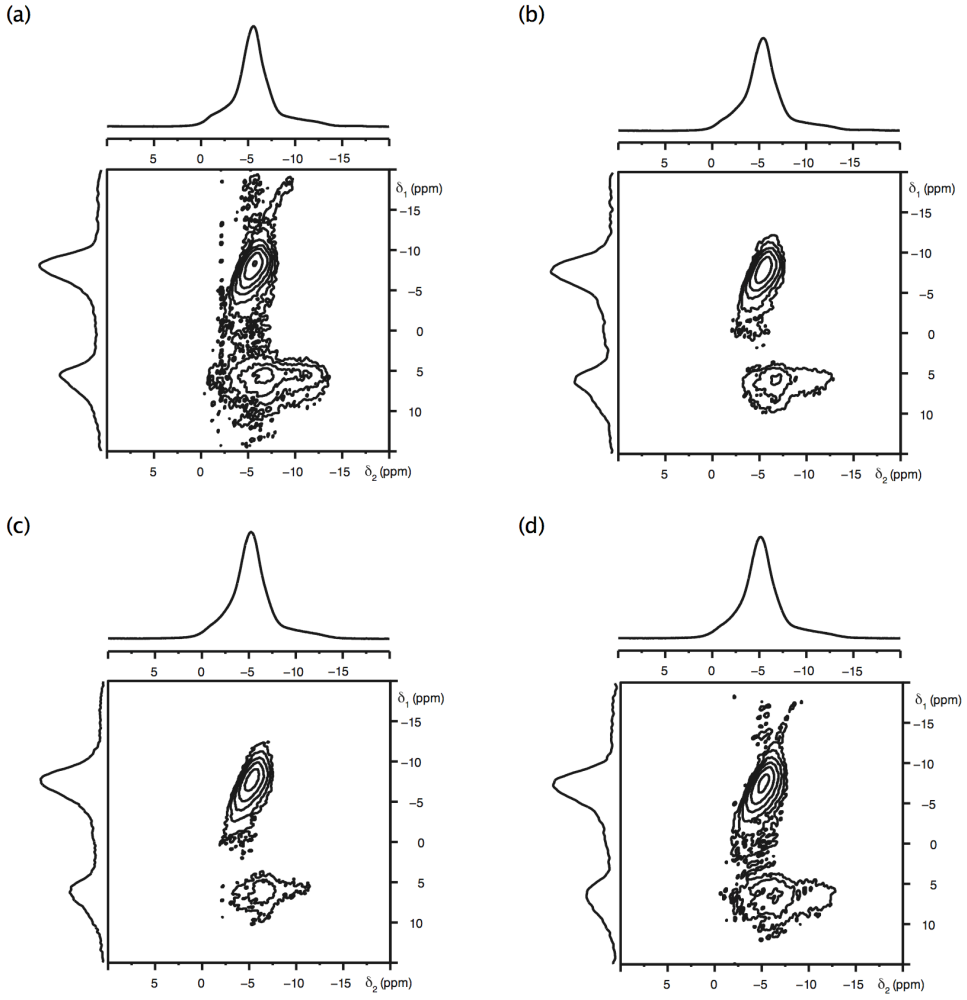

Figure 4.36: ^{23}Na MAS NMR spectra, triple-quantum MAS NMR spectra (14.1 T), and corresponding isotropic projections for (a) $Li_{0.05}Na_{0.95}NbO_3$, (b) $Li_{0.06}Na_{0.94}NbO_3$, (c) $Li_{0.07}Na_{0.93}NbO_3$ and (d) $Li_{0.08}Na_{0.92}NbO_3$. The extent of spectral broadening increases with increasing x, indicating the presence of disorder.

quadrupolar interaction and the gradual introduction of disorder to the system. The ^{23}Na MQMAS NMR spectra recorded for each composition are shown in Figures 4.35, 4.36 and 4.37 respectively. Each composition displays two relatively broadened Na sites. The ridge broadening exhibited by each site appears to be predominantly along +2.125, suggesting it is owing to a distribution of chemical shifts. This appears to be in agreement with the findings previously observed for the KNN series. These findings are also in good agreement with the peak broadening exhibited earlier in both the NPD and s-PXRD data. The two sites

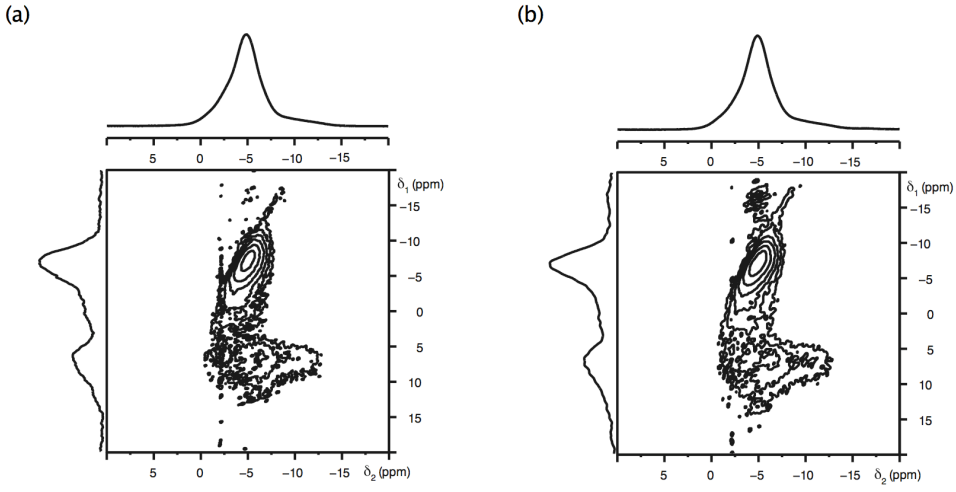

Figure 4.37: ^{23}Na MAS NMR spectra, triple-quantum MAS NMR spectra (14.1 T), and corresponding isotropic projections for (a) $Li_{0.09}Na_{0.91}NbO_3$ and (b) $Li_{0.10}Na_{0.90}NbO_3$. The extent of spectral broadening increases with increasing x, indicating the presence of disorder.

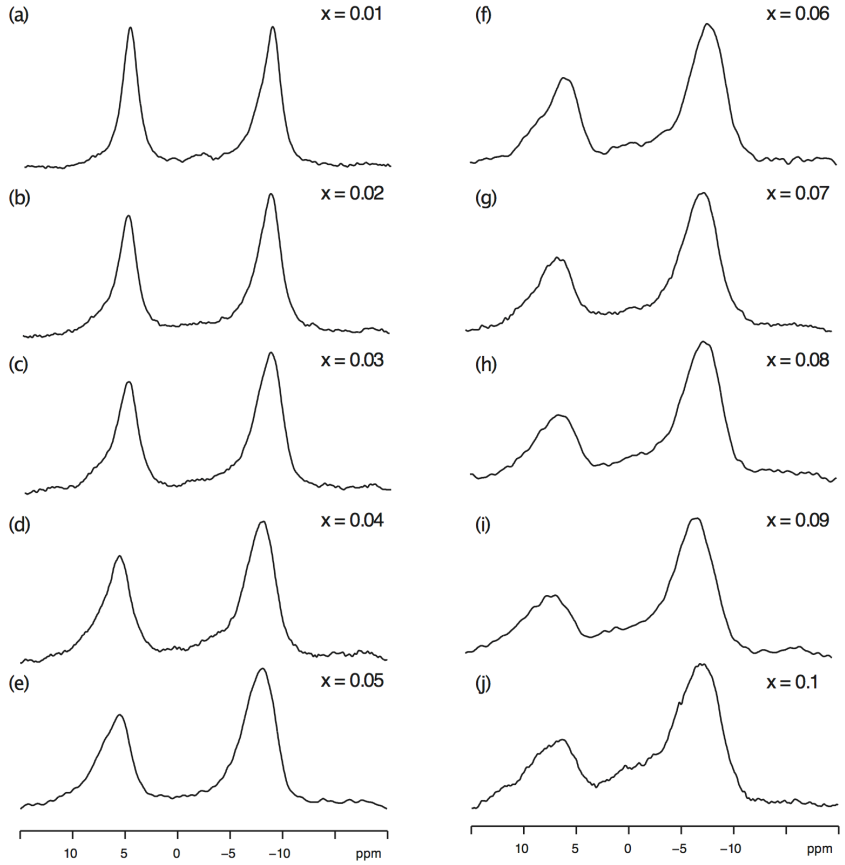

Figure 4.38: Comparison of the isotropic projections obtained from all two-dimensional ^{23}Na MQMAS NMR spectra recorded in the LNN series.

Table 4.17: ^{23}Na (14.1 T) MAS NMR parameters obtained for the $Li_{1-x}Na_xNbO_3$, where $0.01 \leq x \leq 0.1$. All parameters were obtained from the position of the centre of gravity.

x	$\langle\delta_1\rangle$ (ppm)	$\langle\delta_{iso}\rangle$ (ppm)	$\langle P_Q\rangle$ / MHz
0.01	−8.3	−4.7(5)	1.2(2)
	5.0	−1.2(5)	2.4(2)
0.02	−8.2	−4.7(5)	1.2(2)
	5.4	−1.0(5)	2.5(2)
0.03	−7.9	−4.5(5)	1.2(2)
	5.7	−0.9(5)	2.5(2)
0.04	−7.7	−4.5(5)	1.2(2)
	5.7	−1.0(5)	2.5(2)
0.05	−7.7	−4.4(5)	1.1(2)
	6.3	−0.6(5)	2.5(2)
0.06	−7.7	−4.4(5)	1.1(2)
	6.0	−0.8(5)	2.5(2)
0.07	−7.2	−4.1(5)	1.1(2)
	6.3	−0.5(5)	2.4(2)
0.08	−7.1	−4.1(5)	1.1(2)
	6.6	−0.4(5)	2.5(2)
0.09	−6.8	−4.0(5)	1.1(2)
	6.6	−0.4(5)	2.5(2)
0.10	−6.8	−3.9(5)	1.1(2)
	7.1	0.0(5)	2.4(2)

displayed in each spectrum appear to correlate with the two known Na sites identified earlier in the $P2_1ma$ polymorph of $NaNbO_3$. This broadening is mirrored in the isotropic projection of each site onto the δ_1 axis in each spectrum. To highlight the extent of broadening exhibited a comparison of all isotropic projections obtained from each spectrum recorded in the LNN series are shown in Figure 4.38. Considerable spectral broadening was exhibited by many of the samples in this series, particularly for the latter members. To highlight the variation observed in peak broadening with increasing x the linewidth ($\Delta\upsilon_{1/2}$) for each peak in the isotropic projection has been plotted against x. The variation of each peak with increasing x is shown in Figures 4.39(a) and (b). The broadening exhibited appears to increase linearly with increasing Li content. Owing to the presence of disorder $\langle P_Q \rangle$ values have been obtained for each site and are given in Table 4.17.

Both the high-resolution diffraction and ^{23}Na MAS NMR data presented are in good agreement. Each suggests doping the $NaNbO_3$ structure with Li in the range $0.01 \leq x \leq 0.1$ produces the polar $P2_1ma$ polymorph of $NaNbO_3$. The system does, however, become increasingly disordered with increasing Li content. The findings presented are in good agreement with recent work by Yuzyuk *et al.*,[283] in which a phase transition from the orthorhombic Pbma phase (alternative setting Pbcm) to a polar orthorhombic $P2_1ma$ phase was observed when small quantities of Li were added to the system (~2-3%). Hence, both investigations suggest the addition of Li into the $NaNbO_3$ structure consistently produces the $P2_1ma$ polymorph of $NaNbO_3$. Our findings also suggest that doping with quantities as low as 1% can produce the same polar phase. However, it must be noted that it becomes increasingly challenging to investigate materials such as the LNN series as the presence of disorder can often hinder the extraction of important structural information. There are, at present, several different techniques and methods being developed within NMR to aid in both the investigation and understanding of complex disordered materials.

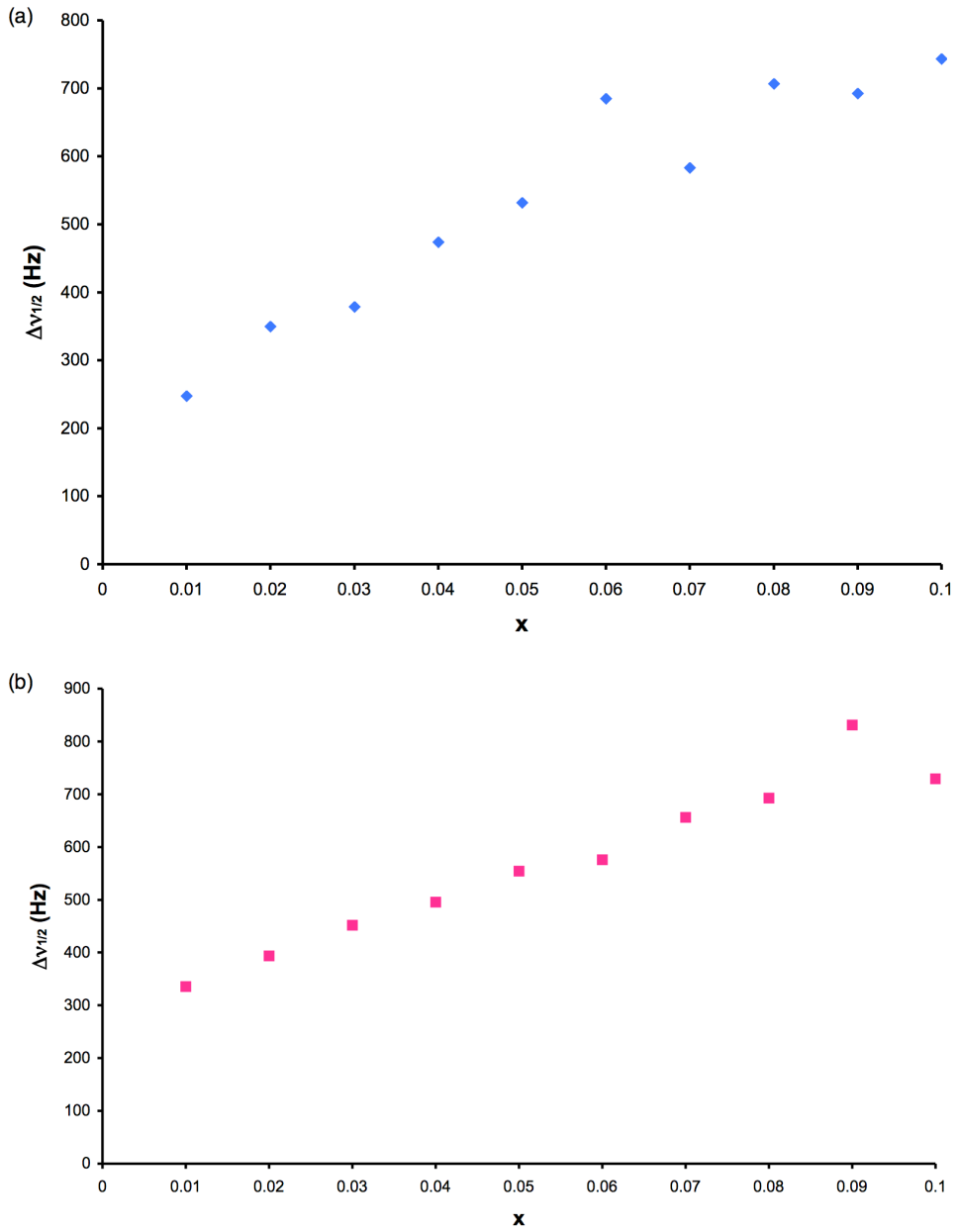

Figure 4.39: Variation in δ_1 linewidth of the resonances corresponding to the two Na sites (a) $\langle\delta_1\rangle \approx 5.0$ ppm and (b) $\langle\delta_1\rangle \approx -8.3$ ppm extracted from the spectra of $Li_xNa_{1-x}NbO_3$, with increasing x in Figures 4.35, 4.36 and 4.37, respectively.

4.3.3 The $Na_{1-x}Sr_{x/2}\square_{x/2}NbO_3$ Solid-Solution

Unlike the KNN and LNN series relatively large quantities of Sr (~10-40%) were doped into the $NaNbO_3$ structure, producing the solid-solution $Na_{1-x}Sr_{x/2}\square_{x/2}NbO_3$. In this particular system an A site vacancy is produced each time a strontium atom is introduced to the structure. This

is owing to an aliovalent substitution on the A site. The phase purity of each sample in the series was initially verified using l-PXRD and in each there appeared to be the presence of an unknown impurity phase, believed to be either a non-stoichiometric mix of reagents or unreacted metal oxides and/or carbonates. However, recent work by Torres-Pardo *et al.*,[287] suggests that for compositions greater than x = 0.4 a tetragonal tungsten bronze (TTB) phase is present as an impurity phase. Therefore, it is possible the unknown phase is a TTB composition. The quantity of this unknown phase appeared to vary from as little as a few percent up to ~10-15% depending on composition. This made it difficult to establish adequate reaction conditions to remove it completely from each composition. Samples containing the smallest quantities of the unknown phase were subsequently investigated using high-resolution s-PXRD. Peaks belonging to the unknown phase were clearly visible in each diffraction pattern recorded. Torres-Pardo *et al.*,[285] recently investigated the $Na_{1-x}Sr_{x/2}\square_{x/2}NbO_3$ series, concentrating on the compositional region $0 < x \leq 0.2$. Their work suggests the introduction of Sr into the $NaNbO_3$ structure produced a polar orthorhombic phase in space group $P2_1ma$. Interestingly, however, their x = 0.1 sample appeared to display a region of phase coexistence between two very similar orthorhombic phases, Pbma (alternative setting Pbcm) and $P2_1ma$. It was, therefore, of particular interest to determine whether a similar region of phase coexistence was exhibited in our x = 0.1 sample. Interestingly, the two phase region identified by Torres-Pardo and co-workers was found using TEM rather than the more conventional technique of powder diffraction. The room temperature study completed earlier for $NaNbO_3$ highlighted that the two orthorhombic phases of $NaNbO_3$ possessed virtually identical X-ray diffraction patterns and a considerable amount of work was required to accurately distinguish between the two. The superstructure peaks identified in both the NPD and s-PXRD data have thus far proved vital in separating the two phases. Therefore, to accurately determine precisely which phase(s) were present in the solid-solution $Na_{1-x}Sr_{x/2}\square_{x/2}NbO_3$ the region $2\theta = 18.5 – 22°$ was closely examined in each diffraction pattern.

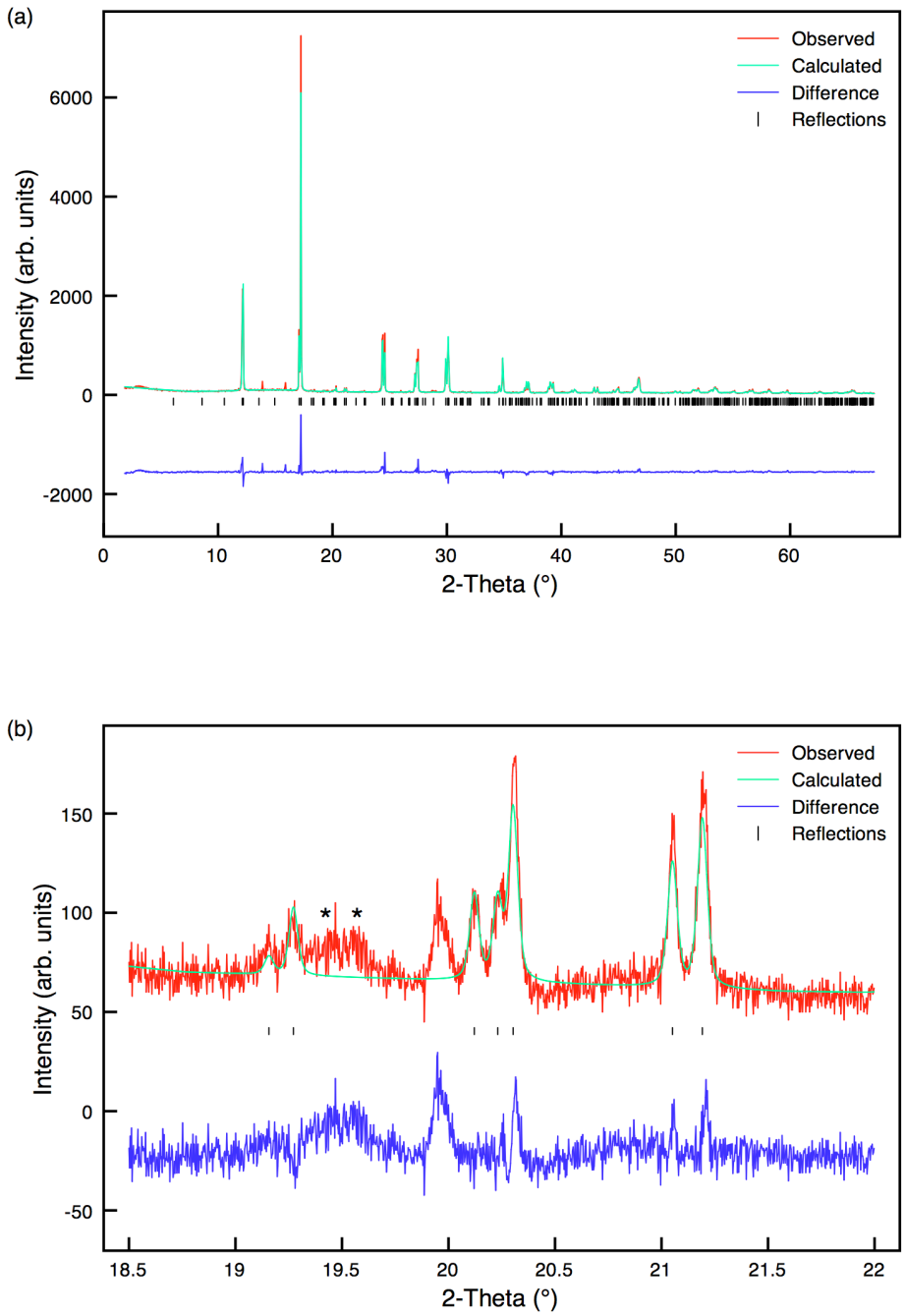

Figure 4.40: (a) Single phase Rietveld refinement completed for $Na_{0.9}Sr_{0.05}\square_{0.05}NbO_3$ using the s-PXRD data and the $P2_1ma$ structural model. (b) An expansion of the superstructure region, 18.5° - 22°, highlighting the presence of very small quantities of the Pbcm polymorph, denoted *. Small quantities of a third phase are also clearly visible in the diffraction pattern. The exact composition of this phase is, at this stage, unknown therefore it could not be correctly modelled during the structural refinement.

Table 4.18: Structural parameters for $Na_{0.9}Sr_{0.05}\square_{0.05}NbO_3$ from s-PXRD data, using isotropic thermal factors. Space group $P2_1ma$, a = 5.56748(4) Å, b = 7.77743(5) Å, c = 5.51270(4) Å and V = 238.704(3) Å^3. $\chi^2 = 1.8$, $wR_p = 13.9\%$ and $R_p = 10.6\%$.

Atom	Site	x	y	z	U(iso) × 100 / Å^2
Na1*	2a	0.270(2)	0	0.7440(10)	2.22(4)
Na2	2b	0.2865(16)	0.5	0.7483(12)	2.22(4)
Nb1	4c	0.2602	0.2503(4)	0.2425(2)	1.35(1)
O1	2a	0.286(3)	0	0.2932(7)	1.49(8)
O2	2b	0.280(3)	0.5	0.1806(16)	1.49(8)
O3	4c	−0.0359(12)	0.2871(10)	0.4746(19)	1.49(8)
O4	4c	−0.0060(15)	0.2273(11)	0.0527(13)	1.49(8)
*Na 0.9, Sr 0.05					

Given the recent findings by Torres-Pardo *et al.*,[285] all Rietveld refinements for the $Na_{1-x}Sr_{x/2}\square_{x/2}NbO_3$ series were completed using the $P2_1ma$ structural model.[228] The Rietveld refinement for the x = 0.1 sample indicated good agreement with the $P2_1ma$ phase with $wR_p = 13.9\%$ and $\chi^2 = 1.8$, as shown in Figure 4.40(a). Small quantities (~1-5%) of the impurity phase were also identified in the Rietveld profile. An expansion of the superstructure region, 18.5° - 22°, for the x = 0.1 sample is also shown in Figure 4.40(b) and upon close inspection of the peaks the $P2_1ma$ polymorph (19.2° and 19.3°) is clearly present, in addition to very small quantities of the Pbcm phase, corresponding to peaks at ~19.4° and ~19.55° (denoted by * in the Rietveld profile). It must be noted that the superstructure peaks observed possess very low intensity and are relatively broad. This broadening is, most probably, owing to disorder in the $Na_{1-x}Sr_{x/2}\square_{x/2}NbO_3$ system. As a result, it becomes extremely challenging to accurately determine which phase(s) are present in the sample and in which quantities. The identification of both the Pbcm and $P2_1ma$ phases in the x = 0.1 sample is in good agreement with the findings of Torres-Pardo *et al.*[285] Note that a multiphase Rietveld refinement was not completed for this sample as the quantities of the Pbcm phase present were too small to be accurately refined. All structural parameters

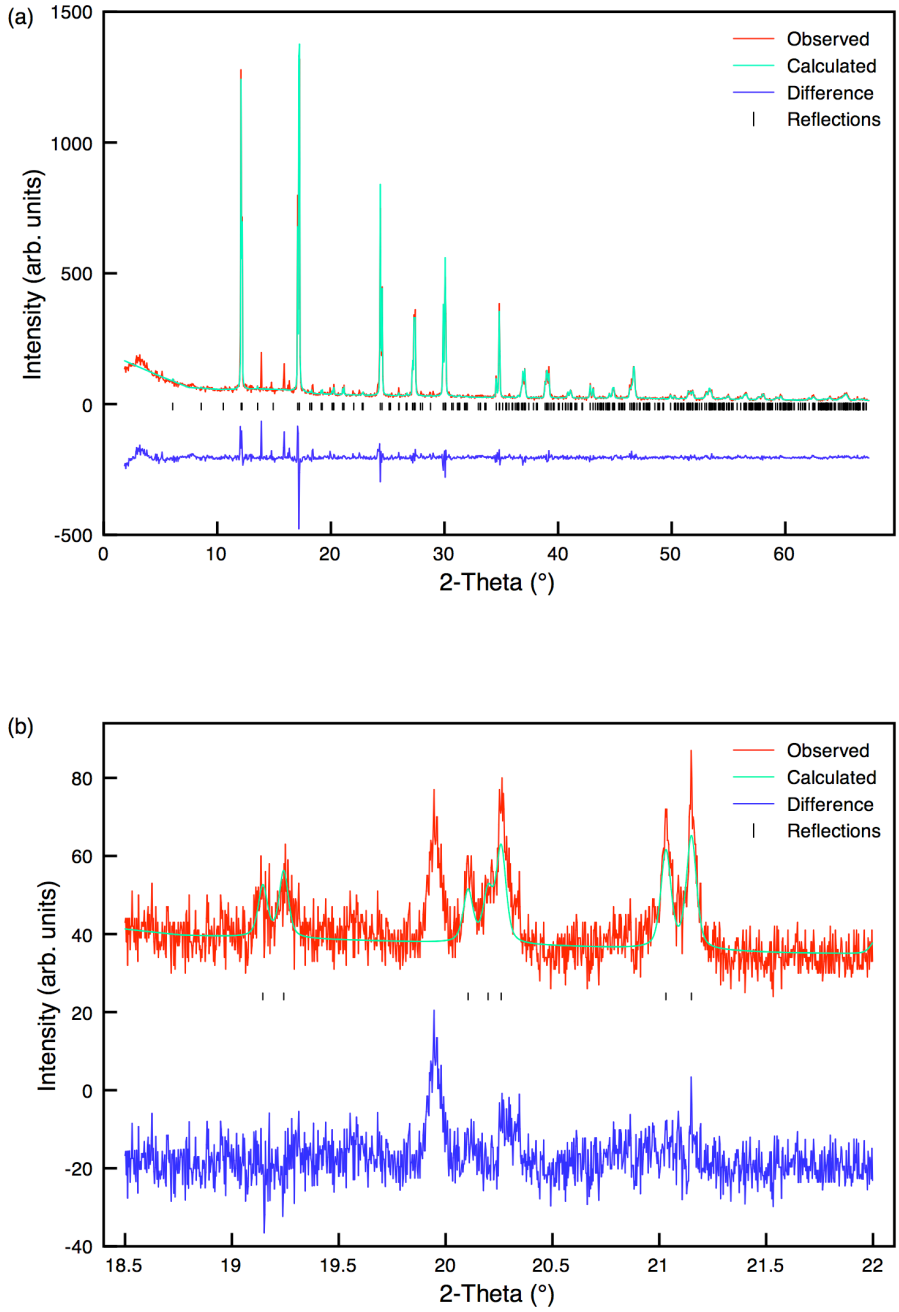

Figure 4.41: (a) Single phase Rietveld refinement completed for $Na_{0.8}Sr_{0.1}\square_{0.1}NbO_3$ using the s-PXRD data and the $P2_1ma$ structural model. (b) An expansion of the superstructure region, 18.5° - 22°, highlighting the possible presence of trace quantities of the Pbcm polymorph. It is, however, difficult to distinguish peaks belonging to this phase from the background in this superstructure region. Small quantities of a third phase are also clearly visible in the diffraction pattern. The exact composition of this phase is, at this stage, unknown therefore it could not be correctly modelled during the structural refinement.

Table 4.19: Structural parameters for $Na_{0.8}Sr_{0.1}\square_{0.1}NbO_3$ from s-PXRD data, using isotropic thermal factors. Space group $P2_1ma$, a = 5.56945(5) Å, b = 7.79448(6) Å, c = 5.52275(5) Å and V = 239.748(4) Å^3. χ^2 = 1.1, wR_p = 14.4% and R_p = 10.7%.

Atom	Site	x	y	z	U(iso) × 100 / Å^2
Na1*	2a	0.278(3)	0	0.7539(13)	3.63(6)
Na2	2b	0.2810(4)	0.5	0.7580(19)	3.63(6)
Nb1	4c	0.2604	0.2501(3)	0.2427(3)	1.73(1)
O1	2a	0.230(3)	0	0.2794(19)	0.76(10)
O2	2b	0.234(3)	0.5	0.1874(17)	0.76(10)
O3	4c	−0.0438(10)	0.2802(8)	0.472(2)	0.76(10)
O4	4c	0.0109(13)	0.2363(10)	0.0670(13)	0.76(10)

*Na 0.8, Sr 0.1

obtained from the single phase refinement of the x = 0.1 sample can be found in Table 4.18.

Similar Rietveld refinements were completed for compositions x = 0.2, 0.3 and 0.4 in the $Na_{1-x}Sr_{x/2}\square_{x/2}NbO_3$ series. Greater quantities (~10-15%) of the impurity phase were present in the x = 0.2 sample, as shown in Figure 4.41(a). Torres-Pardo *et al.*,[285] concluded that no two phase regions of coexistence existed in the x = 0.2 sample, instead domains of solely the $P2_1ma$ phase were observed. Close examination of the superstructure peaks in our s-PXRD data suggest that the quantity of the $P2_1ma$ phase in this particular composition had increased relative to the x = 0.1 sample. In addition, there appeared to be less of the Pbcm phase present in the sample. As greater quantities of Sr were doped into $NaNbO_3$ the peaks observed in the diffraction pattern were increasingly broadened, making it difficult to distinguish between the different phases. An expansion of the region 18.5° - 22° is shown in Figure 4.41(b) where peaks belonging to the $P2_1ma$ phase are clearly visible. It is less obvious, however, whether peaks belonging to the Pbcm phase are also present. Therefore, in the x = 0.2 sample the bulk phase appears to be the $P2_1ma$ polymorph and the single phase refinement completed reflects this. All structural parameters

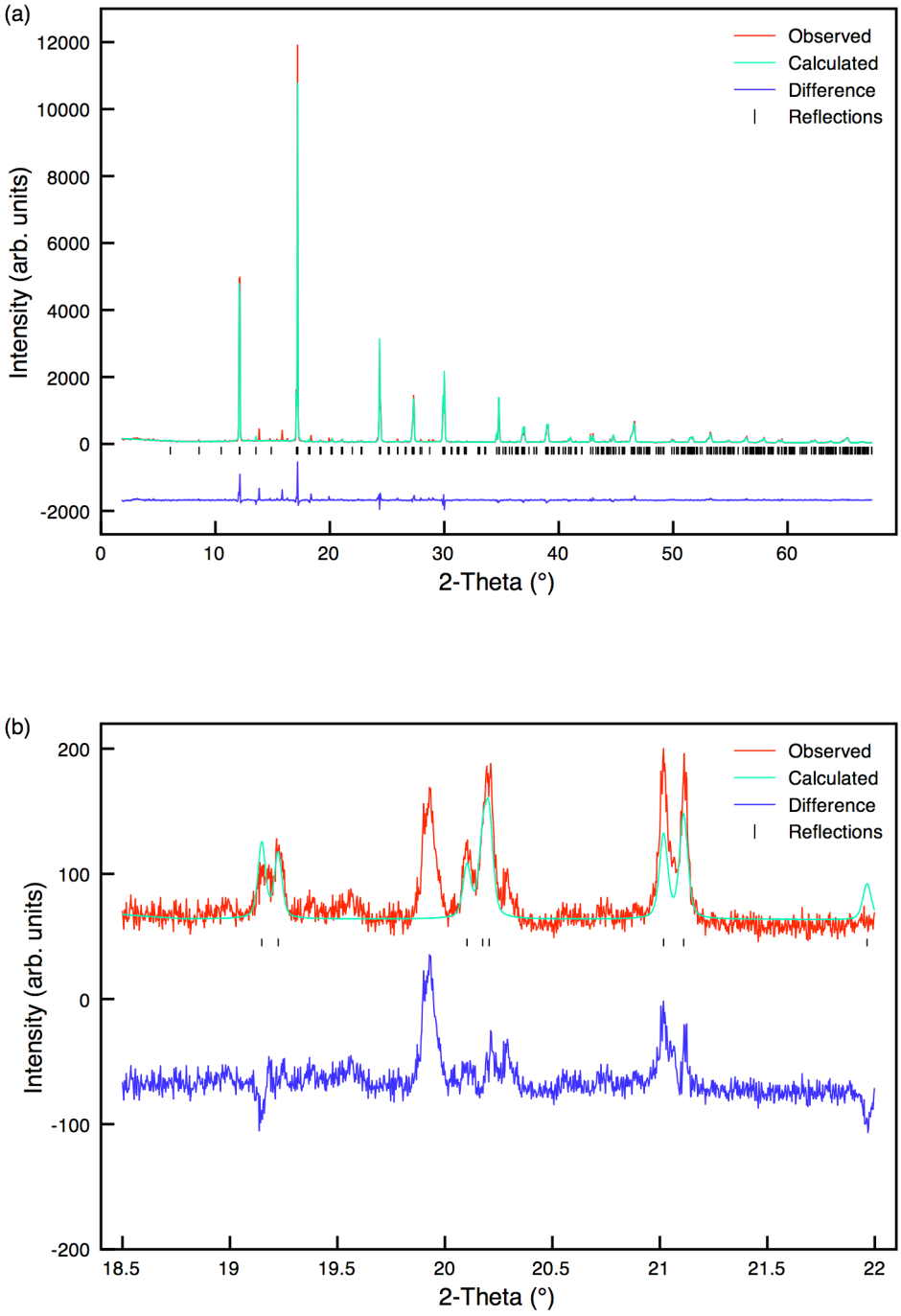

Figure 4.42: (a) Single phase Rietveld refinement completed for $Na_{0.7}Sr_{0.15}\square_{0.15}NbO_3$ using the s-PXRD data and the $P2_1ma$ structural model. (b) An expansion of the superstructure region, 18.5° - 22°, highlighting the gradual removal of the Pbcm polymorph.

Table 4.20: Structural parameters for $Na_{0.7}Sr_{0.15}\square_{0.15}NbO_3$ from s-PXPD data, using isotropic thermal factors. Space group $P2_1ma$, a = 5.56637(3) Å, b = 7.81746(4) Å, c = 5.52982(3) Å and V = 240.630(3) Å^3. $\chi^2 = 2.9$, $wR_p = 15.9\%$ and $R_p = 11.0\%$.

Atom	Site	x	y	z	U(iso) × 100 / Å^2
Na1*	2a	0.2792(11)	0	0.7540(7)	3.27(4)
Na2	2b	0.278(2)	0.5	0.7512(13)	3.27(4)
Nb1	4c	0.2614(6)	0.2502(1)	0.2428(1)	0.99(1)
O1	2a	0.2273(16)	0	0.2869(13)	0.84(8)
O2	2b	0.2217(15)	0.5	0.1951(12)	0.84(8)
O3	4c	−0.0291(11)	0.2834(6)	0.4680(17)	0.84(8)
O4	4c	0.0311(12)	0.2420(6)	0.0545(11)	0.84(8)
*Na 0.7, Sr 0.15					

obtained from this refinement are given in Table 4.19. Smaller quantities of the impurity phase were identified in the x = 0.3 sample and a single phase Rietveld refinement was completed using the $P2_1ma$ structural model,[228] as shown in Figure 4.42(a). A relatively good level of fit was obtained with wR_p = 15.9% and χ^2 = 2.9. All associated structural parameters obtained from this refinement are given in Table 4.20. An expansion of the superstructure peaks is also shown in Figure 4.42(b), in which peaks belonging to the $P2_1ma$ phase are clearly visible. As in the x = 0.2 sample, it is less obvious whether any of the Pbcm phase remains in the sample owing to the relatively poor signal-to-noise observed. A single phase Rietveld refinement was also completed for the x = 0.4 sample. Greater quantities of the impurity phase (~5-10%) were visible in this sample, as shown in Figure 4.43(a). A reasonably good level of fit was obtained with wR_p = 18.9 and χ^2 = 2.2. Examination of the superstructure peaks, 18.5° - 22°, highlighted a considerable reduction in intensity of the two peaks belonging to the $P2_1ma$ phase (19.2° and 19.3°), as shown in Figure 4.43(b). This, in turn, suggested the quantity of this phase was severely reduced in the x = 0.4 sample, possibly signifying there to be an optimal level of Sr doping that consistently produces the polar $P2_1ma$ phase. It is, therefore, possible a structural phase transition could be

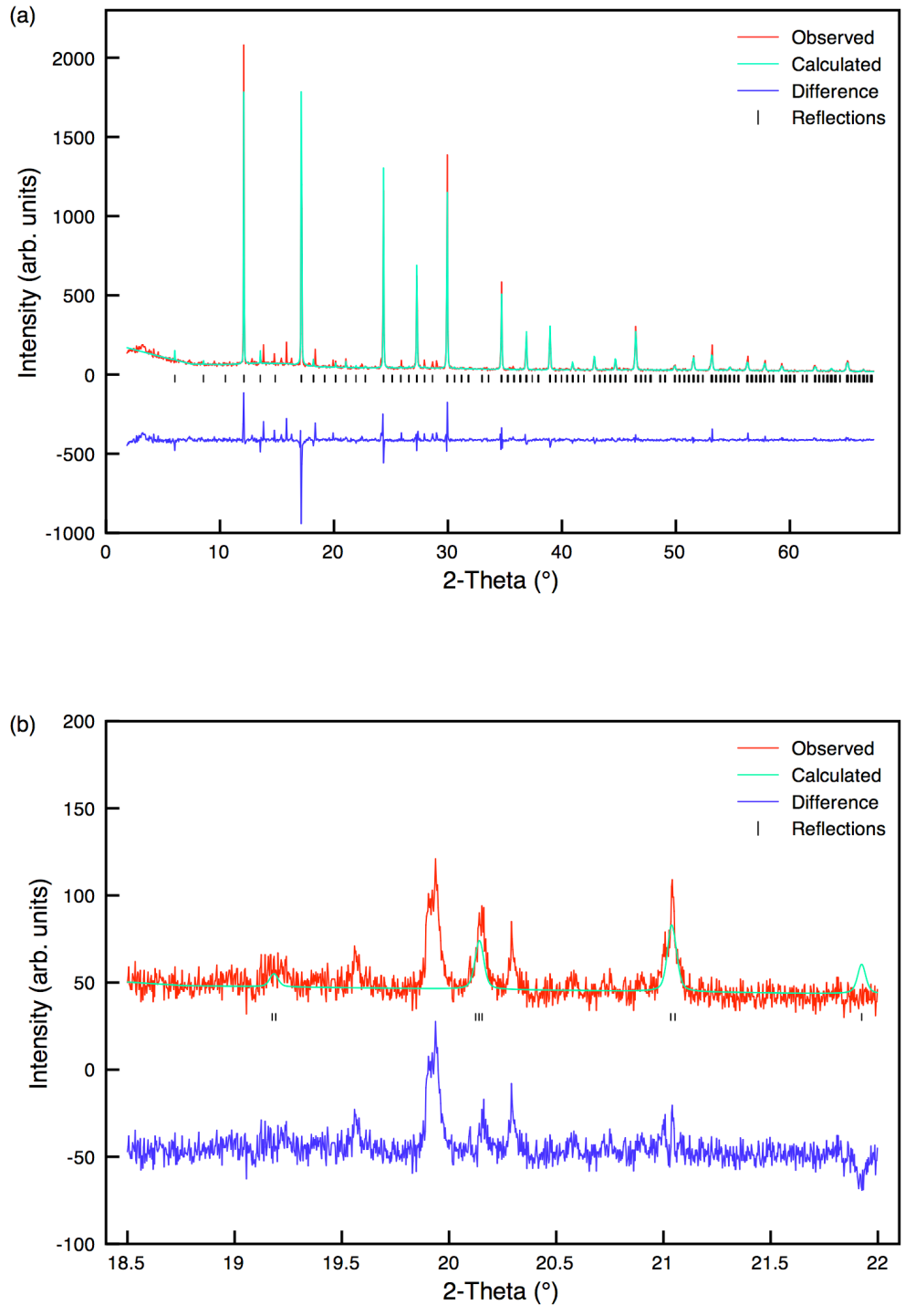

Figure 4.43: (a) Single phase Rietveld refinement completed for $Na_{0.6}Sr_{0.2}\square_{0.2}NbO_3$ using the s-PXRD data and the $P2_1ma$ structural model. (b) An expansion of the superstructure region, 18.5° - 22°, highlighting the removal of the $P2_1ma$ polymorph, suggesting the sample is past the optimal composition required to produce the polar $P2_1ma$ phase.

Table 4.21: Structural parameters for $Na_{0.6}Sr_{0.2}\square_{0.2}NbO_3$ from s-PXPD data, using isotropic thermal factors. Space group $P2_1ma$, a = 5.55268(7) Å, b = 7.83700(8) Å, c = 5.54486(8) Å and V = 241.292(4) Å^3. $\chi^2 = 2.2$, $wR_p = 18.9\%$ and $R_p = 13.4\%$.

Atom	Site	x	y	z	U(iso) × 100 / Å^2
Na1*	2a	0.2884(13)	0	0.7647(14)	3.53(4)
Na2	2b	0.2850(4)	0.5	0.751(3)	3.53(4)
Nb1	4c	0.2673(9)	0.2505(2)	0.2433(3)	1.46(1)
O1	2a	0.201(3)	0	0.272(3)	0.84(8)
O2	2b	0.203(3)	0.5	0.213(3)	0.84(8)
O3	4c	−0.015(3)	0.2774(2)	0.451(3)	0.84(8)
O4	4c	0.005(3)	0.2480(2)	0.038(3)	0.84(8)

*Na 0.6, Sr 0.2

observed at marginally higher levels of Sr doping. However, this was out with the scope of this particular investigation. All structural parameters obtained from the Rietveld refinement for the x = 0.4 sample are given in Table 4.21. All corresponding bond lengths obtained from each refinement in the $Na_{1-x}Sr_{x/2}\square_{x/2}NbO_3$ series are given in Appendix III. The findings presented suggest some degree of uncertainty regarding the exact composition of the samples synthesised in the $Na_{1-x}Sr_{x/2}\square_{x/2}NbO_3$ series. In order to identify which polymorph(s) are present in each sample NPD data is required as neutrons will enhance the superstructure region of the diffraction pattern and enable conclusions to be drawn regarding the exact composition.

The substitution of Sr into the $NaNbO_3$ structure produced a corresponding change in the lattice parameters and unit cell volume. As x was increased a slight increase in the lattice parameters a, b and c was observed and, as a result, an associated increase in the unit cell volume was also observed. The variation of each parameter with increasing Sr content is shown in Figures 4.44 and 4.45. The ionic radius of Sr^{2+} (1.26 Å)[4] is greater than that of Na^+ (1.02 Å).[4] Therefore, as Sr is introduced to the $NaNbO_3$ structure an increase in the unit cell parameters is expected, which will, in turn, cause the cell volume to increase. The findings

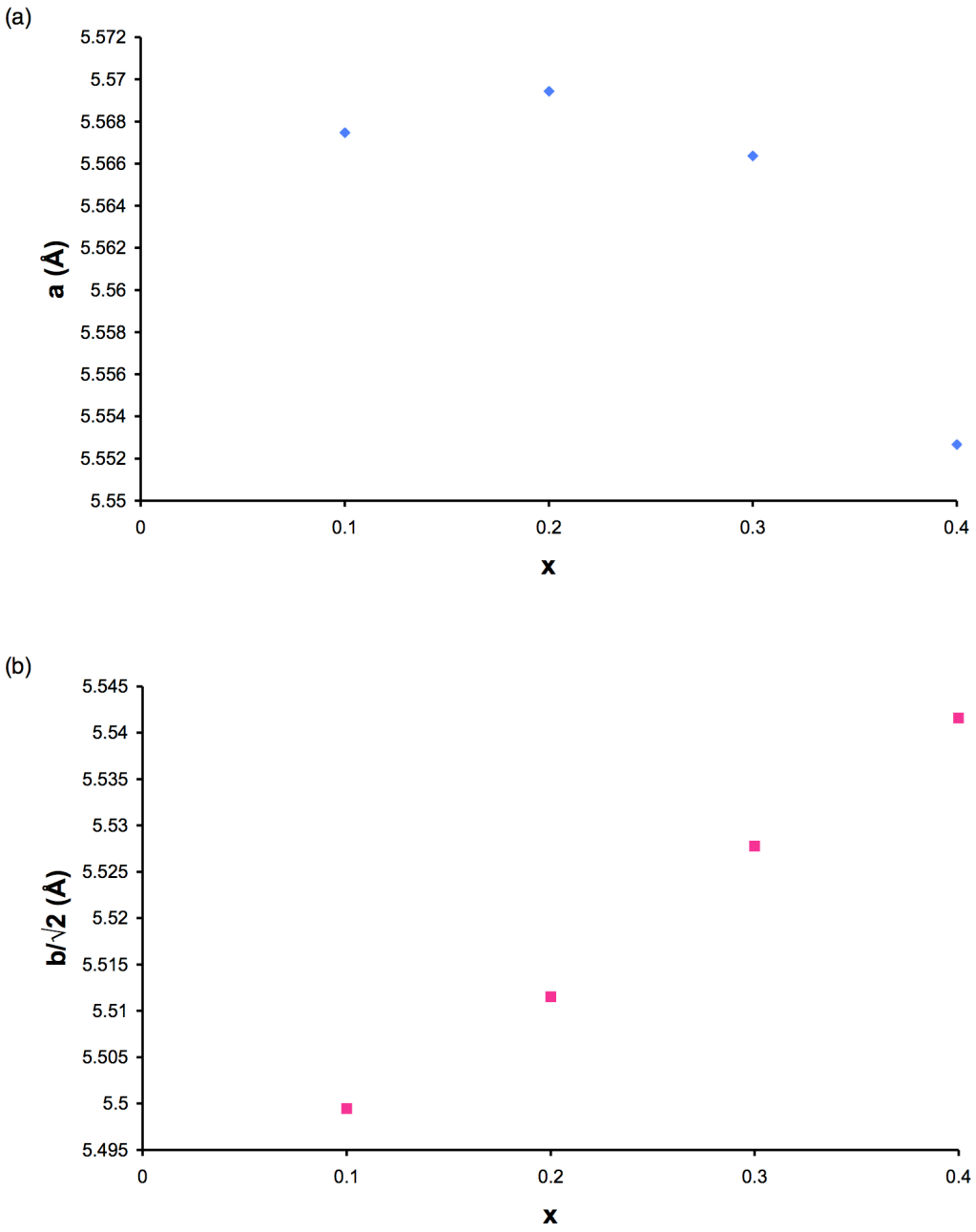

Figure 4.44: Variation observed in the unit cell parameters (a) a and (b) b with increasing x in the SNN series using s-PXRD data. Note that for ease of comparison with the unit cell parameters a and c, the b parameter has been divided by √2. The estimated error bars are smaller than the symbols used and are therefore not shown.

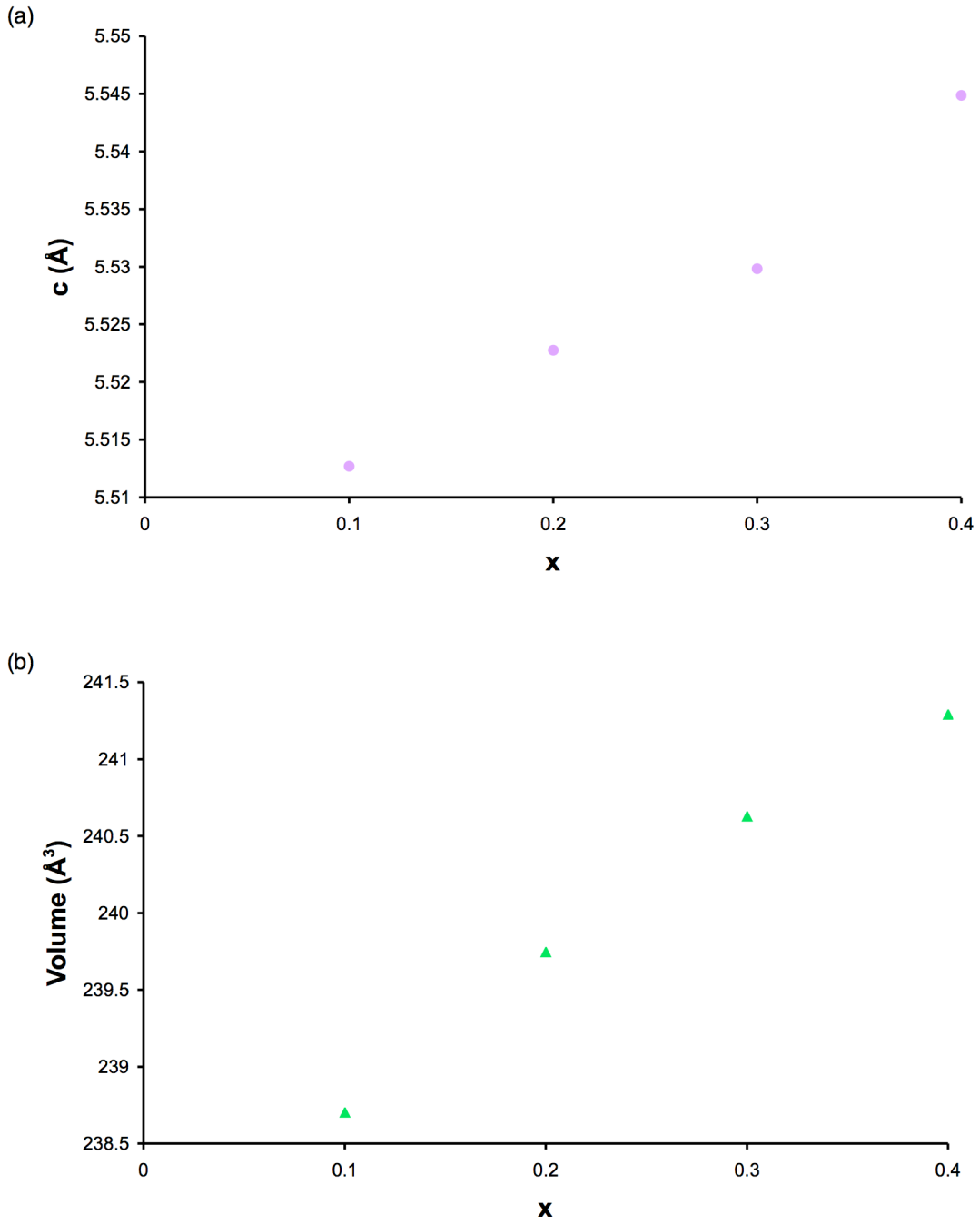

Figure 4.45: Variation observed in (a) the unit cell parameter c and (b) the unit cell volume with increasing x in the SNN series using the s-PXRD data. The estimated error bars are smaller than the symbols used and are therefore not shown.

observed and presented in Figures 4.44 and 4.45 are therefore in good agreement with the expected trends.

4.4 Discussion

The evidence presented suggests the substitution of Li^+, K^+ and Sr^{2+} into the $NaNbO_3$ structure produces the same structural effect; the formation of the polar orthorhombic $P2_1ma$ phase. Both Li^+ and K^+ possess significantly different ionic radii when compared with Na^+ and the abrupt change observed is believed to provoke a structural distortion causing the loss of the antiphase tilts around the orthorhombic b axis, those which are responsible for the antiferroelectric fourfold superstructure. Whilst the difference in ionic radii between Sr^{2+} and Na^+ is not as great as in the KNN and LNN series it must be noted that for each Sr^{2+} cation substituted into the structure an A site vacancy is produced. It is this pair, i.e., the [Sr – vacancy], that are believed to force the loss of the fourfold superstructure in the $Na_{1-x}Sr_{x/2}\square_{x/2}NbO_3$ system. This suggests that the formation of the $P2_1ma$ phase requires an optimal [Sr - vacancy] concentration to be obtained. Our findings suggest that samples with compositions x = 0.1 and 0.2 continue to possess trace amounts of the Pbcm phase, indicating the antiferroelectric fourfold superstructure remains in these samples. However, in samples with compositions x = 0.3 and 0.4 the Pbcm phase was fully eradicated, leaving solely the $P2_1ma$ phase. The diffraction data presented also appeared to suggest the quantity of the $P2_1ma$ phase to be considerably reduced in the x = 0.4 sample, thereby indicating that the optimal [Sr - vacancy] ratio has been achieved. The gradual removal of this phase with increasing Sr content is believed to occur owing to an increasing number of randomly distributed A site vacancies as this is believed to limit the growth of the structural domains and diminish their average size. The removal of the $P2_1ma$ phase from the sample suggests the existence of a phase transition in samples x > 0.4. It is, however, difficult to distinguish peaks belonging to this 'new' phase from those of the impurity phase. Ultimately, in order to establish whether a phase transition is observed in the x = 0.4 sample a phase pure sample is needed. Only then can accurate conclusions be drawn regarding the addition or removal of peaks from the diffraction pattern.

High-resolution ^{23}Na solid-state NMR was utilised to investigate both the KNN and LNN series. All spectra recorded appeared to display good agreement with the diffraction data presented, i.e., the formation of the $P2_1ma$ phase. An important observation in each spectrum, however, was the substantial effect of disorder. As greater quantities of K and Li were introduced to each system the spectral broadening observed gradually increased. Owing to the presence of impurities in each sample in the $Na_{1-x}Sr_{x/2}\square_{x/2}NbO_3$ series solid-state NMR techniques were not utilised. Additional work is required to obtain phase pure samples before more advanced characterisation techniques such as solid-state NMR can be performed.

4.5 Conclusions

Using high-resolution powder diffraction and two-dimensional ^{23}Na MAS NMR the solid-solutions $K_xNa_{1-x}NbO_3$, $Li_xNa_{1-x}NbO_3$ and $Na_{1-x}Sr_{x/2}\square_{x/2}NbO_3$ were investigated and in most cases the polar $P2_1ma$ polymorph was formed. Associated changes in the lattice parameters and unit cell volume were observed, each of which was in good agreement with the respective sizes of the cations substituted into the $NaNbO_3$ structure. There was no evidence of cation ordering in any of the three solid-solutions investigated. In particular, the findings presented for the KNN series are in good agreement with data by both Ahtee and Shuvaeva, whilst those for the LNN series displayed consistent agreement with recent work by Yuzyuk *et al*. Good agreement was also observed with the recent findings by Torres-Pardo *et al*. for the $Na_{1-x}Sr_{x/2}\square_{x/2}NbO_3$ series. Unfortunately, in this particular investigation it was difficult to synthesise phase pure samples in this series. In addition, using s-PXRD data it was challenging to accurately identify the exact phases present in each sample as the only observed subtleties were in the low intensity superstructure peaks. Therefore, in order to characterise this particular series phase pure samples and high-resolution NPD data are required. This will enable any structural subtleties to be identified with greater ease. This is undoubtedly work for the future study of this particular system.

The polar, and potentially ferroelectric, $P2_1ma$ phase produced in each solid-solution may possess many interesting and useful physical properties. Given the current motivation to establish lead free alternatives to PZT such compositions could provide further insight into potential green replacements. Although an investigation of the electrical properties of these systems was out with the scope of this particular structural study it would be, at some stage in the future, interesting to assess the magnitude of the piezoelectric responses observed for the samples synthesised in the KNN, LNN and $Na_{1-x}Sr_{x/2}\square_{x/2}NbO_3$ series.

Chapter 5

A Low Temperature s-PXRD Study of $NaNbO_3$

5.1 Introduction

Sodium niobate, $NaNbO_3$, possesses an extremely complex phase diagram with many temperature- and pressure-induced phase transitions. The room temperature region of this phase diagram has been a cause of considerable confusion for many years with several inconsistent and contradictory phases having been suggested. However, the comprehensive structural study completed earlier in this work has aided considerably in the understanding of room temperature $NaNbO_3$. Samples are now known to routinely comprise of two, structurally very similar, polymorphs of $NaNbO_3$, and only by careful monitoring of the reaction conditions can a phase pure sample of either be obtained.

To date, many investigations have focused solely on one of the six reported temperature induced phase transitions of $NaNbO_3$. The high and low temperature regions of the phase diagram have been heavily investigated in previous years and are currently considered, by many, to be largely resolved.[221-223,263-266,288] For example, it is widely known that the antiferroelectric Pbcm phase undergoes a severely hysteretic transition to the polar, ferroelectric R3c phase at ~173 K.[265] Recent neutron diffraction studies have also shown this transition results in the coexistence of the R3c and Pbcm phases over a relatively large temperature range, $12 < T < 245$ K, on thermal cycling.[224] Therefore, to date the low temperature region of the $NaNbO_3$ phase diagram is known to exhibit only a single phase transition from the antiferroelectric Pbcm phase to the ferroelectric R3c phase. In contrast, high temperature studies for $NaNbO_3$ report as many as five structural phase transitions occurring between 643 K and 914 K, as summarised in Table 5.1.[222,223]

To date, almost all variable temperature studies completed for $NaNbO_3$ have utilised solely diffraction methods for structural

Table 5.1: Several of the suggested phases of sodium niobate, $NaNbO_3$.[222,223]

Temperature / K	Phase	Symmetry
	N	Rhombohedral
193	P	Monoclinic
643	R	Orthorhombic
753	S	Orthorhombic
793	T_1	Orthorhombic
848	T_2	Tetragonal
914	U	Cubic

characterisation and each is reported as starting with 'phase pure' Pbcm $NaNbO_3$. The findings presented earlier in this work have, however, shown it is extremely difficult to accurately determine the exact phase(s) of $NaNbO_3$ present in any sample using diffraction methods alone. Consistently, samples have been shown to comprise of two structurally very similar polymorphs of $NaNbO_3$ and the two phases, characterised in space groups Pbcm and $P2_1ma$, possess virtually identical diffraction patterns. The only visible discrepancies occurred in the superstructure peaks. Initially these differences were extremely difficult to detect using conventional laboratory-based X-ray diffraction methods; hence high-resolution X-ray and neutron powder diffraction techniques were required. Therefore, given these recent findings all previous variable temperature studies completed using 'phase pure' samples of Pbcm $NaNbO_3$ should be treated with some degree of caution. Only when the starting composition of each sample is accurately known can conclusions be drawn regarding the existence of any structural phase transitions.

At present no low temperature investigations have been completed using the polar $P2_1ma$ polymorph of $NaNbO_3$ as the initial room temperature phase. Therefore, it is of interest to determine whether a

similar phase transition occurs from this to the R3c phase. Similarly, we wish to establish whether any regions of phase coexistence occur between the R3c and $P2_1ma$ phases. If the $P2_1ma$ polymorph can be eradicated from the sample at low temperatures which phase(s) will return to the sample upon heating to room temperature; the thermodynamically stable Pbcm or polar $P2_1ma$ phase? Shiratori *et al.*,[226] suggest strain and particle size are important factors in determining the phases produced in any sample. Hence, factors such as strain and the development of domain structure may contribute in determining the stability of the phases of $NaNbO_3$ formed upon returning to room temperature. Therefore, in an attempt to accurately probe and re-investigate the low temperature region of the $NaNbO_3$ phase diagram a high-resolution variable temperature X-ray powder diffraction study has been completed for the $P2_1ma$ polymorph of $NaNbO_3$, using the sol-gel sample of $NaNbO_3$ previously studied as part of the room temperature investigation. This has been completed to establish whether any similar or additional phase transitions occur to those previously reported for the Pbcm polymorph of $NaNbO_3$. It is anticipated the $P2_1ma$ phase will be eradicated from the sample at low temperatures, leaving solely the R3c phase. Therefore, upon heating to 295 K it is of interest to determine which phase(s) of $NaNbO_3$ will be formed.

5.2 Experimental

5.2.1 Synthesis

The $P2_1ma$ sample of $NaNbO_3$ used in this low temperature study was synthesised using sol-gel methods. It must be noted that the same sol-gel sample was also used in the earlier room temperature investigation of $NaNbO_3$. Refer to Chapter 3, section 3.2.1 for specific experimental details.

5.2.2 High-Resolution X-ray Diffraction

High-resolution low temperature powder diffraction studies were completed using Beamline I11 at the Diamond Light Source Synchrotron (λ = 0.826952 Å).[K122,123] The investigation was conducted using a PheniX cryostat (11 – 295 K). The sample was loaded into an aluminium capillary and mounted onto a flat brass plate that employed a continuous 'rocking' motion throughout data collection. Peaks resulting from the aluminium capillary were present in all diffraction patterns obtained; hence, for ease of analysis these peaks were excluded from the data during Rietveld refinement. Prior to cooling of the sample a room temperature diffraction pattern was recorded. The sample was then quenched to 12 K and allowed to equilibrate for ~10 minutes before a diffraction pattern was recorded. The sample was then gradually warmed to room temperature in 10 and 20 K intervals. Diffraction patterns were recorded for ~30 minutes at each temperature and all datasets were analysed using the GSAS software package.[125]

5.3 Results and Discussion

The room temperature study completed earlier for the sol-gel sample of $NaNbO_3$ concluded that the sample was composed of a mix of two very similar phases, the polar orthorhombic $P2_1ma$ (~90%) and antiferrolectric Pbcm (~10%) phases. Specific details regarding the complete room temperature characterisation of the sol-gel $NaNbO_3$ sample can be found in Chapter 3, section 3.3.4.

Prior to cooling of the sol-gel sample a diffraction pattern was recorded at room temperature using the PheniX cryostat. The room temperature data obtained was in good agreement with earlier data and confirmed the presence of both the $P2_1ma$ and Pbcm phases of $NaNbO_3$. Owing to the very small quantities of the Pbcm phase present in the sample a single phase Rietveld refinement was completed using the $P2_1ma$ model. The full Rietveld refinement obtained for the room temperature dataset is shown in Figure 5.1(a). Also shown in Figure 5.1(b) is an expansion of the corresponding superstructure peaks, 19.0° - 19.9°. The

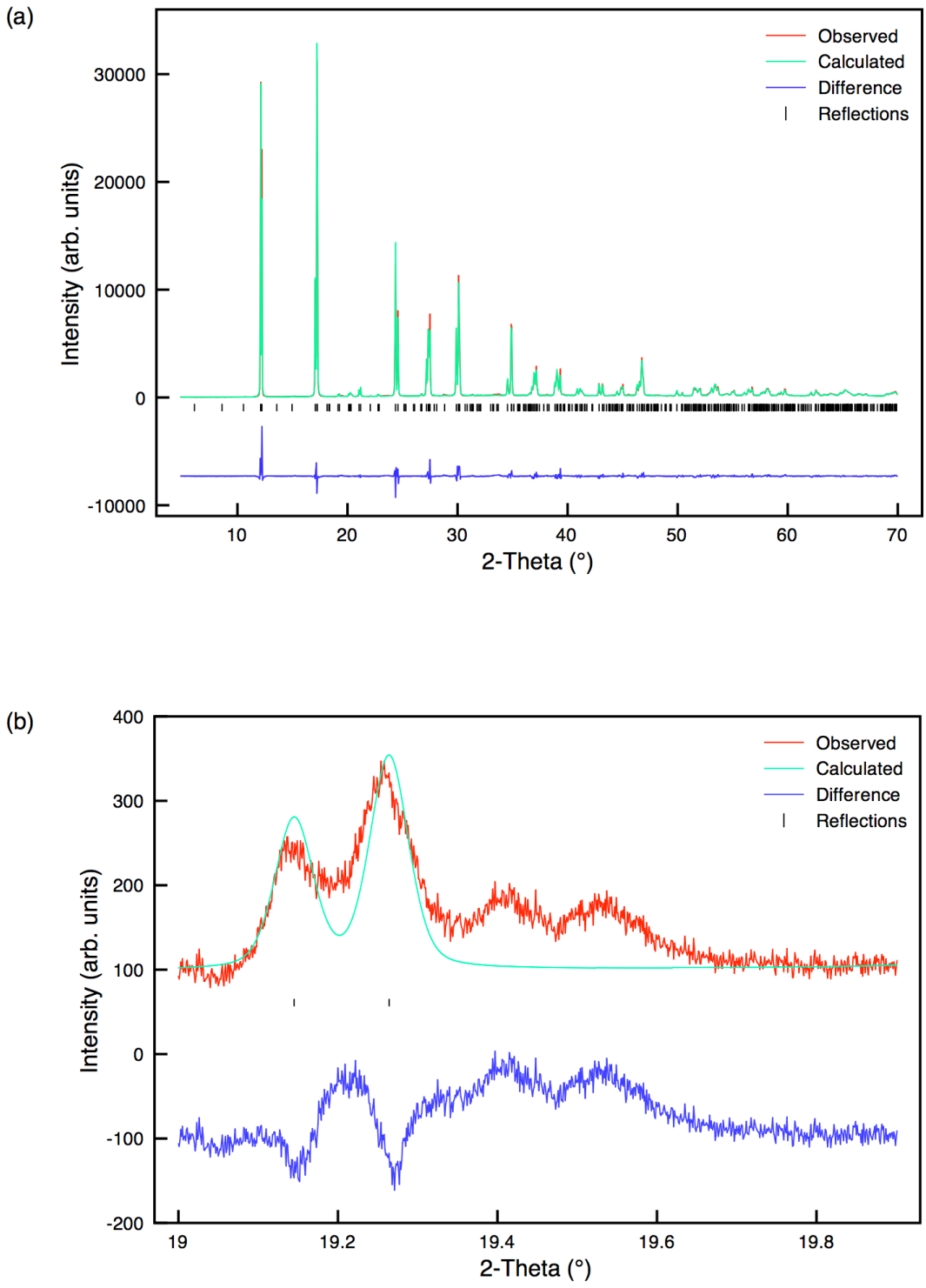

Figure 5.1: (a) Rietveld profile of s-PXRD data (room temperature) for sol-gel $NaNbO_3$ using model $P2_1ma$ and (b) corresponding expansion of the superstructure peaks in the region 19° - 19.9°.

Table 5.2: Structural parameters for sol-gel $NaNbO_3$ (room temperature) from s-PXRD data, using isotropic thermal factors. Space group $P2_1ma$, a = 5.56960(2) Å, b = 7.76598(3) Å, c = 5.51287(3) Å and V = 238.450(2) Å^3. χ^2 = 16.1, wR_p = 13.0% and R_p = 9.7%.

Atom	Site	x	y	z	U(iso) × 100 / Å^2
Na1	2a	0.2276(6)	0	0.7539(8)	1.12(19)
Na2	2b	0.2472(11)	0.5	0.7568(7)	1.18(18)
Nb1	4c	0.2513(4)	0.2505(2)	0.2549(1)	0.58(1)
O1	2a	0.2412(15)	0	0.3073(12)	1.23(3)
O2	2b	0.2251(9)	0.5	0.1869(13)	1.23(3)
O3	4c	0.0527(5)	0.2748(6)	0.5415(9)	1.23(3)
O4	4c	−0.0010(7)	0.2193(5)	0.0181(9)	1.23(3)

two peaks fitted using the calculated model correspond to the $P2_1ma$ phase whilst the peaks at 19.4° and 19.5° correspond to the Pbcm phase of $NaNbO_3$. Hence, the Pbcm phase is clearly visible in the sol-gel sample and is in good agreement with the earlier room temperature study completed. All corresponding structural parameters obtained from the Rietveld refinement can be found in Table 5.2. All associated bond lengths are given in Appendix IV. The sample was then quenched to 12 K. A diffraction pattern was collected and Rietveld refinement of the data was completed. Initially, a single phase refinement was completed using the known low temperature R3c phase of $NaNbO_3$. However, the fit obtained was relatively poor (wR_p = 40.0% and χ^2 = 146.9), as shown in Figure 5.2. In particular, the profile parameters used in the calculated model grossly underestimated the observed peak intensity. Such a poor level of fit suggested the possible presence of either a structural phase transition or second phase. Close examination of the diffraction data suggested the room temperature $P2_1ma$ phase remained in the sample, thereby ruling out the possibility of a phase transition. Hence, a multiphase Rietveld refinement was completed using the rhombohedral R3c and orthorhombic $P2_1ma$ phases. Upon the addition of the $P2_1ma$ phase the quality of fit obtained improved considerably, with wR_p = 10.9% and χ^2 = 10.9. It was possible to refine the respective phase fractions of the two phases present.

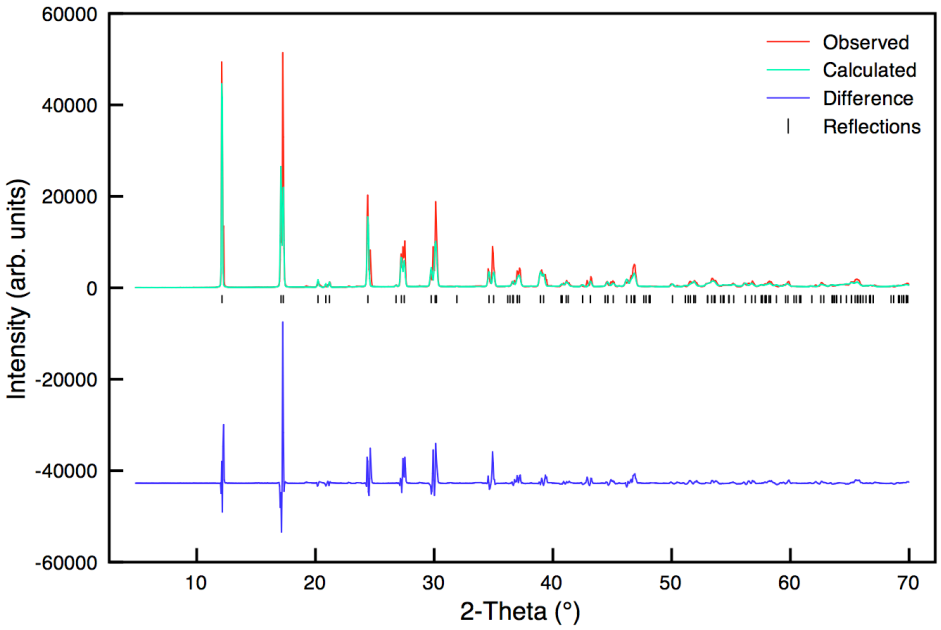

Figure 5.2: Rietveld profile of s-PXRD data (12 K) for sol-gel $NaNbO_3$ using model R3c.

Rather surprisingly, the refined phase fractions suggested the $P2_1ma$ polymorph to be the abundant phase at 12 K, with 66.3(2)% and 33.7(2)% of the $P2_1ma$ and R3c phases, respectively. The multiphase Rietveld refinement completed for the 12 K data is shown in Figure 5.3 and all structural parameters obtained for each phase can be found in Table 5.3. All associated bond lengths are given in Appendix IV. Also shown in Figure 5.3(b) is an expansion of the corresponding superstructure region, 19.0° - 19.9 °. Inspection of this region confirms the presence of the $P2_1ma$ phase and also indicates that the Pbcm phase of $NaNbO_3$ remains in the sample. When Figures 5.1(b) and 5.3(b) are compared it is clear to see that both the $P2_1ma$ and Pbcm phases of $NaNbO_3$ are present in the sol-gel sample when cooled to 12 K. Hence, at 12 K there is a three phase coexistence between the $P2_1ma$, Pbcm and R3c phases. A similar phase coexistence was recently reported by Mishra *et al.*[224] Using variable temperature NPD studies the R3c and Pbcm phases of $NaNbO_3$ were found to coexist over a relatively large temperature range, $12 < T < 245$ K. However, their work found that the R3c phase was the most abundant phase at 12 K, indicating they achieved greater conversion of the Pbcm phase to the low temperature R3c phase. One possible reason for this is

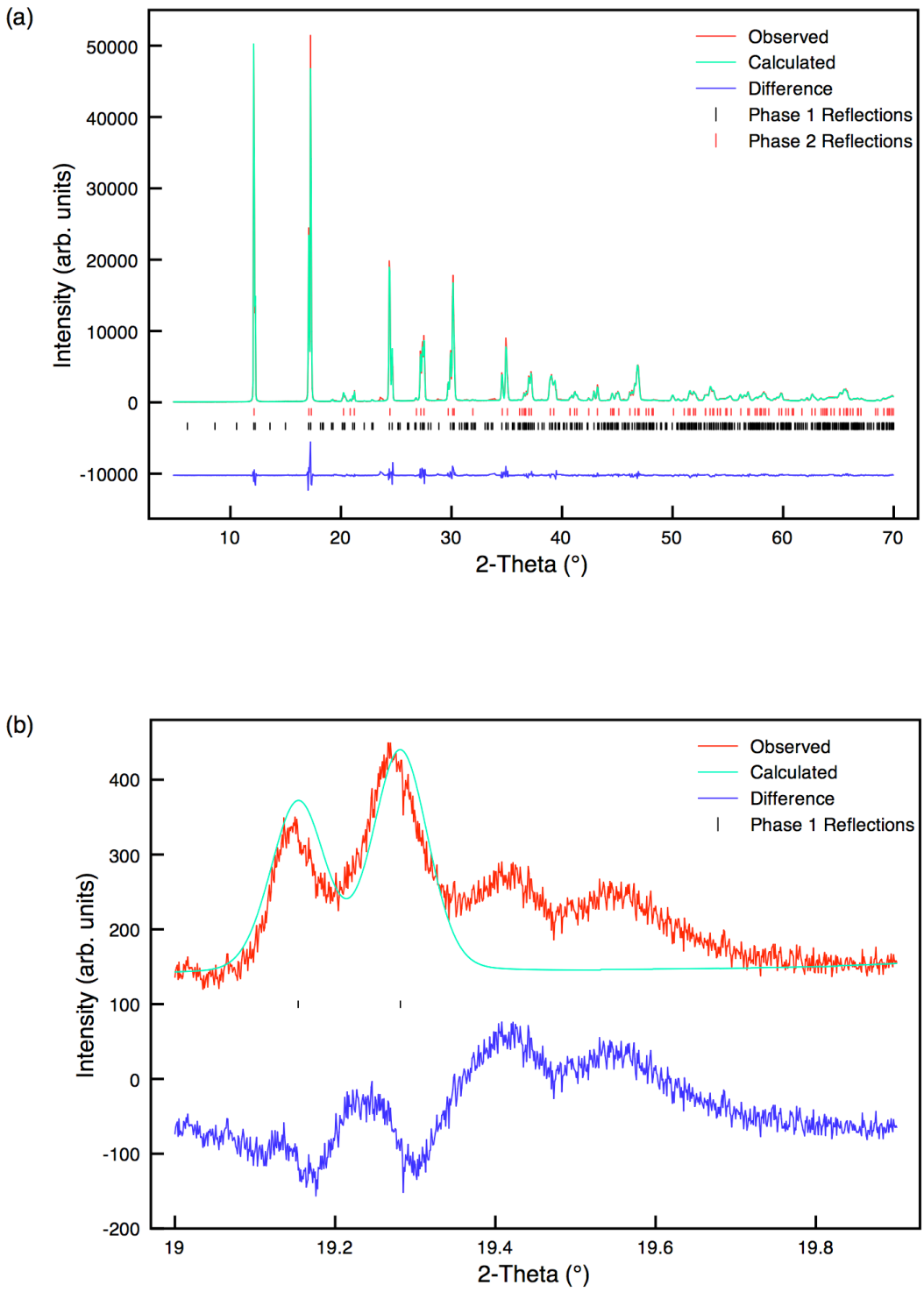

Figure 5.3: (a) Multiphase Rietveld profile of s-PXRD data (12 K) for sol-gel $NaNbO_3$ using models $P2_1ma$ (Phase 1) and R3c (Phase 2). (b) Corresponding expansion of the superstructure peaks in the region 19° - 19.9°.

Table 5.3: Structural parameters for sol-gel $NaNbO_3$ (12 K) from s-PXRD data, using isotropic thermal factors. Space group $P2_1ma$, a = 5.56811(3) Å, b = 7.75278(4) Å, c = 5.50730(4) Å and V = 237.741(2) Å^3. Space group R3c, a = 5.56246(3) , α = 59.142(1)° and V = 119.32(1) Å^3. χ^2 = 10.9, wR_p = 10.9% and R_p = 7.8%

Phase	Atom	Site	x	y	z	U(iso) × 100 / Å^2
$P2_1ma$	Na1	2a	0.2323(7)	0	0.7545(9)	0.25(2)
	Na2	2b	0.2478(12)	0.5	0.7544(9)	0.25(2)
	Nb1	4c	0.2565(4)	0.2507(2)	0.2551(1)	0.17(1)
	O1	2a	0.2421(15)	0	0.3185(12)	0.75(4)
	O2	2b	0.2173(10)	0.5	0.1819(13)	0.75(4)
	O3	4c	0.0540(6)	0.2762(5)	0.5404(11)	0.75(4)
	O4	4c	0.0017(9)	0.2138(4)	0.0154(11)	0.75(4)
R3c	Na1	2a	0.2580(7)	0.2580(7)	0.2580(7)	0.73(4)
	Nb1	2a	0.0048(4)	0.0048(4)	0.0048(4)	0.51(9)
	O1	6b	0.3068(5)	−0.2715(13)	0.1849(4)	0.05(5)

that their sample was cooled for a long period of time, thereby enabling more of the Pbcm phase to convert to the low temperature phase. However, no information regarding sample exposure times was provided. Therefore, it is difficult to determine precisely which factor enabled them to achieve greater percentage of the R3c phase. Mishra *et al*. also reported the observation of smeared dielectric responses for $NaNbO_3$ over the temperature range 12 – 280 K, believed to result from competing ferroelectric and antiferroelectric interactions from the R3c and Pbcm phases respectively. Interestingly, all such findings were reported for a 'phase pure' sample of Pbcm $NaNbO_3$. However, no information regarding the synthesis method used to prepare the sample was provided. Therefore, it is difficult to confirm whether the sample in which the region of phase coexistence was identified was single phase Pbcm $NaNbO_3$ initially. It is possible their sample contained the same mix of two phases identified in many of our room temperature samples. However, it is also highly likely the quantity of the second phase present was extremely small

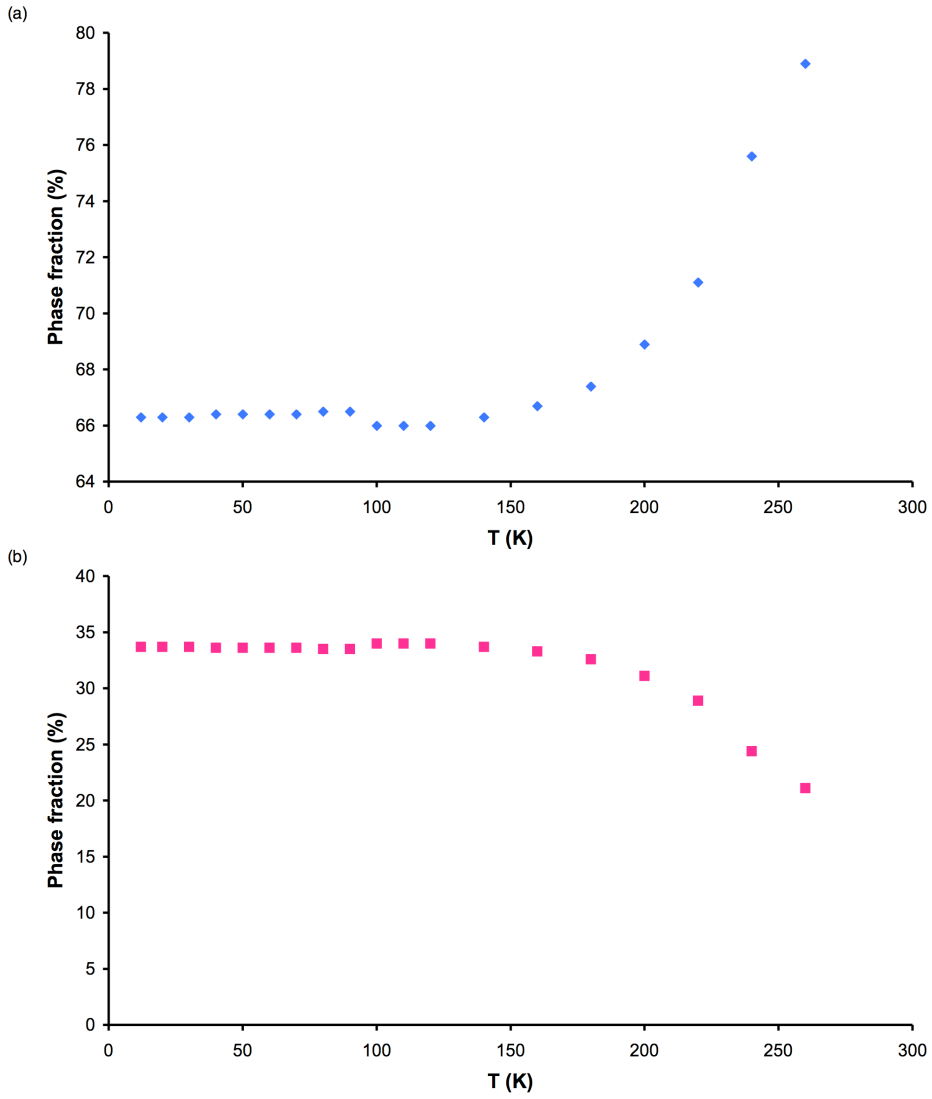

Figure 5.4: Variation of the phase fractions with increasing temperature for the (a) $P2_1ma$ and (b) R3c phases in the sol-gel sample of $NaNbO_3$. Owing to the very small quantities of the Pbcm phase it was not included in any of the multiphase low temperature Rietveld refinements.

and therefore lay undetected in the sample. Hence, it is possible that the smeared dielectric responses obtained in their study could be the result of competing interactions from the presence of *three* different phases of $NaNbO_3$; the R3c, Pbcm and $P2_1ma$ phases.

The sol-gel sample was then gradually warmed to room temperature in 10 K intervals and a diffraction pattern was recorded at each temperature. Rietveld refinements were completed for all datasets obtained, and in the range $20 < T < 260$ K phase coexistence was observed

between the $P2_1ma$, Pbcm and R3c phases. Multiphase Rietveld refinements were completed for each dataset using the $P2_1ma$ and R3c phases and each displayed good agreement with the 12 K data. Interestingly, the refined phase fractions obtained for all datasets ≤ 160 K indicated virtually identical ratios of the two refined phases, ~66% and ~33% of the $P2_1ma$ and R3c phases respectively. A plot highlighting the change in phase fraction of the $P2_1ma$ and R3c phases with increasing temperature is shown in Figure 5.4(a) and (b), respectively. The existence of the $P2_1ma$ phase over such a large temperature range suggests it is a relatively stable polymorph, both at room and low temperatures. The Rietveld refinements completed for the datasets collected at 20 K, 50 K, 100 K and 160 K are shown in Figures 5.5, 5.6, 5.7 and 5.8, respectively.

To monitor the variation observed in the superstructure peaks as a function of temperature peaks from each dataset corresponding to this region have been overlaid and compared, as shown in Figure 5.9. When directly compared it is clear to see the superstructure peaks for the $P2_1ma$ phase appear broadened at low temperatures and much narrower at higher temperatures. All associated structural parameters obtained for the Rietveld refinement completed for the 20 K, 50 K, 100 K and 160 K data can be found in Tables 5.4 – 5.7, respectively, and all corresponding bond lengths are given in Appendix IV. The Rietveld refinements completed for all remaining datasets in this temperature range are given in Appendix IV. All corresponding structural parameters, including refined atomic coordinates and bond lengths are also given in Appendix IV.

During this investigation it was not possible to achieve greater than ~34% of the R3c phase. One possible reason for this is that the sample was not cooled for long enough at 12 K to enable full conversion to the R3c phase. The sample was quenched to 12 K and allowed to equilibrate for approximately 10 minutes before any diffraction data was collected. Both short (30 minutes) and long (2 hours) datasets were obtained at 12 K and both appeared identical. When refined, each indicated identical ratios of the two phases. It is therefore possible that the time allocated to enable the sample to equilibrate was not sufficient to allow the inner most regions of the sample to fully cool. The sol-gel sample remained at 12 K for ~4 hours. However, in that time the sample did not fully convert to the R3c

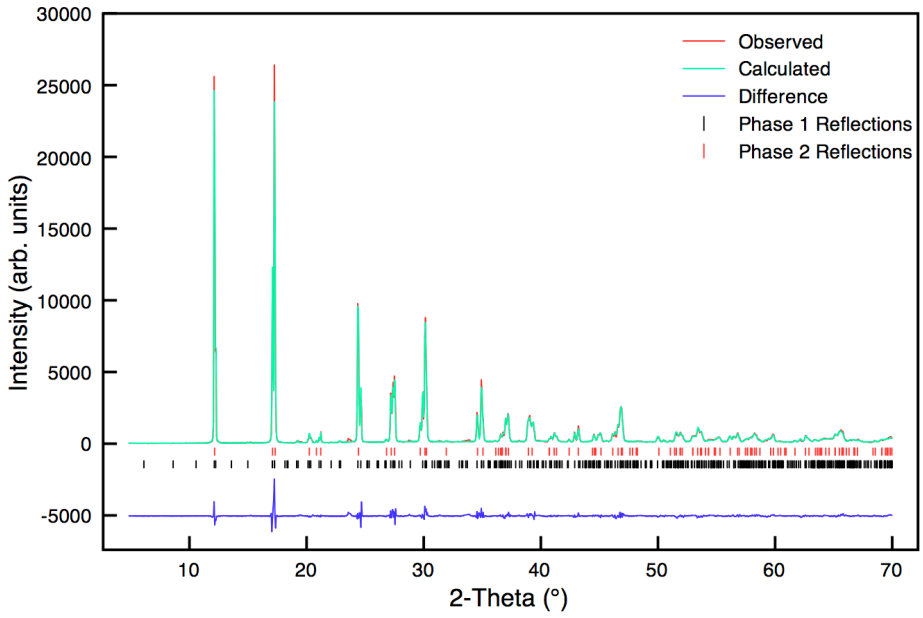

Figure 5.5: Multiphase Rietveld profile of s-PXRD data (20 K) for sol-gel $NaNbO_3$ using models $P2_1ma$ (Phase 1) and R3c (Phase 2).

Table 5.4: Structural parameters for sol-gel $NaNbO_3$ (20 K) from s-PXRD data, using isotropic thermal factors. Space group $P2_1ma$, a = 5.56806(3) Å, b = 7.75318(3) Å, c = 5.50728(3) Å and V = 237.750(1) Å^3. Space group R3c, a = 5.56238(3) , α = 59.142(1)° and V = 119.313(1) Å^3. $\chi^2 = 5.7$, $wR_p = 11.2\%$ and $R_p = 7.9\%$.

Phase	Atom	Site	x	y	z	U(iso) × 100 / Å^2
$P2_1ma$	Na1	2a	0.2286(9)	0	0.7571(10)	0.13(3)
	Na2	2b	0.2491(12)	0.5	0.7566(9)	0.13(3)
	Nb1	4c	0.2574(5)	0.2506(2)	0.2550(1)	0.19(1)
	O1	2a	0.2450(17)	0	0.3204(14)	1.05(4)
	O2	2b	0.2287(12)	0.5	0.1844(14)	1.05(4)
	O3	4c	0.0489(9)	0.2772(6)	0.5375(14)	1.05(4)
	O4	4c	−0.0061(13)	0.2143(5)	0.0153(14)	1.05(4)
R3c	Na1	2a	0.2580(7)	0.2580(7)	0.2580(7)	0.73(4)
	Nb1	2a	0.0043(4)	0.0043(4)	0.0043(4)	0.51(9)
	O1	6b	0.3069(5)	−0.2733(13)	0.1853(4)	0.05(5)

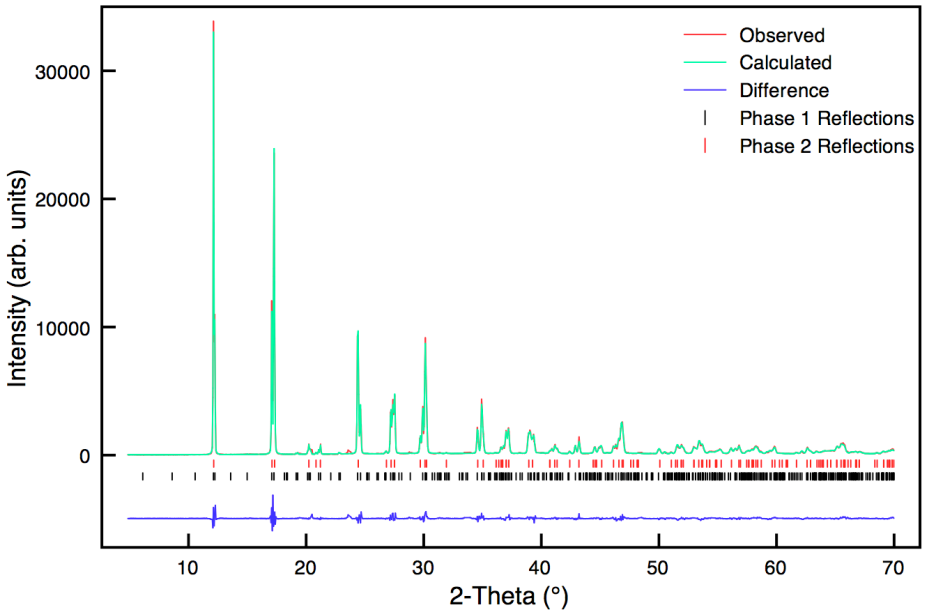

Figure 5.6: Multiphase Rietveld profile of s-PXRD data (50 K) for sol-gel $NaNbO_3$ using models $P2_1ma$ (Phase 1) and R3c (Phase 2).

Table 5.5: Structural parameters for sol-gel $NaNbO_3$ (50 K) from s-PXRD data, using isotropic thermal factors. Space group $P2_1ma$, a = 5.56811(4) Å, b = 7.75422(4) Å, c = 5.50736(4) Å and V = 237.788(3) Å^3. Space group R3c, a = 5.56240(3) , α = 59.143(1)° and V = 119.319(1) Å^3. $\chi^2 = 5.6$, $wR_p = 11.0\%$ and $R_p = 7.9\%$

Phase	Atom	Site	x	y	z	U(iso) × 100 / Å^2
$P2_1ma$	Na1	2a	0.2292(9)	0	0.7574(10)	0.14(3)
	Na2	2b	0.2468(13)	0.5	0.7558(10)	0.14(3)
	Nb1	4c	0.2575(6)	0.2505(3)	0.2551(2)	0.22(1)
	O1	2a	0.2475(17)	0	0.3221(14)	1.13(5)
	O2	2b	0.2275(13)	0.5	0.1823(15)	1.13(5)
	O3	4c	0.0485(9)	0.2771(6)	0.5379(15)	1.13(5)
	O4	4c	−0.0054(14)	0.2148(6)	0.0151(15)	1.13(5)
R3c	Na1	2a	0.2588(6)	0.2588(6)	0.2588(6)	0.73(4)
	Nb1	2a	0.0046(4)	0.0046(4)	0.0046(4)	0.51(9)
	O1	6b	0.3059(5)	−0.2721(13)	0.1860(4)	0.05(5)

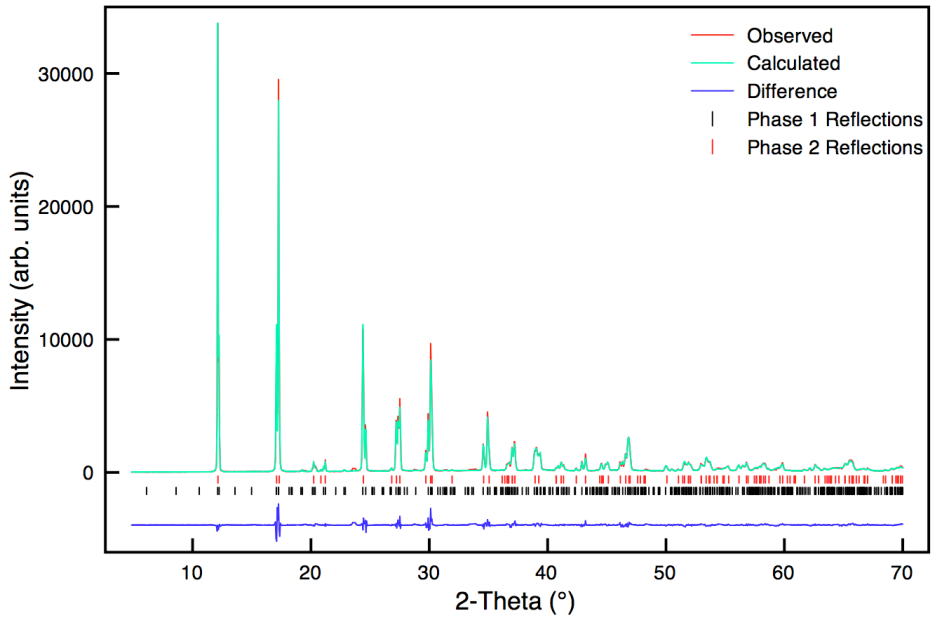

Figure 5.7: Multiphase Rietveld profile of s-PXRD data (100 K) for sol-gel $NaNbO_3$ using models $P2_1ma$ (Phase 1) and R3c (Phase 2).

Table 5.6: Structural parameters for sol-gel $NaNbO_3$ (100 K) from s-PXRD data, using isotropic thermal factors. Space group $P2_1ma$, a = 5.56861(3) Å, b = 7.75369(4) Å, c = 5.50772(4) Å and V = 237.808(2) Å^3. Space group R3c, a = 5.56246(3) , α = 59.162(3)° and V = 119.374(1) Å^3. χ^2 = 4.9, wR_p = 10.3% and R_p = 7.3%.

Phase	Atom	Site	x	y	z	U(iso) × 100 / Å^2
$P2_1ma$	Na1	2a	0.2279(9)	0	0.7555(9)	0.17(3)
	Na2	2b	0.2425(13)	0.5	0.7532(9)	0.17(3)
	Nb1	4c	0.2547(5)	0.2505(2)	0.2550(1)	0.20(1)
	O1	2a	0.2477(17)	0	0.3211(14)	0.88(5)
	O2	2b	0.2262(12)	0.5	0.1798(14)	0.88(5)
	O3	4c	0.0516(7)	0.2770(6)	0.5408(12)	0.88(5)
	O4	4c	0.0010(11)	0.2150(5)	0.0131(12)	0.88(5)
R3c	Na1	2a	0.2591(6)	0.2591(6)	0.2591(6)	0.73(4)
	Nb1	2a	0.0046(4)	0.0046(4)	0.0046(4)	0.51(9)
	O1	6b	0.3054(5)	−0.2716(12)	0.1865(4)	0.05(5)

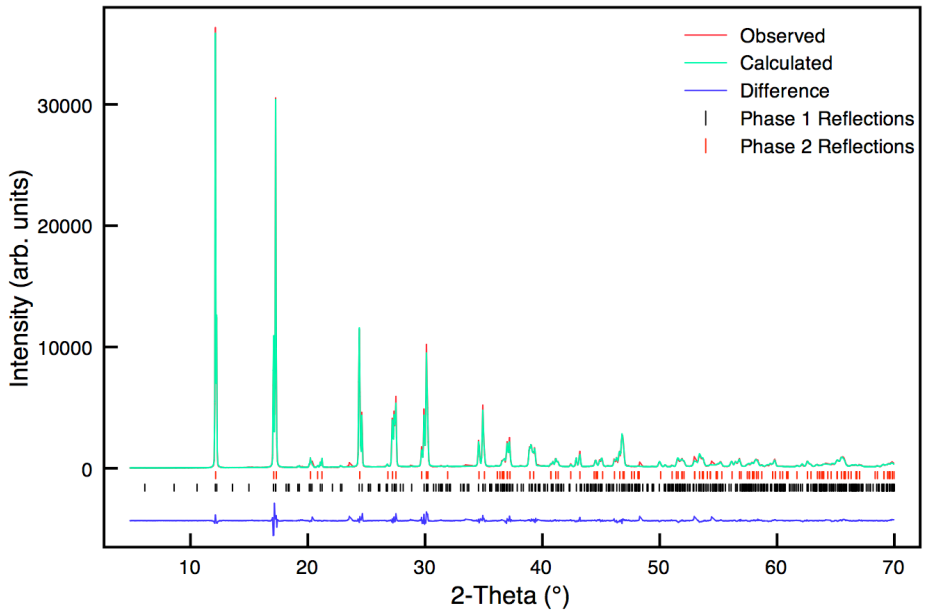

Figure 5.8: Multiphase Rietveld profile of s-PXRD data (160 K) for sol-gel $NaNbO_3$ using models $P2_1ma$ (Phase 1) and R3c (Phase 2).

Table 5.7: Structural parameters for sol-gel $NaNbO_3$ (160 K) from s-PXRD data, using isotropic thermal factors. Space group $P2_1ma$, a = 5.56924(3) Å, b = 7.75867(3) Å, c = 5.50984(3) Å and V = 238.079(2) Å^3. Space group R3c, a = 5.56297(3) , α = 59.198(1)° and V = 119.507(1) Å^3. $\chi^2 = 5.2$, $wR_p = 10.4\%$ and $R_p = 7.2\%$.

Phase	Atom	Site	x	y	z	U(iso) × 100 / Å^2
$P2_1ma$	Na1	2a	0.2312(9)	0	0.7539(9)	0.48(3)
	Na2	2b	0.2442(12)	0.5	0.7531(9)	0.48(3)
	Nb1	4c	0.2557(5)	0.2504(3)	0.2552(1)	0.28(1)
	O1	2a	0.2462(16)	0	0.3176(14)	0.86(5)
	O2	2b	0.2222(11)	0.5	0.1780(14)	0.86(5)
	O3	4c	0.0514(7)	0.2773(6)	0.5429(12)	0.86(5)
	O4	4c	0.0005(11)	0.2167(5)	0.0115(12)	0.86(5)
R3c	Na1	2a	0.2611(5)	0.2611(5)	0.2611(5)	0.73(4)
	Nb1	2a	0.0048(4)	0.0048(4)	0.0048(4)	0.51(9)
	O1	6b	0.3038(5)	−0.2723(12)	0.1879(4)	0.05(5)

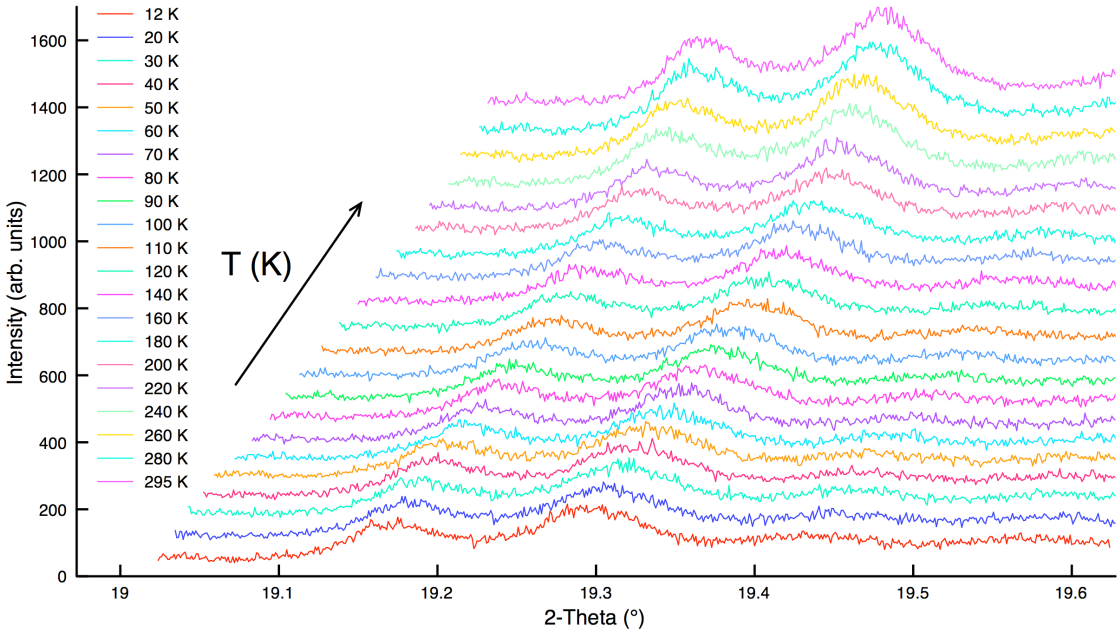

Figure 5.9: Variation of peak intensity with increasing temperature for the region 2θ = 19.0° - 19.6° for sol-gel $NaNbO_3$.

phase. This suggests that to produce the R3c phase the sample would need to remain at very low temperatures for a considerably longer period of time. It is therefore likely that Mishra *et al*. cooled their sample for a much longer period of time during the course of their variable temperature study to achieve 78% and 22% of the R3c and Pbcm phases respectively. However, no specific experimental details were provided regarding the period of time that the sample remained at low temperatures. The findings presented therefore suggest that it is not possible to achieve full conversion of the $P2_1ma$ phase to the low temperature phase using the conditions utilised during this particular s-PXRD variable temperature study. Realistically, to achieve full conversion the sample would need to be cooled for long enough to enable the inner region of the sample to be fully cooled. This could potentially take many days or even weeks to achieve. At present, the user time available on machines such as I11 and HRPD is highly competitive and over subscribed. Therefore it is unlikely an experiment requiring many days or even weeks would be allocated a sufficient amount of user time. A method is therefore required that will sufficiently cool the sample prior to mounting on the diffractometer for analysis. This way it is possible to

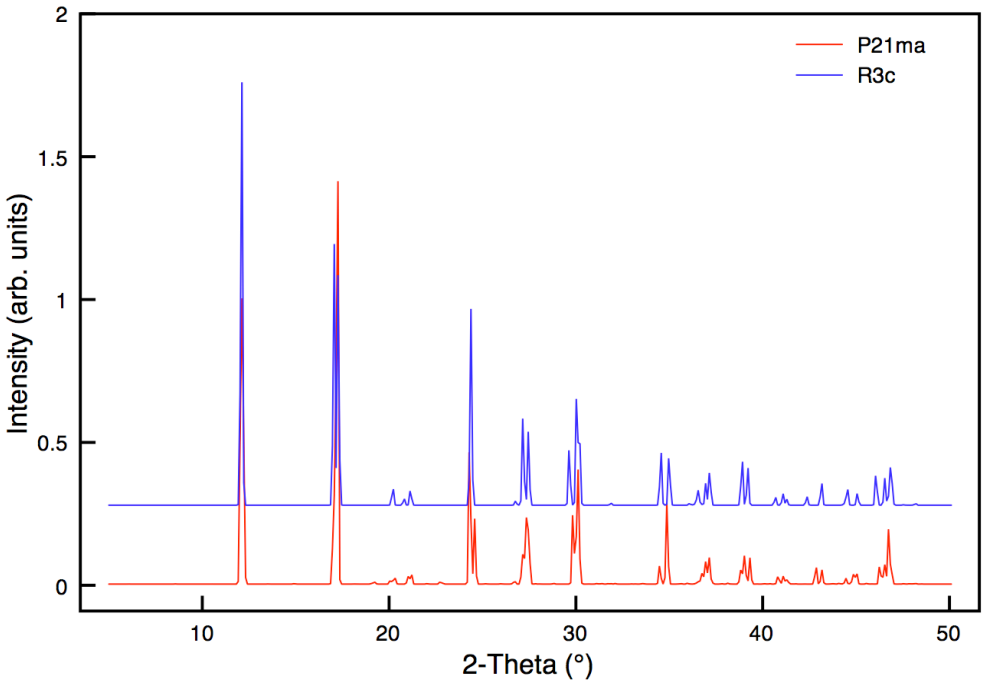

Figure 5.10: Simulated diffraction patterns (using λ = 0.826952 Å) for the $P2_1ma$ and R3c phases of $NaNbO_3$.

ensure complete conversion of the sample to the correct phase has occurred prior to the high-resolution diffraction study.

The Rietveld refinements completed for datasets in the temperature region 180 < T < 280 K suggest the gradual removal of the R3c phase from the sample. This was confirmed by the refined phase fractions obtained for the two phases, as shown in Figure 5.4. It is, however, much harder to visually observe the removal of the R3c phase by examination of solely the diffraction patterns obtained. The $P2_1ma$ and R3c phases of $NaNbO_3$ possess very similar diffraction patterns, as shown in Figure 5.10 where the two have been simulated and overlaid. When compared it is clear to see that many of the observed peak positions for the two phases are severely overlapped. The three phase coexistence observed at 12 K highlights how difficult it can be to distinguish between the two phases and identify which peaks belong to which phase. However, the simulated diffraction patterns shown in Figure 5.10 highlight a very important point. The most intense peaks for the $P2_1ma$ and R3c phases appear at different values of 2θ. The most intense reflection for the $P2_1ma$ phase appears at

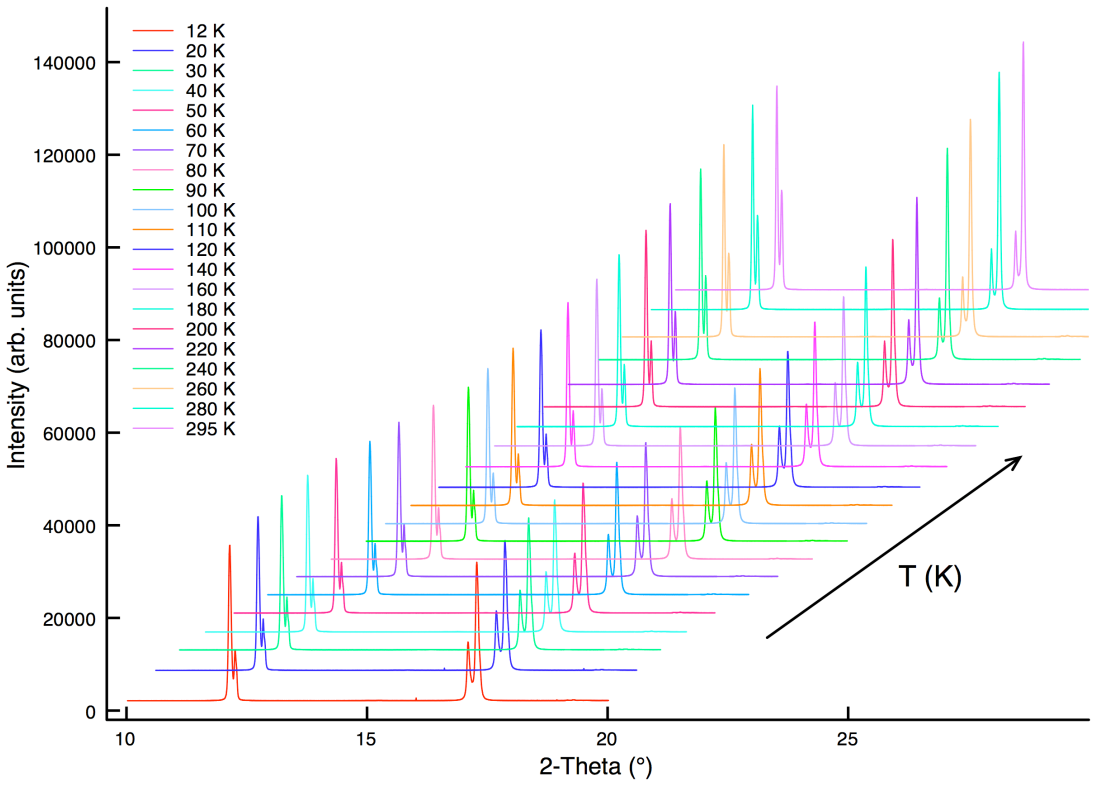

Figure 5.11: Variation of peak intensity with increasing temperature for the region 2θ = 10° – 20° for the sol-gel $NaNbO_3$.

2θ = 17°, whereas the largest peak in the R3c phase appears at 2θ = 12°. The relative intensities of the two peaks at 2θ = 12° and 17° are therefore key in distinguishing between the $P2_1ma$ and R3c phases in each of the datasets obtained. Expansions of this particular region for each dataset have been overlaid and compared, and are shown in Figure 5.11. In the 12 K dataset the doublet at 2θ = 12° possesses greater intensity than that at 2θ = 17°. This appears to be in good agreement with the presence of the R3c phase at low temperatures, as it corresponds to the most intense peak initially identified in the simulated diffraction pattern for the R3c phase. The intensity of each peak in the doublet then gradually increases with increasing temperature. The second doublet, at 2θ = 17°, appears to correlate with the most intense peak identified in the simulated diffraction pattern for the $P2_1ma$ phase of $NaNbO_3$. The intensity of this doublet increases with temperature and is in good agreement with earlier discussions regarding the return of the $P2_1ma$ phase to the sol-gel sample upon warming to room temperature. It is important to note that the ratio

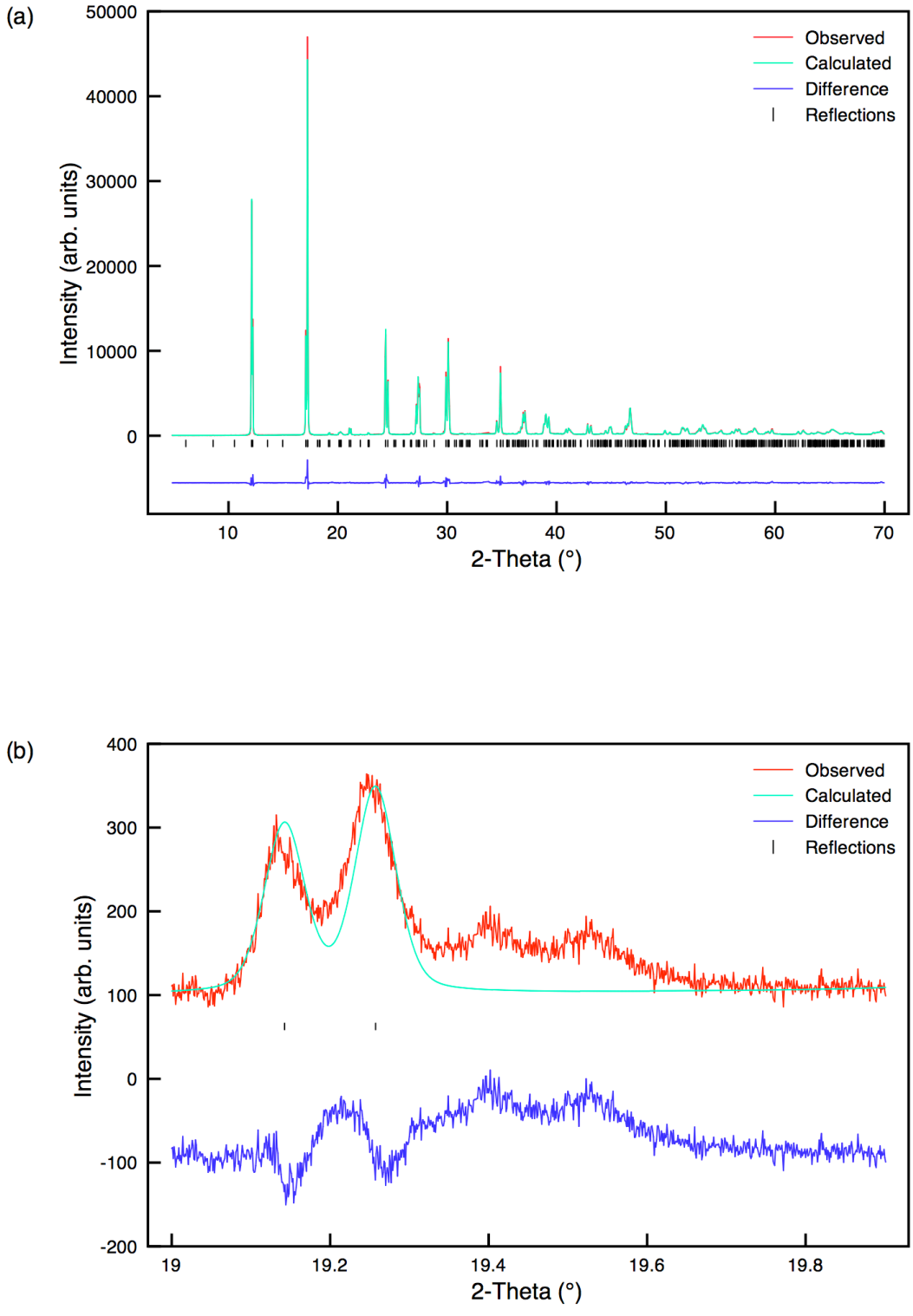

Figure 5.12: (a) Rietveld profile of s-PXRD data (280 K) for sol-gel $NaNbO_3$ using model $P2_1ma$ and (b) corresponding expansion of the superstructure peaks in the region 19° - 19.9°.

Table 5.8: Structural parameters for sol-gel $NaNbO_3$ (280 K) from s-PXRD data, using isotropic thermal factors. Space group $P2_1ma$, a = 5.57014(2) Å, b = 7.77311(3) Å, c = 5.51541(2) Å and V = 238.802(2) Å^3. $\chi^2 = 5.3$, $wR_p = 10.3\%$ and $R_p = 7.3\%$.

Atom	Site	x	y	z	U(iso) × 100 / Å^2
Na1	2a	0.2238(9)	0	0.7568(7)	1.2(2)
Na2	2b	0.2403(13)	0.5	0.7537(6)	1.4(2)
Nb1	4c	0.2456(5)	0.2506(2)	0.2550(1)	0.64(1)
O1	2a	0.2476(17)	0	0.3100(10)	1.04(3)
O2	2b	0.2346(14)	0.5	0.1879(10)	1.04(3)
O3	4c	0.0520(6)	0.2768(5)	0.5404(7)	1.04(3)
O4	4c	0.0001(7)	0.2176(4)	0.0172(7)	1.04(3)

of the two peaks at 12 K were very similar. However, upon warming the peak at 2θ = 17° is considerably more intense. Again this is in agreement with an increase in the amount of the $P2_1ma$ phase present in the sample.

Gradually, the R3c phase was reduced from ~33% at 12 K to ~21% at 260 K and was fully eradicated from the sample at ~280 K. It must be noted that the precise temperature required to fully eradicate the R3c phase is currently unknown. Single phase Rietveld refinements were therefore completed for the datasets collected at 280 K and 295 K, these are shown in Figure 5.12 and 5.13, respectively. Also shown in Figures 5.12(b) and 5.13(b) are expansions of the superstructure region, 19.0° - 19.9°, for each Rietveld refinement. Superstructure peaks belonging to the Pbcm phase (19.4° and 19.5°) are clearly present in each, confirming the presence of the Pbcm phase for the duration of the variable temperature study of $NaNbO_3$. Specific structural details obtained from each refinement can be found in Tables 5.8 and 5.9, respectively. The associated bond lengths obtained from each refinement are given in Appendix IV.

Work by Mishra *et al*. concluded that a phase coexistence occurred between the Pbcm and R3c phases over a large temperature range.

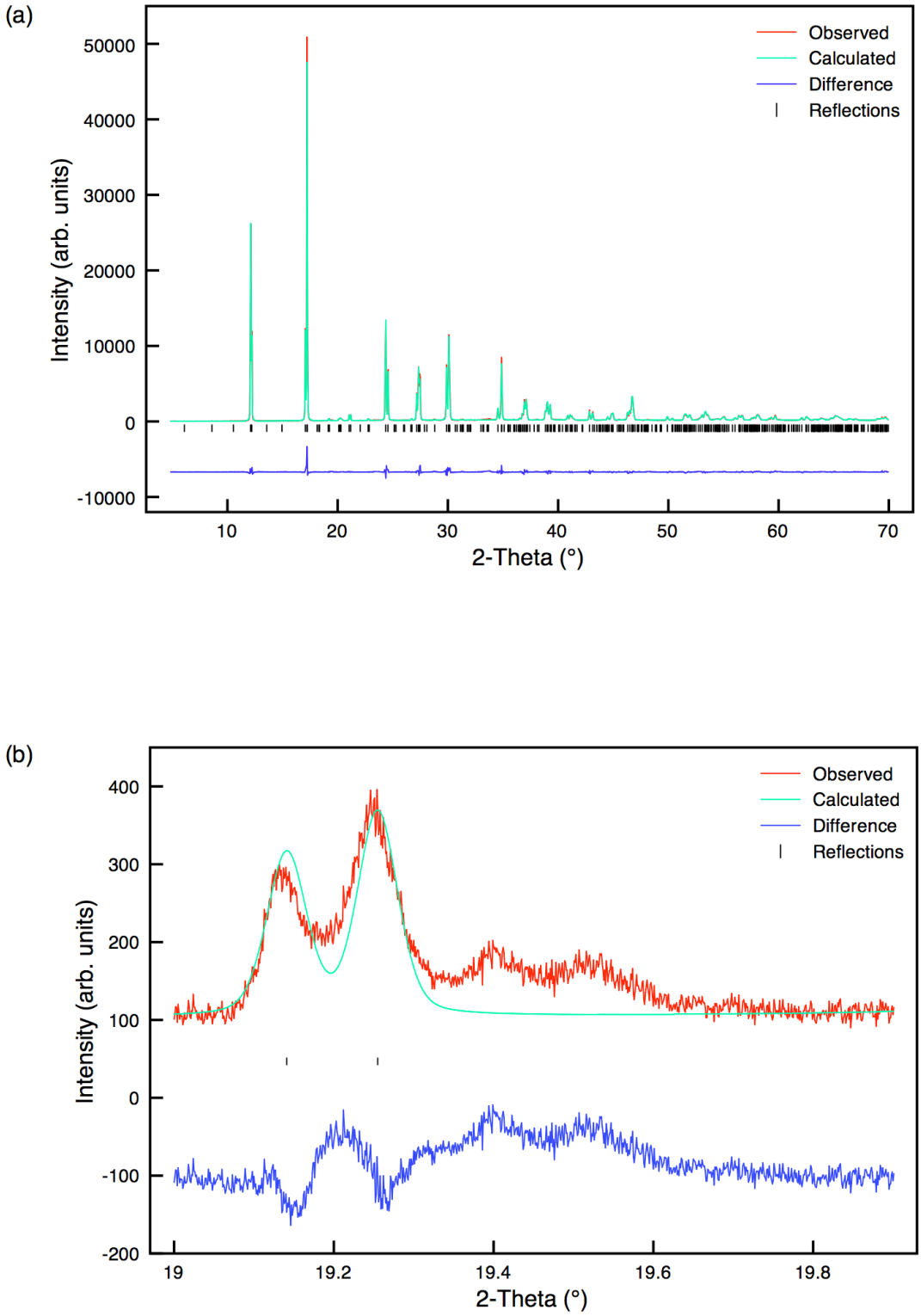

Figure 5.13: (a) Rietveld profile of s-PXRD data (295 K) for sol-gel $NaNbO_3$ using model $P2_1ma$ and (b) corresponding expansion of the superstructure peaks in the region $2\theta = 19° - 19.9°$.

Table 5.9: Structural parameters for sol-gel $NaNbO_3$ (295 K) from s-PXRD data, using isotropic thermal factors. Space group $P2_1ma$, a = 5.57034(2) Å, b = 7.77443(2) Å, c = 5.51611(2) Å and V = 238.828(2) Å^3. $\chi^2 = 4.6$, $wR_p = 9.5\%$ and $R_p = 6.9\%$.

Atom	Site	x	y	z	U(iso) × 100 / Å^2
Na1	2a	0.2272(7)	0	0.7547(6)	1.31(19)
Na2	2b	0.2466(11)	0.5	0.7557(6)	1.4(2)
Nb1	4c	0.2484(4)	0.2506(2)	0.2552(1)	0.63(1)
O1	2a	0.2426(14)	0	0.3092(9)	1.19(3)
O2	2b	0.2269(9)	0.5	0.1880(9)	1.19(3)
O3	4c	0.0524(4)	0.2753(5)	0.5408(6)	1.19(3)
O4	4c	−0.0001(6)	0.2193(4)	0.0167(7)	1.19(3)

However, it is difficult to establish whether their sample was initially phase pure Pbcm as no information was provided regarding the synthesis method used. Furthermore, the superstructure region of their published diffraction data was not clearly shown. Therefore, it is possible that their sample also contained small quantities of the $P2_1ma$ polymorph that remained undetected during the course of the experiment. Within this particular investigation we have identified a region of phase coexsistence, between the $P2_1ma$, Pbcm and R3c phases of $NaNbO_3$ in the temperature range $12 < T < 280$ K. Upon heating to room temperature associated trends were observed in both the lattice parameters and unit cell volume for both the $P2_1ma$ and R3c phases. A gradual increase in the lattice parameters was observed for each phase with increasing temperature and, as a direct consequence, an increase in the cell volume was also observed. Plots highlighting the variation in the unit cell parameters and cell volume with increasing temperature for the $P2_1ma$ and R3c phases are shown in Figures 5.14, 5.15 and 5.16, respectively. The variation observed in the unit cell angle, α, for the R3c phase is also shown in Figure 5.16. Megaw and Darlington,[8] developed a convenient set of structural parameters to describe the atomic positions in rhombohedral perovskites. The five parameters, sc, tc, e, ω and d, allow easy recognition of physically important properties. The parameters sc and tc describe the displacements of the A- and B-site cations from their ideal perovskite

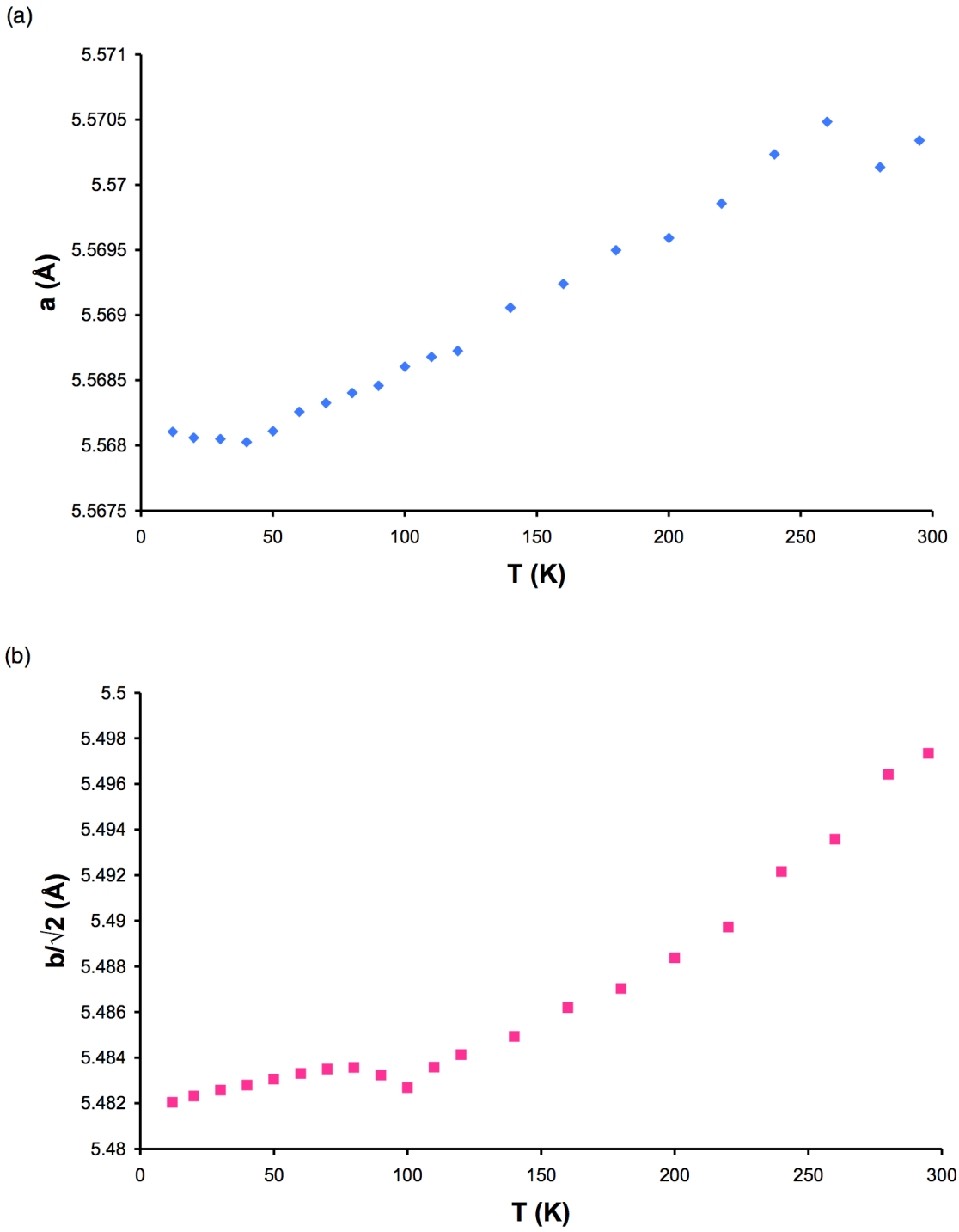

Figure 5.14: Variation of the lattice parameters (a) a and (b) b/√2 with increasing temperature for the $P2_1ma$ phase in the sol-gel sample of $NaNbO_3$. Note that the lattice parameter b has been divided by √2 to enable direct comparison with lattice parameters a and c. The estimated error bars are smaller than the symbols used and are therefore not shown.

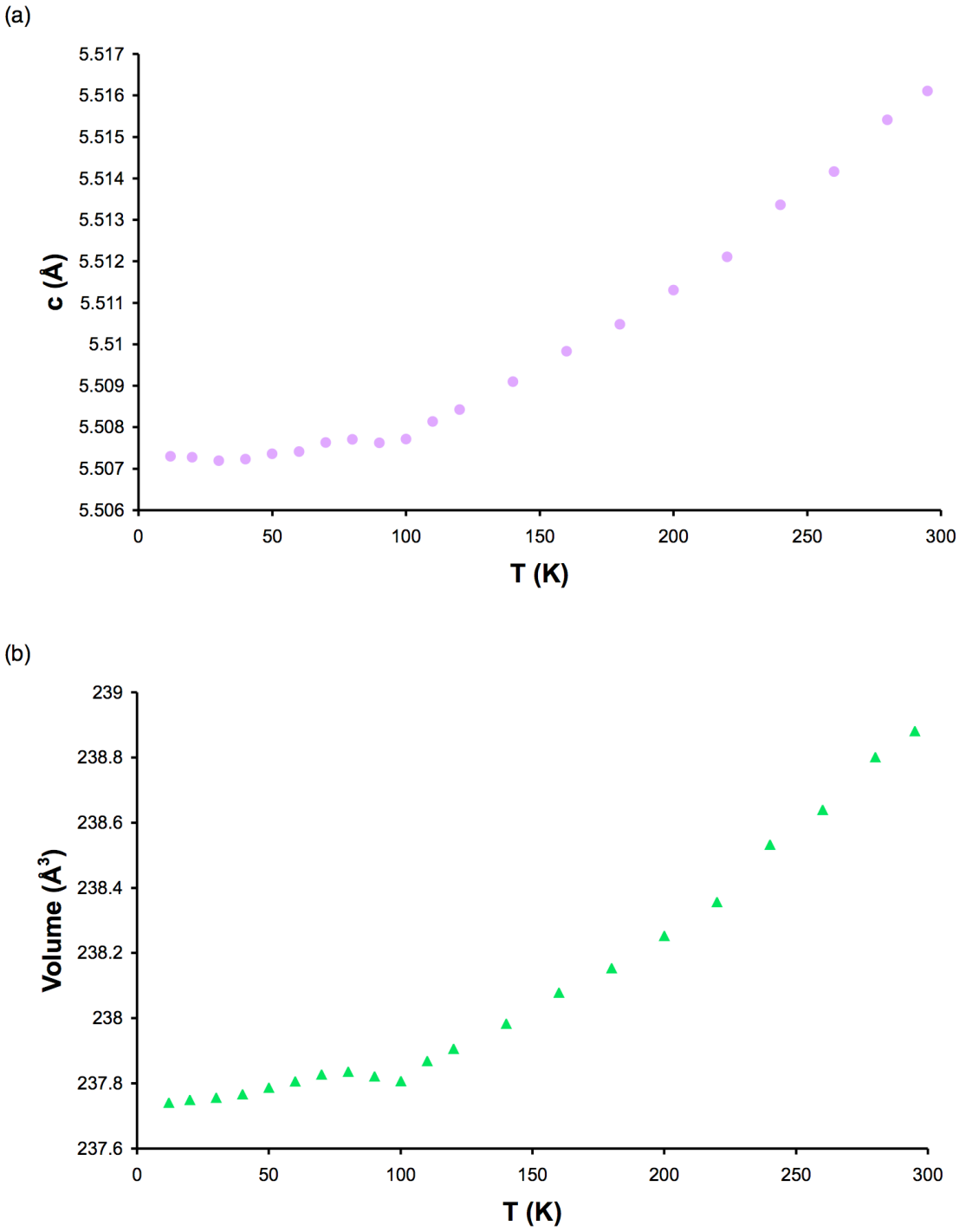

Figure 5.15: Variation of (a) the unit cell parameter c and (b) the unit cell volume with increasing temperature for the $P2_1ma$ phase in the sol-gel sample of $NaNbO_3$. The estimated error bars are smaller than the symbols used and are therefore not shown.

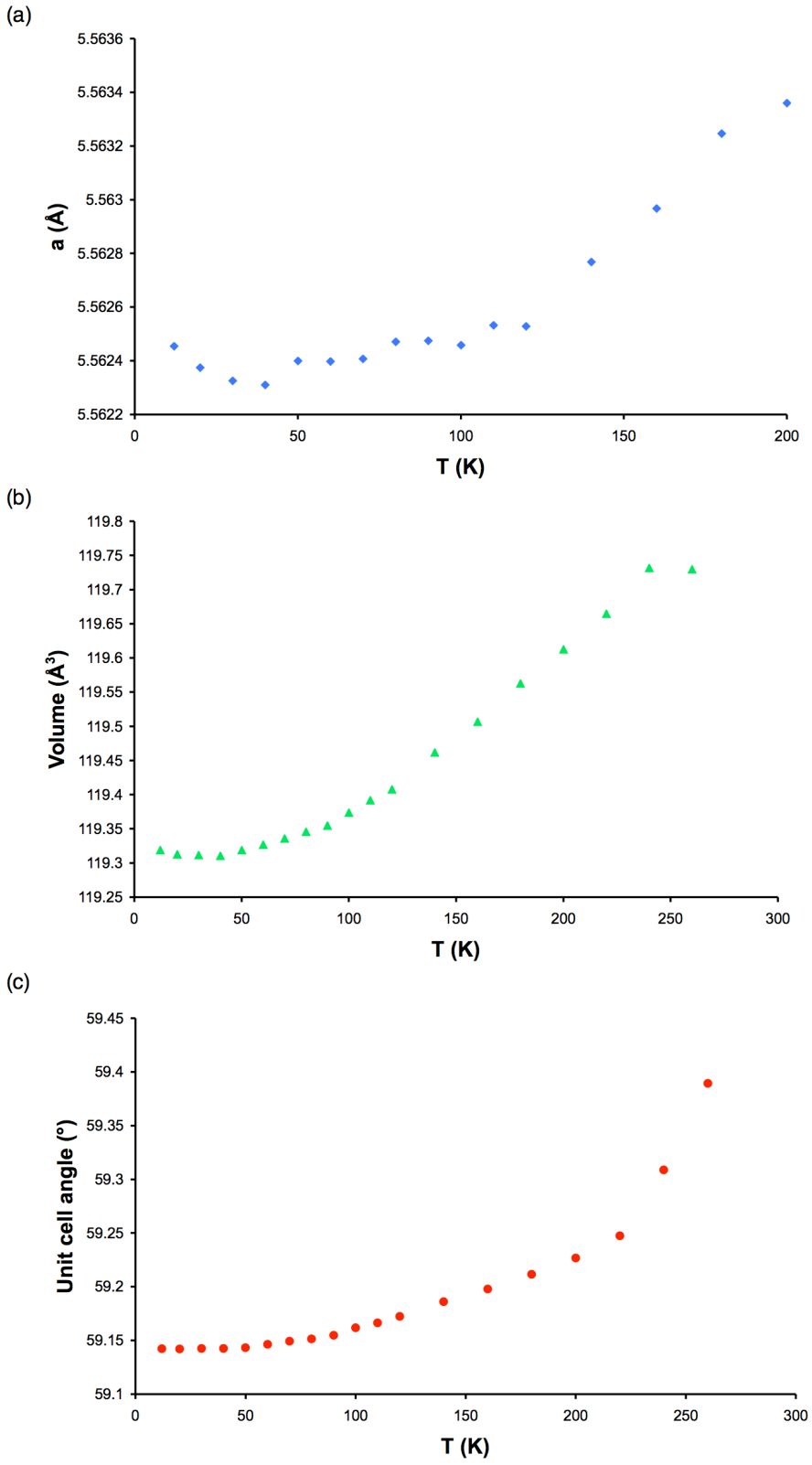

Figure 5.16: Variation of (a) the unit cell parameter a, (b) the unit cell volume and (c) the unit cell angle with increasing temperature for the R3c phase in the sol-gel sample of $NaNbO_3$. The estimated error bars are smaller than the symbols used and are therefore not shown.

positions, giving rise to a dipole moment and, hence, spontaneous polarisation. The parameter e is related to the tilt angle, ω, of the oxygen octahedra by

$$\tan\omega = 4\sqrt{3e} \quad , \tag{5.1}$$

whilst the parameter d describes the distortion of the octahedra in the rhombohedral perovskite. Each of the parameters developed by Megaw and Darlington have been calculated for the R3c phase of $NaNbO_3$, and the variation of each with increasing temperature is shown in Figures 5.17 and 5.18. The oxygen octahedral rotation angle, ω, gradually decreases with increasing temperature whilst the octahedral distortion, gradually increases with temperature, as shown in Figure 5.17. Hence, at low temperatures the octahedra in the R3c phase of $NaNbO_3$ exhibit small distortions and large tilt angles. The parameters sc and tc increase with temperature, indicating large displacements of the A- and B-site cations from their ideal positions, as shown in Figure 5.18.

Shiratori *et al.*[226] suggested factors such as strain, particle size and domain structure influence the phases of $NaNbO_3$ formed. Hence, it is believed intrinsic effects such as the strain and development of domain structure could determine specific polymorph stability. Throughout this study the $P2_1ma$ polymorph was consistently found to be the most favourable phase in the sol-gel $NaNbO_3$ sample at both room and low temperatures. The continued presence and overall stability of this phase therefore suggests intrinsic effects such as particle size, domain structure, stress and strain may heavily influence the phases of $NaNbO_3$ formed.

5.4 Conclusions

To summarise, we have shown it is not possible to eradicate the $P2_1ma$ polymorph from the sol-gel sample of $NaNbO_3$ at temperatures as low as 12 K (at least under these cooling conditions). However, we have shown, using high-resolution variable temperature s-PXRD studies, that over a relatively large temperature range, $12 < T < 280$ K, a region of considerable phase coexistence is observed between the $P2_1ma$, Pbcm and

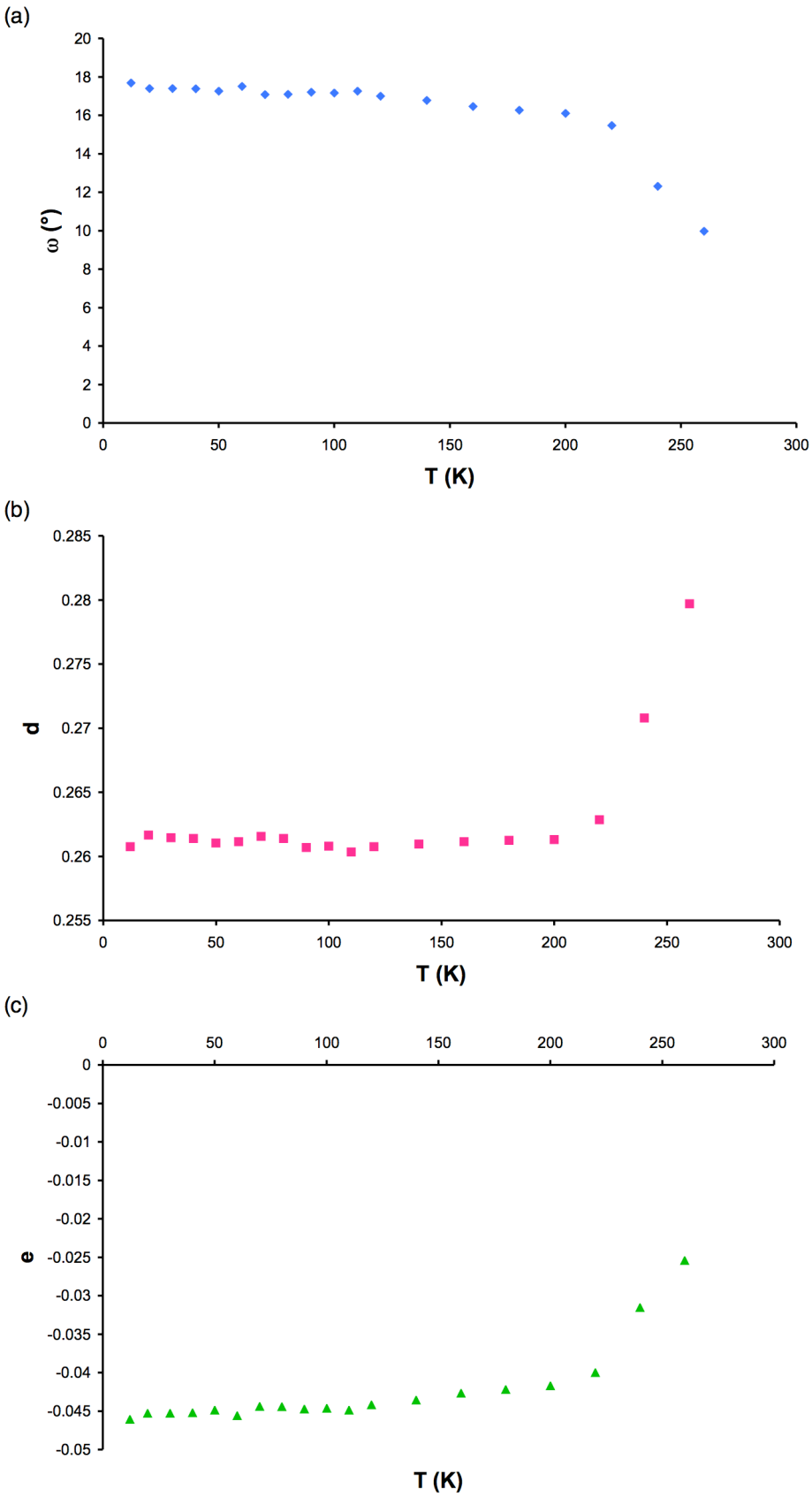

Figure 5.17: Variation of (a) the octahedral rotation angle, ω, and parameters (b) d and (c) e with increasing temperature for the R3c phase in sol-gel $NaNbO_3$.

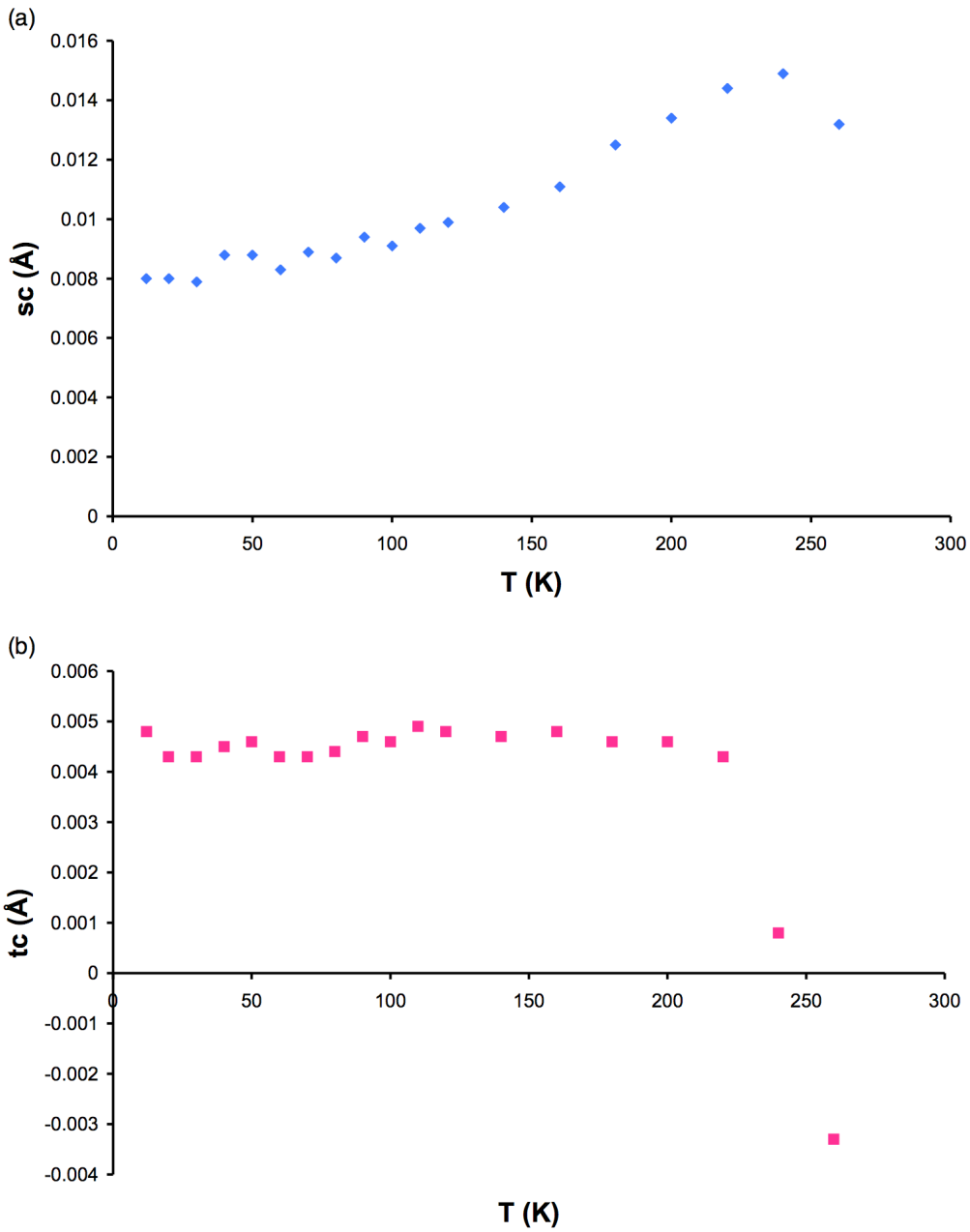

Figure 5.18: Variation of parameters (a) sc and (b) tc with increasing temperature for the R3c phase in sol-gel $NaNbO_3$.

R3c phases of $NaNbO_3$. These findings are in good agreement with recent NPD studies by Mishra *et al.*,[224] completed for Pbcm $NaNbO_3$ in which a similar region of phase coexistence was observed between the ferroelectric R3c and antiferroelectric Pbcm polymorphs. Consistently in this work the $P2_1ma$ phase of $NaNbO_3$ was found to be the abundant phase at both room and low temperatures and this is believed to be the result of various different effects within the sample. Factors such as structural strain,

crystallite size, morphology and domain structure are believed to contribute significantly to the exact phase of $NaNbO_3$ formed at any one time. Hence, there are many contributing factors as to the phase(s) of $NaNbO_3$ formed, both at room and low temperatures.

Chapter 6

The Synthesis and Characterisation of $La_{1-x}Y_xScO_3$

6.1 Introduction

From the mid 1950s to the late 1970s a considerable amount of work was completed on the synthesis, characterisation and crystallographic properties of ternary perovskite-type oxides of transition metals, $LnBO_3$, where Ln and B are trivalent lanthanides and first row transition metals, respectively. In particular, work concentrated on rare earth scandates, vanadates, gallates, orthochromates and orthoferrites.[289-295] Many of these compounds exhibit interesting physical properties which have, in turn, led to important academic and industrial applications. In recent years Liferovich and Mitchell[218] have reinvestigated several ternary lanthanide orthoscandate perovskites and discovered much of the earlier literature to be largely correct. Of the nine compounds investigated many, including $LaScO_3$, were found to be isotructural with $GdFeO_3$.[292,296,297] The $LaScO_3$ structure, in space group Pbnm, contains corner sharing ScO_6 octahedra which display strong orthorhombic tilting about [001], [110] and [111] respectively, as shown in Figure 6.1. At present, materials such as $DyScO_3$ are used as crystal substrates to grow thin films for use in electronic devices.

The closely-related rare earth scandate $YScO_3$ has been investigated numerous times in previous years and is well documented as requiring high-pressure techniques for successful synthesis.[218,298] Although several attempts have been made to synthesise $YScO_3$ using conventional solid-state methods, almost all have been unsuccessful in synthesising phase pure $YScO_3$. Much of the literature in this area suggests the use of exceptionally high annealing temperatures, often in excess of 1600 °C. Samples synthesised using solid-state methods commonly contain only

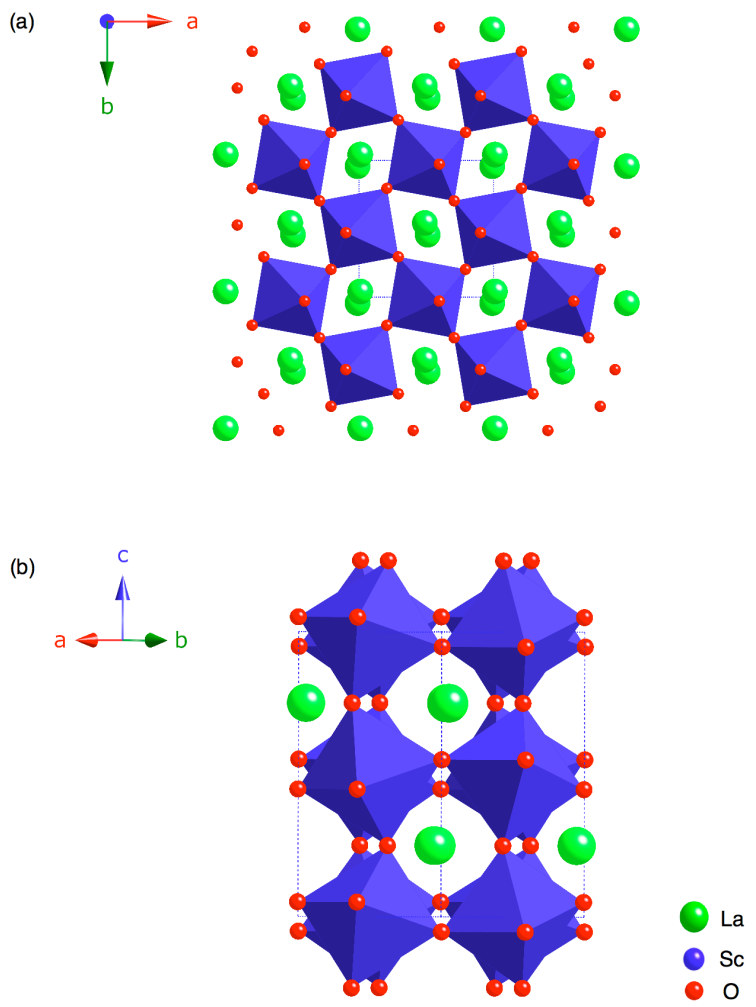

Figure 6.1: The crystal structure of $LaScO_3$ viewed (a) along the c axis and (b) across the ab plane.

trace amounts of the desired $YScO_3$ and large quantities of different impurity phases.[298]

Interestingly, Clark[298] and co-workers in 1978 identified a complex series of rare earth scandates that, in theory, should have produced perovskite-type structures. In reality, however, they preferred to adopt 'C-type' solid-solutions, where preference for both the A- and B-site cations to be on the octahedral site becomes predominant. Under ambient pressure conditions and annealing at 1600 °C many of the compounds identified in this series contained only trace amounts of the desired perovskite and large quantities of a C-type solid-solution. $YScO_3$ was amongst this series. The application of pressure to any system is widely known to favour higher coordinated sites. Hence, Clark *et al.*[298]

reinvestigated this scandate series using pressures of 20 and 30 kbar. Their study concluded that several of the scandates responded well to the application of pressure and phase pure samples were synthesised after only one hour at 20 kbar and 1000 °C. A phase pure sample of $YScO_3$ was reported using these conditions. However, two compounds in this series, $YbScO_3$ and $LuScO_3$, continued to produce C-type solid-solutions even after the application of higher pressures, thus indicating it is not feasible to synthesise these perovskites. When the tolerance factors of these two compounds are considered it becomes apparent as to why these small lanthanides cannot form perovskites. $LaScO_3$ has a tolerance factor of 0.843, indicating it is capable of forming a perovskite structure or suitably distorted version of a perovskite. In contrast, the tolerance factors for $YbScO_3$ (0.799) and $LuScO_3$ (0.783) are lower than the allowed limit, $0.85 < t < 1.06$. Hence it is not physically possible to synthesise either of these compounds.

In 1980 Porotnikov *et al*.[299] reported the first successful synthesis of $YScO_3$ using a two-stage solid-state reaction under ambient pressure conditions. This method of synthesis used very high annealing temperatures for substantial periods of time. To date, no complete structural model is available for $YScO_3$, however, lattice parameters have been suggested from previous high-pressure studies. $YScO_3$ is thought to be isostructural with $HoScO_3$, shown in Figure 6.2.[218] Hence, for accurate structural refinement of any $YScO_3$ diffraction data the reported lattice parameters for $YScO_3$ and the structural model for $HoScO_3$ obtained from the literature can be used.

To date the related solid-solution, $La_{1-x}Y_xScO_3$, has not been reported in the literature. Owing to its small ionic radius, yttrium substitution is feasible, and indeed favourable, on both the A and B sites within the perovskite structure. However, it must be noted that all cations present in the structure will influence precisely at which site yttrium will substitute. It is, therefore, of considerable interest to determine whether any 'C-type' solid-solutions form during the synthesis of the $La_{1-x}Y_xScO_3$ series. The work presented within this chapter concentrates on the synthesis and structural characterisation of the solid-solution $La_{1-x}Y_xScO_3$, for $x = 0, 0.2,$

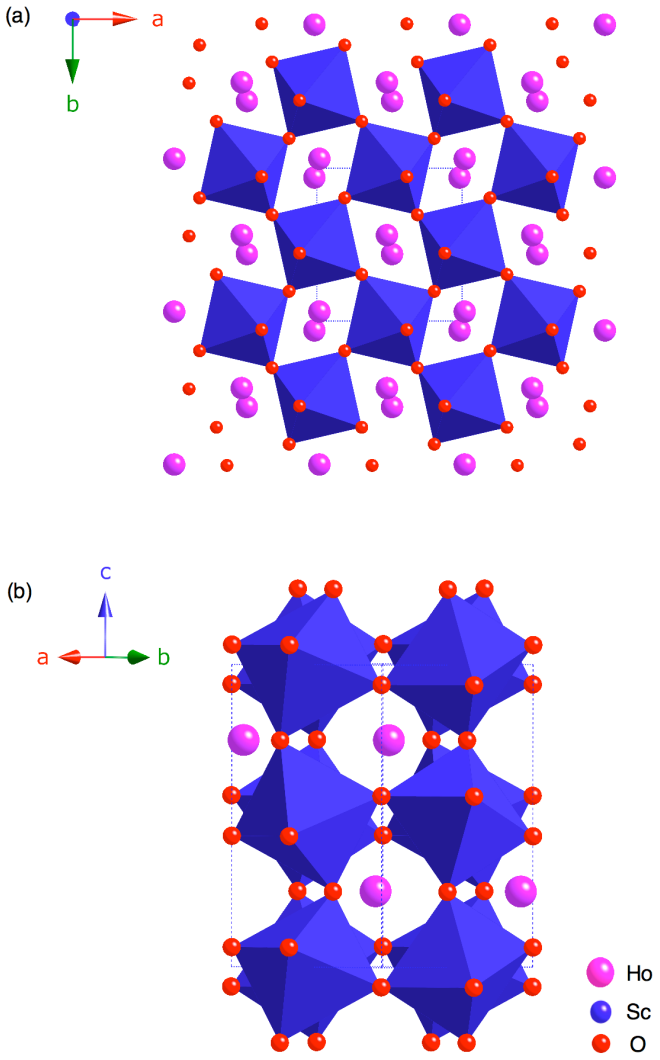

Figure 6.2: The crystal structure of $HoScO_3$ viewed (a) along the c axis and (b) across the ab plane.

0.4, 0.6, 0.8 and 1, using high-resolution powder diffraction, ^{45}Sc (I = 7/2), ^{89}Y (I = 1/2) and ^{17}O (I = 5/2) solid-state NMR and density functional theory (DFT) calculations.

6.2 Experimental

6.2.1 Synthesis

All samples in the series $La_{1-x}Y_xScO_3$ were synthesised using conventional solid-state methods. Stoichiometric amounts of commercial La_2O_3 (Sigma-Aldrich, 99.99%), Y_2O_3 (Sigma-Aldrich, 99.999%) and Sc_2O_3

(Stanford Materials Ltd, 99.995%) were mixed and ground in an agate mortar and pestle with a small quantity of acetone, to aid in the mixing process. Samples were pressed into 1 cm pellets, using a pressure of 10 tons cm^{-2}, and heated at temperatures ranging from 1200 °C to 1450 °C. $LaScO_3$ was prepared using an annealing temperature of 1400 °C for 3 days. Samples in the series $La_{1-x}Y_xScO_3$ (x = 0.2, 0.4, 0.6 and 0.8) were synthesised by heating at 1450 °C for up to 4 days, with intermediate regrinding. $YScO_3$ was synthesised in a two-stage reaction, 1200 °C for 65 hours followed by 1450 °C for 7 days, with intermediate regrinds. After the initial solid-state preparation a small quantity of the $LaScO_3$ sample was enriched using ^{17}O gas. Enrichment was performed by heating the sample under 50% ^{17}O enriched O_2 gas (Isotec, 99% ^{17}O) for 7 days at 950 °C. All ^{17}O enrichments were completed in collaboration with Professor Clare Grey and Dr Frédéric Blanc at the State University of New York, Stony Brook, United States of America.

6.2.2 X-ray and Neutron Powder Diffraction

Room temperature 'laboratory' X-ray diffraction experiments (l-PXRD) were carried out on a Stoe STADI-P diffractometer using Cu $K_{\alpha 1}$ (λ = 1.54056 Å) radiation. Room temperature time-of-flight neutron powder diffraction (NPD) experiments were completed using POLARIS[130-134] at the ISIS neutron spallation source, Rutherford-Appleton Laboratories. All diffraction data were analysed by Rietveld refinement using the GSAS software package.[125]

6.2.3 NMR Spectroscopy

Solid-state NMR spectra were acquired using either Bruker 400 Avance I or 600 Avance III spectrometers, equipped with wide-bore 9.4 T and 14.1 T magnets, respectively using Larmor frequencies of 97.2 MHz and 145.8 MHz for ^{45}Sc (I = 7/2), 29.41 MHz for ^{89}Y (I = 1/2) and 81.4 MHz for ^{17}O (I = 5/2). The finely powdered samples were tightly packed into conventional 4- and 2.5-mm ZrO_2 rotors and magic-angle spinning (MAS)

rates of 14 kHz and 35 kHz, respectively were employed. Chemical shifts were referenced to 0.2 M $ScCl_3$ (aq), 1 M YCl_3 (aq) and H_2O (aq), using $LaScO_3$ (s) (δ = 162.9 ppm), $Y_2Sn_2O_7$ (s) (δ = 65.0 ppm) and 35% ^{17}O enriched clinohumite (δ = 57.0 ppm) as secondary references.

Conventional ^{45}Sc MAS NMR spectra were obtained using single pulse experiments at 9.4 T and 14.1 T with typical pulse lengths of 1.25 μs and 1 μs, respectively. Conventional ^{89}Y and ^{17}O MAS NMR spectra were obtained using single pulse experiments at 14.1 T with typical pulse lengths of 8 μs and 1.5 μs respectively. Optimised recycle intervals for ^{45}Sc, ^{89}Y and ^{17}O were 3 s, 20 s and 20 s, respectively. Typical radiofrequency field strengths employed were 100-150 kHz. Two-dimensional triple-quantum ^{45}Sc MAS NMR experiments were recorded at 14.1 T using the z-filtered pulse sequence shown in Figure 2.28.[178] Spectra result from the averaging of 96 transients with a recycle interval of 3 s for each of the 256 increments of 20 μs. Additional experimental details can be found in the relevant figure captions. Spectral analysis and fitting was performed using the Solids Line Shapes Analysis (SOLA) program within the Topspin 2.1 package.

6.2.4 Scandium Referencing

There is some degree of confusion regarding the most suitable primary reference for ^{45}Sc (I = 7/2).[300-303] Several reference compounds have been suggested in the literature, most commonly $Sc(NO_3)_3$ (aq) and $ScCl_3$ (aq). The concentration of each solution quoted in the literature often varies, thereby making it difficult to establish a consistent primary reference. Within this particular investigation a reliable scandium reference was required to accurately reference all ^{45}Sc MAS and MQMAS NMR spectra. Systematic studies as a function of concentration were therefore completed for $Sc(NO_3)_3$ (aq) and $ScCl_3$ (aq) to establish the most suitable reference.

Nine solutions of $Sc(NO_3)_3$ were prepared with the following concentrations; 2, 1, 0.5, 0.2, 0.1, 0.05, 0.0375, 0.025 and 0.0125 M. In a similar manner seven solutions of $ScCl_3$ were prepared with

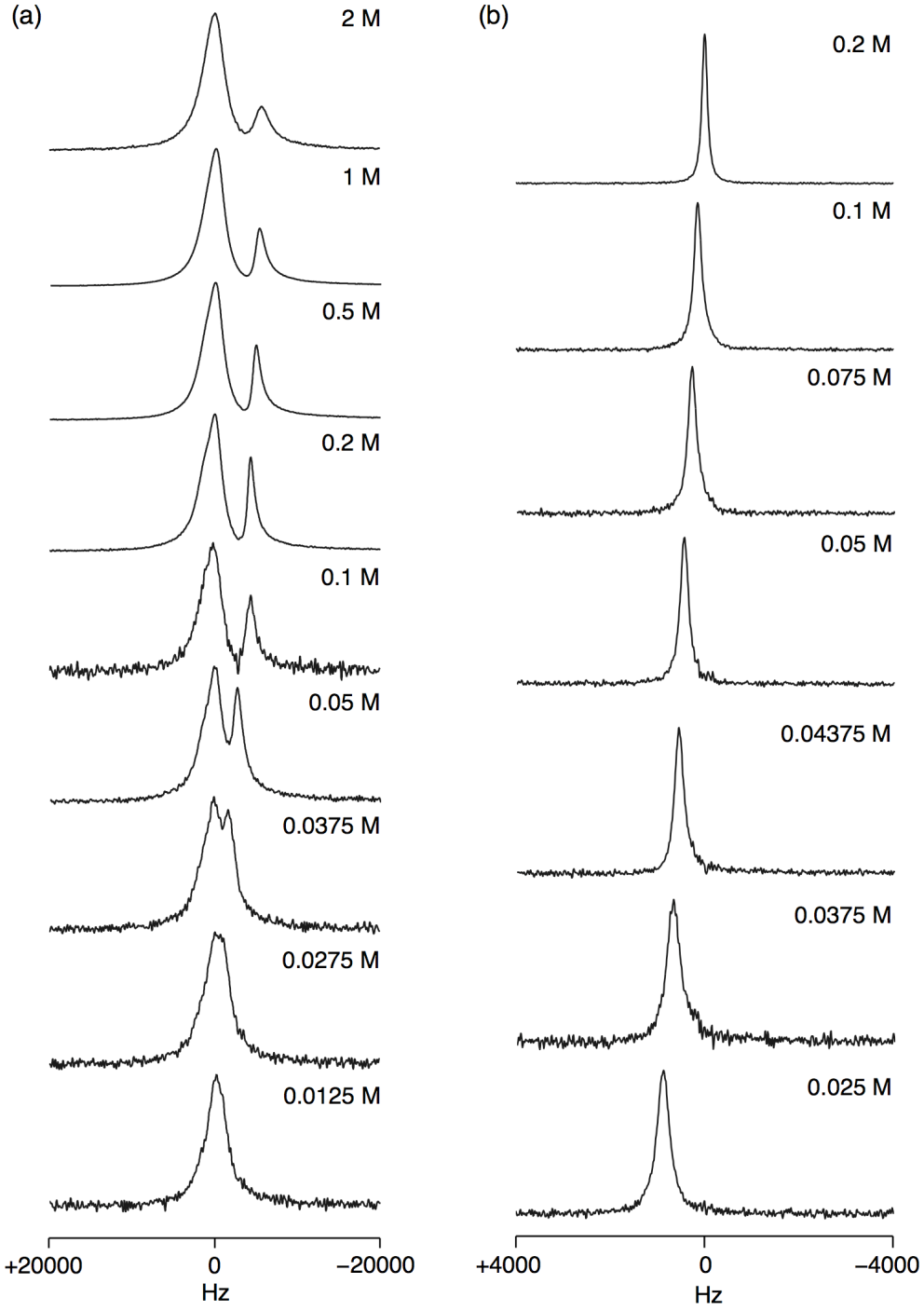

Figure 6.3: ^{45}Sc NMR spectra of solutions of (a) $Sc(NO_3)_3$ and (b) $ScCl_3$ at varying concentrations. The spectra are referenced (in Hz) relative to the transmitter offset in each case.

concentrations; 0.2, 0.1, 0.075, 0.05, 0.04375, 0.0375, 0.025 M. A small quantity of each solution was placed into a 4-mm ZrO_2 rotor and static ^{45}Sc NMR spectra were recorded for each using conventional experiments. All

experimental parameters were initially optimised using 2 M $Sc(NO_3)_3$ (aq) and 0.2 M $ScCl_3$ (aq). Typical pulse lengths were 5 μs with a recycle interval of 0.5 s in each case.

Static ^{45}Sc NMR spectra were recorded for all $Sc(NO_3)_3$ (aq) concentrations. The 2 M solution displayed two resonances, as shown in Figure 6.3(a). Note that all ^{45}Sc NMR spectra shown in Figure 6.3 are referenced relative to the transmitter offset. The 1 M solution also exhibited two resonances. However, one of the two resonances appeared shifted relative to the 2 M $Sc(NO_3)_3$ (aq) spectrum, also shown in Figure 6.3(a). As the concentration was reduced a similar trend was exhibited, as the same resonance continued to shift in each spectrum until the two solutions with the lowest concentrations, 0.025 M and 0.0125 M, displayed a single resonance, as shown in Figure 6.3(a). Spectra recorded for $Sc(NO_3)_3$ (aq) therefore exhibit an obvious concentration dependent shift, most probably owing to hydration of the Sc and the varying number of H_2O molecules in the surrounding coordination environment. Therefore it would not seem feasible to utilise $Sc(NO_3)_3$ as a reliable primary reference.

Static ^{45}Sc NMR spectra were also recorded for all $ScCl_3$ (aq) solutions prepared. The 0.2 M solution displayed a single sharp resonance, as shown in Figure 6.3(b). However, in a similar manner to $Sc(NO_3)_3$ (aq), as the concentration was reduced the resonance was shifted, as shown in Figure 6.3(b). However, a relatively small shift in peak position was observed as a function of concentration, suggesting $ScCl_3$ to be a more consistent and reliable primary reference. Therefore, the resonance displayed in the 0.2 M $ScCl_3$ (aq) was set to be 0 ppm. From this, at 14.1 T, the peak with maximum intensity in the spectrum of $LaScO_3$ was at 162.9 ppm. Therefore, $LaScO_3$ was used as a solid secondary reference. It must be noted that the secondary reference used is field dependent.

6.2.5 Calculations

^{45}Sc, ^{89}Y and ^{17}O density functional theory (DFT) calculations were completed using the CASTEP[214] code. Calculations were converged as far

as possible with respect to k-point spacing and cut-off energy, with typical values of 0.04 $Å^{-1}$ and 60 Ry, respectively. Crystal structures were obtained from both the literature and Rietveld refinement of the NPD data. Where necessary, geometry optimisation of the structure was performed prior to calculation of the NMR parameters. The isotropic chemical shift, δ_{iso}, was obtained from the isotropic shielding, σ_{iso}, using $\delta_{iso} = -(\sigma_{iso} - \sigma_{ref})$, where σ_{ref} is the isotropic shielding (788.6 ppm for ^{45}Sc, 2624.5 ppm for ^{89}Y and 253.7 ppm for ^{17}O), determined from calculations on $LaScO_3$, $YScO_3$ and Mg_2SiO_4, respectively.

6.3 Results and Discussion

6.3.1 $LaScO_3$

Several samples of $LaScO_3$ were initially synthesised to establish feasible reaction conditions. The structure and phase purity of each sample were verified using l-PXRD, and all displayed excellent agreement with the orthorhombic structure (Pbnm) reported in the literature.[218] A Rietveld refinement of $LaScO_3$ using l-PXRD data is shown in Figure 6.4(a). A sample of $LaScO_3$ was also analysed in more detail using high-resolution neutron powder diffraction (NPD). Rietveld refinement of the NPD data also displayed excellent agreement with the orthorhombic structure reported and is shown in Figure 6.4(b). Full refinement details obtained from the NPD data, including anisotropic temperature factors, can be found in Table 6.1.

^{45}Sc is a spin I = 7/2 nucleus with 100% natural abundance and a quadrupole moment of −22.0 fm^2. Given the quadrupolar nature of ^{45}Sc there is, inevitably, the added complication of quadrupolar broadening in the spectra recorded.[304-306] Despite being an extremely attractive nucleus to study by NMR there are, at present, relatively few publications regarding ^{45}Sc solid-state NMR[300-303,306-317] and, as a consequence, little information is known regarding the relationship between observed ^{45}Sc NMR parameters and local structure. A recent study by Kim *et al.*,[191] investigated the ^{45}Sc NMR isotropic chemical shifts and quadrupolar coupling constants of several scandium-containing solid

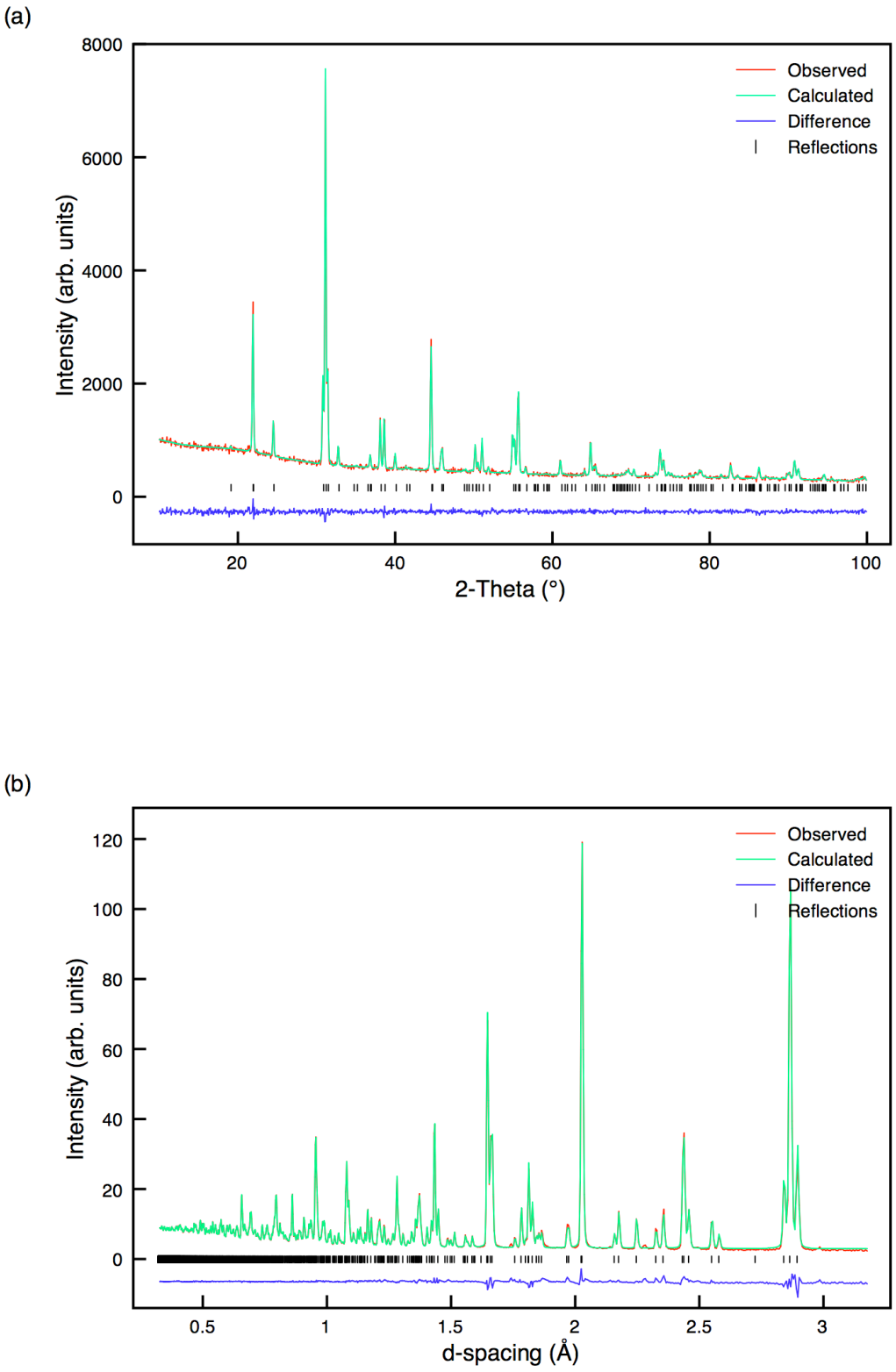

Figure 6.4: Rietveld profiles of (a) l-PXRD and (b) NPD data for $LaScO_3$ using the structural model Pbnm. Anisotropic thermal parameters were used during refinement of the NPD data.

Table 6.1: Structural parameters for $LaScO_3$ from NPD data using anisotropic thermal factors. Space group Pbnm, a = 5.67942(6) Å, b = 5.78720(6) Å, c = 8.09438(8) Å and V = 266.046(6) Å^3. $\chi^2 = 6.8$ and $wR_p = 1.5\%$.

Atom	Site	x	y	z	U_{11} × 100 / Å^2	U_{22} × 100 / Å^2	U_{33} × 100 / Å^2
La	4c	0.0102(1)	0.9565(1)	0.25	0.45(2)	0.48(1)	0.41(2)
Sc	4a	0	0.5	0	0.43(1)	0.42(1)	0.38(1)
O1	4c	0.9047(2)	0.5313(2)	0.25	0.62(2)	0.89(3)	0.19(2)
O2	8d	0.7046(1)	0.2958(1)	0.9493(1)	0.51(2)	0.53(2)	0.79(2)

oxides, including $NaScO_2$, $LiScO_2$, Sc_2O_3, $ScPO_4$ and $ScVO_4$. It was found that both the ^{45}Sc isotropic chemical shifts and quadrupolar coupling constants were highly sensitive to local structure. In particular, it was shown that the ^{45}Sc isotropic chemical shift is largely dominated by coordination number. A difference of more than 150 ppm was observed between shifts for six- and eight-coordinate scandium. In addition, a number of the compounds investigated exhibited very large quadrupolar coupling constants. For example, Sc_2O_3 possesses two Sc sites, each with $C_Q = 23.4$ MHz and $C_Q = 15.3$ MHz respectively.

It must be noted that the cost associated with synthesising scandium-containing compounds is often extremely high. At present in the world there are very few mines that extract scandium. In addition, scandium is sparsely distributed and occurs only in trace amounts in many minerals. Hence, owing to its rarity and difficulties in separation very high cost are often associated with its extraction. These high costs are then mirrored in the cost of commercially available starting reagents. For example, the cost of 5 g of Sc_2O_3 can range from £240 - £1000 depending on the sample purity and exact supplier. This is, however, just one of the many reasons as to why such little ^{45}Sc solid-state NMR has been completed to date. For example, at present, relatively little is known regarding the chemical importance of Sc-containing compounds. Scandia-stabilised zirconia (SSZ) is currently the most widely used Sc-bearing compound and is predominantly utilised as a high efficiency electrolyte in

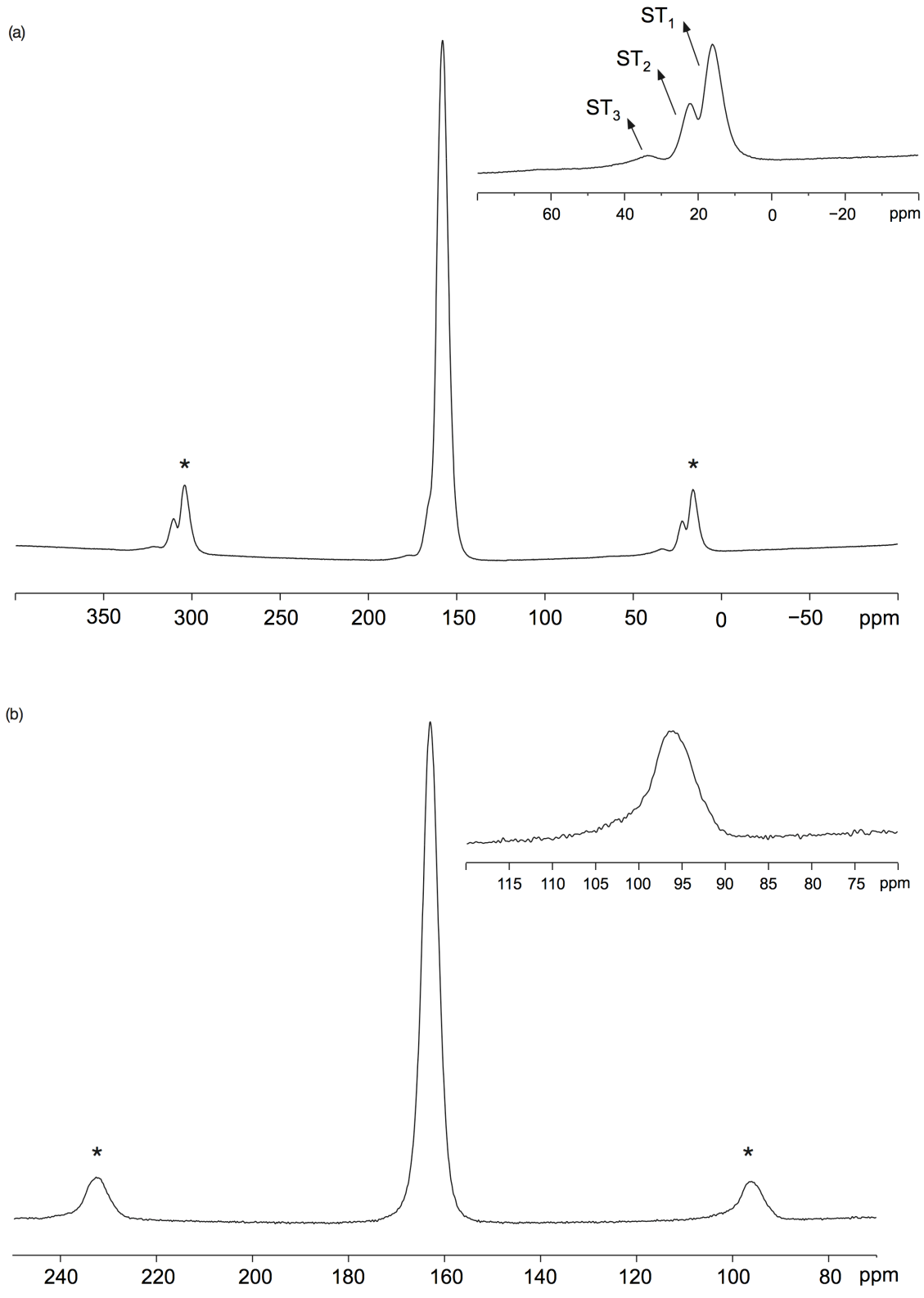

Figure 6.5: Conventional ^{45}Sc MAS NMR spectra for $LaScO_3$ at (a) 9.4 T and (b) 14.1 T. Also shown in each are expansions of the satellite transition spinning sidebands, marked with an *. Spectra are the result of averaging (a) 96 and (b) 24 transients with a recycle interval of (a) 5 and (b) 3 s. The MAS rate was (a) 14 kHz and (b) 10 kHz.

Table 6.2: Transition-dependent coefficients for spin I = 7/2 nuclei.[318]

	A^0 (I, q)	A^2 (I, q)	A^4 (I, q)
CT (q = 1/2)	−2	−40/7	54/7
ST_1 (q = 3/2)	−4/5	−4	24/5
ST_2 (q = 5/2)	14/5	8/7	−138/35
ST_3 (q = 7/2)	44/5	68/7	−648/35

solid oxide fuel cells. However, the potential application of many other Sc-based compounds is currently unknown and therefore requires a more detailed investigation. Therefore, in an attempt to contribute to the current literature all samples in the solid-solution $La_{1-x}Y_xScO_3$ have been investigated using ^{45}Sc solid-state NMR.

The ^{45}Sc (9.4 T) MAS NMR spectrum of $LaScO_3$ contained a single sharp resonance, as shown in Figure 6.5(a). ^{45}Sc is well documented as often exhibiting large quadrupolar coupling constants[191] and, as a result, multiple-quantum (MQ) MAS techniques are required to fully remove inhomogeneous second-order quadrupolar broadenings and resolve distinct resonances. The ^{45}Sc (9.4 T and 14.1 T) MAS NMR spectra obtained for $LaScO_3$ are shown in Figures 6.5(a) and (b) respectively and each suggests the presence of a single six coordinate site. Eight-coordinated Sc sites typically possess much lower chemical shifts when compared with six-coordinate Sc.[191] Therefore, the shift observed for the single resonance in each spectrum is indicative of a six-coordinate Sc environment. Each ^{45}Sc MAS NMR spectrum of $LaScO_3$ exhibits a range of spinning sidebands (denoted by *) associated with three satellite transitions; ST_1, ST_2 and ST_3 found for a I = 7/2 nucleus. When the spectra are compared, these sidebands are well resolved in the ^{45}Sc (9.4 T) MAS NMR spectrum shown in Figure 6.5(a). It is important to note the large anisotropic broadening associated with ST_3 when compared with ST_1 and ST_2. The values in Table 6.2 correspond to the coefficients $A^0(I,q)$, $A^2(I,q)$ and $A^4(I,q)$ in an equation similar to that of Equation 2.50 used to describe the second-order quadrupolar interaction, where q denotes a transition $m_I = \pm(q - 1) \leftrightarrow \pm q$. $A^0(I,q)$ relates to the isotropic shift whilst

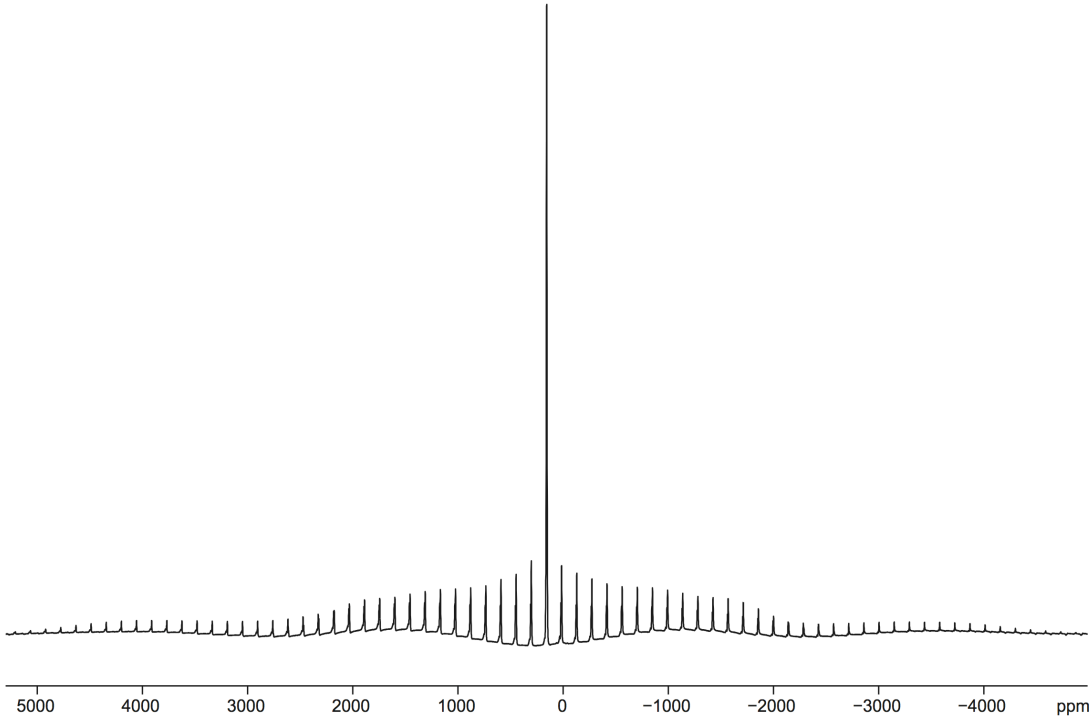

Figure 6.6: Conventional ^{45}Sc (9.4 T) MAS NMR spectrum of $LaScO_3$ with a wide spectral width of $LaScO_3$. The spectrum is the result of averaging 192 transients with a recycle interval of 5 s. The MAS rate was 14 kHz.

$A^2(I,q)$ and $A^4(I,q)$ correspond to the anisotropic terms. The extent of broadening exhibited by ST_3 is given by the $A^4(I,q)$ value displayed in Table 6.2 and is considerably greater than those for ST_1 and ST_2, indicating second-order broadening has a substantially greater effect on the third satellite transition when compared with the first and second. At 14.1 T it is not possible to distinguish the different satellite transitions, as shown in the expansion in Figure 6.5(b). Here, the three satellite transitions appear at similar positions owing to their respective quadrupolar shifts being smaller at higher field strength. A ^{45}Sc (9.4 T) MAS NMR spectrum with wide spectral width was also recorded for $LaScO_3$, as shown in Figure 6.6. In this spectrum the satellite transitions are clearly visible which, in turn, enables the lineshape to be fitted and NMR parameters to be obtained. The central and satellite transitions, ST_1, ST_2 and ST_3, were therefore fitted using SOLA and the single site has δ_{iso} = 162.0 ppm and C_Q = 3.9 MHz. Full details of the NMR parameters for $LaScO_3$ are given in Table 6.3.

Table 6.3: Experimental ^{45}Sc NMR parameters, δ_{iso}, P_Q, C_Q and η_Q, for $LaScO_3$ (9.4 T) and $YScO_3$ (14.1 T), obtained from the wide spectral width MAS NMR spectrum and MAS spectrum in Figures 6.6 and 6.9, respectively.

Sample	δ_{iso} (ppm)	P_Q / MHz	C_Q / MHz	η_Q
$LaScO_3$	162.0(5)	4.0(1)	3.9(1)	0.3(1)
$YScO_3$	163.2(5)	8.2(1)	7.6(1)	0.7(1)

To confirm no additional sites lay under the ^{45}Sc MAS lineshape a MQMAS experiment was completed on the phase pure sample of $LaScO_3$ previously analysed by NPD. The ^{45}Sc triple-quantum MAS spectrum (14.1 T) is shown in Figure 6.7, displaying a single resonance. The presence of a single site is in good agreement with published crystallographic data.[218] Although the quadrupolar contribution appears to be relatively small, it is sufficiently large that one might expect to observed a quadrupolar lineshape at 9.4 T. However, the ^{45}Sc MAS NMR spectrum for $LaScO_3$ does not exhibit a quadrupolar lineshape, suggesting there is an additional degree of broadening present, most probably owing to factors such as positional or geometrical disorder. This additional broadening is also observed in the MQMAS spectrum obtained, as the single ridge is not aligned along 101/45 (the MQMAS ratio for a spin I = 7/2 nucleus). When compared with other scandium-bearing compounds[300,301] the quadrupolar interaction observed for $LaScO_3$ (C_Q = 3.9 MHz) is relatively small, suggesting the Sc environment is highly symmetrical. $LaScO_3$ is an orthorhombic perovskite composed of corner sharing ScO_6 octahedra where the Sc cation is directly bonded to six oxygen atoms. The Sc – O bond distances obtained from Rietveld refinement of the NPD data are given in Table 6.4. Crystallographically Sc is positioned on an inversion centre. Therefore, by definition, the Sc should reside in the centre of the octahedron. However, the O – Sc – O bond angles obtained for $LaScO_3$ appear to indicate mild distortions of the octahedra, suggesting the ScO_6 octahedra are not fully regular. All O - Sc – O bond angles obtained from Rietveld refinement of the NPD data for $LaScO_3$ are given in Table 6.5. The irregular nature of the octahedra

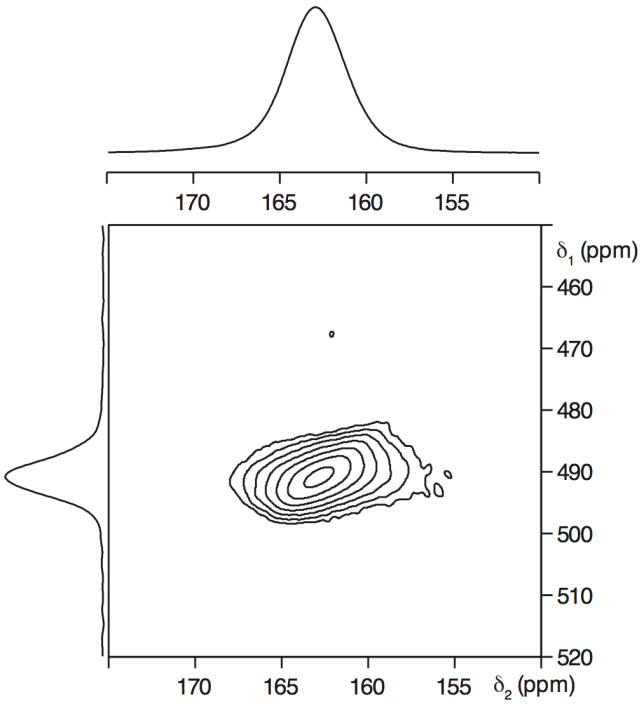

Figure 6.7: Conventional ^{45}Sc (14.1 T) MAS NMR spectrum, triple-quantum MAS NMR spectrum and corresponding projection of $LaScO_3$, recorded using the z-filtered pulse sequence shown in Figure 2.28. The spectrum is the result of averaging 96 transients with a recycle interval of 3 s for each of the 256 increments of 20 μs. The MAS rate was 10 kHz.

within $LaScO_3$ may give rise to disorder within the structure. However, it is likely that diffraction is not capable of detecting the disorder because 'on average' the octahedra appear regular. It is only by using a more local probe such as NMR that it is possible to identify such disorder.

When the C_Q is very small, as in the case of $LaScO_3$, the extent of disorder exhibited becomes important as the lineshape displays a greater effect. At 9.4 T the linewidth of the resonance exhibited for $LaScO_3$ is ~120 Hz greater than that at 14.1 T. The increase in linewidth at low field suggests that the origin of the dominant interaction is quadrupolar (decreases with field), not a distribution of shifts (increases with field). However, if only quadrupolar broadening was present the linewidth would decrease by a factor of 2/3, and this does not appear to be the case. Therefore, a contribution which scales with field must also be present,

Table 6.4: Sc-O and La-O bond lengths obtained from Rietveld refinement of NPD data for $LaScO_3$.

Bond	Bond Length / Å	Bond	Bond Length / Å
Sc1-O1 ×2	2.103(2)	La1-O1	2.533(1)
Sc1-O2 ×2	2.093(1)	La1-O1	2.396(1)
Sc1-O2 ×2	2.109(1)	La1-O2 ×2	2.877(1)
		La1-O2 ×2	2.424(1)
		La1-O2 ×2	2.713(1)

Table 6.5: All O-Sc-O, Sc-O-Sc and Sc-La-Sc bond angles obtained from Rietveld refinement of the NPD data for $LaScO_3$.

Bond	Bond Angle (°)	Bond	Bond Angle (°)
O1-Sc-O1	180	Sc-O1-Sc	148.50(4)
O1-Sc-O2 ×2	91.77(3)	Sc-O2-Sc	149.53(3)
O1-Sc-O2 ×2	88.59(3)	Sc-La-Sc	73.46(1)
O1-Sc-O2 ×2	88.23(3)	Sc-La-Sc	71.85(2)
O1-Sc-O2 ×2	91.41(3)	Sc-La-Sc	115.39(2)
O2-Sc-O2 ×2	88.77(1)		
O2-Sc-O2 ×2	180.00		
O2-Sc-O2 ×2	91.23(1)		

resulting in a distribution of both quadrupolar parameters and chemical shifts.

6.3.2 $YScO_3$

Using conventional solid-state techniques several attempts were made to synthesise $YScO_3$. Various experimental conditions were tested several times, including annealing temperature, annealing time and the effect of different cooling rates (e.g., quench vs. slow cool). All samples

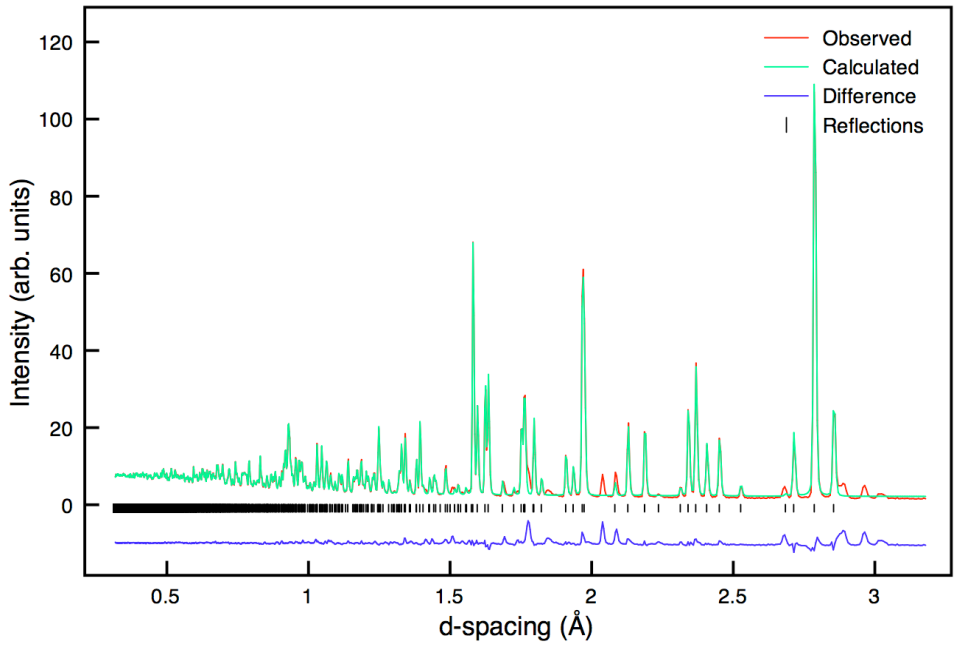

Figure 6.8: Rietveld profile of NPD data for $YScO_3$ using the structural model Pbnm. Anisotropic thermal parameters were utilised during the refinement.

synthesised were analysed using l-PXRD and contained very little of the desired product. All variations to the synthesis method used produced little or no effect on the resultant product(s). Routinely, samples contained only trace amounts of $YScO_3$ and large quantities of either an unidentified impurity phase or unreacted starting reagents.

After an extensive investigation into various solid-state techniques, the preparative method proposed by Porotnikov *et al.*[299] was tested. Phase purity was verified using l-PXRD and confirmed the presence of $YScO_3$, in addition to very small quantities of an unknown impurity phase. Various adjustments were made to the original synthesis conditions, including higher annealing temperatures and longer heating times. Many of these were tested several times in an attempt to remove the impurity phase; however, these proved unsuccessful and small quantities remained in each sample. As previously stated, no complete structural model is currently available in the literature for $YScO_3$. However, accurate lattice parameters have been reported from an earlier study by Clark *et al.*[298] in which $YScO_3$ was synthesised using high-pressures. Therefore, to obtain accurate crystallographic data a sample of $YScO_3$ was investigated using

Table 6.6: Structural parameters for $YScO_3$ from NPD data using anisotropic thermal factors. Space group Pbnm, a = 5.42666(10) Å, b = 5.70859(10) Å, c = 7.89309(14) Å and V = 244.517(10) Å^3. χ^2 = 32.0 and wR_p = 3.0%.

Atom	Site	x	y	z	U_{11} × 100 / Å^2	U_{22} × 100 / Å^2	U_{33} × 100 / Å^2
Y	4c	0.0182(2)	0.9382(1)	0.25	0.42(3)	0.35(3)	0.69(4)
Sc	4a	0	0.5	0	0.48(2)	0.49(2)	0.45(2)
O1	4c	0.8722(2)	0.5580(2)	0.25	0.39(4)	0.71(5)	0.21(4)
O2	8d	0.6900(2)	0.3071(2)	0.9331(1)	0.56(3)	0.53(3)	0.85(4)

high-resolution NPD. The sample containing the smallest quantities of the impurity phase (< 5%) was used. $YScO_3$ and $HoScO_3$ are believed to be isostructural owing to their similar ionic radii. Therefore, all Rietveld refinements for $YScO_3$ were completed using an initial structural model for $HoScO_3$[218] (obtained from the literature) and the lattice parameters suggested by Clark *et al*.[298] The Rietveld refinement for $YScO_3$, using NPD data, displays very good agreement with the calculated model (wR_p = 2.9% and χ^2 = 31.9), as shown in Figure 6.8. It must be noted that the impurity phase is believed to be a mixed $(Y,Sc)_2O_3$-type phase, however, the exact composition is not yet known. Therefore, it was not possible to complete a two-phase structural refinement for $YScO_3$ and peaks belonging to the unknown impurity phase are clearly visible in the Rietveld refinement. Full refinement details obtained from the NPD data for $YScO_3$, including anisotropic temperature factors, can be found in Table 6.6.

The ^{45}Sc MAS NMR spectrum for $YScO_3$ contained a single resonance and, in contrast to $LaScO_3$, a characteristic second-order quadrupolar lineshape was exhibited, as shown in Figure 6.9. As observed for $LaScO_3$, the chemical shift of the resonance was in the known shift range for 6-coordinate Sc. The resonance does, however, appear to display additional broadening under MAS, possibly indicating small distributions in environment and in the NMR parameters. Using SOLA the MAS lineshape for $YScO_3$ was fitted and the ^{45}Sc NMR parameters

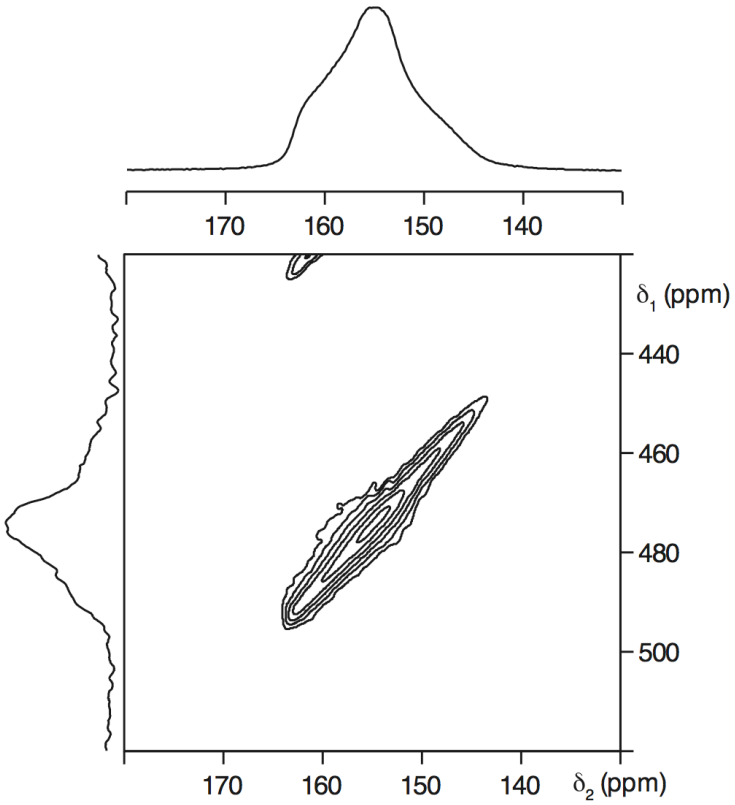

Figure 6.9: Conventional ^{45}Sc (14.1 T) MAS NMR spectrum, triple-quantum MAS NMR spectrum and corresponding projection of $YScO_3$, recorded using the z-filtered pulse sequence shown in Figure 2.28. The spectrum is the result of averaging 96 transients with a recycle interval of 3 s for each of the 256 increments of 20 μs. The MAS rate was 10 kHz.

δ_{iso} = 163.3 ppm and C_Q = 7.6 MHz were obtained. Details of all NMR parameters for $YScO_3$ can be found in Table 6.3. To identify the nature and extent of broadening exhibited MQMAS experiments were performed. The two-dimensional ^{45}Sc MQMAS NMR spectrum is shown in Figure 6.9, displaying a single six coordinate site. This therefore confirmed no additional resonances lay under the lineshape observed in the ^{45}Sc MAS NMR spectrum. The quadrupolar interaction for $YScO_3$ is ~5 MHz greater than that of $LaScO_3$. This suggests the Sc environment in $YScO_3$ is less symmetrical than that found in $LaScO_3$. Both structures refine well to the orthorhombic Pbnm structure, indicating the two are, structurally very similar. The Sc – O bond distances obtained for $YScO_3$ from Rietveld refinement are listed in Table 6.7, where the Sc – O2 and Y –

Table 6.7: Sc-O and Y-O bond lengths obtained from Rietveld refinement of NPD data for $YScO_3$.

Bond	Bond Length / Å	Bond	Bond Length / Å
Sc1-O1 ×2	2.118(1)	Y1-O1	2.310(2)
Sc1-O2 ×2	2.079(1)	Y1-O1	2.226(2)
Sc1-O2 ×2	2.101(1)	Y1-O2 ×2	2.845(1)
		Y1-O2 ×2	2.253(1)
		Y1-O2 ×2	2.561(1)

Table 6.8: All O-Sc-O, Sc-O-Sc and Sc-Y-Sc bond angles obtained from Rietveld refinement of NPD data for $YScO_3$.

Bond	Bond Angle (°)	Bond	Bond Angle (°)
O1-Sc-O1	179.97	O2-Sc-O2	180
O1-Sc-O2 ×2	93.11(5)	O2-Sc-O2	91.08(2)
O1-Sc-O2 ×2	86.72(5)	O2-Sc-O2	179.96
O1-Sc-O2 ×2	86.89(5)	Sc-O1-Sc	137.44(7)
O1-Sc-O2 ×2	93.28(5)	Sc-O2-Sc	140.84(5)
O2-Sc-O2 ×2	88.92(2)	Sc-Y-Sc ×2	74.80(2)
		Sc-Y-Sc ×2	118.65(3)
		Sc-Y-Sc	76.50(2)
		Sc-Y-Sc	73.59(2)

O bond lengths are marginally smaller than those obtained for $LaScO_3$. In contrast, the Sc – O1 bond distances are slightly greater than those in $LaScO_3$. To highlight how subtly different the two are isolated ScO_6 octahedra obtained from Rietveld refinement of each structure are shown in Figures 6.10(a) and (b), and they appear very similar. In contrast, large differences are exhibited in the bond angles obtained for $LaScO_3$ and $YScO_3$, as detailed in Tables 6.5 and 6.8, respectively. The differences

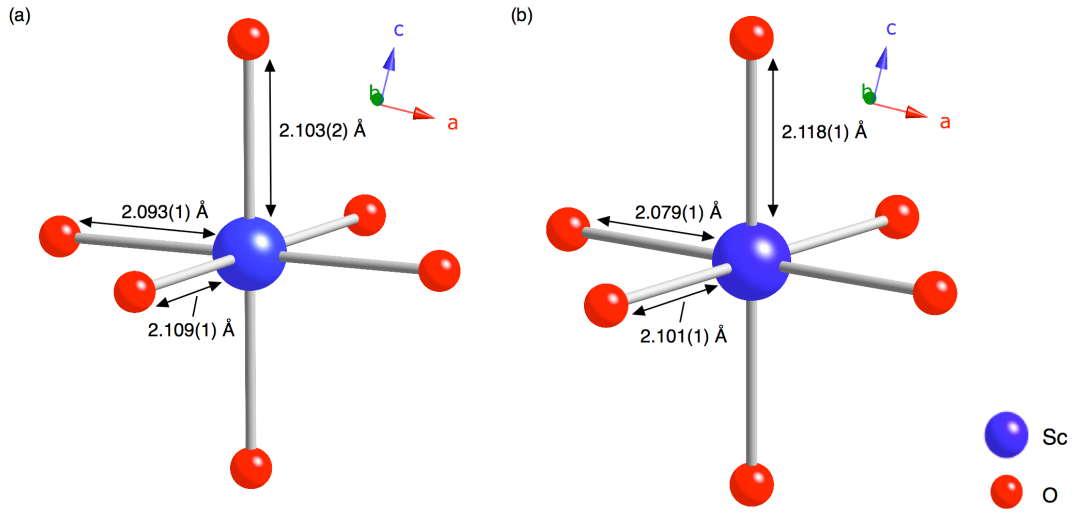

Figure 6.10: Isolated ScO_6 octahedra for (a) $LaScO_3$ and (b) $YScO_3$ obtained from Rietveld refinement of NPD data, showing the Sc – O bond distances.

observed suggest that, in particular, greater octahedral tilts and distortions are exhibited in the $YScO_3$ structure when compared with $LaScO_3$. ^{45}Sc NMR parameters are known to be sensitive to changes in the local coordination sphere. The subtle changes in bond length observed between $LaScO_3$ and $YScO_3$ do not appear sufficiently large enough to cause the large difference in C_Q observed between the two. However, the large differences in bond angle would be sufficient to cause such a large change. Yttrium possesses a relatively small ionic radius (1.02 Å)[4] when compared with lanthanum (1.18 Å)[4] and, as a direct consequence, when Y is substituted onto the A site the unit cell is forced to contract. As stated previously, the substitution of a smaller cation onto the A site results in a certain degree of strain being imposed on the structure. Therefore, to compensate for this and relieve such strain, the surrounding octahedra are forced to undergo small rotations. The degree of strain exhibited in any orthorhombic structure can be measured relatively easily using a parameter known as the orthorhombic strain parameter, s, given by

$$s = \frac{2(b-a)}{a+b} \qquad (6.1)$$

Table 6.9: The orthorhombic strain, s, tilting angle, φ, and bond deviation, Δ_d, values obtained for the solid-solution $La_{1-x}Y_xScO_3$.

x	s	φ (°)	Δ_d (× 10^4)
0	0.0188	15.49	0.099
0.2	0.0254	16.42	0.051
0.4	0.0315	17.42	0.119
0.6	0.0383	18.49	0.183
0.8	0.0444	19.62	0.414
1	0.0506	20.43	0.878

where a and b are the lattice parameters obtained from Rietveld refinement of the structure.[319] The degree of orthorhombic strain exhibited by $LaScO_3$ and $YScO_3$ can be found in Table 6.9. As expected, s is greater for $YScO_3$ owing, presumably, to the small nature of the A-site cation. It is therefore likely that the large quadrupolar interaction exhibited by $YScO_3$ is due to several effects, namely the increase in orthorhombic strain and pronounced tilting of the octahedra.

6.3.3 $La_{1-x}Y_xScO_3$

6.3.3.1 Neutron Diffraction Analysis

Samples in the solid-solution $La_{1-x}Y_xScO_3$, with compositions x = 0.2, 0.4, 0.6 and 0.8, were synthesised using conventional solid-state methods and relatively high annealing temperatures. Structure and phase purity were initially verified using l-PXRD and later analysed using NPD. All compositions in the solid-solution refined well to the orthorhombic model Pbnm. Rietveld refinements completed for compositions x = 0.2 and 0.4 used the $LaScO_3$ structure as the initial model. The converse was true for compositions x = 0.6 and 0.8, where the $YScO_3$ structure was used as the initial model in each refinement. In a similar manner to $YScO_3$ it was very difficult to synthesise a phase pure sample for the composition x = 0.8, as the same impurity phase, believed to be a mixed $(Y,Sc)_2O_3$-type phase, was consistently present in all samples synthesised. Although

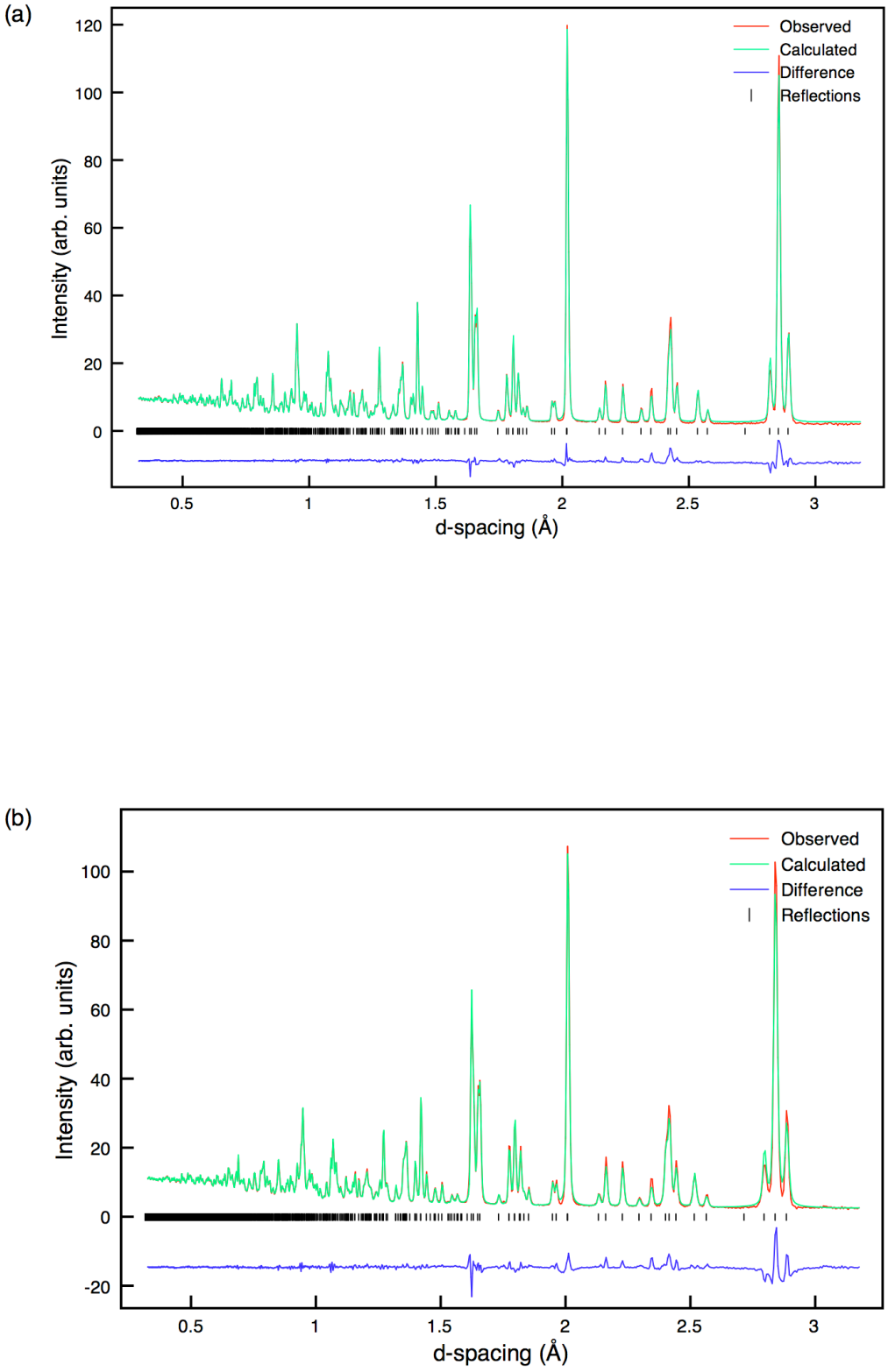

Figure 6.11: Rietveld refinements completed using the NPD data and structural model Pbnm for (a) $La_{0.8}Y_{0.2}ScO_3$ and (b) $La_{0.6}Y_{0.4}ScO_3$. Anisotropic thermal parameters were utilised during each refinement.

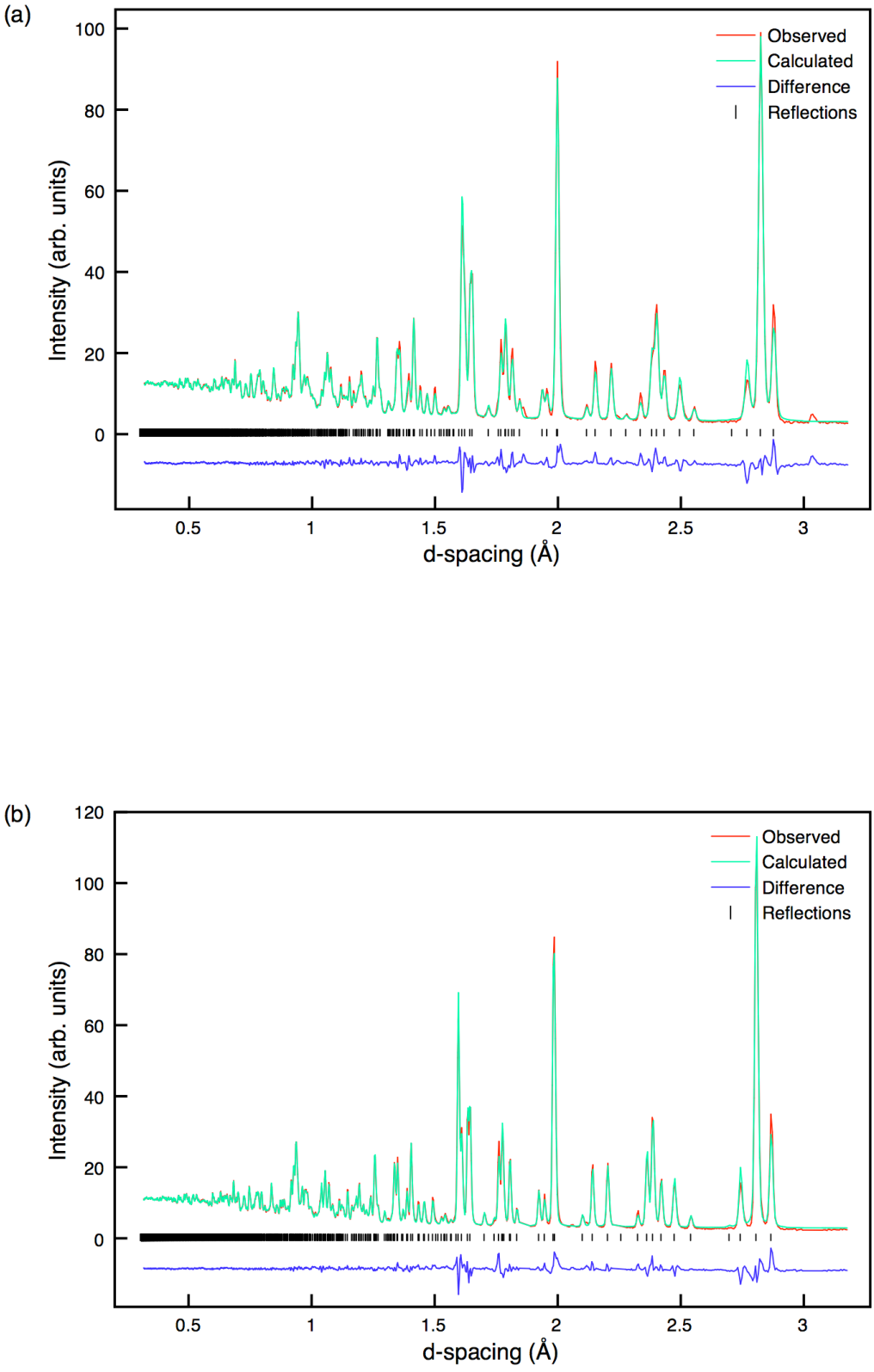

Figure 6.12: Rietveld refinements completed using the NPD data and structural model Pbnm for (a) $La_{0.4}Y_{0.6}ScO_3$ and (b) $La_{0.2}Y_{0.8}ScO_3$. Anisotropic thermal parameters were utilised during each refinement.

Table 6.10: Structural parameters for $La_{0.8}Y_{0.2}ScO_3$ from NPD data using anisotropic thermal factors. Space group Pbnm, a = 5.63797(8) Å, b = 5.78312(8) Å, c = 8.06670(11) Å and V = 263.015(8) Å^3. $\chi^2 = 9.6$ and $wR_p = 1.7\%$.

Atom	Site	x	y	z	U_{11} × 100 / Å^2	U_{22} × 100 / Å^2	U_{33} × 100 / Å^2
La1*	4c	0.0116(2)	0.9528(1)	0.25	0.76(2)	0.57(2)	0.61(2)
Sc1	4a	0	0.5	0	0.73(1)	0.60(1)	0.50(1)
O1	4c	0.8992(2)	0.5370(2)	0.25	1.54(4)	1.03(4)	0.31(3)
O2	8d	0.7016(1)	0.2973(1)	0.9461(1)	0.78(2)	0.59(2)	1.11(2)
*La 0.8,Y 0.2							

Table 6.11: Structural parameters for $La_{0.6}Y_{0.4}ScO_3$ from NPD data using anisotropic thermal factors. Space group Pbnm, a = 5.59023(13) Å, b = 5.76907(13) Å, c = 8.03151(17) Å and V = 259.020(14) Å^3. $\chi^2 = 17.3$ and $wR_p = 2.3\%$.

Atom	Site	x	y	z	U_{11} × 100 / Å^2	U_{22} × 100 / Å^2	U_{33} × 100 / Å^2
La1*	4c	0.0121(3)	0.9492(1)	0.25	0.92(4)	0.50(3)	0.55(3)
Sc1	4a	0	0.5	0	0.95(2)	0.58(2)	0.46(2)
O1	4c	0.8928(3)	0.5427(3)	0.25	2.25(7)	1.03(5)	0.32(4)
O2	8d	0.6989(2)	0.2996(2)	0.9428(1)	1.10(4)	0.53(3)	1.04(3)
*La 0.6, Y 0.4							

Table 6.12: Structural parameters for $La_{0.4}Y_{0.6}ScO_3$ from NPD data using anisotropic thermal factors. Space group Pbnm, a = 5.5364(2) Å, b = 5.75241(19) Å, c = 7.99153(3) Å and V = 254.51(2) Å^3. χ^2 = 19.6 and wR_p = 2.4%.

Atom	Site	x	y	z	U_{11} × 100 / Å^2	U_{22} × 100 / Å^2	U_{33} × 100 / Å^2
La1*	4c	0.0138(3)	0.9456(1)	0.25	1.04(5)	0.39(3)	0.41(4)
Sc1	4a	0	0.5	0	1.08(3)	0.50(2)	0.39(2)
O1	4c	0.8858(4)	0.5479(3)	0.25	2.36(8)	0.90(6)	0.13(5)
O2	8d	0.6959(2)	0.3016(2)	0.9388(2)	1.04(4)	0.47(4)	1.24(4)

*La0.4, Y 0.6

Table 6.13: Structural parameters for $La_{0.2}Y_{0.8}ScO_3$ from NPD data using anisotropic thermal factors. Space group Pbnm, a = 5.48259(13) Å, b = 5.73172(13) Å, c = 7.94657(17) Å and V = 249.718(13) Å^3. χ^2 = 16.9 and wR_p = 2.2%.

Atom	Site	x	y	z	U_{11} × 100 / Å^2	U_{22} × 100 / Å^2	U_{33} × 100 / Å^2
La1*	4c	0.0164(2)	0.9419(1)	0.25	0.72(4)	0.45(3)	0.62(3)
Sc1	4a	0	0.5	0	0.90(2)	0.44(2)	0.46(2)
O1	4c	0.8780(3)	0.5540(2)	0.25	1.53(6)	0.91(5)	0.20(4)
O2	8d	0.6926(2)	0.3049(2)	0.9356(1)	0.92(3)	0.49(3)	1.26(4)

*La 0.2, Y 0.8

Table 6.14: Sc-O, La-O and Y-O bond lengths obtained from Rietveld refinement of NPD data for $La_{0.8}Y_{0.2}ScO_3$.

Bond	Bond Length / Å	Bond	Bond Length / Å
Sc1-O1 ×2	2.106(3)	La1/Y1-O1	2.487(1)
Sc1-O2 ×2	2.096(1)	La1/Y1-O1	2.366(1)
Sc1-O2 ×2	2.106(1)	La1/Y1-O2 ×2	2.874(1)
		La1/Y1-O2 ×2	2.396(1)
		La1/Y1-O2 ×2	2.685(10)

Table 6.15: Sc-O, La-O and Y-O bond lengths obtained from Rietveld refinement of NPD data for $La_{0.6}Y_{0.4}ScO_3$.

Bond	Bond Length / Å	Bond	Bond Length / Å
Sc1-O1 ×2	2.110(1)	La1/Y1-O1	2.438(2)
Sc1-O2 ×2	2.093(1)	La1/Y1-O1	2.327(2)
Sc1-O2 ×2	2.106(1)	La1/Y1-O2 ×2	2.868(1)
		La1/Y1-O2 ×2	2.364(1)
		La1/Y1-O2 ×2	2.659(2)

Table 6.16: Sc-O, La-O and Y-O bond lengths obtained from Rietveld refinement of NPD data for $La_{0.4}Y_{0.6}ScO_3$.

Bond	Bond Length / Å	Bond	Bond Length / Å
Sc1-O1 ×2	2.114(1)	La1/Y1-O1	2.395(2)
Sc1-O2 ×2	2.092(1)	La1/Y1-O1	2.289(3)
Sc1-O2 ×2	2.104(1)	La1/Y1-O2 ×2	2.867(2)
		La1/Y1-O2 ×2	2.325(2)
		La1/Y1-O2 ×2	2.623(2)

Table 6.17: Sc-O, La-O and Y-O bond lengths obtained from Rietveld refinement of NPD data for $La_{0.2}Y_{0.8}ScO_3$.

Bond	Bond Length / Å	Bond	Bond Length / Å
Sc1-O1 ×2	2.119(1)	La1/Y1-O1	2.349(2)
Sc1-O2 ×2	2.086(1)	La1/Y1-O1	2.256(2)
Sc1-O2 ×2	2.105(1)	La1/Y1-O2 ×2	2.859(1)
		La1/Y1-O2 ×2	2.284(1)
		La1/Y1-O2 ×2	2.593(1)

variations of the original synthesis method were attempted numerous times this phase was consistently produced. As observed for $YScO_3$, peaks belonging to this phase are clearly visible in the Rietveld refinement. Lattice parameters and atomic coordinates were obtained for each composition from Rietveld refinement of the NPD data. Rietveld refinements for samples x = 0.2, 0.4, 0.6 and 0.8 are shown in Figures 6.11(a) and (b), and Figures 6.12(a) and (b). Full refinement details, including anisotropic temperature factors, for all samples in this series can be found in Tables 6.10 - 6.13. Details of all bond lengths obtained from each refinement in this series can be found in Tables 6.14 – 6.17. All corresponding bond angles can be found in Appendix V.

Diffraction indicates the orthorhombic Pbnm structure is retained as greater quantities of Y are substituted into the $LaScO_3$ structure. This was, to some extent, as expected because $YScO_3$ is also an orthorhombic structure in space group Pbnm. As the yttrium content is increased several important structural changes are observed. For example, the lattice parameters a, b and c gradually decrease and, as a direct consequence, the unit cell volume is also reduced as Y is introduced to the structure. The variation of each lattice parameter and cell volume with increasing Y content is shown in Figures 6.13 and 6.14. A near linear variation is observed with increasing x for both the lattice parameters and cell volume, in good agreement with Végards Law. As Y is substituted onto the A site the unit cell is forced to contract and, as a result, the strain

imposed on the structure increases. In a similar manner to the orthorhombic strain, it is possible to calculate the tilt angle Sc – O – Sc of the ScO_6 octahedra in any $RScO_3$ perovskite. This can be obtained using the formula for the tilt angle, φ, given by

$$\varphi = \frac{180 - \langle Sc - O - Sc \rangle}{2} \quad , \tag{6.2}$$

where ⟨Sc – O – Sc⟩ is the average Sc – O – Sc bond angle obtained from Rietveld refinement.[319] In addition, to accurately quantify the relative distortion exhibited by the octahedra in any perovskite structure the parameter Δ_d is commonly used, given by

$$\Delta_d = 1.6\left[\frac{(d_n - \langle d \rangle)}{\langle d \rangle}\right]^2 \quad . \tag{6.3}$$

This parameter describes the deviation of the Sc – O distances (d_n) with respect to the average ⟨Sc – O⟩ value, ⟨d⟩, in each ScO_6 octahedron.[319] The values of s, φ and Δ_d obtained from Rietveld refinement of the NPD data for each sample in the series $La_{1-x}Y_xScO_3$ are shown in Table 6.9. The variation in parameters, s and φ with x composition is shown in Figure 6.15. As x is increased a gradual increase in both the orthorhombic strain and tilt angle of the ScO_6 octahedra is observed. This is in good agreement with earlier discussions regarding the placement of a small cation onto the A site, i.e., an increase in the strain imposed on the structure owing to larger rotations of the ScO_6 octahedra. The variation of Δ_d with increasing x is shown in Figure 6.16. The value of Δ_d observed for both $LaScO_3$ and $La_{0.8}Y_{0.2}ScO_3$ is very small. This parameter does, however, substantially increase for the latter members of this series. A maximum is observed in Δ_d for $YScO_3$, indicating good agreement with the orthorhombic strain and Sc – O – Sc tilt angle observed for $YScO_3$. It must be noted that the values of Δ_d obtained for this particular solid-solution are extremely small when compared with those observed in other perovskite series such as $RMnO_3$, where the Jahn-Teller character of the Mn^{3+} produces a dramatic electronic-driven distortion. For example, extremely large octahedral distortions are exhibited for $DyMnO_3$ at room temperature, with Δ_d =

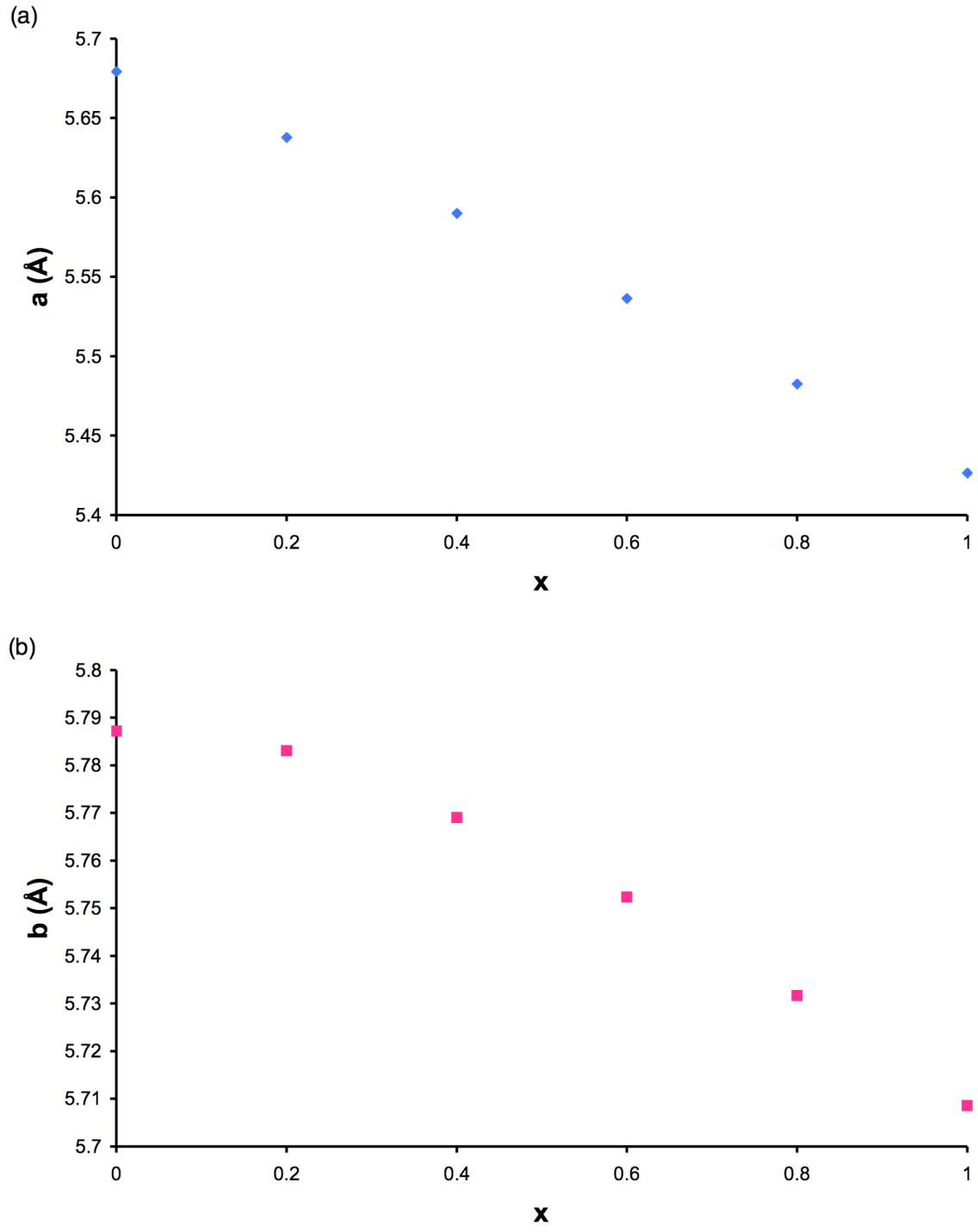

Figure 6.13: Variation observed in the unit cell parameters (a) a and (b) b with increasing x in the solid-solution $La_{1-x}Y_xScO_3$. The estimated error bars are smaller than the symbols used and are therefore not shown.

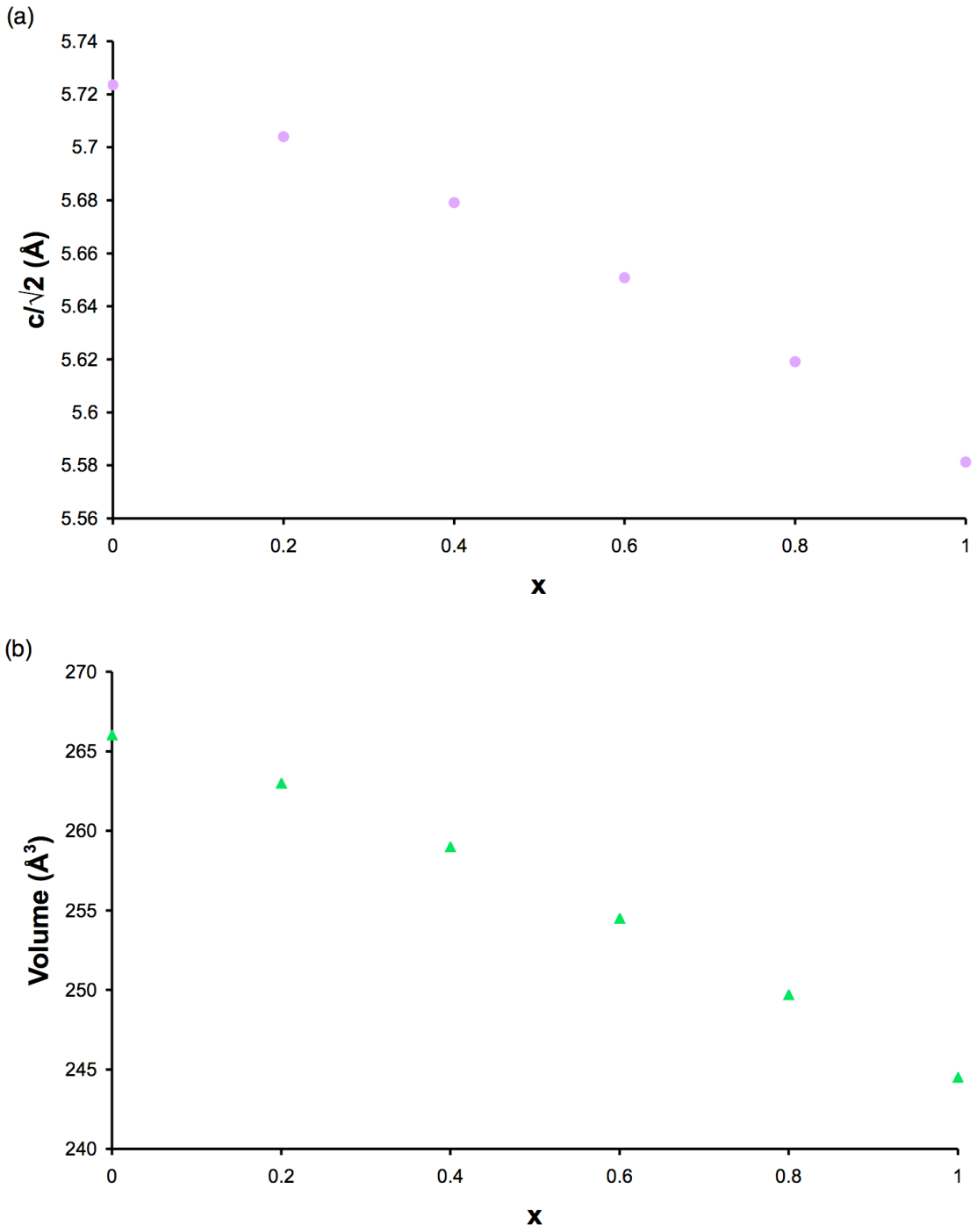

Figure 6.14: Variation observed in (a) the unit cell parameter c and (b) the unit cell volume with increasing x for $La_{1-x}Y_xScO_3$. Note that for ease of comparison with unit cell parameters a and b, the c parameter has been divided by √2. The estimated error bars are smaller than the symbols used and are therefore not shown.

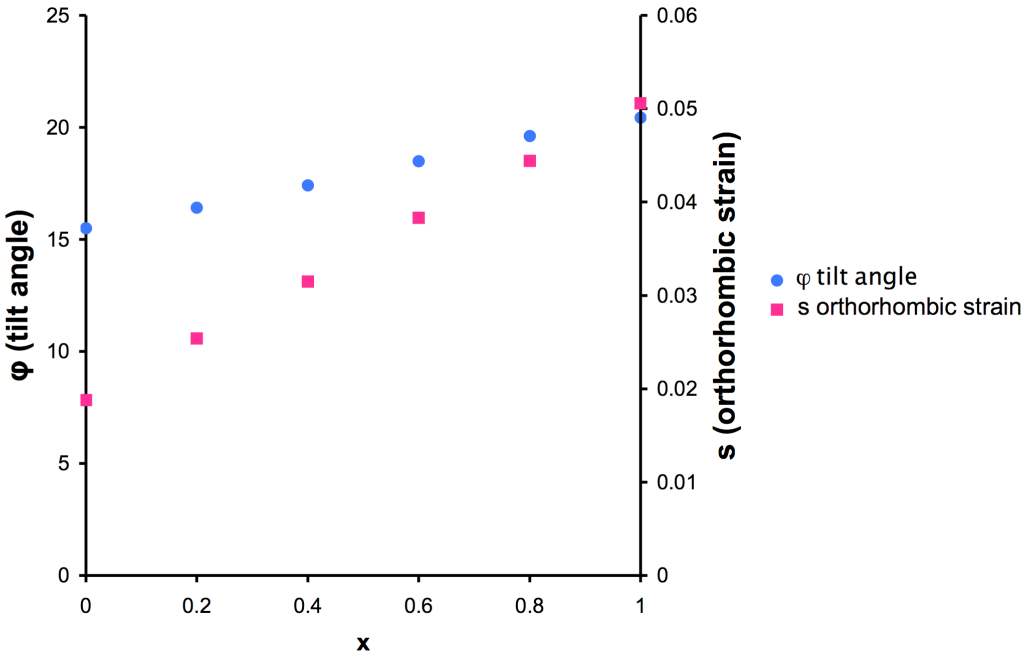

Figure 6.15: The variation observed in the tilt angle, φ, and orthorhombic strain, s, with increasing x in $La_{1-x}Y_xScO_3$.

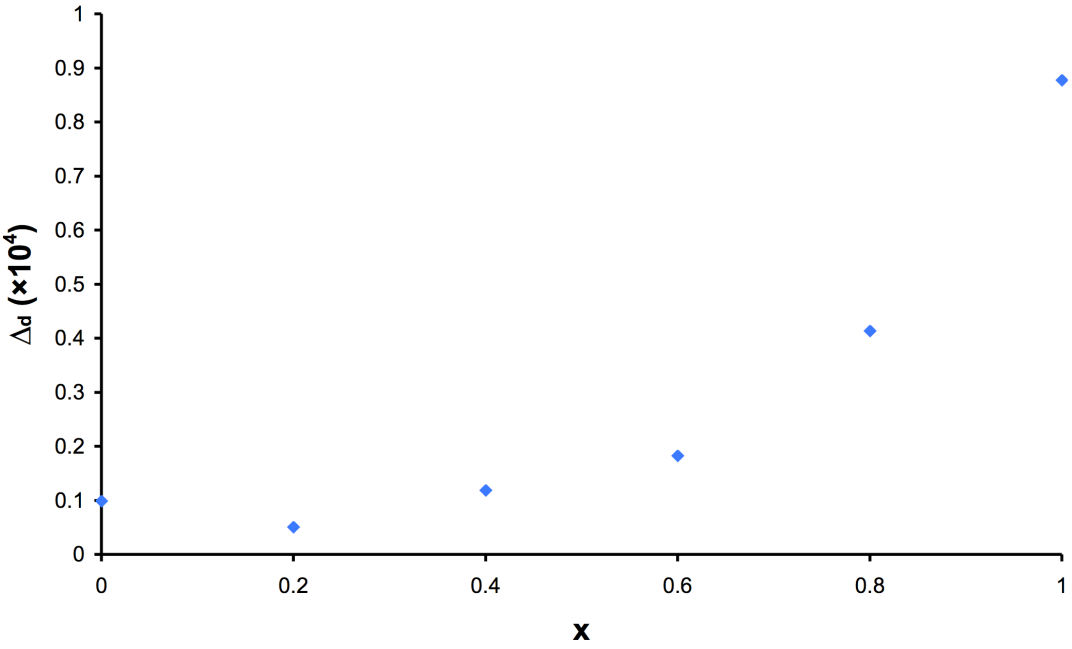

Figure 6.16: The variation observed in the bond deviation, Δ_d, defined in Equation 6.3, with increasing x for $La_{1-x}Y_xScO_3$.

49.7.[320] Analysis of the NPD data for the $La_{1-x}Y_xScO_3$ series, therefore, suggests the level of strain imposed on the structure increases as Y is added to the system. Each of the parameters calculated for the solid-solution $La_{1-x}Y_xScO_3$ indicates a linear variation with increasing x. This therefore confirms that a true solid-solution is formed between $LaScO_3$ and $YScO_3$. The trends observed indicate that yttrium is randomly distributed across the A site, i.e., there is no evidence of cation or layered ordering within the structure. In addition, the trends observed indicate there are no phase transitions observed with increasing x.

The substitution of Y^{3+} into the $LaScO_3$ structure inevitably introduces disorder to the system and, upon closer inspection, the presence of disorder is evident from the NPD data obtained. Examination of the anisotropic temperature factors obtained from each refinement indicates the largest values to be exhibited for the x = 0.4 and 0.6 samples. This therefore suggests that the greatest degree of disorder is exhibited between the two, presumably close to x = 0.5.

6.3.3.2 ^{45}Sc MAS NMR Analysis

^{45}Sc (9.4 T and 14.1 T) MAS NMR spectra were acquired for all compositions in the series $La_{1-x}Y_xScO_3$, and are shown in Figures 6.17(a) and (b) respectively. For comparison the two end-members, $LaScO_3$ and $YScO_3$, have also been included. Each spectrum displays a single resonance, suggesting the presence of a single Sc site. As observed for $LaScO_3$ the isotropic chemical shift of each resonance is indicative of a 6 coordinate Sc site. In each, the central transition appears broadened relative to $LaScO_3$. In addition, a degree of asymmetric broadening is observed, with a 'tail' occurring to low frequency. This particular type of lineshape is characteristic of disorder and typically indicative of systems exhibiting a distribution of quadrupolar parameters or chemical shifts. The extent of broadening displayed in the ^{45}Sc MAS NMR spectra of $La_{1-x}Y_xScO_3$ increases with increasing Y content. Spectra recorded (14.1 T) for each composition in this series have been overlaid to highlight the extent of broadening exhibited as x is increased. An expansion of the

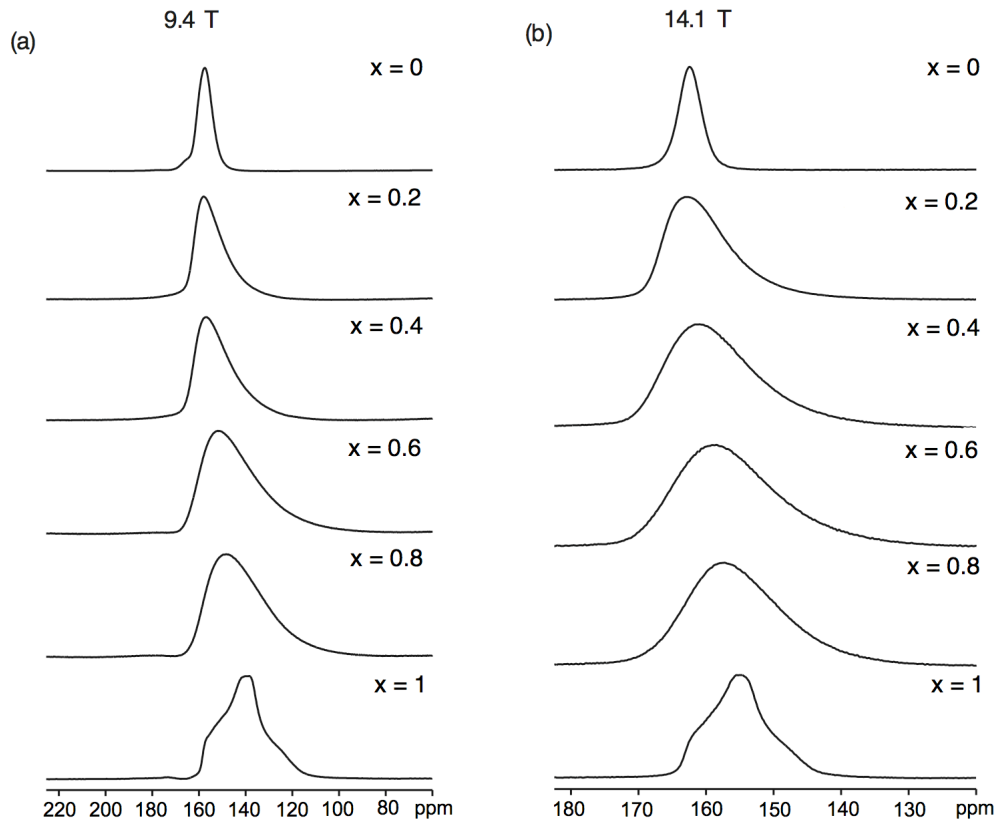

Figure 6.17: Comparison of ^{45}Sc (a) 9.4 T and (b) 14.1 T MAS NMR spectra obtained for $La_{1-x}Y_xScO_3$. Spectra are the result of averaging (a) 96 and (b) 24 transients with a recycle interval of (a) 5 s and (b) 3 s. The MAS rate was (a) 14 kHz and (b) 10 kHz.

central transition displayed for each sample is shown in Figure 6.18, where the extent of broadening and the shift in the position of each lineshape are clearly visible. For completeness the variation in linewidth observed with increasing x for each spectrum recorded (9.4 T and 14.1 T) is shown in Appendix V.

When the series of spectra recorded for the solid-solution are compared with the ^{45}Sc MAS NMR spectrum recorded for $YScO_3$ it becomes clear what is happening. $YScO_3$ possesses a large quadrupolar interaction when compared with $LaScO_3$ and as greater quantities of Y are introduced to the system it appears a structure similar to $YScO_3$ is adopted. As x is increased the degree of strain imposed on the structure continues to increase, as highlighted earlier in Figure 6.15. Hence, the broad ^{45}Sc MAS NMR spectra and large quadrupolar interactions

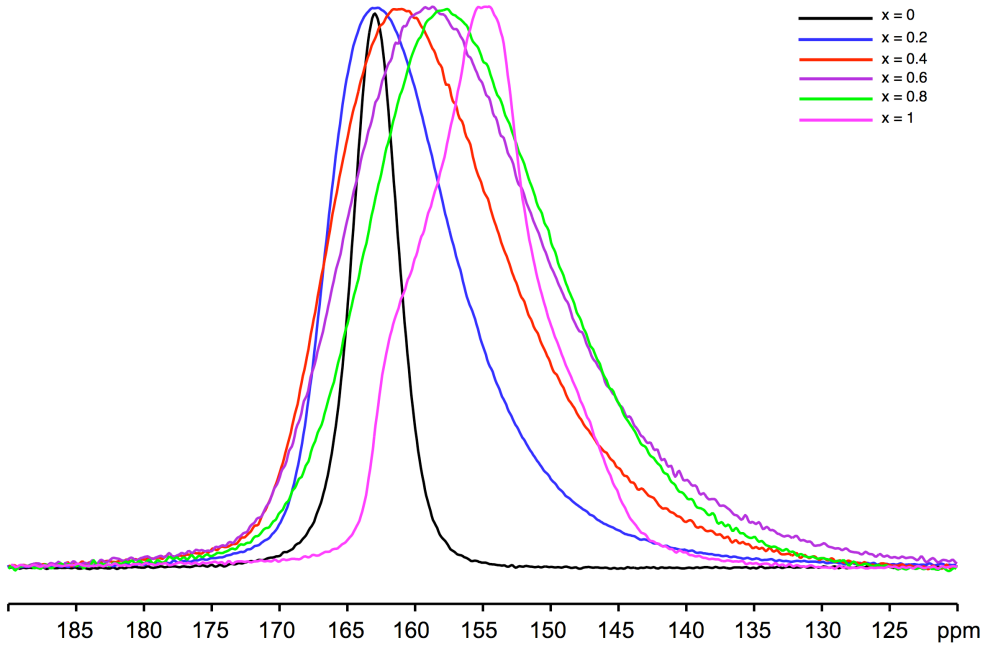

Figure 6.18: An expansion of the central transition of the ^{45}Sc (14.1 T) MAS NMR spectra for each sample in the series $La_{1-x}Y_xScO_3$ shown in Figure 6.17.

exhibited for the latter samples of this series are, most probably, owing to increased stress and strain on the structure.

To gain resolution and insight into the nature and extent of the disorder exhibited in the $La_{1-x}Y_xScO_3$ series, MQMAS experiments were performed. The triple-quantum ^{45}Sc MAS spectrum for $La_{0.8}Y_{0.2}ScO_3$ is shown in Figure 6.19(a), displaying a single ridge. When no disorder is present in a system the ridge observed in any z-filtered experiment (prior to shearing) will be aligned along a gradient equal to the MQMAS ratio, R, i.e., for a I = 7/2 nucleus the ridge will be aligned along 101/45 (+2.24). To illustrate this an MQMAS spectrum has been simulated and is shown in Figure 6.20(a) displaying a single ridge aligned along R. When disorder is present in a system the direction along which the ridge is aligned changes depending on the precise nature of the disorder. For example, when a distribution of chemical shifts is present the centre of the different environments will be aligned along a gradient of +3, as shown in Figure 6.20(b). If, however, a distribution of quadrupoles is present this alignment will be along a gradient of +1.8, as shown in Figure 6.20(c). In reality, many disordered systems exhibit contributions from both a distribution of chemical and quadrupolar shift interactions. Therefore, in

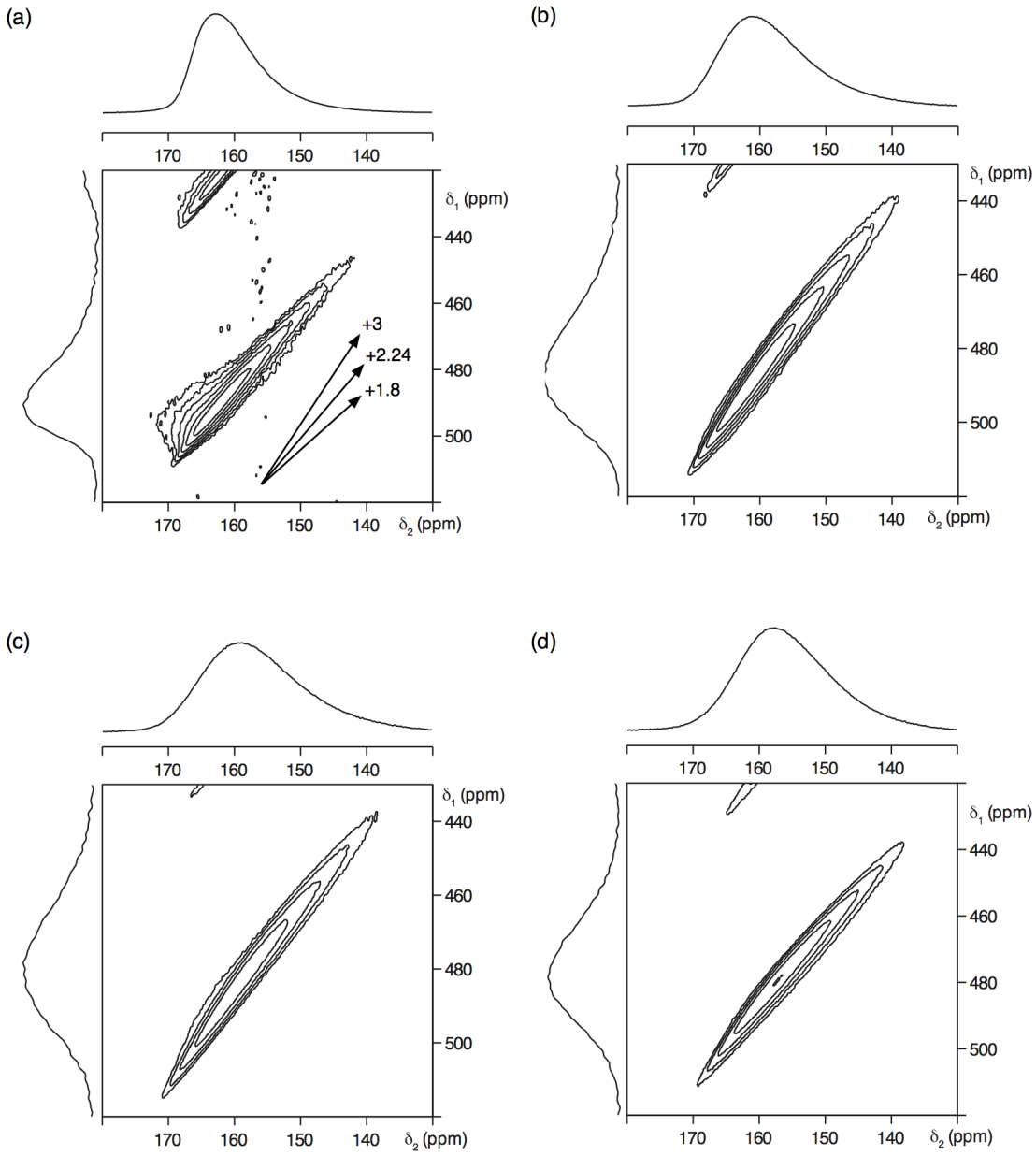

Figure 6.19: Conventional ^{45}Sc (14.1 T) MAS NMR spectra, triple-quantum MAS NMR spectra and corresponding projections for (a) $La_{0.8}Y_{0.2}ScO_3$, (b) $La_{0.6}Y_{0.4}ScO_3$, (c) $La_{0.4}Y_{0.6}ScO_3$ and (d) $La_{0.2}Y_{0.8}ScO_3$. Spectra were recorded using the z-filtered pulse sequence shown in Figure 2.28. Also shown in (a) are axes highlighting the respective gradients along which samples exhibiting a distribution of chemical shift or quadrupolar interaction will lie. Spectra are the result of averaging 96 transients with a recycle interval of 3 s for each of 256 t_1 increments of 20.0 μs. The MAS rate was 10 kHz.

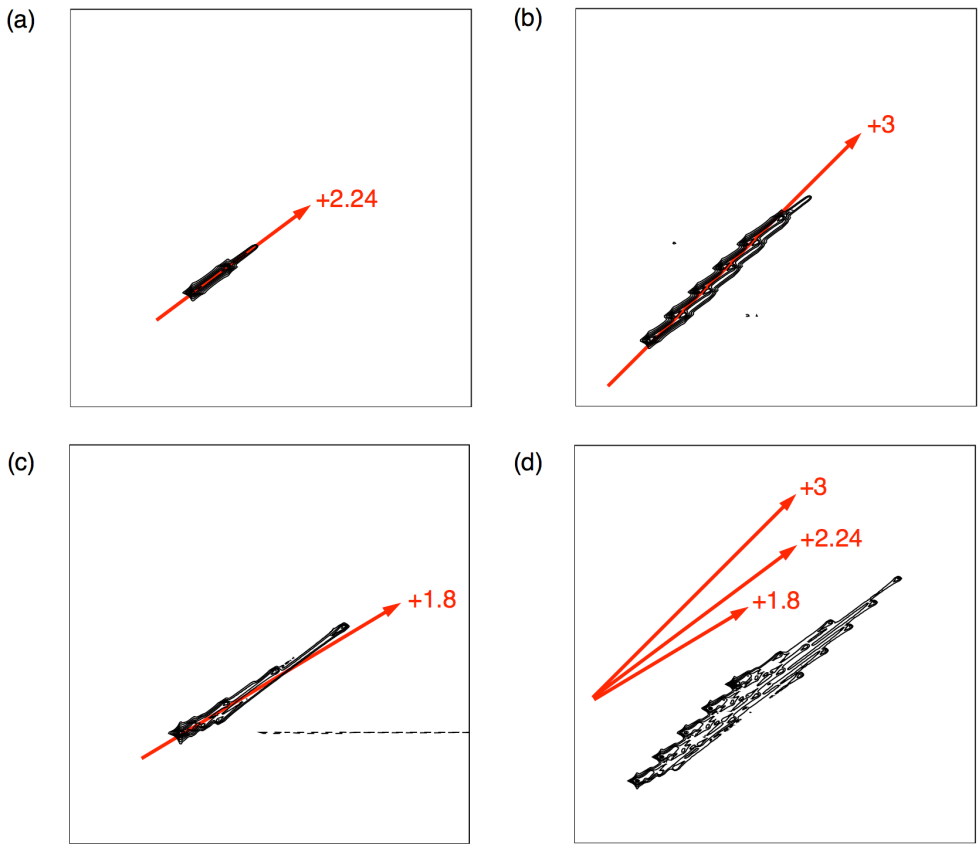

Figure 6.20: Simulated ^{45}Sc (9.4 T) MAS NMR spectra for (a) a single Sc site exhibiting no disorder, aligned along a gradient of 101/45 (+2.24), (b) sites resulting from a distribution of chemical shifts, aligned along a gradient of +3, (c) sites resulting from a distribution of the quadrupolar interaction, aligned along a gradient of +1.8, and (d) sites resulting from a distribution of both chemical shifts and quadrupolar parameters. Also shown are axes representing the different gradients along which each distribution will exhibit broadening. Simulation parameters include C_Q = 8 MHz, η_Q = 0 and δ_{iso} = 0. Boxcar distributions of C_Q (± 2 MHz) and δ_{iso} (± 8 ppm) were used.

such cases, the ridge in an MQMAS experiment will be broadened along a gradient between +3 and +1.8. An example of a spectrum exhibiting contributions from both is shown in Figure 6.20(d). The single ridge present in the ^{45}Sc MQMAS spectrum for $La_{0.8}Y_{0.2}ScO_3$ indicates the presence of a single Sc site, in good agreement with the diffraction data refined earlier. The ridge displayed appears to be aligned along a gradient of +2.24. However, the ridge exhibits a degree of additional broadening that is characteristic of disorder and owing to a distribution of

Table 6.18: Experimental ^{45}Sc NMR parameters, $\langle\delta_{iso}\rangle$ and $\langle P_Q\rangle$ for x = 0.2, 0.4, 0.6 and 0.8 in the series $La_{1-x}Y_xScO_3$, obtained from the MQMAS spectra in Figures 6.7, 6.9 and 6.19.

x	$\langle\delta_{iso}\rangle$ (ppm)	$\langle P_Q\rangle$ / MHz
0	164.6(5)	3.9(2)
0.2	165.8(5)	5.0(2)
0.4	166.0(5)	6.2(2)
0.6	164.8(5)	6.5(2)
0.8	164.1(5)	7.4(2)
1	163.0(5)	8.4(2)

chemical and/or quadrupolar shift interactions. In this particular case the ridge does not appear to be predominantly aligned along any one axis, suggesting the disorder exhibited is owing to a distribution of both quadrupoles and chemical shifts. In a similar manner to $LaScO_3$, the ridge exhibited is relatively narrow. This therefore makes it difficult to quantify the disorder resulting from each distribution.

Two-dimensional ^{45}Sc MAS NMR spectra were also recorded for all remaining samples in the $La_{1-x}Y_xScO_3$ series. Spectra corresponding to compositions x = 0.4, 0.6 and 0.8 are shown in Figures 6.19(b-d) respectively. As observed for the $La_{0.8}Y_{0.2}ScO_3$ sample, all spectra exhibit a single broadened ridge. For the x = 0.4 and 0.6 samples (Figures 6.19(b) and (c)) the ridges appear to be aligned along a gradient of +2.24 with a small amount of additional broadening. As observed for the x = 0.2 sample, the disorder exhibited in each sample is believed to result from both a distribution of quadrupoles and chemical shifts. This appears to be in good agreement with earlier discussions regarding the increase in orthorhombic strain and tilt angle producing a substantial change to the local coordination environment of the Sc and hence the quadrupolar interaction. As greater quantities of Y are introduced to the system the octahedra become more distorted owing to the cation size and associated changes to the bond angle. As x is increased a structure type similar to that of $YScO_3$ is adopted and, as shown previously, a larger value of C_Q is

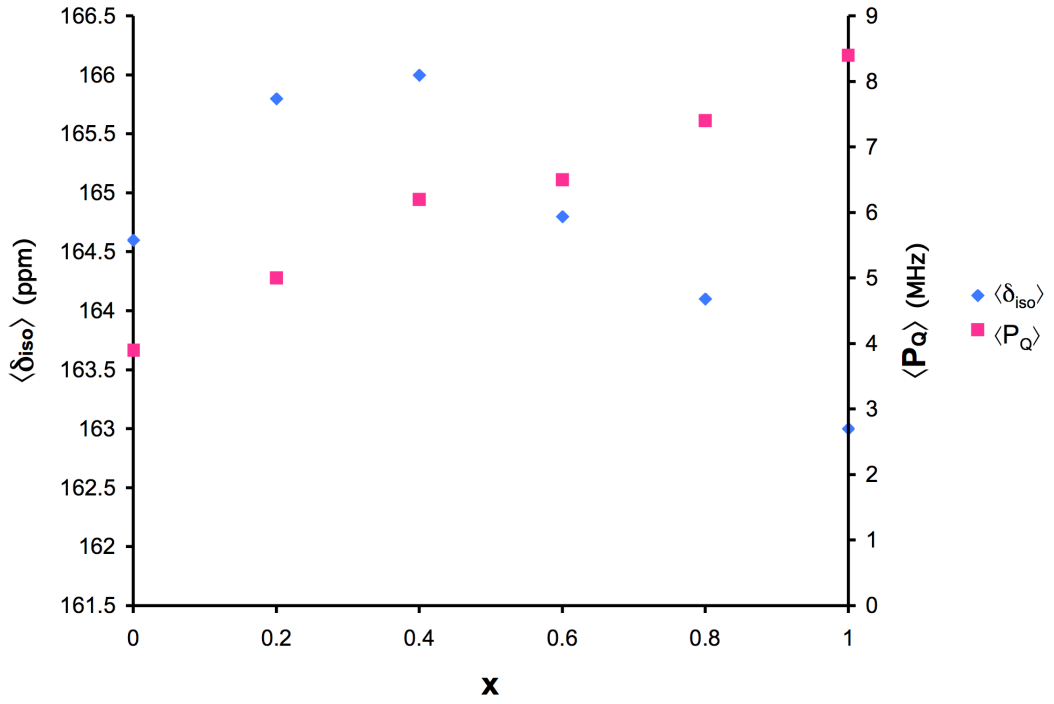

Figure 6.21: The variation in $\langle\delta_{iso}\rangle$ and $\langle P_Q\rangle$ observed with increasing x for $La_{1-x}Y_xScO_3$. All values were obtained from the centre of gravity of the resonance in the two-dimensional ^{45}Sc (14.1 T) MAS NMR spectra shown in Figures 6.7, 6.9 and 6.19.

observed for $YScO_3$. Therefore, a distribution of quadrupolar parameters and chemical shifts is highly likely as x is increased as the solid-solution gradually progresses towards a structure exhibiting a less symmetrical Sc environment.

The MQMAS spectra recorded have therefore confirmed that the disorder exhibited in the $La_{1-x}Y_xScO_3$ solid-solution is owing to a distribution of both quadrupoles and chemical shifts. To aid in the understanding and interpretation of the ^{45}Sc MQMAS spectra recorded for each sample in the series and to obtain information regarding the both the quadrupolar and chemical shift interactions, the position of the centre of gravity of the ridge lineshape (δ_1, δ_2) was obtained. This enabled the average chemical shift, $\langle\delta_{iso}\rangle$, and average quadrupolar product, $\langle P_Q\rangle$, to be determined. Details of these parameters are given in Table 6.18 and a plot highlighting the variation in $\langle\delta_{iso}\rangle$ and $\langle P_Q\rangle$ with increasing x is shown in Figure 6.21. The $\langle P_Q\rangle$ value gradually increases with x and is in good agreement with earlier discussions regarding the larger value of C_Q exhibited for $YScO_3$. The $\langle\delta_{iso}\rangle$ reaches a maximum at x = 0.4 then

gradually reduces with greater values of x. However, the change in chemical shift between the two end-members is relatively small.

6.3.3.3 ^{89}Y NMR Analysis

^{45}Sc is a quadrupolar nucleus and, as already highlighted, quadrupolar broadening and the presence of disorder can often hinder the extraction of important information. As a result, this can make the study of quadrupolar nuclei less appealing. The series $La_{1-x}Y_xScO_3$ does, however, possess three additional NMR active nuclei, ^{89}Y (I = 1/2), ^{139}La (I = 7/2) and ^{17}O (I = 5/2). ^{89}Y is, in theory, an attractive proposition for study using NMR. However, like ^{45}Sc there are some limitations to its practical use and implementation. ^{89}Y is a spin I = 1/2 nucleus with 100% abundance and large chemical shift range (~4000 ppm). However, it possesses an extremely low receptivity (0.681 relative to ^{13}C). In addition, relaxation times for ^{89}Y are typically on the order of tens to thousands of seconds, meaning to obtain spectra of sufficiently high quality very long experiments are required. However, an associated advantage of ^{89}Y is that as a spin I = 1/2 nucleus it is therefore free from the added complication of the quadrupolar interaction, and spectral interpretation is therefore considerably easier. Investigation of the yttrium environment may offer additional insight into the disorder exhibited within the system. Furthermore, it may enable us to quantify the disorder exhibited. Therefore, in an attempt to gain additional structural information regarding the A site in $La_{1-x}Y_xScO_3$ the local Y environment was probed using ^{89}Y NMR.

Conventional ^{89}Y MAS NMR spectra were recorded for compositions x = 0.2, 0.4, 0.6, 0.8 and 1. All ^{89}Y MAS NMR spectra recorded for this series exhibited a single resonance, as shown in Figure 6.22. As x was increased a shift in the average isotropic chemical shift, $\langle\delta_{iso}\rangle$, was exhibited. The known chemical shift range for ^{89}Y is extremely large. However, the shift exhibited in this particular series was very

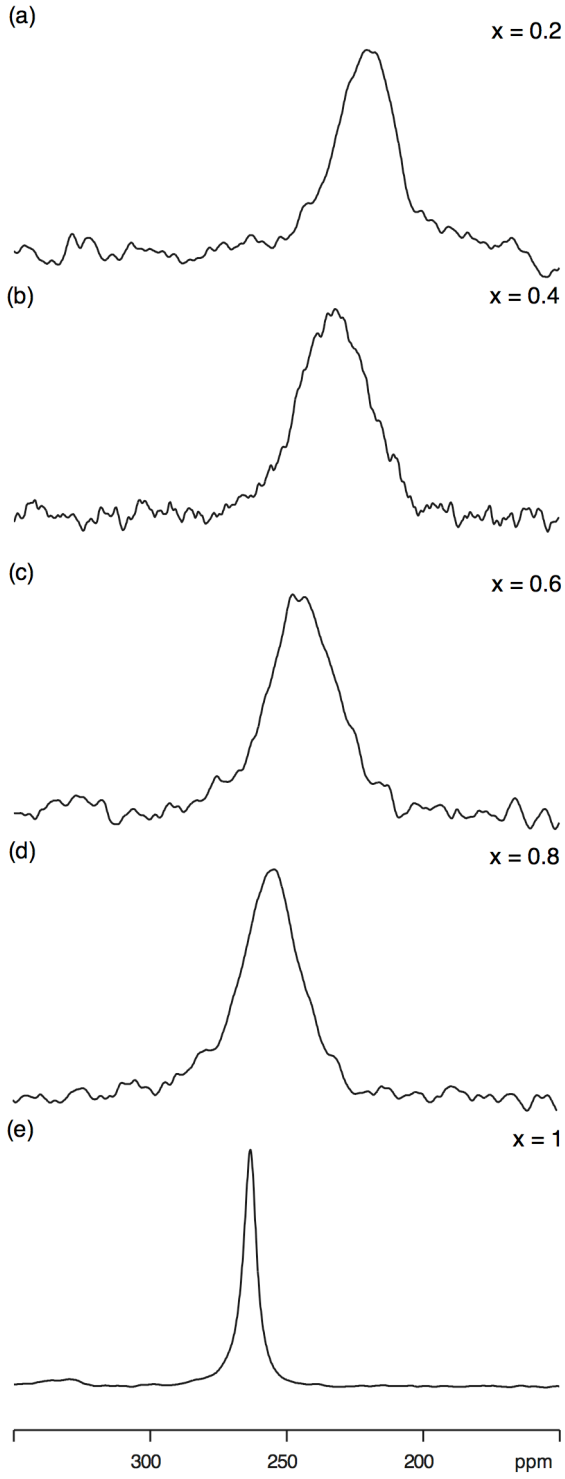

Figure 6.22: Conventional ^{89}Y (14.1 T) MAS NMR spectra recorded for compositions x = 0.2, 0.4, 0.6, 0.8 and 1 in the series $La_{1-x}Y_xScO_3$. Spectra are the result of averaging (a) 4096, (b) 3072, (c) 1080 and (d, e) 720 transients with a recycle intervals of 20 s. The MAS rate was 10 kHz.

Table 6.19: Experimental ^{89}Y NMR parameters, $\langle\delta_{iso}\rangle$ and $\Delta\nu_{1/2}$ for the series $La_{1-x}Y_xScO_3$, obtained from the MAS spectra in Figure 6.22.

x	$\langle\delta_{iso}\rangle$ (ppm)	$\Delta\nu_{1/2}$ / Hz
0.2	219(4)	740(10)
0.4	232(4)	1018(10)
0.6	246(4)	934(10)
0.8	254(4)	865(10)
1	263.3(2)	179(10)

small, suggesting a relatively small change is observed in the local Y environment. Each of the observed chemical shifts was in good agreement with the known chemical shift range of twelve coordinate Y^{3+}.[321,322] All $\langle\delta_{iso}\rangle$ values extracted from the ^{89}Y MAS NMR spectra recorded can be found in Table 6.19. The variation in $\langle\delta_{iso}\rangle$ observed with increasing x is linear, as shown in Figure 6.23(a). In a similar manner to the ^{45}Sc MAS NMR spectra recorded, compositions x = 0.2, 0.4, 0.6 and 0.8 exhibit broadening of the lineshape, most probably owing to Y being disordered across the A site. In contrast, the ^{89}Y MAS NMR spectrum for $YScO_3$ is relatively narrow, confirming an ordered Y environment. The linewidth, $\Delta\nu_{1/2}$, of each ^{89}Y spectrum was also measured as a function of x and all values of $\Delta\nu_{1/2}$ extracted from the ^{89}Y MAS NMR spectra recorded are given in Table 6.19. The variation in $\Delta\nu_{1/2}$ exhibited with increasing x is shown in Figure 6.23(b). For I = 1/2 nuclei it is considerably easier to quantify the disorder present in any system, as the magnitude of the linewidth is expected to be directly proportional to disorder and the trend exhibited in Figure 6.23(b) suggests the maximum level of disorder in the $La_{1-x}Y_xScO_3$ is close to x = 0.4. The linewidth of the lineshape exhibited in the ^{89}Y MAS NMR spectrum for the x = 0.4 sample is ~280 Hz greater than that of the x = 0.2 sample, suggesting that there is a sharp increase in the disorder exhibited in the x = 0.4 sample, as highlighted in Figure 6.23(b). A slow spinning MAS spectrum was also recorded for $YScO_3$, as shown in Figure 6.24. Fitting a slow spinning MAS NMR spectrum enables the

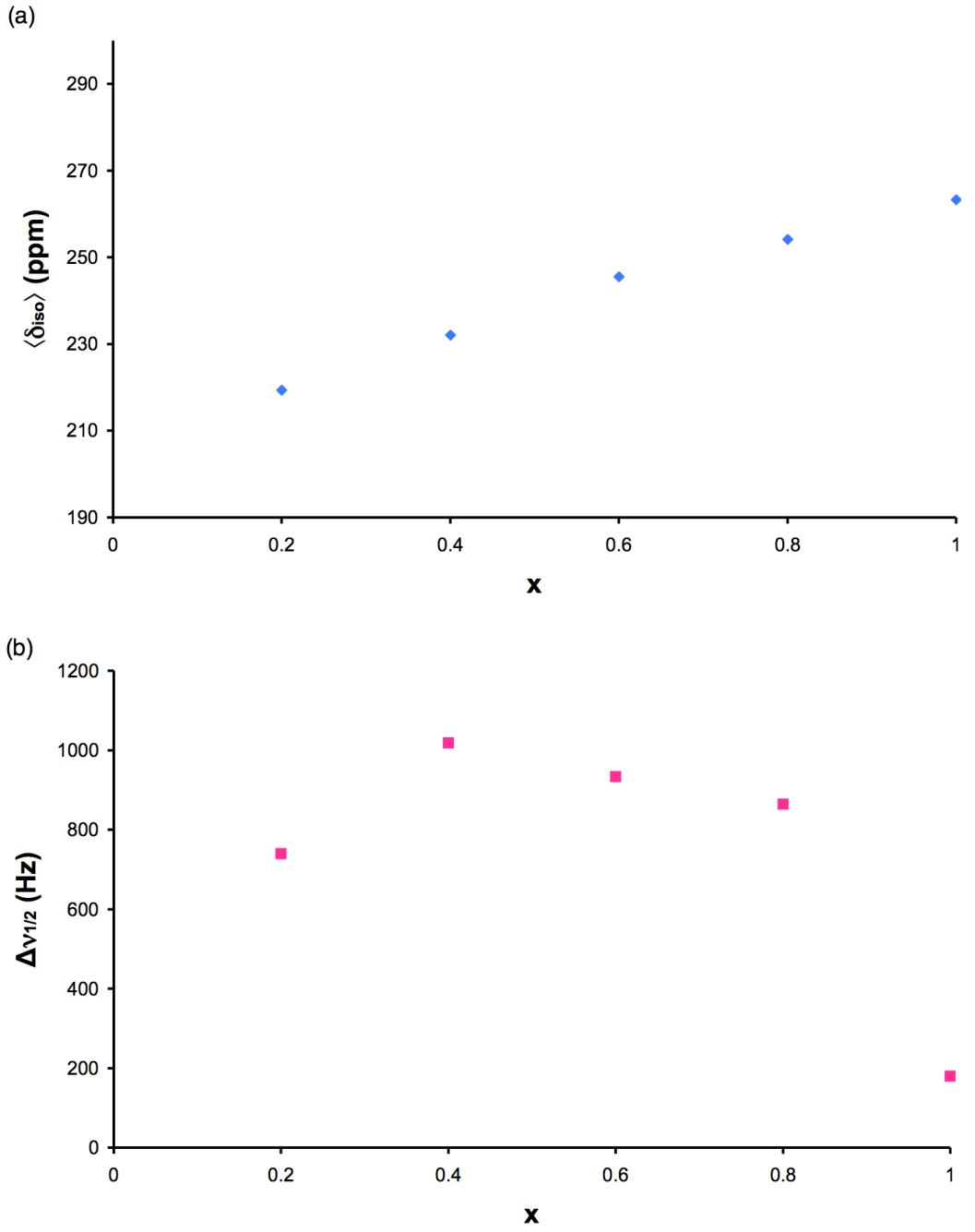

Figure 6.23: The variation of (a) $\langle\delta_{iso}\rangle$ and (b) $\Delta\upsilon_{1/2}$ observed with increasing x in $La_{1-x}Y_xScO_3$. All values were obtained from the ^{89}Y NMR spectra in Figure 6.22.

parameters δ_{iso}, $\Delta\sigma_{CS}$, and η_{CS}, to be determined, the parameters obtained for $YScO_3$ (using SOLA) are given in Table 6.20.

The ^{89}Y MAS NMR spectra recorded aided in confirming the disorder previously identified using ^{45}Sc MAS NMR. In addition, the extraction of information regarding the linewidth of each spectrum enabled the disorder to be quantified. This confirmed earlier suggestions

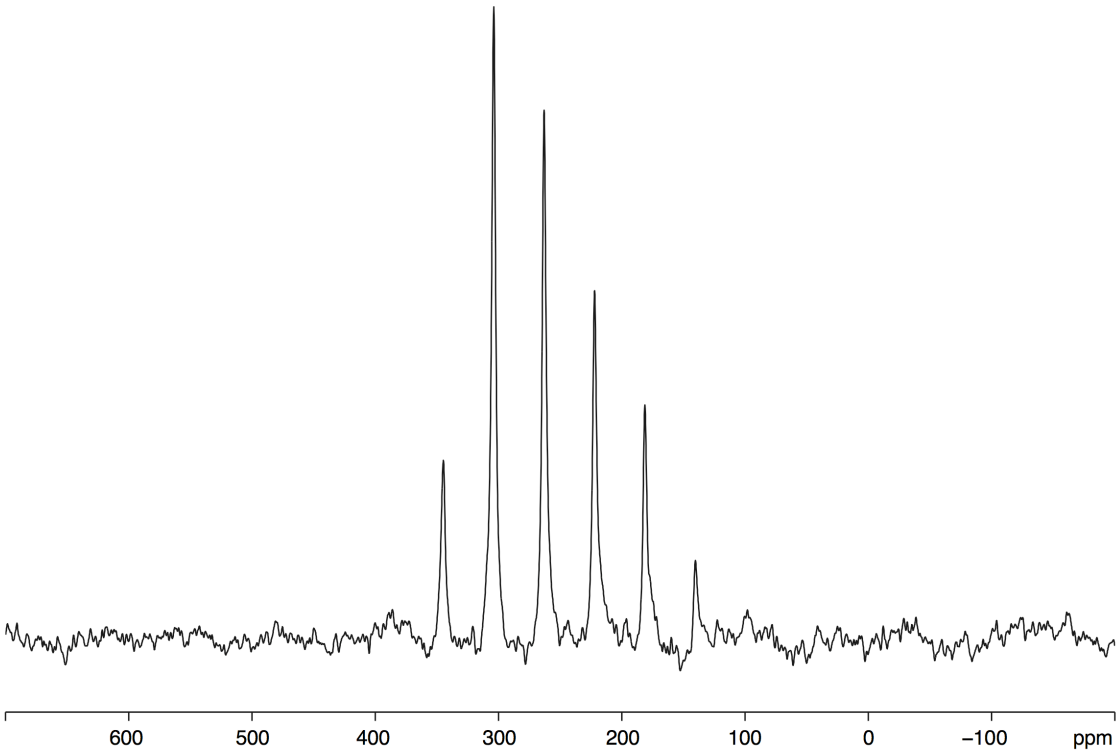

Figure 6.24: ^{89}Y (14.1 T) MAS NMR spectrum of $YScO_3$, acquired by averaging 720 transients with a recycle interval of 20 s. The MAS rate was 1.2 kHz.

from the ^{45}Sc MAS NMR data and NPD data obtained that the greatest degree of disorder was exhibited close to x = 0.5. The substitution of Y into the $LaScO_3$ structure appears to produce a greater effect on the local environment of the Sc and this, in turn, suggests that the B site is more sensitive to changes occurring on the A site. Upon closer inspection of the La – Y/La and Sc – Y/La distances it becomes apparent as to why this is the case. The distance between the A- and B-site cations is smaller than the distance between two A-site cations. The B site is therefore 'closer' to the A site and, as a result, is more sensitive to any substitutions. The Y environment in $La_{1-x}Y_xScO_3$ would therefore experience a greater effect if the Sc was substituted with an isovalent cation. Both the ^{45}Sc and ^{89}Y MAS NMR spectra recorded confirm no structural phase transitions occur in this series and an orthorhombic structure is retained throughout. This is in good agreement with the findings observed from the NPD data.

Table 6.20: ^{89}Y NMR parameters, δ_{iso},$\Delta\sigma_{CS}$ and η_{CS}, for $YScO_3$ obtained from fitting of the slow spinning MAS spectrum shown in Figure 6.24.

	δ_{iso} (ppm)	$\Delta\sigma_{CS}$ / ppm	η_{CS}
$YScO_3$	263.1(5)	−122(4)	0.55(5)

6.3.4 ^{17}O enrichment of $LaScO_3$

As previously stated in Chapter 3 information regarding the local environment of oxygen is highly desirable. However, it is often extremely difficult to obtain such information as the most abundant oxygen isotope, ^{16}O (I = 0), is NMR inactive. To overcome such issues samples are commonly enriched with ^{17}O. In an attempt to gain additional structural information regarding the local environment of oxygen in $LaScO_3$ the sample previously investigated using high-resolution NPD and ^{45}Sc MAS NMR was post-synthetically enriched using ^{17}O enriched gas.

Structure and phase purity of the sample, post enrichment, were verified using l-PXRD. This confirmed the sample had not been changed during the enrichment process. In addition, a ^{45}Sc MAS NMR spectrum was recorded, which also confirmed the sample had not changed. The ^{17}O MAS NMR spectrum, shown in Figure 6.25(a), displays two distinct O sites, δ = 392.8 ppm and δ = 373.2 ppm, in good agreement with published crystallographic data. Both sites appear to exhibit small values of C_Q, suggesting each O is in a symmetrical environment. The ^{17}O MAS NMR spectrum with wide spectral width is shown in Figure 6.25(b). This spectrum was fitted using SOLA and the NMR parameters obtained confirmed initial suggestions of two resonances with very small values of C_Q, as shown in Table 6.21. To highlight how similar and highly symmetrical the two oxygen sites in $LaScO_3$ are isolated oxygen environments for sites O1 and O2 are shown in Figure 6.26(a) and (b), respectively. The ⟨Sc - O⟩ bond distance exhibited for each site is very similar. This confirms the similar nature of the two sites and verifies the findings by NMR. $LaScO_3$ is well documented as being an ordered perovskite with two distinct oxygen environments, therefore this was an

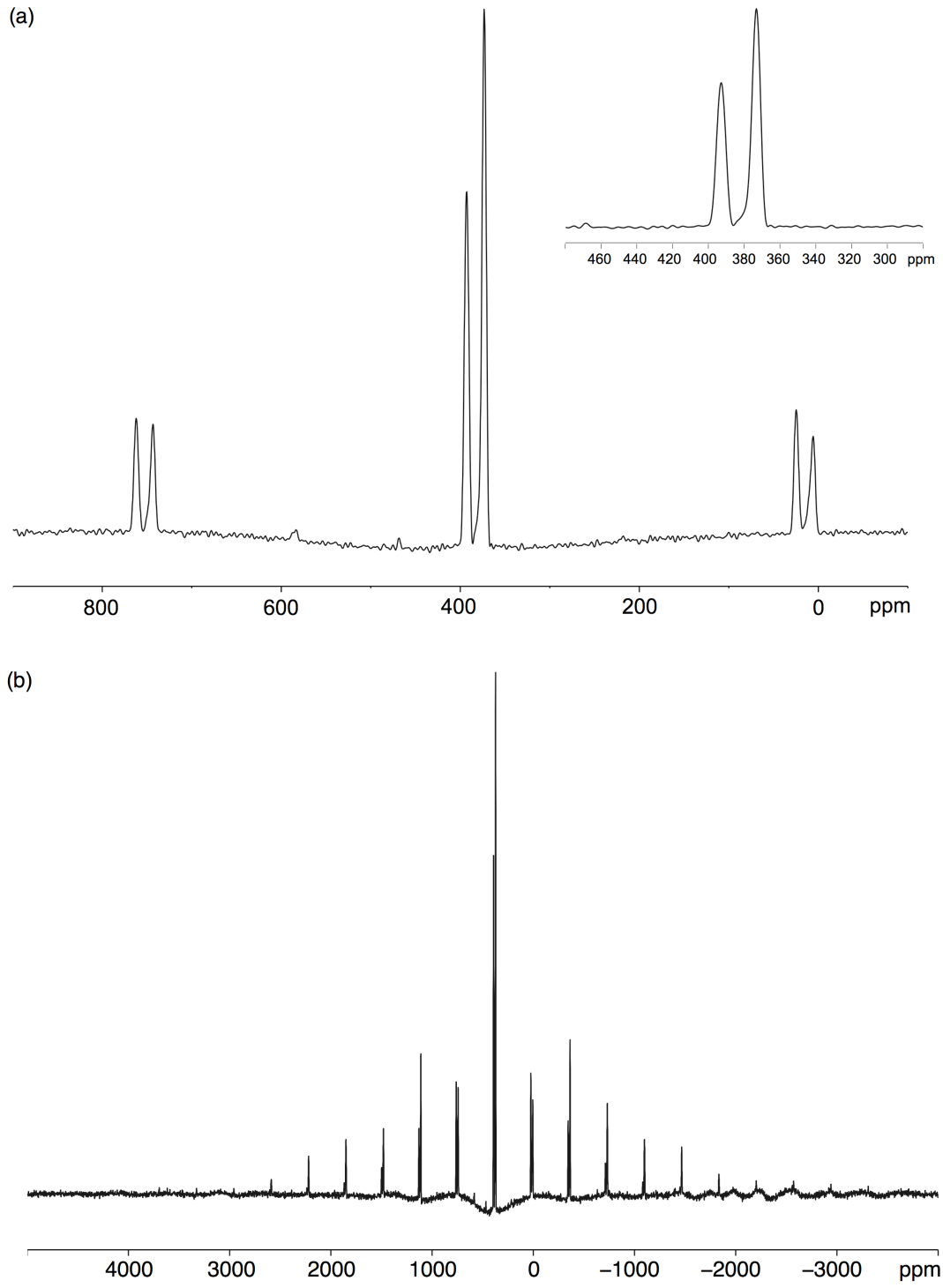

Figure 6.25: Conventional ^{17}O (14.1 T) MAS NMR spectrum of $LaScO_3$ with spectral widths of (a) 80 kHz and (b) 800 kHz. Also shown as an insert in (a) is an expansion of the centreband in the spectrum. Spectra are the result of averaging 576 transients with 20 s recycle interval. The MAS rate was 30 kHz.

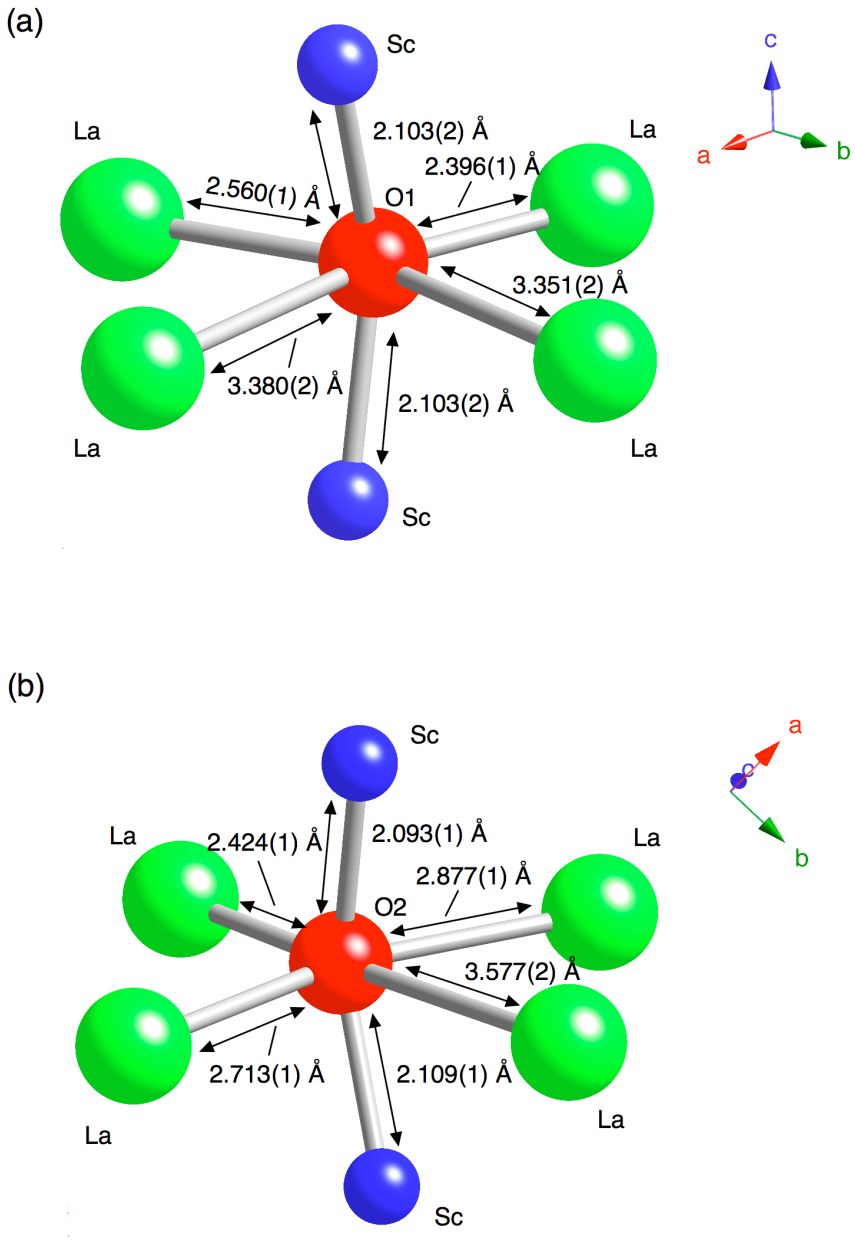

Figure 6.26: The coordination environments for sites O1 and O2 in $LaScO_3$, obtained from Rietveld refinement of the NPD data shown in Figure 6.4(b).

ideal 'test' compound to determine whether ^{17}O enrichment of perovskite-based materials was feasible. The initial results obtained are extremely encouraging, as we have shown it is possible to successfully enrich dense perovskite-based compounds using $^{17}O_2$ gas. For disordered materials, such as the solid-solution $La_{1-x}Y_xScO_3$, this type of enrichment would be hugely beneficial as it would provide information regarding the precise number of oxygen environments present and could, in turn, provide

Table 6.21: ^{17}O NMR parameters, δ_{iso}, P_Q and η_Q, for $LaScO_3$ obtained from the wide spectral width MAS spectrum shown in Figure 6.25.

	Site	δ_{iso} (ppm)	P_Q / MHz	C_Q / MHz	η_Q
$LaScO_3$	O1	393.1(5)	0.57(1)	0.56(1)	0.3(1)
	O2	374.3(5)	1.10(1)	1.09(1)	0.2(1)

valuable insight into the nature of the disorder exhibited. Unfortunately within this investigation it was not possible to enrich any additional samples in the $La_{1-x}Y_xScO_3$ series. However, it is hoped the findings presented will encourage future investigations into the study of disordered materials using ^{17}O MAS NMR. At present, work has concentrated solely on the substitution of isovalent cations onto the A site in the $LaScO_3$ structure. However, the introduction of a vacancy, i.e., doping the structure with an aliovalent cation could potentially provide a greater degree of information. Using ^{17}O MAS NMR it would be possible to probe the vacancy sites and gain information regarding coordination and bonding. In addition, the introduction of vacancies could potentially introduce conduction capabilities in these types of materials. This could, in turn, lead to future applications in a range of different devices. In addition, this could provide important information regarding the chemical importance of Sc-containing compounds. This would then ultimately contribute to the little knowledge currently known regarding the importance of Sc-based compounds. It must be noted that whilst the procedure for ^{17}O enrichment of $LaScO_3$ was relatively straightforward (heated in 50% ^{17}O enriched O_2 gas at 950 °C for 7 days) the costs associated with ^{17}O enrichment are often extremely high (see Chapter 3, section 3.3.7). Hence, cost is often a limiting factor when deciding whether the enrich samples. Ultimately if the gain in structural information is high then it is hugely beneficial to enrich samples.

6.3.5 Density Functional Theory (DFT) Calculations

6.3.5.1 $LaScO_3$ and $YScO_3$

In conjunction with experiment, ^{45}Sc, ^{89}Y and ^{17}O DFT calculations were completed, to aid spectral interpretation. In order to establish the accuracy and feasibility of ^{45}Sc NMR calculations using CASTEP initial calculations were completed on several 'model' compounds, including Sc_2O_3, $LiScO_2$, $NaScO_2$, $ScPO_4$ and $ScVO_4$. To date, our calculated results indicate excellent agreement with experimental data,[191] as shown in Figure 6.27(a). The NMR parameters calculated for all model compounds appeared to display better correlation with experiment after geometry optimisation of each structure. In particular, $NaScO_2$ displayed considerably better agreement with experiment post geometry optimisation. Similar calculations were completed for several Y-containing compounds, including Y_2O_3, $Y_2Sn_2O_7$, $Y_2Ti_2O_7$, Y_2O_2S, YF_3, $YAlO_3$, β-$Y_2Si_2O_7$ and α-$Y_2Si_2O_7$. The experimental ^{89}Y NMR chemical shifts for each compound are plotted against the calculated ^{89}Y NMR shifts in Figure 6.27(b) and very good agreement is observed between the two. For each of the model compounds shown in Figure 6.27 the structure was geometry optimised prior to calculation of the NMR parameters, as better correlation with experiment was observed post optimisation. Each of the model compounds investigated indicated good agreement with the literature. This, therefore, confirmed that the Sc and Y pseudopotentials used in each calculation were accurate for ^{45}Sc and ^{89}Y DFT calculations using the CASTEP[214] code. Hence, DFT calculations were completed for $LaScO_3$ and $YScO_3$.

Initially, ^{45}Sc and ^{17}O NMR parameters were calculated for $LaScO_3$ using a structural model obtained from the literature, and are given in Table 6.22. When compared with the experimentally obtained parameters, shown in Tables 6.3 and 6.21, very little agreement was observed between the two. However, better correlation was observed post optimisation of the structure, during which both the unit cell and atomic coordinates were allowed to vary simultaneously. All ^{45}Sc and ^{17}O NMR parameters calculated for $LaScO_3$ (post optimisation) can also be found in Table 6.22.

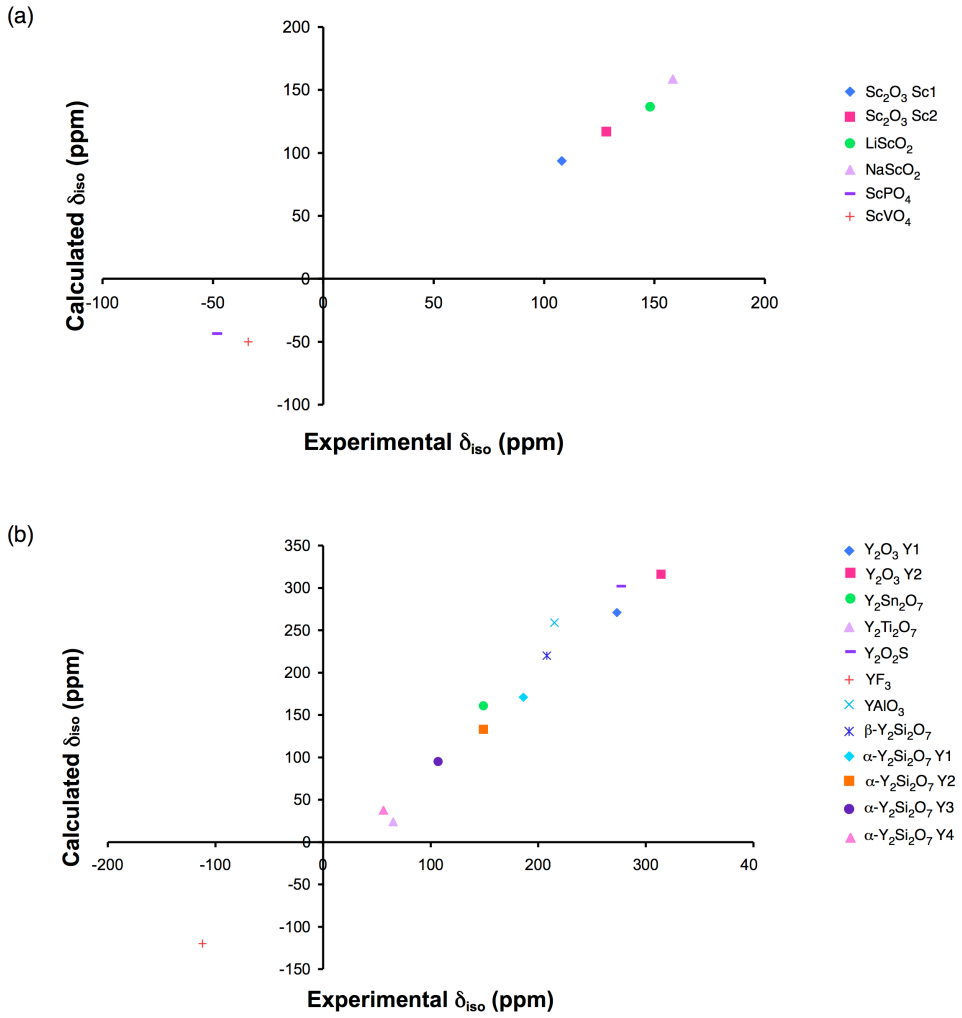

Figure 6.27: Comparison of experimental and calculated (a) ^{45}Sc and (b) ^{89}Y δ_{iso} for a series of simple inorganic compounds. All calculations were performed after full geometry optimisation of each structure.

The poor agreement with experiment observed prior to optimisation of the structure indicates the need for geometry optimisation. The structural optimisation of $LaScO_3$ was discussed earlier in Chapter 2 (section 2.11.2), where it was shown that optimisation of the initial structure obtained from diffraction was necessary to reduce the atomic forces and ensure the structure was in an energy minimum. It was also highlighted in section 2.11.2 that optimisation of the structure did not visibly change the structure in any way or the resulting diffraction pattern. (Refer to section section 2.11.2. for specific details). It must be noted that whilst the calculated values of C_Q for sites O1 and O2 appear in reasonable agreement with experiment, the calculated values δ_{iso} and η_Q do not

Table 6.22: Calculated (using CASTEP) ^{45}Sc and ^{17}O NMR parameters, δ_{iso}, P_Q, C_Q and η_Q, for $LaScO_3$ obtained (a) prior to and (b) post optimisation of the structure.

	Site	δ_{iso} (ppm)	P_Q / MHz	C_Q / MHz	η_Q
[(a)]$LaScO_3$	Sc1	160.9	6.49	5.89	0.80
	O1	424.1	−0.80	−0.80	0.17
	O2	407.2	−1.34	−1.32	0.31
[(b)]$LaScO_3$	Sc1	162.0	3.26	3.05	0.66
	O1	430.6	−0.70	−0.70	0.16
	O2	413.8	−1.29	−1.27	0.28

appear in as good agreement. The discrepancy observed in the isotropic chemical shift is, most probably, owing to the reference used for the calculation, i.e., Mg_2SiO_4. It is possible that this is not a suitable reference for this particular series of compounds and a better one is required. To establish whether this is the case an investigation into alternative reference compounds is required. There are many reports within the literature of poor agreement between calculated and experimental values of η_Q and, as discussed in Chapter 3, section 3.4, there are many reasons for such behaviour.

In a similar manner ^{45}Sc, ^{17}O and ^{89}Y calculations were completed for $YScO_3$. As previously stated, during this investigation it was difficult to successfully synthesise $YScO_3$ and, as a result, it was not initially possible to record an MAS spectrum for this sample. DFT calculations therefore provided a convenient method for predicting the ^{45}Sc and ^{89}Y NMR parameters. This, in turn, enabled the ^{45}Sc and ^{89}Y MAS NMR spectra to be simulated for $YScO_3$. In an attempt to calculate the parameters for $YScO_3$ a model for the isostructural $HoScO_3$ was used, replacing the Ho atoms for Y. This worked extremely well, producing the ^{45}Sc and ^{89}Y parameters shown in Tables 6.23 and 6.24. Note that the structure was fully optimised (allowing both the unit cell and atomic coordinates to vary simultaneously) prior to calculation of the NMR parameters to ensure that the atomic forces were minimised and the

Table 6.23: Calculated (using CASTEP) ^{45}Sc and ^{17}O NMR parameters, δ_{iso}, P_Q, C_Q and η_Q, for $YScO_3$ obtained (a) replacing all Ho atoms in the $HoScO_3$ with Y and (b) replacing all La atoms in the $LaScO_3$ structure with Y and (c) the structural model for $YScO_3$ obtained from Rietveld refinement of the NPD data.

	Site	δ_{iso} (ppm)	P_Q / MHz	C_Q / MHz	η_Q
[(a)]$YScO_3$	Sc1	156.6	−9.35	−8.32	0.89
	O1	404.8	0.60	0.59	0.27
	O2	385.6	−1.44	−1.39	0.45
[(b)]$YScO_3$	Sc1	156.3	−9.38	−8.44	0.84
	O1	404.3	0.62	0.61	0.25
	O2	385.5	−1.44	−1.39	0.45
[(c)]$YScO_3$	Sc1	156.3	−9.08	−8.06	0.90
	O1	404.5	0.59	0.58	0.34
	O2	385.6	−1.44	−1.39	0.45

Table 6.24: Calculated (using CASTEP) ^{89}Y NMR parameters, δ_{iso}, $\Delta\sigma_{CS}$ and η_{CS}, for $YScO_3$ obtained (a) replacing all Ho atoms in the $HoScO_3$ with Y, (b) replacing all La atoms in the $LaScO_3$ structure with Y and (c) the structural model for $YScO_3$ obtained from Rietveld refinement of the NPD data.

	Site	δ_{iso} (ppm)	$\Delta\sigma_{CS}$ / ppm	η_{CS}
[(a)]$YScO_3$	Y1	263.1	−140.7	0.32
[(b)]$YScO_3$	Y1	263.2	−140.3	0.32
[(c)]$YScO_3$	Y1	263.3	−142.0	0.30

structure was in a local energy minimum. The parameters obtained displayed very good agreement with those subsequently obtained experimentally. A second calculation was completed for $YScO_3$ using the structural model for $LaScO_3$, where all the La atoms were replaced with Y atoms. Again, prior to calculation of the NMR parameters the structure was fully optimised. The calculated parameters were again in good agreement with those obtained experimentally. All ^{45}Sc and ^{17}O NMR parameters calculated post optimisation of the two structures are given in Table 6.22. The calculated ^{45}Sc NMR parameters obtained for $YScO_3$ were extremely useful as they predicted a single ^{45}Sc site with $C_Q = -8.3$ MHz. It must be noted that the sign discrimination of C_Q is difficult to obtain experimentally. However, this information is automatically generated during the calculation. For completeness, NMR parameters were also subsequently calculated for $YScO_3$ using the structural model obtained from Rietveld refinement of the NPD data. The parameters were calculated prior to and post optimisation of the structure and, as previously observed, the greatest agreement with experiment was obtained post optimisation of the structure, as highlighted in Table 6.23. All parameters obtained prior to and post optimisation (using a fixed cell) are given in Appendix V. The $YScO_3$ structure obtained directly from Rietveld refinement was compared with the structures obtained post optimisation and each appeared virtually identical, suggesting that very little movement of the atoms was required to reduce the atomic forces sufficiently and ensure the structure was in an energy minimum. This therefore indicated that the Rietveld refinement completed for $YScO_3$ using the NPD data was reasonably accurate and the structure was already close to an energy minimum. The ^{89}Y DFT calculations completed for $YScO_3$ indicate good agreement with the single site observed experimentally. Details of all ^{89}Y calculated parameters for each of the $YScO_3$ calculations are given in Table 6.24. All ^{45}Sc, ^{17}O and ^{89}Y DFT calculations completed for $LaScO_3$ and $YScO_3$ in which solely the atomic coordinates were allowed to vary (i.e., the unit cell was fixed) can be found in Appendix V.

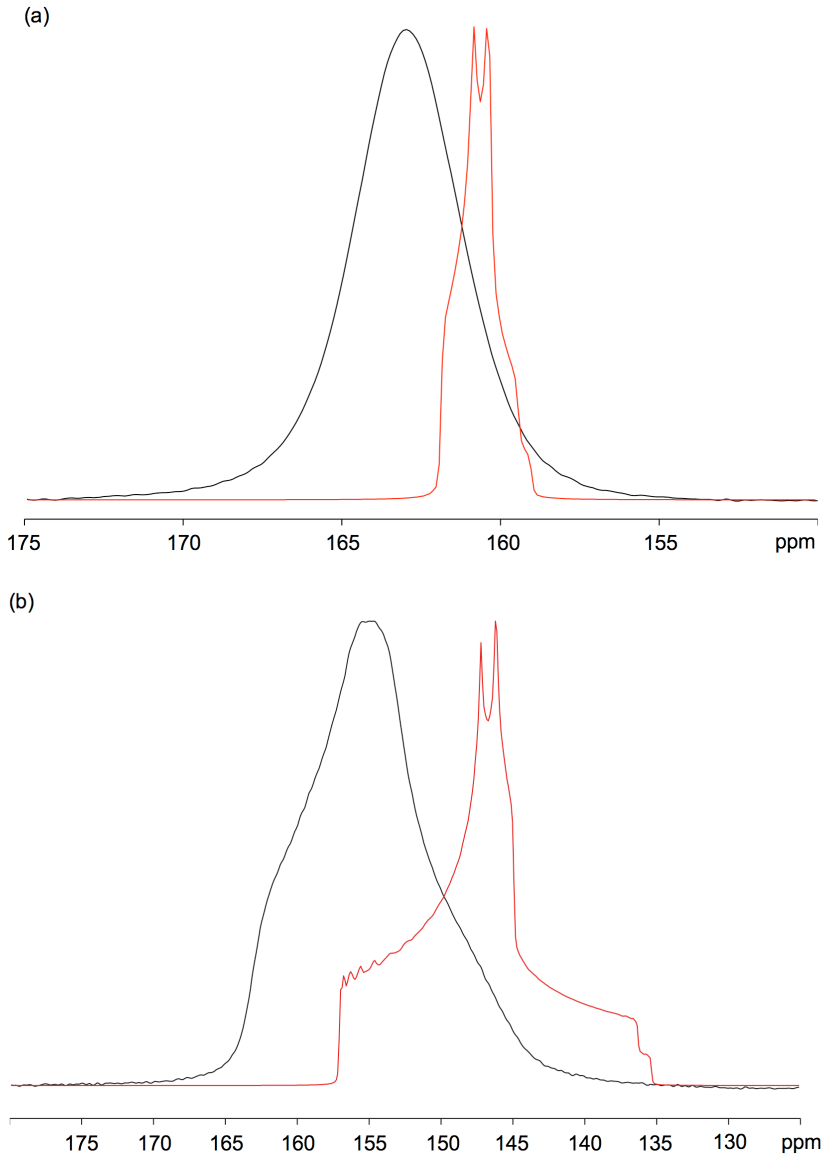

Figure 6.28: Comparison of experimental ^{45}Sc (14.1 T) MAS NMR spectra (shown in black) and lineshapes simulated using the calculated parameters (shown in red) for (a) $LaScO_3$ and (b) $YScO_3$.

Prior to the successful synthesis of $YScO_3$ there was considerable confusion regarding the ^{45}Sc MAS NMR results obtained. Experimentally, all samples in the $La_{1-x}Y_xScO_3$ series exhibited broadening characteristic of disorder. However, this broadening appeared to gradually increase for the latter members. Initially this behaviour was confusing and only when the calculated ^{45}Sc NMR parameters were considered did it become apparent that $YScO_3$ possessed a larger quadrupolar interaction when compared with $LaScO_3$. Hence, the broadening exhibited experimentally

by compositions x = 0.6 and 0.8 confirmed that these samples were gradually moving towards a structure type similar to that of $YScO_3$. ^{45}Sc MAS NMR spectra have been simulated for $LaScO_3$ and $YScO_3$ using the NMR parameters obtained post optimisation of each structure. The simulated spectra have been overlaid and compared with the experimental spectra and are shown in Figures 6.28(a) and (b). In contrast to the ^{45}Sc MAS NMR spectra obtained experimentally, the simulated ^{45}Sc NMR spectra for $LaScO_3$ and $YScO_3$ exhibit quadrupolar lineshapes. Experimentally, each resonance displays broadening of the main features. This therefore aids in confirming the presence of an additional broadening in each, most probably owing to a small distribution of environment types. It must be noted that the slight difference in shift exhibited between the two is probably owing to referencing differences between experiment and calculation.

6.3.5.2 Gaining Insight into Disorder using DFT

In perovskite structures yttrium substitution can be favourable both on the A and B sites. In the solid-solution $La_{1-x}Y_xScO_3$, the trends observed from Rietveld refinement of the NPD data appeared to suggest that the Y had been substituted onto the A site only. However, in order to verify that Y was being substituted onto the A site a DFT calculation was completed where the B site was substituted with Y to produce the composition, $LaY_{0.25}Sc_{0.75}O_3$. The site (0.5, 0, 0.5) was replaced with an Y atom and the structure was fully optimised prior to calculation of the NMR parameters. The substitution of Y onto the B site produces three crystallographically distinct Sc sites and a single Y site. Furthermore, a large range of values of C_Q were predicted for each of the Sc sites, from ~4 – 15 MHz, as shown in Table 6.25. Whilst this displays good agreement with the distribution of quadrupoles observed experimentally the parameters for the single Y site predicted exhibit very little agreement with experiment. The chemical shift for the single site was ~167 ppm greater than that observed experimentally. In addition, the predicted

Table 6.25: Calculated (using CASTEP) ^{45}Sc and ^{17}O NMR parameters, δ_{iso}, P_Q, C_Q and η_Q, for composition $LaSc_{0.75}Y_{0.25}O_3$, where Y is substituted onto the B site.

	Site	δ_{iso} (ppm)	P_Q / MHz	C_Q / MHz	η_Q
$LaSc_{0.75}Y_{0.25}O_3$	Sc1	170.6	−4.48	−4.11	0.75
	Sc2	162.3	10.36	9.19	0.90
	Sc3	149.6	−15.17	−14.80	0.39
	O1	429.7	1.07	0.93	0.99
	O2	442.2	0.49	0.47	0.51
	O3	416.1	−1.74	−1.61	0.70
	O4	416.1	−1.18	−1.12	0.57
	O5	419.7	−1.18	−1.13	0.54
	O6	414.5	−1.71	−1.65	0.46

chemical shift was not in the allowed chemical shift range for six coordinate Y on the B site, the chemical shift was instead much larger. This therefore appears to confirm initial suggestions from the NPD data that Y is substituted onto the A site.

In an attempt to gain insight into the disorder exhibited in the $La_{1-x}Y_xScO_3$ series several additional DFT calculations were performed, where the La atoms in the $LaScO_3$ structure were substituted with Y. Initially one La atom in the $LaScO_3$ unit cell was replaced with an Y atom, producing a structure with composition $La_{0.75}Y_{0.25}ScO_3$, shown in Figure 6.29(a). In a similar manner, two La atoms were substituted to produce the composition $La_{0.5}Y_{0.5}ScO_3$. However, there were three possible ways in which to complete this particular substitution, and all three are shown in Figures 6.29(b-d). The composition $La_{0.25}Y_{0.75}ScO_3$ was modelled by substituting three La atoms with Y, as shown in Figure 6.29(e). (Full details of all atoms substituted can be found in Appendix V). All structures were geometry optimised prior to calculation of the NMR parameters. The ^{45}Sc and ^{89}Y parameters calculated for each composition can be found in Tables 6.27 and 6.28, respectively. The number of Sc and Y sites predicted for each composition varied as a function of symmetry, i.e., each time a different atom was changed the symmetry was also

Table 6.26: Calculated (using CASTEP) ^{89}Y NMR parameters, δ_{iso}, $\Delta\sigma_{CS}$ and η_{CS}, for composition $LaSc_{0.75}Y_{0.25}O_3$, where Y is substituted onto the B site.

	Site	δ_{iso} (ppm)	$\Delta\sigma_{CS}$ (ppm)	η_{CS}
$LaSc_{0.75}Y_{0.25}O_3$	Y1	430.0	−50.4	0.87

changed. For each of the compositions calculated a range of C_Q values were predicted for ^{45}Sc that varied from ~5 – 12 MHz, as shown in Table 6.27. It must be noted that several of the predicted values of C_Q were extremely large and would therefore result in very broad resonances. To determine whether any of the calculated compositions could, realistically, be observed experimentally the values obtained for each composition were 'summed', i.e., their contributions were added and a corresponding spectrum was simulated. The spectrum produced is shown (in blue) in Figure 6.30. Rather surprisingly, when compared with the broad ^{45}Sc MAS NMR spectra obtained for samples in the $La_{1-x}Y_xScO_3$ series (Figure 6.17) relatively good agreement was observed in both the position (shifted upfield from $LaScO_3$) and the shift range observed. This suggests all possible compositions simulated using DFT methods are potentially present in each of the samples synthesised.

The ^{89}Y NMR parameters calculated for each composition described above indicated a range of chemical shifts, as shown in Table 6.28. To determine whether any of these shifts were feasible experimentally NMR spectra for each were simulated and compared with the observed experimental resonances. Tick marks corresponding to each of the predicted Y sites have been added to the ^{89}Y MAS NMR spectrum of $La_{0.6}Y_{0.4}ScO_3$, and are shown in Figure 6.31. Each of the predicted sites appear close to one another, highlighting the range of shifts exhibited. This range predicted using DFT methods resides under the experimental lineshape and therefore suggests that each one could be observed experimentally. Good agreement was therefore observed between experiment and the calculated values.

In reality, to gain further insight into the disorder exhibited DFT calculations using much larger cells are required. Using the supercell

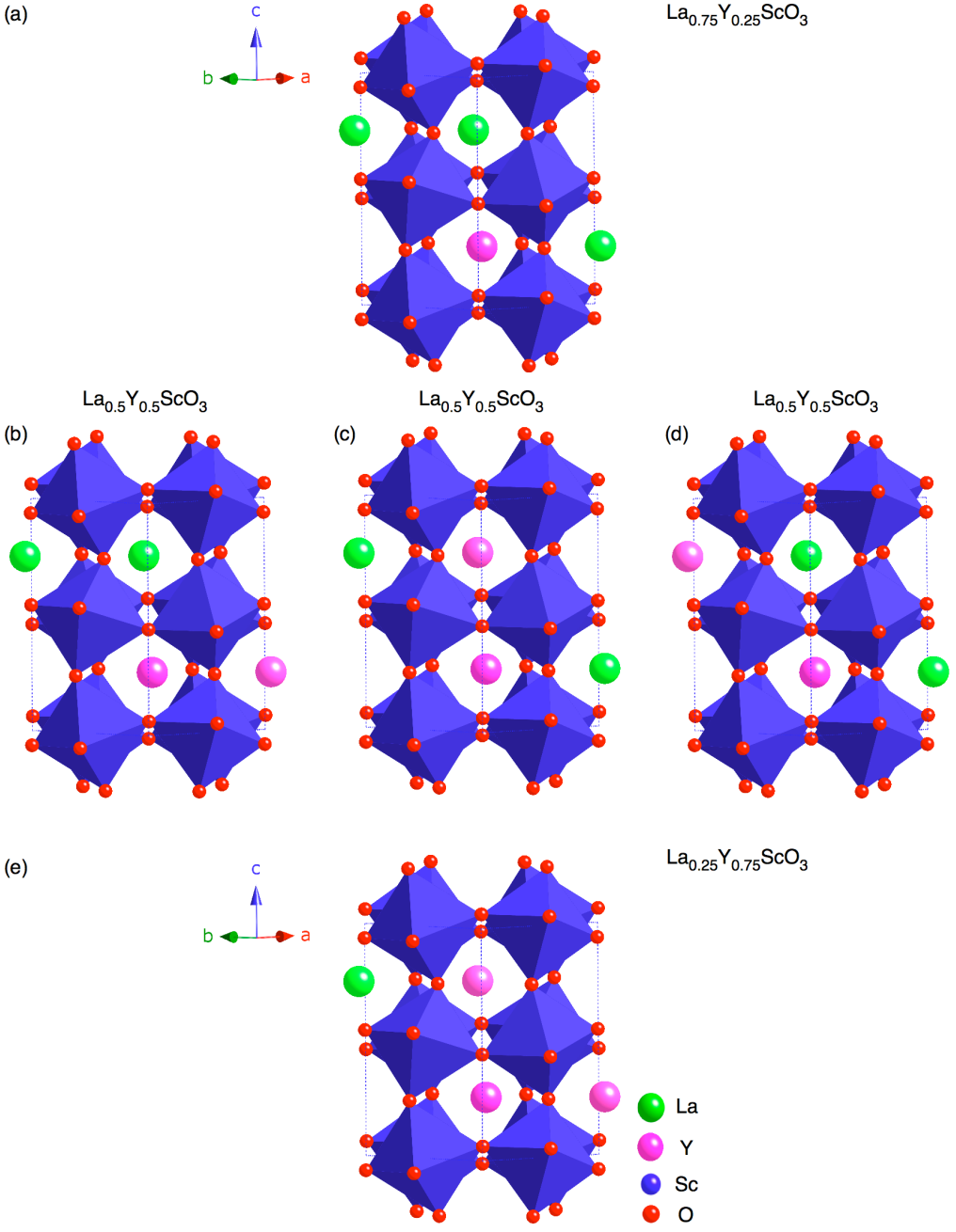

Figure 6.29: The structures of (a) $La_{0.75}Y_{0.25}ScO_3$, (b-d) $La_{0.5}Y_{0.5}ScO_3$ and (e) $La_{0.25}Y_{0.75}ScO_3$ used to gain insight into the disorder exhibited in the $La_{1-x}Y_xScO_3$. Each structure was geometry optimised prior to calculation of the ^{45}Sc and ^{89}Y NMR parameters given in Tables 6.27 and 6.28.

Table 6.27: Calculated (using CASTEP) ^{45}Sc NMR parameters, δ_{iso}, P_Q, C_Q and η_Q, for x = 0, 0.25, 0.5, 0.75 and 1 in the series $La_{1-x}Y_xScO_3$. The initial $LaScO_3$ structure was obtained from literature.[218] To 'model' disorder Y atoms were placed on different La sites, structures were then relaxed and subsequent NMR parameters were calculated, as described in Appendix V.

	Site	δ_{iso} (ppm)	P_Q / MHz	C_Q / MHz	η_Q
$La_{0.75}Y_{0.25}ScO_3$	Sc1	159.2	7.82	7.62	0.40
	Sc2	164.9	−5.15	−4.64	0.83
$La_{0.5}Y_{0.5}ScO_3$ (A)	Sc1	159.8	7.46	6.59	0.92
$La_{0.5}Y_{0.5}ScO_3$ (B)	Sc1	156.7	12.29	12.03	0.36
	Sc2	164.8	9.13	8.25	0.82
$La_{0.5}Y_{0.5}ScO_3$ (C)	Sc1	162.3	5.52	4.8	0.98
$La_{0.25}Y_{0.75}ScO_3$	Sc1	157.7	9.99	9.76	0.38
	Sc2	160.2	−8.07	−7.77	0.49

approximation and the inherent periodic boundary conditions of each system, the structure can be extended in all three dimensions by a greater number of unit cells. A 2 × 2 × 2 supercell therefore extends the structure in three dimensions by an additional unit cell. Calculations of this type are, however, computationally demanding and often require large computational resources. To determine the feasibility of completing supercell calculations using the computational resources currently available to us a 2 × 1 × 1 supercell calculation was completed. Initially a single La atom was replaced in the 2 × 1 × 1 cell with Y, producing the composition $La_{0.875}Y_{0.125}ScO_3$, shown in Figure 6.32(a). In a similar manner to earlier calculations, the structure was geometry optimised prior to calculation of the NMR parameters. The calculated ^{45}Sc and ^{89}Y NMR parameters can be found in Table 6.29 and 6.30, respectively. For example, geometry optimisation calculations can take from between two

Table 6.28: Calculated (using CASTEP) ^{89}Y NMR parameters, δ_{iso}, $\Delta\sigma_{CS}$ and η_{CS}, for x = 0, 0.25, 0.5, 0.75 and 1 in the series $La_{1-x}Y_xScO_3$. The initial $LaScO_3$ structure was obtained from literature.[218] To 'model' disorder Y atoms were placed on different La sites, structures were then relaxed and subsequent NMR parameters were calculated, as described in Appendix V.

	Site	δ_{iso} (ppm)	$\Delta\sigma_{CS}$/ ppm	η_{CS}
$La_{0.75}Y_{0.25}ScO_3$	Y1	234.8	−136.8	0.57
$La_{0.5}Y_{0.5}ScO_3$ (A)	Y1	229.1	−131.1	0.75
$La_{0.5}Y_{0.5}ScO_3$ (B)	Y1	246.4	−156.0	0.38
$La_{0.5}Y_{0.5}ScO_3$ (C)	Y1	255.5	−124.7	0.14
$La_{0.25}Y_{0.75}ScO_3$	Y1	242.2	−150.9	0.52
	Y2	247.7	−121.0	0.44
	Y3	267.5	−140.6	0.17

and seven days to complete using 20 processors. Calculations were also attempted, substituting two La atoms in the 2 × 1 × 1 supercell with Y, producing the composition $La_{0.75}Y_{0.25}ScO_3$. Note that there were several possible ways in which to complete this particular substitution. Shown in Figure 6.32(b) and (c) are the two methods of substitution used for this particular composition. Again, each structure was optimised prior to calculation of the NMR parameters to ensure each structure was in a local energy minimum. The calculated ^{45}Sc NMR parameters for the two structures are given in Table 6.29. The number of sites predicted again varied as a function of symmetry. As observed for earlier single cell calculations, a large range of values of C_Q (~4 – 14 MHz) were predicted for each of the ^{45}Sc sites. The contribution from each of these sites was also summed and the spectrum obtained is shown (in purple) in Figure 6.30. The simulated spectrum again highlights that each composition calculated could be present in each sample experimentally. Also shown in Figure 6.30, and denoted in green, is the summation of the two simulated spectra.

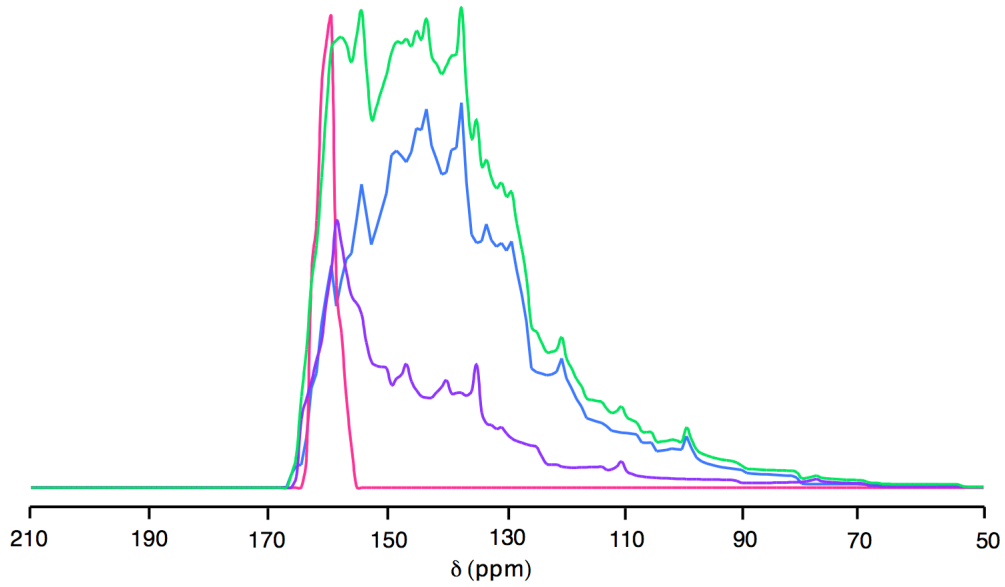

Figure 6.30: Simulated ^{45}Sc MAS NMR spectra obtained by 'summing' the NMR parameters obtained from the ^{45}Sc DFT calculations completed for a single unit cell (1 × 1 × 1), shown in blue, and a 2 × 1 × 1 supercell, shown in purple. Also shown in green is the summation of the two simulated patterns.

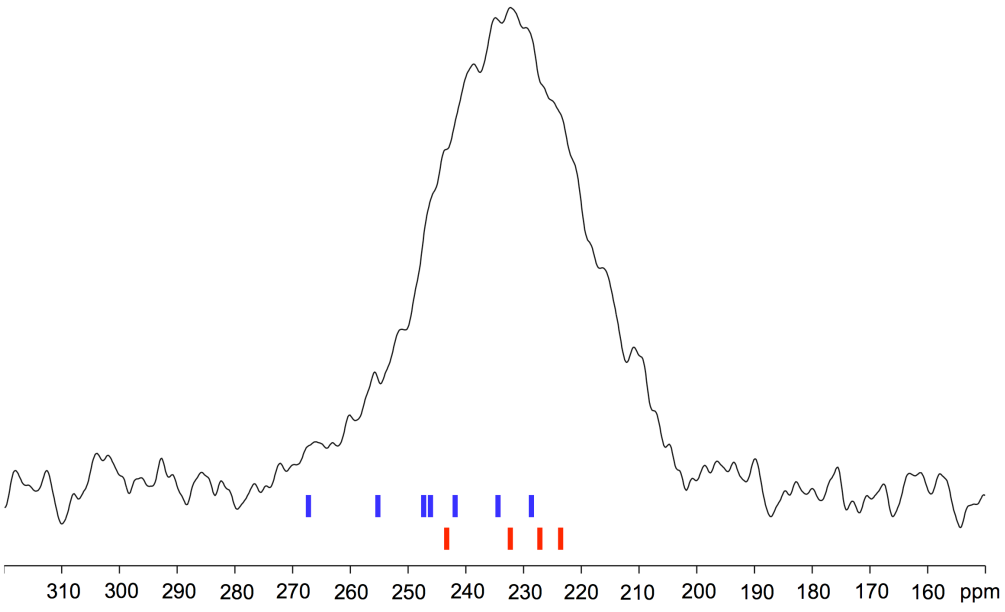

Figure 6.31: The ^{89}Y (14.1 T) MAS NMR spectrum of $La_{0.6}Y_{0.4}ScO_3$ (see Figure 6.22) with tick marks corresponding to the calculated chemical shifts of Y sites in a 1 × 1 × 1 single cell (shown in blue) and 2 × 1 × 1 supercell (shown in red) calculations.

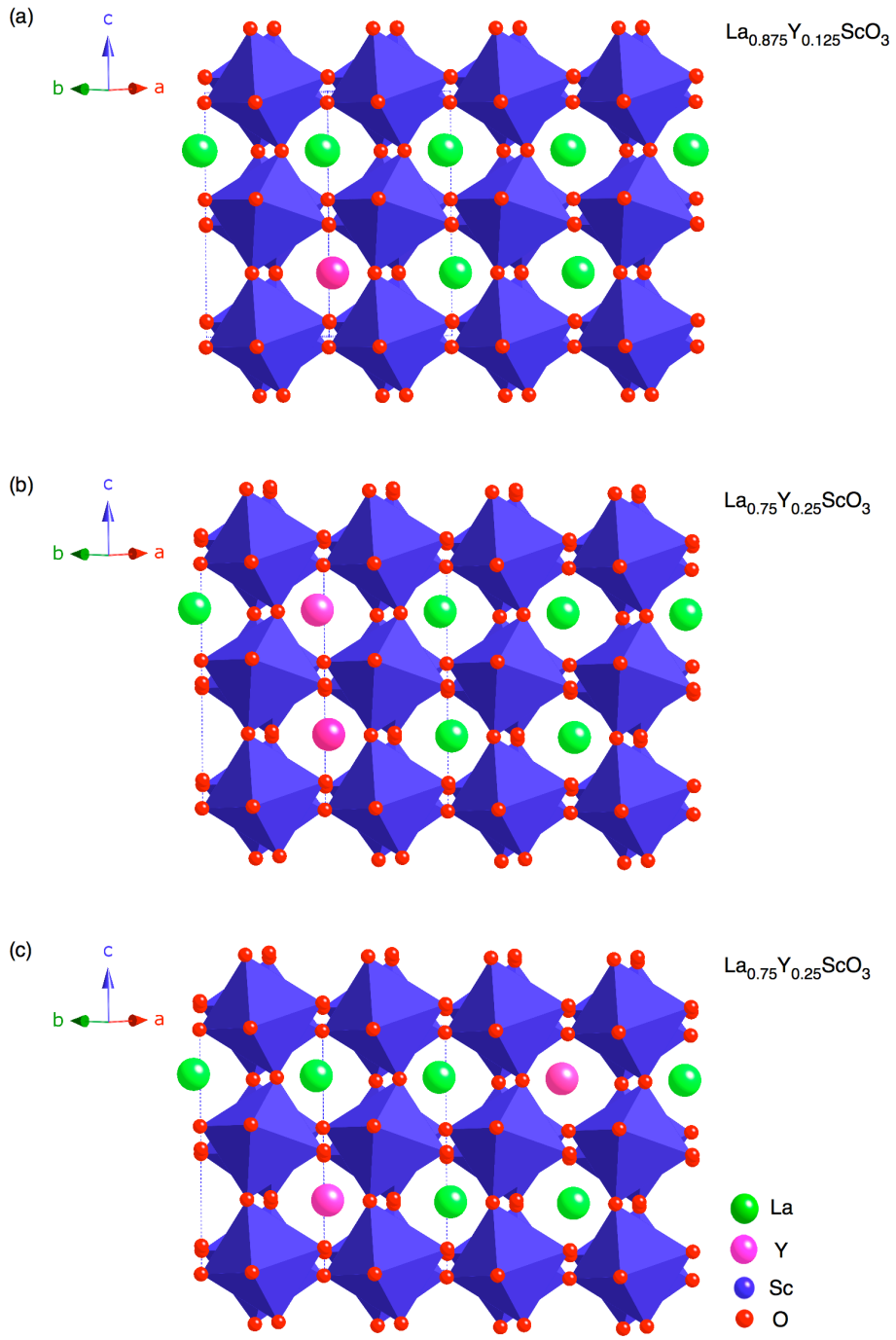

Figure 6.32: The structures of (a) $La_{0.875}Y_{0.125}ScO_3$ and (b-c) $La_{0.75}Y_{0.25}ScO_3$ used to calculate the NMR parameters in a 2 × 1 × 1 supercell. Each structure was geometry optimised prior to calculation of the ^{45}Sc and ^{89}Y NMR parameters given in Tables 6.29 and 6.30.

Table 6.29: Calculated (using CASTEP) ^{45}Sc NMR parameters, δ_{iso}, P_Q, C_Q and η_Q, for compositions x = 0.125 and 0.25. To 'model' disorder Y atoms were placed on different La sites in the $LaScO_3$ structure obtained for the literature.[218] All structures were relaxed prior to the NMR parameters being calculated.

	Site	δ_{iso} (ppm)	P_Q / MHz	C_Q / MHz	η_Q
$La_{0.875}Y_{0.125}ScO_3$	Sc1	158.6	8.58	8.48	0.26
	Sc2	163.4	−4.63	−4.39	0.58
	Sc3	163.1	−4.22	−3.79	0.85
	Sc4	163.6	−6.58	−6.06	0.73
$La_{0.75}Y_{0.25}ScO_3$ (A)	Sc1	155.2	13.66	13.62	0.13
	Sc2	163.6	−4.65	−4.05	0.98
	Sc3	163.7	−5.73	−5.05	0.93
	Sc4	163.1	−4.82	−4.25	0.93
$La_{0.75}Y_{0.25}ScO_3$ (B)	Sc1	159.6	8.34	8.06	0.46
	Sc2	164.8	−8.07	−7.99	0.25
	Sc3	163.4	−11.90	−11.58	0.41

The same upfield shift from $LaScO_3$ is observed and good agreement in the linewidth is also observed. Similar ^{89}Y NMR calculations were also completed for each composition, details of which are given in Table 6.30. As previously observed for the single cell calculations, a range of chemical shifts were predicted. To illustrate whether any of these sites could be observed experimentally in the $La_{1-x}Y_xScO_3$ series, tick marks corresponding to each shift have been added to the ^{89}Y MAS NMR spectrum for the x = 0.4 sample, and are shown in red in Figure 6.31. The range of chemical shifts is relatively small and realistically each site could reside under the experimental lineshape, as highlighted in Figure 6.31.

Unfortunately, it was not possible to complete any larger supercell calculations as our computational resources are, at present, limited. In reality, to complete calculations of this nature greater computational resources would be required. However, the calculations completed have

Table 6.30: Calculated (using CASTEP) ^{89}Y NMR parameters, δ_{iso}, $\Delta\sigma_{CS}$ and η_{CS}, for compositions x = 0.125 and 0.25. To 'model' disorder Y atoms were placed on different La sites in the $LaScO_3$ structure obtained for the literature.[218] All structures were relaxed prior to the NMR parameters being calculated.

	Site	δ_{iso} (ppm)	$\Delta\sigma_{CS}$ / ppm	η_{CS}
$La_{0.875}Y_{0.125}ScO_3$	Y1	230.6	−129.5	0.24
$La_{0.75}Y_{0.25}ScO_3$ (A)	Y1	239.3	−142.1	0.22
	Y2	234.1	−144.1	0.26
$La_{0.75}Y_{0.25}ScO_3$ (B)	Y1	250.4	−142.8	0.21

provided valuable insight into the possibility of modelling disorder using DFT calculations.

6.4 Conclusions

In summary, we have successfully synthesised and characterised the solid-solution $La_{1-x}Y_xScO_3$ for compositions x = 0, 0.2, 0.4, 0.6, 0.8 and 1 using high-resolution neutron powder diffraction, solid-state NMR and DFT calculations. All samples in this series were found to be orthorhombic and isostructural with $GdFeO_3$, in space group Pbnm. As Y was gradually introduced to the $LaScO_3$ structure a corresponding decrease in both the lattice parameters and unit cell volume was observed. In addition, as x was increased the degree of orthorhombic strain placed on the structure gradually increased and, as a direct consequence, the tilt angle(s) observed for the ScO_6 octahedra steadily increased. Structurally, only minor changes in the Sc – O bond lengths were observed as x was increased. As the level of strain gradually increased with x a substantial effect on the magnitude of the quadrupolar interaction was observed.

^{45}Sc MAS NMR was shown to be highly sensitive to substitutions occurring on the A site. In contrast, the ^{89}Y MAS NMR completed indicated the Y environment to be less sensitive to changes on the A site. The Sc – La/Y distances are shorter than the La – La/Y distances. The

local environment of the Sc is therefore severely affected by cation substitution on the A site owing to the close proximity of the Sc to a substituted La atom. Each sample in the series $La_{1-x}Y_xScO_3$ was shown to exhibit disorder and using two-dimensional ^{45}Sc MAS NMR techniques and it was found to result from both a distribution of quadrupoles and chemical shifts. Using ^{45}Sc, ^{89}Y MAS NMR in conjunction with high-resolution NPD data the greatest disorder is believed to be in compositions close to $x = 0.5$ in the solid-solution $La_{1-x}Y_xScO_3$.

In addition, we have successfully implemented ^{45}Sc, ^{89}Y and ^{17}O DFT calculations using CASTEP for $LaScO_3$, $YScO_3$ and a series of model compounds, the results of which displayed very good agreement with those obtained experimentally. Several additional calculations were completed in an attempt to provide insight into the disorder exhibited in the $La_{1-x}Y_xScO_3$ solid-solution. Initial calculations were successful and suggested a variety of different compositional environments could be present in each sample. It is highly likely that, experimentally, a 'summation' of all the calculated environments is observed. The preliminary calculations completed therefore suggest that 'modelling' disorder using DFT could aid considerably in the understanding and interpretation of complex NMR spectra of disordered materials.

Also in this investigation we have managed to successfully enrich $LaScO_3$ using $^{17}O_2$ enriched gas, suggesting post-synthetic enrichment of dense perovskite-based compounds is feasible. This, in turn, suggests it would be highly advantageous to enrich disordered samples and probe the local oxygen environment using ^{17}O MAS NMR in an attempt to gain insight into the nature and extent of the disorder exhibited. Finally, we emphasise the importance of using a multidisciplinary approach to the structural investigation of complex solid-state systems such as $La_{1-x}Y_xScO_3$. Using a variety of highly complementary techniques it is possible to gain important additional structural information that may be lost by the use of a one technique alone.

Chapter 7
Conclusions and Future Work

7.1 Conclusions

The primary focus of this thesis was to synthesise and characterise several perovskite systems using high-resolution powder diffraction, solid-state NMR and first-principles DFT calculations.

Initial investigations concentrated on $NaNbO_3$ at room temperature and the work presented has shown that laboratory-synthesised samples of $NaNbO_3$ routinely comprise of two structurally very similar orthorhombic phases; the centrosymmetric Pbcm and polar $P2_1ma$ polymorphs. In addition, the quantity of each phase present has been shown to vary as a function of the preparative method. It was possible to synthesise a phase pure sample of Pbcm $NaNbO_3$ using molten salt techniques. However, it was considerably harder to synthesise a phase pure sample of the $P2_1ma$ polymorph, as small quantities of the more thermodynamically stable Pbcm phase were consistently produced. Using high-resolution s-PXRD and NPD data it was possible to distinguish between the two phases. Close examination of the superstructure peaks in each dataset proved key in identifying precisely which phase(s) were present in each sample. Using conventional and two-dimensional solid-state NMR techniques it was only possible to distinguish between the Pbcm and $P2_1ma$ phases using ^{23}Na MQMAS NMR. The ^{93}Nb MAS and static NMR spectra appeared virtually identical for the two phases, indicating the Nb environment to be very similar in each. Using $^{17}O_2$ gas it was possible to post-synthetically enrich selected samples of $NaNbO_3$. However, considerable spectral overlap was observed in each ^{17}O MAS NMR spectrum owing to the extreme similarities of sites O1 and O2, and sites O3 and O4 in both the Pbcm and $P2_1ma$ phases. The spectral overlap exhibited confirmed previous conclusions drawn from ^{23}Na and ^{93}Nb MAS NMR as to the very similar nature of the two $NaNbO_3$ polymorphs.

The ^{23}Na, ^{93}Nb and ^{17}O DFT calculations completed for the different phases of $NaNbO_3$ displayed very good agreement with the observed experimental findings. In particular, the ^{17}O DFT calculations aided in confirming the spectral assignment initially made using published crystallographic data. Using AIRSS, structure searching methods were also employed for $NaNbO_3$ and, consistently, the most energetically favourable phases of $NaNbO_3$ found were the R3c, $Pmc2_1$ (i.e., $P2_1ma$) and Pbcm phases. This was in good agreement with the observed experimental findings. The structure searching results obtained were extremely encouraging as they suggest that this method could be utilised with similar success for many other perovskite-based systems in the future.

Using ^{23}Na MQMAS techniques a third, unknown Na-based phase was consistently found in all samples of $NaNbO_3$ investigated, including the commercially purchased sample. However, owing to the exceptionally small quantities of this phase present in each sample (~1-2%) it was not possible to identify its presence in any diffraction pattern and, as a result, the phase could not be successfully characterised.

The effect of low percentage doping was investigated in the $NaNbO_3$-related solid-solutions KNN (1-5%), LNN (1-10%) and SNN (10-40%) and, in most cases, the $P2_1ma$ polymorph of $NaNbO_3$ was formed. Associated changes in both the lattice parameters and unit cell volume were observed as each cation was substituted into the $NaNbO_3$ structure. The substitution of K^+ and Li^+ cations into the $NaNbO_3$ structure appears to result in a structural distortion which results in the loss of the antiphase tilts responsible for the antiferroelectric fourfold superstructure of the Pbcm phase, and subsequently produces the $P2_1ma$ phase. The introduction of vacancies and, in particular, the concentration of [Sr-vacancy] in the SNN solid-solution is believed to play a crucial role in determining the phases formed. Disorder was identified in each series, believed to be primarily owing to a distribution of chemical shifts.

The low temperature s-PXRD study completed for the sol-gel sample of $NaNbO_3$ identified a region of phase coexistence between the $P2_1ma$, R3c and Pbcm phases of $NaNbO_3$ over a relatively large

temperature range, 12 < T < 280 K. The observed phase coexistence was in good agreement with earlier NPD studies completed by Mishra *et al.*,[224] in which a two phase region of coexistence was identified between the Pbcm and R3c phases. It is believed that to achieve full conversion of the $P2_1ma$ and/or Pbcm phases of $NaNbO_3$ to the low temperature R3c phase each sample would need to remain at low temperatures for a substantial period of time. The time taken to complete the low temperature s-PXRD study was therefore insufficient to adequately cool the entire sample and achieve full conversion to the low temperature phase.

The compositions x = 0, 0.2, 0.4, 0.6, 0.8 and 1 in the solid-solution $La_{1-x}Y_xScO_3$ were successfully synthesised and characterised. All samples were found to be isostructural with $GdFeO_3$ and refined NPD data indicated that an orthorhombic structure was retained throughout the solid-solution, in space group Pbnm. The structure of the end member, $YScO_3$, was correctly ascertained for the first time by structural refinement of high-resolution NPD data using the Rietveld method. This was completed using $HoScO_3$[218] as the initial model and lattice parameters estimated by Clark *et al*.[298] A gradual decrease in the lattice parameters and unit cell volume was observed with increasing x. The degree of orthorhombic strain and the tilt angle(s) observed for the ScO_6 octahedra steadily increased with x. Using ^{45}Sc and ^{89}Y NMR each sample in the series was found to exhibit disorder. Using ^{45}Sc MAS NMR the disorder was found to result from both a distribution of quadrupoles and chemical shifts. The sample $La_{0.6}Y_{0.4}ScO_3$ was found to exhibit the greatest degree of disorder, confirmed both by the NPD and NMR data obtained. The ^{45}Sc MAS NMR data indicates that Sc NMR parameters are highly sensitive to cation substitutions on the A site. In contrast, the ^{89}Y MAS NMR data suggests yttrium shift is less sensitive to substitution on the A site, most probably owing to the large distance between two A-site cations. The findings presented do, however, suggest that the Y environment would experience a much greater effect if substitution was to occur on the B site. A sample of the end-member, $LaScO_3$, was post-synthetically enriched using $^{17}O_2$ gas and subsequently investigated using ^{17}O NMR. The ^{17}O MAS NMR spectrum obtained for $LaScO_3$ displayed two resonances, in

good agreement with published crystallographic data. Very small values of C_Q were exhibited for each site, indicating two highly symmetrical oxygen environments. This, therefore, indicates that the post-synthetic enrichment of dense perovskite phases such as $LaScO_3$ is feasible and could potentially be applied to many other perovskite phases. In particular, enrichment of disordered perovskites would be hugely informative as this would aid in identifying any subtle differences exhibited in the different oxygen environments. ^{45}Sc, ^{89}Y and ^{17}O DFT calculations were also carried out for the end-members, $LaScO_3$ and $YScO_3$ and the results obtained indicated very good agreement with the experimental findings. Furthermore, to gain insight into disorder several calculations were attempted in which different La atoms in the unit cell were substituted with Y to produce compositions $La_{0.75}Y_{0.25}ScO_3$, $La_{0.5}Y_{0.5}ScO_3$ and $La_{0.25}Y_{0.75}ScO_3$. This proved highly successful and when the contribution from each was 'summed' and a spectrum was simulated, good agreement was observed with experiment, indicating that each of the calculated environments could realistically be found experimentally. This result is particularly encouraging as it suggests that similar and more complex methods such as supercells could be adopted and utilised to investigate other disordered materials.

The work presented in this thesis has demonstrated the effectiveness of combining three very powerful techniques. Furthermore, this work has highlighted the importance of using a multidisciplinary approach for the investigation of structurally complex systems. Using a single characterisation technique it is often difficult to gain an accurate and robust structural characterisation. Therefore, it is often better to utilise a variety of different techniques to gain a complete and comprehensive structural solution to the system under investigation.

7.2 Future Work

Although a largely exhaustive and comprehensive study has been completed for each of the systems investigated, several additional areas of interest and future investigation still remain. For example, it would be

beneficial to accurately charcterise the 'third phase' consistently present in all samples of $NaNbO_3$ as this could potentially provide additional information regarding the formation of the different phases of $NaNbO_3$. This could, in turn, provide further insight into the $NaNbO_3$ system. However, to do so, a sample composed of principally this phase is needed. Therefore, a systematic study of reaction conditions is necessary to identify the exact synthetic method required to synthesise such a sample. Once known, a sample could be synthesised and using a combination of high-resolution NPD and ^{23}Na MQMAS NMR techniques it would be possible to characterise this phase.

The KNN and LNN solid-solutions possesses additional NMR active species, namely ^{39}K (I = 3/2), ^{7}Li (I = 3/2) and ^{17}O (I = 5/2). It would be particularly useful to complete ^{39}K and ^{7}Li NMR studies on the KNN and LNN series as each could potentially provide additional, complementary, information regarding the A site environment in each. Furthermore, ^{17}O enrichment of each sample in both series could, potentially, aid in interpreting the disorder exhibited in each sample.

Within this particular invstigation no NMR studies were completed for samples in the SNN series owing, principally, to large quantities of an impurity phase in each. The initial diffraction studies completed suggest that this may be an interesting series to study by NMR. However, phase pure samples would be required before any detailed studies could be completed. Hence, a thorough investigation of the synthesis conditions required to synthesise phase pure samples is necessary. Many of the samples in the KNN, LNN and SNN series were found to comprise of the same polar, and potentially ferroelectric, $P2_1ma$ phase. Therefore, it would be particularly interesting to assess the magnitude of the piezoelectric responses exhibited by samples in each series. Dielectric measurements of each sample are therefore required.

The low temperature study completed for the sol-gel sample of $NaNbO_3$ indicated that at low temperatures a mix of three phases was exhibited. Given these findings, it would be interesting to determine whether any similar regions of phase coexistence are exhibited at high temperatures. We recently completed a preliminary high temperature

study using NPD for the sol-gel sample of $NaNbO_3$ and initial results appear promising. We have also recently been allocated beamtime at I11 to complete a more comprehensive high temperature study on the sol-gel sample of $NaNbO_3$. It is hoped that this will aid in confirming the preliminary results obtained from the NPD data. In addition, it would be highly informative to complete low temperature ^{23}Na and ^{93}Nb NMR studies. This would aid in confirming the findings already obtained from the low temperature diffraction study completed.

The structural characterisation completed for the solid-solution $La_{1-x}Y_xScO_3$ was comprehensive. However, a number of minor areas of investigation still remain. For example, it would be advantageous to ^{17}O enrich all remaining samples in the series as this could, potentially, provide additional information regarding the disorder exhibited in the system. Furthermore, it would be highly desirable to complete a $2 \times 2 \times 2$ supercell calculation to determine whether computational methods can provide any additional insight into the disorder exhibited experimentally. However, to feasibly undertake such a calculation, access to large computational resources would be required. The preliminary calculations completed to date suggest that a calculation of this magnitude would require a large amount of computational time. However, if this could be achieved the results obtained could potentially aid in confirming initial conclusions drawn from the single cell calculations that all possible environments calculated could feasibly be present in each sample.

References

1. M. T. Weller, "Inorganic Materials Chemistry", p. 38-44, Oxford University Press, Oxford, 1994.
2. A. R. West, "Solid State Chemistry and Its Applications", p. 204-207, Wiley, Chichester, 1984.
3. V. M. Goldschmidt, *Naturwissenschaften*, 1926, **14**, 477.
4. R. D. Shannon, *Acta Cryst.*, 1976, **A32**, 751.
5. R. D. Shannon and C. T. Prewitt, *Acta Cryst.*, 1969, **B25**, 925.
6. W. Cochran, *Phys. Rev. Lett.*, 1959, **3**, 412.
7. W. Cochran, *Adv. Phys.*, 1960, **9**, 387.
8. H. D. Megaw and C. N. W. Darlington, *Acta Cryst.*, 1975, **A31**, 161.
9. M. O'Keeffe and B. G. Hyde, *Acta Cryst.*, 1977, **B33**, 3802.
10. N. W. Thomas, *Acta Cryst.*, 1989, **B45**, 337.
11. N. W. Thomas, *Acta Cryst.*, 1996, **B52**, 16.
12. N. W. Thomas and A. Beitollahi, *Acta Cryst.*, 1994, **B50**, 549.
13. J.-S. Zhou and J. B. Goodenough, *Phys. Rev. Lett.*, 2005, **94**, 065501.
14. C. J. Howard and H. T. Stokes, *Acta Cryst.*, 1998, **B54**, 782.
15. C. J. Howard and H. T. Stokes, *Acta Cryst.*, 2004, **A61**, 93.
16. A. M. Glazer, *Acta Cryst.*, 1972, **B28**, 3384.
17. A. Okazaki and Y. Suemune, *J. Phys. Soc. Jpn.*, 1961, **28**, 443.
18. S. Y. Wu, S. R. Hwang, W.-H. Li, K. C. Lee, J. W. Lynn and R. S. Liu, *Chin. J. Phys.*, 2000, **38**, 354.
19. K. Leinenweber and J. Parise, *J. Solid State Chem.*, 1995, **114**, 277.
20. P. M. Woodward, *Acta Cryst.*, 1997, **B53**, 32.
21. P. M. Woodward, *Acta Cryst.*, 1997, **B53**, 44.
22. A. Arulraj, K. Ramesha, J. Gopalakrishnan and C. N. R. Rao, *J. Solid State Chem.*, 2000, **155**, 233.
23. K. Tezuka, K. Henmi, Y. Hinatsu and N. M. Masaki, *J. Solid State Chem.*, 2000, **154**, 591.
24. B. Jaffe, R. S. Roth and S. Marzullo, *J. Res. Natl. Bur. Stand.*, 1955, **55**, 239.
25. E. Cross, *Nature*, 2004, **432**, 24.

26. Y. Saito, H. Takao, T. Tani, T. Nonoyama, K. Takatori, T. Homma, T. Nagaya and M. Nakamura, *Nature*, 2004, **432**, 84.
27. K.-I. Kobayashi, T. Kimura, H. Sawada, K. Terakura and Y. Tokura, *Nature*, 1998, **395**, 677.
28. L. Dupont, L. Chai and P. K. Davies, *Mater. Res. Soc. Symp. Proc.*, 1999, **547**, 93.
29. C. Chaillout, M. A. Alario-Franco, J. J. Capponi, J. Chenavas, J. L. Hodeau and M. Marezio, *Phys. Rev. B: Conden. Matter Mater. Phys.*, 1987, **36**, 7118.
30. C. Chaillout, M. A. Alario-Franco, J. J. Capponi, J. Chenavas, P. Strobel and M. Marezio, *Solid State Commun.*, 1988, **65**, 283.
31. P. Karen, P. M. Woodward, J. Linden, T. Vogt, A. Studer and P. Fischer, *Phys. Rev. B: Conden. Matter Mater. Phys.*, 2001, **64**, 214405.
32. P. M. Woodward and P. Karen, *Inorg. Chem.*, 2003, **42**, 1121.
33. P. M. Woodward, E. Suard and P. Karen, *J. Am. Chem. Soc.*, 2003, **125**, 8889.
34. P. Karen, A. Kjekshus, Q. Huang, V. L. Karen, J. W. Lynn, N. Rosov, I. N. Sora and A. Santoro, *J. Solid State Chem.*, 2003, **174**, 87.
35. A. R. Chakhmouradian, R. H. Mitchell and P. C. Burns, *J. Alloys Comp.*, 2000, **307**, 149.
36. B. J. Kennedy, C. J. Howard, Y. Kubota and K. Kato, *J. Solid State Chem.*, 2004, **177**, 4552.
37. A. S. Sefat, G. Amow, M-Y. Wu, G. A. Bottom and J. E. Greedan, *J. Solid State Chem.*, 2005, **178**, 1008.
38. J. Darriet, S. G. Mayarga and A. Tressaud, *Eur. J. Solid State Inorg. Chem.*, 1990, **27**, 783.
39. V. Caignaert, F. Millange, B. Domenges, B. Raveau and E. Suard, *Chem. Mater.*, 1999, **11**, 930.
40. F. Millange, V. Caignaert, B. Domenges, B. Raveau and E. Suard, *Chem. Mater.*, 1998, **10**, 1974.
41. M. C. Knapp and P. M. Woodward, *J. Solid State Chem.*, 2006, **179**, 1076.
42. R. Ranjan, A. Senyshyn, H. Boysen, C. Baehtz and F. Frey, *J. Solid State Chem.*, 2007, **180**, 995.

43. C. J. Howard, B. J. Kennedy and P. M. Woodward, *Acta Cryst.*, 2003, **B59**, 463.
44. M. T. Anderson, K. B. Greenwood, G. A. Taylor and K. R. Poeppelmeier, *Prog. Solid State Chem.*, 1993, **22**, 197.
45. P. W. Barnes, M. W. Lufaso and P. M. Woodward, *Acta Cryst.*, 2006, **B62**, 384.
46. R. Liu, Y. Xuan and Y. Q. Jia, *J. Solid State Chem.*, 1997, **134**, 420.
47. P. K. Davies, *Current Opinion in Solid State and Materials Science*, 1999, **4**, 467.
48. K. S. Aleksandrov and S. V. Misjul, *Sov. Phys. Crystallogr.*, 1981, **26**, 612.
49. S.-J. Kim, M. D. Smith, J. Darriet and H. C. zur Loye, *J. Solid State Chem.*, 2004, **177**, 1493.
50. F. Galasso, L. Katz and R. Ward, *J. Am. Chem. Soc.*, 1959, **81**, 820.
51. F. Galasso and W. Darby, *J. Phys. Chem.*, 1962, **66**, 131.
52. C. A. Randail, A. S. Bhalla, T. R. Shrout and L. E. Cross, *J. Mater. Res.*, 1990, **4**, 829.
53. N. Setter and L. E. Cross, *J. Mater. Sci.*, 1980, **15**, 2478.
54. T. Sekiya, T. Yamamoto and Y. Torii, *Bull. Chem. Soc. Jpn.*, 1984, **57**, 1859.
55. G. King, L. M. Wayman and P. M. Woodward, *J. Solid State Chem.*, 2009, **182**, 1319.
56. G. King, S. Thimmaiah, A. Dwived and P. M. Woodward, *Chem. Mater.*, 2007, **19**, 6451.
57. M. L. Lopez, M. L. Veiga and C. Pico, *J. Mater. Chem.*, 1994, **4**, 547.
58. M. A. Arillo, J. Gomez, M. L. Lopez, C. Pico and M. L. Veiga, *Solid State Ionics*, 1997, **7**, 801.
59. M. A. Arillo, J. Gomez, M. L. Lopez, C.Pico and M. L. Veiga, *J. Mater. Chem.*, 1997, **7**, 801.
60. P. G. Radaelli, D. G. Hinks, A. W. Mitchell, B. A. Hunter, J. L. Wagner, B. Dabrowski, K. G. Vandervoort, H. K. Viswanathan and J. D. Jorgensen, *Phys. Rev. B*, 1994, **49**, 4163.
61. C. Rial, U. Amador, E. Moran, M. A. Alario-Franco and N. H. Anderson, *Physica C*, 1994, **243**, 237.

62. C. Steudtner, E. Moran, M. A. Alario-Franco and J. L. Martinez, *Mater. Chem.*, 1997, **7**, 661.
63. D. Balz and K. Plieth, *Zeitschrift für Elektrochemie*, 1955, **59**, 545.
64. S. N. Ruddlesden and P. Popper, *Acta Cryst.*, 1957, **10**, 538.
65. B. Aurivillius, *Ark. Kemi.*, 1949, **1**, 463.
66. B. Aurivillius, *Ark. Kemi.*, 1949, **1**, 499.
67. A. D. Rae, J. G. Thompson and R. L. Withers, *Acta Cryst.*, 1991, **B47**, 870.
68. C. A. P de Araujo, J. D. Cuchiaro, L. D. McMillan, M. C. Scott and J. F. Scott, *Nature*, 1995, **374**, 627.
69. R. L. Withers, J. G. Thompson and A. D. Rae, *J. Solid State Chem.*, 1991, **94**, 404.
70. R. E. Newnham, R. W. Wolfe and J. F. Dorrian, *Mater. Res. Bull.*, 1971, **6**, 1029.
71. F. Kubel and H. Schmidt, *Ferroelectrics*, 1992, **129**, 101.
72. S. N. Ruddlesden and P. Popper, *Acta Cryst.*, 1957, **10**, 583.
73. S. N. Ruddlesden and P. Popper, *Acta Cryst.*, 1958, **11**, 54.
74. G. Blasse, *J. Inorg. Nucl. Chem.*, 1967, **30**, 656.
75. M. M. Elcombe, E. H. Kisi, K. D. Hawkins, T. J. White, P. Goodman and S. Matheson, *Acta Cryst.*, 1991, **B47**, 305.
76. A. J. Wright and C. Greaves, *J. Mater. Chem.*, 1996, **6**, 1823.
77. K. Park and S.-H. Byeon, *Bull. Korean Chem. Soc.*, 1996, **17**, 168.
78. V. Thangdurai, A. K. Shukla and J. Gopalakrishnan, *Solid State Ionics*, 1994, **73**, 9.
79. J. G. Bednorz and K. A. Muller, *Z. Phys.*, 1986, **B64**, 189.
80. M. Dion , M. Ganne and M. Tournoux, *Mater. Res. Bull.*, 1981, **16**, 1429.
81. A. J. Jacobson, J. W. Johnson and J. T. Lewandowski, *Inorg. Chem.*, 1985, **24**, 3727.
82. M. Sato, J. Abo and T. Jin, *Solid State Ionics*, 1992, **51**, 285.
83. K. Toda, T. Teranishi, Z-G. Ye, M. Sato and Y. Hinatsu, *Mat. Res. Bull.*, 1999, **34**, 971.
84. Y.-S. Hong, S.-J. Kim and J.-H. Choy, *J. Mater.Chem.*, 2000, **10**, 1209.

85. A. J. Jacobson, J. W. Johnson and J. T. Lewandowski, *Inorg. Chem.*, 1985, **24**, 3727.
86. M. M. J. Treacy, S. B. Rice, A. J. Jacobson and J. T. Lewandowski, *Chem. Mater.*, 1990, **2**, 279.
87. J. Gopalakrishnan, T. Sivakumar, V. Thangadurai and G. N. Subbanna, *Inorg. Chem.*, 1999, **38**, 2902.
88. Neues Jahrb. Mineral, Monatsh, 1964, **1**, 22.
89. J. Handermann, A. M. Abakumov, H. D'Hondt, A. S. Kalyuzhnaya, M. G. Rozova, M. M. Markina, M. G. Mikheev, N. Tristan, R. Klingeler, B. Büchner and E. V. Antipov, *J. Mater. Chem.*, 2007, **17**, 692.
90. T. Omata, T. Fuke, S. Otsuka-Yao-Matsuo, *Solid State Ionics*, 2006, **177**, 2447.
91. S. B. Adler, J. A. Reimer, J. Baltisberger and U. Werner, *J. Am. Chem. Soc.*, 1994, **116**, 675.
92. A. R. West, "Solid State Chemistry and Its Applications", p. 549, Wiley, Chichester, 1984.
93. E. Wainer and A. N. Salomon, Titanium Alloy Manufacturing Co., Electrical Report No. 9, 1943.
94. S. Nomura, T. Takahashi and Y. Yokomizo, *Jpn., J. Appl., Phys.*, 1969, **27**, 262.
95. S. J. Zhang, C. A. Randall and T. R. Shrout, *Appl. Phys. Lett.*, 2003, **83**, 3150.
96. J. Rouquette, J. Haines, V. Bornand, M. Pintard, Ph. Papet, C. Bousquet, L. Konczewicz, F. A. Gorelli and S. Hull, *Phys. Rev. B*, 2004, **70**, 1.
97. A. R. West, "Solid State Chemistry and Its Applications", p. 548, Wiley, Chichester, 1984.
98. R. E. Newnham and L. E. Cross, *MRS Bulletin*, 2005, **30**, 845.
99. A. R. West, "Solid State Chemistry and Its Applications", p. 540-548, Wiley, Chichester, 1984.
100. A. R. West, "Solid State Chemistry and Its Applications", p. 550, Wiley, Chichester, 1984.
101. F. Bloch, W. W. Hansen and M. Packard, *Phys. Rev.*, 1946, **69**, 127.

102. E. M. Purcell, H. C. Torrey and R. V. Pound, *Phys. Rev.*, 1946, **69**, 37.
103. J. Virlet in "Encyclopedia of Nuclear Magnetic Resonance" (D. M. Grant and R. K. Harris Eds.), 1996, Vol. 4, p. 2694, Wiley, Chichester.
104. U. Shmueli, in "Theories and Techniques of Crystal Structure Determination", Chap. 1-2, Oxford University Press, Oxford, 2007.
105. M. T. Weller, in "Inorganic Materials Chemistry", p. 3-6, Oxford Univeristy Press, Oxford, 1994.
106. U. Shmueli, in "Theories and Techniques of Crystal Structure Determination", Chap. 3, Oxford University Press, Oxford, 2007.
107. International Tables for Crystallography, Volume A, 4th Ed., 1995.
108. A. R. West, in "Solid State Chemistry and Its Applications", Chap. 5, Wiley, Chichester, 1984.
109. M. T. Weller, in "Inorganic Materials Chemistry", p. 6-8, Oxford Univeristy Press, Oxford, 1994.
110. W. L. Bragg, *Nature*, 1912, **90**, 410.
111. M. T. Dove, in "Structure and Dynamics An Atomic View of Materials", p. 16., Oxford University Press, Oxford, 2003.
112. M. T. Dove, in "Structure and Dynamics An Atomic View of Materials", p. 78-90., Oxford University Press, Oxford, 2003.
113. N. W. Ashcroft and N. D. Mermin, in "Solid State Physics", Thomson Learning Inc., Chap. 5, 1976.
114. U. Shmueli, in "Theories and Techniques of Crystal Structure Determination", p. 10, Oxford University Press, Oxford, 2007.
115. http://www.esrf.eu/AboutUs/AboutSynchrotron/XRays
116. U. Shmueli, in "Theories and Techniques of Crystal Structure Determination", Chap. 4, Oxford University Press, Oxford, 2007.
117. W. Clegg, in "Crystal Structure Determination", p. 25, Oxford University Press, Oxford, 1998.
118. P. Atkins and J. de Paula, in "Atkins Physical Chemistry", p. 700, Oxford University Press, Oxford, 2006.
119. http://www.diamond.ac.uk/Home/About/Synchrotrons/Machine.html
120. Synchrotron Soleil: Schéma de Principe Copyright © Chaix & Morel et Associés.

121. Diamond Light Source Ltd, Harwell Science and Innovation Campus, Didcot, Oxforshire, OX11 0DE, UK.
122. C. C. Tang, S. P. Thompson, T. P. Hill, G. R. Wilkin and U. H. Wagner, *Z. Kristallogr. Suppl.*, 2007, **26**, 153.
123. S. P. Thompson, J. E. Parker, J. Potter, T. P. Hill, A. Birt, T. M. Cobb, F. Yuan and C. C. Tang, *Review Sci. Instrum.*, 2009, **80**, 075107.
124. http://www.diamond.ac.uk/Home/Beamlines/I11.html
125. A. C. Larson and R. B. von Dreele, Los Alamos National Laboratory, Report No. LA-UR-86-748, 1987.
126. G. L. Squires, in "Introduction to the Theory of Thermal Neutron Scattering", Chap. 1, Dover Publications, New York, 1996.
127. The 11th Ocford School on Neutron Scattering, "Introduction to Neutron Scattering", September 2009.
128. http://www.ill.eu/instrumentssupport/instrumentsgroups/instruments/d2b/
129. ISIS Facility, Rutherford Appleton Laboratory, Chilton, Didcot, OX11 0QX, UK.
130. R. I. Smith, S. Hull and A. R. Armstrong, *Mater. Sci. Forum*, 1993, **166**, 251.
131. S. Hull, R. I. Smith, W. I. F. David, A. C. Hannon, J. Mayers and R. Cywinski, *Physica B*, 1992, **180**, 1000.
132. R. I. Smith and S. Hull, User Guide for the Polaris Powder Diffractometer at ISIS; Rutherford Appleton Laboratory Report: 1997.
133. http://www.isis.stfc.ac.uk/instruments/polaris/polaris4643.html
134. R. M. Ibberson, W. I. F. David and K. S. Knight The High Resolution Neutron Powder Diffractometer (HRPD) at ISIS - A User Guide Report RAL-92-031 (1992).
135. http://www.isis.stfc.ac.uk/instruments/hrpd/hrpd.html
136. R. A. Young, in "The Rietveld Method", Oxford University Press, Oxford, 1996.
137. H. M. Rietveld, *Acta Cryst.*, 1966, **20**, 508.
138. H. M. Rietveld, *J. Appl. Cryst.*, 1969, **2**, 65.
139. A. Albinati and B. T. M. Willis, *J. Appl. Cryst.*, 1982, **15**, 365.

140. Inorganic Crystal Structure Database, Fachinformationszentrum (FIZ): Karlsruhe, Germany, 2007.
141. F. Bloch, *Phys. Rev.*, 1946, **70**, 460.
142. A. Abragam, in "Principles of Nuclear Magnetism", p. 33, Oxford Science Publications
143. R. R. Ernst and W. A. Anderson, *Rev. Sci. Instr.*, 1966, **37**, 93.
144. A. E. Derome, in "Modern Techniques for Chemistry Research", p. 77, Pergamon Press, Oxford, 1991.
145. P. J. Hore, J. A. Jones and S. Wimperis, in "NMR: The Toolkit", Chap. 2 , Oxford University Press, Oxford, 2000.
146. P. J. Hore, in "Nuclear Magnetic Resonance", p. 9, Oxford University Press, Oxford, 1995.
147. C. P. Slichter, in "Principles of Magnetic Resonance", p. 157-165, Springer-Verlag, Berlin, 1990.
148. R. R. Ernst, G. Bodenhausen and A. Wokaun, in "Principles of Nuclear Magnetic Resonance in One and Two Dimensions", p. 44, Clarendon Press, Oxford, 1987.
149. P. J. Hore, in "Nuclear Magnetic Resonance", p. 9, Oxford University Press, Oxford, 1995.
150. A. Abragam, in "Principles of Nuclear Magnetism", p. 103, Oxford Science Publications, 1961.
151. R. R. Ernst, G. Bodenhausen and A. Wokaun, in "Principles of Nuclear Magnetic Resonance in One and Two Dimensions", p. 47, Clarendon Press, Oxford, 1987.
152. J. McManus, R. Kemp-Harper and S. Wimperis, *Chem. Phys. Lett.*, 1999, **311**, 292.
153. A. Abragam, in "Principles of Nuclear Magnetism", p. 104-105, Oxford Science Publications, 1961.
154. A. Abragam, in "Principles of Nuclear Magnetism", p. 480-495, Oxford Science Publications, 1961.
155. E. R. Andrew, A. Bradbury and R. G. Eades, *Nature*, 1958, **182**, 1659.
156. E. R. Andrew, A. Bradbury and R. G. Eades, *Nature*, 1959, **183**, 1802.
157. I. Lowe, *Phys. Rev. Lett.*, 1959, **22**, 133.

158. E. A. Andrew in "Encyclopedia of Nuclear Magnetic Resonance" (D. M. Grant and R. K. Harris, Eds.), p. 2891, Wiley, Chichester, 1996.
159. U. Haeberlen, in "High Resolution NMR in Solids: Selective Averaging", New York, 1976.
160. M. Mehring, A. Pines, W.-K. Rhim and J. S. Waugh, *J. Chem. Phys.*, 1971, **54**, 3239.
161. M. J. Duer, in "Introduction to Solid-State NMR Spectroscopy", p. 78-81, Blackwell Publishing, Oxford, 2004.
162. A. E. Bennett, C. M. Rienstra, M. Auger, K. V. Lakshmi and R. G. Griffin, *J. Chem. Phys.*, 1995, **103**, 6951.
163. A. J. Vega, in "Encyclopedia of Nuclear Magnetic Resonance" (D. M. Grant and R. K. Harris, Eds.), p. 3869, Wiley, Chichester, 1996.
164. A. Abragam, in "Principles of Nuclear Magnetism", p. 232, Oxford Science Publications, 1961.
165. P. W. Atkins, in "Molecular Quantum Mechanisms", Chap. 8, Oxford University Press, Oxford, 1983.
166. R. N. Zare, in "Angular Momentum", Chap. 5, Wiley, Chichester, 1996.
167. A. Samoson, E. Lippmaa and A. Pines, *Mol. Phys.*, 1988, **65**, 1013.
168. A. Samoson and E. Lippmaa, *J. Magn. Reson.*, 1989, **84**, 410.
169. K. T. Mueller, B. Q. Sun, G. C. Chingas, J. W. Zwanziger, T. Terao and A. Pines, *J. Magn. Reson.*, 1990, **86**, 470.
170. A. Llor and J. Virlet, *Chem. Phys. Lett.*, 1988, **152**, 248.
171. L. Frydman and J. S. Harwood, *J. Am. Chem. Soc.*, 1995, **117**, 5367.
172. A. Wokaun and R. R. Ernst, *J. Chem. Phys.*, 1977, **67**, 1752.
173. S. Vega and Y. Naor, *J. Chem. Phys.*, 1981, **75**, 75.
174. A. Medek, J. S. Harwood and L. Frydman, *J. Am. Chem. Soc.*, 1995, **117**, 12779.
175. G. Wu, D. Rovnyak, B. Sun and R. G. Griffin, *Chem. Phys. Lett.*, 1996, **249**, 210.
176. S. P. Brown, S. J. Heyes and S. Wimperis, *J. Magn. Reson. A*, 1996, **119**, 280.

177. J.-P. Amoureux, C. Fernandez and S. Steuernagel, *J. Magn. Reson.*, 1996, **123**, 116.
178. C. Fernandez and J.-P. Amoureux, *Solid State Nucl. Magn. Reson.*, 1996, **5**, 315.
179. P. J. Grandinetti, J. H. Baltisberger, J. Stebbins, U. Werner, M. A. Eastman and A. Pines, *Mol. Phys.*, 1994, **81**, 1109.
180. D. Massiot, B. Touzo, D. Trumeau, J. P. Coutures, J. Virlet, P. Florian and P. J. Grandinetti, *Solid State Nucl. Magn. Reson.*, 1996, **6**, 73.
181. S. P. Brown and S. Wimperis, *J. Magn. Reson.*, 1997, **124**, 279.
182. C. Fernandez and J.-P. Amoureux, *Chem. Phys. Lett.*, 1995, **242**, 449.
183. J.-P. Amoureux and C. Fernandez, *Solid State Nucl. Magn. Reson.*, 1998, **10**, 211.
184. S. H. Wang, Z. Xu, J. H. Baltisberger, L. M. Bull, J. F. Stebbins and A. Pines, *Solid State Nucl. Magn. Reson.*, 1997, **8**, 1.
185. K. J. Pike, R. P. Malde, S. E. Ashbrook, J. McManus and S. Wimperis, *Solid State Nucl. Magn. Reson.*, 2000, **16**, 203.
186. A. Goldbourt, P. K. Madhu and S. Vega, *Chem. Phys. Lett.*, 2000, **320**, 448.
187. P. K. Madhu, A. Goldbourt, L. Frydman and S. Vega, *Chem. Phys. Lett.*, 1999, **307**, 41.
188. P.K. Madhu, A. Goldbourt, L. Frydman and S. Vega, *J. Chem. Phys.*, 2000, **112**, 5.
189. Z. Gan and H. Kwak, *J. Magn. Reson.*, 2004, **168**, 346.
190. T. J. Ball and S. Wimperis, *J. Magn. Reson.*, 2007, **187**, 343.
191. N. Kim, C.-H. Hsieh and J. F. Stebbins, *Chem. Mater.*, 2006, **18**, 3855.
192. K. T. Mueller, Y. Wu, B. F. Chmelka, J. Stebbins and A. Pines, *J. Am. Chem. Soc.*, 1991, **113**, 32.
193. R. W. Broach, S. T. Wilson and R. M. Kirchner, *Proc. 12th Int. Zeolite Conf.*, 1999, **III**, 1715.
194. S. Antonijevic, S. E. Ashbrook, S. Biedasek, R. I. Walton, S. Wimperis and H. Yang, *J. Am. Chem. Soc.*, 2006, **128**, 8054.
195. S. E. Ashbrook, M. Cutajar, C. J. Pickard, R. I. Walton and S. Wimperis, *Phys. Chem. Chem. Phys.*, 2008, **10**, 5754.

196. M. D. Segall, P. J. D. Lindan, M. J. Probert, C. J. Pickard, P. J. Hasnip, S. J. Clark and M. C. Payne, *J. Phys.: Condens. Matter*, 2002, **1**, 2717.
197. V. Fock, *Z. Physik*, 1930, **61**, 126.
198. D. R. Hartree and W. Hartree, *Proc. Roy. Soc.*, 1935, **A150**, 9.
199. J. C. Slater, *Phys. Rev.*, 1930, **35**, 210.
200. J. C. Slater, *Phys. Rev.*, 1951, **81**, 385.
201. M. Born and R. Oppenheimer, *Annalen der Physik*, 1927, **389**, 457.
202. P. Hohenberg and W. Kohn, *Phys. Rev. B*, 1964, **136**, 864.
203. W. Kohn and L. J. Sham, *Phys. Rev. A*, 1965, **140**, 1133.
204. D. M. Ceperley and B. J. Alder, *Phys. Rev. Lett.*, 1980, **45**, 566.
205. J. Perdew and A. Zunger, *Phys. Rev. B*, 1981, **23**, 5048.
206. Y. M. Juan and E. Kaxiras, *Phys. Rev. B*, 1993, **48**, 14944.
207. J. P. Perdew, in "Electronic Structure of Solids '91", Akademie Verlag, Berlin, 1991.
208. J. P. Perdew, K. Burke and M. Ernzerhof, *Phys. Rev. Lett.*, 1996, **77**, 3865.
209. R. Car and M. Parrinello, *Phys. Rev. Lett.*, 1985, **55**, 2471.
210. M. L. Cohen and V. Heine, in "Solid State Physics", Vol. 24, p. 1, Academic Press, New York, 1970.
211. M. L. Cohen and V. Heine, in Solid State Physics, Vol. 24, p. 250, New York, 1970.
212. C. G. van de Walle and P. E. Blöchl, *Phys. Rev. B*, 1993, **47**, 4244.
213. C. J. Pickard and F. Mauri, *Phys. Rev. B*, 2001, **63**, 245101.
214. S. J. Clark, M. D. Segall, C. J. Pickard, P. J. Hasnip, M. I. J. Probert, K. Refson and M. C. Payne, *Z. Kristallogr.*, 2005, **220**, 567.
215. J. R. Yates, C. J. Pickard and F. Mauri, *Phys. Rev. B*, 2007, **76**, 024401.
216. M. Profeta, F. Mauri and C. J. Pickard, *J. Am. Chem. Soc.*, 2003, **125**, 541.
217. A. C. Sakowski-Cowley, K. Lukaszewicz and H. D. Megaw, *Acta Cryst.*, 1969, **B25**, 851.
218. R. P. Liferovich and R. H. Mitchell, *J. Solid State Chem.*, 2004, **177**, 2188.
219. D. Vanderbilt, *Phys. Rev. B*, 1990, **41**, 7892.

220. V. A. Shuvaeva and M. Yu. Antipin, *Crystallography Reports*, 1995, **40**, 466.
221. A. M. Glazer and H. D. Megaw, *Acta Cryst.*, 1973, **A29**, 489.
222. C. N. W. Darlington and K. S. Knight, *Physica B*, 1999, **266**, 368.
223. C. N. W. Darlington and K. S. Knight, *Acta Cryst.*, 1999, **B55**, 24.
224. S. K. Mishra, N. Choudhury, S. L. Chaplot, P. S. R. Krishna and R. Mittal, *Phys. Rev. B*, 2007, **76**, 024110.
225. D. R. Modeshia, R. J. Darton, S. E. Ashbrook and R. I. Walton, *Chem. Commun.*, 2009, 68.
226. Y. Shiratori, A. Magrez, J. Dornseiffer, F-H. Haegel, C. Pithan and R. Waser, *J. Phys. Chem. B*, 2005, **109**, 20122.
227. H. D. Megaw, *Proc. Phys. Soc.*, 1946, **58**, 133.
228. V. A. Shuvaeva, M. Yu. Antipin, S. V. Lindeman, O. E. Fesenko, V. G. Smotrakov and Yu. T. Struchkov, *Ferroelectrics*, 1993, **141**, 307.
229. Y. Shiratori, A. Magrez, W. Fischer, C. Pithan and R. Waser, *J. Phys. Chem. C*, 2007, **111**, 18493.
230. F. Wolf, D. Kline and H. S. Story, *J. Chem. Phys.*, 1970, **53**, 3538.
231. S. E. Ashbrook, L. Le Polles, R. Gautier, C. J. Pickard and R. I. Walton, *Phys. Chem. Chem. Phys.*, 2006, **8**, 3423.
232. R. K. Harris, S. A. Joyce, C. J. Pickard, S. Cadars and L. Emsley, *Phys. Chem. Chem. Phys.*, 2006, **8**, 137
233. J. M. Griffin, S. Wimperis, A. J. Berry, C. J. Pickard and S. E. Ashbrook, *J. Phys. Chem. C*, 2009, **113**, 465
234. S. E. Ashbrook, A. J. Berry, D. J. Frost, A. Gregorovic, C. J. Pickard, J. E. Readman and S. Wimperis, *J. Am. Chem. Soc.*, 2007, **129**, 13213
235. F. Pourpoint, C. Gervais, L. Bonhomme-Coury, T. Azais, C. Coelho, F. Mauri, B. Alonso, F. Babonneau and C. Bonhomme, *Appl. Magn. Reson.*, 2007, **32**, 435
236. L. A. O'Dell and R. W. Schurko, *Phys. Chem. Chem. Phys.*, 2009, **11**, 7069
237. R. P. Chapman and D. L. Bryce, *Phys. Chem. Chem. Phys.*, 2009, ***11***, 6987
238. P. J. Pallister, I. L. Moudrakovski and J. A. Ripmeester, *Phys. Chem. Chem. Phys.*, 2009, **11**, 11487

239. S. W. Reader, M. R. Mitchell, K. E. Johnston, C. J. Pickard, K. R. Whittle and S. E Ashbrook, *J. Phys. Chem. C*, 2009, **113**, 18874.
240. A. Castro, B. Jimenez and T. Hungria, *J. Eur. Ceram. Soc.*, 2004, **24**, 941.
241. L. Wu, J. Zhang, C. Wang and J. Li, *J. Appl. Phys.*, 2008, **103**, 084116.
242. R. Arendt and J. Rosolowski, US Patent 4234557, Molten salt synthesis of alkali niobate powders.
243. K. Tanaka, K. Kakimoto and H. Ohsato, *J. Eur. Ceram. Soc.*, 2007, **27**, 3591.
244. C. J. Pickard and R. J. Needs, *Phys. Rev. Lett.*, 2006, **97**, 045504.
245. C. J. Pickard and R. J. Needs, *Nature Phys.*, 2007, **3**, 473.
246. C. J. Pickard and R. J. Needs, *Phys. Rev. B*, 2007, **76**, 144114.
247. C. J. Pickard and R. J. Needs, *Nature Mater.*, 2008, **7**, 775.
248. E. A. Chizhova, A. I. Klyndyuk, L. A. Bashkirov, G. S. Petrov, L. V. Makhnach, *Neorganicheskie Materialy*, 2004, **40**, 1508.
249. Y. Shiratori, A. Magrez, K. Kasezawa, M. Kato, S. Rohrig, F. Peter, C. Pithan and R. Waser, *J. Electroceram.*, 2007, **19**, 273.
250. K. J. D. MacKenzie and M. E. Smith, in "Multinuclear Solid-State NMR of Inorganic Materials", p. 662-665, Pergamon Materials Series, 2002.
251. J. V. Hanna, K. J. Pike, T. Charpentier, T. F. Kemp, M. E. Smith, B. E. G. Lucier, R. W. Schurko and L. S. Cahill, *Chem. Eur. J.*, 2010, **16**, 3222.
252. M. Bak, J. Rasmussen and N. C. Nielsen, *J. Magn. Reson.*, 2000, **147**, 296.
253. N. Kim and C. P. Grey, *Science*, 2002, **297**, 1317.
254. K. J. D. MacKenzie and M. E. Smith, in "Multinuclear Solid-State NMR of Inorganic Materials", p. 333-390, Pergamon Materials Series, 2002.
255. T. J. Bastow and S. N. Stuart, *Chem. Phys.*, 1990, **143**, 459.
256. L. Jahnberg, *J. Solid State Chem.*, 1970, **1**, 454.
257. N. Zhang, A. M. Glazer, D. W. Baker and P. A. Thomas, *Acta Cryst.*, 2009, **B65**, 291.
258. C. J. Pickard and R. J. Needs, *Phys. Rev. Lett.*, 2009, **102**, 125702.

259. C. J. Pickard and R. J. Needs, *Phys. Rev. Lett.*, 2009, **102**, 146401.
260. C. J. Pickard and R. J. Needs, *J. Phys. Condens. Matter*, 2009, **21**, 452205.
261. A. J. Morris, C. J. Pickard and R. J. Needs, *Phys. Rev. B*, 2008, **78**, 184102.
262. A. J. Morris, C. J. Pickard and R. J. Needs, *Phys. Rev. B*, 2009, **80**, 144112.
263. A. M Glazer and H. D. Megaw, *Phil. Mag.*, 1972, **25**, 1119.
264. M. Athee, A. M. Glazer and H. D. Megaw, *Phil. Mag.*, 1972, **26**, 995.
265. C. N. W. Darlington and H. D. Megaw, *Acta Cryst.*, 1973, **B29**, 2171.
266. H. D. Megaw, *Ferroelectrics*, 1974, **7**, 87.
267. M. Athee and A. M. Glazer, *Acta Cryst.*, 1976, **A32**, 434.
268. M. Athee and A. W. Hewat, *Acta Cryst.*, 1975, **A31**, 846.
269. M. Athee and A. W. Hewat, *Acta Cryst.*, 1978, **A34**, 309.
270. V. J. Tennery and K. W. Kang, *J. Appl. Phys.*, 1968, **39**, 4749.
271. L. Egerton and D. M. Dillon, *J. Am. Ceram. Soc.*, 1959, **42**, 438.
272. R. E. Jaeger and L. Egerton, *J. Am. Ceram. Soc.*, 1962, **45**, 209.
273. Y. Guo, K. Kakimoto and H. Ohsato, *Mater. Lett.*, 2004, **59**, 241.
274. H. Birol, D. Damjanovic and N. Setter, *J. Eur. Ceram. Soc.*, 2006, **26**, 861.
275. T. R. Shrout and S. J. Zhang, *J. Electroceram.*, 2007, **19**, 111.
276. S. Zhang, R. Xia, H. Hao, H. Liu and T. R. Shrout, *Appl. Phys. Lett.*, 2008, **92**, 1-152904/3.
277. D. W. Baker, P. A. Thomas, N. Zhang and A. M. Glazer, *Acta Cryst.*, 2009, **B65**, 22.
278. N. N. Krainik, *Izv. Akad. Nauk SSSR*, Ser. Fiz, 1958, **22**, 1492.
279. T. Nitta, *J. Am. Ceram. Soc.*, 1968, **51**, 626.
280. R. van der Mühll, A. Sadel, J. Ravez and P. Hagenmuller, *Solid State Commun.*, 1979, **31**, 151.
281. Y. D. Juang, S. B. Dau, Y. C. Wang, W. Y. Chou, J. S. Hwang, M. L. Hu and W. S. Tse, *Solid State Commun.*, 1999, **111**, 723.
282. L. A. Reznitchenko, L. A. Shilkina, O. N. Razumovskaya and S. I. Dudkina, *Inorg. Mater. (Transl. Neorg. Mater.)*, 2003, **39**, 139.

283. Yu. I. Yuzyuk, E. Gararina, P. Simon, L. A. Reznitchenko, L. Hennet and D. Thiaudière, *Phys. Rev. B*, 2004, **69**, 144105.
284. D. Mori, J-P. Colin, G. Le Roux, L. Pateau and J-C. Toledano, *Mater. Res. Bull.*, 1973, **8**, 1089.
285. A. Torres-Pardo, R. Jiménez, J. M. González-Calbet and E. Garía-González, *Chem. Mater.*, 2008, **20**, 6957.
286. S. C. Abrahams, H. J. Levinstein and J. M. Reddy, *J. Phys. Chem. Solids*, 1966, **27**, 1019.
287. A. Torres-Pardo, R. Jiménez, J. M. González-Calbet and E. Garía-González, *Chem. Mater.*, 2009, **21**, 2193.
288. K. Ishida and G. Honjo, *J. Phys. Soc. Jpn.*, 1972, **34**, 1279.
289. M. L. Keith and R. Roy, *Am. Mineral.*, 1954, **39**, 1.
290. S. Geller and E. A Wood, *Acta Cryst.*, 1956, **9**, 563.
291. S. Geller and V. B. Bala, *Acta Cryst.*, 1956, **9**, 1019.
292. S. Geller, *J. Chem. Phys.*, 1956, **24**, 1236.
293. M. A. Gilleo, *Acta Cryst.*, 1957, **10**, 161.
294. S. Geller, *Acta Cryst.*, 1957, **10**, 243.
295. S. J. Schneider, R. S. Roth and J. L. Waring, *J. Res. Nat. Bur. Stand. A*, 1961, **65**, 345.
296. M. Marezio, J. P. Remeika and P. D. Dernier, *Acta Cryst.*, 1970, **B26**, 2008.
297. J. Pérez-Cacho, J. Blasco, J. García and R. Sanchez, *J. Solid State Chem.*, 2000, **150**, 145.
298. J. B. Clark, P. W. Richter and L. Du Toit, *J. Solid State Chem.*, 1978, **23**, 129.
299. N. V. Porotnikov, K. I. Petrov, V. N. Tsygankov and M. E. Bogdanova, *Inorg. Mater. (Transl. of Neorg. Mater.)*, 1980, **16**, 62.
300. C. P. Sebastian, L. Zhang, C. Fehse, R-D. Hoffmann, H. Eckert and R. Pöttgen, *Inorg. Chem.*, 2007, **46**, 771.
301. D. Mohr, A. S. S. de Camargo, C. C. de Araujo and H. Eckert, *J. Mater. Chem.*, 2007, **17**, 3733.
302. A. Y. H. Lo, V. Sudarsan, S. Sivakumar, F. van Veggel and R. W. Schurko, *J. Am. Chem. Soc.*, 2007, **129**, 4687.

303. C. Vinod Chandran, J. Cuny, R. Gautier, L. Le Pollès, C. J. Pickard and T. Bräuniger, *J. Magn. Reson.*, 2010, **203**, 226.
304. A. P. M. Kentgens, *Geoderma*, 1997, **80**, 271.
305. M. E. Smith and E. R. H. van Eck, *Prog. NMR Spectrosc.*, 1999, **34**, 159.
306. A. R. Thompson and E. Oldfield, *J. Chem. Soc., Chem. Commun.*, 1987, **1**, 27.
307. J. A. Davies and S. Dutremez, *Coord. Chem. Rev.*, 1992, **114**, 201.
308. S. E. Ashbrook and S. Wimperis, *J. Magn. Reson.*, 2002, **156**, 269.
309. C. Tien, E. V. Charnaya, S. Y. Sun, R. R. Wu, S. N. Ivanov and E. N. Khazanov, *Phys. Stat. Sol.*, 2002, **233B**, 222.
310. D. Riou, F. Fayon and D. Massiot, *Chem. Mater.*, 2002, **14**, 2416.
311. T. J. Bastow and S. Celotto, *Mater. Sci. Eng.*, 2003, **C23**, 757.
312. C. M. Morais, M. Lopes, C. Fernandez and J. Rocha, *Magn. Reson. Chem.*, 2003, **41**, 679.
313. T. J. Bastow, T. Mathews and J. R. Sellar, *Solid State Ionics*, 2004, **175**, 415.
314. T. Brauniger, K. Ramaswamy and P. K. Madhu, *Chem. Phys. Lett.*, 2004, **383**, 403.
315. V. V. Laguta, M. D. Glinchuk, I. P. Bykov, R. Blinc and B. Zalar, *Phys. Rev.*, 2004, **B69**, 54103/1.
316. H. S. Park, I. Bull, L. M. Peng, G. Y. J. Victor, C. P. Grey and J. B. Parise, *Chem. Mater.*, 2004, **16**, 5350.
317. A. J. Rossini and R. W. Schurko, *J. Am. Chem. Soc.*, 2006, **128**, 10391.
318. S. E. Ashbrook and S. Wimperis, *Prog. Nucl. Magn. Reson. Spectrosc.*, 2004, **45**, 53.
319. M. J. Martínez-Lope, J. A. Alonso, M. Retuerto and M. T. Fernández-Díaz, *Inorg. Chem.*, 2008, **47**, 2634.
320. J. A. Alonso, M. J. Martínez-Lope, M. T. Casais and M. T. Fernández-Díaz, *Inorg. Chem.*, 2000, **39**, 917.
321. A. I. Becerro, A. Escudero, P. Florian, D. Massiot and M. D. Alba, *J. Solid State Chem.*, 2004, **177**, 2783.
322. R. Dupree and M. E. Smith, *Chem. Phys. Lett.*, 1988, **148**, 41.